

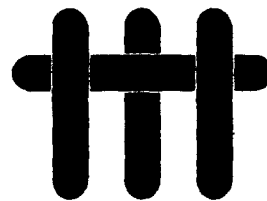
①

ANNUAL REPORT  
University Research Initiative

Contract No.: N00014-92-J-1808

March 1993 - April 1994

AD-A279 739

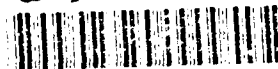


The Processing and Mechanical  
Properties of High Temperature/  
High Performance Composites

by

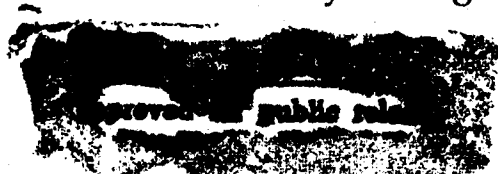
A.G. Evans & F. Leckie  
University of California,  
Santa Barbara

94-15994



University of Pennsylvania  
Harvard University  
Washington State University  
Carnegie Mellon University  
University of Virginia

DTIC  
ELECTE  
MAY 27 1994  
S G D



Book 4 of 7:

Processing/Property Correlations

DTIC QUALITY INSPECTED 1

94 5 26 148

**SUMMARY**  
**OF**  
**TABLE OF CONTENTS**

Accession For	
NTIS CRA&I	<input checked="" type="checkbox"/>
DTIC TAB	<input type="checkbox"/>
Unannounced	<input type="checkbox"/>
Justification <i>PC-A266398</i>	
By .....	
Distribution /	
Availability Codes	
Dist	Avail and/or Special
<i>A-1</i>	

**EXECUTIVE SUMMARY**

**BOOK 1: MECHANISM-BASED CONSTITUTIVE LAWS AND DESIGN**

**BOOK 2: STRESS REDISTRIBUTION AND NOTCH PROPERTIES**

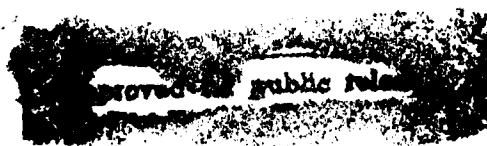
**BOOK 3: FATIGUE AND CREEP**

**BOOK 4: PROCESSING/PROPERTY CORRELATIONS**

**BOOK 5: INTERFACE EFFECTS**

**BOOK 6: DELAMINATION AND COMPRESSIVE BEHAVIOR**

**BOOK 7: *IN-SITU* MEASUREMENTS OF STRESS AND DAMAGE**





## BOOK 4

### PROCESSING/PROPERTY CORRELATIONS

- |  |  |
|--|--|
| 46. A Fiber Fracture Model for Metal Matrix Composite Monotape Consolidation   | D. M. Elzey<br>H. N. G. Wadley   |
| 47. Effects of Composite Processing on the Strength of Sapphire Fiber-Reinforced Composites                                    | J. B. Davis<br>J. Yang<br>A. G. Evans  |
| 48. On the Flexural Properties of Brittle Multilayer Materials: I. Modeling  | C. A. Folsom<br>F. W. Zok<br>F. F. Lange   |
| 49. On the Flexural Properties of Brittle Multilayer Materials: II. Experiments  | C. A. Folsom<br>F. W. Zok<br>F. F. Lange   |
| 50. The Microstructure of SiC/C Composites and Relationships with Mechanical Properties  | X. Bourrat<br>K. S. Turner<br>A. G. Evans  |
| 51. Microstructural Observations on Constrained Densification of Alumina Powder Containing a Periodic Array of Sapphire Fibers | D. C. C. Lam<br>F. F. Lange  |
| 52. Material Issues in Layered Forming   | C. Amon<br>J. Beuth<br>H. Kirchner<br>R. Merz<br>F. Prinz<br>K. Schmaltz<br>L. Weiss |
| 53. Thermal Modelling and Experimental Testing of MD* Spray Shape Deposition Processes   | C. H. Amon<br>R. Merz<br>F. B. Prinz<br>K. S. Schmaltz                               |



- |   |  |
|---|--|
| 54. Liquid Precursor Infiltration and Pyrolysis of Powder Compacts, I: Kinetic Studies and Microstructure Development | W. C. Tu<br>F. F. Lange  |
| 55. Liquid Precursor Infiltration and Pyrolysis of Powder Compacts: II, Fracture Toughness and Strength               | W. C. Tu<br>F. F. Lange  |
| 56. Influence of Interparticle Forces on the Rheological Behavior of Pressure-Consolidated Alumina Particle Slurries  | B. V. Velamakanni<br>F. F. Lange<br>F. W. Zok<br>D. S. Pearson |
| 57. Evolution of a Metastable FCC Solid Solution during Sputter Deposition of Ti-Al-B Alloys                          | J. P. A. Löfvander<br>U. Ruschewitz<br>C. G. Levi              |
| 58. Novel ODS Copper Alloys from Rapidly-Solidified Precursors—I: Microstructural Development                         | M. S. Nagorka<br>C. G. Levi<br>G. E. Lucas                     |
| 59. Novel ODS Copper Alloys from Rapidly-Solidified Precursors—II: Creep Behavior                                     | M. S. Nagorka<br>G. E. Lucas<br>C. G. Levi                     |
| 60. Mechanical Properties of Partially Dense Alumina Produced from Powder Compacts                                    | D. C. C. Lam<br>F. F. Lange<br>A. G. Evans                     |

## **EXECUTIVE SUMMARY**

The general emphasis for 1994 would be on increased software development, testing of subelements and design calculations. For these purposes, the constitutive law coding and development would be coordinated by Nick Aravas, and implemented in ABAQUS. The initial implementation would be the elastic/plastic model for MMCs with interface debonding developed in 1993 (Leckie). This would be extended in 1994 to include creep and some aspects of thermomechanical cycling. The code would be used for design calculations concerned with MMC rotors, actuators and vanes (Leckie). A plan is being formulated to collaborate with Pratt and Whitney to acquire MMC sub-elements representative of these components during 1994. Experimental tests on these subelements would be capable of providing a direct validation of the code capabilities.

Constitutive law and fatigue life software would be created for CMCs using continuum damage mechanics (CDM) approaches (Leckie, McMeeking). The approach has been motivated by micromechanics models developed in 1993 (Hutchinson, Zok, Evans). These codes would be used to calculate stress redistribution effects and fatigue life on simple subelements, such as center notched and pin-loaded plates. Comparison with experimental measurements needed to test the fidelity of the models will be based on moiré interferometry and thermoelastic emission. This effort is coordinated with the NASA EPM program through both General Electric and Pratt and Whitney. A plan for acquiring sub-elements from DuPont Lanxide is being formulated.

A new emphasis for 1994 would be on the transverse properties of CMCs. The measurements and calculations performed in 1993 have indicated a strategy for curved sections and junctions that would establish a consistent design approach. The basic approach for resisting failures from combinations of interlaminar shear and transverse tension involves the use of stitching and angle ply weaving patterns that inhibit major reductions in stiffness when matrix cracks are induced by transverse loads and bending moments. For this purpose, calculations would be performed that combine

the mechanics of delamination cracks with models of bridging by inclined fiber bundles (Hutchinson, Ashby, Evans, McMeeking). The insight gained from these calculations would be used to design and acquire sub-elements, such as C sections and T junctions.

Additional software development will be for creep and creep rupture (McMeeking). The models devised in 1993 and test data relevant to MMCs will be combined into a code that predicts the creep and rupture of unidirectional MMCs subject to multiaxial loads. Some aspects of this code will also be applicable to CMCs.

Two new activities will be introduced in 1994: thermal properties and damping. The thermal properties will be studied on both CMCs and MMCs (Ashby, Hutchinson). Measurements of thermal diffusivity will be made by the laser flash method and related to the properties of the interface and the density of matrix damage in the material. Thermal expansion measurements will also be performed with emphasis on determining hysteresis effects, which can be related to the temperature dependence of the interfaces properties, through cell models. The latter might evolve into a diagnostic for establishing relationships between the interface properties and thermomechanical fatigue.

The processing activities in the program will have newly established goals in 1994. The principal emphasis will be on concepts for affordable manufacturing. The issues selected for investigation will be consistent with manufacturing processes that allow near-net shape consolidation while still yielding reasonable combinations of longitudinal and transverse properties. Performance models developed in the program would be used as an initial test of concept viability.

Beyond these general trends, specific activities are planned for 1994. These are elaborated below. The status of understanding and development in each of these areas is summarized in Table I. Increasing magnitudes between 0 and 1 designate a knowledge range from limited to comprehensive.

**TABLE 1A****Status of Design Knowledge for MMCs**

	[0°] <sub>n</sub> MMC				[0°/90°] <sub>n</sub>	
	LONG.		TRANS.			
	P	S	P	S	P	S
<b>Tensile Strength</b>	3/4	1	1	1/2	1/4	~ 0
<b>Creep and Creep Rupture</b>	3/4	0	1	0	0	0
<b>Cyclic Flow (Isothermal, TMF)</b>	1/4	0	1	1/2	0	0
<b>Crack Growth (Isothermal Fatigue)</b>	1	1	0	1/2	0	0
<b>Crack Growth (TMF)</b>	1/2	1/2	0	0	0	0
<b>Compressive Strength</b>	3/4	0	0	0	0	0

**TABLE 1B****Status of Design Knowledge for CMCs**

	<b>[0/90]</b>		<b>[45/45]</b>	
	<b>P</b>	<b>S</b>	<b>P</b>	<b>S</b>
<b>Stress/Strain</b>	3/4	1/4	1/2	0
<b>Fatigue</b>	3/4	0	0	0
<b>TMF</b>	1/4	0	0	0
<b>Creep and Rupture</b>	1/2	0	0	0
<b>Compression Strength</b>	3/4	1/4	0	0
<b>Transverse Properties</b>	3/4	1/2	—	—
<b>Thermal Properties</b>	1/4	0	—	—

**P**      **Primary Structure**

**S**      **Secondary Structure**

## 2. CONSTITUTIVE LAWS

Two approaches will be used to create a formulation capable of representing the in-plane properties of CMCs. One would be based on Continuum Damage Mechanics (CDM) (Leckie). The other would use concepts analogous to those used in plasticity theory (Hutchinson). The CDM approach uses damage parameters that relate explicitly to micromechanics models. A potential function has already been identified as the state variable which separately represents the strain from the elastic compliance change caused by the matrix cracks and the inelastic strains associated with the debonding and sliding interfaces. Derivatives of the potential with regard to strain and damage give the relationships between variables, such as stress, interface sliding resistance, matrix crack density, etc.

The first version of the CDM model would use the minimum number of damage variables potentially capable of representing the behavior of laminated or woven composites. Cross terms between the damage variables would not be considered at this stage. Moreover, matrix cracks would be introduced normal to the maximum principal tensile stress, consistent with the experimental observations.

The plasticity theory approach would seek a formulation based on matrix cracks occurring normal to the maximum principal tension. It would introduce parameters that reflect the inelastic strain caused by interface sliding upon off-axis loading which would be calibrated from tests performed in tension in 0/90 and 45/45 orientations.

The insight needed to characterize off-axis loading effects will be gained from cell models (Hutchinson) in a manner analogous to that previously used for axial loads. The principal objective will be to understand trends in matrix crack opening and interface debonding/sliding with applied loads. The stress on the fibers will be calculated with the intent of predicting effects of loading orientation on fiber failure. The models will be compared with measurements made in 45/45 tension, using various CMCs (Evans).

Calibration of the damage parameters for each material would be made from hysteresis loop measurements in accordance with procedures developed in 1993. Experimental results obtained in 0/90 tension, 45/45

tension and in-plane shear will be used. In future work, it is hoped that shear tests will not be necessary.

The validation of the constitutive laws will be achieved by comparing calculations with measurements made on sub-elements, especially pin-loaded holes (Evans). The experimental results include residual strains obtained by Moiré interferometry (Fig. 2.1), ultimate loads for either tensile or shear failure and principal strain trajectories delineated by matrix cracking patterns. Acoustic methods will also be developed to probe the local values of the elastic modulus (Clarke, Wadley) which could be compared directly with the CDM predictions.

### **3. FATIGUE LIFING**

#### **3.1 CMCs**

A software program for isothermal low cycle fatigue (LCF) of CMCs, developed in 1993 (Fig. 3.1) will be extended in 1994. The present program asserts that fatigue is associated with cyclic degradation of the interface sliding resistance,  $\tau$ , which can be characterized by analyzing hysteresis loops measured periodically during a fatigue test. With this methodology, S-N curves have been predicted for both unidirectional and woven 0/90 composites tested in cyclic tension as well as changes in compliance and permanent strain. Some additional effort is required to analyze data on 0/90 laminates in order to validate the model predictions. The extensions envisaged for 1994 include thermomechanical fatigue (TMF), strain controlled LCF and off-axis fatigue (Zok, Evans). Experiments are planned which would assess the effects of temperature cycling and of inclined fibers on  $\tau$  degradation, measured from hysteresis loops. Various cell model calculations (Hutchinson) will be used to interpret the experiments. The results will be used to establish general *rules* for interface degradation in CMCs.

The off-axis experiments will also give insight into the fiber failure criterion that replaces the global load sharing (GLS) results successfully used for 0/90 loadings. This study will coordinate with the cell calculations described above, and the 45/45 tensile experiments.

Notch fatigue studies will be initiated. These will examine cyclic stress redistribution and notch sensitivity (Evans).

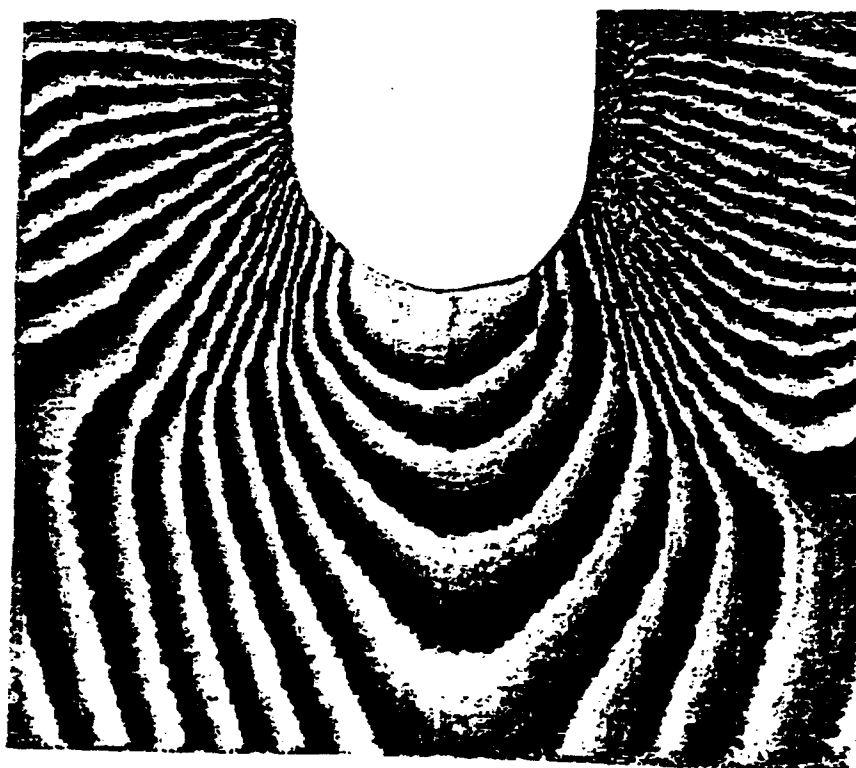
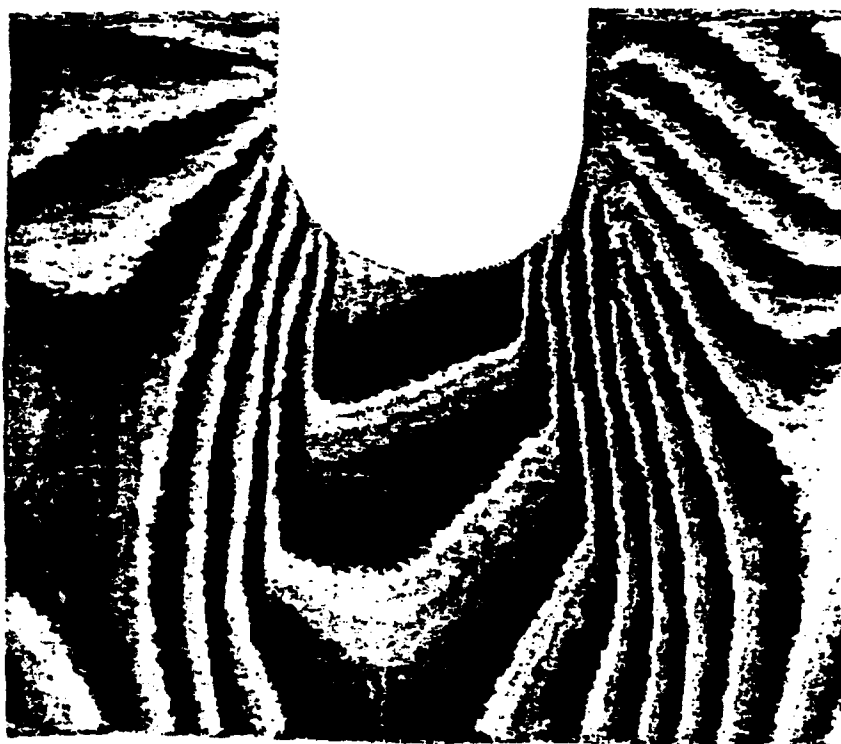


Figure 2.1



# Fatigue Methodology

## CMC Life Program

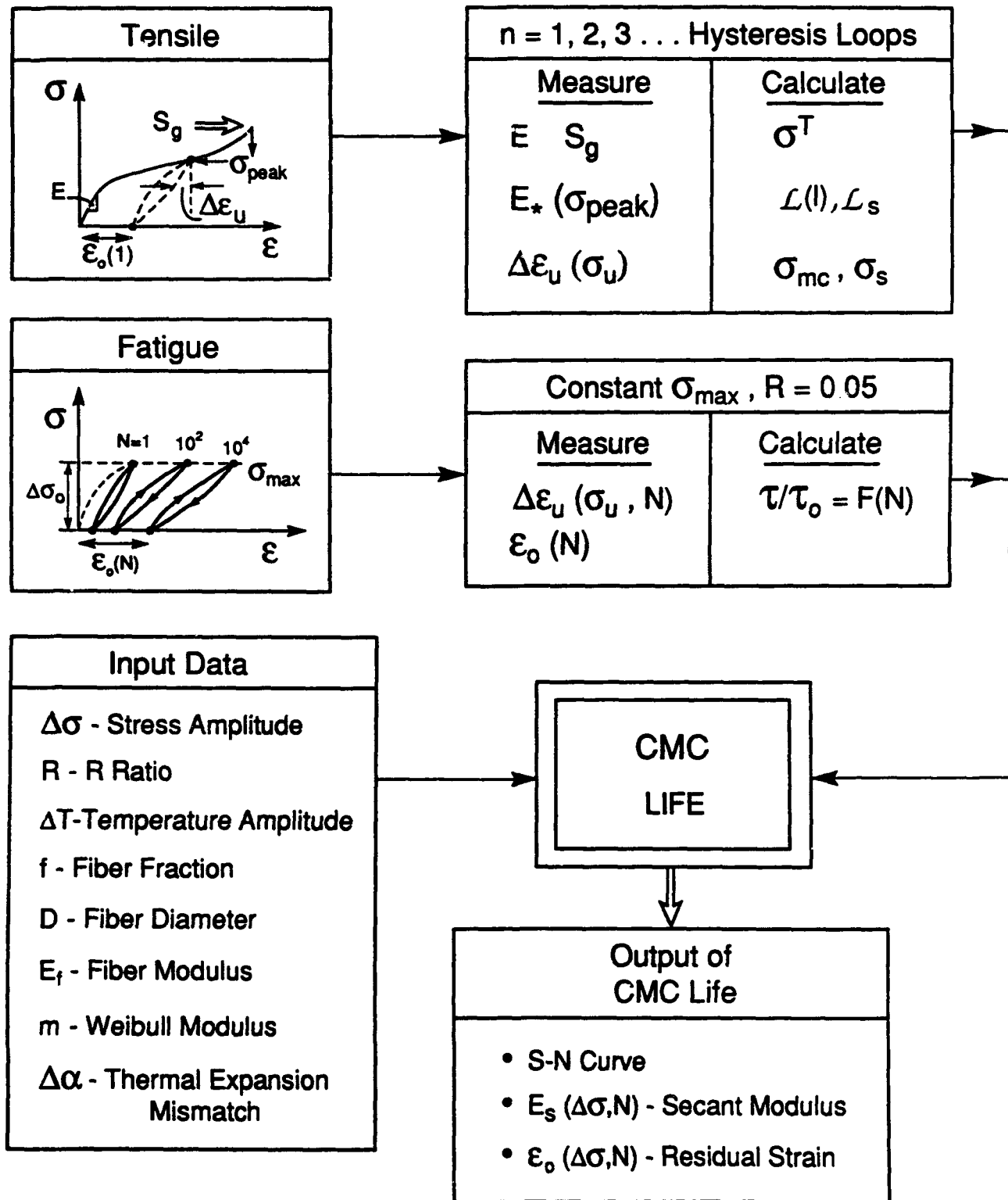


Figure 3.1

### **3.2 MMCs**

Fatigue crack growth and notch strength studies in MMCs will be extended to 0/90 laminates (Zok, Suo). The experiments concerned with crack growth will be interpreted using crack bridging models. The utility of such models has been validated in previous years through studies on unidirectional MMCs. It is envisaged that the fatigue crack growth characteristics of the unidirectional and 0/90 configurations will be related through the volume fraction of fibers aligned with the loading direction. The notch strength behavior will also be interpreted using crack bridging models. Such models have been developed in 1993 and found to be useful in rationalizing the behavior of unidirectional materials (Zok, Suo). In all cases, the mechanical measurements will be augmented by *in-situ* observations to identify changes in damage mechanisms with temperature, fiber architecture, etc. Plans to study the influence of panel thickness on fatigue and fracture resistance are also being developed, as well as tests to understand the potential for crack growth in mixed mode loadings (Hirth, Zok).

Studies of the TMF response of MMCs loaded parallel to the fiber axis will be initiated (Zok, Leckie). Experiments will evaluate both in-phase and out-of-phase loadings. Models of load shedding (matrix-fibers) will be used to interpret the hysteresis loops and to develop fatigue life models applicable to low cycle, high strain TMF.

## **4. CREEP AND RUPTURE**

### **4.1 MMCs**

The considerable progress made in 1993 towards identifying and understanding the mechanisms of creep and rupture in unidirectional MMCs containing non-creeping fibers (McMeeking, Zok) will be used to develop creep rupture software. The longitudinal creep model to be used incorporates stochastic fiber fracture and interface sliding in a format amenable to the prediction of primary and tertiary creep in terms of matrix creep strength, interface sliding resistance, fiber strength, Weibull modulus, etc. The concepts would be visualized in a rupture mechanisms map

(Fig. 4.1). The transverse creep behavior would include interface debonding, which greatly accelerates the creep, leading to marked anisotropy. A constitutive law for creep that includes these effects will be developed (Aravas, McMeeking).

Additional experiments and calculations will be conducted to assess the effects of notches and holes on creep rupture (Zok, Suo). Experience with MMCs at ambient temperature indicates that the notch sensitivity is largely dictated by matrix properties (i.e., strength and ductility). The reduction in matrix properties at elevated temperatures may lead to a substantial elevation in notch sensitivity. However, this behavior may be complicated by the development of alternate damage processes, such as shear bands.

#### **4.2 CMCs**

Studies of the creep and rupture of CMCs will continue with emphasis on materials containing creeping fibers. A particular emphasis will be on matrix cracking that arises as fiber creep relaxes fiber bridging tractions (McMeeking, Evans). The experimental studies will be performed on SiC/SiC composites. Hysteresis loop measurements will be used to monitor matrix damage during composite creep, using procedures devised in 1993. Models will be developed based on time dependent fiber bridging concepts (McMeeking, Cox).

It is envisioned that the lifetime of some CMCs will be dictated by time-dependent rupture of the fibers. A lifetime prediction tool for such a composite *must* incorporate the knowledge of fiber strength degradation over time. A new activity will be initiated to address this problem (Suo, Evans). The initial work will involve a survey of data in the existing literature, and a comparison with available models. A new model is being developed for single crystal fibers. This model involves a residual pore inside a fiber which changes shape, under stress, via surface diffusion, to become a crack. These issues will be viewed in the broad context of fiber and composite manufacture.

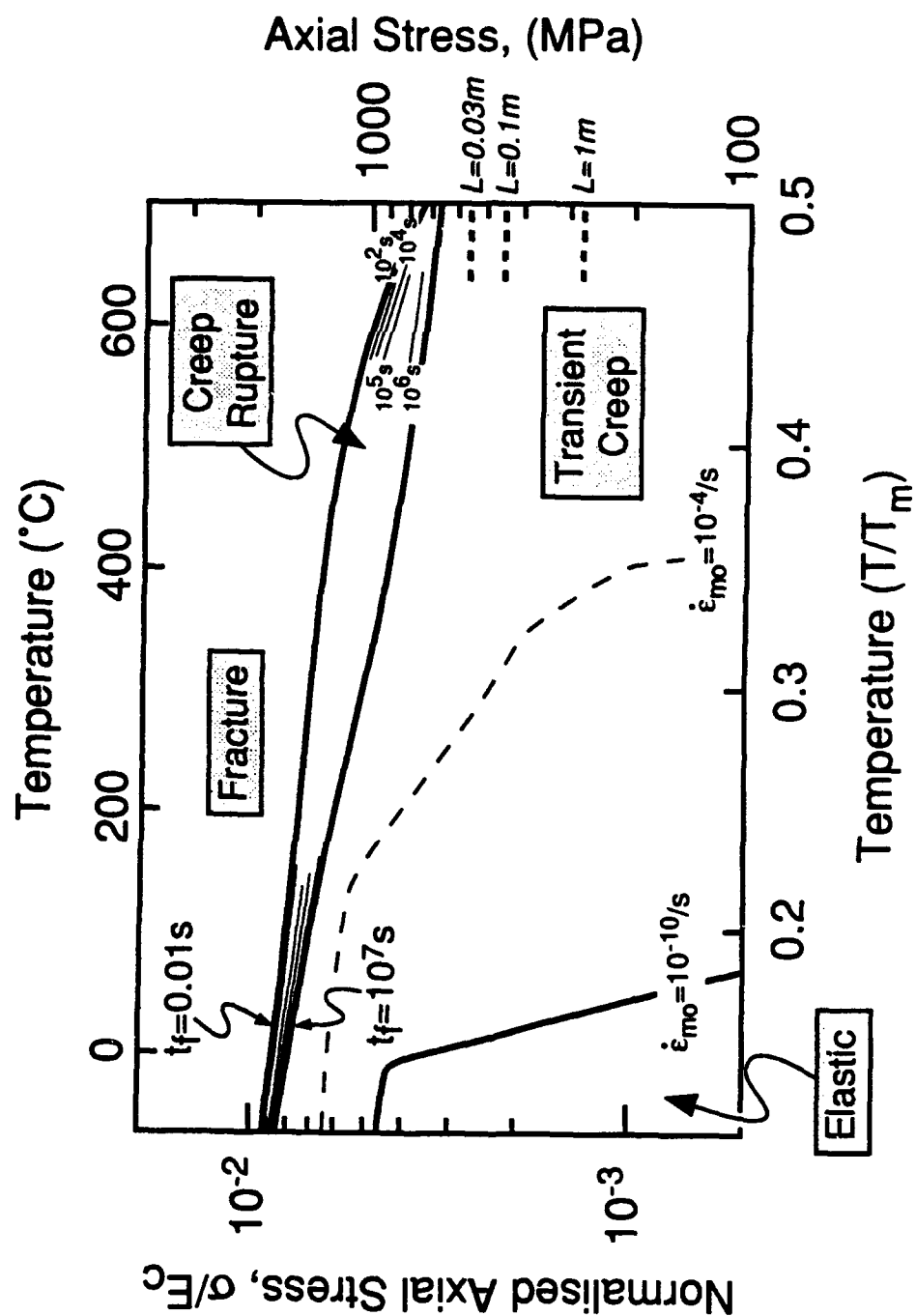


Figure 4.1

## 5. TRANSVERSE PERFORMANCE OF CMCs

Analyses and tests performed in 1993 (Ashby, Hutchinson, Bao) have highlighted the essential issues related to components that experience combinations of transverse tension and interlaminar shear. In both loadings, matrix cracks form at manufacturing flaws at low stresses, of order 10-100 MPa. These cracks extend across the plies and interact minimally with the fibers. Although the crack configurations differ for transverse tension and interlaminar shear loadings, multiple cracks always form. This multiplicity of cracking causes a major reduction in stiffness, which can cause unacceptably large displacements and also redistribute stress into other areas. The formation of the matrix cracks is probabilistic in nature and governed by the size distribution of manufacturing flaws. Design based on the prevention of such transverse cracks must rely on weakest link statistics, usually with a low Weibull modulus. Alternatively, it may be assumed that cracks *inevitably* form and, instead, reliance is placed on *controlling* the diminished modulus of the material, after matrix cracking has occurred. This approach relies on having 3-D architectures, with transverse fibers introduced locally either by stitching or by using angle plies. To explore this possibility, calculations will be performed (Hutchinson, Evans) to examine fiber architectures that lead to minimum stiffness loss, subject to acceptable in-plane properties. Based on these calculations, sub-elements will be designed that test out the concepts.

## 6. COMPRESSIVE BEHAVIOR

The studies completed in 1993 on the compressive failure of polymer matrix composites by the growth of kink bands (Budiansky, Fleck) will be extended to metal matrix composites, through a coordination with 3M. Compressive failure of Al and Ti MMCs with small diameter fibers has been observed by 3M to occur in accordance with the same kink band mechanism known to operate in PMCs and in C/C composites. The theory should thus extend to the MMCs, with the fiber misalignment, the shear yield strength of the matrix and its work hardening coefficient as the principal variables. A comparison between the theory and experimental

results would provide the basis for specifying the compressive properties of MMCs.

Compression failure of CMCs occurs by different mechanisms (Ashby). The dominant failure modes are similar to those that operate in porous brittle solids such as monolithic ceramics, concrete and rocks. The theory is well established and validated for these materials. Applications of the theory to various CMCs will be made and applied to the understanding of a behavior of pin-loaded holes (Evans, Ashby).

## **7. THERMAL PROPERTIES**

A new focus on the thermal properties of CMCs and MMCs will be initiated in 1994. Calculations of the effects of matrix cracks in the thermal expansion of CMCs will be made (Hutchinson). These will be compared with data obtained from TMF testing (Zok). The effects of such cracks on the in-plane thermal conductivity will also be calculated (Hutchinson). Measurements will be performed using the laser flash method (Ashby).

Thermal conductivity measurements will be initiated on Ti MMCs (Ashby). These will be used to understand the effects of the fiber/matrix interphases and of matrix damage on the transverse and in-plane thermal conduction.

## **8. MATERIALS SELECTION**

The Cambridge Materials Selector software will be expanded in 1994 to include high temperature creep design with the corresponding data base (Ashby). This expanded version will permit estimates to be made of temperature limits for MMCs based on creep controlled TMF and on the transverse creep of components with unidirectional reinforcements.

## **9. DESIGN CALCULATIONS AND SUB-ELEMENT TESTS**

A larger fraction of the effort in 1994 will be on design and sub-element testing, particularly for MMCs. Discussions are now in progress with Pratt and Whitney, Textron and 3M to perform design calculations using the

constitutive equations developed at UCSB and to produce sub-elements for testing.

The design emphasis for MMCs will be on various diffusion bonded joints with Ti matrices and monolithic Ti attachments. Two specific subelements are envisaged. The first involves unidirectionally reinforced rods (or plates), clad with monolithic metal. The purpose of the cladding is to prevent exposure of the fibers to the environment and to mechanical abrasion. The design of clad MMC structures requires consideration of (i) the residual stresses resulting from thermal mismatch between the cladding and the composites section, (ii) the potential for fatigue cracks to initiate and grow through the monolithic material, and (iii) the interaction of such cracks with the composite section and their influence on the strength and life of the structure. The design and testing of such subelements (Zok, Leckie) will be augmented by calculations of crack growth and fracture, incorporating the effects of thermal and elastic mismatch between the cladding and the composite (McMeeking). The clad structures will also be used to initiate studies on the reinforcement of holes in composite sections with monolithic metal patches, as drawn in Fig. 9.1 (Zok, Suo). The second subelement involves the attachment of a MMC actuator rod to a pin-loaded monolithic section (Fig. 9.2). The critical design issues relate to the strength and fatigue resistance of the interfaces between the composite and monolithic matrices. Design studies shall also be completed on rotor rings with special efforts made to produce rule-based design procedures which would be used by industry at the conceptual level of design to determine sizes and the efficient disposition of material.

For CMCs, the sub-element studies would be based on the calculations described above in Section 5. These would include C sections and T junctions (Fig. 9.3) Negotiations for manufacturing these sub-elements will be initiated and tests performed at UCSB.

## **10. AFFORDABLE MANUFACTURING**

As our understanding of composite mechanics and its interplay with design and performance has evolved, it has become increasingly evident that *cost* and *reproducibility*, are major constraints. Even as processing

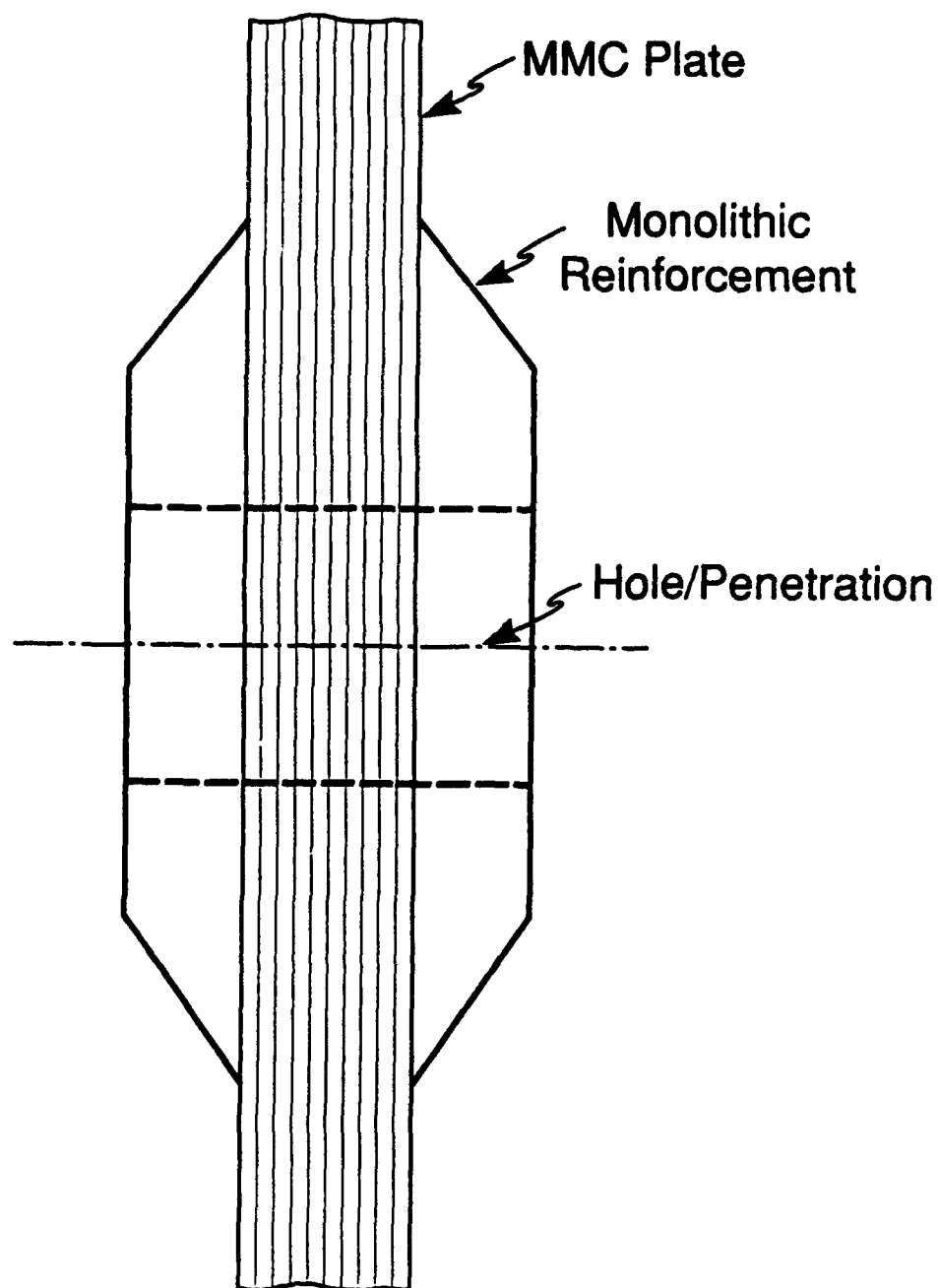


Figure 9.1



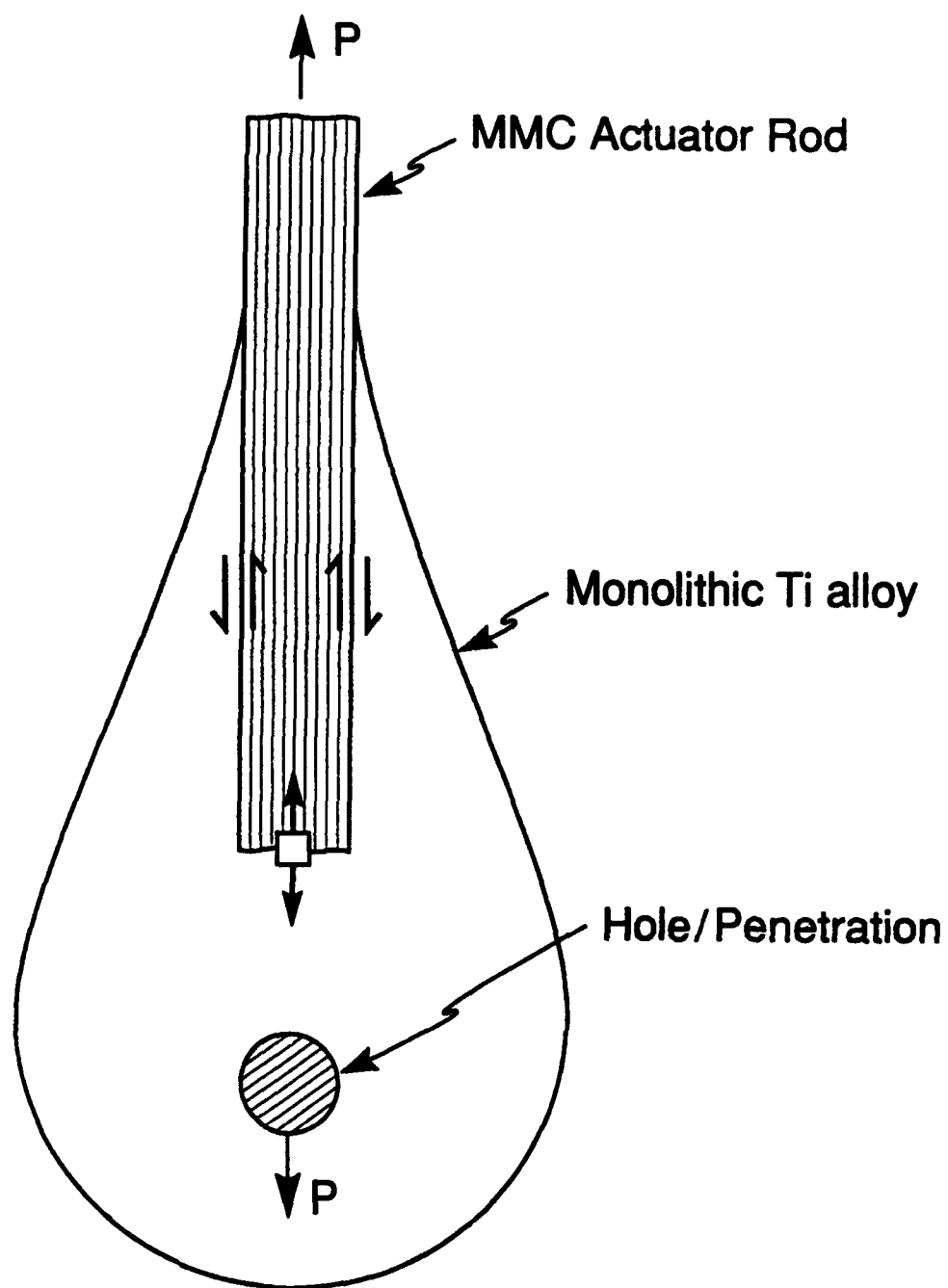


Figure 9.2

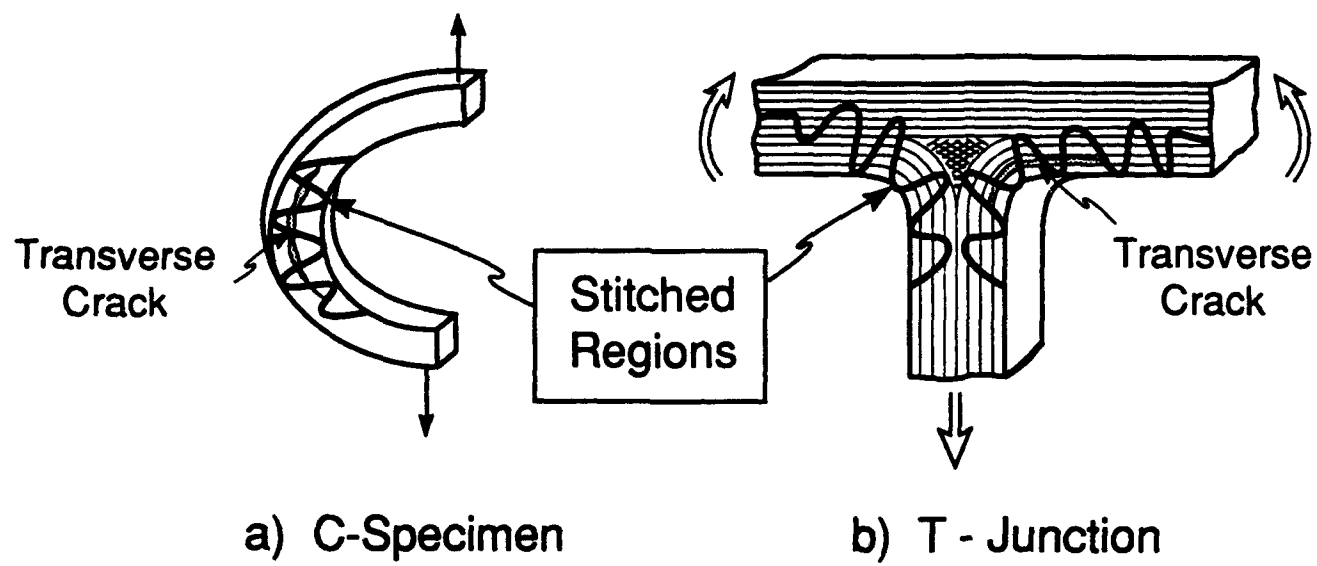


Figure 9.3

developments make the prospect of affordable high temperature fibers more realistic, evolving knowledge on the mechanical and thermochemical functions of interfaces have led to design concepts involving carefully tailored interphase layers, with unfavorable impact on cost. Moreover, if affordable coated fibers were available today, fabrication costs associated with consolidation and pressure densification would often remain prohibitive. Future processing and manufacturing activities are predicated on these issues, especially the need for new ideas, and the related knowledge base.

### 10.1 MMCs

Melt processing methods provide the more affordable options in composite synthesis with the added benefit of near-net shape capability. For continuous fiber composites melt infiltration also enables full density while minimizing the consolidation stresses that typically cause premature reinforcement failure in solid state processes. However, melt processing requires a high degree of thermochemical compatibility between matrix and reinforcement since deleterious diffusional interactions would be accelerated by the liquid phase. Conventional melt processing also exhibits limited ability to control the volume fraction and spatial uniformity of the reinforcements.

Among metal matrices, Ti alloys epitomize unsuitability for direct melt infiltration owing to aggressive reactivity. Fiber clustering is also a concern, even in solid state processes based on powder or foil matrices. Composite consolidation by vapor deposition (PVD) of the matrix on the fibers provides an avenue for improving *homogeneity of fiber spacing*. However, present schemes require expensive pressure densification with its many problems. A potential solution involves a hybrid manufacturing route wherein part of the matrix is first applied to the fibers by PVD. The pre-metallized fibers are then assembled into a preform having the desired shape and then infiltrated with the remaining matrix in liquid form.

Direct infiltration with Ti alloys could be feasible owing to the protection of the fiber by the PVD layer, but the high temperatures involved would exacerbate the diffusional interactions at the fiber-matrix interface. An alternate approach involves depositing the more refractory constituents of

the matrix (e.g., Ti, Nb, Mo, etc.) by PVD and then infiltrating with the lower melting point constituents (e.g. Al). Based on stoichiometric considerations, the latter approach would be suitable for matrices with  $\geq 25$  at.% Al, notably the orthorhombic and  $\alpha_2$  alloys. The obvious problem with this approach is the homogenization of the matrix after consolidation, which may require lengthy high temperature treatments in the solid state. However, a significant part of the matrix synthesis reaction could be effected in the presence of molten Al, followed by a final heat treatment in the solid state. While this lower temperature infiltration approach is evidently desirable from a manufacturing viewpoint, it is not clear that matrix homogenization can be achieved.

A program involving modeling and experimental work will be initiated in 1994 to generate the knowledge base appropriate to hybrid approaches for Ti matrix composites (Levi, Evans). Cell models (single fiber environment) would be developed to study diffusional interactions and remelting/solidification phenomena as a function of processing cycle (temperature-time history). Experiments would be performed to elucidate the relevant aspects of microstructural evolution and provide the reaction and interdiffusion kinetics needed to calibrate the models. Initial experiments would be performed by infiltrating pure Ti-wire preforms with molten Al and subjecting the "composite" to different treatments in the semi-solid state. Subsequent experiments would focus on developing a metallization route for Ti-Nb alloys on SiC fibers and on the relevant interactions with infiltrated Al. Larger scale modeling issues would be tackled in 1995 if the proposed approach appears promising.

Ongoing activities on the understanding of microstructure evolution and its relationship to properties in *in-situ* TMC systems based on TiB reinforcements would be continued (Levi). These are by nature affordable composites which exhibit inherent thermochemical stability and may be cast into shapes using conventional Ti processing techniques. A potential application of these materials would be in joints with unidirectionally reinforced composites, wherein their higher modulus and creep resistance combined with acceptable toughness and isotropic properties could be advantageous. It is also anticipated that these materials could be used for cladding in PVD or plasma-sprayed form, thereby reducing the potential for fatigue crack initiation in the cladding. Since TiB is thermochemically stable

with practically all Ti matrices of interest in fiber composites, such strengthening concepts may be readily implemented.

## 10.2 CMCs

Measurements and observations in 1993 have shown that strong, high strain to failure CMCs can be fabricated using an inexpensive method that involves a) packing a powder around fibers within a fiber preform using pressure filtration and b) making the powder matrix strong by heat treatment followed by infiltration with a liquid precursor that decomposes to an inorganic material. A composite made this way, with polycrystalline alumina fibers in a silicon nitride matrix, demonstrated that the *matrix* deflects the crack. This observation is significant since it suggests that a class of CMCs can be processed without needing weak fiber/matrix interfaces. The potential of this observation will be explored (Lange, Evans), by processing a composite with strong, polycrystalline alumina fibers in a mullite matrix because the thermomechanical properties of mullite minimize thermal stresses and resist creep. In addition, the thermal expansion mismatch is relatively small. Mixed Al, Si metal alkoxide precursors which can be gelled *in-situ*, prior to decomposition, will be used to strengthen the matrix.

Manufacturing studies would initiate with understanding the precursor infiltration into mullite power compacts. The densification of the matrix would be determined as a function of the cyclic infiltration. Microstructure changes would be controlled to avoid flaw populations during densification. The fracture toughness and the strength of the matrix would be determined as a function of the number of precursor infiltration cycles. Composite processing would initiate with precursor infiltration into alumina fiber preforms by pressure filtration, with emphasis on the colloidal aspects of this processing step. The goal would be to determine the processing conditions needed to produce a matrix that optimizes the ability to deflect cracks without degrading fiber strength. To optimize composite processing, panels for testing under conditions of both strain and stress control would be manufactured.

## 11. STRESS AND DAMAGE SENSORS

The extensive exploitation of the optical fluorescence method of measuring stresses in sapphire fiber and alumina-containing ceramic composites begun in 1993 will be continued in 1994 (Clarke, Wadley). The emphasis is on using the method to understand basic, unresolved issues in stress redistribution in composites by the direct measurement, with high spatial resolution, of the stresses themselves. Particular attention will be paid to determining the stress distribution associated with interfacial sliding. One of the problems to be addressed relates to new concepts for oxidation resistant interfaces within MMCs and CMCs, particularly the concomitant roles of fiber roughness and sintering on interface sliding and debonding, after exposure to high temperatures and cyclic loadings. For this purpose, fibers with fugitive, low modulus coatings will be explored and fluorescence measurements used to understand stress evolution and its connection with fiber durability within the composite. A second problem relates to the distinction between the line spring and large scale sliding models for fiber bridging (Budiansky, Hutchinson), so as to determine the range of applicability of the two models. The two competing models predict different distributions of stresses in the fibers within the bridging zone and hence are amenable to validation on the basis of the measured stress distribution.

Two approaches to measuring local damage are under development and will be the focus of the sensor activities. One is the use of acoustic methods (Wadley) to probe local variations in the elastic modulus of CMCs as a function of load. This should provide a means of mapping the distribution of damage which can be compared directly with the predictions of continuum damage mechanics models. The second approach (Clarke) is to detect the third harmonic signal generated by the presence of local damage. Preliminary experimental results obtained in 1993 concerned with the detection of crack-like voids in thin metal lines, together with computer simulation studies, have demonstrated the viability of the technique. This work will be extended in order to detect damage accumulation in CMCs and MMCs.



# A FIBER FRACTURE MODEL FOR METAL MATRIX COMPOSITE MONOTAPE CONSOLIDATION<sup>1</sup>

Dana M. Elzey and Haydn N. G. Wadley  
Department of Materials Science and Engineering  
University of Virginia  
Charlottesville, VA 22903

## ABSTRACT

The consolidation of plasma sprayed monotapes is emerging as a promising route for producing metal and intermetallic matrix composites reinforced with continuous ceramic fibers. Significant fiber fracture has been reported to accompany the consolidation of some fiber/matrix systems, particularly those with creep resistant matrices. J.F. Groves et al (*Acta Metall. et Mater.* 1994) determined the predominant mechanism to be bending at monotape surface asperities and showed a strong dependence of damage upon process conditions. Here, a previous model for the densification of monotapes (Elzey and Wadley, *Acta Metall. et Mater.* 41, 2297, 1993) has been used with a stochastic model of the fiber failure process to predict the evolution of fiber fracture during either hot isostatic or vacuum hot pressing. Using surface profilometer measured roughness data for the monotapes and handbook values for the mechanical properties of different matrices and fibers, this new model is used to elucidate the damage dependence on process conditions, monotape surface roughness, and the mechanical properties both of the fiber and matrix. The model is used to investigate the "processability" of several currently important matrix and fiber systems and to identify the factors governing this. An example is also given of its use for the simulation of a representative consolidation process cycle. This approach to the analysis of a complex, nonlinear, time-varying process has resulted in a clear understanding of the causal relationships between damage and the many process, material and geometric variables of the problem and identified new strategies for its elimination.

## 1. INTRODUCTION

Interest in metal and intermetallic matrix composites reinforced with continuous fibers is growing because of their superior specific modulus, strength and creep resistance[1,2]. For example, one emerging system based upon a  $\text{Ti}_3\text{Al}+\text{Nb}$  matrix reinforced with 40 vol% of Textron's SCS-6 fibers has a specific strength double that of wrought superalloys at 25°C and single crystal superalloys at 1100°C[3]. They are viewed as potential (but costly) materials for future gas turbine engines and the airframes of high speed aircraft.

These composite systems are difficult to process by conventional solidification pathways because of extreme reactivity between the fiber and many of the matrix materials of interest. Novel methods are being investigated to bypass this problem including solid state

---

<sup>1</sup>Submitted to *Acta metall. et mater.* (1994).



techniques such as foil-fiber-foil[4] and powder cloth[5], vapor deposition techniques[6] and various thermal spray processes such as induction coupled plasma deposition (ICPD)[7]. The ICPD method has attracted interest because the contact time between the liquid alloy and the fiber is short ( $\sim 10^{-4}$  s), fiber alignment and uniform spacing are retained in the final composite, high temperature matrix alloys (that are difficult to produce in the rolled foil form needed for a foil/fiber/foil approach) can be used, and alloy compositions can be maintained (unlike vapor deposition where the wide variation in partial pressures of some alloy elements results in a loss of stoichiometry). For many fiber/matrix systems it is also potentially the lowest cost processing route.

ICPD results in sheets (usually called monotapes) containing a single layer of unidirectional fibers surrounded by matrix. These can be layed up and either hot isostatically or vacuum hot pressed (HIP/VHP) to densify and form a near net shape component, Figure 1. A

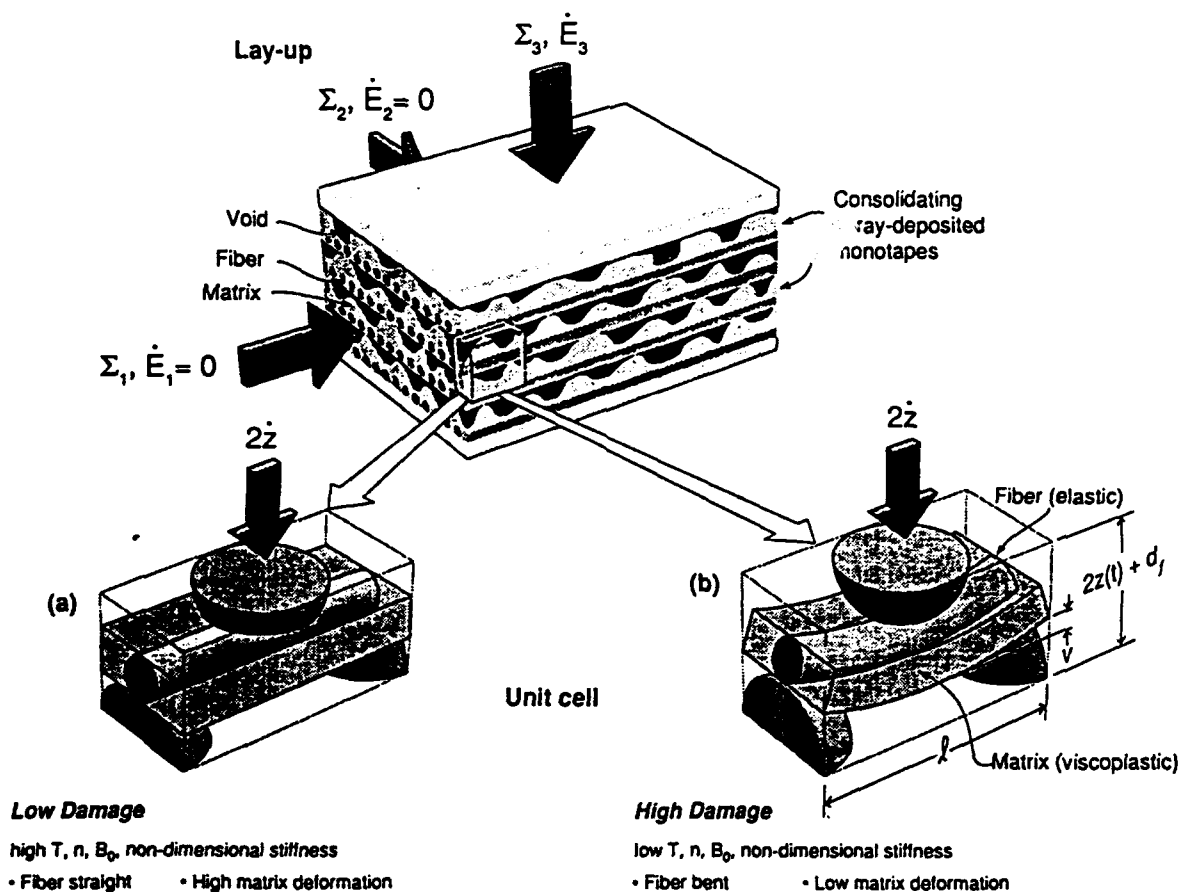


Figure 1. The fiber fracture model is based on the analysis of a representative volume element in which a single fiber segment is subjected to bend forces by contacting asperities; fiber damage is predicted by summing the failure probabilities of a statistical distribution of such cells within the lay-up. Fiber damage during consolidation is lowest when the matrix flows into and fills voids without deflecting the fibers.

recent study has analyzed the consolidation process and developed expressions for densification by plasticity, power law creep and diffusional flow at asperity contacts and voids[8]. It resulted in the development of a predictive model that calculated the temporal evolution of density during any (arbitrary) HIP/VHP temperature/pressure cycle. It was also used to find optimum process conditions (i.e. accomplish a fully dense consolidation in minimum time).

Recent experimental studies of monotape consolidation have revealed the sometimes widespread occurrence of fiber fracture during consolidation[9], a potentially serious drawback to this processing approach. However, these studies indicated that the extent of fiber fracture was sensitive to the conditions used to consolidate the monotapes and raised the possibility that for some process conditions/material systems it could be avoided. In particular it was shown that high consolidation temperatures and low densification rates greatly reduced the fiber damage, at least in the  $\text{Ti}_3\text{Al}+\text{Nb}/\text{SCS}-6$  system. Unfortunately, extended exposure of the monotapes to high temperature during consolidation results in the deleterious dissolution of the fiber's protective coating, increased fiber-matrix sliding resistance[10] and (eventually) a loss of the fiber's strength[11]. The rates at which these effects occur depend on the fiber coating and matrices and the process temperature used. Thus, for each fiber/matrix system of potential interest, it becomes necessary to make a trade-off between fiber fracture, interfacial reaction severity and relative density to determine the best consolidation process. There is the possibility that for some systems no acceptable compromise exists.

This trade-off could be sought empirically but would require numerous experiments (and their time consuming characterization) with test materials that are expensive, sometimes irreproducible and often difficult to obtain. In addition, such an approach would have to be repeated each time the matrix alloy, the fiber or the fiber coating was changed. Instead, we have resorted to a modeling approach, the development and results of which are presented here. It will be shown that simulations with the model allows identification of the properties of potential fiber/matrix systems that govern fiber fracture during consolidation. This enables the selection of fiber/matrix combinations that can be processed successfully (and a determination made of those that cannot). Together with the model developed earlier for densification[8], it can also be used for model-based control (optimization) of both densification and fiber fracture during the consolidation process[12].

## 2. PROBLEM DEFINITION

Composite monotapes can be produced by winding ceramic fiber (e.g., Textron's SCS-6 fiber) on large diameter drums. These are then heated to  $\approx 850^\circ\text{C}$  (to avoid thermal shock to the fibers during subsequent deposition) and rotated/translated under a stream of plasma melted alloy droplets (see [7] for further details). The resulting monotapes are characterized by one, quite rough surface (the one built up by successive droplet solidification), one, much smoother surface (the one in contact with the drum surface) and upto 10% of internal (closed) porosity. A full characterization of the monotape's geometry can be found in [8,9] and of its sometimes metastable microstructure (and evolution during the consolidation thermal cycle) in [13,14].

Near net shape composite components can be produced by cutting and stacking the monotapes in a suitably shaped cannister or die and subjecting this to a consolidation cycle designed to eliminate porosity and promote monotape diffusion bonding[8]. For sheet-like samples almost all the consolidation strain is accommodated by a reduction of component thickness (sheet widths and lengths show no appreciable strains), especially at low density where the plastic Poisson's ratio of the porous laminate is very low ( $< 0.1$ ). Therefore regardless of the type of consolidation process (HIP or VHP), monotape consolidation can, to a good approximation, be treated as occurring under conditions of constrained uniaxial compression.

During consolidation, fibers can be fractured, especially during the early stages of densification[9]. A number of potential mechanisms of fiber fracture can be envisioned. In principle, tensile fiber stresses could be generated on heating to the consolidation temperature because the matrix often has double the thermal expansion coefficient of the fiber[15]. A second possibility is that transformations of some metastable ICPD alloys on heating cause matrix dilatation and tensile fiber stressing[13,14]. Both of these have been discounted for many of the systems studied here because experiments in which the foils were thermally cycled (without an applied pressure) to the consolidation temperature showed no fiber damage[9]. Fractures due to fiber/matrix thermal expansion coefficient mismatch did not occur because, at the start of consolidation, the fibers are in residual compression after cooling from the ICPD process temperature ( $\approx 800\text{--}900^\circ\text{C}$  for  $\text{Ti}_3\text{Al+Nb}$  deposition), and would go into tension only upon heating above the deposition temperature. Consolidation is typically performed  $100\text{--}200^\circ\text{C}$  above that of deposition, resulting in

tensile fiber stresses of 150–300 MPa, which are small compared to typical fiber strengths of 3–5 GPa. Evidence is beginning to emerge that a more significant axial fiber stress can be developed if there is a large CTE mismatch between the composite and the tooling used for its consolidation[16]. This would result in an additional damage mechanism not analyzed here.

The mechanism we examine results from *nonuniform* mechanical loading of the fibers which causes the fibers to deform by bending. Axial and torsional fiber deformations can also be created, but the experimental work of Groves et al[9] has identified bending as the main damage source. The nonuniform forces that cause fiber bending were shown to result from the surface roughness of the monotapes; forces were essentially transmitted from one monotape to the next only at points of (asperity) contact, resulting in local fiber bending and potential fiber fracture. This mechanism of damage occurs only when densification is by contact deformation (Stage I[8]). When the composite relative density approaches 0.9 and beyond, the asperities create isolated voids (Stage II). In this regime, densification is accomplished by void shrinkage and, if these are uniformly distributed, the loads on the fiber become more homogeneous and further bending is not expected. Thus fiber bending is expected in the range of densities where asperity contact deformation dominates densification.

To be of greatest value for process design (and control), a model is required that predicts fiber damage accumulation throughout a consolidation cycle of arbitrary pressure and temperature profile so that the effect of changes to these profiles can be evaluated. It must also fully capture the relevant features of a randomly rough monotape surface so that one can assess its contribution to damage. The model should also be capable of generalization so that the effects of changing either the fiber or matrix properties could be predicted and the best combinations identified. Lastly, since there is interest in the use of the model for model-based process design (optimization) and possibly feedback control, it should not require overly extensive computation, and in particular, the need for human intervention during its iterative application (i.e., it should not be a finite element model).

### 3. MODEL DEVELOPMENT

When monotapes are compressed, fibers bend (and possibly fracture) because they are loaded only at the contact points between adjacent foils, Figure 1. Each fiber span bridging a pair of asperities suffers a bending that depends upon the span length and the asperities'

height and shape which are all statistical quantities determined by the surface roughness. As densification proceeds, and the monotapes are pressed more closely together, the number of contacting asperities increases and the average spacing between the contacts decreases. Given an initial distribution of asperity spacings and heights (simply determined from a single profilometer line scan), we first seek to calculate the distribution of fiber bend lengths at any given density. Each fiber segment length within the distribution will suffer a deflection governed by the constitutive response of the asperity, its geometry and the fiber stiffness. The probability that a fiber segment's deflection causes its fracture can be determined by calculating the maximum fiber tensile stress (due to the bend deflection) and comparing this with the (statistically distributed) fiber strength. Summing this fracture probability over all the fiber length segments present will give the desired overall probability of fiber fracture for any point in the densification process.

If we assume macroscopic isostrain conditions (the  $\dot{\epsilon}_3$  strain rate component in Figure 1 is independent of position), the monotapes will remain planar throughout consolidation and their position and approach rate are defined by the macroscopic (lay-up) density and densification rate, respectively. These could be obtained experimentally, but instead we prefer to use calculated values (for a given applied pressure,  $\Sigma_3(t)$  and temperature cycle) using the densification model developed in [8]. Thus the current density and densification rate are available as an inputs to a fiber fracture model; a choice that favors a displacement analysis of fiber bending/fracture rather than one based on equilibrium of (applied and internal) stresses.

The model's development is presented in two steps. First, we analyze (to obtain the fiber deflection) a geometrically representative volume element consisting of a fiber segment and three contacting asperities responsible for its bending (Figure 1). The fibers' deflection arises from the asperities' resistance to inelastic deformation. This is assumed to occur by either plastic yielding or power-law creep or a combination of both. The unit cell analysis results in a single nonlinear differential equation relating the instantaneous density and densification rate (the inputs to the model obtained using the results of [8]) to the fiber's deflection (the model's output). The second step (§3.2) combines the unit cell response with a statistical model of a randomly rough surface to calculate the distribution of fiber deflections (and fiber fracture probabilities) in the macroscopic body. A significant complication with the second step is the need to include the evolving nature of the fiber span length distribution since segments are continuously formed, deformed and eliminated (predominantly by subdivision as new contacts are made) throughout the consolidation process.

### 3.1 Single Fiber Segment Analysis

Figure 1 illustrates a typical fiber segment forced into three-point bending by asperity contacts. Each plasma sprayed monotape may be envisioned as consisting of two regions (laminae), one containing the parallel array of fibers and the other composed only of the surface roughness[8]. As shown in Figure 1, the unit cell consists of a fiber reinforced lamina (which is subjected to bending), a surface asperity of the same monotape as the fiber segment (shown inverted), and asperities of an adjacent monotape. Although the fibers are embedded in matrix material, the resistance of the reinforced lamina to bending is assumed to be entirely due to the fiber because of its much higher stiffness and large volume fraction (about 70% of the volume of the reinforced lamina). The fiber segment and associated asperities define a unit cell of length,  $\ell$  (defined by the distance between contacting asperities) and height,  $2 \cdot z(t) + d_f$  where  $z(t)$  is the current thickness of the surface roughness lamina within a compressed foil and  $d_f$ , the fiber diameter, approximates the thickness of the reinforced lamina. Although the reinforced lamina thickness does change slightly during densification[8], it can be regarded as a constant for the purpose of modeling the fiber fracture (since its contribution to the bend stiffness of the r-lamina is neglected). Thus the contribution of the reinforced lamina to the cell height can be omitted from the derivation of the unit cell model, so that the monotape thickness is taken to be simply  $z(t)$ . The initial dimensions of the unit cell to be analyzed are then given by  $\ell$  and  $2h$ , where  $h$  is the (original) undeformed asperity height. Both  $\ell$  and  $h$  vary statistically for a rough surface and are later treated as random variables, but to begin we consider just a single combination.

The thickness of a monotape lay up changes with time due to densification, eventually bringing the fiber (i.e. the reinforced lamina) of one foil into full contact with all the asperities of an adjacent foil. As the compaction of each newly formed unit cell occurs, the asperities press against the fiber, causing it to deflect. In turn, reaction forces exerted by the fiber lead to deformation of the asperities. The rate of change of height ( $\dot{y}$ ) for a deforming asperity can be taken as the sum of the asperity's plastic ( $\dot{y}_p$ ) and creep ( $\dot{y}_c$ ) deformation rates; i.e.  $\dot{y} = \dot{y}_p + \dot{y}_c$  (where dots indicate differentiation with respect to time). The instantaneous monotape thickness ( $z[t]$ ) and the deformed asperity height ( $y[t]$ ) govern the fiber deflection ( $v[t]$ ):

$$(1) \quad v(t) = 2[z(t) - y(t)].$$

The monotape thickness ( $z[t]$ ) is governed by the lay-up's macroscopic density. It can be

determined by simulation using a previously developed model for densification[8]. By conservation of mass, the predicted relative density,  $D$  of a monotape is related to the thickness during constrained uniaxial compression by  $z(t) = z_0 \cdot D_0/D(t)$ , where  $z_0$  and  $D_0$  are the initial monotape thickness and relative density.

The output desired from the unit cell analysis is the fiber's deflection ( $v$ ), which in turn determines the tensile stresses in the fiber and therefore the probability that the fiber will fail. Since  $z(t)$  is available as an independent input, it is only necessary to compute  $y(t)$  to obtain the deflection using (1). Expressions for  $y(t)$  can be calculated assuming either plasticity or creep to be the dominant mode of asperity deformation using the approach in [8].

**3.1.1 Plasticity** Plastic deformation is the primary densification mechanism of metals and alloys when consolidation is conducted at temperatures below about  $0.4T_m$ , where  $T_m$  is the absolute melting point. The contact stress required to cause an asperity's plastic yielding generates the forces that cause fiber bending[8,17]. The uniaxial yield criterion for a hemispherical asperity can be written:

$$(2) \quad \frac{F_c}{a_c} = \sigma_c \geq \beta \cdot \sigma_0$$

where  $\sigma_c$  is the average asperity contact stress,  $F_c$  is the normal contact force,  $a_c$  the contact area,  $\sigma_0$  the uniaxial yield stress of the matrix and  $\beta$  a numerical factor accounting for the increase in the stress required for elastically constrained or workhardening plastic flow. Gampala et al have shown that the degree of elastic constraint is strongly dependent on the evolving shape of the deforming contact, quickly reaching a maximum value of about 3 and then decreasing for a perfectly plastic material[17]. Work hardening counteracts this decrease and to a reasonably good approximation,  $\beta$  can be assumed to have a constant value of 3 with relatively little loss of precision<sup>2</sup>.

From (2), the force acting on a single asperity to cause its plastic deformation is given by

$$(3) \quad F_c = -\beta \cdot \sigma_0 \cdot a_c \approx 6\pi\tau\sigma_0(y_p - h)$$

---

<sup>2</sup>This represents a worst case since allowing  $\beta$  to decrease with continued deformation (geometric softening) leads to plastic flow at lower contact stresses, and thus a smaller probability of failure.

where  $r$  is the mean asperity radius,  $y_p$  is the asperity height following plastic deformation and  $a_c$  has been approximated by  $2\pi r(h-y_p)$  for a hemispherical asperity[18]. We define a "plastic stiffness",  $k_p (\equiv 6\pi r\sigma_0)$ , so that equation 3 becomes  $F_c = k_p(y_p-h)$ .

Given the contact forces, the deflection of a fiber segment can be obtained from simple beam theory. The force-deflection relation for a simply supported segment subjected to three-point elastic bending is:

$$(4) \quad F = k_s v$$

where  $v$  is the fiber's midpoint deflection and, for central loading of a cylindrical fiber, the elastic bend stiffness,  $k_s$  is given by[19]:

$$(5) \quad k_s = \frac{3\pi}{4} \cdot E_f \cdot \frac{d_f^4}{l^3}$$

where  $E_f$  is the fiber's Young's modulus and  $d_f$  its diameter.

Equating (3) and (4), (the force acting through both asperity and fiber must be equal), and using (1) gives the change in asperity height due to plastic yielding as  $y_p-h = 2(z-y) \cdot k_s/k_p$ , which upon differentiation, leads to an expression for the rate of plastic displacement:

$$(6) \quad \dot{y}_p(t) = \xi [\dot{z}(t) - \dot{y}(t)]$$

where  $\xi (\equiv 2k_s/k_p)$  is a non-dimensional stiffness equal to twice the ratio of the elastic bend stiffness of the fiber to the "plastic" stiffness of the asperity. High values of the non-dimensional stiffness are desirable since this increases the rate of asperity compaction for a fixed deflection force rate, and results in a lower fiber deflection rate.

**3.1.2 Power Law Creep** At higher temperatures ( $T \geq 0.4T_m$ ), densification is dominated by power law creep. We assume that a uniaxial power-law stress-strain rate ( $\sigma-\dot{\epsilon}$ ) relation holds for the matrix material:

$$(7) \quad \dot{\epsilon} = B\sigma^n$$



where  $n$  is the creep exponent (often a function of stress and temperature) and  $B$  is a temperature dependent constant conventionally expressed as  $B = B_0 \exp(-Q_c/RT)$  in which  $Q_c$  is the activation energy for power law creep. Rewriting (7) in terms of the asperity height ( $y$ ) and the force applied to the asperity contact gives:

$$(8) \quad \frac{\dot{y}_c}{y} = -B \left[ \frac{F_c}{a_c} \right]^n$$

Equating the force ( $F_c$ ) in (8) required to creep deform the asperity at a rate  $\dot{y}_c/y_c$  with that required to bend the fiber (equation 4) and substituting for  $a_c$  gives:

$$(9) \quad \dot{y}_c = -By(t) \left[ \frac{2k_s[z(t)-y(t)]}{2\pi r[y(t)-h]} \right]^n$$

This is an ordinary nonlinear differential equation ( $n$  typically ranges from 2 to 5) that can be solved numerically, using, for example, a Runge-Kutta numerical integration scheme.

**3.1.3 Combined Response** The total displacement rate for an asperity is assumed to be the sum of the rates due to creep and plasticity, i.e.  $\dot{y} = \dot{y}_p + \dot{y}_c$ . Substituting expressions (6) and (9) for  $\dot{y}_p$  and  $\dot{y}_c$  results in a nonlinear ordinary differential equation in the asperity height:

$$(10) \quad \dot{y} = -\frac{By(t)}{1+\xi} \left[ \frac{2k_s[z(t)-y(t)]}{2\pi r[y(t)-h]} \right]^n + \frac{\xi}{1+\xi} \dot{z}$$

Equation (10) can be solved numerically to give the asperity height,  $y(t)$ , given  $z(t)$  as input. The time-dependent fiber deflection can then be obtained using (1).

**3.1.4 Fiber Fracture** The unit cell response of a fiber segment can be used to determine the deflection, given values of  $\ell$  and  $h$  for the cell, and  $z(t)$  for the consolidating body. The maximum tensile stress,  $\sigma_b$ , in the fiber is related its deflection:

$$(11) \quad \sigma_b(t) = 6E_f \frac{d_f}{\ell^2} \cdot v(t)$$

The bending fracture strength is proportional to the tensile fracture stress,  $\sigma_f$ [20]

$$(12) \quad \sigma_b = \sigma_f \left[ \frac{V_t}{V_b} \cdot \frac{1}{\kappa} \right]^{\frac{1}{m}}$$

where  $V_t$  and  $V_b$  are the volumes of tensile stressed fiber during tension and bend testing, respectively. For fiber strengths that obey Weibull statistics, the factor  $\kappa$  depends only on the fibers' Weibull modulus,  $m$ . For example, SCS-6 (SiC) fibers with  $m = 13$  have  $\kappa = 1.45 \cdot 10^{-2}$ [9]. Taking  $V_t$  to be the gage length of tensile fiber samples and  $V_b$  to be governed by the mean asperity spacing (for asperities of all heights),  $V_t/V_b \approx 100$  for ICPD monotapes[9], and thus

$$(13) \quad \sigma_b \approx 1.9 \cdot \sigma_f$$

The constant in (13) is insensitive to values of  $V_b$ ; for the entire range of fiber segment lengths (i.e., asperity spacings) encountered here,  $\sigma_b/\sigma_f = 1.9 \pm 0.1$ . From (11) and (13), the tensile fiber stress is

$$(14) \quad \sigma_f(t) \approx 3E_f \cdot \frac{d_f}{72} \cdot v(t)$$

Since the deflection,  $v(t)$  in (14) is obtained by solution of (10) for a given  $\ell$ ,  $h$  and foil thickness,  $z(t)$ , the fiber stress at some time  $\tau$  depends on  $\ell$ ,  $h$  and the densification history,  $z(t)$ : i.e.  $\sigma_f = \sigma_f(\ell, h, z(t), \tau)$ .

With the fiber stress given by (14), the probability of fracture is obtained from the fiber strength distribution,  $\varphi_f(\sigma_f)$ . For a two-parameter Weibull distribution[21], the strength distribution function is

$$(15) \quad \varphi_f(\sigma_f) = \frac{m}{\sigma_{ref}} \cdot \sigma_f^{m-1} \exp \left[ - \left[ \frac{\sigma_f}{\sigma_{ref}} \right]^m \right]$$

where  $\sigma_f$  is the fiber stress and  $\sigma_{ref}$  is a reference stress (the stress below which 37% of fibers survive). The ratio of the volume of material stressed in bending to the volume stresses during tensile testing,  $V/V_0$ , does not appear in (15) since it has already been accounted for by equations (12) and (13). Integration of (15) gives the cumulative strength distribution

$$(16) \quad \Phi_f(\sigma_f) = 1 - \int_0^{\sigma_f} \varphi_f d\sigma = 1 - \exp \left[ - \left[ \frac{\sigma_f}{\sigma_{ref}} \right]^m \right]$$

For any given cell (i.e. for a given fiber span length and asperity height) and densification path,  $z(t)$ , the fiber stress ( $\sigma_f$ ) needed to determine the cumulative probability of fracture is obtained by first solving the ODE (10) for the asperity height,  $y(t)$ , substituting this into (1) to obtain the deflection, and then substituting  $v(t)$  into (14).

### 3.2 Macroscopic Response

In principle, the macroscopic response of a monotape lay-up could be evaluated by summing the failure probabilities for all the possible unit cell lengths present. It is complicated however, because at any instant in the process, not only are there continuous distributions of cell lengths, cell heights and fiber fracture strengths, but the cells are continually being created, deformed and eliminated throughout the consolidation cycle. The new problems of cell creation/elimination arise because a cell, formed at some earlier time in the cycle, is eliminated when it encounters a new asperity, and two new cells (with new lengths) are formed. The distribution of cell lengths therefore evolves during the process.

Let us consider how a single cell response like that developed above (§3.1) could be integrated into a macroscopic (many-celled) lay-up response. Suppose a particular cell of interest has a fiber segment length,  $\ell$ . It would have been created earlier in the process of consolidation by the addition of an asperity to subdivide an existing cell of length  $> \ell$  when the compacted monotape height  $z(t) = z_c$ . During subsequent densification, the new fiber span thus created undergoes deflection until it is eliminated (by the addition of a contact) at some height,  $z$  (where  $z < z_c$ , see Figure 2). Obviously, if  $z_c - z$  is small, the fiber will

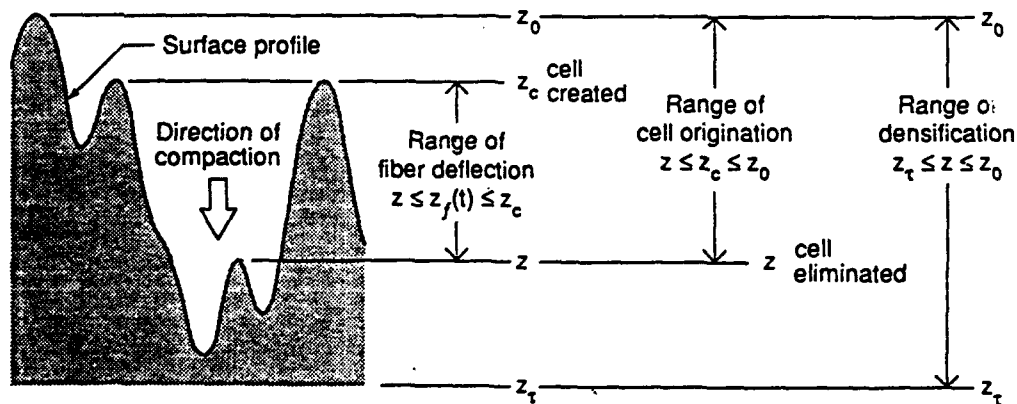


Figure 2. Integration variables used in the fiber fracture model: the composite monotape is compacted from an initial height,  $z_0$  to  $z_t$  at time,  $\tau$ . At each height,  $z$ , the cells eliminated by new contacts are considered;  $z_c$  is the height at which a cell, eliminated at  $z$ , was created.  $z_t$  is a measure of the amount of deformation of the cell created at  $z_c$  and eliminated at  $z$ .

probably not have suffered a very significant deflection and its failure probability will be small. Thus, the cumulative probability that this fiber segment would have failed ( $\Phi_f$ , defined by equation 16), will be a function of  $z_c$ ,  $z$  and  $L$ .

By introducing a change of variable to relate stress in the fiber ( $\sigma_f$ ), given by (14), to the extent of monotape compaction ( $z_f$ ), we can write the failure probability as:

$$(17) \quad \Phi_f(z_c, z, L) = \int_{z_c}^z \varphi_f(L; \sigma_f) \cdot \frac{d\sigma_f}{dz_f} dz_f$$

where  $z_f$  represents the height as the cell is compacted from  $z_c$  to  $z$  (Figure 2).  $\Phi_f(z_c, z, L)$  represents the fraction of those cells created at  $z_c$  and subsequently eliminated at  $z$  which had fractured. The cumulative number of these fractures can be obtained by summing the product of (the fraction of cells eliminated at  $z$ )  $\times$  (the fraction of these created at  $z_c$ )  $\times$  (the cumulative probability of failure), for all cells created during consolidation to a height,  $z(\tau)$ .

However, the fraction of cells of a given length eliminated at  $z$  and the fraction of these which were created at  $z_c$  must also be expressed as probabilities. Therefore the macroscopic model must be able to predict the probability that a cell of given length is eliminated when a new contact is added and the probability that this particular cell was created at any previous height,  $z_c$ . These two probability density functions are referred to as the probability of elimination,  $\varphi_e$  and the probability of origination,  $\varphi_o$  and are derived below ( §3.2.2 and §3.2.3). However, since the probability of eliminating a cell depends on the number of cells of this particular length in existence at any moment, the total number of cells and their length distribution must first be determined.

**3.2.1 Number of Cells and Cell Length Distribution** Suppose a randomly rough surface, Figure 2, is contacted by a straight fiber. If the fiber compresses the surface (along its line of contact) to a height,  $z$ , then the number of asperities per unit length in contact with the fiber ( $n_c$ ) is

$$(18) \quad n_c(z) = \rho \cdot \int_z^{z_0} \varphi_h(h) dh = \rho \cdot \Phi_h(z)$$

where  $z_0$  is the undeformed surface height,  $\varphi_h(h)$  is the probability density function (PDF)

describing the distribution of asperity heights,  $h$ ,  $\rho$  is a lineal asperity density (with units of  $m^{-1}$ ) and  $\Phi_h(z)$  is the cumulative height probability function, i.e., the probability of finding an asperity of height  $\geq z$ . Both  $\varphi_h(h)$  and  $\rho$  can be experimentally determined by stylus profilometry.

These contacts result in cells like those shown schematically in Figure 1. Because of the randomness of the surface, the cells are of a variable length. We let  $\varphi_1(z; \ell)$  be the PDF describing the distribution of cell lengths at any compacted height,  $z$ . It must depend on the current compacted monotape thickness since, as  $z$  decreases, the number of contacts, and therefore the number of cells, increases, with the result that the mean cell length continually decreases with densification. Additionally,  $\varphi_1(z; \ell)$  will have to allow for the occurrence of very closely spaced asperities which cannot be further subdivided by an additional contact.  $\varphi_1(z; \ell)$  could be determined experimentally, but only with great difficulty. A simplified derivation of  $\varphi_1(z; \ell)$  can be achieved if we assume an average asperity radius,  $r$  (sprayed monotapes exhibit a statistical distribution of asperity sizes, i.e. radii for hemispherical asperities), such that the shortest possible cell length<sup>3</sup> will be  $2r$  and restrict  $\varphi_1(z; \ell)$  to  $\ell \geq 2r$ . This assumption allows use of the method of Widom[22] for analyzing random sequential addition processes like this and we find (Appendix I):

$$\varphi_1(z; \ell) = \frac{1}{4n_c(z) \cdot r^2} \cdot q(\rho; \lambda)$$

where  $q(\rho; \lambda)$  is defined in the Appendix. Even if this were not a reasonable assumption to invoke, we find that fiber lengths this short are anyway unlikely to fracture and the assumption minimally perturbs our result.

**3.2.2 Cell Creation/Elimination** If the monotape is deformed from  $z$  to  $z+dz$ , a number of new contacts,  $\Delta N$ , will be established as indicated by equation (18). Consider the fraction of cells that are of a length, say  $\ell$ ; the additional contacts may either eliminate (i.e., subdivide) longer cells to create additional cells of length,  $\ell$ , or the new contacts can eliminate cells of length,  $\ell$  to create cells of a shorter length. Provided  $\varphi_1(z; \ell)$  is known, the probabilities that added contacts either eliminate or create cells of a given length can be obtained as follows.

---

<sup>3</sup>The minimum spacing does not correspond to  $1/\rho$  (where  $\rho$  is the measured line density of asperities) since the asperities are not close packed, but may be separated by shallow valleys or flats.

Suppose a fiber of overall length,  $L$  has  $N_c(z)$  contacts. Since new contacts cannot be formed where gaps of less than  $2r$  exist, the total length of fiber accessible to a potential contact is

$$A(z) = N_c(z) \int_{2r}^L (\ell - 2r) \cdot \varphi_1(z; \ell) d\ell$$

The probability that the next contact to form will subdivide a cell of length between  $\ell$  and  $\ell + d\ell$  is just the fraction of the accessible length occupied by all lengths between  $\ell$  and  $\ell + d\ell$ , i.e.

$$\frac{N_c(z) \cdot \varphi_1(z; \ell) d\ell \cdot (\ell - 2r)}{A(z)}$$

Since  $N_c(z)/L = n_c(z)$ , the current contact density, and  $n_c(z) \cdot \varphi_1(z; \ell) \cdot (\ell - 2r)/A(z)$  is recognized as a PDF describing the (evolving) distribution of eliminated cells:

$$(19) \quad \varphi_e(z; \ell) = n_c(z) \cdot \varphi_1(z; \ell) \cdot (\ell - 2r)/A(z)$$

where  $\varphi_e(z; \ell)$  represents the probability of subdividing a segment of length,  $\ell$  per contact added. (Note its units of per meter per contact.) The fraction of the  $\Delta N$  eliminated cells with length between  $\ell$  and  $\ell + d\ell$  is thus  $\varphi_e(z; \ell) d\ell \cdot \Delta N$ .

Turning next to the creation of cells, we note that any cell length,  $\ell' > \ell - 2r$  could be subdivided to create a cell of length,  $\ell$ . For this to occur, a newly added asperity must first contact a cell of length  $\ell'$  and then subdivide it such that a cell of length,  $\ell$  is created. The probability of contacting a cell with a length between  $\ell'$  and  $\ell' + d\ell'$  is  $\varphi_e(z; \ell') d\ell'$ . Since the contact has an equal probability of occurring anywhere within  $\ell' - 2r$ , the probability of creating cells having lengths between  $\ell$  and  $\ell + d\ell$  is uniform, i.e., it is just  $d\ell/(\ell' - 2r)$ . The fraction of cells with lengths between  $\ell$  and  $\ell + d\ell$  created by the subdivision of cells having lengths between  $\ell'$  and  $\ell' + d\ell'$  is therefore  $2 \cdot [n_c(z)/A(z)] \cdot \varphi_1(z; \ell') d\ell' \cdot d\ell$ . The factor 2 arises because the new cell could be created to the left or right of the added contact. For all  $\ell' \geq \ell$ , the fraction of created cells of length between  $\ell$  and  $\ell + d\ell$  is:

$$2 \cdot \frac{n_c(z)}{A(z)} \cdot \left\{ \int_{\ell+2r}^L \varphi_1(z; \ell') d\ell' \right\} \cdot d\ell$$

from which we define a PDF describing the distribution of created cells:

$$(20) \quad \varphi_c(z; \ell) = 2 \cdot \frac{n_c(z)}{A(z)} \cdot \int_{\ell+2r}^L \varphi_1(z; \ell') d\ell'$$

$\varphi_c(z; \ell)$  represents the probability of creating a segment of length,  $\ell$  per contact added when the compacted height is  $z$ . The fraction of the  $2 \cdot \Delta N$  newly created cells with length between  $\ell$  and  $\ell + d\ell$  is thus  $\varphi_c(z; \ell) d\ell \cdot \Delta N$ .

**3.2.3 Probability of Cell Origination** When a cell is subdivided by the addition of a contact, the cell must be replaced by two cells, each of a shorter length, and the subdivided cell must be removed from the cell length population. To calculate the failure probability for the cell at the point of its removal, it is necessary to know the height,  $z_c$ , at which the cell was formed. The probability that a cell was originally created at a height between  $z$  and  $z_0$  (the initial monotape thickness) is the number of cells created between  $z_c$  and  $z_c + dz_c$  divided by the total number of cells (of length,  $\ell$ ) created between  $z_0$  and  $z$ :

$$(21) \quad \varphi_o(z_c, z, \ell) \cdot d\ell = \frac{\varphi_c(z_c; \ell) d\ell \cdot \frac{dn_c}{dz_c} dz_c}{\int_z^{z_0} \varphi_c(z'_c; \ell) d\ell \cdot \frac{dn_c}{dz'_c} dz'_c} \quad (z \leq z_c \leq z_0)$$

Note that the population described by  $\varphi_o$  includes all cells created between  $z_0$  and  $z$  whereas  $\varphi_c$  includes only the cells created between  $z_c$  and  $z_c + dz_c$ .

**3.2.4 Cumulative Fiber Damage** Finally, the probability that a cell of length,  $\ell$ , created at  $z_c$ , is subdivided at  $z$  and subsequently fails at a height,  $z_f$  can be expressed as  $\varphi_c(z; \ell) \cdot \varphi_o(z_c, z, \ell) \cdot \varphi_f(\ell; \sigma_f) \cdot d\sigma_f / dz_f$ . Thus, the total number of fractures associated with cells eliminated at or before  $z(\tau) \equiv z_r$  is

$$(22) \quad N_a(z_r) = \int_{2r}^{\infty} \int_{z_r}^{z_0} \left\{ \varphi_c(z; \ell) \cdot \int_z^{z_0} \left\{ \varphi_o(z_c, z; \ell) \cdot \int_z^{z_c} \left\{ \varphi_f(\ell; \sigma_f) \cdot \frac{d\sigma_f}{dz_f} \right\} dz_f \right\} dz_c \right\} \cdot \frac{dn_c}{dz} \cdot dz \cdot d\ell$$

where  $dn_c/dz \cdot dz$  gives the number of cells removed between  $z$  and  $z + dz$ .

Equation (22) represents the total number of cells which have failed and subsequently been

eliminated by subdivision prior to reaching  $z(\tau)$ . However, at  $z(\tau)$ , many cells will not have been eliminated, but are still subjected to various levels of stress and some may have fractured. The contribution of these to the number of fractures is:

$$(23) \quad N_b(z_\tau) = n_c(z_\tau) \cdot \int_{z_r}^{\infty} \left\{ \varphi_1(z_\tau; \ell) \cdot \int_{z_\tau}^{z_0} \left\{ \varphi_0(z_c, z; \ell) \cdot \int_{z_\tau}^{z_c} \left\{ \varphi_f(\ell; \sigma_f) \cdot \frac{d\sigma_f}{dz_f} \right\} dz_f \right\} dz_c \right\} d\ell$$

where  $\varphi_1$  has replaced  $\varphi_e$  since it is not the distribution of subdivided cells that are of interest (these have already been accounted for in (22)), but the distribution of existing cells at  $z_\tau$ . The total accumulated damage after densifying to  $z(\tau)$  is therefore the sum of (22) and (23):

$$(24) \quad N_f(z_\tau) = N_a(z_\tau) + N_b(z_\tau)$$

The fiber fracture predictive model, given by (24), requires knowledge of three probability distribution functions;  $\varphi_h(h)$ , the distribution of asperity heights,  $\varphi_f(\sigma_f)$ , the distribution of fiber strengths and  $\varphi_1(z; \ell)$ , the distribution of asperity spacings, which depends on the deformed height,  $z$  (i.e. the current density). The PDF for asperity heights can be determined easily by means of stylus profilometry. The distribution of fiber strengths is usually described by Weibull statistics and is available for different types of fiber.  $\varphi_1(z; \ell)$  could be determined by surface profilometry or analytically as described in Appendix I using the method of Widom[22]. The model, (24) can be regarded as predicting the number of fractures as a function of monotape thickness (which can be converted into relative density) or time (for a prescribed consolidation cycle) since the height is known or predictable as a function of time using the densification model[8] for any process cycle.

In attempting to keep the model formulation as simple as possible, (since for some of its intended applications the model should take only minutes to run), a number of idealizations have been introduced including: (i) the fiber segments are treated as bare, although they are actually embedded within a porous matrix, (ii) the fiber segments are assumed to be simply supported as though isolated – the fact that the fibers are continuous and bonded to the deforming metal matrix makes the actual end constraints considerably more complicated, (iii) central three-point bending is treated – in reality, the intermediate loading point may occur anywhere between the end supports, (iv) the deforming asperity contacts are treated as point loads rather than distributed, (v) fiber fracture has been neglected as a means of cell elimination since the number of fractures is usually much less



than the number of asperity contacts (0–300 compared to 1500–2500), and (vi) fiber segments are assumed to be stress-free at the instant they are created. Assumptions (i) – (v) cause the model to overestimate the actual damage while (vi) result in an underestimation. Some of these deficiencies could be corrected if experience with the model shows the additional computation to be justified.

### 3.3 Implementation

In principle, the fracture density,  $N_f$ , can be determined by direct, numerical integration of (24). In practice, the large number of integrals involved, and the need to solve a nonlinear ODE (10) (describing the single cell response) for each combination of  $z_c$ ,  $z$  and  $\ell$  results in an excessively large computation. An alternative is to simulate the cell creation/elimination process using random sampling techniques in such a way that the governing probabilities ( $p_c, p_e$ ) are satisfied. Monte Carlo methods allow one to do this and to evaluate and sum the cumulative probabilities of failure for all cells. This approach also exploits the independence of the fiber strength and the surface roughness distributions. It can be implemented efficiently so that parametric investigations of materials and process paths (which affect only the unit cell response) can be conducted without having to repeat the computationally expensive cell distribution analysis.

The simulation of the cell creation/elimination process can be conducted by treating  $\ell$  as a discrete random variable and using discrete forms of the probability densities given in §3.2. The distribution of fiber bend segment lengths at any time consists of  $n_c(z)+1$  segments, all of different lengths,  $\ell_i$ . The number of asperity contacts,  $n_c(z)$ , is given by (18) with the probability density function describing the distribution of asperity heights,  $p_h$ , and the asperity density,  $\rho$ , determined experimentally by stylus profilometry. Typically the surface is found to be isotropic and the asperity heights to be normally distributed[8]:

$$(25) \quad p_h(h) = \frac{1}{\sqrt{2\pi} \cdot \sigma_h} \exp \left[ -\frac{1}{2} \left( \frac{h-\bar{h}}{\sigma_h} \right)^2 \right]$$

where  $\bar{h}$  is the mean asperity height and  $\sigma_h$  is the standard deviation.

Monte Carlo techniques allow the process of elimination to be simulated by random sampling in such a way that the frequency with which a particular segment length is eliminated by added contacts is given by  $p_e$ . Recalling (from §3.2) that the probability

that the next contact added to a fiber intercepts a cell of length,  $\ell$  is just the length occupied by cells of length,  $\ell$  divided by the total length of fiber accessible to the contact, the probability that any one of the discrete lengths,  $\ell_i$  will be contacted in a meter of fiber (i.e.  $\sum \ell_i = 1$ ) is just the length itself divided by  $1 - n_c(z) \cdot 2r$ :  $p_e(\ell_i) = (\ell_i - 2r) / (1 - n_c(z) \cdot 2r)$ . Using the Monte Carlo technique, a pseudorandom number,  $\chi$ , is generated (on the interval 0,1);  $\chi$  represents the cumulative probability of elimination and the corresponding (expected) event is determined by adding the probabilities associated with each segment length,  $p_e(\ell_i)$ , until the sum (i.e. the cumulative probability) is greater than or equal to  $\chi$ :

$$(26) \quad \chi \leq \sum_{i=0}^N p_e(\ell_i) = \sum_{i=0}^N \frac{\ell_i - 2r}{1 - n_c(z) \cdot 2r}$$

This is easily solved for  $N$  (the only unknown) in the numerical implementation since all the  $\ell_i$  are known (and are unique) at the moment an additional contact is made.

Determination of the lengths of the two cells created when a longer cell is eliminated can be treated likewise using the Monte Carlo method. Since the probability of subdividing any cell of length,  $\ell'$  to create cells, for which at least one has a length,  $\ell$ , is uniform, the created lengths are determined from:

$$(27) \quad \chi \leq \sum_{i=0}^N \frac{\Delta \ell_i}{\ell'} = \frac{N \Delta \ell}{\ell'}$$

where  $\Delta \ell$  represents the smallest segment which can be created when  $\ell'$  fractures (typically  $\Delta \ell$  is chosen such that  $\Delta \ell \ll \ell$ ). The two created lengths are then  $\ell_1 = N \cdot \Delta \ell$  with  $N = \chi \ell' / \Delta \ell$  so that  $\ell_1 = \chi \ell'$ , and  $\ell_2 = (\ell' - \ell_1)$ . Following the elimination of a cell and its replacement by two cells of shorter length, the list of cell lengths is sorted in order of increasing length. This process (i.e., addition of a contact, eliminating a segment and replacing it with two shorter segments) can then be repeated.

Finally, the problem of determining the point during densification at which the eliminated cell was created becomes simple in the discrete formulation since a running list is maintained of all cell lengths ( $\ell$ ), their point of creation ( $z_c$ ) and elimination ( $z$ ). Thus since all cells are unique, it is easy to find the corresponding height of creation when a particular cell is eliminated.

Equations (26) and (27) allow the evolution of the cell length distribution to be simulated. Figure 3 gives an example of the change in lengths of created cells as densification proceeds

(decreasing  $z$ ). For the case shown,  $z_0 = 208 \mu\text{m}$  and the final relative density reached (at  $z = 82 \mu\text{m}$ ,  $z/z_0 \approx 0.4$ ) was 0.89. The longer cells have the greatest probability of being eliminated and are seen to be quickly subdivided. The length of most of the roughly 1800 cells present at the end of this example (the actual number depends on the surface roughness characteristics) are too small to be seen on the linear scale of the figure.

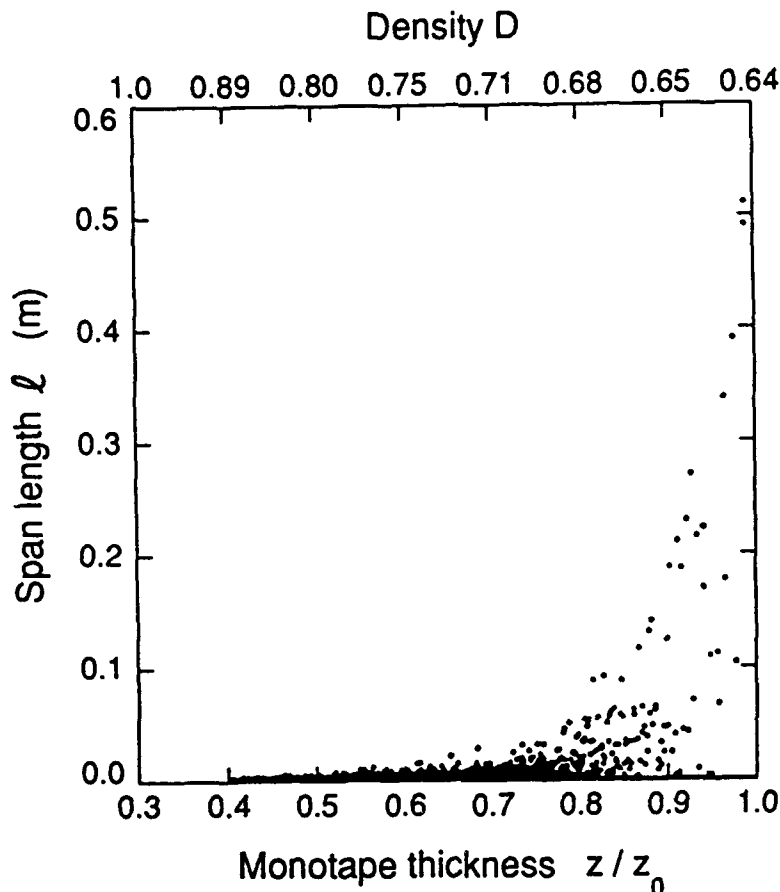


Figure 3. The creation of fiber span lengths with decreasing monotape thickness (from  $z_0 = 208 \mu\text{m}$  to  $z_f = 82 \mu\text{m}$ , corresponding to a final relative density of 0.9). Typically, 1800–2500 fiber bend segments are created, depending on the surface roughness characteristics of the monotape.

With the evolution of cell lengths and their heights of creation and elimination determined, equation (17) can be applied to determine the cumulative probability of failure for each cell. These failure probabilities are summed for all cells to obtain the total number of accumulated fractures. The unit cell response,  $y(t)$  given by (10) can be solved by numerical integration using a Runge–Kutta scheme, from which the fiber stress during bending (equations 1 and 14) and the rate of change of fiber stress with respect to  $z$  ( $d\sigma_f/dz = \dot{\sigma}_f/\dot{z}$ ) are determined.

The fiber fracture model (Monte Carlo simulation and unit cell constitutive response) has been implemented using MATHEMATICA™ [23]. Separate subroutines treated the cell evolution and damage. Input to the model was the monotape thickness as a function of time (predicted using a monotape densification model[8]). The Monte Carlo approach, had a  $\pm 2\%$  variability for the predicted number of fractures at a relative density of 0.9, (the highest density at which the model was presumed accurate). Simulation of a typical process cycle required about 15 minutes to complete on a 66 MHz 486 PC, depending on the constitutive model nonlinearity, complexity of the process schedule and lineal asperity density.

#### 4. RESULTS AND DISCUSSION

Damage accumulation during consolidation processing of spray deposited monotapes is affected by many parameters, e.g. the dimensions and mechanical properties of the constituent materials (fiber and matrix), surface roughness, and the process path. Damage dependence upon these parameters is not always intuitive because of the coupled, nonlinear behavior of the system. This complexity also denies one the opportunity to analytically derive relationships between damage and the parameters affecting it. However, the model enables numerical experiments to be conducted (more easily than real experiments) and these can be used to explore and better understand the influence of these parameters on the fiber fracture density (and thus the quality of the resulting composite). We begin with the study of a benchmark problem and subsequently investigate systematic variations of the damage controlling parameters. An analysis of the processibility of typical composite systems is also presented and an example is shown of the application of both the fiber fracture and densification[8] models to the simulation of a typical consolidation cycle.

##### *4.1 Benchmark Problem*

The matrix material used for the benchmark problem was the intermetallic alloy, Ti-24Al-11Nb(at%) used in an experimental study of damage[9]. It was assumed to have the properties given in Table I. Table II lists the properties assumed for a SCS-6 (SiC) fiber reinforcement used in [9] and Table III gives the measured surface statistical parameters for this type of monotape[8].

Table I. Ti-24Al-11Nb Matrix Material Data[24-30]

Parameter, symbol	Units	Value
<i>Plasticity</i>		
Yield strength, $\sigma_0$	[MPa]	539.9
20° C		
20 ≤ T ≤ 800° C		$\sigma_0(T) = 539.9 - 0.32 \cdot T$
T > 800° C		$\sigma_0(T) = 1019.9 - 0.92 \cdot T$
<i>Steady State Creep</i>		
Power law creep constant, $B_0$	[Pa <sup>-n</sup> s <sup>-1</sup> ]	$2.72 \cdot 10^{-14}$
Stress exponent, n		2.5
Activation energy, $Q_c$	[kJ/mol]	285

Table II. SCS-6 (SiC) Fiber Properties[21]

Parameter, symbol	Units	Value
Diameter, $d_f$	[ $\mu\text{m}$ ]	142
Young's Modulus, $E_f$	[GPa]	425
Reference Strength, $\sigma_{ref}$	[GPa]	$4.5 \pm 0.2$
Weibull Modulus, m		$13.0 \pm 2.1$

Table III. Plasma Sprayed Ti-24Al-11Nb/SCS-6 Monotape Surface Statistical Data[8]

Parameter, symbol	Units	Value
Mean asperity height, h	[ $\mu\text{m}$ ]	91.06
Asperity height deviation, $\sigma_h$	[ $\mu\text{m}$ ]	39.82
Lineal asperity density, $\rho$	[ $\mu\text{m}^{-1}$ ]	$3.87 \cdot 10^{-3}$

A constant consolidation temperature of 900°C and a (constant) densification rate of 0.55 hr<sup>-1</sup> were assumed.<sup>4</sup> With all of the benchmark values inserted into the model, 62 fractures per meter of fiber were found to have occurred by the time the relative density had reached 90%. This amounted to about 3% of the total number of spans formed. Practically all fractured fiber segments had  $l/d_f$  ratios between 4 and 20 with the most frequently fractured segments having an  $l/d_f$  ratio of around 8. Fiber segments first began to fracture at a relative density of about 0.76 (the starting relative density was 0.64). The number of predicted fractures lay within the range of experimental observations where, under similar conditions (870–955°C, 5.5 hr<sup>-1</sup>), 50 to 140 fractures/meter were measured[9].

#### *4.2 Influence of Process Conditions*

The model was next used to explore the effects of consolidation conditions. Figure 4 shows a damage contour plot relating densification rate and consolidation temperature (i.e. process variables) to fiber fracture. Damage was reduced by lowering the rate of compaction (i.e. smaller displacement rates for VHP or a slower application of pressure during HIP) and by raising the consolidation temperature. These conditions favor asperity flow (Figure 1a) as opposed to fiber deflection (Figure 1b). The accumulated damage is seen to be more sensitive to changes in temperature than to densification rate because of the rapid matrix softening and higher creep rates associated with an increase in temperature.

Support for these predicted trends can be found in experimental studies[9]. For example, the measured fracture density decreased by about a factor of 2 as the displacement rate during VHP consolidation at 955°C was decreased from 1.7 to 0.4 cm/hr. Furthermore, increasing the process temperature from 900° to 975°C while keeping the applied stress (of 100 MPa) constant also resulted in a decrease in fracture density from 140 to about 60 m<sup>-1</sup>[9]. Figure 5 summarizes the results of Groves et al[9] for three compaction rates at 955°C and compares them to the model predictions. The model gives good agreement with the experiments even though the monotapes were consolidated to full density.

During the consolidation of alloy or ceramic powders, one normally applies pressure and

---

<sup>4</sup>In reality the densification rate depends on the applied stress, temperature and current density and varies throughout a real process cycle. It was kept constant here to simplify elucidation of the fracture behavior. A constant densification rate at fixed temperature requires the applied stress to increase as the density increases.

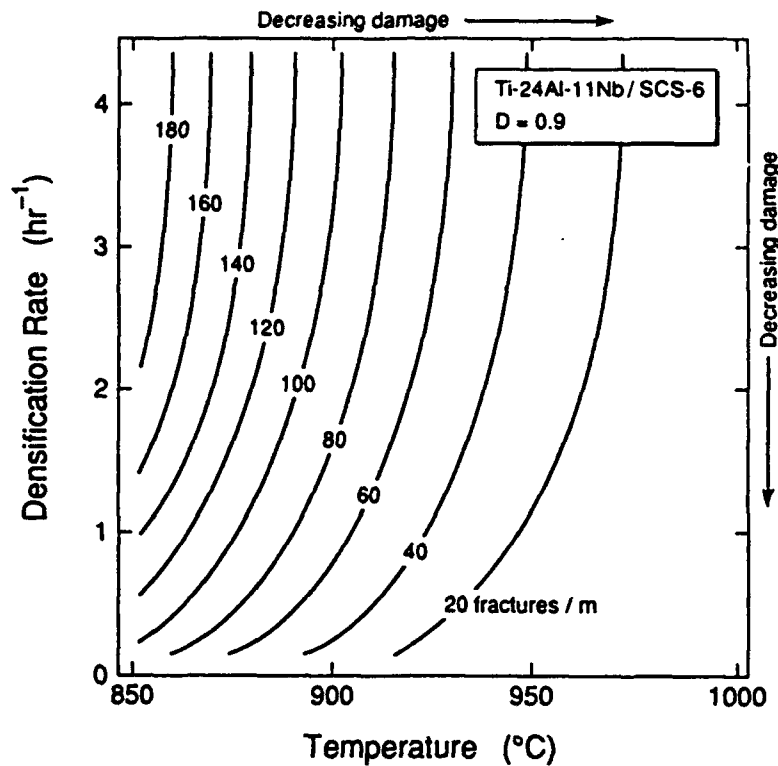


Figure 4. Influence of processing conditions: lower consolidation rates and higher temperatures lead to fewer accumulated fractures by promoting matrix deformation as opposed to fiber deflection.

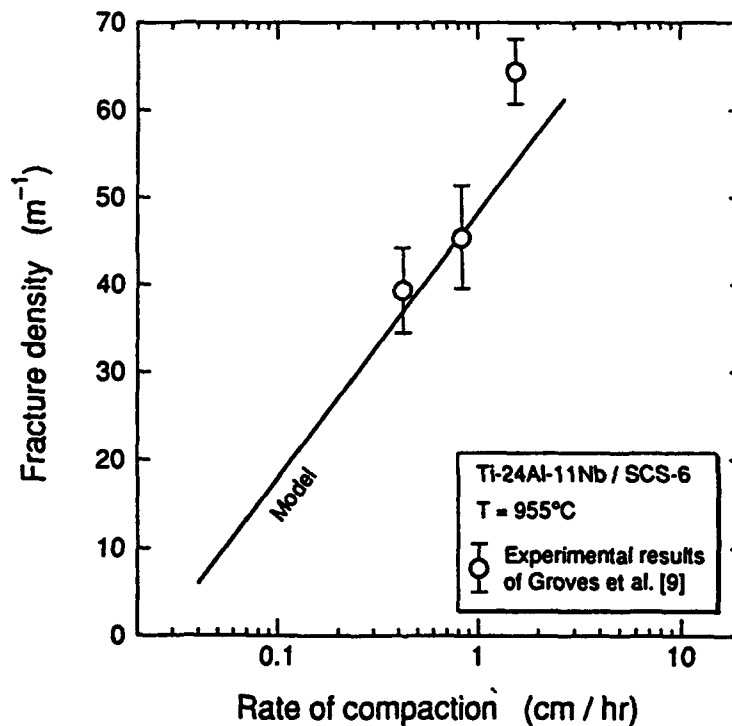


Figure 5. Comparison of experimental and predicted fracture densities at several consolidation rates. The results are for a laminate of five Ti-24Al-11Nb/SCS-6 monotapes consolidated at 955°C.

temperature simultaneously to reduce consolidation time. Figure 4 can be used to demonstrate the importance of heating a lay-up to its process temperature before applying the consolidation pressure in order to avoid fracture. It can be seen that if the temperature were first raised to 950°C and the lay-up were then subjected to an applied pressure sufficient to cause a densification rate = 1 hr<sup>-1</sup>, the fracture density would not exceed 20 m<sup>-1</sup>. However, much higher levels of damage would have resulted from simultaneously increasing both the temperature and pressure (densification rate) to these values. The damaging effect of applying pressures at low processing temperatures has been observed by Groves[21]. Stresses even as small as 3.5 MPa, when applied at room temperature, resulted in up to 20 fractures per meter in the Ti-24Al-11Nb/SCS-6 system because of the high matrix yield strength at this temperature.

It can be seen in Figure 4 that the processing temperature required for a fixed degree of damage decreases as the densification rate is reduced (i.e. consolidation time increased). However this must be balanced against the need to also minimize interfacial reactions in order to obtain low interfacial sliding friction stresses. The thickness of the interfacial reaction has been shown to obey Arrhenius kinetics and therefore the use of lower temperature/shorter times is necessary to avoid interfacial property degradation[31]. The relatively simple models for predicting the growth rate of fiber/matrix reaction zones during consolidation processing[31] could be combined with those for densification[8] and fiber fracture to enable a quantitative trade-off to be made.

#### *4.3 Influence of Material Properties*

The extent of fiber deflection and thus fracture during consolidation is controlled by complex combinations of matrix and fiber properties. We can use the model to explore this, and to identify which properties are the most critical for the control of damage.

*4.3.1 Matrix* Using the benchmark fiber properties (those for SCS-6) and process conditions ( $\dot{D} = 0.55 \text{ hr}^{-1}$ ,  $T = 900^\circ\text{C}$ ), the effect of the matrix material's resistance to plastic and creep deformation (as represented by its yield strength,  $\sigma_0$  and power law creep stress exponent,  $n$ ) is shown in Figure 6. It is seen that fiber damage can be reduced by using matrix materials with a low resistance to inelastic deformation (i.e. low  $\sigma_0$ , high  $n$ ) because in this case smaller contact forces are required to deform the asperities (and accommodate an imposed densification rate) resulting in smaller fiber deflections and thus bend stresses. Depending on the yield strength value, reducing the creep exponent below



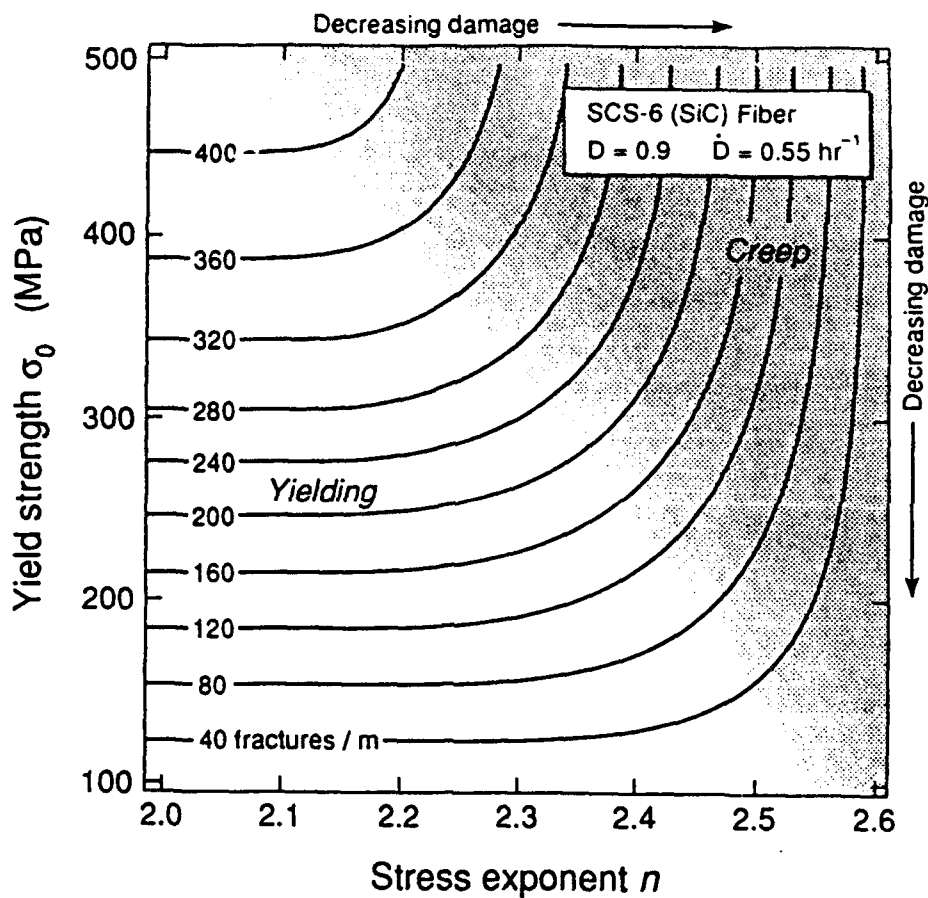


Figure 6. Influence of matrix properties on fiber damage: matrices with low resistance to deformation (low yield strength/high creep stress exponent) are favored. For matrices with high creep resistance (low  $n$ ), fiber damage is controlled by the yield strength (regime labeled "Yielding") while for matrices with low creep strength (high  $n$ ), damage is controlled by the creep response (regime labeled "Creep"). (The benchmark value for the power-law creep constant,  $B_0$  (see Table I) was used for calculations.)

about 2.2 is seen to have surprisingly little effect on the fracture density. For  $n < 2.2$ , we find the creep contribution to the asperities' deformation to be negligible compared to that of yielding, and in this region, the matrix yield strength alone determines the amount of damage. The converse can also be seen: changing the yield strength of the matrix when  $n$  is large has little effect on damage because the asperities are able to deform readily by creep. The fracture behavior in this region is then controlled by only the matrix creep strength.

The results shown in Figure 6 were calculated using a fixed value of the power-law creep constant,  $B_0$ . Variation of  $n$  (by changing alloy composition or microstructure) also usually changes  $B_0$ . From equation 7, it can be seen that increasing  $B_0$  has a similar effect on the strain rate (and hence on the fracture density) to increasing  $n$ , although it would have to be varied over a much greater range in order to obtain the same effect because of the linear dependence of creep strain rate on  $B_0$ .

**4.3.2 Fiber** Intuitively, the incidence of consolidation damage is expected to depend on fiber properties such as stiffness, diameter and strength distribution, but these dependencies are complicated by the interaction between the fiber and the inelastically deforming asperities. Intuition alone cannot predict the best combinations of say, fiber reference strength ( $\sigma_{ref}$ ) and Weibull modulus ( $m$ ) to reduce damage, nor the relative worth of increasing the elastic stiffness or diameter. We shall show that it can even lead to completely erroneous conclusions.

As an illustration of this, it could be argued that the fiber's flexibility, as defined by  $1/MR$  (where  $M$  is the bending moment and  $R$  the minimum radius of curvature), determines the susceptibility of fibers to bend fracture. For cylindrical elastic fibers,  $1/MR = 64/(E_f \pi d_f^4)$ . Thus fibers having both a small diameter and low Young's modulus are the most flexible and might be expected to undergo a very large deflection without breaking. However, the model (Figure 7a) predicts that for the fibers usually used in monotapes ( $d_f \approx 150 \mu m$ ) it is generally not flexibility, but rather the fiber's resistance to bending that is important in avoiding fiber damage. Flexibility is favored only for very small diameter ( $d_f < 35 \mu m$ ) fibers. In fact, for the matrix material and processing conditions used to produce Figure 7a, only fibers with very high flexibility (e.g.  $d_f < 10 \mu m$ ,  $E_f \ll 275$  GPa), would be able to suffer the deflections required during consolidation without substantial fiber damage.

For fibers with  $d_f > 35 \mu m$ , damage is most easily decreased by increasing their diameter. The influence of the fiber's elastic modulus is a relatively weak one; it is the size effect that is strong. For this region of the map (labeled "RIGIDITY" in Fig. 7a), damage is lessened by promoting asperity deformation rather than fiber deflection and this is best achieved with large diameter fibers that have the greatest bend stiffness. The relative importance of flexibility (fibers bend without breaking) or rigidity (fibers that resist bending), depends on the matrix material and the process conditions during consolidation. For the case examined in Figure 7a, efforts to develop slightly smaller, more flexible fibers than those used today are predicted to be a futile approach to damage reduction.

Similar difficulties can emerge when attempting to predict the effect of a fiber's strength distribution on damage; obviously, increasing the fiber's average (or reference) strength will lessen the likelihood of fracture, but it is not as intuitively clear how the Weibull modulus affects damage, or how the fiber's reference strength might affect this. The model can be used to explore these issues and to provide guidelines to the developers of fibers for

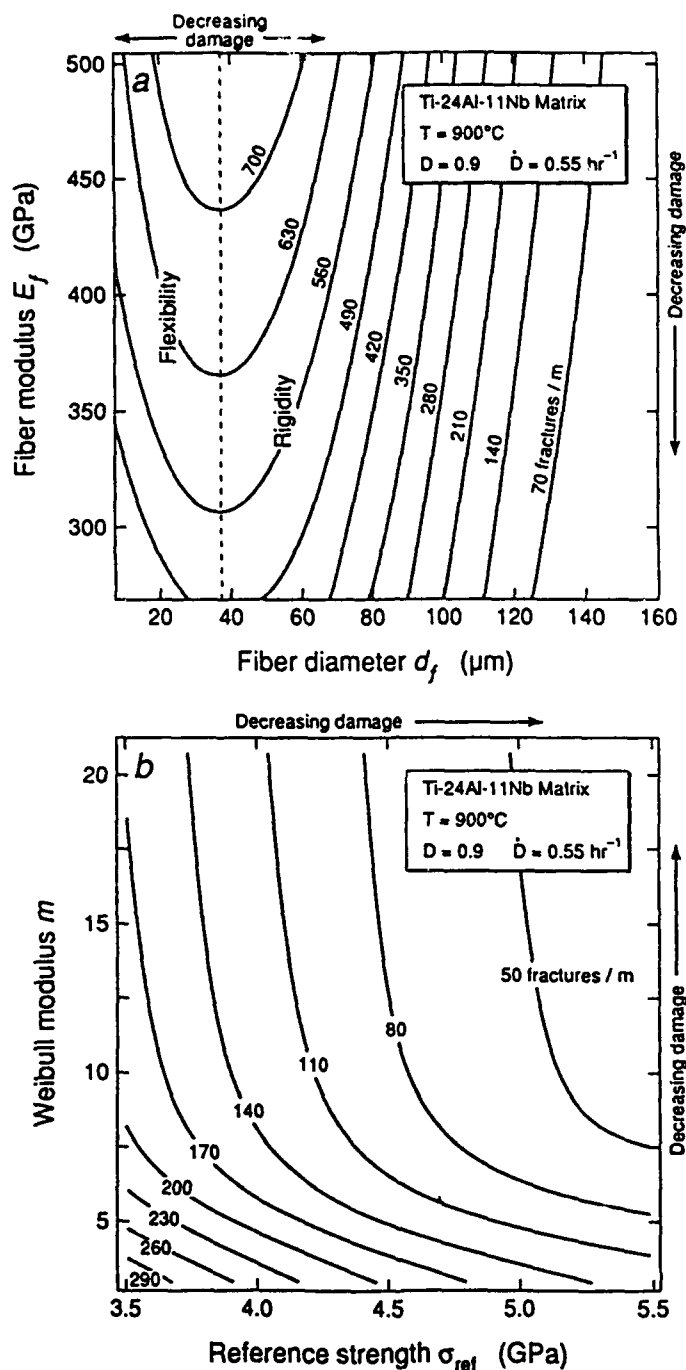


Figure 7. The influence of fiber properties on damage: (a) the damage map indicates two approaches to minimizing damage: fibers having high flexibility (small diameter, low modulus) can bend without breaking while larger diameter fibers resist bending so that densification must be achieved via matrix flow (regime labeled "Rigidity"). Improved rigidity (bend resistance) is the favored approach for the fibers usually used in these composites ( $d_f \approx 140 \mu\text{m}$ ), (b) the map indicates that high reference strength fibers with low strength variability (high Weibull modulus) are preferred.

improving their processability. Using the benchmark process conditions and matrix properties, we show in Figure 7b the effect of a fiber's Weibull modulus (i.e. its fracture strength variability) and reference strength on damage. In general, increasing both  $m$  and  $\sigma_{ref}$  reduces the incidence of fracture. Fracture densities are lowered by high values of  $m$  and/or  $\sigma_{ref}$  because, for given matrix properties and processing conditions, the fraction of fiber strengths in the range of bend stresses (created by asperity forces) is reduced. It is interesting to see that the influence of the Weibull modulus is strongest when the modulus and reference strength are both low. The results indicate that damage becomes practically independent of  $m$  once the modulus exceeds about 10 for the range of fiber reference strengths available in today's fibers (see Table IV) so fiber development efforts to further reduce variability are, from the processing viewpoint, unnecessary. Improving the processability of fibers by reducing  $m$ , may in fact reduce the strength of brittle matrix composites, which is enhanced by a high fiber strength variability[32,33].

#### *4.4 Influence of Monotape Surface Roughness*

Monotape surface roughness is the fundamental reason for fiber damage in this approach to composite processing. Removing the roughness would eliminate the damage. The surface roughness of these monotapes is determined by conditions prevailing during the plasma spray deposition process (e.g. it is probably reduced by increasing the molten droplet superheat or velocity which both promote droplet spreading). We can use the model to investigate how much of a reduction in asperity height is needed to overcome the damage problem.

Figure 8 shows the influence of the initial surface roughness as characterized by the standard deviation of asperity heights,  $\sigma_h$ . All the material properties and process conditions correspond to the benchmark values used earlier. It should also be noted that altering the conditions under which materials are spray deposited in order to vary the surface roughness also affects the initial relative density of the deposit. As the deviation in asperity heights goes to zero (assuming the average size and density of asperities remain constant), the initial relative density is expected to increase. For this reason, the initial relative density used to obtain Figure 8 was varied linearly from 0.52 (the ratio of the volume of a hemisphere to that of an enclosing parallelepiped) at  $\sigma_h = 0$ , to 0.35, the value measured experimentally and corresponding to  $\sigma_h = 39.82 \mu\text{m}$ . The accumulation of damage is seen to be extremely sensitive to  $\sigma_h$  for  $\sigma_h > 30 \mu\text{m}$ . In the experiments of Ref[9],  $\sigma_h = 39.82 \mu\text{m}$ . Reducing the deviation in asperity heights to  $30 \mu\text{m}$  or below is

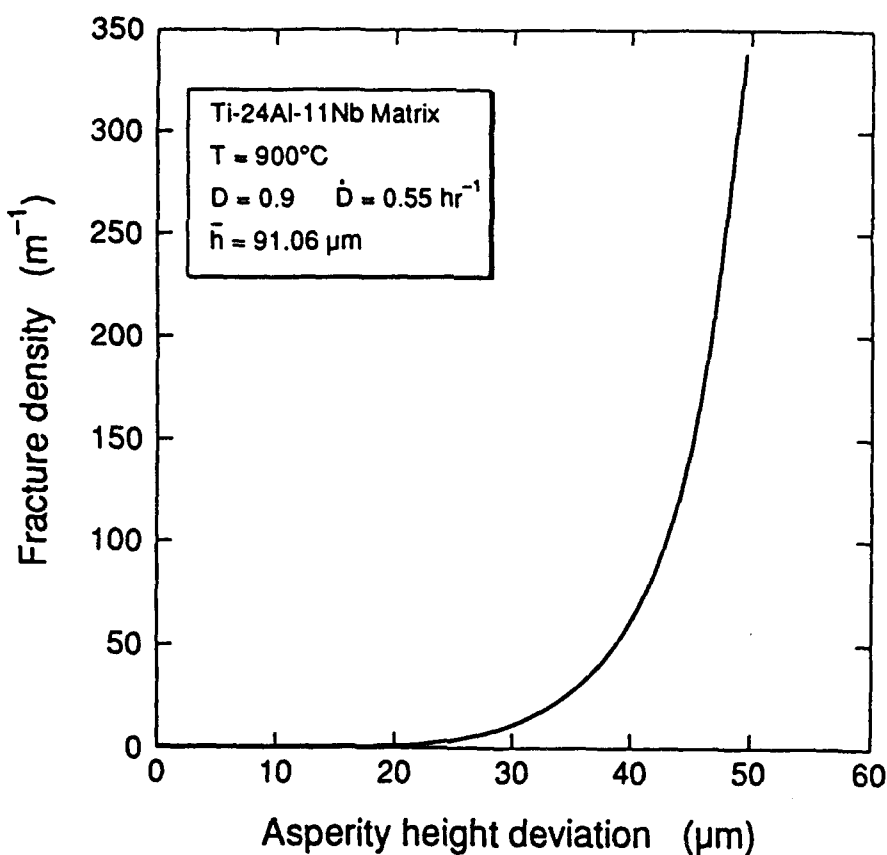


Figure 8. The effect of monotape surface roughness (determined by conditions during plasma spraying of the monotapes) on fiber damage: reducing surface roughness (lower deviation in asperity height,  $\sigma_h$ ) strongly reduces the predicted damage.

predicted to be an effective method for reducing (or even eliminating) fiber fracture during consolidation. Damage is predicted to be much less sensitive to changes in the mean asperity height; it is the variability in roughness which determines the deflections and hence the stresses in the fibers.

#### 4.5 Materials Selection for Process Tolerance

Fiber fracture results from a competition between an asperity's inelastic contact deformation and a fiber's elastic deflection and we have shown that this has a complex dependence upon matrix and fiber properties. Many fibers and matrix alloys are available today and others are in development. It is not at all obvious which combinations are likely to result in the least damage. The model can be used to determine this (i.e. to conduct a

**4.5.1 Fiber Selection** Figure 9 compares the fracture density after densifying a  $\text{Ti}_3\text{Al}+\text{Nb}$  matrix composite (using the benchmark problem's matrix properties and process conditions) reinforced with either BP's Sigma 1240 (SiC with a C/ $\text{TiB}_2$  coating) fiber, Sigma 1040 (uncoated 1240), Saphikon's single crystal  $\text{Al}_2\text{O}_3$  fiber or Textron's SCS-6 fiber (SiC with a duplex C coating). The properties of these fibers, used in calculating the results shown in Figure 9, are summarized in Table IV. We see that the SCS-6 fiber is the best choice from the viewpoint of process induced damage; a consequence of its favorable combination of large diameter, high reference strength, low strength variability (high  $m$  value) and good stiffness. The Sigma 1240 fiber is the second best choice; the loss in processability due to its smaller diameter and lower reference strength (compared to the Saphikon and SCS-6 fibers) is offset by its lower strength variability. The relatively poorer processability of the Saphikon and Sigma 1040 fibers results from unfortunate combinations of  $d_f$ ,  $m$  and  $\sigma_{\text{ref}}$ . The big difference in the processability of the two Sigma fiber types (even though the differences in their properties is relatively small) is a dramatic demonstration of how processability is magnified by the nonlinearity of the damage process.

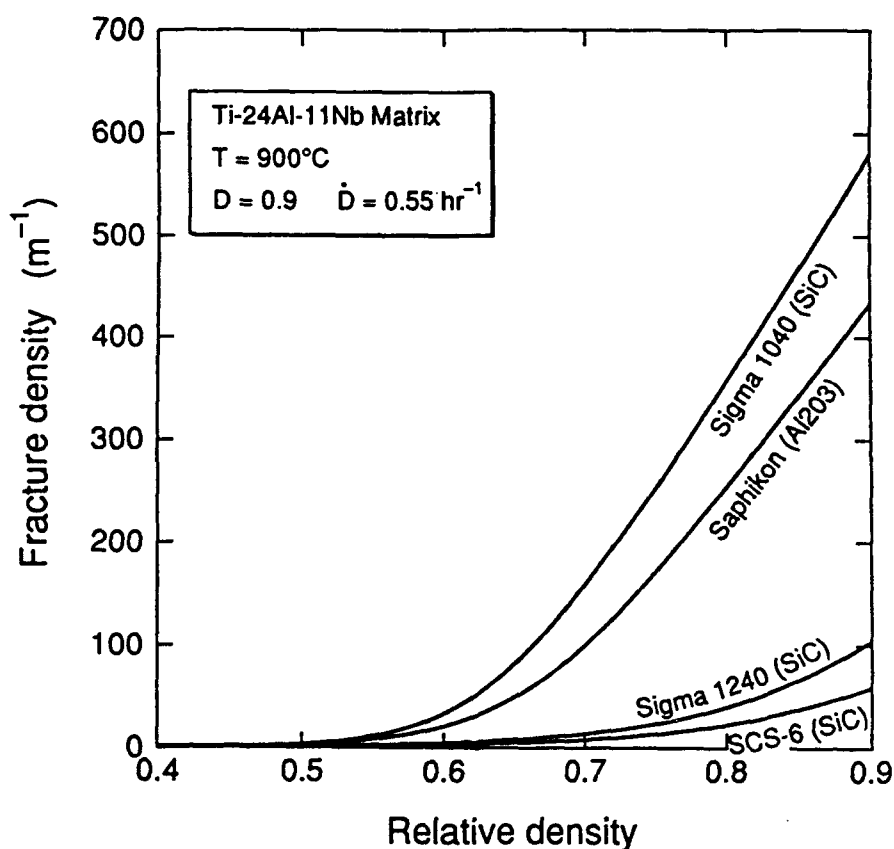


Figure 9. Comparison of fibers for consolidation processability: the SCS-6 fiber's combination of large diameter and high reference strength make it the most attractive from the processing viewpoint.

combinations of  $d_f$ ,  $m$  and  $\sigma_{ref}$ . The big difference in the processibility of the two Sigma fiber types (even though the differences in their properties is relatively small) is a dramatic demonstration of how processibility is magnified by the nonlinearity of the damage process.

Table IV. Fiber Properties used for Processibility Study

Fiber	Material	Diameter [ $\mu\text{m}$ ]	Modulus [GPa]	Ref Strength [GPa]	Weibull Modulus	Reference
Sigma 1240	SiC	100	400	3.87	18	[34],[35]
Sigma 1040	SiC	100	400	$3.3 \pm 0.1$	$12 \pm 3$	[34],[35]
Saphikon	$\text{Al}_2\text{O}_3$	135	460	$3 \pm 0.3$	$6 \pm 1$	[36]
SCS-6	SiC	142	425	$4.5 \pm 0.2$	$13 \pm 2.1$	[21]

**4.5.2 Matrix Selection** Use of the model for selecting a matrix material is not as straightforward as fiber selection; the temperature and rate dependence of the matrix properties prevent a simple comparison of damage under identical process conditions. Instead, we have calculated the damage as a function of consolidation temperature. Using the matrix properties given in Table V and a densification rate of  $0.55 \text{ hr}^{-1}$ , Figure 10 compares the damage produced during the consolidation of a variety of matrix alloys. It can be seen that a Ti-6Al-4V matrix (containing SCS-6 fibers) can be successfully consolidated at temperatures below  $650\text{--}700^\circ\text{C}$  whereas the more creep resistant intermetallic matrices, such as  $\alpha_2 + \beta$  Ti-24Al-11Nb alloy and  $\gamma$ -TiAl, require temperatures in the range  $950\text{--}1000^\circ\text{C}$  or above. The Ni-base superalloy, Nimonic 80A, can be processed in an intermediate range,  $850\text{--}900^\circ\text{C}$ . Lower densification rates shift the curves to the left, allowing use of lower processing temperatures (see Figure 4), but at the expense of increased process time.

It is interesting to note that although the steady state creep strength of  $\gamma$ -TiAl is considerably greater than that of the  $\alpha_2 + \beta$  alloy, the latter's higher yield strength (at the process temperature) makes it the more difficult material to consolidate without fracturing fibers. Figure 10 indicates that alloys such as Ti-6Al-4V are preferred candidates for this class of MMC's, but such a matrix restricts their use to low to intermediate temperatures ( $600^\circ\text{C}$ ). The intermetallic alloys needed for higher temperature applications are seen to be

difficult to composite via the plasma spray route because of fiber/matrix reactions at the high processing temperatures that are always needed to avoid fracture. Further improvements in fiber strength and protective coatings (to avoid degradation during high temperature processing) together with modification of the monotape roughness could allay these difficulties, and enable the more successful manufacture of higher temperature composites.

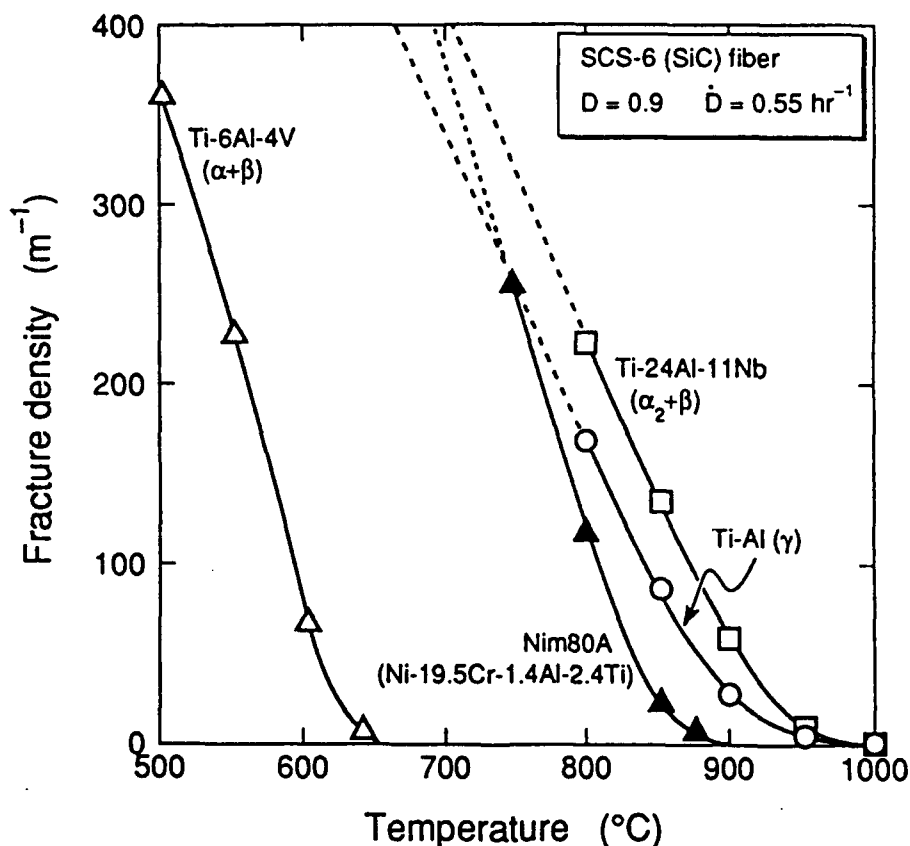


Figure 10. A comparison of the processability of several matrix alloys (all reinforced with SCS-6 fiber): successful consolidation of the creep resistant intermetallic alloys, TiAl( $\gamma$ ) and Ti-24Al-11Nb( $\alpha_2+\beta$ ) requires high processing temperatures (and consequent risk of fiber degradation due to reactions with the matrix) compared with the  $\alpha+\beta$  alloys, such as Ti-6Al-4V. The Ni-base superalloy, Nimonic 80A, can be processed in an intermediate range of temperature.



Table V. Matrix Properties used for Processibility Study

Parameter, symbol	Ti-Al[37-39]	Units	Value
<i>Elastic Properties</i>			
Young's modulus, E as f(temp)		[GPa]	
20° C			173.0
T ≥ 20° C			$E(T) = 172.0 - 0.03 \cdot T$
<i>Plasticity</i>			
Yield strength, $\sigma_0$ as f(temp)		[MPa]	
20° C			473.0
20 ≤ T ≤ 600° C			$\sigma_0(T) = 475.0 - 0.10 \cdot T$
T > 600° C			$\sigma_0(T) = 875.0 - 0.76 \cdot T$
<i>Steady State Creep<sup>5</sup></i>			
Power law creep constant, A		[s <sup>-1</sup> ]	2.12x10 <sup>19</sup>
Stress exponent, n			4.0
Activation energy, Q <sub>c</sub>		[kJ/mol]	300
Ti-6Al-4V[40-45]			
<i>Elastic Properties</i>			
Young's modulus, E as f(temp)		[GPa]	
20° C			114.0
T ≤ 500° C			$E(T) = 115.0 - 0.056 \cdot T$
T > 500° C			$E(T) = 172.4 - 0.16 \cdot T$
<i>Plasticity</i>			
Yield strength, $\sigma_0$ as f(temp)		[MPa]	
20° C			970.0
T < 960° C			$\sigma_0(T) = 884.0 - 0.92 \cdot T$
<i>Steady State Creep<sup>4</sup></i>			
Power law creep constant, A		[s <sup>-1</sup> ]	2.3x10 <sup>21</sup>
Stress exponent, n			4.0
Activation energy, Q <sub>c</sub>		[kJ/mol]	280
Nim 80A[46-48]			
<i>Plasticity</i>			
Yield strength, $\sigma_0$ as f(temp)		[MPa]	
20° C			620.0
20 ≤ T ≤ 760° C			$\sigma_0(T) = 622.0 - 0.14 \cdot T$
T > 760° C			$\sigma_0(T) = 2198.0 - 2.23 \cdot T$
<i>Steady State Creep</i>			
Power law creep constant, B <sub>0</sub>		[Pa <sup>-n</sup> s <sup>-1</sup> ]	1.08x10 <sup>-21</sup>
Stress exponent, n			4.2
Activation energy, Q <sub>c</sub>		[kJ/mol]	410

<sup>5</sup>The steady state creep rate is described by  $\dot{\epsilon}_c = A \cdot (\sigma/E)^n \exp(-Q_c/RT_k)$ .

#### 4.6 Process Simulation

The fiber fracture model can be used to simulate an entire consolidation process including its response to transients. Implementation of the model is no different to that for the process planning and materials selection applications considered above; only the densification path, taken to be constant earlier is instead, generated for an entire pressure-temperature-time cycle (including ramp-up) using the monotape densification model in [8].

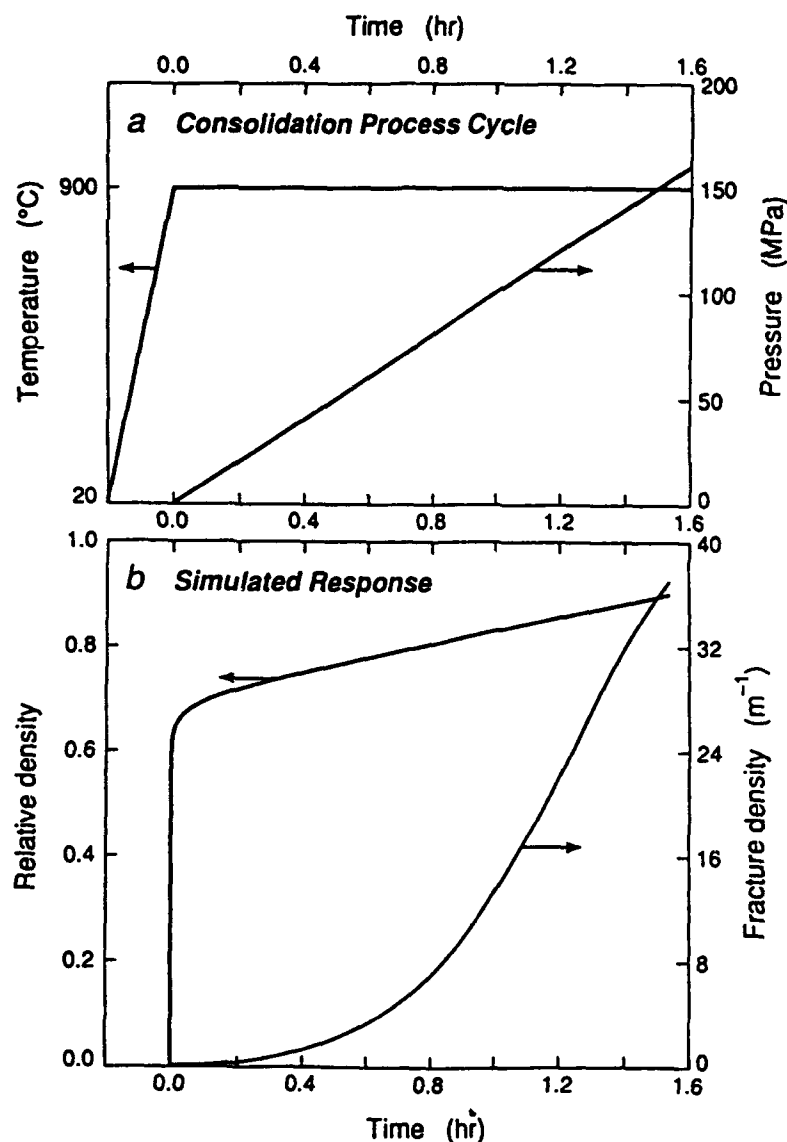


Figure 11. An example of the model's use to simulate fiber damage for arbitrary pressure-temperature-time cycles. (a) Process schedule, (b) predicted densification (from model given in [8]) and fiber damage.

Figures 11a and b show an example of this application of the model. For this hypothetical process cycle the temperature was first ramped to 900°C and held constant, and a linear ramp in pressure (at 100 MPa/hr) then applied. Figure 11b shows the time dependent evolution of composite relative density (obtained using the model in [8]) and the normalized fiber fracture density predicted by the fracture model. The damage accumulation rate is seen to be at first slow (despite the high densification rate) because initially, most fiber segments are long ( $\ell/d_f > 20$ ) and do not suffer large bending stresses (cf. equation 11) for the small deflections associated with initial densification. The rate of fracture achieves a maximum at about 1.1 hr into the process (composite relative density of 0.85) when the most probable segment lengths approach  $\ell/d_f$  values of 12 and lower. The fracture rate then begins to decrease as the relative density approaches 0.9 as an increasing fraction of the fiber segments become too short to fail ( $\ell/d_f < 4$ ), (though in this region the model's validity is also diminishing, because the assumption of point contacts becomes unreasonable). This ability of the model to simulate fiber damage accumulation for arbitrary consolidation cycles enables exploration of new approaches to process planning and on-line control by coupling the model with an optimization scheme[12].

## CONCLUDING REMARKS

A micromechanical model for predicting the rate of fiber fracture during the consolidation processing of spray deposited metal matrix composite monotapes has been developed and combined with stochastic descriptions of fiber strength and randomly rough surfaces to investigate the fiber damage during MMC processing. The model has been used to investigate the sensitivity of damage to process conditions, matrix and fiber materials and monotape surface roughness. It has been found that:

- 1) The model successfully predicts the damage experimentally observed in Ti-24Al-11Nb/SCS-6 composites and reproduced the experimentally observed dependence of damage on consolidation process conditions.
- 2) The model predicts that fiber damage can be avoided (or at least minimized) by increasing temperature and lowering the densification rate (i.e. pressure) during consolidation: the optimal conditions are shown to depend on the properties of the fiber and matrix
- 3) The "processing window", where high composite density can be achieved while fiber fracture is avoided, is reduced as the matrix yield strength and creep resistance are increased (e.g. titanium aluminides and Ni-base superalloys). The selection of fiber and processing conditions is critical for these materials.
- 4) Fiber properties have a strong effect on damage. Depending on the matrix and process conditions, those least likely to be damaged during consolidation have either a high resistance to bending or are highly flexible. Resistance to bending is achieved by fibers with a large diameter. Flexibility is an attribute of small, compliant fibers which can suffer the deflections incurred during consolidation without failure. Most currently available fibers fall in the "rigidity" regime and damage is reduced by increasing their diameter (reducing their flexibility).
- 5) Reducing the monotape's surface roughness (particularly the variability in asperity height) even by modest amounts can greatly reduce fiber damage. Improved control of the plasma deposition process to reduce roughness offers the potential to eliminate fiber fracture during consolidation, even for creep resistant materials.

## Acknowledgements

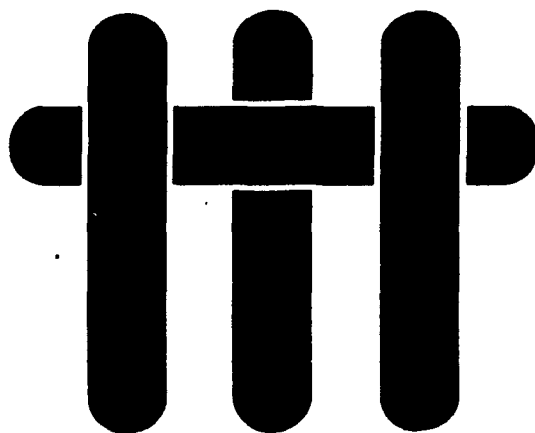
The authors wish to thank D.G.Backman and E.S.Russell of General Electric Aircraft Engines for helpful discussions of the fiber damage problem. We also gratefully acknowledge the support for this work by an ARPA/NASA contract (No. NAGW-1692) managed by W.Barker(ARPA) and R.Hayduk(NASA) and a grant from ARPA/ONR from the UCSB-URI (No. 5158-91) directed by Prof. A.Evans and managed by W.Coblentz(ARPA) and S.Fishman(ONR).

## REFERENCES

1. R.A.MacKay, P.K.Brindley and F.H.Froes, JOM, 43(5), 23 (1991).
2. J.Doychak, JOM, 44(6), 46 (1992).
3. J.R.Stephens and M.V.Nathal, "Status and Prognosis for Alternative Engine Materials" in: *Superalloys 1988*, ed., D.N.Duhl, TMS (Warrendale, PA), p.183 (1988).
4. P.D.Nicolaou, H.R.Piehler and S.Saigal, "Finite Element Analysis of the Consolidation Behavior of Composite Materials Using the Foil/Fiber/Foil Technique" in: *Concurrent Engineering Approaches to Materials Processing*, eds., A.J.Paul, S.N.Dwivedi and F.R.Dax, TMS (Warrendale, PA), p.247 (1993).
5. P.K.Brindley, "SiC Reinforced Aluminide Composites" in: *High Temperature Ordered Intermetallic Alloys II*, eds., N.S.Stoloff, C.C.Koch, C.T.Liu and O.Izumi, MRS (Pittsburgh, PA), 81, p.419 (1987).
6. D.A.Hardwick and R.C.Cordi, "Intermetallic Matrix Composites by Physical Vapor Deposition" in: *Intermetallic Matrix Composites*, eds., D.L.Anton, P.L.Martin, D.B.Miracle and R.McMeeking, MRS (Pittsburgh, PA) 194, p.65 (1990).
7. E.S.Russell, "Thermomechanical Effects in Plasma-Spray Manufacture of MMC Monotapes" in: *Thermal Structures and Materials for High Speed Flight*, ed., E.A.Thornton, *Progress in Astronautics and Aeronautics* 140, AIAA (Washington D.C.), p. 437 (1992).
8. D.M.Elzey and H.N.G.Wadley, *Acta metall. mater.* 41, 2297 (1993).
9. J.F.Groves, D.M.Elzey and H.N.G.Wadley, *Acta metall. mater.*, 1993 (Submitted).
10. J.-M. Yang and S.M.Jeng, JOM, 44(6), 52 (1992).
11. J.-M. Yang, S.M.Jeng and C.J. Yang, *Mat. Sci. & Eng.*, A138, 155 (1991).
12. D.G.Meyer, R.Vancheeswaran and H.N.G.Wadley, "Application of Micromechanical Models for On-Line Control of MMC Consolidation" in: *Model-Based Design of Materials and Processes*, eds., E.S.Russell, D.M.Elzey and D.G.Backman, TMS (Warrendale, PA), p.163 (1993).
13. L.M.Hsiung, W.Cai and H.N.G.Wadley, *Mat. Sci. & Eng.*, A125, 295 (1992).
14. L.M.Hsiung, W.Cai and H.N.G.Wadley, *Acta metall. mater.*, 40(11), 3035 (1992).
15. T.A.Kuntz, H.N.G.Wadley and D.G.Black, *Metall. Trans. A* 24, 1117 (1993).
16. H.Hough, J.Demas, T.O.Williams and H.N.G.Wadley, submitted to *Acta metall. et mater.* (1994).
17. R.Gampala, D.M.Elzey and H.N.G.Wadley, *Acta metall. mater.* (1993). Submitted.
18. K.L.Johnson, *Contact Mechanics*, Cambridge Univ. Press, Cambridge, p.412 (1985).
19. C.W.MacGregor, *Mechanical Properties of Materials* in: *Marks Standard Handbook for Mechanical Engineers*, 8<sup>th</sup> Edition, eds. Theodore Baumeister et al, McGraw-Hill, New York, p.5-24 (1978).
20. P.A.Siemers, R.L.Mehan and H.Moran, JOM, 23, 1329 (1988).
21. J.F.Groves, M.S.Thesis, University of Virginia, p.32 (1992).
22. B.Widom, *J. Chem. Phys.* 44, 3888 (1966).
23. Wolfram Research, Inc., *Mathematica*, vers. 2.2, publ. by Wolfram Research, Inc (Champaign, IL), 1992.
24. S.J. Balsone, *Proc. Conf. on Oxidation of High Temperature Intermetallics*, eds. T.Grobstein and J.Doychak, TMS (Warrendale, PA), p.219 (1989).
25. D.A. Koss et al, *Proc. Conf. on High Temperature Aluminides and Intermetallics*, eds. S.H.Whang et al, TMS (Warrendale, PA), p.175 (1990).
26. J.M. Larsen et al, *Proc. Conf. on High Temperature Aluminides and Intermetallics*, eds. S.H.Whang et al, TMS (Warrendale, PA), p.521 (1990).
27. D.A. Lukasak, *Metall. Trans. A* 21, 135 (1990).
28. M.G. Mendiratta and H.A. Lipsitt, *J. Mat. Sci.* 15, 2985 (1980).
29. R.W. Hayes, *Scripta Metall.* 23, 1931 (1989).
30. W. Cho et al, *Metall. Trans. A* 21, 641 (1990).
31. P.E.Cantonwine and H.N.G.Wadley, *Comp. Eng.* (1994). In Press.
32. W.A.Curtin, *J.Am.Ceram.Soc.* 74, 2837 (1991).
33. W.A.Curtin, *J.Mech.Phys.Solids* 41, 217 (1993).

34. British Petroleum, Product Data Sheet, BP Metal Composites, Ltd., Farnborough, Hampshire, U.K.
35. P.E.Cantonwine, M.S. Thesis, University of Virginia, p.11 (1993).
36. Saphikon, Product Data Sheet, Saphikon, Inc., Milford, NH.
37. P.L. Martin, M.G. Mendiratta and H.A. Lipsitt, Met. Trans. A 14, 2170 (1983).
38. H.A. Lipsitt, D. Shechtman and R.E. Schafrik, Met. Trans. A 6, 1991 (1975).
39. T. Takahashi and H. Oikawa, Mat. Res. Soc. Symp. Proc. 133, p.699. MRS, Pittsburgh, Pa (1989).
40. C.J. Smithell, Metals Reference Book, 5<sup>th</sup> ed., pp.14-21. Butterworths, Boston, Ma (1961).
41. M.J. Donachie, Jr., Titanium A Technical Guide, p.173. ASM, Metals Park, Ohio (1988).
42. E.W. Collings, The Physical Metallurgy of Ti Alloys, pp.111-21-. ASM, Metals Park, Ohio (1984).
43. C.R. Brooks, Heat Treatment, Structure and Properties of Nonferrous Alloys, pp.361-376. ASM, Metals Park, Ohio (1982).
44. W.C. Harrigan, Jr., Met. Trans. A 5, 565 (1974).
45. J. Pilling et al, Metal Science 18, 117 (1984).
46. Superalloys II, edited by. C.T.Sims et al, p.595. John Wiley & Sons, New York (1987).
47. H.Riedel, Fracture at High Temperatures, p.390. Springer-Verlag, New York (1987).
48. R.W.Evans and B.Wilshire, Introduction to Creep, p.62. Bourne Press Ltd., Bournemouth, UK (1993).

# M A T E R I A L S



## **EFFECTS OF COMPOSITE PROCESSING ON THE STRENGTH OF SAPPHIRE FIBER-REINFORCED COMPOSITES**

by

J.B. Davis, J. Yang and A.G. Evans  
Materials Department  
College of Engineering  
University of California, Santa Barbara  
Santa Barbara, California 93106-5050

## ABSTRACT

The current interest in tough, high-temperature materials has motivated fiber coating development for sapphire fiber-reinforced alumina composites. For this system, it has been demonstrated that the interfacial properties can be controlled with coatings which can be eliminated from the interface subsequent to composite consolidation. However, these fugitive coatings can contribute to the high temperature strength degradation of sapphire fibers. Such degradation, which compromises the composite strength and toughness, is the focus of the current investigation. It has been observed that, in some cases, by selecting appropriate composite processing conditions, such effects can be minimized. But overcoming fiber strength loss remains an important issue.



## 1. INTRODUCTION

The current limitations to the advancement of ceramic matrix composites are associated with the development of high strength, oxidation and creep resistant fiber-reinforcements and the control of the interfacial debonding and sliding behaviors. One approach to reinforcements has been to develop single crystal oxide fibers. The most thoroughly studied of these is sapphire. One promising class of coating is fugitive,<sup>1-2</sup> whereby the coating is removed from the interface subsequent to composite consolidation in order to leave a gap between the fiber and matrix. Carbon and molybdenum are examples of such coatings. The coating thickness and resulting gap size are used to manipulate the interfacial sliding resistance. However, the coating chemistry and thickness can affect the surface morphology of the fibers during either composite processing or subsequent exposures to high temperatures. This can lead to pronounced changes in fiber strengths. Such effects are the focus of this investigation.

This study has five essential elements. (i) Uncoated fibers were heat treated and their strengths measured in order to classify inherent strength degradation mechanisms. (ii) Coated fibers were given similar heat treatments and tested to establish additional degradation phenomena that may arise. (iii) Fibers with thick fugitive coatings of C and Mo were introduced into an alumina matrix by hot pressing. The fibers were removed by using the fugitive character of the coating. The withdrawn fibers were tested. These tests identified new degradation mechanisms that may operate with this coating. (iv) Unidirectional composites were fabricated with several coating thicknesses. The tensile properties of the composite were measured and fiber push-out tests performed. These tests indicated whether there are other strength loss phenomena associated with composite consolidation. They also allowed correlation to be made between composite behavior, the fiber strength and the interface debonding/sliding resistance. (v) The fiber

morphological changes were examined in order to provide an understanding of the mechanisms involved.

## **2. EXPERIMENTAL PROCEDURES**

### **2.1 Fiber Strength Tests**

The fibers were obtained from a single spool of Saphikon sapphire fiber (diameter  $\sim 130\text{ }\mu\text{m}$ ). Their tensile strengths were measured for several fiber conditions by using a commercially available fiber testing machine\* and a one-inch gauge length. The first set was tested in the as-received state. The second was washed in cold water followed by acetone and ethanol, and then subjected to the series of heat-treatments summarized in Table I. The remaining two sets were first washed and then coated with either Mo or C to a thickness of  $\sim 10\text{--}15\text{ }\mu\text{m}$ . These were hot pressed into a high purity alumina matrix using the conditions specified in Table I. After hot pressing, the composites were heat treated at  $1100^\circ\text{C}$  in air for  $\sim 2\text{ h}$  to remove the coatings from the interfaces. The fibers were extracted from the matrix and their strengths were measured directly.

Fiber strength data sets were comprised of  $\sim 20$  measurements. While this set size is too small to give an accurate determination of the fiber strength distribution parameters, it is sufficient to establish definitive trends in the median fiber strength.<sup>3,4</sup>

### **2.2 Composite Specimen Fabrication**

Unidirectional alumina matrix composites containing Mo coated sapphire fibers were produced for correlating composite behavior with the properties of the fibers and interfaces. Coatings with three thicknesses ( $0.2$ ,  $0.7$  and  $1.4\text{ }\mu\text{m}$ ) were used. Composites were produced by hot isostatic pressing (HIPing). These have been made by first

---

\* Micropull Sciences, Thousand Oaks, California

fabricating a preform comprising coated fibers within a slurry of the matrix material. These composites were sealed in an evacuated niobium can. Consolidation was achieved at a pressure of 30 MPa at 1350°C for 30 min (Fig. 1). Dog-bone shaped tensile specimens were diamond machined from the consolidated composite and the coatings were removed from the interface by heat-treating in air at 1150°C for 50 h.

### 2.3 Microstructural Characterization

Scanning electron microscopy (SEM) techniques with energy dispersive X-ray analysis were used to identify the strength limiting flaws for each data set. In addition, the morphologies of heat-treated fibers were examined in a field emission scanning electron microscope (JEOL 6300F) in order to classify and compare various surface and fracture features.

The interfaces in the composites were examined by transmission electron microscopy (TEM). For this purpose, electron transparent foils were prepared as described elsewhere. After tensile testing, the fiber pull-out length distributions were measured from scanning electron micrographs and the surface features of the fibers characterized. In addition, interactions between the fibers and the matrix were also classified.

### 2.4 Composite Testing

Tension tests were performed on the composite in a fixture located within a scanning electron microscope (Fig. 2). The forces were measured from a load cell. The behavior at small strains was monitored from strain gauges affixed to the specimen. At larger strains, the specimen displacement was measured with an LVDT. These strain data were compared with photomicrographic measurements.

The interfacial sliding resistances were measured by using the fiber push-through technique.<sup>6</sup>

### 3. FIBER STRENGTHS

The fibers in the as-received condition were found to have a median strength,  $\bar{S} \approx 2.7$  GPa, and a Weibull modulus,  $m \approx 6.5$  (Fig. 3a), consistent with values reported in the literature.<sup>5</sup> After heating the washed, uncoated fibers to successively higher temperatures (1250°C, 1350°C and 1450°C), there were small, though significant, reductions in either the mean strength,  $\bar{S}$ , or the Weibull modulus,  $m$ , (Fig. 3b, Table I). Conversely, extracted fibers originally coated with Mo showed considerable strength loss, at all heat-treatment temperatures (Fig. 3b). The fibers originally coated with carbon exhibited a smaller reduction in median strength but had the most substantial strength *variability*, reflected in the highest coefficient of variation and the low Weibull modulus ( $m \approx 2.6$ ).

### 4. FIBER MORPHOLOGY

Upon heat treatment, the fiber morphology was found to be strongly influenced by both diffusional effects and chemical reactions, especially in the presence of either fiber coatings or a composite matrix. There are four basic phenomena (Fig. 4), each exemplified by the observations presented below. (i) Surface diffusion causes fiber facetting, even in isolated fibers. (ii) Thin polycrystalline coatings, when chemically inert (no reaction products), are morphologically unstable and develop holes. Equilibrium at the hole edges then motivates surface diffusion and induces the formation of ridges on the fibers. (iii) Chemical reactions occur between the coating and the fiber resulting in fiber surface damage. This may produce either solid or gaseous reaction products. (iv) After a coating has either become discontinuous during composite consolidation or has been removed by oxidation, the matrix may sinter to the

fiber. This results in localized bonding, causing matrix grains to remain attached to the fiber during pull-out, upon composite testing.

#### **4.1 Uncoated Fibers**

The fibers display sinusoidal diameter modulations along their length with characteristic wavelengths and amplitudes, described elsewhere.<sup>6</sup> Flaws observed in the as-received fibers were primarily associated with porosity. Pores develop during fiber growth and have been observed within the fibers and at the fiber surfaces (Fig. 5). The strength range is consistent with calculations for cylindrical rods containing cracks having the same dimensions as the pores<sup>7</sup> (Fig. 6).

The surface features were altered by high temperature heat-treatments. The fibers facet (Fig. 7), illustrating the inherent morphological instability of single crystal fibers. Frequently, local surface damage was evident resulting from chemical reactions (Fig. 8a). These sites usually correlate with failure origins and account for the strength loss. Energy dispersive X-ray spectroscopy measurements identified Si and Mg at these sites (Fig. 8b). Two likely sources of contamination include the incomplete removal of the fiber sizing and reactions with inorganic contaminants that condense onto the fiber surfaces during heat treatment in the air furnace. Such contaminant reactions are avoidable upon encapsulation of the fibers and are of moderate practical concern.

#### **4.2 Carbon Coated Fibers**

The heat treated carbon coated fibers displayed surface regions indicative of a chemical reaction between the coating and the fiber, localized near fiber ends and at locations where the coatings were discontinuous. The reaction product, identified by X-ray analysis as  $Al_4C_3$ , severely degraded the fiber surface. The extent of reaction increased with temperature (Fig. 9). In addition, accentuated fiber facetting occurred near the reaction sites.

Thermodynamic calculations (Appendix I) indicate that alumina and C can react to form volatile aluminum suboxides at temperatures as low as 1100°C, at least when heat treatments are conducted in an open system.<sup>8-11</sup> The progress of these reactions requires a means of removing CO from the reaction site, consistent with the reactions being preferentially located at the fiber ends and at coating discontinuities. This tendency for localized attack is presumably responsible for the strength *variability* of the fibers. Some fibers were relatively undamaged in the gauge section and exhibit strengths similar to the uncoated fibers heat treated to the same temperature. Others were damaged in the gauge length associated with areas where the coating was discontinuous.

#### 4.3 Mo Coated Fibers

Observations of the extracted Mo coated fibers reveal substantial changes in surface morphology. At least two phenomena contribute. The first involves the breakup of the polycrystalline Mo coating.<sup>12,13</sup> The Mo/Al<sub>2</sub>O<sub>3</sub> interface then forms ridges on the surface of the sapphire, at the Mo grain edges. This process proceeds by *surface and interface diffusion*. The ridges are visible when the coating is chemically etched from the fibers (Fig. 10). They heighten as the heat treatment temperature increases. Upon removing the coating, further heat treatment causes the ridges to become unstable. The morphology then resembles fiber facetting, but with an additional surface roughness that originates with the ridges.

A second potential phenomenon involves the dissolution of alumina in Mo. If it occurs, the same morphological changes discussed above would proceed, but the kinetics could be more rapid than those for interface diffusion. Such dissolution has been well documented for Nb/Al<sub>2</sub>O<sub>3</sub> interfaces<sup>14</sup> and has also been reported to occur for Mo/Al<sub>2</sub>O<sub>3</sub> at temperatures similar to those used in this study.<sup>15</sup> However, Mo dissolution not been verified, because high resolution TEM specimens are difficult to produce without interface debonding.

The large strength reduction found for the Mo coated fibers is presumed to relate to the ridges and troughs formed by diffusion or dissolution. It has not been possible to quantify the measured strengths, because an appropriate surface flaw model has not been developed. However, the general trend toward a lower strength with increased ridge height, as the temperature increases, suggests a model based on the stress intensification caused by ridges and troughs.

#### 4.4 Fibers Within A Composite

Thin (0.2 and 0.7  $\mu\text{m}$ ) Mo fiber coatings do not remain continuous after composite consolidation (Fig. 11). Consequently, submicron thick Mo fiber coatings permit the fibers to sinter to the matrix, during HIPing, in those areas where the coating has become discontinuous. The thicker (1.4  $\mu\text{m}$ ) Mo coatings are continuous (Fig. 11), but the thickness is non-uniform. For these coatings, local sintering of the fiber to the matrix does not occur upon HIPing, but can still occur *after the coating has been removed*. In such cases, upon debonding, some matrix grains remain attached to the fiber, with associated ridge formation and fiber damage (Fig. 12). Chipping of the fibers can also occur (Fig. 13). Such visual evidence of fiber, matrix sintering allows measurement of the sintered regions to give the area fraction of fiber bonded to the matrix, designated  $f_A$  (Table II). In some locations, additional features are evident, manifest as large ridges and troughs between neighboring sintered sites (Fig. 14).

Sintered areas resist debonding and increase the interfacial fracture energy in proportion to the area fraction of bonding. Moreover, when the matrix sinters to the fibers, the resulting damage (Figs. 12, 13) reduces the fiber strength. The relatively large depth of these damaged regions compared with the size of the ridges and troughs found for the extracted Mo coated fibers (Fig. 10) suggests that the strengths may be substantially lower in the HIPed composites. The magnitude of the additional strength reduction is implied from analyses conducted below.

Localized sintering would also induce residual stress upon cooling, because of the thermal expansion mismatch between c-axis sapphire and polycrystalline  $\text{Al}_2\text{O}_3$ . Such stresses should be of order 100 MPa and may influence trough formation (Appendix II).

## 5. COMPOSITE PROPERTIES

Composites with Mo coated fibers were tested after removing the Mo. All failed from a single dominant crack because of the low fiber volume fractions ( $f < 0.20$ ). However, the fracture resistance and the extent of fiber pull-out were very different for the three coating thicknesses (Table II). The specimens with thin ( $0.2 \mu\text{m}$ ) gaps had low toughness and exhibited co-planar fracture (Fig. 15a), with no pull-out. Conversely, appreciable pull-out was evident for the two larger interfacial gaps (Figs. 15b,c). Moreover, the material with the  $1.4 \mu\text{m}$  interface gaps exhibited substantially more pull-out (average pull-out length,  $\bar{h} \sim 640 \mu\text{m}$ ) than the material with the  $0.7 \mu\text{m}$  gaps ( $\bar{h} \sim 90 \mu\text{m}$ ). A typical load-displacement curve for these materials illustrates the fiber pull-out contribution to the composite fracture resistance (Fig. 16). The magnitude of the fracture dissipation is  $\sim 40 \text{ k J m}^{-2}$ . The associated ultimate tensile strengths (UTS), summarized in Table I indicate a similar trend, with the larger gap giving a considerably higher UTS.

The corresponding push-out behaviors are summarized in Fig. 17. The composite with the thinnest coating did not exhibit push-out. The inability of this interface to slide and pull-out results from sintering. Conversely, sliding was induced in the other two composites. Both materials exhibited essentially the same sliding resistance. This similarity suggests that sliding is dominated by local variations in the coating thickness, rather than by the average gap width.



## 6. ANALYSIS

### 6.1 Method and Assumptions

An attempt is made to interpret the above composite behavior in terms of the fiber strength degradation phenomena, discussed above, in conjunction with related trends in interface properties. For this purpose, three basic assumptions are made and used together with models of interface debonding and sliding, as well as fiber pull-out. It is assumed that, when the fiber sinters to the matrix, debonding occurs when the energy release rate reaches the mode I fracture energy of the fine-grained alumina polycrystals ( $\Gamma_c = 25 \text{ Jm}^{-2}$ ). The debond energy  $\Gamma_i$  is then,

$$\Gamma_i = f_A \Gamma_c \quad (1)$$

with  $f_A$  given in Table II. It is also assumed that a sliding zone exists behind the debond, subject to a constant sliding resistance,  $\tau$ . In this case, the debond length,  $\ell$ , at stress,  $\sigma$ , is<sup>16</sup>

$$\ell = \frac{R(1-f)}{2\tau f}(\sigma - \sigma_i) \quad (2)$$

where  $R$  is the fiber radius,  $f$  is the fiber volume fraction and  $\sigma_i$  is the debond stress given by,

$$\sigma_i = \frac{1}{c_1} \sqrt{E\Gamma_i/R} - \sigma^T \left( \frac{c_2}{c_1} \right) \quad (3)$$

where  $\sigma^T$  is the axial misfit stress caused by thermal expansion mismatch and  $c_1$  and  $c_2$  are constants defined by Hutchinson and Jensen.<sup>16</sup>

Finally, it is assumed that fiber failure occurs *within the debond zone*, in accordance with weakest link statistics. The fiber pull-out length  $\bar{h}$  should then be related to  $\ell$ . The relationship between  $\ell$  and  $\bar{h}$  is considered to be similar to that derived by Curtin,<sup>17</sup>

$$\bar{h} = \ell \lambda' (m) \quad (4)$$

where  $\lambda'$  is a function of the Weibull modulus of the fibers. Equation (4) must be a lower bound for the pull-out length when a non-zero debond energy obtains.

## 6.2 Interpretation

The preceding formulae allow an understanding and rationalization of the observation that composites with the 0.7  $\mu\text{m}$  gap have smaller pull-out lengths than materials with a 1.4  $\mu\text{m}$  gap, but yet have similar sliding resistance. There are two factors involved. (i) A smaller debond length is expected with the narrower gap, because of the larger debond resistance induced by the more extensive fiber/matrix sintering. Slip is limited by the debond length. (ii) Fiber weakening occurs when matrix grains sinter to the fibers and create damage sites (Figs. 12, 13).

The measured UTS,  $\sigma_u$ , may be inserted into Eqn. (2) and, upon using Eqns. (1) and (3), the debond lengths at failure may be estimated. The results (Table II) verify that a considerably larger debond length develops for the composite with the wider interface gap. Moreover, the proportionality constant,  $\lambda'$ , between the pull-out length,  $\bar{h}$ , and the debond length  $\ell$  (Eqn. 4) is similar for both materials.

The strengths of the fibers in the composite  $S_c$  is of order,

$$S_c \approx \sigma_u / f \quad (5)$$

These strengths (Table II) are considerably lower than those measured on the extracted fibers with the thick coatings. It is implied that the strengths have been markedly degraded by sintering of the matrix to the fibers. Furthermore, because  $S_c$  represents the strength measured at a gauge length of order the debond length,<sup>17</sup> even smaller values would obtain at a 1" gauge length.

## 7. SUMMARY

Single crystal sapphire fibers have been suggested as a high strength reinforcement for ceramic matrix composites. Interfaces have been developed based on a fugitive coating concept which satisfies the fiber debonding and sliding conditions for toughness enhancement. However, the strengths of the fibers are reduced by the presence of the coatings and are further reduced upon forming a composite. The mechanisms for the strength loss of coated fibers include: i) gas phase reactions with the coating which produce aluminum sub-oxides and etch the fibers ii) chemical reactions which form solid state reaction products and iii) facetting or ridging by surface diffusion. Carbon coated fibers are susceptible to the first two modes of degradation. However, it should be possible to minimize these effects by selecting composite processing conditions that provide a controlled CO/CO<sub>2</sub> atmosphere. For the Mo coatings, the degradation mechanisms are primarily of the third type and more difficult to eliminate.

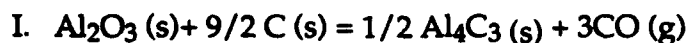
Additional fiber strength reduction results after composite processing with thin coatings, due to localized sintering of the matrix to the fiber. Such bonding affects the surface of the fibers. It also imposes a residual stress, which may further alter the surface morphology. It is believed that this strength loss could be minimized by

manipulating the matrix microstructure and chemistry (by incorporating segregants) to reduce the sintering potential.

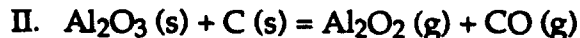
## APPENDIX I

### Thermodynamic Calculations

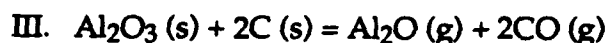
For alumina to be reduced by carbon during diffusion bonding, a maximum pressure for the reaction system can be determined. The chemical reactions of interest and their standard free energies,\*  $\Delta G^\circ$  (J/ mole), per mole of CO, are as follows:



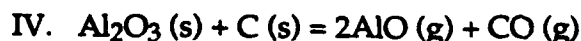
$$\Delta G^\circ = 1260904.5 - 575.5 T$$



$$\Delta G^\circ = 1141595 - 389.3 T$$



$$\Delta G^\circ = 1262879 - 551.7 T$$



$$\Delta G^\circ = 1600515 - 522.2 T$$



$$\Delta G^\circ = 1929403 - 799.7 T$$



$$\Delta G^\circ = -111700 - 87.65 T$$



$$\Delta G^\circ = -564800 + 173.6 T \quad (\text{A1})$$

where T is the temperature. Reaction I was calculated to have the lowest free energy for the temperature range of interest (1250°C–1450°C). Furthermore, since this reaction

---

\* Thermodynamic data are taken from references 8-11.

involves the formation of one gaseous species, the equilibrium CO partial pressure can be determined as a function of temperature.\* The equilibrium CO partial pressure is calculated (Table A.1), using

$$P_{\text{co}} = \exp\left[\frac{\Delta G^\circ}{3RT}\right] \quad (\text{A2})$$

For Reaction I to proceed, the CO partial pressures in the system must not exceed the equilibrium values. Such pressures cannot develop in the vacuum system used for the present experiments, indicating that the reaction is likely to occur.

With  $P_{\text{co}}$  specified at its equilibrium value, the partial pressures of the aluminum suboxides can be determined for Reactions II to V (Table AII). From these results, it is apparent that both  $\text{Al}_2\text{O}$  and Al have significant partial pressures under conditions that also permit the formation of  $\text{Al}_4\text{C}_3$ . The formation of these volatile phases could occur by reaction with CO in regions adjacent to the C coating, consistent with the observation of rapid facetting near discontinuities in the coating (Fig. 9).

---

\* It is assumed that the buffer system described by reactions VI and VII does not dictate the CO partial pressure in the system.

## APPENDIX II

### Crack-Like Surface Instabilities

Recent analyses have shown that surface perturbations can grow into crack-like flaws, by surface diffusion, in bodies subject to stress.<sup>19</sup> The flux is provided by the strain energy contribution to the chemical potential, which can exceed the surface curvature term, at sufficiently high stress. The consequence is that there is a critical stress,  $\sigma_c$ , above which such flaws can develop. The surface troughs observed in some of the fibers may be caused by this phenomenon. In order to explore this possibility, analysis of the critical stress is performed.

The basic requirement for the development of crack-like flaws is that the change in strain energy,  $dU$ , upon crack extension,  $da$ , exceed the increase in surface energy,  $dU_s$ , as in the original Griffith analysis. This condition defines the critical stress. For an array of surface flaws of depth,  $a$ , and separation,  $b$ , the energy release rate at stress,  $\sigma$ , is<sup>7</sup>

$$\frac{dU}{da} = \left( \frac{\sigma^2 \pi b}{E} \right) F(a/b) \quad (B1)$$

where the function  $F(a/b)$  is plotted on Fig. A1. The corresponding change in surface energy is

$$\frac{dU}{da} = 2\gamma_s \quad (B2)$$

where  $\gamma_s$  is the surface energy per unit area. Hence, for flaw growth to be possible,

$$dU/da \geq dU_s/da \quad (B3)$$

resulting in a critical stress,

$$\sigma_c = \sqrt{\frac{2E\gamma_s}{\pi b} F(a/b)} \quad (B4)$$

For flaws with depths in the micron range to extend in sapphire, Eqn. (A4) indicates that stresses of order 500 MPa are required (Fig. A2). While such stresses are unlikely, the mechanism has not been ruled out because of the morphological similarity of the observed trough with the profile predicted for diffusive crack growth.



**TABLE I**  
**Fiber Strength Data**

Heat Treatment*		Median Strength (GPa)	Coefficient of Variation	Weibull Modulus
As-Received		2.9	0.13	6.5
Uncoated	1250°C	2.6	0.10	9.8
	1350°C	2.0	0.15	6.8
	1450°C	2.1	0.18	5.8
Mo Coated: Extracted	1250°C	1.9	0.16	6.2
	1350°C	1.4	0.32	2.2
	1450°C	1.0	0.33	3.2
C Coated: Extracted	1450°C	1.6	0.38	2.6

\* With the exception of the As-Received set, all fibers were heated in an air furnace at 1150°C for 2 hours subsequent to the heat treatments shown above.

**TABLE II**

**Constituent Properties of Composite**

Coating Thickness ( $\mu\text{m}$ )	Measured				Inferred		
	$\tau$ (MPa)	$\bar{h}$ ( $\mu\text{m}$ )	Area Fraction of Fiber Bonded to Matrix $f_A$	UTS (MPa)	$S_c$ (GPa)	$\ell$ ( $\mu\text{m}$ )	$\lambda'$ (m)
0.7	17	90	$\sim 0.05$	22	0.1	250	0.3
1.4	15	640	$\sim 0.01$	79	0.4	1000	0.7

**TABLE AI**

**Equilibrium Partial Pressure of CO for Reaction I**

T (°C)	pCO (atm)
1250	$4.0 \cdot 10^{-5}$
1350	$3.1 \cdot 10^{-4}$
1450	$1.9 \cdot 10^{-3}$

TABLE AII

Partial Pressures of Gas Phases for the Aluminum Oxide/Carbon System\*

T (°C)	pCO (atm)	pAl <sub>2</sub> O <sub>3</sub> (atm)	pAl (atm)	pAl <sub>2</sub> O (atm)	pAlO (atm)
1250	4.0*10 <sup>-5</sup>	3.0*10 <sup>-15</sup>	2.0*10 <sup>-6</sup>	1.6*10 <sup>-6</sup>	2.3*10 <sup>-12</sup>
1350	3.1*10 <sup>-4</sup>	1.3*10 <sup>-13</sup>	1.2*10 <sup>-5</sup>	1.4*10 <sup>-5</sup>	4.0*10 <sup>-11</sup>
1450	1.9*10 <sup>-3</sup>	2.8*10 <sup>-12</sup>	5.0*10 <sup>-4</sup>	1.3*10 <sup>-4</sup>	5.0*10 <sup>-10</sup>

---

\* These results are in reasonable agreement with literature values. (Ref.: Sprague in Ref. of High Temp. Sys. vol. 1., ed. G.S. Bahn, Gordon & Breach (1964).

## REFERENCES

- [1] T. Mah, K. Keller, T.A. Parthasarathy and J. Guth, *Ceram. Eng. Sci. Proc.*, **12** [9-10] pp. 1802-15 (1991).
- [2] J.B. Davis, J.P.A. Löfvander, E. Bischoff, A.G. Evans and M.L. Emiliani, *J. Am. Ceram. Soc.*, **76** [5] 1249-57 (1993).
- [3] K. Trustrum, and A. De S. Jayatilaka, *J. Mat. Sci.*, **14** 1080-1084 (1979).
- [4] J.R. Porter, *MRS Symp. Proc.*, **273** 315-324 (1992).
- [5] E. Trembauer and R. Tressler, *HITEMP Conference Proceedings* (1992).
- [6] T.J. Mackin, J. Yang and P.D. Warren, *J. Am. Ceram. Soc.*, **75** [12] 3358-62 (1992).
- [7] H. Tada, P.C. Paris and C.R. Irwin, *The Stress Analysis of Cracks Handbook*, Del Research Corp., Pennsylvania (1973).
- [8] L.M. Foster, G. Long and M.S. Hunter, *J. Am. Ceram. Soc.*, **39** [1] 1-11 (1956).
- [9] D.R. Stull and H. Prophet, *JANAF Thermochemical Tables*, 2nd ed., NSRDS-NBS 37, U.S. Department of Commerce, Washington, D.C., 1971.
- [10] I. Barin and O. Knacke, *Thermochemical Properties of Inorganic Substances*, Springer-Verlag, New York, 1973.
- [11] I. Barin, O. Knacke, and O. Kubaschewski, *Thermochemical Properties of Inorganic Substances, Supplement*, Springer-Verlag, New York, 1977.
- [12] W.W. Mullins, *Journal of Applied Physics*, **28** [3] 333-339 (1957).
- [13] K.T. Miller, F.F. Lange and D.B. Marshall, *Mat. Res. Soc. Proc. Sym. on Ultrastr. Proc.*, **121** [3] 823-30 (1988) and *J. Mater. Res.*, **1** [5] 151-60 (1990).
- [14] M. Rühle and A.G. Evans, *Materials Science and Engineering*, **A107** 187-197 (1989).
- [15] G.H.M. Gubbels, *Materials Science and Engineering*, **A135** (1991) 135-139.
- [16] J. W. Hutchinson and H. M. Jensen, *Mech. Mtls.*, **9** 139 (1990).
- [17] W.A. Curtin, *J. Am. Ceram. Soc.*, **74** [11] 2837-45 (1991).
- [18] M.Y. He, A. Bartlett, A.G. Evans and J.W. Hutchinson, *J. Am. Ceram. Soc.*, **74** [4] 767-71 (1991).

- [19] W.H. Yang and D.J. Srolovitz, "Crack-Like Surface Instabilities in Stressed Solids," *Phys. Rev. Lett.*, in press.

## FIGURE CAPTIONS

- Fig. 1. Cross section of composite produced by HIPing.
- Fig. 2. Composite tensile test geometry for *in situ* studies in the SEM.
- Fig. 3. a) Fiber strength data plotted as the cumulative probability of fracture.  
b) Effect of heat treatment on median strengths and standard deviation.
- Fig. 4. Schematic representations of the surface morphology changes found to occur when coated sapphire fibers are heat treated.
- Fig. 5. Pores observed on the surface of a sapphire fiber.
- Fig. 6. Fiber strength predictions obtained upon assuming that the porous behaviors are penny-cracks. The fracture energy for sapphire was assumed to be  $15 \text{ Jm}^{-2}$ . Typical pore diameters are  $\sim 1 \text{ }\mu\text{m}$ .
- Fig. 7. Facets observed on the surfaces of uncoated, heat treated fibers.
- Fig. 8. a) Surface damage was observed on uncoated, heat-treated fibers near the failure plane. A chemical reaction has occurred between the fiber and the contaminant. b) The reaction site examined by EDS, reveals Si and Mg.
- Fig. 9. The fiber surface degradation (near the coating edge) for the carbon coated fibers increases with the heat-treatment temperature. a) Surface features of a fiber heated in vacuum for 2 h at  $1250^{\circ}\text{C}$ . b) Surface features of a fiber heated in vacuum for 2 h at  $1350^{\circ}\text{C}$ . c) Surface features of a fiber heated in vacuum for 2 h at  $1450^{\circ}\text{C}$ .
- Fig. 10. Ridges on the sapphire surface observed when Mo coated fibers were heat treated. The coating has been chemically etched from the fiber surface.
- Fig. 11. TEM micrographs reveal that a)  $0.7 \text{ }\mu\text{m}$  thick Mo coatings do not remain continuous during HIPing. b)  $1.4 \text{ }\mu\text{m}$  thick Mo coatings are continuous.
- Fig. 12. A view of a section of the fiber surface after pull-out. Matrix grains which sinter to the fiber remain attached.

Fig. 13. Surface grooves observed on sapphire fibers in HIPed composites, after fiber pull-out. Also evident are the patches that sintered and then debonded.

Fig. 14. Sliding between the matrix and fiber during pull-out degrades the fiber surface by forming a chip.

Fig. 15. a) Extensive bonding between the fiber and matrix led to co-planar fracture of the composite produced with 0.2  $\mu\text{m}$  thick gaps.

b) Composites produced with the 0.7  $\mu\text{m}$  thick coatings exhibited moderate fiber pull-out.

c) The greatest extent of fiber pull-out was found for the composites produced with 1.4  $\mu\text{m}$  thick coatings.

Fig. 16. Load-displacement curve for composite produced with 1.4  $\mu\text{m}$  thick interface gaps reveals contribution to crack growth resistance from fiber pull-out. The corresponding energy dissipation is 40  $\text{kJm}^{-2}$ .

Fig. 17. Shear resistance of interface measurements by fiber push-out.

Fig. A1 The strain energy density function for an array of surface cracks.

Fig. A2 The critical stress required for deepening of surface troughs by surface diffusion.



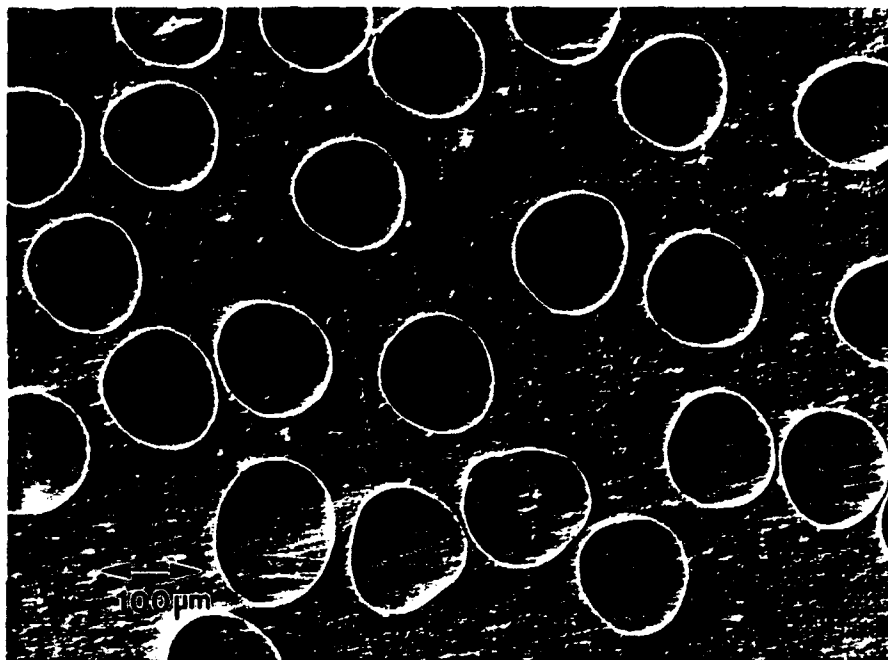


Figure 1

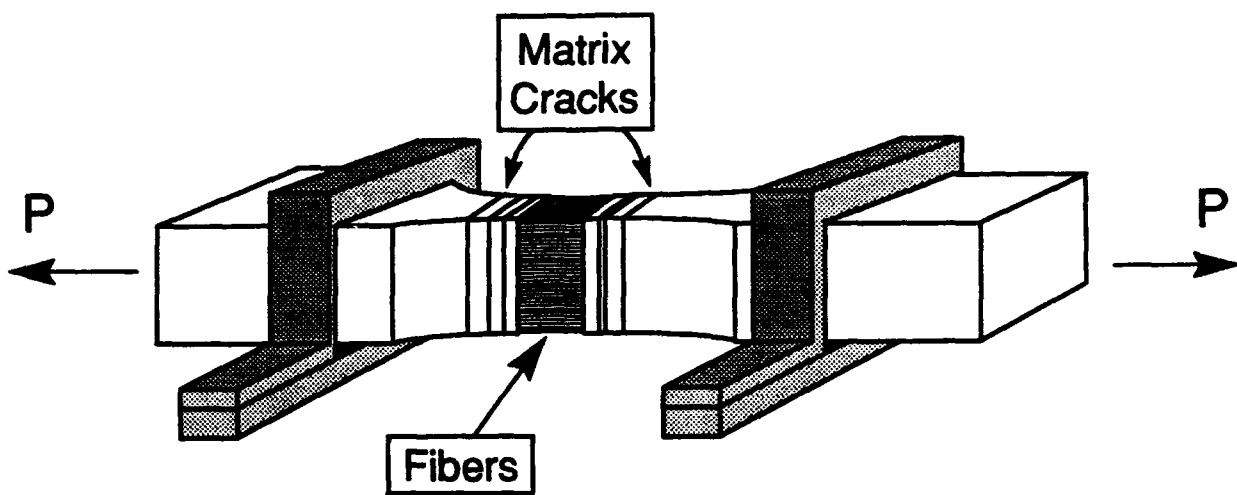


Figure 2

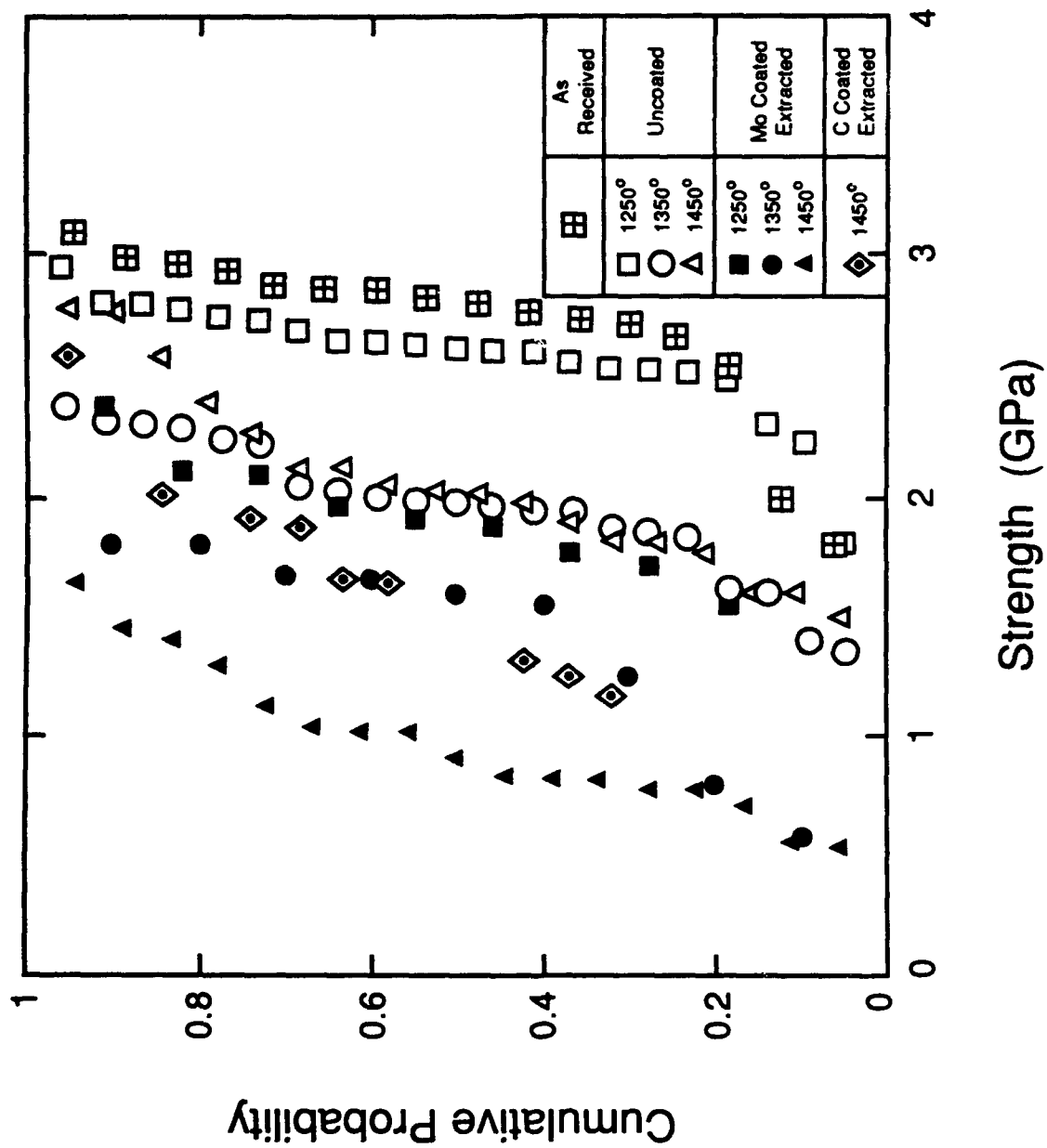


Figure 3a

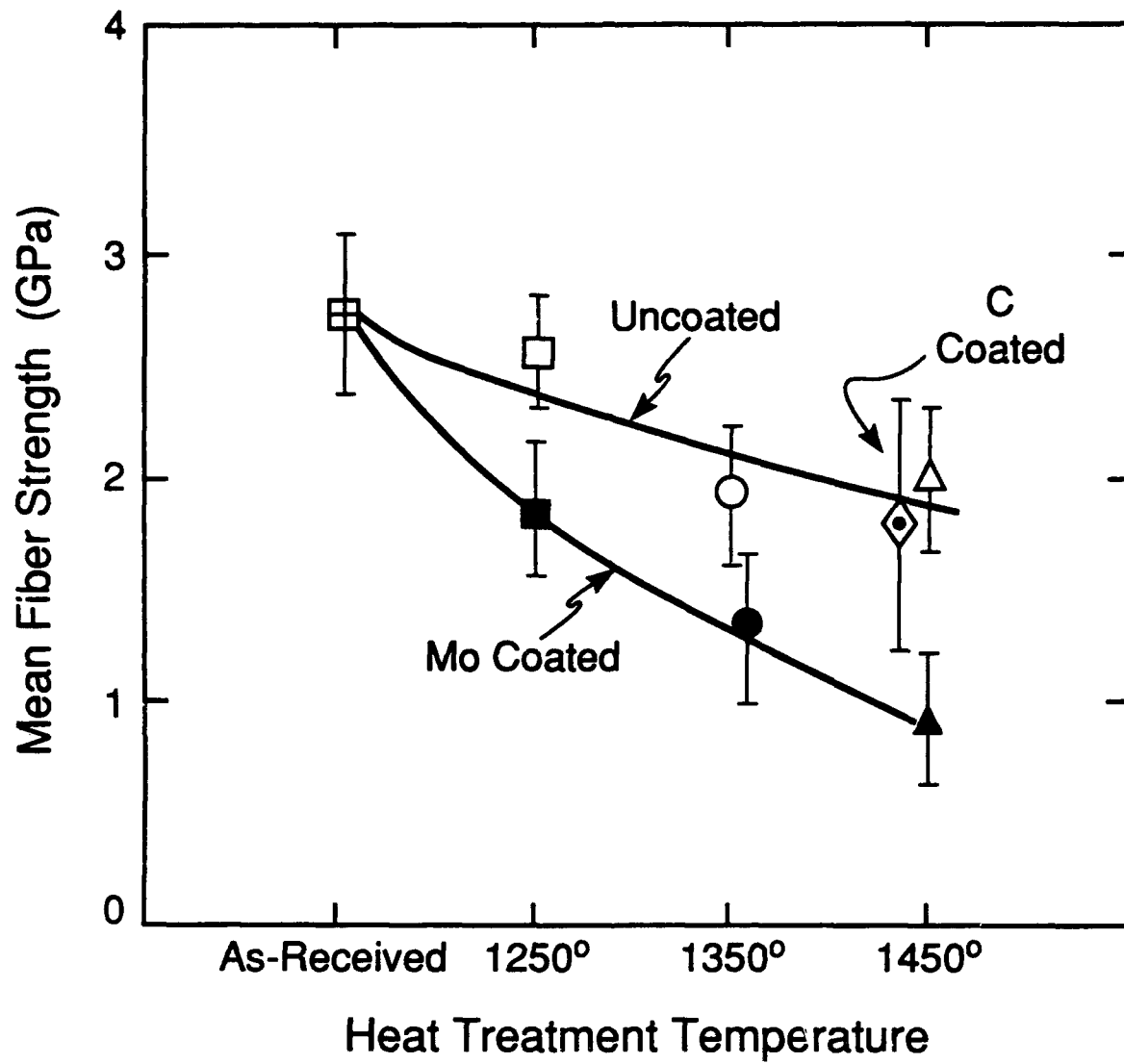


Figure 3b

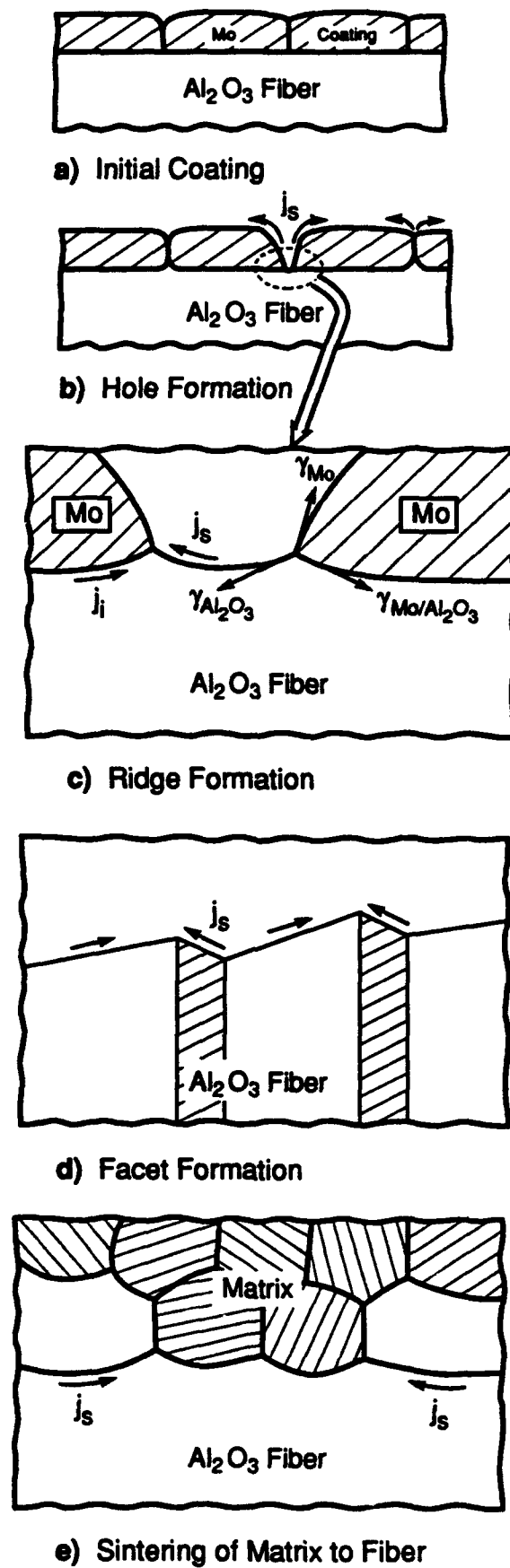


Figure 4



Figure 5

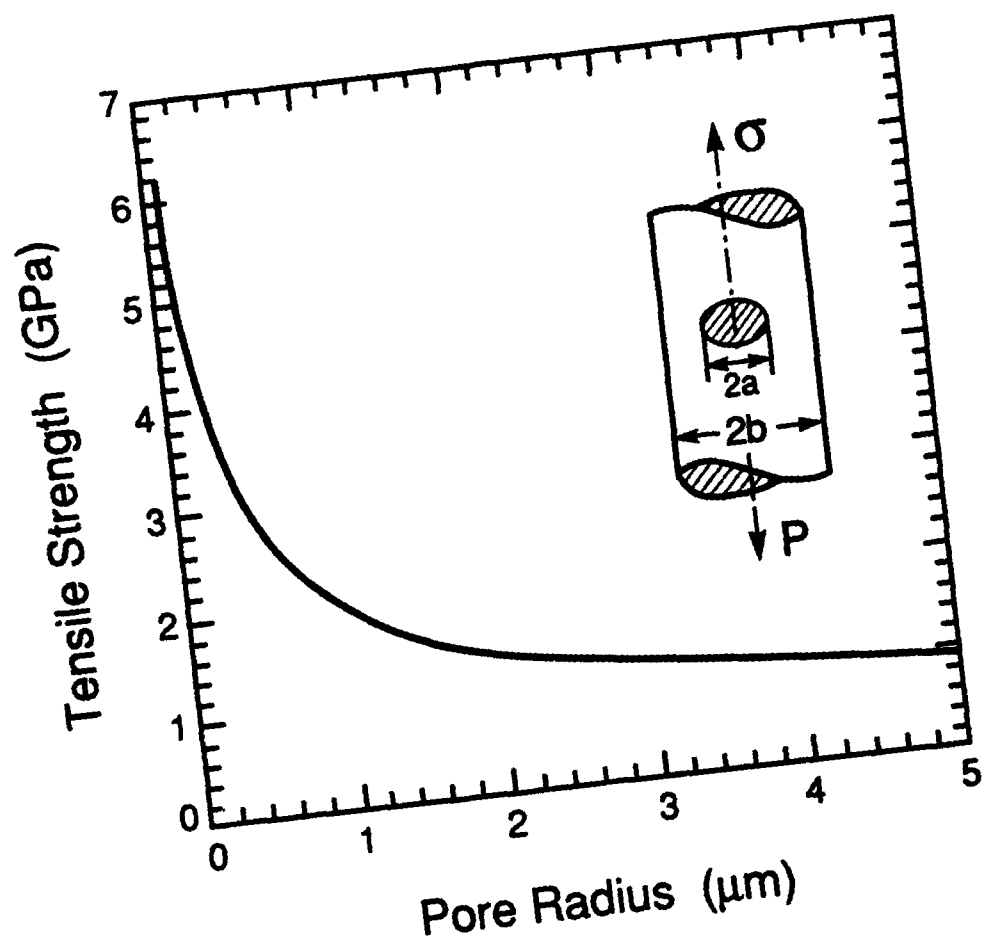


Figure 6

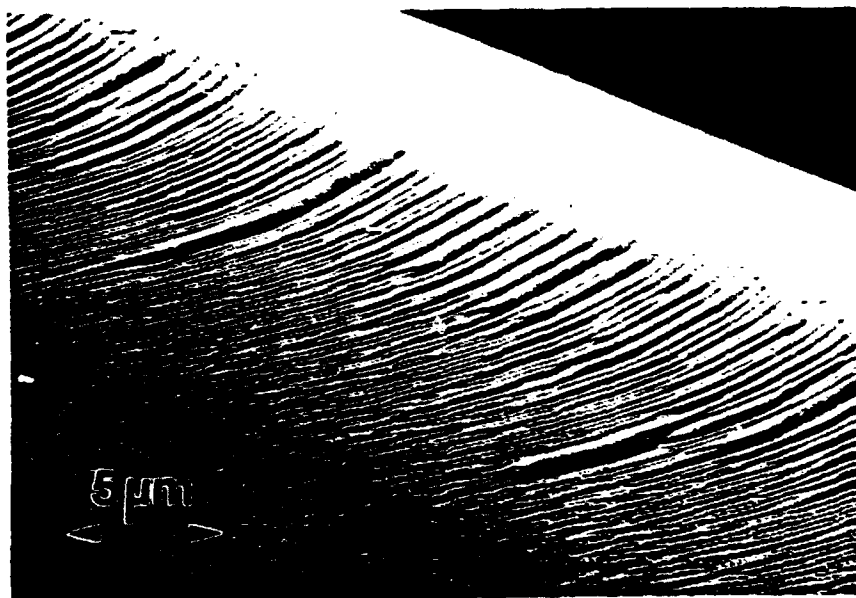


Figure 7



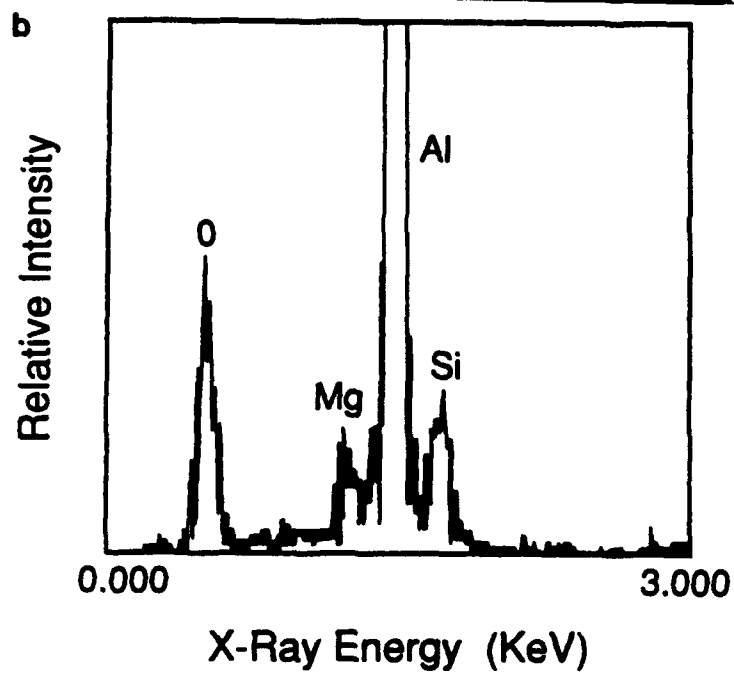
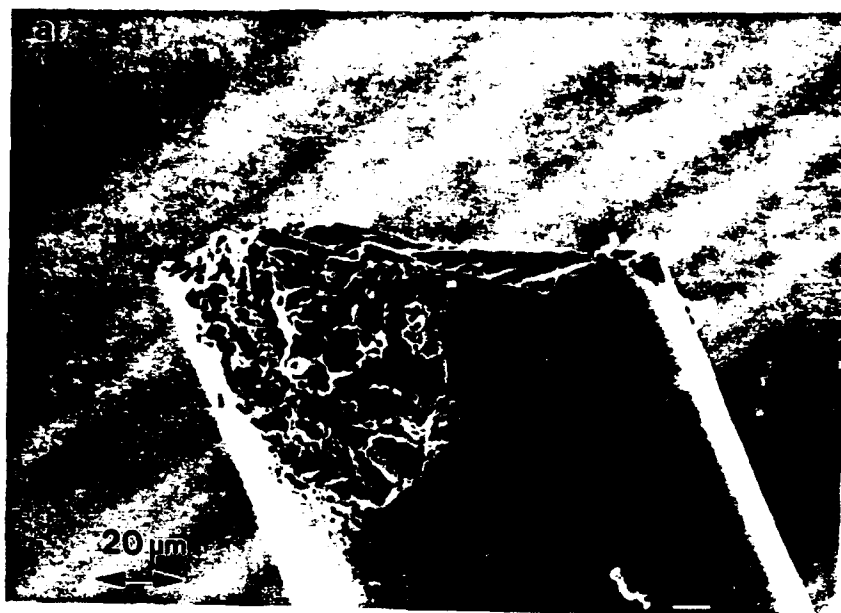


Figure 8

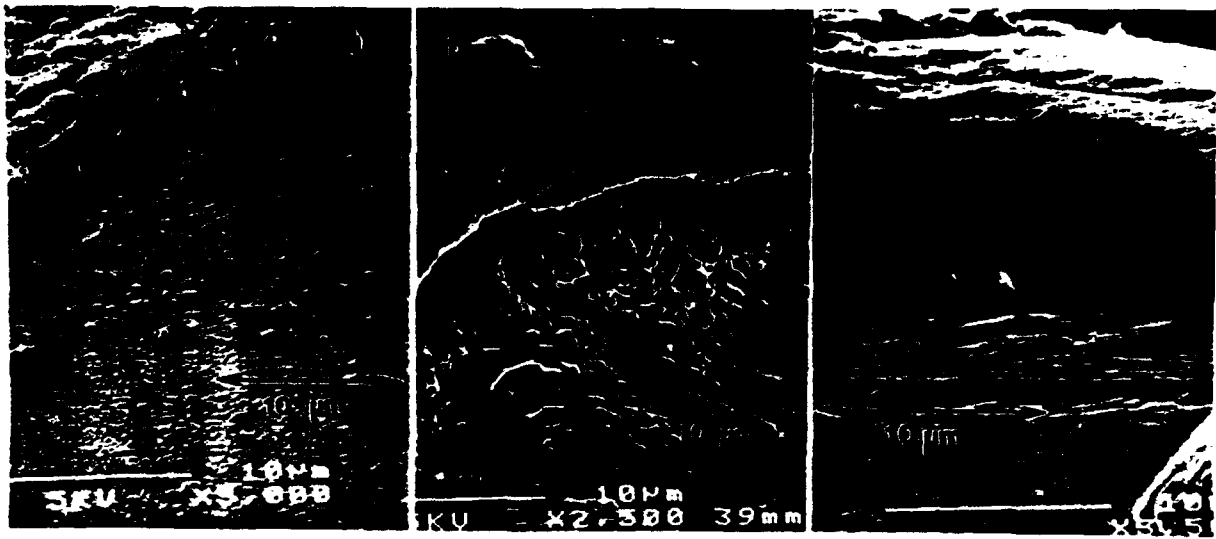


Figure 9

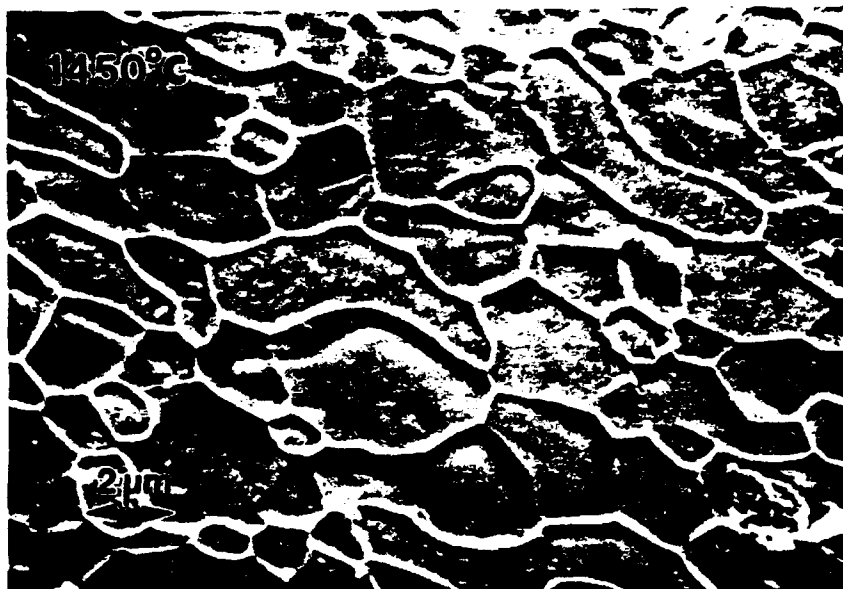


Figure 10

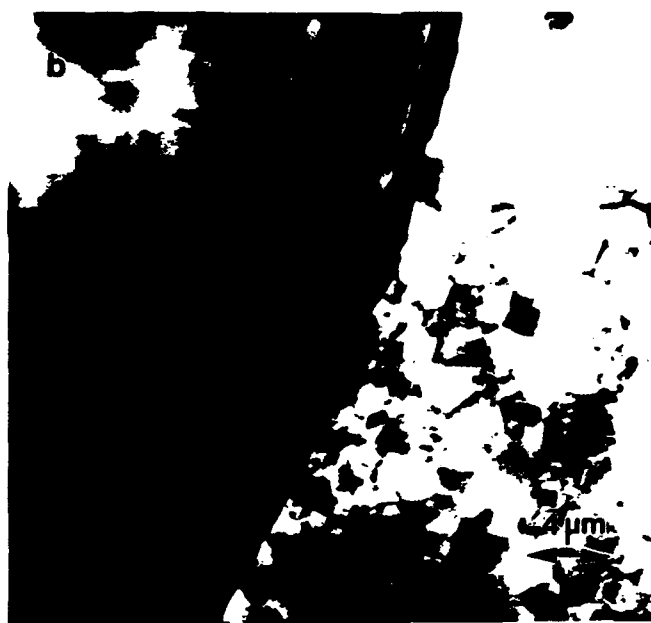
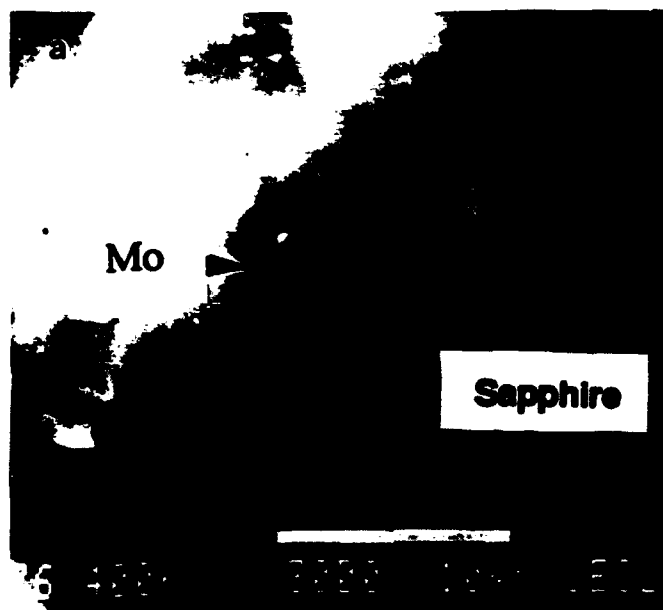


Figure 11

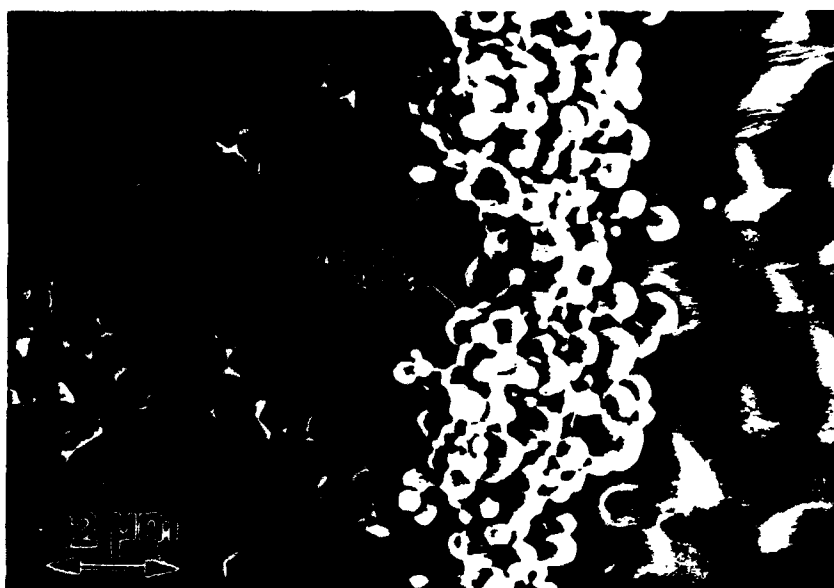


Figure 12



Figure 13

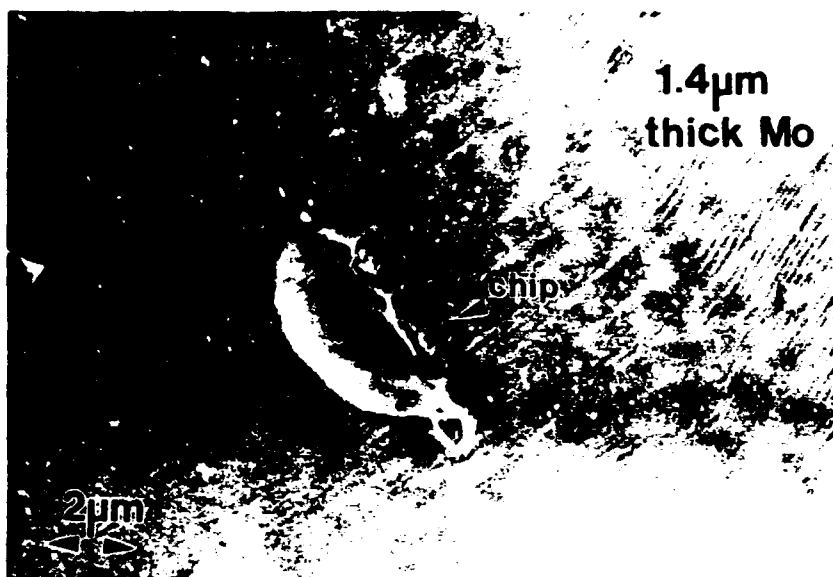


Figure 14

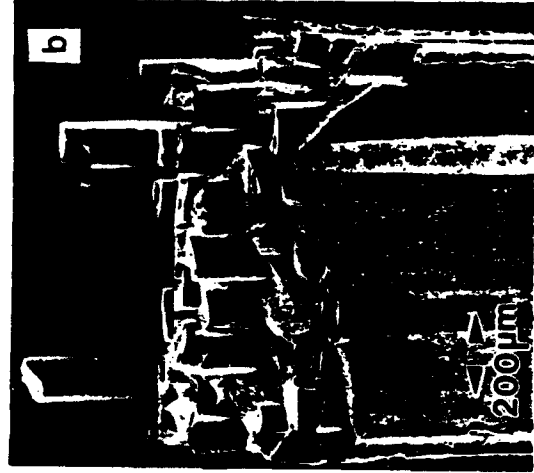
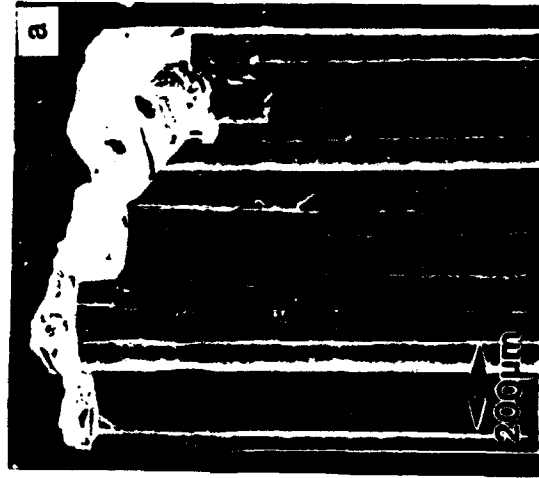


Figure 15



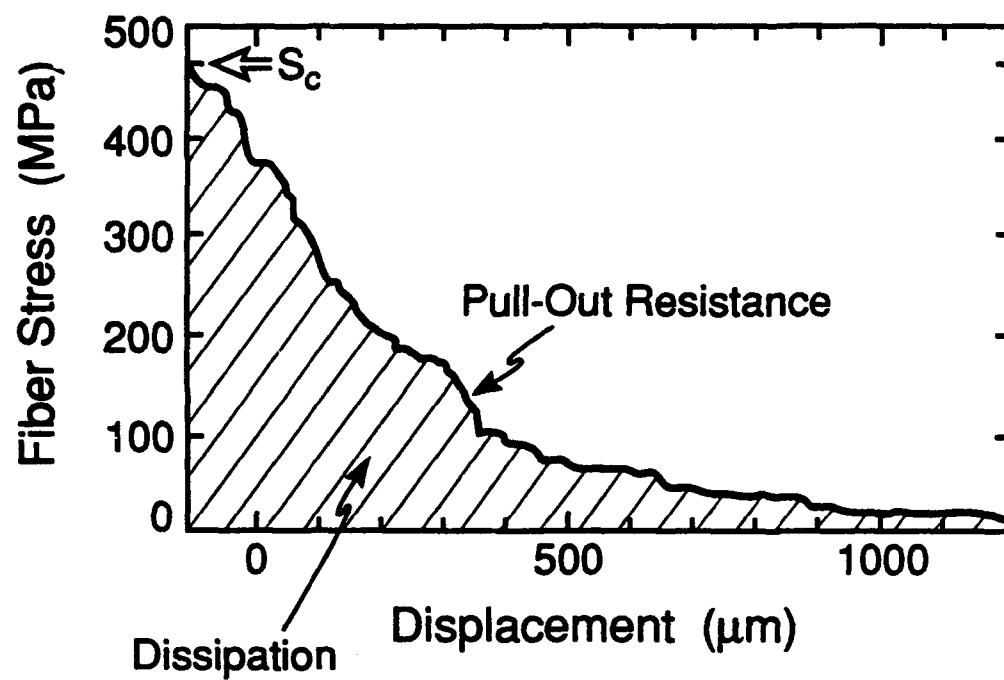


Figure 16

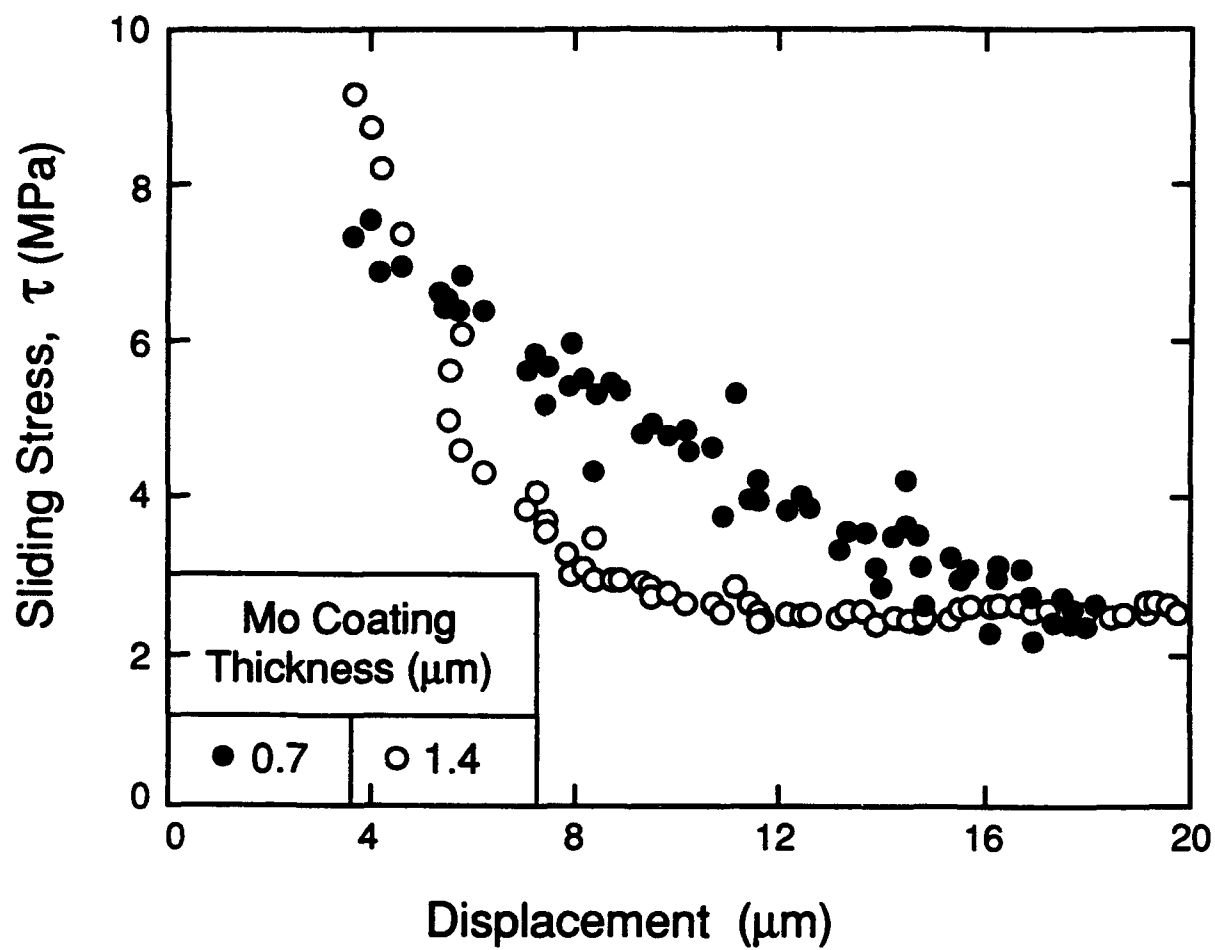


Figure 17

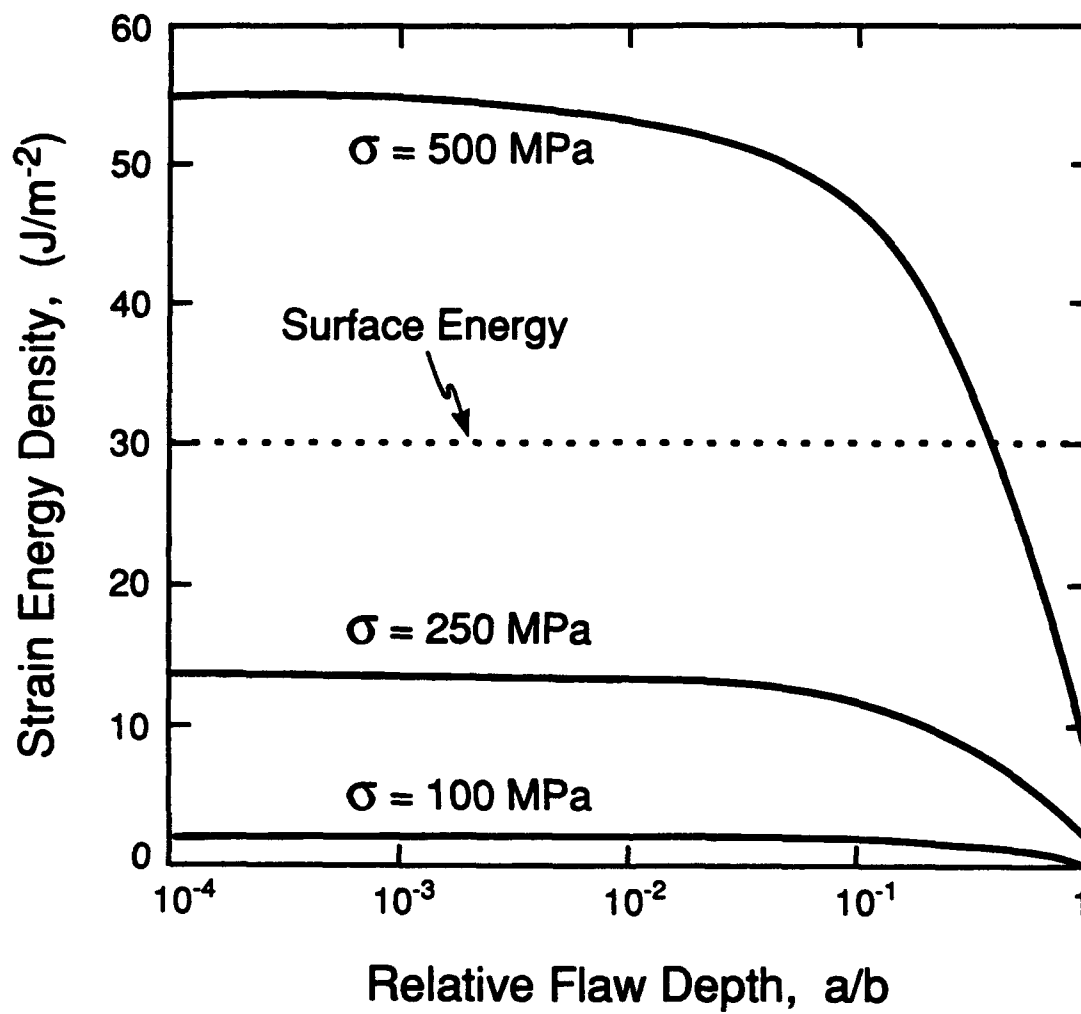


Figure A1

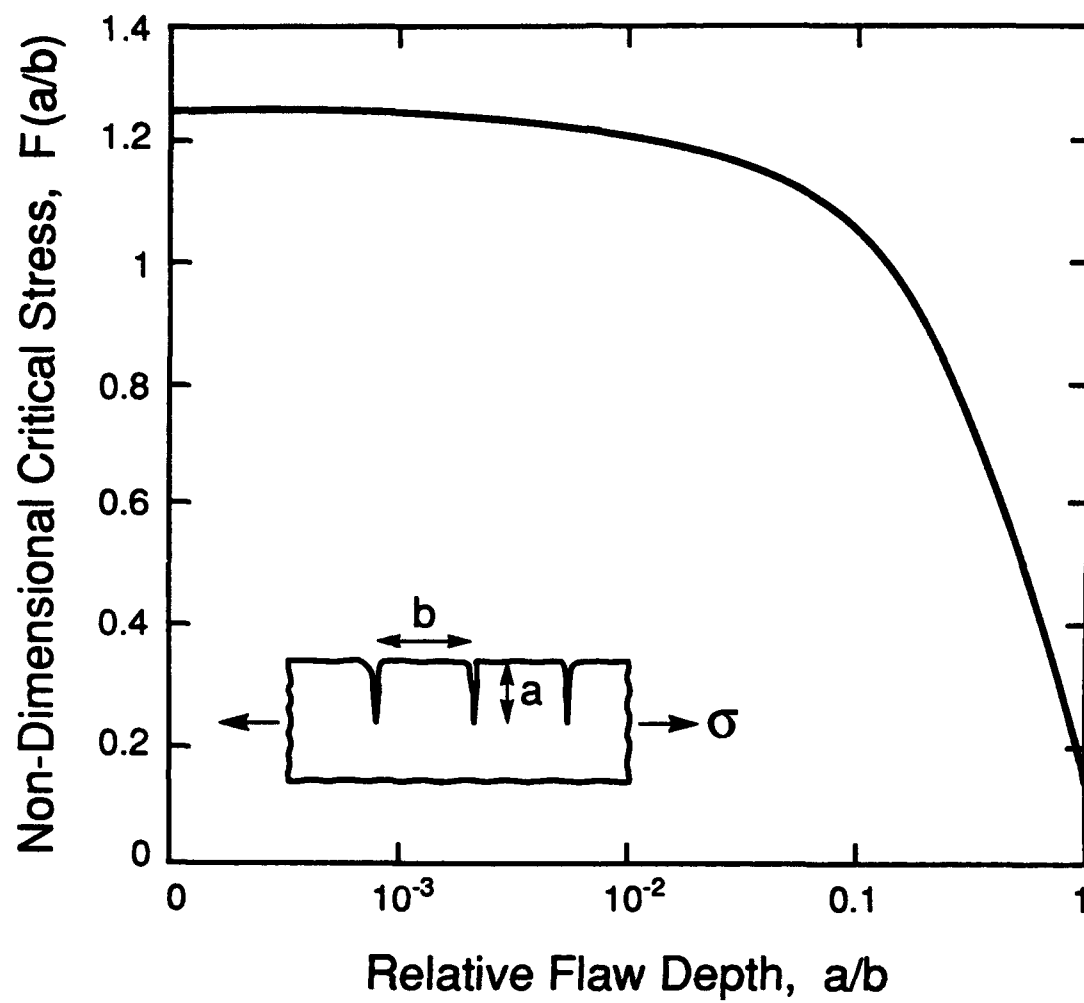
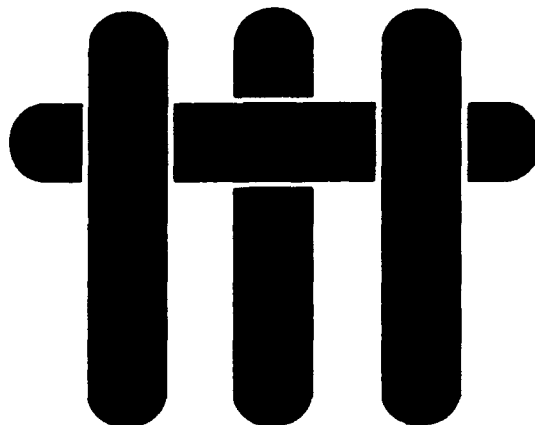


Figure A2

# M A T E R I A L S



## ON THE FLEXURAL PROPERTIES OF BRITTLE MULTILAYER MATERIALS: I. MODELING

by

C.A. Folsom\*, F.W. Zok and F.F. Lange  
Materials Department  
College of Engineering  
University of California  
Santa Barbara, California 93106-5050

\*Presently at  
Wright Laboratories  
Materials Directorate  
Wright Patterson Air Force Base, OH  
45433-7817

*To be published in the Journal of the American Ceramic Society*  
*Revised version, August 1993*

## ABSTRACT

Multilayer systems comprised of brittle materials can exhibit substantially different behaviors under *flexural* and tensile loadings. The present article addresses the origins of such differences, with emphasis on the modeling of the *flexural* stress-strain response. Systems with both a deterministic tensile strength and a distribution in strengths (characterized by Weibull statistics) are considered. The model predictions show that both the ultimate strength and strain-to-failure in flexure exceed the corresponding values in uniaxial tension. In addition, systems comprised of alternating layers of two different materials are examined, and disparities in the flexural and tensile behaviors addressed.

## 1. INTRODUCTION

There has recently been considerable interest in the mechanical behavior of a wide range of multilayer systems. Some of these systems are man-made,<sup>1-4</sup> whereas others occur in nature (e.g., shells of mollusks<sup>5,6</sup>). The key feature that imparts good mechanical properties in many of these materials is the presence of crack-deflecting interfaces between layers: cracks that form in one layer are deflected along the interfaces with adjacent layers, preventing catastrophic failure.

Characterization of the mechanical properties of multilayer systems usually involves two types of tests: flexure and uniaxial tension. Flexure tests are frequently chosen because of limitations of small specimen volumes, and ease of both sample preparation and testing procedure. However, it has become clear that layered materials exhibit rather different characteristics in the two tests<sup>1-4</sup>. In particular, the nominal failure strain measured in flexure can be substantially higher than that measured in uniaxial tension.<sup>1,2</sup> The purpose of the present article is to address the origins of such disparities.

It should be emphasized that neither test is necessarily "better" than the other in terms of characterizing mechanical properties: they are simply *different* from one another. The uniaxial tensile test simulates loading that leads to in-plane tensile stresses, whereas the flexure test simulates loading that involves stress gradients across the layers. Such gradients can arise through either mechanical loading, e.g., a plate, simply supported at discrete points on one side, with a uniformly distributed load on the other; or thermal loading, e.g., a plate with a temperature gradient across it. Consequently, it is necessary to understand the mechanics of failure in both cases.

Multilayer systems comprised of brittle layers can exhibit three types of behavior under flexural loading. The behavior is dictated by the properties of the interfaces between the layers as well as the loading configuration. (i) When the layers are strongly

bonded, the system behaves essentially as a monolithic ceramic: a crack in one layer can propagate readily into adjacent layers, with no beneficial effect of the interface. In this case, the flexural stress-strain response is linear elastic up to fracture (as it is in uniaxial tension). (ii) The second type of behavior involves sliding of the layers past one another prior to cracking. This occurs when the sliding resistance of the interface is low. The stress-strain response of such systems is characterized by a linear region with a low modulus, given approximately by  $E/N$  where  $E$  is the modulus of the ceramic and  $N$  is the number of layers. In principle, the sliding can be prevented by increasing the aspect ratio of the beam such that the interlaminar shear stresses are minimized. (iii) The third, and most desirable, type of behavior occurs when the interface is sufficiently strong to prevent sliding, but its fracture resistance is sufficiently small to allow cracks to be deflected along the interfaces. In order to get crack deflection, the interface toughness,  $\Gamma_i$ , must be less than ~25% of the toughness of the ceramic,  $\Gamma_c$ <sup>12</sup>. The flexural stress-strain response of these systems is characterized by a linear elastic region with a modulus equivalent to that of the monolithic ceramic, followed by a step-like reduction in stress as the layers crack<sup>1,4</sup>. Systems that exhibit the latter characteristics are the focus of the present study.

This paper considers, theoretically, the flexural stress-strain response of three types of brittle, multilayer systems, all containing crack-deflecting interfaces. (i) In the first, all the layers are assumed to be the same and to have a deterministic tensile strength. This simple case demonstrates that the nominal failure strain in flexure is larger than that in tension. The flexural strength, however, remains the same as the tensile strength. (ii) In the second system, the strengths of the individual layers are assumed to follow a two-parameter Weibull distribution. In this case, both the strength and the strain to failure in flexure exceed the corresponding values for uniaxial tension. (iii) The third system is comprised of alternating layers of two different materials, both of which have a deterministic tensile strength. This configuration is chosen to provide insight into the



behavior of hybrid composites comprised of monolithic ceramics and fiber-reinforced composite layers.<sup>2,7</sup> A notable feature that emerges from these calculations is the difference in the critical volume fraction of reinforcement needed for strength enhancement: the critical value being lower in flexure than in tension. Comparisons between the model predictions and experimental measurements are presented in a companion paper<sup>8</sup>.

A key assumption invoked in the present analysis is that the *stress everywhere within cracked layer is zero*. In essence, the interface toughness is taken to be zero. The effects of finite interface toughness have recently been examined by Phillips et al.<sup>3</sup>, using an approach similar to the one presented here. In that study, numerical simulations of the flexural stress-strain response were conducted for several combinations of material properties. In the present article, comparisons between the analytical solutions for one of the material systems (designated (i) above) assuming zero interface toughness and the numerical simulations for finite interface toughness are also presented.

## 2. SYSTEMS WITH DETERMINISTIC STRENGTH

The flexural stress-strain response of a weakly-bonded multilayer material with a deterministic tensile strength  $\sigma_c$  is evaluated following Euler-Bernoulli beam theory<sup>9</sup>. The compressive strength of the material is assumed to be very much larger than the tensile strength and the material is taken to be linear elastic up to fracture. These characteristics are representative of many brittle solids, including ceramics. The loading is assumed to be pure bending. The results are presented in terms of nominal stresses and strains, calculated on the basis of the overall beam dimensions.

Upon initial loading, the system behaves like a monolithic solid in the sense that both the stress and the strain distributions across the beam are linear. The maximum values of tensile stress and tensile strain are thus given by<sup>9</sup>

$$\sigma = 6M/b(N_0 t)^2 \quad (1)$$

and

$$\epsilon = \sigma/E = 6M/b(N_0 t)^2 E \quad (2)$$

where  $M$  is the applied bending moment,  $N_0$  is the number of layers,  $t$  is the thickness of each layer and  $b$  is the beam width. When  $\sigma$  reaches  $\sigma_*$ , the layer on the tensile face breaks: the remaining layers are assumed to stay intact since the crack deflects along the interface with the second layer. The corresponding values of *nominal* stress and strain are simply

$$\sigma_1 = \sigma_* \quad (3)$$

and

$$\epsilon_1 = \sigma_*/E = \epsilon_* \quad (4)$$

For the purpose of calculating the subsequent stress-strain response, it is assumed that the stress everywhere in the first layer is reduced to zero following cracking. In essence, the outer layer is removed from the composite, leaving  $(N_0 - 1)$  intact layers. As a result, the stress and strain distributions can be assumed to remain linear, with a

shift in the neutral axis by a distance of  $t/2$ . The reduction in plate stiffness following the initial cracking event leads to a drop in the nominal stress to the value

$$\sigma'_1 = \sigma_* \left( \frac{N_o - 1}{N_o} \right)^3 \quad (5)$$

In order to break the next layer, the plate must be loaded further until, once again, the stress in that layer reaches  $\sigma_*$ . The loading conditions required for this event are described by

$$\sigma_2 = \sigma_* \left( \frac{N_o - 1}{N_o} \right)^2 \quad (6)$$

and

$$\epsilon_2 = \epsilon_* \left( \frac{N_o - 1}{N_o} \right)^{-1} \quad (7)$$

Following the second cracking event, the load drops again, and the stress for further cracking calculated assuming that *both* cracked layers do not support any stress. Using this approach, the nominal stress,  $\sigma_i$ , and the nominal strain,  $\epsilon_i$ , for cracking the  $i^{\text{th}}$  layer are

$$\frac{\sigma_i}{\sigma_*} = \left( \frac{N_i}{N_o} \right)^2 \quad (8)$$

and

$$\frac{\epsilon_i}{\epsilon_*} = \left( \frac{N_i}{N_o} \right)^{-1} \quad (9)$$

where  $N_i$  is the number of intact layers. Similarly, the nominal stress *after failure* of the  $i$ th layer is

$$\frac{\sigma'_i}{\sigma_*} = \left( 1 - \frac{1}{N_i} \right)^3 \left( \frac{N_i}{N_o} \right)^2 \quad (10)$$

The preceding results can be combined to describe two relevant curves: one is the locus of nominal stress and nominal strain values *at* each cracking event; the other is the locus of the corresponding values *following* each cracking event. The stress-strain curves oscillate between these loci in a saw-tooth fashion until all the layers have broken. This behavior is illustrated in Fig. 1. (For comparison, the behavior corresponding to uniaxial tensile loading is also shown.) The former locus is obtained by combining Eqns. (8) and (9), resulting in

$$\frac{\sigma_i}{\sigma_*} = \left( \frac{\epsilon_i}{\epsilon_*} \right)^{-2} \quad (11)$$

This relationship does not depend on the number of layers. The latter locus is obtained from Eqns. (9) and (10), resulting in

$$\frac{\sigma'_i}{\sigma_*} = \left[ 1 - \frac{1}{N_o} \left( \frac{\epsilon_i}{\epsilon_*} \right) \right]^3 \left( \frac{\epsilon_i}{\epsilon_*} \right)^{-2} \quad (12)$$

In this case, the stress increases with increasing number of layers,  $N_0$ , as shown in Fig. 2. As  $N_0$  approaches  $\infty$ , the lower curve converges with the upper curve and the stress-strain curve becomes a smooth, monotonically decreasing function beyond the stress maximum. It should be noted that the flexural strength of these systems (defined by the maximum point in the nominal stress/nominal strain curve) is identical to the tensile strength. However, the nominal strain-to-failure can be substantially higher in flexure: by a factor of  $> 3$  for large values of  $N_0$ .

To evaluate the role of interface toughness, comparisons have been made between the predictions of Eqns. (11) and (12), and the numerical simulations of Phillips et al.<sup>3</sup>. In those simulations, a similar approach, based on Euler-Bernoulli beam theory, was used to develop the flexural stress-strain relations, taking into account the progressive delamination that occurs when the interface toughness,  $\Gamma_i$ , is finite. Figure 3 shows such comparisons for two values of interface toughness: (a)  $7.5 \text{ Jm}^{-2}$ , and (b)  $50 \text{ Jm}^{-2}$ . Evidently, for the lower value of  $\Gamma_i$ , the present model is in good agreement with the numerical simulations. For the higher value, the present model predictions lie slightly above those of the simulations.

### 3. ROLE OF FRACTURE STATISTICS

Many brittle materials, including ceramics, exhibit a distribution in strengths. This distribution can be described by the empirical Weibull function

$$P = 1 - \exp \left[ -\frac{V}{V_0} \left( \frac{\sigma}{\sigma_0} \right)^m \right] \quad (13)$$

where  $P$  is the cumulative probability of failure at stresses up to  $\sigma$ ,  $V$  is the sample volume,  $V_0$  and  $\sigma_0$  are the reference values of volume and stress, and  $m$  is the Weibull

modulus. The approach developed in the previous section is used here to describe the flexural response of multilayer systems in which the strength of the layers follows such a distribution. For convenience,  $N_0$  is assumed to be large, allowing the stress gradients across individual layers to be neglected. To provide a basis for comparison, the results for uniaxial tensile loading are presented first. The latter results are not new: they are equivalent to those obtained in the theory of fiber bundle failure.

During uniaxial *tensile* loading, the stress in each intact layer is simply  $\epsilon E$ , where  $\epsilon$  is the remote tensile strain. The stress in the broken layers is assumed to be zero, as in the preceding section. Consequently, the variation in nominal stress with nominal strain can be written as

$$\frac{\sigma}{\sigma_0} = \frac{\epsilon E(1-P)}{\sigma_0} = \left( \frac{\epsilon E}{\sigma_0} \right) \exp \left[ \frac{-V}{V_0} \left( \frac{\epsilon E}{\sigma_0} \right)^m \right] \quad (14)$$

Typical tensile stress-strain curves, presented in the normalized form  $\sigma/\sigma_0$  vs.  $\epsilon E/\sigma_0$ , for several values of  $m$  are shown in Fig. 3(a). The tensile strength,  $\bar{\sigma}_T$ , is obtained by setting

$$\frac{d(\sigma/\sigma_0)}{d(\epsilon E/\sigma_0)} = 0, \quad (15)$$

whereupon

$$\frac{\bar{\sigma}_T}{\sigma_0} = \frac{1}{(m V/V_0)^{1/m}} \quad (16)$$

Trends in  $\bar{\sigma}_T/\sigma_0$  with  $m$  for  $V/V_0 = 1$  are presented in Fig. 4.

The corresponding results for *flexural* loading are more complicated and, as shown below, require numerical integration. The assumptions used in deriving the equations here are essentially the same as those outlined in Section 2, with one notable exception. Since the strength of the layers is assumed to follow a Weibull distribution, cracking does not necessarily occur sequentially through the layers in order of their positions. Consequently, the stress distribution across the beam does not remain linear, though the *strain* distribution does.

Evaluation of the nominal stress-strain behavior of such systems involves two steps. In the first, the applied bending moment,  $M$ , is equated to the moment induced by the stresses within the beam. This condition can be written as

$$M = \frac{b(N_0 t)^2}{(\epsilon_t - \epsilon_c)^2} \int_{\epsilon_c}^{\epsilon_t} \sigma(\epsilon) \cdot (\epsilon - \epsilon_c) d\epsilon \quad (17)$$

where  $\epsilon_c$  and  $\epsilon_t$  are the maximum values of compressive and tensile strains, respectively. Furthermore, assuming the stress-strain relation  $\sigma(\epsilon)$  to be linear in the compressive region ( $\epsilon < 0$ ) and to follow Eqn. (14) in the tensile region ( $\epsilon > 0$ ) allows Eqn. (17) to be re-written in the non-dimensional form

$$\frac{\sigma}{\sigma_0} = \frac{6}{(e_t - e_c)^2} \left[ \int_{e_c}^0 e(e - e_c) de + \int_0^{e_t} e(e - e_c) \exp\left[\frac{-V}{V_0} e^m\right] de \right], \quad (18)$$

where  $e$  is a normalized strain ( $\epsilon E / \sigma_0$ ), and the subscripts  $c$  and  $t$  represent compression and tension, respectively. In the second step, the sum of the forces acting parallel to the plate is set equal to zero, enforcing static equilibrium. This condition can be expressed as

$$\int_{e_c}^0 e de + \int_0^{e_t} e \cdot \exp\left[-\left(\frac{V}{V_0}\right)e^m\right] de = 0 \quad (19)$$

Combining Eqns. (18) and (19) leads to the final result

$$\frac{\sigma}{\sigma_0} = \frac{2}{(e_t - e_c)^2} \left\{ 3 \int_0^{e_t} e^2 \cdot \exp\left[-\left(\frac{V}{V_0}\right)e^m\right] de - e_c^3 \right\} \quad (20)$$

where

$$e_c = - \left[ 2 \int_0^{e_t} e \cdot \exp\left[-\left(\frac{V}{V_0}\right)e^m\right] de \right]^{1/2} \quad (21)$$

The integrals in these equations have been solved using a numerical method. The resultant stress-strain curves for  $V/V_0 = 1$  and several values of  $m$  are plotted in Fig. 4(b). Comparison with the tensile curves indicates that the ultimate flexural strength,  $\bar{\sigma}_F$ , consistently exceeds the ultimate tensile strength,  $\bar{\sigma}_T$ ; the difference being largest for low values of  $m$  (Fig. 5). The influence of  $m$  on the strength ratio (flexural to tensile) is plotted in Fig. 6.

It is of interest to note that the trend in Fig. 5 is similar to that obtained when comparing the mean flexural strength  $\hat{\sigma}_F$  of a *monolithic* ceramic with the corresponding mean tensile strength  $\hat{\sigma}_T$ . In the latter case, the strength ratio is given by<sup>10</sup>

$$\frac{\hat{\sigma}_F}{\hat{\sigma}_T} = [c(m+1)]^{1/m} \quad (22)$$



where  $c$  is a numerical coefficient. When the specimen volumes are equivalent,  $c = 2$ . The trend predicted by Eqn. (22) is plotted on Fig. 6 as a dashed line. It appears to scale with the results for multilayer systems over the range of values of  $m$  considered here, suggesting that the present results can be described empirically by a function with a form similar to that of Eqn. (22). Indeed, when  $c$  is taken to be 0.75, Eqn. (22) provides a good approximation to the exact results, with an error  $\leq 0.8\%$ , over the range  $3 \leq m \leq 20$ . This comparison is presented in Fig. 6.

The origin of the disparity in the ultimate strengths in flexural and tensile loading can be understood by examining the stress and strain distributions across a flexural beam at various stages of loading. One such example, for  $m = 5$ , is presented in Fig. 7. Figure 7(a) shows the nominal stress-strain response and Figs. 7(b) and (c) show the corresponding strain and stress distributions at three load levels, represented by points A, B and C. Prior to extensive cracking (A), both the strain and stress distributions remain essentially linear and symmetric about the beam center, as expected for an elastic beam. When extensive cracking occurs, the strain distribution remains linear, though the neutral axis shifts toward the compressive face. At the load maximum (point B in Fig. 7(a)), the stress distribution on the tensile side becomes highly non-linear. The shape of this distribution is identical to the *tensile* stress-strain curve shown in Fig. 4(a) (though with a part of the tail truncated). This similarity arises because the strain distribution is assumed to vary linearly across the beam. The maximum *local* tensile stress in the plate is thus equivalent to the ultimate tensile strength ( $0.59 \sigma_0$  for the present case), whereas the maximum compressive stress reaches significantly higher levels:  $0.85 \sigma_0$  at the load maximum. Consequently, the maximum nominal stress supported by the beam is higher in flexure ( $0.80 \sigma_0$ ) than in tension ( $0.59 \sigma_0$ ). In essence, this difference can be attributed to the process of stress re-distribution following cracking in the flexure specimen, coupled with the high *compressive* strength of the constituent layers.

To provide insight into the relative magnitudes of these effects (one due to the stress re-distribution and the other to the tension-compression strength differential), it is useful to consider a hypothetical case where the *compressive* stress-strain response is the same as that for *tension* (Eqn. 14). This approach allows determination of the ratio of flexural to tensile strength when the only effect is the geometric one associated with stress re-distribution. (Clearly, this is an academic exercise since there are no real materials that exhibit such behavior.) The results of these calculations are plotted as the dotted line in Fig. 6. Apparently, the strength ratio (flexure/tension) is due largely to the stress re-distribution effect, though there is a noticeable contribution associated with the tension-compression strength differential.

#### 4. BIMATERIAL SYSTEMS

The preceding analysis for single-phase systems is extended here to cases in which the beams consist of alternating layers of different phases: one being the 'matrix' phase (material 1) and the other the 'reinforcing' phase (material 2). The motivation for this analysis stems from recent experimental studies on hybrid composites comprised of alternating layers of monolithic ceramics and fiber-reinforced sheets<sup>2</sup>. The present analysis is limited to symmetric lay-ups in which the exterior layers are the 'matrix' phase. Each of the two phases is assumed to be linear elastic and to have a deterministic tensile strength. For simplicity, differences in elastic moduli between the two materials are neglected. (The elastic mismatch is accounted for in a companion paper<sup>8</sup>.) Once again, cracks formed in one layer are assumed to be deflected along the interfaces with adjacent layers, allowing the layers to behave independently of one another. Furthermore, the tensile strength  $\bar{\sigma}_2$  of the reinforcing layers is assumed to be larger than the tensile strength  $\bar{\sigma}_1$  of the matrix layers. The behavior of plates comprised of an

infinite number of layers is considered first, since a closed form expression for the stress-strain response can be readily derived.

The *tensile stress-strain* relationship of such bimaterial beams is a discontinuous linear function of strain in three intervals of strain. This relationship can be expressed in the non-dimensional form

$$\sigma/\epsilon E = 1 \quad \epsilon/\bar{\epsilon}_1 \leq 1 \quad (23a)$$

$$\sigma/\epsilon E = f \quad 1 \leq \epsilon/\bar{\epsilon}_1 \leq \bar{\epsilon}_2/\bar{\epsilon}_1 \quad (23b)$$

$$\sigma/\epsilon E = 0 \quad \epsilon/\bar{\epsilon}_1 > \bar{\epsilon}_2/\bar{\epsilon}_1 \quad (23c)$$

where  $f$  is the volume fraction of the reinforcing phase, and  $\bar{\epsilon}_1$  and  $\bar{\epsilon}_2$  are the failure strains of materials 1 and 2, respectively. Due to the discontinuous nature of the tensile response, the nominal stress in flexure is also a discontinuous function of strain. The flexural response must be determined separately for each of the three intervals and then combined in a piece-wise fashion to determine the overall response. In all cases, the flexural response is determined from static equilibrium (by setting the average longitudinal stress equal to zero) and setting the resultant bending moment equal to the applied moment.

The first interval is simply the trivial case where the body is linear elastic, whereupon the stress-strain relation becomes

$$\frac{\sigma}{\sigma_1} = \frac{\epsilon}{\bar{\epsilon}_1} \quad \frac{\epsilon_t}{\bar{\epsilon}_1} \leq 1, \quad (24)$$

where  $\epsilon_t$  is the maximum tensile strain in the beam.

For the second interval, the nominal stress-strain relation is

$$\frac{\sigma}{\bar{\sigma}_1} = \left( \frac{\left(1 - \left(\frac{\epsilon_c}{\bar{\epsilon}_1}\right)^3\right) + f \left[ \left\{ 2 \left(\frac{\epsilon}{\bar{\epsilon}_1}\right) + \left(\frac{\epsilon_c}{\bar{\epsilon}_1}\right) \right\}^3 - 1 \right]}{2 \left(\frac{\epsilon}{\bar{\epsilon}_1}\right)^2} \right) \quad 1 \leq \frac{\epsilon_t}{\bar{\epsilon}_1} \leq \frac{\bar{\epsilon}_2}{\bar{\epsilon}_1} \quad (25)$$

where  $\epsilon_c$  is the maximum compressive strain and is related to the nominal strain  $\epsilon$  by

$$\frac{\epsilon_c}{\bar{\epsilon}_1} = \frac{2f \left(\frac{\epsilon}{\bar{\epsilon}_1}\right) + \left[ f^2 + 2f \left( 2 \left(\frac{\epsilon}{\bar{\epsilon}_1}\right)^2 - 1 \right) + 1 \right]^{1/2}}{(1-f)} \quad (26)$$

The expression for the third interval is

$$\frac{\sigma}{\bar{\sigma}_1} = \left( \frac{1 - \left(\frac{\epsilon_c}{\bar{\epsilon}_1}\right)^3 + f \left( \left(\frac{\bar{\epsilon}_2}{\bar{\epsilon}_1}\right)^3 - 1 \right)}{2 \left(\frac{\epsilon}{\bar{\epsilon}_1}\right)^2} \right) \quad \frac{\epsilon_t}{\bar{\epsilon}_1} \geq \frac{\bar{\epsilon}_2}{\bar{\epsilon}_1} \quad (27)$$

where the maximum compressive strain is now given by

$$\frac{\epsilon_c}{\bar{\epsilon}_1} = - \left[ f \left( \left(\frac{\bar{\epsilon}_2}{\bar{\epsilon}_1}\right)^2 - 1 \right) + 1 \right]^{1/2} \quad (28)$$

It can readily be shown that, when  $f = 0$ , the results for intervals two and three (Eqns. 25 and 27) are identical, and agree with the results derived for single phase multilayered materials (Eqn. 11).

Similar calculations have also been carried out for plates containing *finite* numbers of layers. In this case, no simple closed form expression for the flexural stress-strain response can be obtained. The approach adopted here was to increase the nominal strain in small increments and, at each interval, evaluate the magnitude of the stresses in both phases. When the stresses reached the corresponding strengths (either  $\bar{\sigma}_1$  or  $\bar{\sigma}_2$ ), then those layers were discounted from subsequent calculations by simply setting their modulus equal to zero, as before. This procedure was repeated until all the layers had failed.

The resulting nominal stress-strain curves for the case where  $\bar{\sigma}_2/\bar{\sigma}_1 = 3$  and  $f = 0.1$  are plotted in Fig. 8(a). In this case, the ultimate strengths in tension and flexure are governed by the strength of the matrix phase (material 1), though the nominal flexural stress at strains beyond the load maximum is larger than that in tension. In general, the stress increases as the number of layers increases. It is also seen that the result for beams containing 20 matrix layers (39 total layers) differ only slightly from the infinite layer solution.

The corresponding stress-strain curves for  $f = 0.5$  are shown in Fig. 8(b). In this case, the ultimate strength is substantially larger than the stress required for the onset of matrix cracking. It is also apparent that the ultimate strength is greater in flexure than in tension and depends to some extent upon the number of layers.

The effects of reinforcement volume fraction  $f$  on the ultimate strengths in tension and flexure for the case where  $\bar{\sigma}_2/\bar{\sigma}_1 = 3$  are shown in Fig. 9. At low values of  $f$ , there is no strength enhancement due to the presence of the reinforcements: once the matrix layers fail, the reinforcements are unable to support the additional load and thus the

strength of the composite is dictated by that of the matrix. However, beyond a critical volume fraction,  $f_c$ , the strength increases with  $f$ , reaching a value of 3 when  $f = 1$ .

A notable feature in Fig. 9 is that the critical volume fraction for flexure is lower than that for tension. This critical volume fraction can be expressed solely in terms of the strength ratio,  $\bar{\sigma}_1/\bar{\sigma}_2$ . For tensile loading, the relationship is simply<sup>11</sup>

$$f_c = \bar{\sigma}_1/\bar{\sigma}_2 \quad (29)$$

For flexure, the critical value is found by setting the maximum nominal stress (given by the intersection of Eqns. (25) and (27)) equal to unity, resulting in

$$f_c = \frac{4\left(\frac{\bar{\sigma}_2}{\bar{\sigma}_1}\right)^2 + 13\left(\frac{\bar{\sigma}_2}{\bar{\sigma}_1}\right) + 7 + \left[8\left(\frac{\bar{\sigma}_2}{\bar{\sigma}_1}\right)^3 + 33\left(\frac{\bar{\sigma}_2}{\bar{\sigma}_1}\right)^2 + 22\left(\frac{\bar{\sigma}_2}{\bar{\sigma}_1}\right) + 1\right]^{1/2}}{8\left[\left(\frac{\bar{\sigma}_2}{\bar{\sigma}_1}\right) + 1\right]^3} \quad (30)$$

The results of Eqns. (29) and (30) are plotted against the strength ratio  $\bar{\sigma}_2/\bar{\sigma}_1$  in Fig. 10, and show that the critical volume fraction in flexure is consistently about half of that required in tension.

## 5. CONCLUDING REMARKS

The main goal of this study has been to quantify the basic trends in the fracture behavior of brittle multilayered systems and address, specifically, the origin of differences between flexural and tensile properties. A simple theory based on the bending of beams has been developed to account for the progressive cracking through such systems and its effects on the nominal stress-strain response. A number of important features have been identified. Firstly, single phase multilayer beams with

deterministic strengths, while not possessing greater strengths than the individual layers, do have the ability to withstand flexural load beyond the initial cracking event under displacement-controlled conditions. When the individual layers possess a statistical distribution of strengths (as expected for most brittle solids), both the strength and the failure strain are higher in flexure than in tension. Secondly, further property improvements can be obtained by introducing reinforcing layers with a high strength and strain-to-failure (e.g. fiber composites). Such hybrid systems are expected to provide a high matrix cracking stress (relative to that of conventional unidirectional CMCs) in combination with a high strain-to-failure. Finally, the critical volume fraction required to strengthen layered ceramic systems under flexural loading is about one half the value corresponding to uniaxial tension. This result is important in designing composites for applications subject to stress gradients across the layers.

## **ACKNOWLEDGMENTS**

Funding of this work was supplied by the DARPA University Research Initiative Program of UCSB under ONR contract N-0014-92-J-1808. In addition, one of the authors (C.A.F.) was supported through the Air Force Palace Knights Program.

## REFERENCES

- [1] W.J. Clegg, K. Kendall, N.McN. Alford, T.W. Burton and J.D. Birchall, "A Simple Way to Make Tough Ceramics, *Nature* [347], No. 6292, pp. 455-57, Oct. 4 (1991).
- [2] C.A. Folsom, F.W. Zok, F.F. Lange and D.B. Marshall, "Mechanical Behavior of a Laminar Ceramic/Fiber-Reinforced Epoxy Composite," *J. Am. Ceram. Soc.*, 75 [11] pp. 2969-75 (1992).
- [3] A.J. Phillips, W.J. Clegg and T.W. Clyne, "Fracture Behaviour of Ceramic Laminates in Bending - I. Modeling of Crack Propagation," *Acta Metall. Mater.*, 41 [3], pp. 805-817 (1993).
- [4] A.J. Phillips, W.J. Clegg and T.W. Clyne, "Fracture Behaviour of Ceramic Laminates in Bending - II. Comparison of Model Predictions with Experimental Data," *Acta Metall. Mater.*, 41 [3], pp. 819-827 (1993).
- [5] J.D. Currey and A.J. Kohn, "Fracture in the Crossed-Lamellar Structure of Conus Shells," *J. Mater. Sci.*, 11, pp. 1615-73 (1976).
- [6] V.J. Laraia and A.H. Heuer, "Novel Composite Microstructure and Mechanical Behavior of Mollusk Shells," *J. Am. Ceram. Soc.*, 72 [11] pp. 2177-79 (1989).
- [7] C.A. Folsom, F.W. Zok and F.F. Lange, "Flexural Properties of Brittle Matrix Laminar Composites," Ceramic Engineering and Science Proceedings of the 16th Annual Conference on Composites and Advanced Ceramic Materials, J.B. Watchman Ed., American Ceramic Society (1992).
- [8] C.A. Folsom, F.W. Zok and F.F. Lange, to be published.
- [9] S. Timoshenko, *Strength of Materials*, 3rd Ed. Princeton (1955) pp. 137-40.
- [10] G.J. DeSalvo, "Theory and Structural Design Applications of Weibull Statistics," WANL-TME-2688, Westinghouse Electric Corp., Pittsburgh, PA, May 1970.
- [11] A. Kelly and N.H. MacMillan, "Strong Solids," Clarendon Press, Oxford (1986).
- [12] M.Y. He and J.W. Hutchinson, "Kinking of a Crack out of an Interface," *J. Appl. Mech.*, 56, 270-78, (1989).



## NOMENCLATURE

$b$	Beam width
$c$	Numerical coefficient
$e$	Normalized strain ( $\epsilon E/\sigma_0$ )
$e_c$	Normalized compressive strain ( $\epsilon_c E/\sigma_0$ )
$e_t$	Normalized tensile strain ( $\epsilon_t E/\sigma_0$ )
$E$	Young's modulus
$f$	Reinforcement volume fraction
$f_c$	Critical reinforcement volume fraction
$m$	Weibull modulus
$M$	Bending moment
$N_0$	Total number of layers
$N_i$	Number of intact layers
$P$	Cumulative failure probability
$t$	Layer thickness
$V$	Specimen volume
$V_0$	Reference volume in Weibull distribution
$\Gamma_c$	Ceramic toughness
$\Gamma_i$	Interface toughness
$\epsilon$	Strain
$\epsilon_c$	Compressive strain
$\epsilon_i$	Nominal strain for cracking $i^{\text{th}}$ layer
$\epsilon_t$	Tensile strain
$\epsilon_0$	Reference strain ( $\sigma_0/E$ )

$\epsilon_*$	Fracture strain ( $\sigma_*/E$ )
$\bar{\epsilon}_1$	Fracture strain of matrix
$\bar{\epsilon}_2$	Fracture strain of reinforcement
$\sigma$	Stress
$\bar{\sigma}_F$	Flexural strength of multilayer system
$\hat{\sigma}_F$	Mean flexural strength of monolithic material
$\sigma_i$	Nominal stress for cracking $i^{\text{th}}$ layer
$\sigma'_i$	Nominal stress following cracking of $i^{\text{th}}$ layer
$\sigma_0$	Reference stress in Weibull distribution
$\bar{\sigma}_T$	Tensile strength of multilayer system
$\hat{\sigma}_T$	Mean tensile strength of monolithic material
$\sigma_*$	Tensile strength of monolithic material
$\bar{\sigma}_1$	Tensile strength of matrix
$\bar{\sigma}_2$	Tensile strength of reinforcement

## FIGURES

- Fig. 1. Comparison of the tensile and flexural stress-strain curves of a system comprised of 8 brittle layers, each with a deterministic tensile strength,  $\sigma_t$ . The dashed lines are calculated from Eqns. (11) and (12), and show the bounds on the flexural stress-strain curve.
- Fig. 2. The locus of points bounding the flexural stress-strain response of systems with finite numbers of layers. The solid curve represents the upper bound, and the dashed curves represent the lower bounds.
- Fig. 3. Comparison of the present model predictions (Eqns. 11 and 12) with the numerical simulations of Phillips et al.<sup>3</sup>, showing the effects of the interface toughness,  $\Gamma_i$ . The total number of layers is 20\* (Simulations adapted from Figs. 7(a) and 8(a) of Ref. 3).
- Fig. 4. Influence of the Weibull modulus,  $m$ , on (a) the tensile and (b) the flexural stress-strain response of multilayer systems.
- Fig. 5. Trends in the ultimate strength with Weibull modulus for flexural and tensile loading.
- Fig. 6. Influence of Weibull modulus on the ultimate strength ratio (flexure-to-tension).
- Fig. 7. (a) The flexural stress-strain curves for  $m = 5$ , and (b) the corresponding strain and (c) stress distributions at three load levels, indicated by points A, B and C on the curve in (a).
- Fig. 8. Comparisons of the tensile and flexural stress-strain curves for bimaterial systems: (a)  $f = 0.1$ , (b)  $f = 0.5$ . Note that the tensile curves do not depend on the number of layers, whereas the flexural curves do.

---

\* Phillips et al.<sup>3</sup> assumed that the first layer was cracked (or notched) prior to loading. Consequently only 19 layers are intact at the onset of loading. For this reason, the peak normalized stress predicted by the present model (Eqn. 8) is  $(19/20)^2 = 0.903$ , rather than unity, and the corresponding normalized strain (Eqn. 9) is  $20/19 = 1.053$ .

**Fig. 9. Influence of reinforcement volume fraction on (a) the flexural and tensile ultimate strengths and (b) the strength ratio (flexure/tension).**

**Fig. 10. Influence of strength ratio  $\bar{\sigma}_2/\bar{\sigma}_1$  on the critical reinforcement volume fractions for both flexural and tensile loading.**



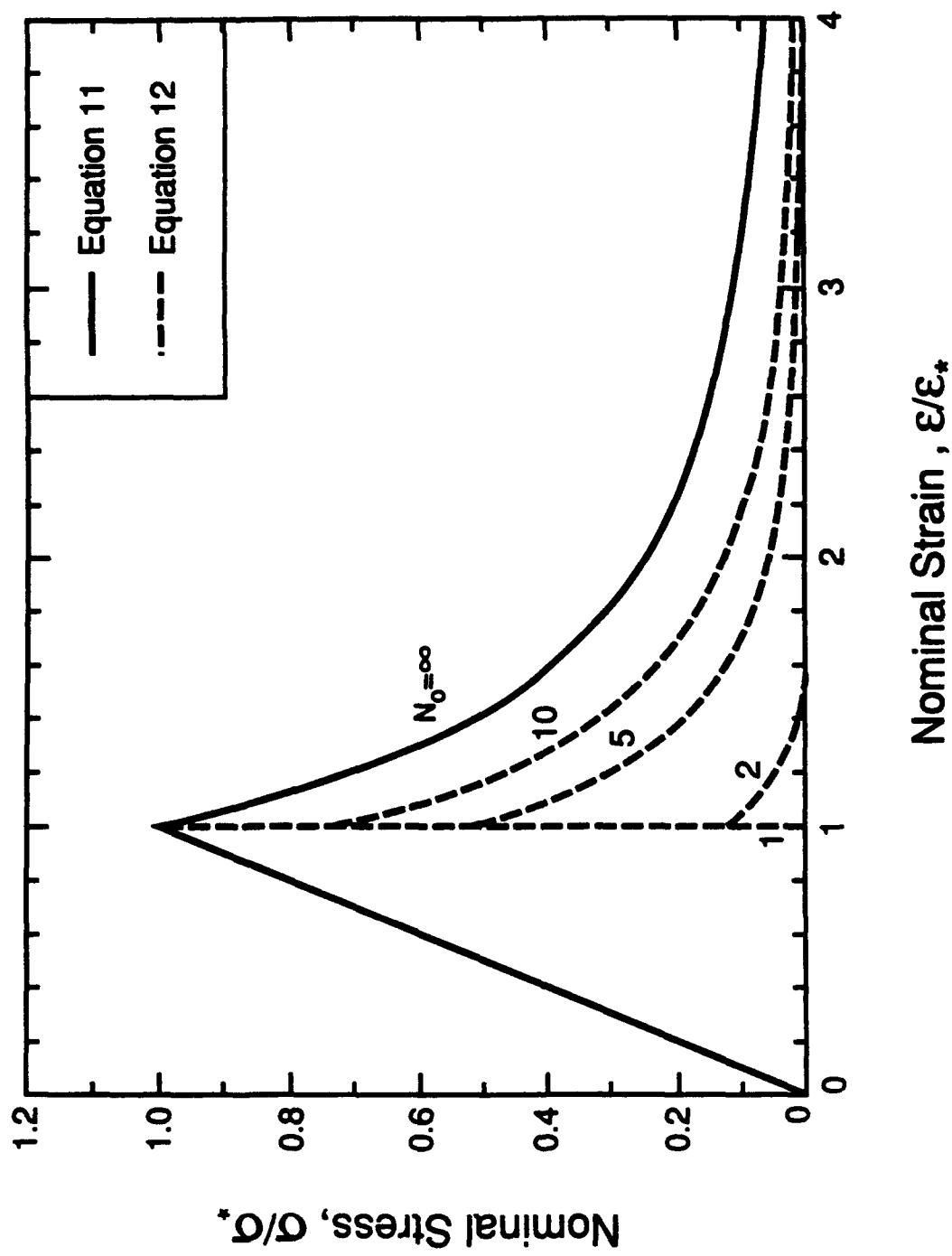


Figure 2

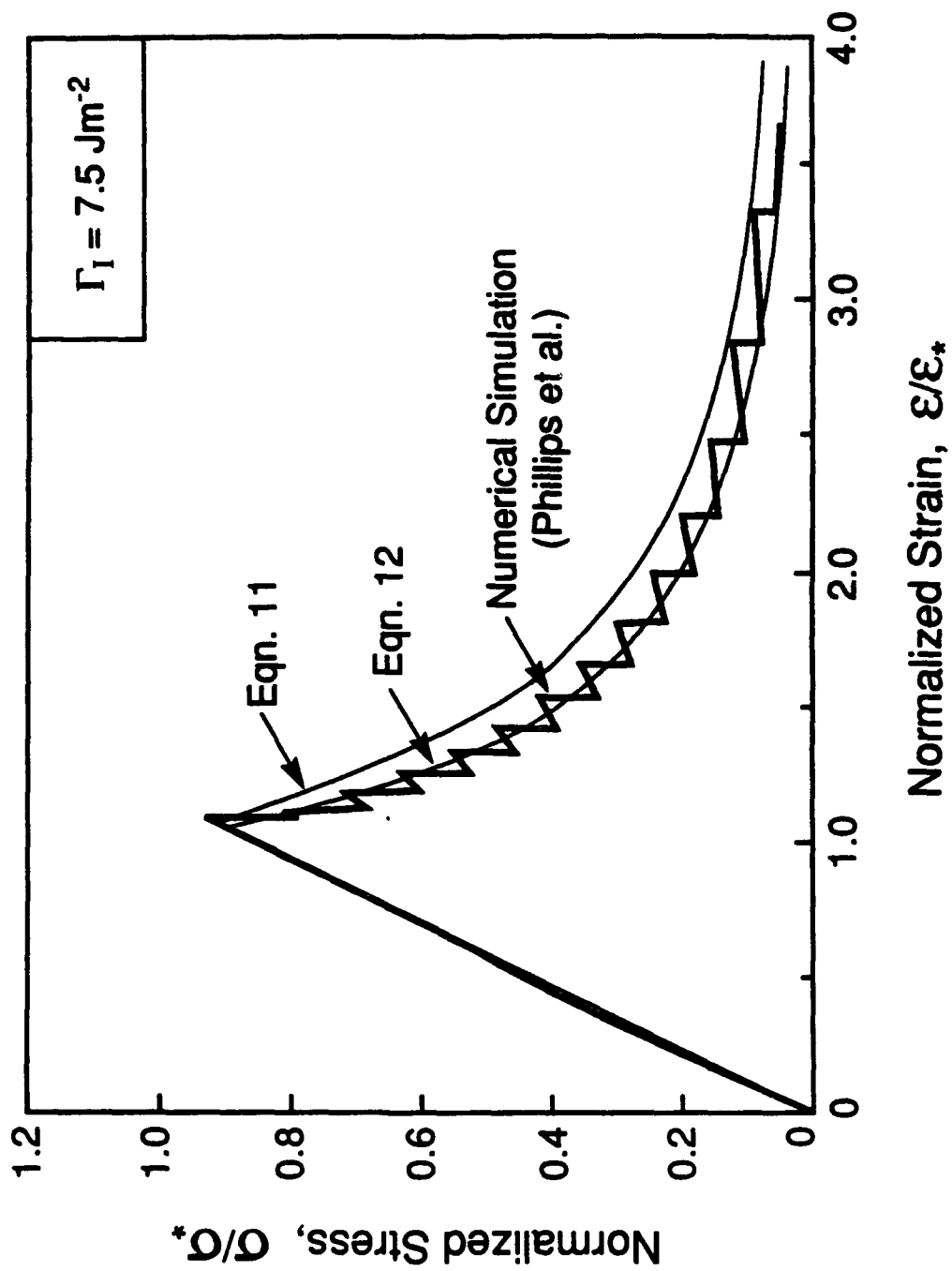


Figure 3(a)

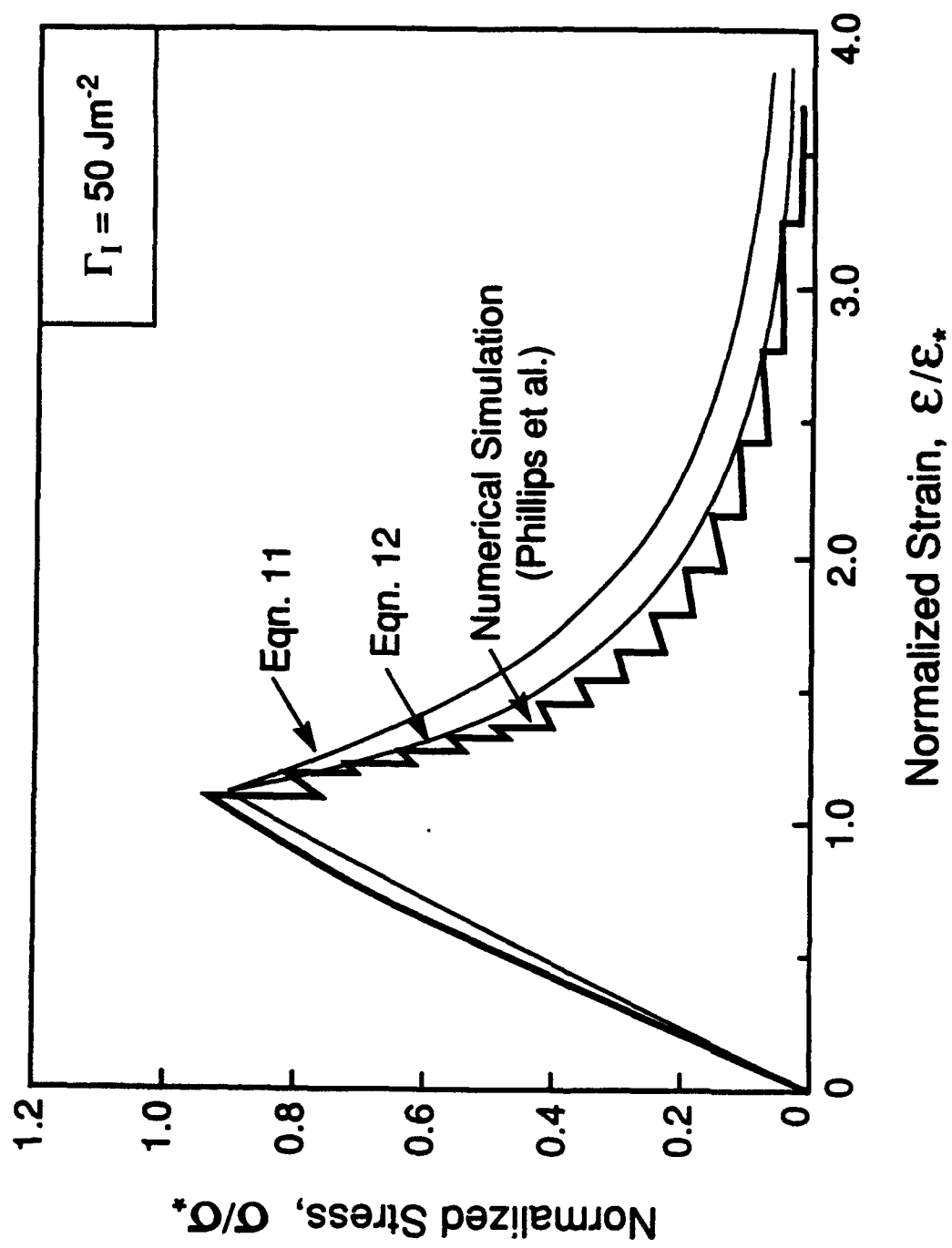


Figure 3(b)



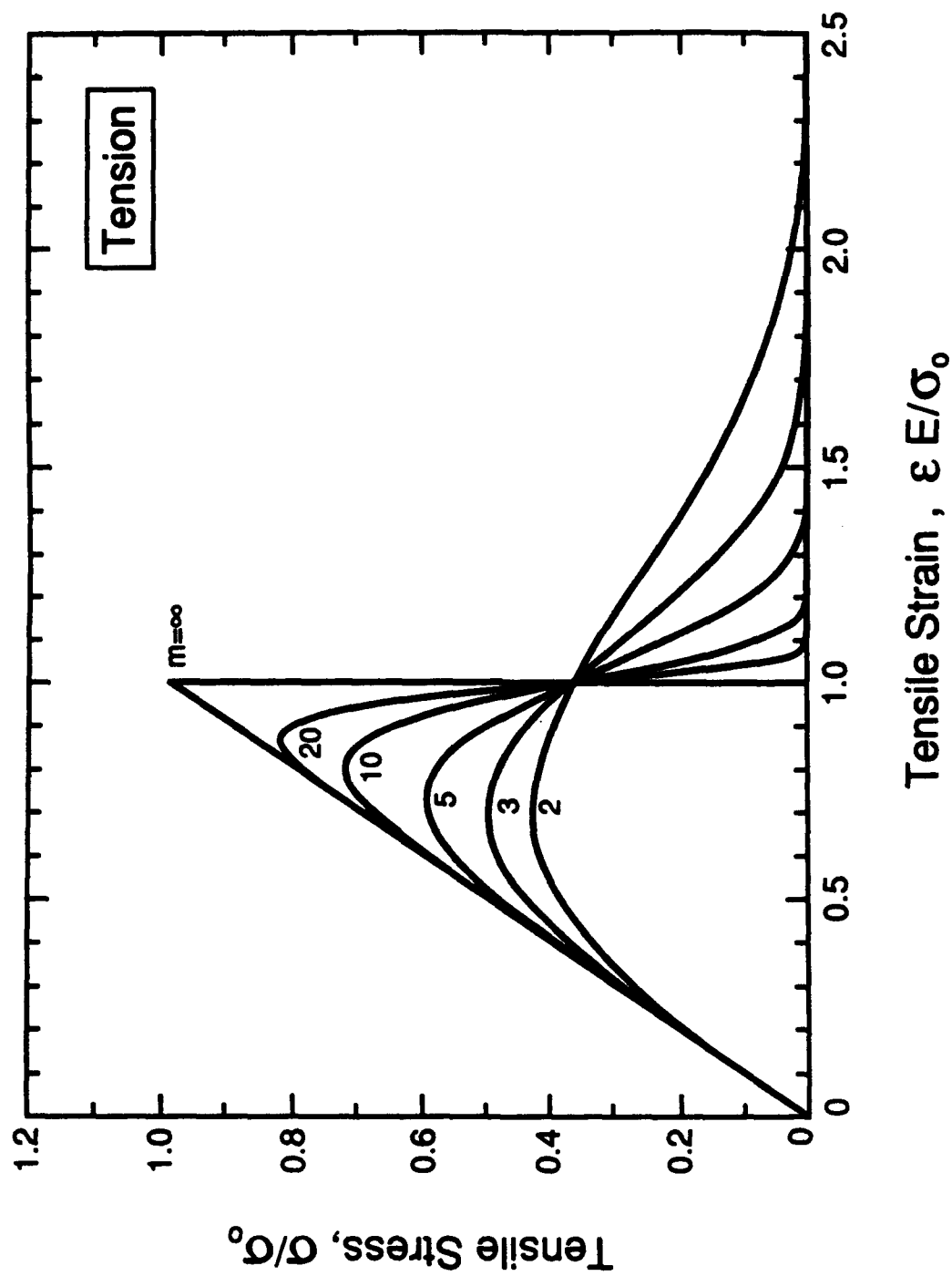


Figure 4(a)

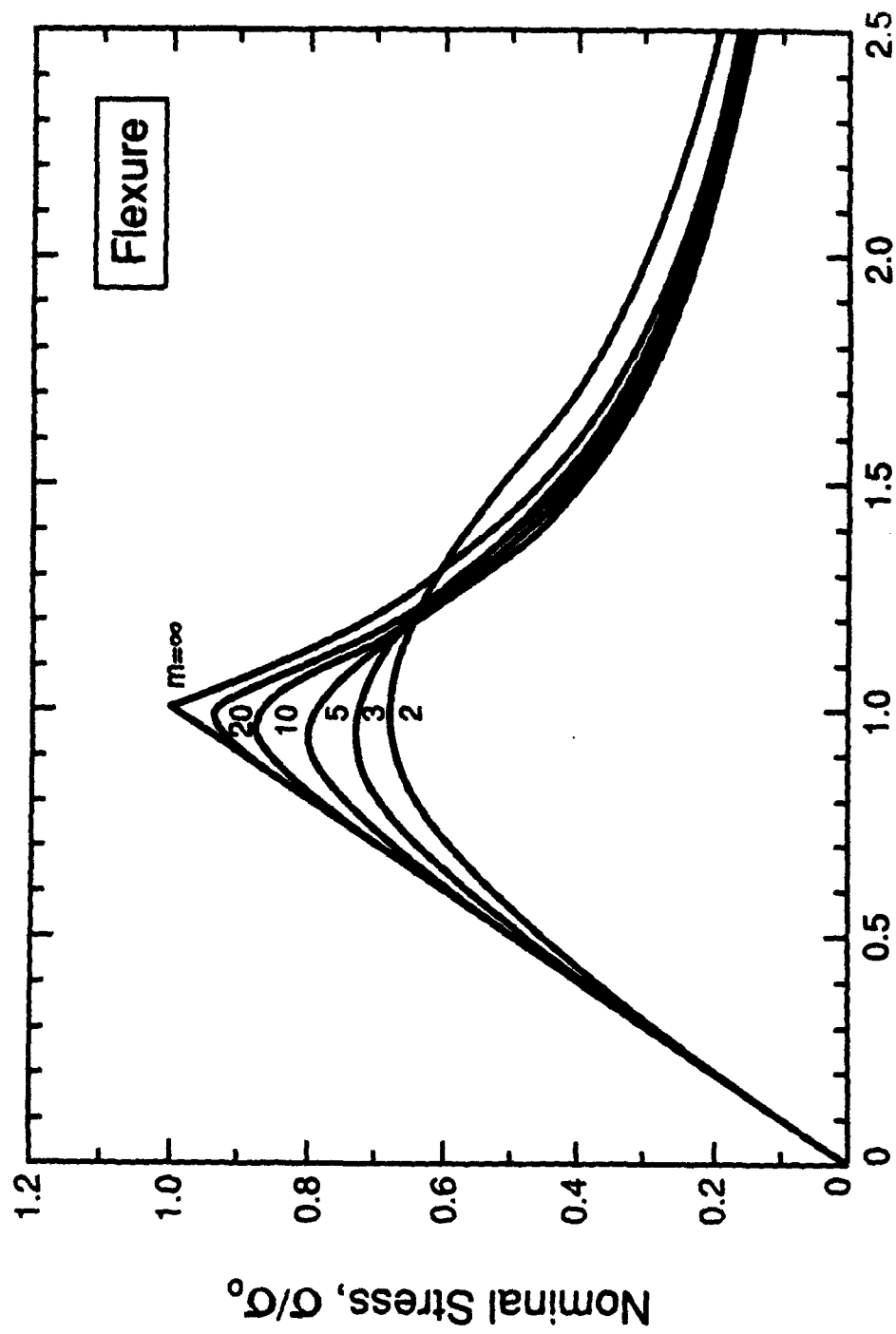


Figure 4(b)

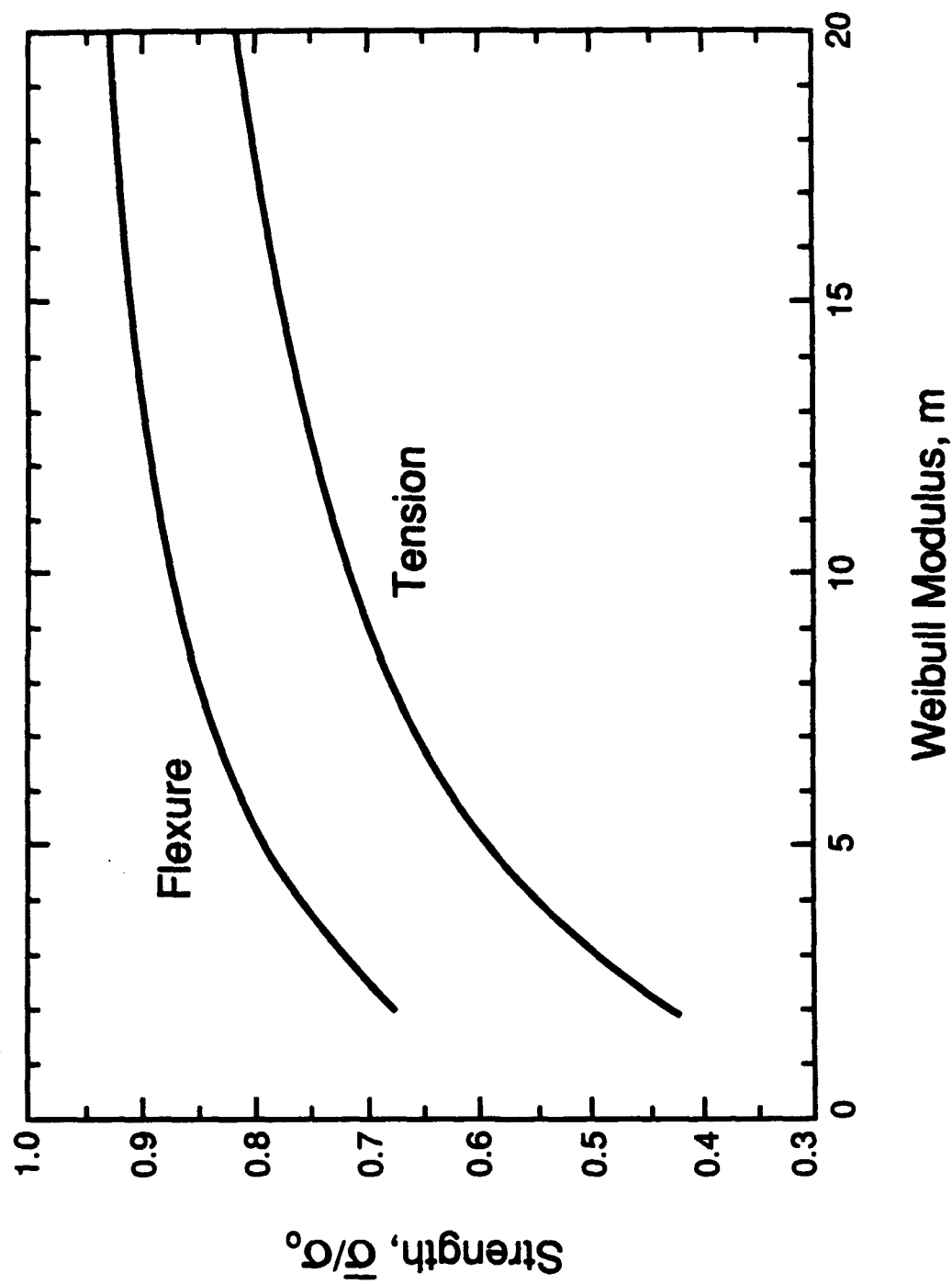


Figure 5

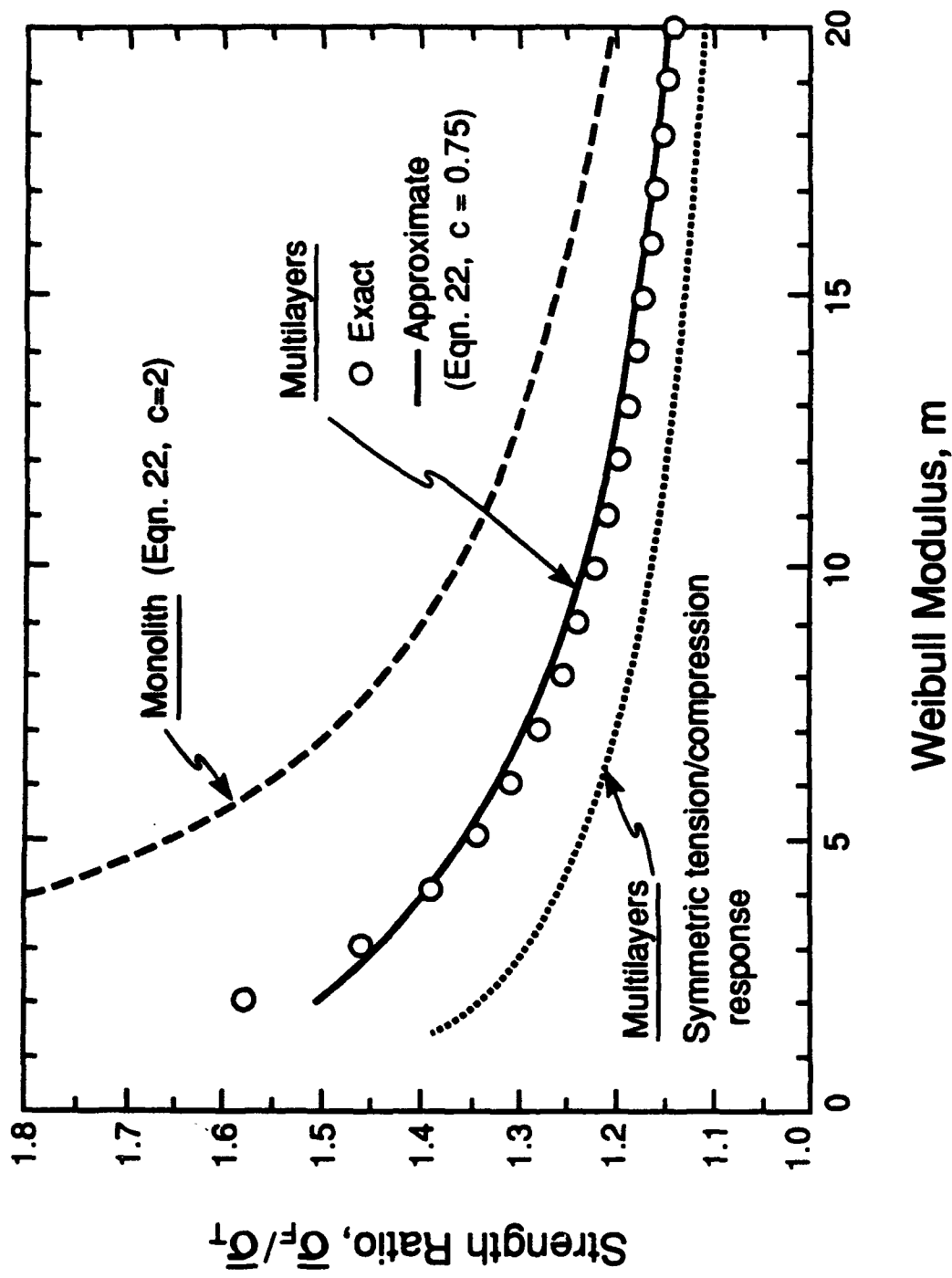


Figure 6

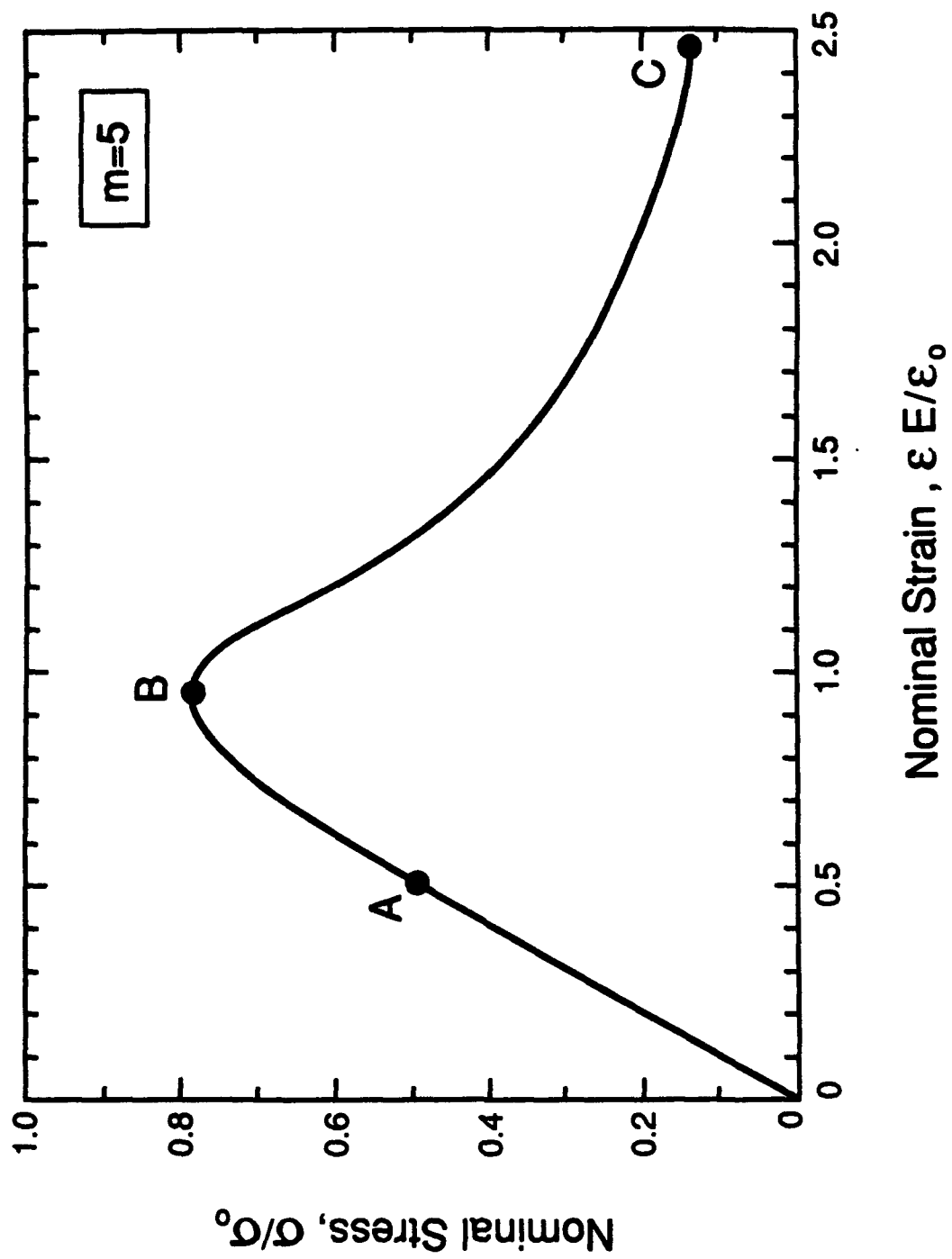


Figure 7(a)

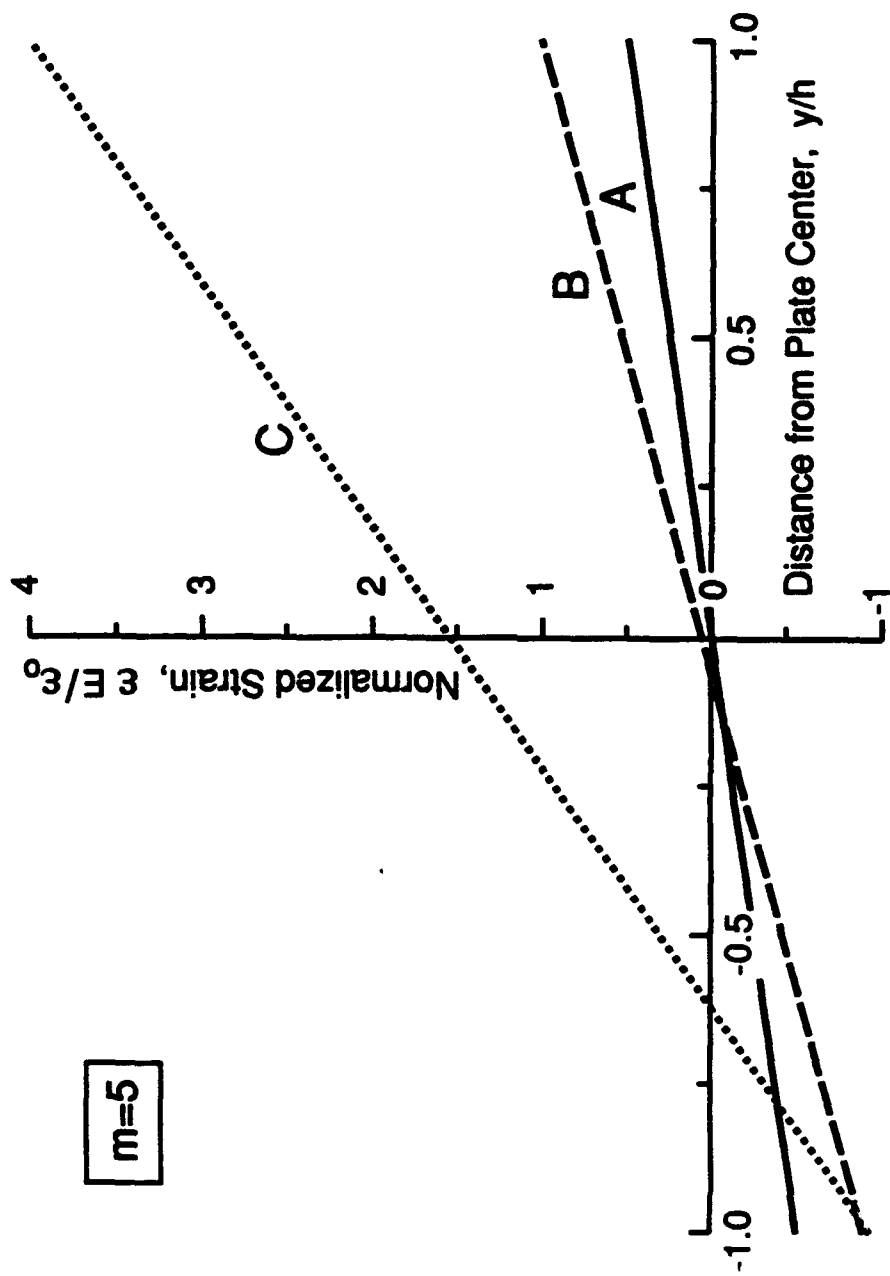


Figure 7(b)

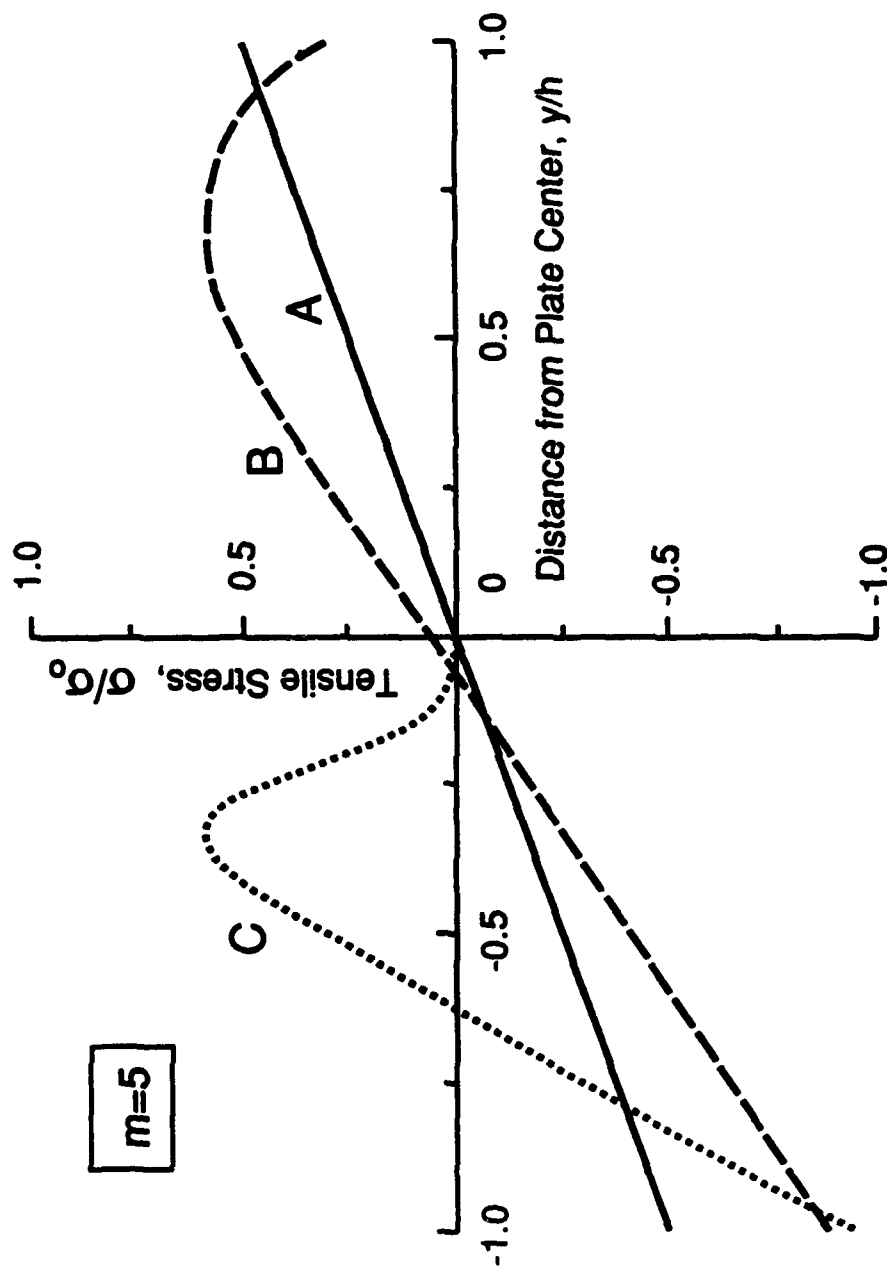


Figure 7(c)

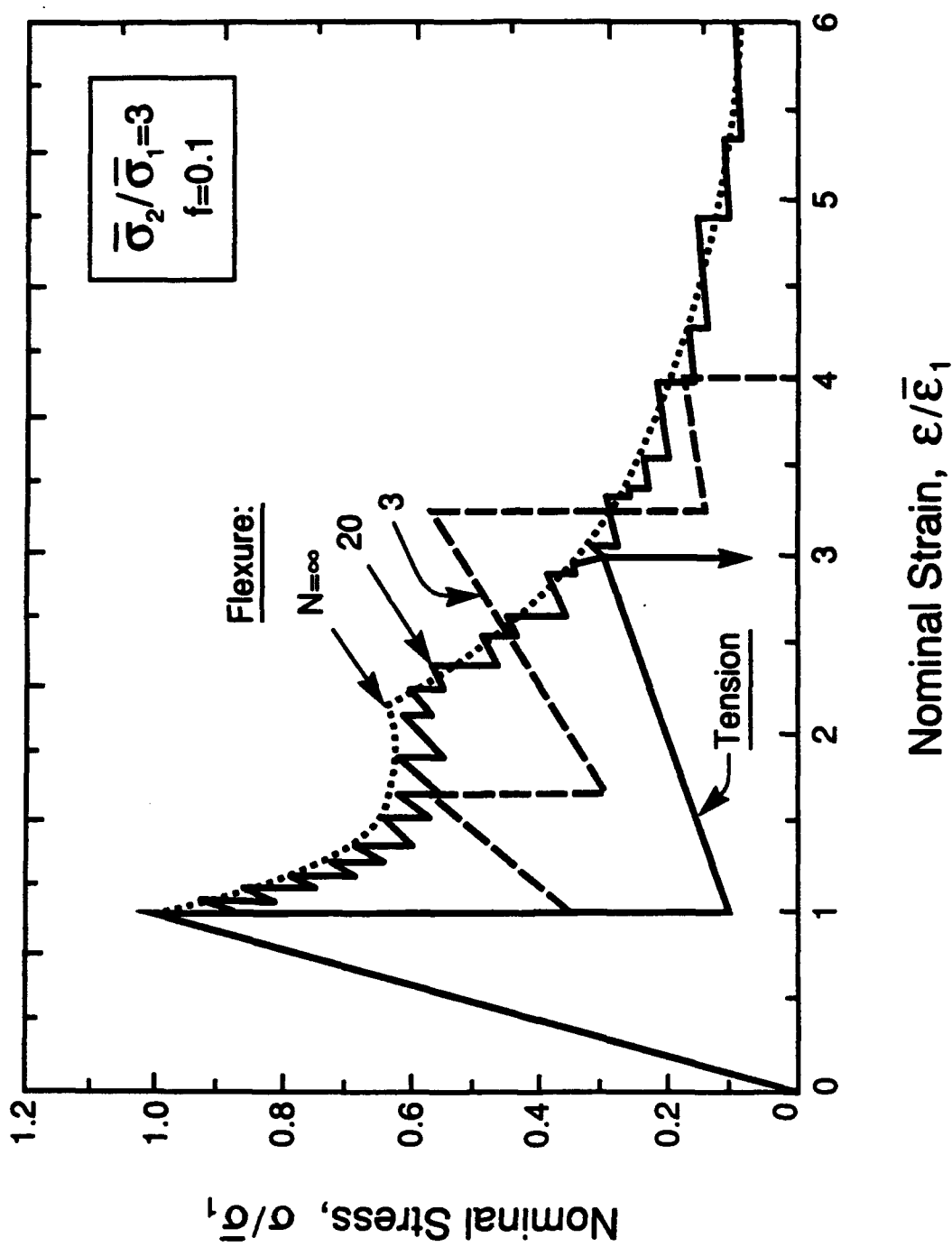


Figure 8(a)



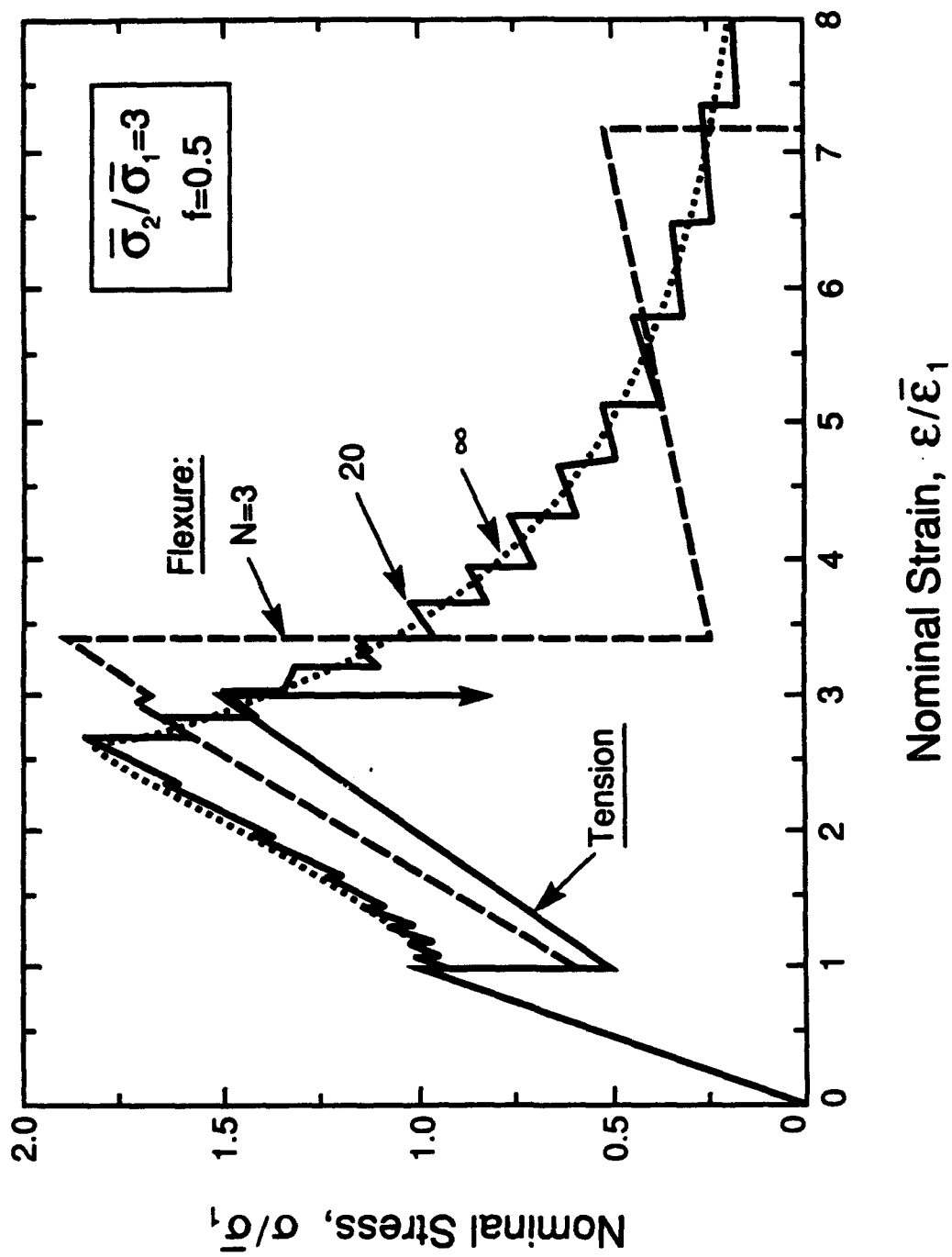


Figure 8(b)

[illegible]

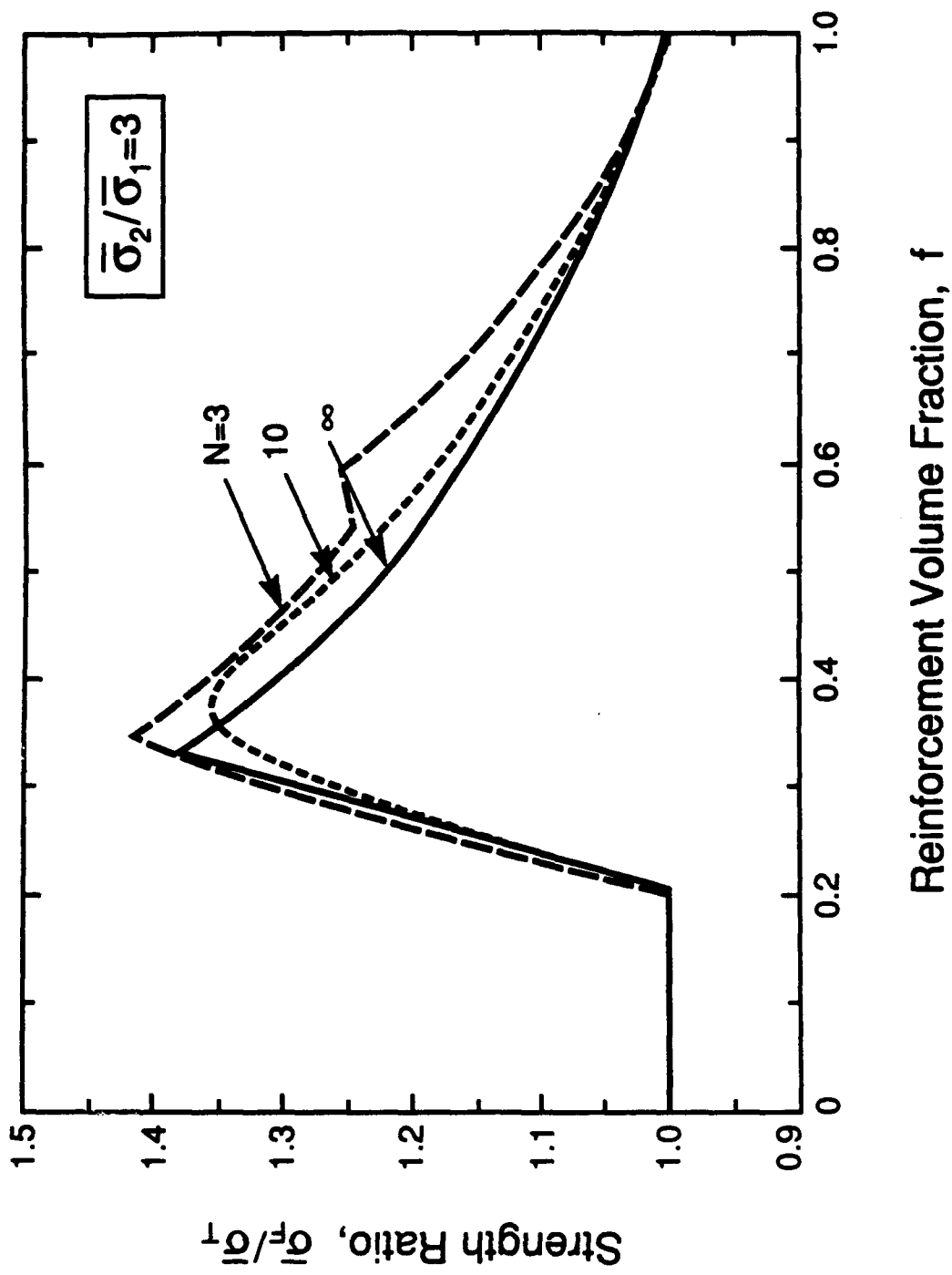
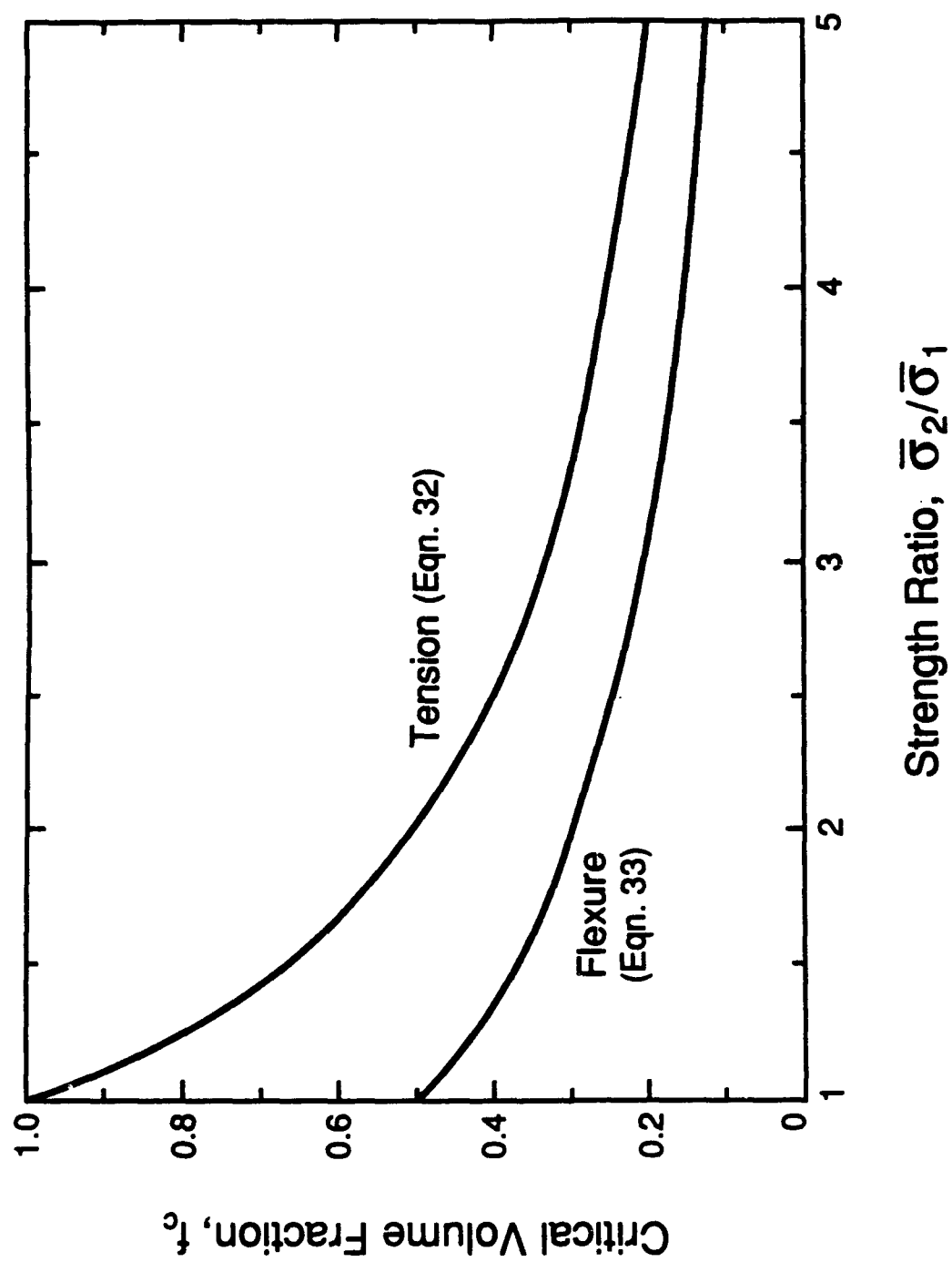
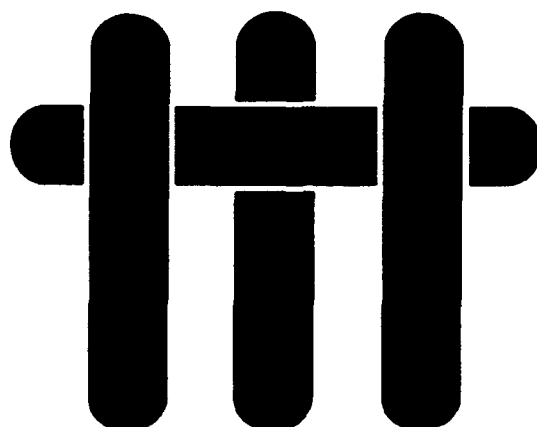


Figure 9(b)



**Figure 10**

# M A T E R I A L S



## ON THE FLEXURAL PROPERTIES OF BRITTLE MULTILAYER MATERIALS: II. EXPERIMENTS

C.A. Folsom\*, F.W. Zok and F.F. Lange

Materials Department  
University of California  
Santa Barbara, California 93106

\*Presently at

Wright Laboratories  
Materials Directorate  
Wright Patterson Air Force Base, OH  
45433-7817

*Submitted to the Journal of the American Ceramic Society, August 1993*

## ABSTRACT

An experimental investigation of the flexural properties of a variety of brittle multilayer materials has been conducted. The results have been compared with the predictions of a model presented in a companion paper<sup>1</sup>. Three types of systems have been studied. The first consisted of glass sheets bonded together with a thermoplastic adhesive. The glass sheets had been pre-cracked by indentation prior to bonding such that their strengths were essentially deterministic. The flexural response of this system is characterized by an initial linear elastic regime, followed by a step-wise reduction in the stress-strain curve during cracking. The second system consisted of thin glass sheets (without indents), also bonded with a thermoplastic adhesive. This system exhibited flexural characteristics similar to those found in the system with indented glass plates. In both systems, the measured stress-strain behavior was in good agreement with the model predictions, incorporating the strength characteristics of the constituent layers. The third type of system was a hybrid composite comprised of alternating layers of a brittle phase (either glass or  $\text{Al}_2\text{O}_3$ ) and a carbon fiber reinforced epoxy composite. These systems exhibited an initial linear elastic response, followed by a regime in which multiple cracks formed in each of the brittle layers, with the exception of the one on the compressive face. This process generally occurred subject to a progressively increasing stress. None of the fiber reinforced layers failed during this stage. The peak stress coincided with the onset of failure of the fiber reinforced layers. The progressive failure of these layers was accompanied by step-like load drops, similar to those observed in the single phase glass multilayer specimens. The measured response of these systems

was qualitatively consistent with the model predictions, though some discrepancies have been noted and their origins briefly discussed.

## 1. INTRODUCTION

Brittle multilayer materials with crack-deflecting interfaces exhibit different characteristics under flexural and tensile loadings. Notably, under flexural loading, the layers crack sequentially from the tensile to the compressive face, giving a series of step-like drops in the stress-strain response following the onset of cracking<sup>2-5</sup>. In this case, the nominal failure strain is substantially higher than the failure strain measured in uniaxial tension. Similar behavior is expected under thermal loading conditions where the thermal gradients occur across the layers.

In order to develop a better understanding of the mechanics of failure of multilayer materials, an experimental investigation of the flexural properties of several model systems has been conducted. The experimental effort complements the modeling work presented in a companion paper<sup>1</sup>.

Three types of systems have been examined. The first consists of a small number of glass plates bonded together with a thermoplastic adhesive. In order to control the strength of the plates, the plates are pre-cracked by indentation prior to bonding. The second system consists of a relatively large number of thin glass sheets (with no indents), also bonded with a thermoplastic adhesive. In this case, the individual sheets exhibit a range of strengths, characterized by a Weibull distribution. The third type of system is a hybrid composite comprised of alternating layers of a brittle phase (either glass or  $\text{Al}_2\text{O}_3$ ) and a fiber reinforced epoxy composite<sup>5</sup>. These systems are bonded together by the epoxy within the fiber composite. The flexural stress-strain responses for each of these systems have been measured and the results compared with the model predictions presented in the companion paper<sup>1</sup>.



## 2. EXPERIMENTAL PROCEDURE

The first system was designed to simulate multilayer materials in which the constituent layers exhibit a *deterministic* tensile strength. For this purpose, multilayer beams comprised of indented glass plates<sup>†</sup> were used. The indents were placed in the center of the plates using a diamond pyramid indenter, with indent loads of either 1, 5 or 10 kg. The plates had dimensions of 25.4 x 76 x 1.0 mm. The strengths of the pre-cracked plates were measured using 4 point flexure. At least 10 tests were performed for each indent load. In addition, the elastic modulus of the glass was measured using (unindented) plates loaded in flexure, with a strain gauge attached to one of the faces within the constant moment region.

Prior to bonding, the indented plates were cleaned in detergent and rinsed in deionized water. A thin layer of a thermoplastic adhesive\* was then applied to one face of each plate at a temperature of 160°C. The plates were stacked on one another such that all the indents were facing the same direction. The stacked plates were then uniaxially hot pressed at 175°C and 350 kPa for ~ 3 minutes, cooled to < 100°C with the pressure applied, and then released. The volume fraction of adhesive, determined from the thickness of the bonded plates, was  $\leq 0.01$ . Systems containing 2, 3, 4 and 5 layers were produced in this manner.

A similar procedure was used to make multilayer beams comprised of 20 thin glass sheets<sup>‡</sup>, each ~ 0.15 mm thick. In this case, the sheets were not indented. A multilayer plate with dimensions 75 x 28 mm was fabricated and cut into four identical

---

<sup>†</sup>Corning Microscope Slides (No. 2947)

<sup>\*</sup>Buehler Lakeside 70 Thermoplastic Cement

<sup>‡</sup>Gold Seal Coverslips

rectangular beams, each ~ 9 mm wide. The individual sheets in two of the beams were subsequently retrieved by dissolving the adhesive in acetone. The strengths of the individual sheets were measured in three-point bending, with an outer loading span of 25 mm. The strength distribution was characterized using the two parameter Weibull function<sup>6</sup>. The two remaining beams were subsequently tested in four point flexure, as described below.

The third type of system was comprised of alternating layers of a brittle material (either glass<sup>\*</sup> or Al<sub>2</sub>O<sub>3</sub><sup>§</sup>) and a unidirectional carbon fiber reinforced epoxy<sup>\*\*</sup> (CFRE) composite<sup>5</sup>. Multilayer plates were produced by uniaxial hot pressing at 135°C and 350 kPa pressure for 90 minutes. The plates contained 6 ceramic or glass layers and 5 CFRE layers. The Al<sub>2</sub>O<sub>3</sub>/CFRE composite contained 15% CFRE. Two volume fractions of CFRE were obtained in the glass/CFRE system (either 13% or 21%) by using different thicknesses of glass plate (either 0.41 or 0.71 mm). The elastic moduli and strengths of the glass and Al<sub>2</sub>O<sub>3</sub> sheets were measured using strain-gauged flexure specimens. The strengths were obtained from at least 10 tests on each material. In addition, unidirectional laminates of the CFRE composite were produced and their properties characterized in a similar fashion. The properties of the constituent layers are summarized in Table 1.

The single phase multilayer specimens were tested in four point flexure. The inner and outer loading spans were 22.2 mm and 63.5 mm, respectively. The tests were conducted in displacement control at a rate of 1.7 µm/s. In some cases, the strain on the compressive face was measured with a resistance strain gauge within the constant

---

<sup>\*</sup>Corning No. 7059

<sup>§</sup>Coors 96% Al<sub>2</sub>O<sub>3</sub>

<sup>\*\*</sup>Fiberite HYE 3071 AC

moment region. In addition, the remote displacement was monitored by an LVDT. The compliance of the testing machine was determined using a thick, strain-gauged glass beam, also loaded in flexure. The machine compliance was subsequently used to determine the load point displacement from the remote displacement. Prior to cracking, the strains computed from the load point displacements were found to be within ~ 2% of those measured with the strain gauges.

The hybrid composite specimens were tested in a similar fashion, except with a smaller outer span (44.4 mm). For comparison, three point tests were also conducted on the hybrid composites, using the same outer span.

The results of the flexural tests are presented in two ways. In the first, the nominal stress,  $\sigma$ , is plotted against the nominal strain,  $\epsilon$ . The two quantities are computed from Euler-Bernoulli beam theory<sup>7</sup> and are given by

$$\sigma = \frac{3FS_o}{2b(N_o t)^2} \quad (1a)$$

$$\text{and} \quad \epsilon = \frac{6\delta N_o t}{S_o^2} \quad (1b)$$

for 3-point loading, and

$$\sigma = \frac{3F(S_o - S_i)}{2b(N_o t)^2} \quad (2a)$$

and

$$\epsilon = \frac{6\delta N_o t}{(S_o - S_i)(S_o + 2S_i)} \quad (2b)$$

for 4-point loading. Here,  $F$  is the applied load,  $S_i$  and  $S_o$  are the inner and outer loading spans,  $b$  is the specimen depth,  $t$  is the thickness of the individual layers,  $N_o$  is the total number of layers and  $\delta$  is the load point displacement. In the second, the nominal stress is plotted against the true compressive strain,  $\epsilon_c$ , measured by the strain gauge.

### 3. INDENTED GLASS MULTILAYERS

#### 3.1 Experimental Results

Examples of the flexural stress-strain responses of the indented multilayer beams are shown in Figs. 1 and 2. Here the stresses are normalized by the strengths of the individual plates,  $\sigma_*$ , and the strains normalized by the corresponding fracture strains,  $\epsilon_* = \sigma_*/E$ , with  $E$  being the Young's modulus. The strengths of the individual indented plates are summarized in Table 2. In all cases, the elastic modulus of the multilayer specimen was within  $\sim 3\%$  of the modulus of the individual plates ( $E = 65.5$  GPa). Furthermore, cracking in the multilayer specimens initiated at a stress,  $\sigma \approx \sigma_*$ . At this stress, the outermost layer cracked entirely, though all the remaining layers stayed intact. In addition, a delamination crack had propagated along the interface between the first and second layers. This cracking process was accompanied by a load drop. During subsequent loading, the tangent modulus,  $d\sigma/d\epsilon$ , was lower than  $E$ , but remained essentially constant until the second layer cracked. Cracking was again

accompanied by a load drop, the propagation of a delamination crack at the interface between the second and third layers, and a further drop in the tangent modulus. The step-like stress-strain response continued until all of the layers had failed. Occasionally, two layers cracked simultaneously, resulting in a relatively large increment of load point displacement. This behavior is presumed to be due to the finite stiffness of the testing machine.

Two features of the stress-strain curves are of interest: (i) the stress required to crack a particular layer, and (ii) the slope (or tangent modulus) following cracking. The trends in these parameters with the fraction of cracked layers,  $N_c/N_0$ , derived from tests on specimens with various indent loads and numbers of layers, are presented in Figs. 3 and 4. Once again the stresses have been normalized by the strengths of the individual indented plates. The tangent modulus is expressed in two ways: (i) in terms of the *nominal* strain,  $d\sigma/d\epsilon$  (Fig. 4(a)), and (ii) in terms of the true *compressive* strain,  $d\sigma/d\epsilon_c$  (Fig. 4(b)). In both cases, the tangent modulus is normalized by the initial elastic modulus,  $E$ . Using these normalizations, the cracking stress and tangent moduli for all specimens exhibit essentially the same decreasing trends with  $N_c/N_0$ , independent of the absolute strengths and the absolute number of layers.

### 3.2 Model Predictions

The experimental results have been compared with the predictions of a model, detailed in the companion paper<sup>1</sup>. The model is based on Euler-Bernoulli beam theory, incorporating the effects of the sequential cracking of the layers. It is assumed that the compressive strength of the material is very much higher than the tensile strength and that the tensile strengths of all layers are equivalent. Furthermore, the material is taken

to be linear elastic up to fracture. The length of the delamination crack following cracking of a given layer is assumed to be large and the shear stress acting along the delamination crack assumed to be negligible, such that the stress everywhere in the cracked layer falls to zero. In essence, the cracked layers are imagined to be removed from the beam, leaving a beam comprised of  $N_i$  intact layers. Throughout, the strain distribution is taken to be linear across the beam. The key results from the model are presented below.

The stress required to crack a particular layer is related to the fraction of cracked layers through

$$\frac{\sigma}{\sigma_*} = \left(1 - \frac{N_c}{N_o}\right)^2 \quad (3)$$

The corresponding nominal strain is

$$\frac{\varepsilon}{\varepsilon_*} = \left(1 - \frac{N_c}{N_o}\right)^{-1} \quad (4)$$

and the true compressive strain on the bottom face is

$$\frac{\varepsilon_c}{\varepsilon_*} = 1 \quad (5)$$

Furthermore, the nominal stress *following cracking* of the  $i^{\text{th}}$  layer is

$$\frac{\sigma}{\sigma_*} = \left(1 - \frac{1}{N_i}\right)^3 \left(\frac{N_i}{N_o}\right)^2 \quad (6)$$

The preceding results can be combined to give the relevant tangent moduli:

$$\frac{1}{E} \frac{d\sigma}{d\epsilon} = \left(1 - \frac{N_c}{N_o}\right)^3 \quad (7)$$

and

$$\frac{1}{E} \frac{d\sigma}{d\epsilon_c} = \left(1 - \frac{N_c}{N_o}\right)^2 \quad (8)$$

Comparisons between the model predictions and the experimental measurements on the indented multilayer beams are presented in Figs. 1-4. A good correlation between the two is obtained in all cases.

#### 4. INDENTED GLASS MULTILAYER BEAMS

##### 4.1 Experimental Results

The strength distribution of the individual glass layers extracted from the multilayer beams is presented in Fig. 5. The results are consistent with the Weibull distribution<sup>6</sup>

$$P = 1 - \exp - \frac{kV}{V_0} \left( \frac{\sigma}{\sigma_0} \right)^m \quad (9)$$

where  $P$  is the cumulative failure probability up to a stress,  $\sigma$ ,  $m$  is the Weibull modulus,  $\sigma_0$  and  $V_0$  are the reference values of stress and volume, respectively, and  $k$  is a geometric parameter, which, for three-point loading, is given by<sup>6</sup>

$$k = \frac{1}{2(m+1)^2} \quad (10)$$

Linear regression analysis of the data in Fig. 5 gives  $m = 6$  and  $\sigma_0 = 72$  MPa.

The stress-strain response of one of the multilayer beams measured in four point flexure is shown in Fig. 6. Here the nominal stress is normalized by the reference stress,  $\sigma_0$ , and the strain normalized by the corresponding reference strain,  $\sigma_0/E$ . Once again, load drops associated with the cracking events are evident. Moreover, large nominal strains ( $\epsilon E/\sigma_0 > 5$ ) are achieved prior to complete failure. The stress-strain response of the other multilayer beam was essentially the same.

Observations made during testing indicated that the layers did not crack exactly in order of their position with respect to the tensile face. This result is consistent with the relatively broad strength distribution associated with the individual layers. The observations also indicated that failure sites were distributed in a more or less random fashion within the constant moment region (Fig. 7) This result suggests that the stress concentrations associated with individual cracks is small and have little influence on the location of failure in the adjacent layers.



## 4.2 Model Predictions

The model described in Section 3.2 has been extended to incorporate the effects of a *distribution* in the tensile strengths of the individual layers. Again, details are presented in the companion paper<sup>1</sup>. In the model, the number of layers is assumed to be large, allowing the effects of stress gradients across individual layers on failure probability to be neglected. Even in this limiting case, the solution to the stress-strain response requires numerical integration (see Eqns. 20 and 21 and Fig. 4(b) in Ref. 1).

The prediction of this model for values of  $m$  and  $\sigma_0$  corresponding to the glass sheets is shown in Fig. 6. In this case, the relevant shape factor,  $k$ , is the one corresponding to pure tension ( $k = 1$ ). The predictions follow trends similar to those of the measurements, though the model slightly underestimates the stress beyond the load maximum. Moreover, the model does not predict the discrete load drops following each cracking event.

## 5. HYBRID LAYERED COMPOSITES

### 5.1 Experimental Results

The flexural responses of the two glass/CFRE composites are shown in Fig. 8. The first non-linearity in these curves is due to cracking of the glass sheet on the tensile face. Beyond this point, multiple cracks are formed in all glass layers, with the exception of the one on the compressive face. Beyond the load maximum, the stress-strain curves exhibit large periodic load drops, each associated with fracture of one of the CFRE layers. A series of micrographs showing the progression of cracking within the glass sheets prior to the load maximum is shown in Fig. 9. The nominal

failure strain in these systems was generally  $\geq 3\%$ . In contrast, the failure strains of similar systems<sup>5</sup> under uniaxial tensile loading is  $\sim 1.5\%$ .

During the cracking process, prior to the load maximum, there is a continual re-distribution of stress occurring across the beam section. The neutral axis shifts toward the compressive face, a result on the loss of load bearing capacity of the cracked layers. This result is consistent with the large stresses developed within the glass layer on the compressive face, as shown in Fig. 10. In this case ( $f = 21\%$ ), the peak *compressive* stress is  $\sim 2.5$  times the peak *nominal* stress and about an order of magnitude larger than the tensile strength of the individual glass layers.

The flexural response of the  $\text{Al}_2\text{O}_3/\text{CFRE}$  composite is shown in Fig. 11. This system exhibits essentially the same features as the glass/CFRE system.

## 5.2 Model Predictions

The model presented in Section 3.2 has been extended to dual phase multilayer beams<sup>1</sup>. Each of the phases is assumed to have a deterministic tensile strength and to be linear elastic up to fracture. The elastic mismatch between the two phases is incorporated into the model by simply replacing one of the phases with an equivalent section of the other, with a thickness ratio equal to the inverse of the modulus ratio<sup>7</sup>.

The model predictions are compared with the experimental measurements in Figs. 8, 10 and 11. The constituent properties used in the model are summarized in Table 1. The predicted stress-strain curves exhibit features similar to those of the experiments, though two discrepancies are found. First, beyond the initial cracking event but prior to the ultimate strength, the predicted stress is consistently below the measure value. This discrepancy is consistent with the assumption that the stress in the

cracked layers falls to zero, whereas the observations of multiple cracking indicate that the stresses in these layers buildup to substantial levels over relatively short distances from any one of the crack planes. Second, the predicted ultimate strength generally exceeds the measured value. This trend is believed to be due to the stress concentrating effects associated with the cracks in the ceramic or glass layers, leading to premature failure of the adjacent CFRE layers. Neither of these effects is accounted for in the present model.

## 6. DISCUSSION

The good correlation between the model predictions and experimental measurements on the *indented* multilayer glass beams provides confidence that the model, though rather simple, captures the essential features of the flexural response of brittle multilayer systems containing crack-deflecting interfaces. In this case, the assumption that the strengths of the layers are equivalent is appropriate, since all the layers had been indented with the same load prior to bonding. This assumption is also supported by the small standard deviations in the strengths of the indented plates (Table 2). In addition, the assumption that the stresses within the cracked layers are reduced to a negligible value is consistent with the delamination cracks observed during testing. An important conclusion emanating from these comparisons is that the step-like stress-strain response and the large nominal strains that are attained prior to complete failure are consequences of the stress re-distribution and stiffness reduction associated with cracking: no additional "toughening mechanisms" are required to produce this behavior.

The study on the *unindented* multilayer beams provides additional verification of these conclusions. Furthermore, it demonstrates that fracture statistics can be incorporated into the model and yield predictions that are broadly consistent with the experimental measurements. The discrepancies that do exist between experiment and theory are believed to be due mainly to the finite number of layers in the real systems. These effects could be incorporated into the model, though the predictions would require numerical simulation and the results would no longer be deterministic<sup>3</sup>.

The discrepancies between the experiment and the model for the hybrid composites are believed to be due to two relevant features of the fracture process being neglected in the model. The first deals with the load transfer from the intact CFRE layers to the cracked ceramic or glass layers. Evidently, the interfaces in these materials are sufficiently strong to allow a stress build-up within the cracked layers. This build-up is manifested in the form of *multiple* cracking in each of the brittle layers. In this case, the assumption that the stress in the cracked layers drops to zero is no longer valid. The second feature involves the stress concentrations associated with the cracks when the interfaces are strong. These effects are expected to lead to premature fracture of the reinforcing layers in the vicinity of the cracks, reducing the ultimate strength. The observations of multiple cracks in the brittle layers within the hybrid composites is consistent with the notion that the interfacial strength in these systems is relatively high. A modeling approach involving damage mechanics is required to describe the flexural response of such systems.

Finally, the present results suggest that brittle multilayer systems both with and without reinforcing layers may be well suited for structural applications *subject to stress gradients across the layers*. These systems may be particularly attractive for thermal shock

applications wherein temperature gradients occur across the layers. Such concepts are currently being explored.

## ACKNOWLEDGMENTS

Funding of this work was supplied by the DARPA University Research Initiative Program of UCSB under ONR contract N-0014-92-J-1808. In addition, one of the authors (C.A.F.) was supported through the Air Force Palace Knights Program.

## REFERENCES

- [1] C.A. Folsom, F.W. Zok and F.F. Lange, "On the Flexural Properties of Brittle Multilayer Materials: I. Modeling," to be published in *J. Am. Ceram. Soc.* (1993).
- [2] W.J. Clegg, K. Kendall, N.McN. Alford, T.W. Burton and J.D. Birchall, "A Simple Way to Make Tough Ceramics, *Nature* [347], No. 6292, pp. 455-57, Oct. 4 (1991).
- [3] A.J. Phillipps, W.J. Clegg and T.W. Clyne, "Fracture Behavior of Ceramic Laminates in Bending: 1. Modelling of Crack-Propagation," *Acta Metall. Mater.*, 41 [3], 805-817 (1993).
- [4] A.J. Phillipps, W.J. Clegg and T.W. Clyne, "Fracture Behavior of Ceramic Laminates in Bending: II. Comparison of Model Predictions with Experimental Data," *Acta Metall. Mater.*, 41 [3], 819-827 (1993).
- [5] C.A. Folsom, F.W. Zok, F.F. Lange and D.B. Marshall, "Mechanical Behavior of a Laminar Ceramic/Fiber-Reinforced Epoxy Composite," *J. Am. Ceram. Soc.*, 75 [11] pp. 2969-75 (1992).
- [6] G.J. DeSalvo, "Theory and Structural Design Applications of Weibull Statistics," WANL-TME-2688, Westinghouse Electric Corp., Pittsburgh, PA, May 1970.
- [7] S. Timoshenko, *Strength of Materials*, 3<sup>rd</sup> Ed. Princeton (1955) pp. 137-40.

**TABLE 1**  
**Summary of Materials used in the Experimental Study**

Material	Thickness (mm)	Young's Modulus (GPa)	Flexural Strength (MPa)
Gold Seal Coverslip	0.13 - 0.15	60	*
Corning Microscope Slides (No. 2947)	0.96 - 1.06	65	‡
Corning Glass Substrates (No. 7059)	0.41	68	69 ± 2
Corning Glass Substrates (No. 7059)	0.71	68	67 ± 14
Coors 96% Al <sub>2</sub> O <sub>3</sub>	0.64	305	339 ± 38
CFRE (Fiberite HYE 3071AC)	0.13 - 0.20	115	1280

---

\*See Fig. 5

‡ See Table 2

**TABLE 2**  
**Strengths of Indented Glass Plates (Corning No. 2947)**

Indentation Load (kg)	Flexural Strength (MPa)
1	$41.9 \pm 2.8$
5	$31.7 \pm 0.7$
10	$27.5 \pm 1.2$

## FIGURES

- Fig. 1 The flexural response of a 3 layer specimen plotted as nominal stress,  $\sigma$ , against (a) the nominal strain,  $\epsilon$  and (b) the true compressive strain,  $\epsilon_c$ . The indentation load was 1 kg.
- Fig. 2 The flexural response of a 4 layer specimen, plotted as nominal stress,  $\sigma$ , against (a) the nominal strain,  $\epsilon$ , and (b) the true compressive strain,  $\epsilon_c$ . The indentation load was 10 kg.
- Fig. 3 Trends in the normalized cracking stress with the fraction of cracked layers.
- Fig. 4 Trends in the normalized tangent modulus, (a)  $(1/E) d\sigma/d\epsilon$  and (b)  $(1/E) d\sigma/d\epsilon_c$ , with the fraction of cracked layers.
- Fig. 5 Strength distribution of the thin glass sheets (Gold Seal Coverslips).
- Fig. 6 Flexural response of the (unindented) multilayer glass specimen.
- Fig. 7 Micrograph showing the crack distribution in (unindented) multilayer glass specimen. The light source was aligned parallel to the beam axis. The internal reflections off the crack surfaces give rise to discontinuities in brightness at the crack planes.
- Fig. 8 Flexural response of glass/CFRE hybrid composites, with (a)  $f = 13\%$  and (b)  $f = 21\%$ .
- Fig. 9 Optical micrographs showing progression of cracking in the glass/CFRE composite with  $f = 13\%$ . The nominal strains are: (a) 0.2%, (b) 0.9% and (c) 1.3%.
- Fig. 10 The variation in the maximum compressive stress (in the glass layer) with nominal strain for the glass/CFRE composite with  $f = 21\%$  (4-point loading). The compressive stress is calculated from the compressive strain and the elastic modulus of the glass.
- Fig. 11 Flexural response of the  $Al_2O_3$ /CFRE composite ( $f = 15\%$ ).



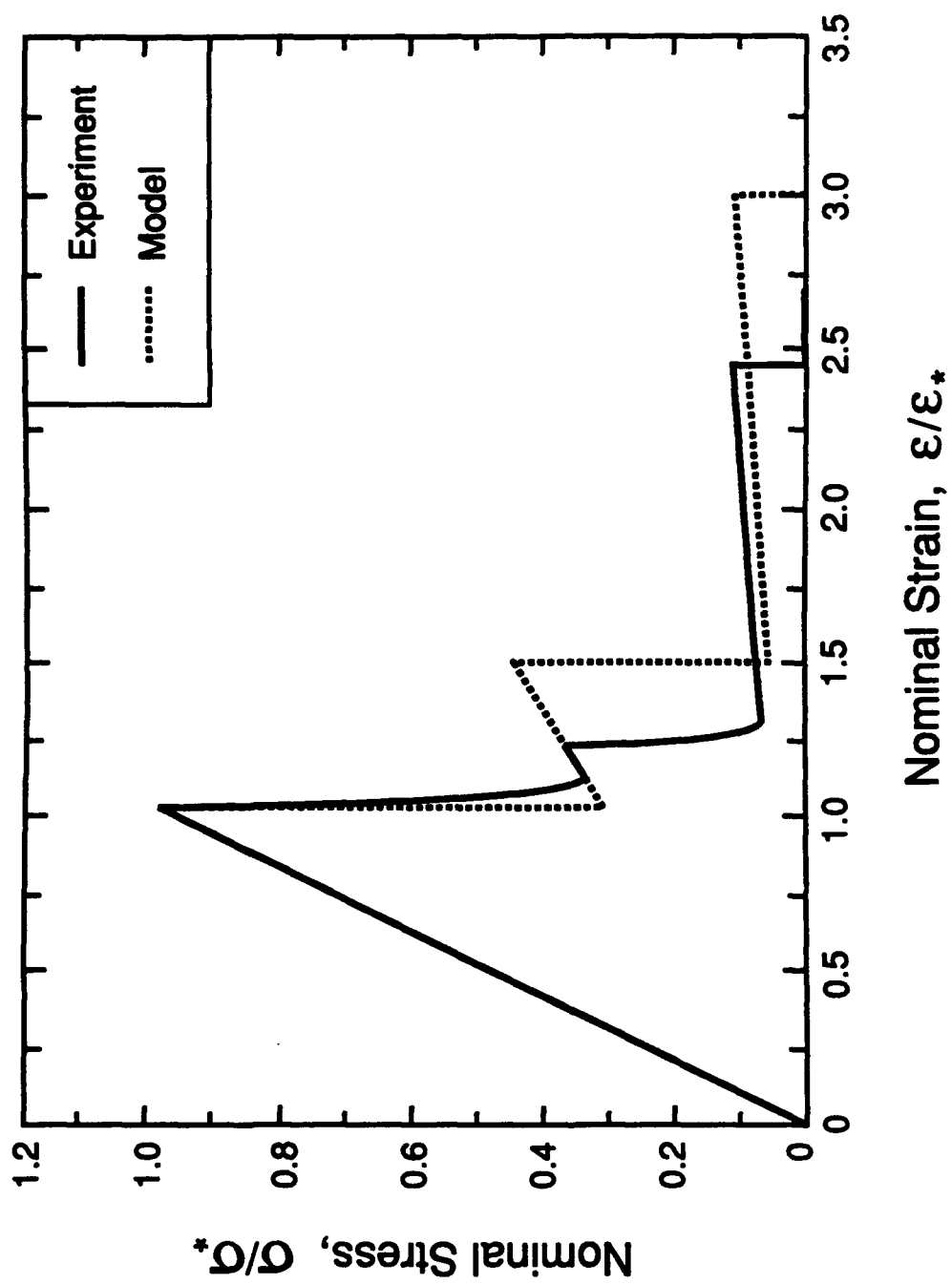


Figure 1(a)

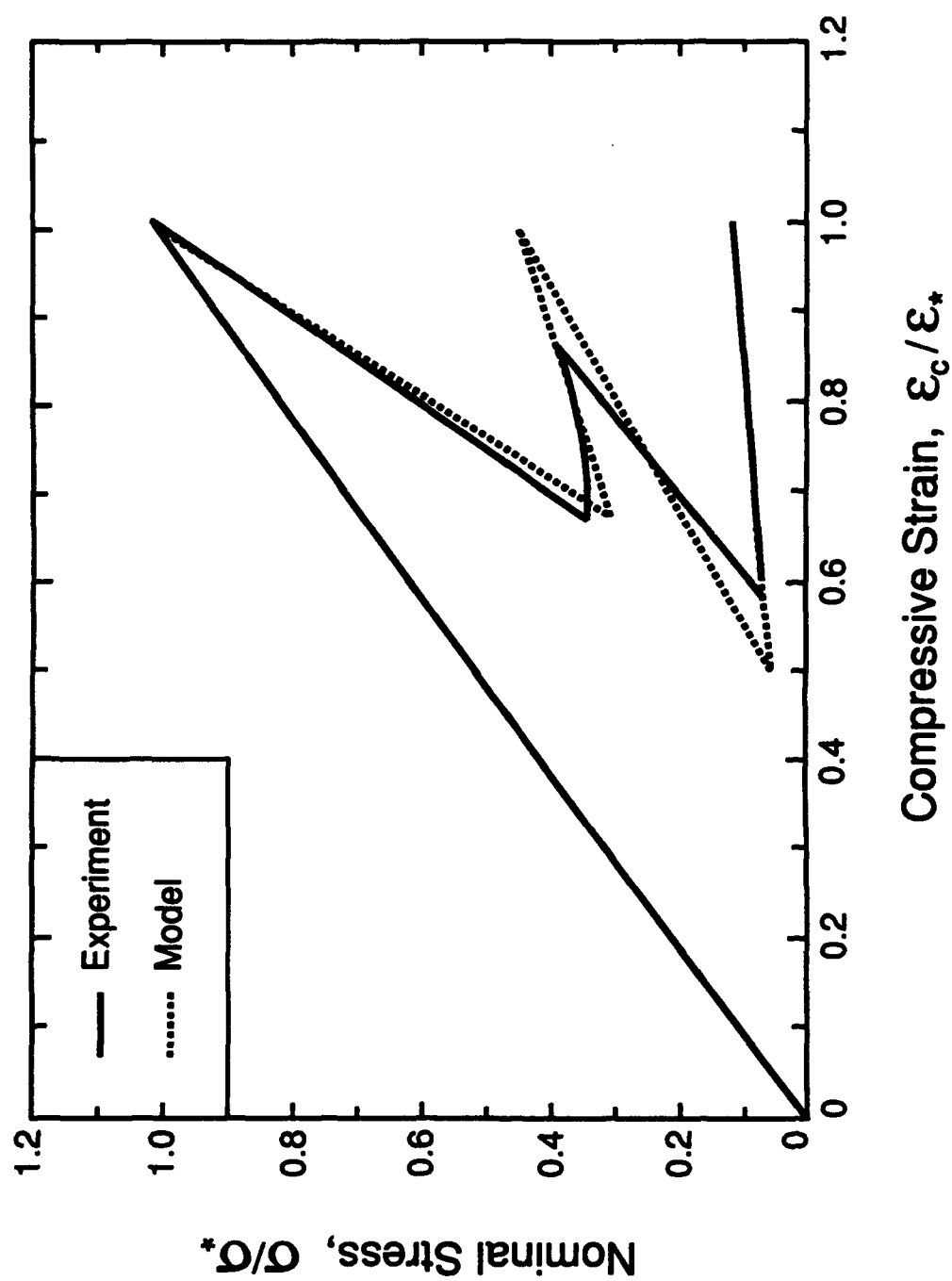


Figure 1(b)

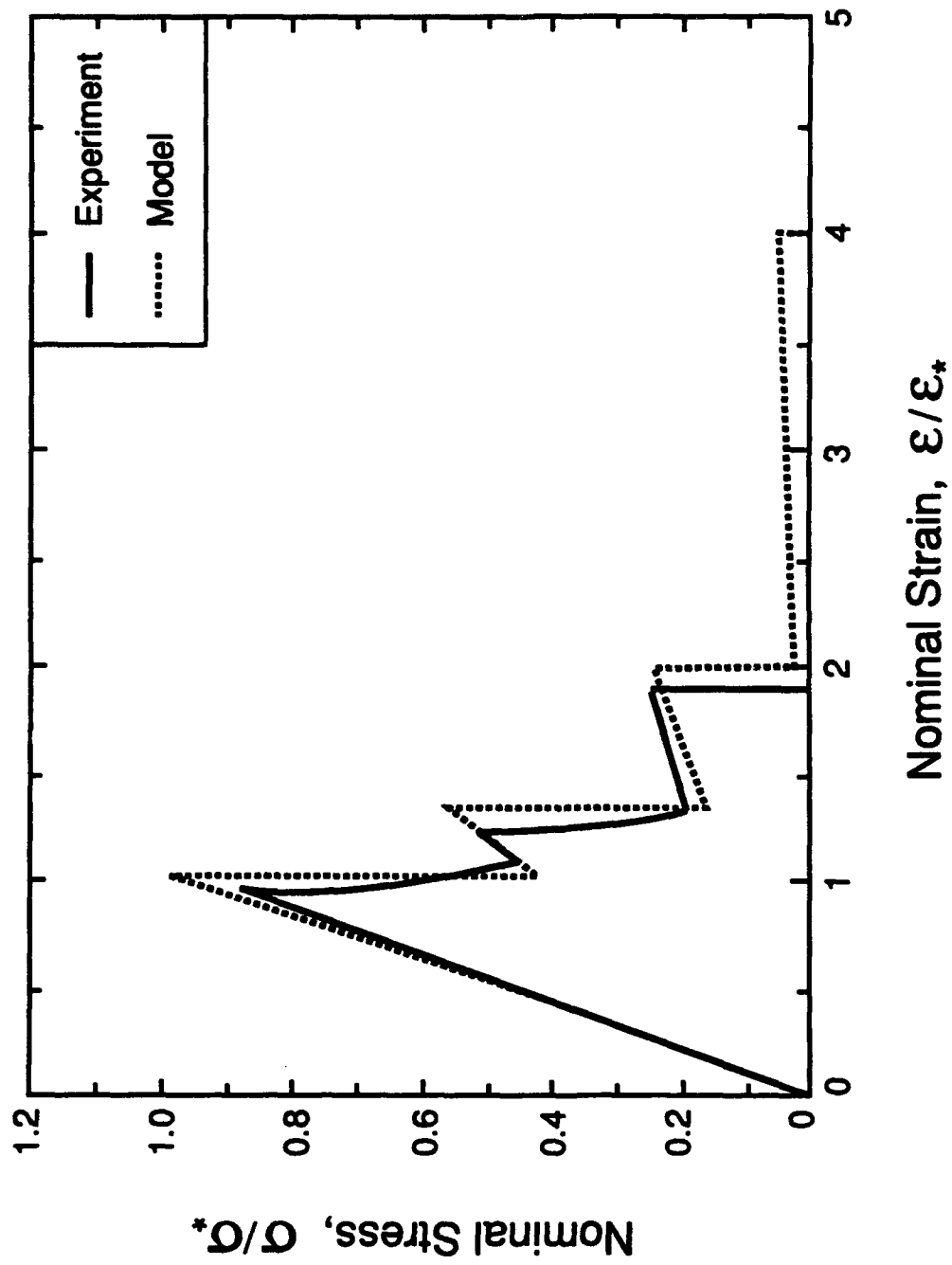


Figure 2(a)

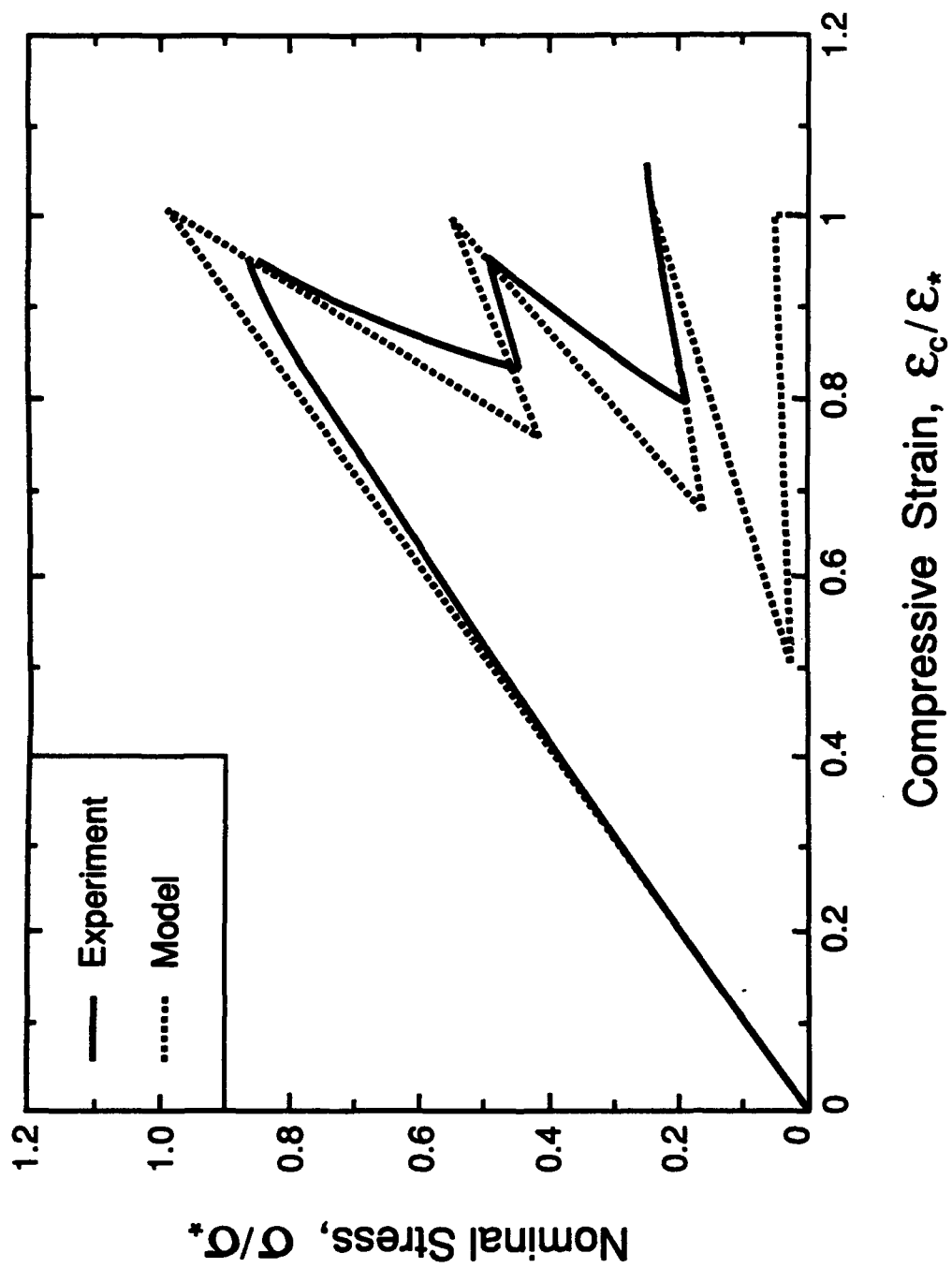


Figure 2(b)

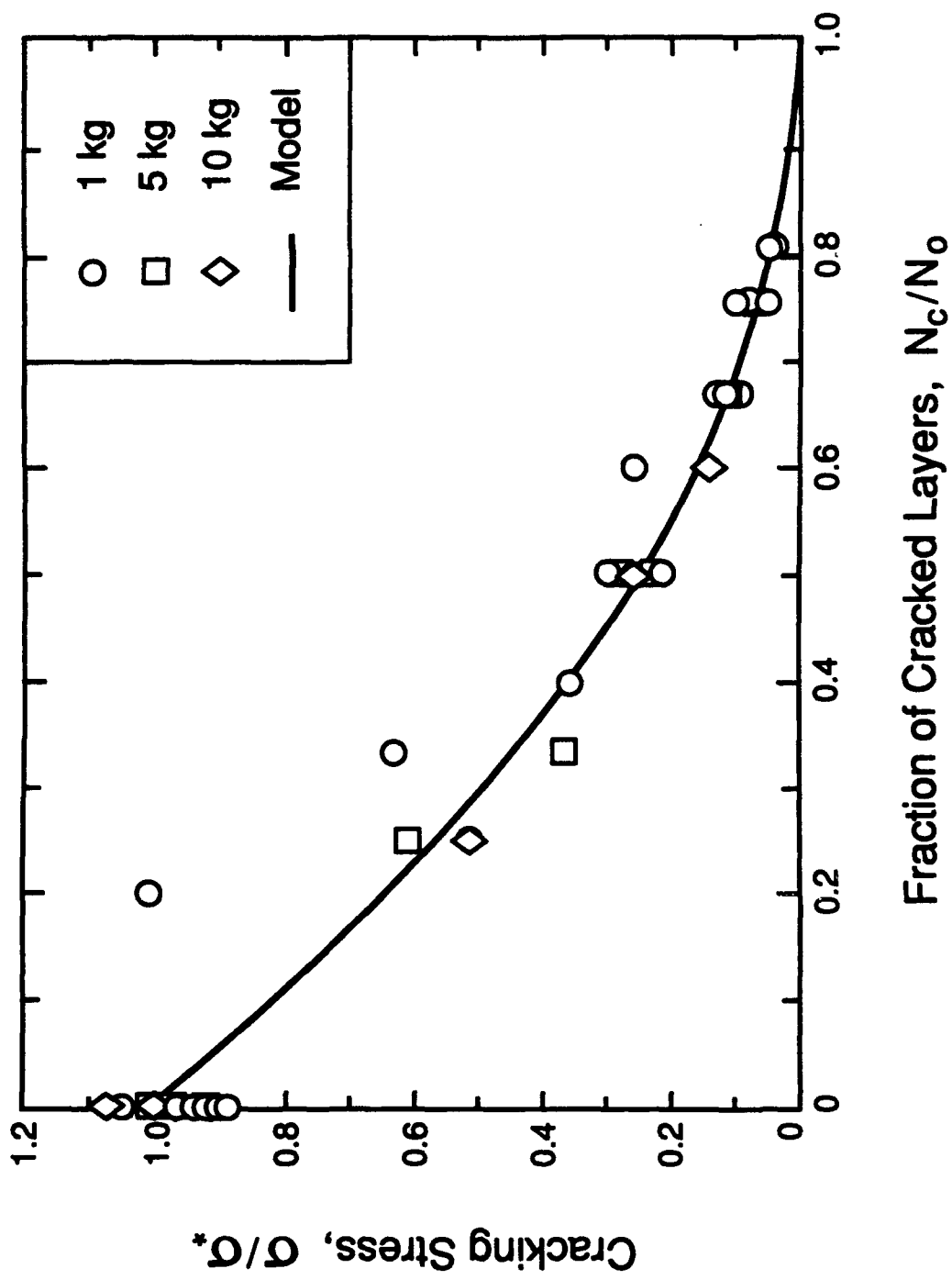


Figure 3

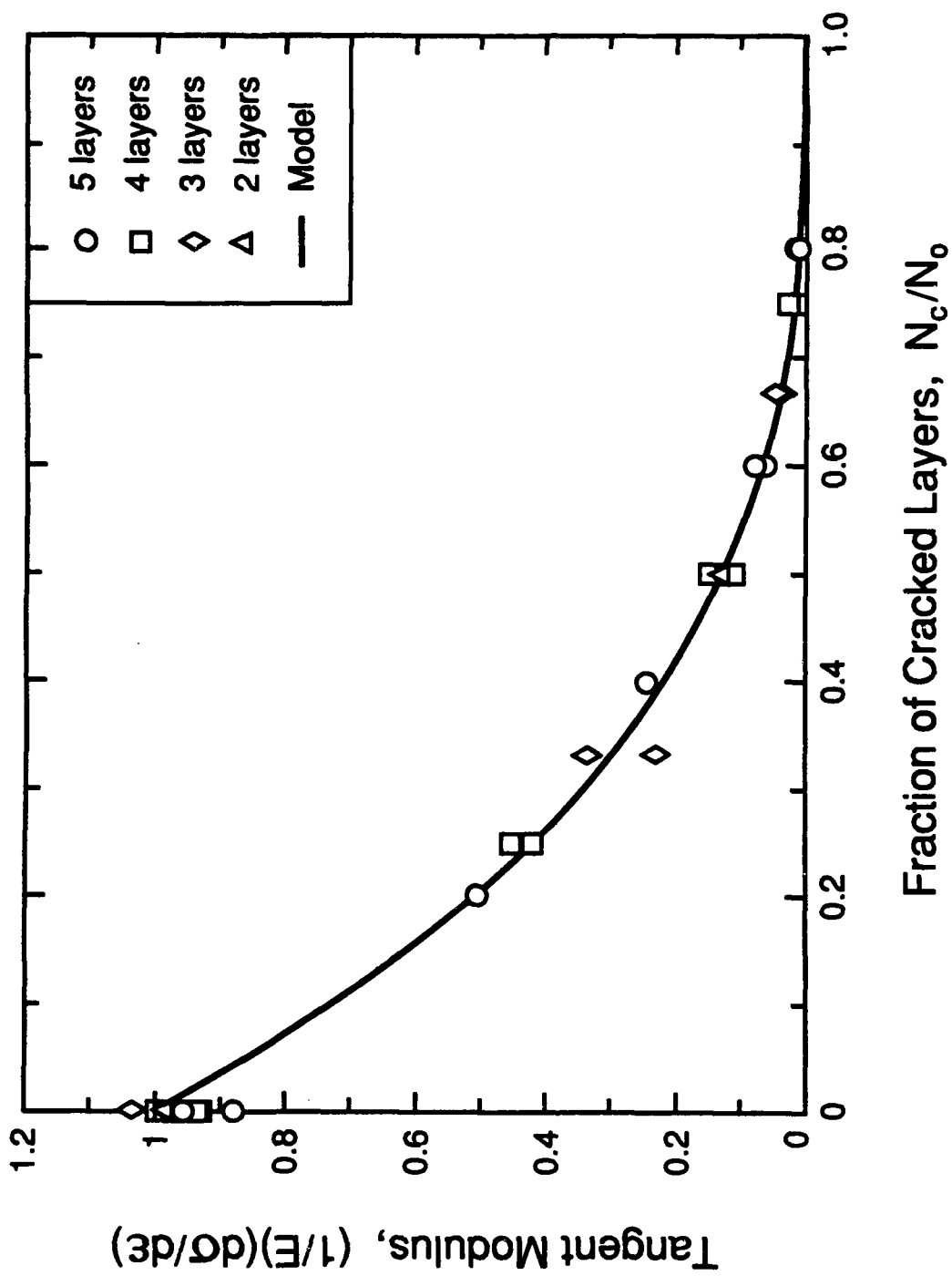


Figure 4(a)

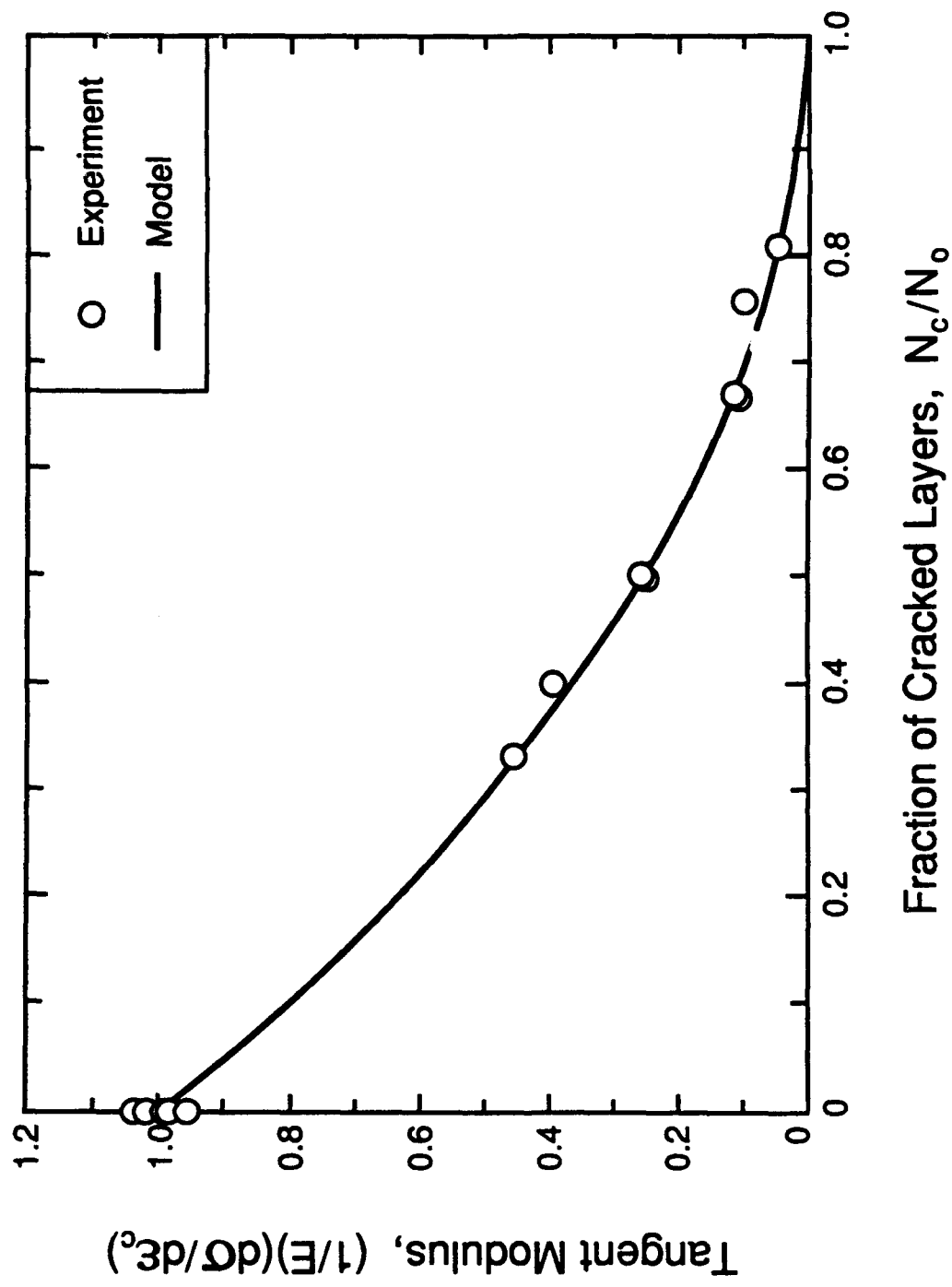


Figure 4(b)

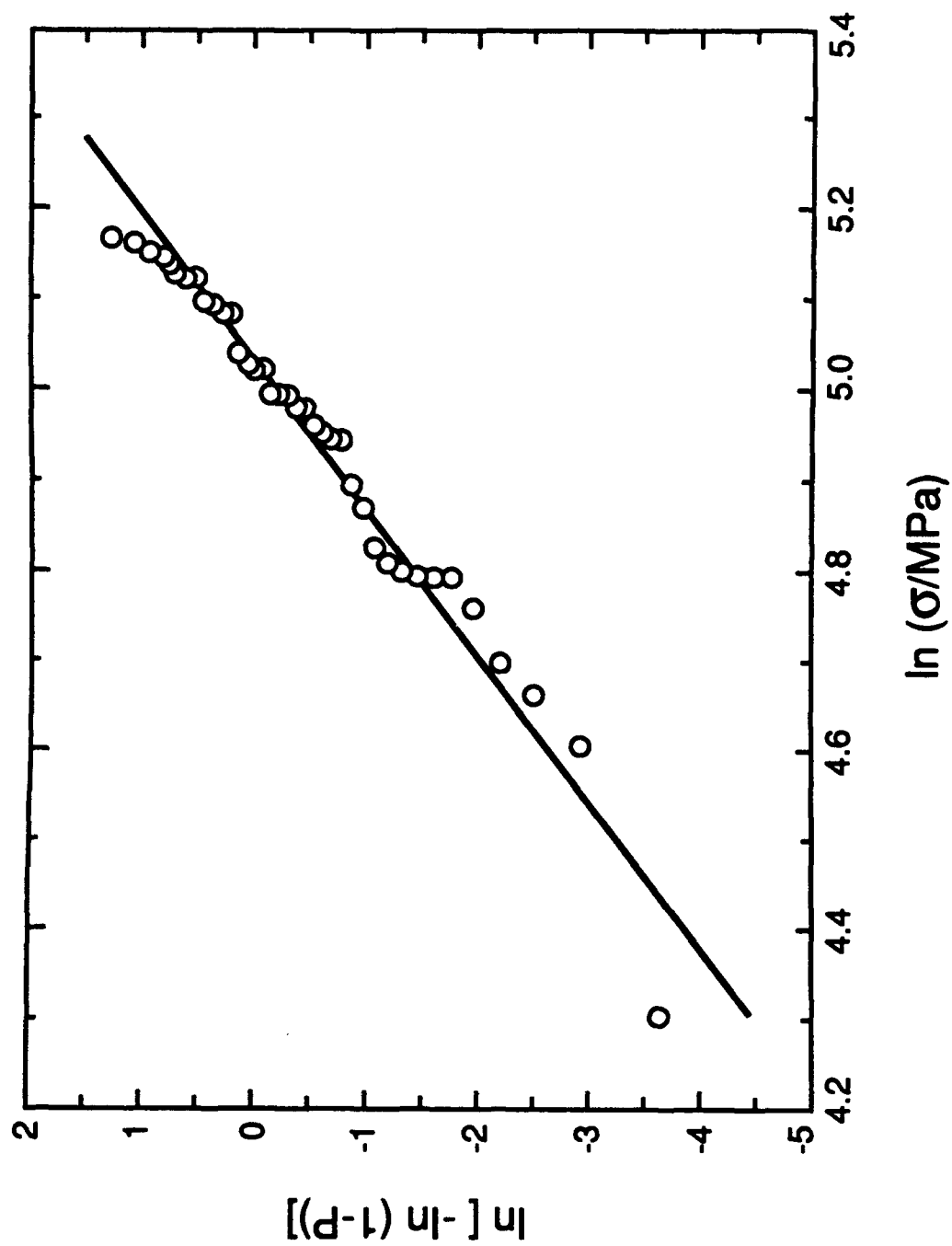


Figure 5



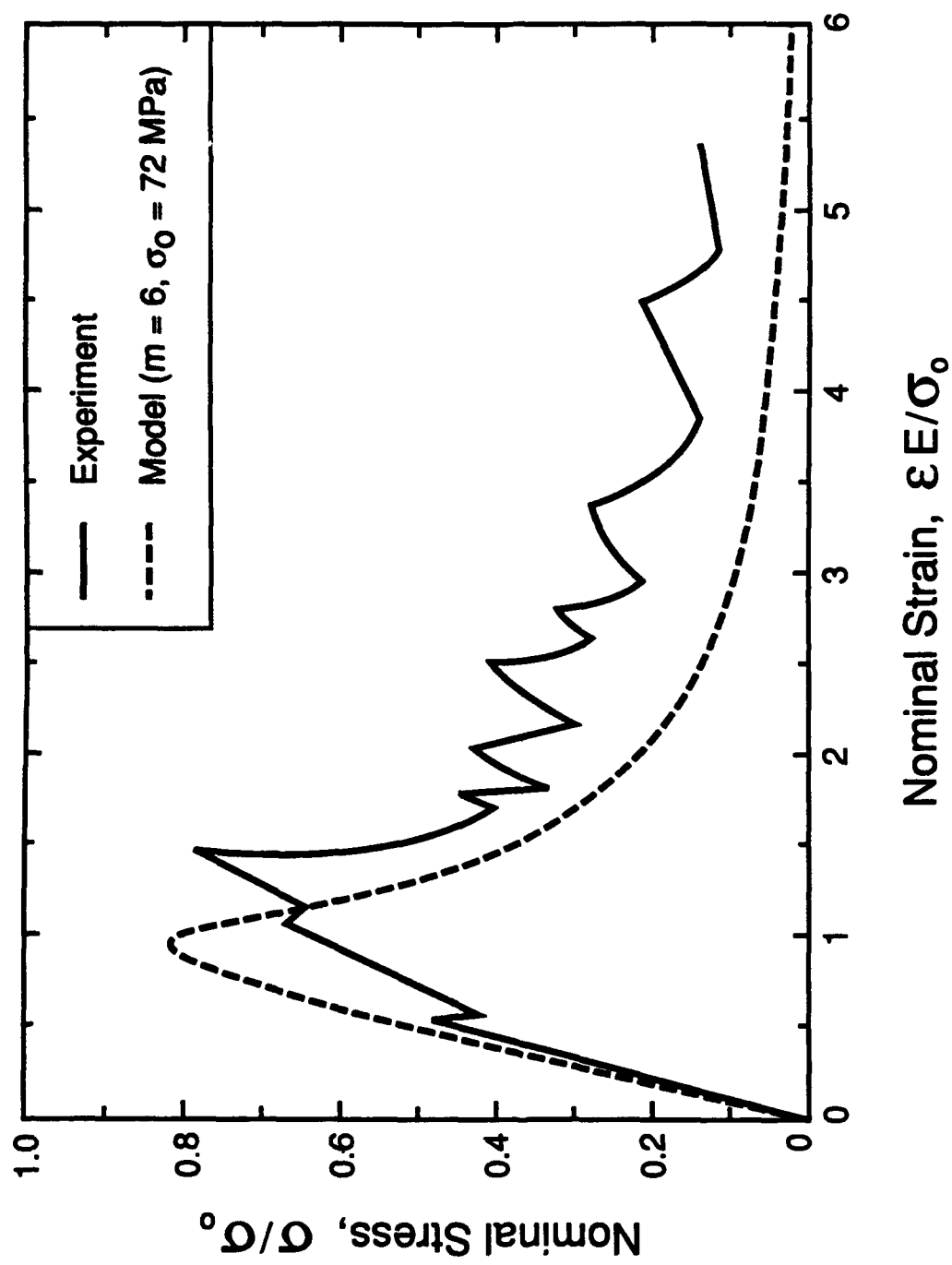


Figure 6



Figure 7

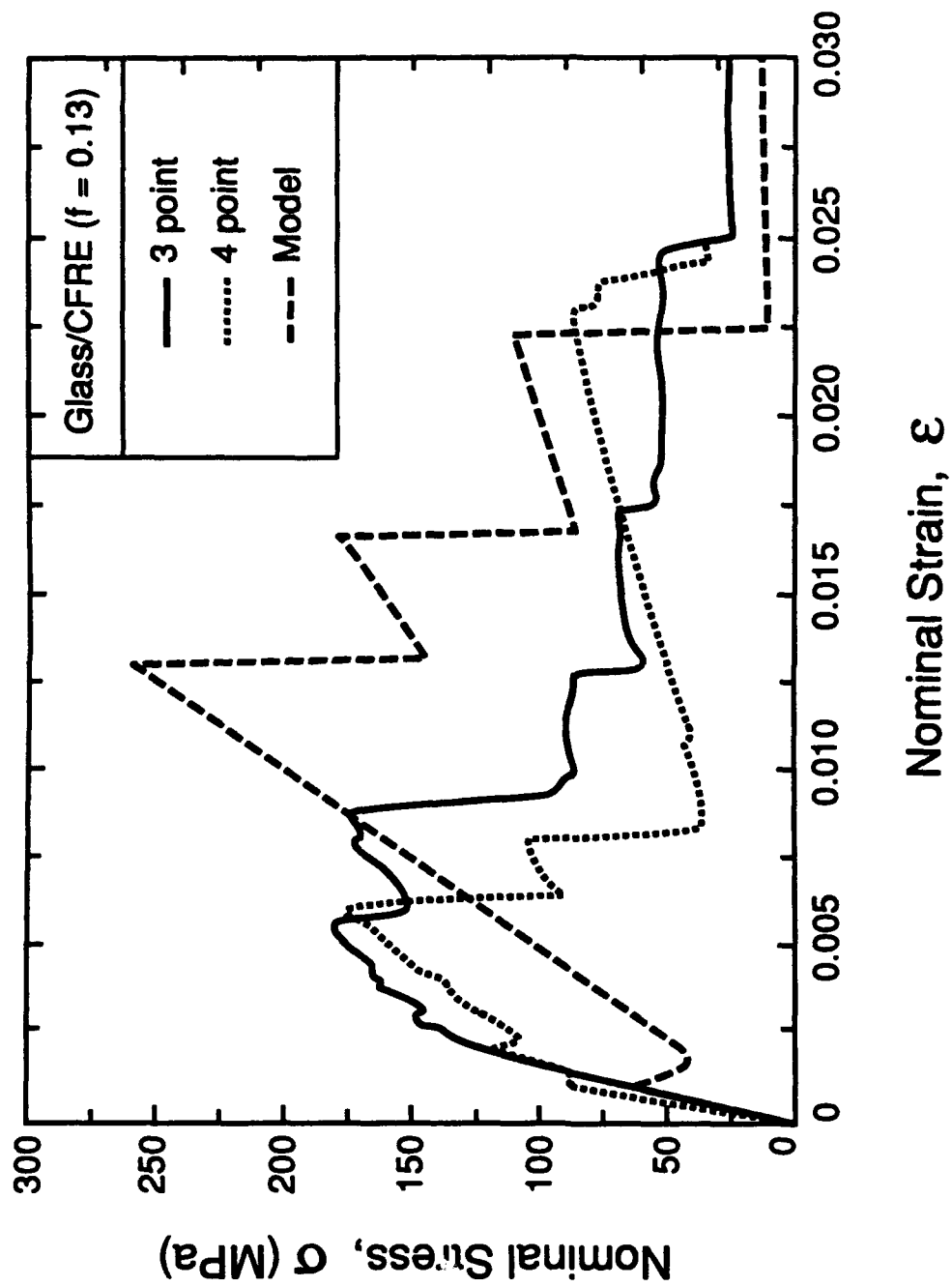


Figure 8(a)

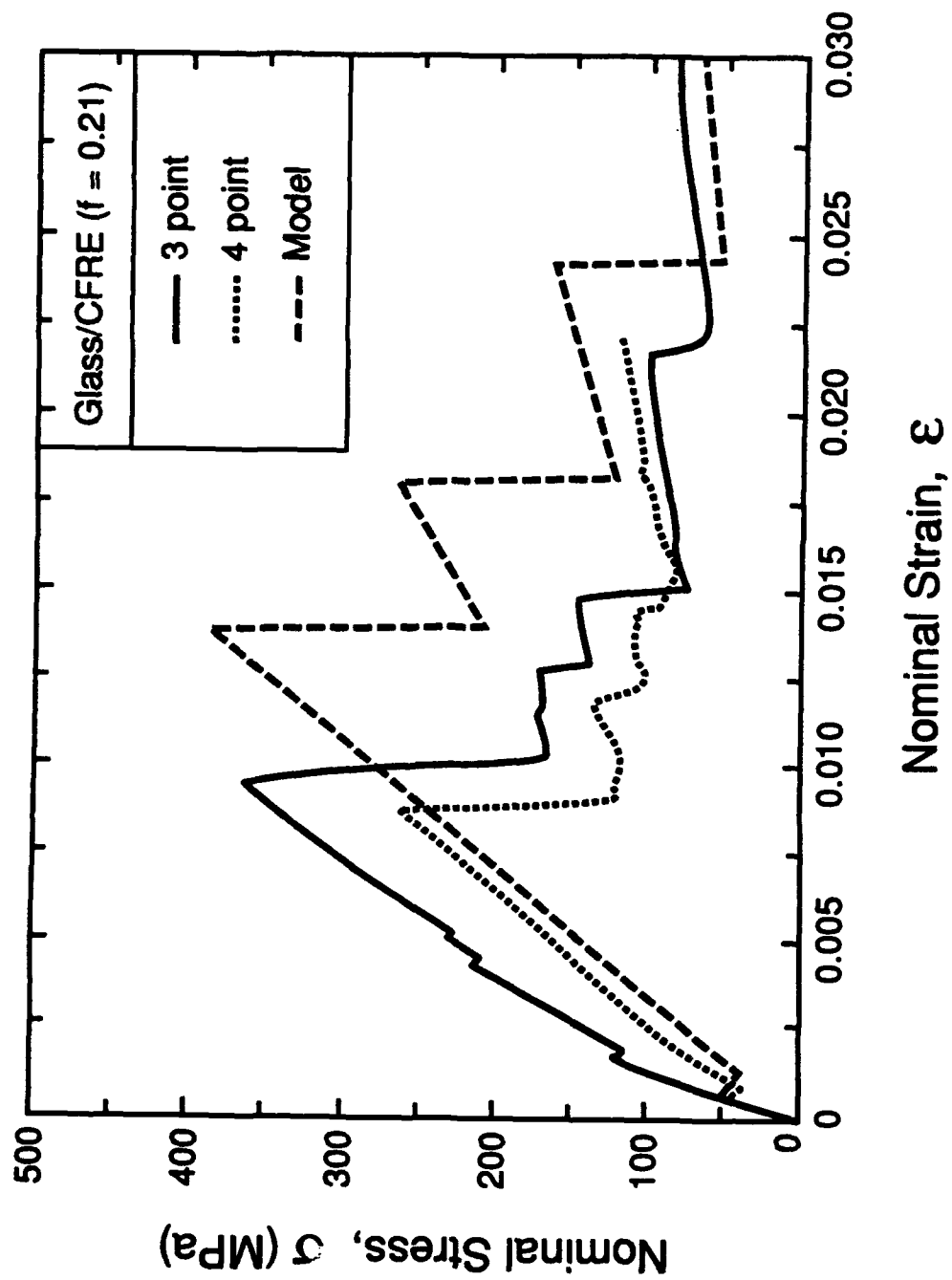


Figure 8(b)

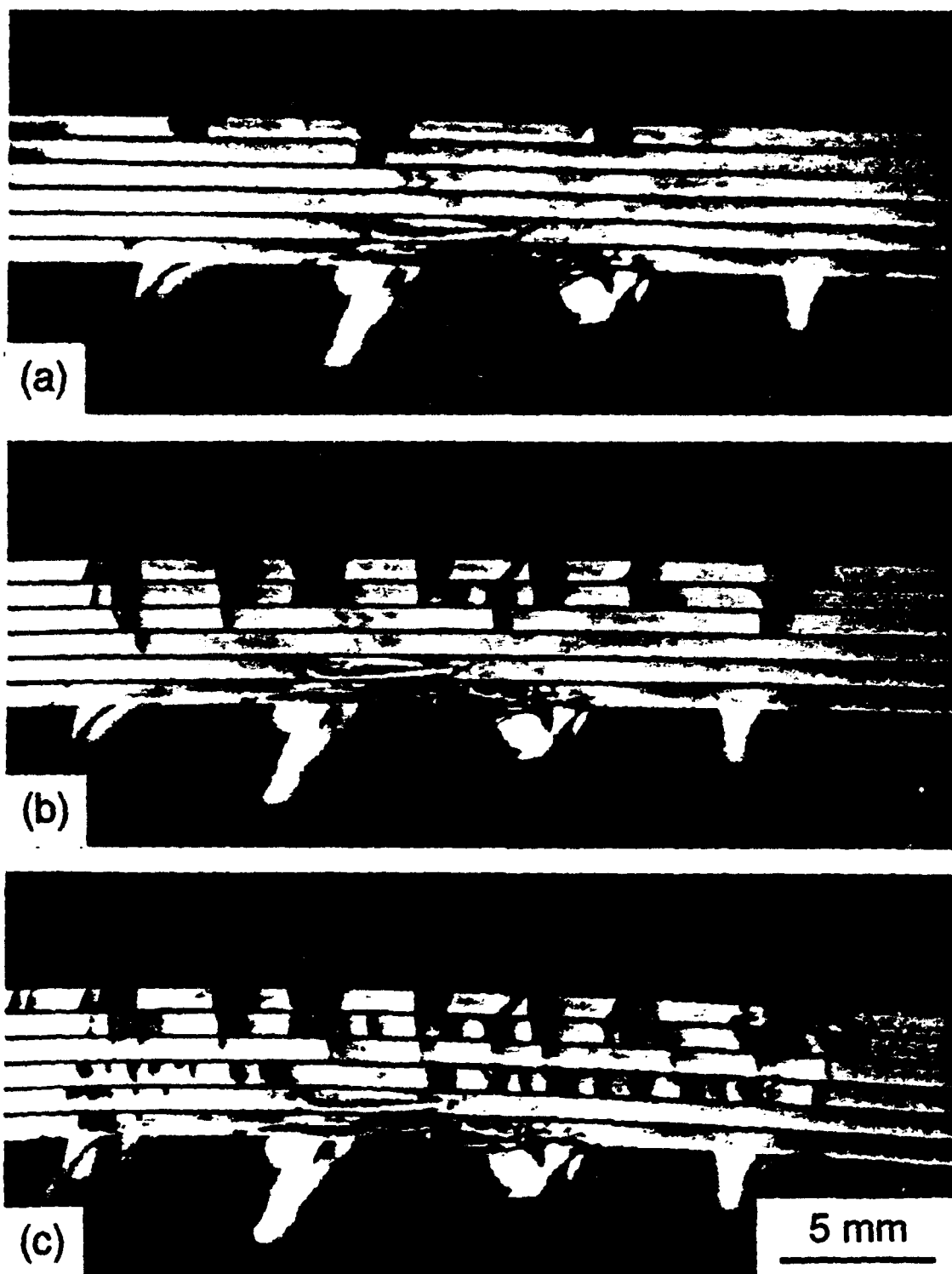


Figure 9

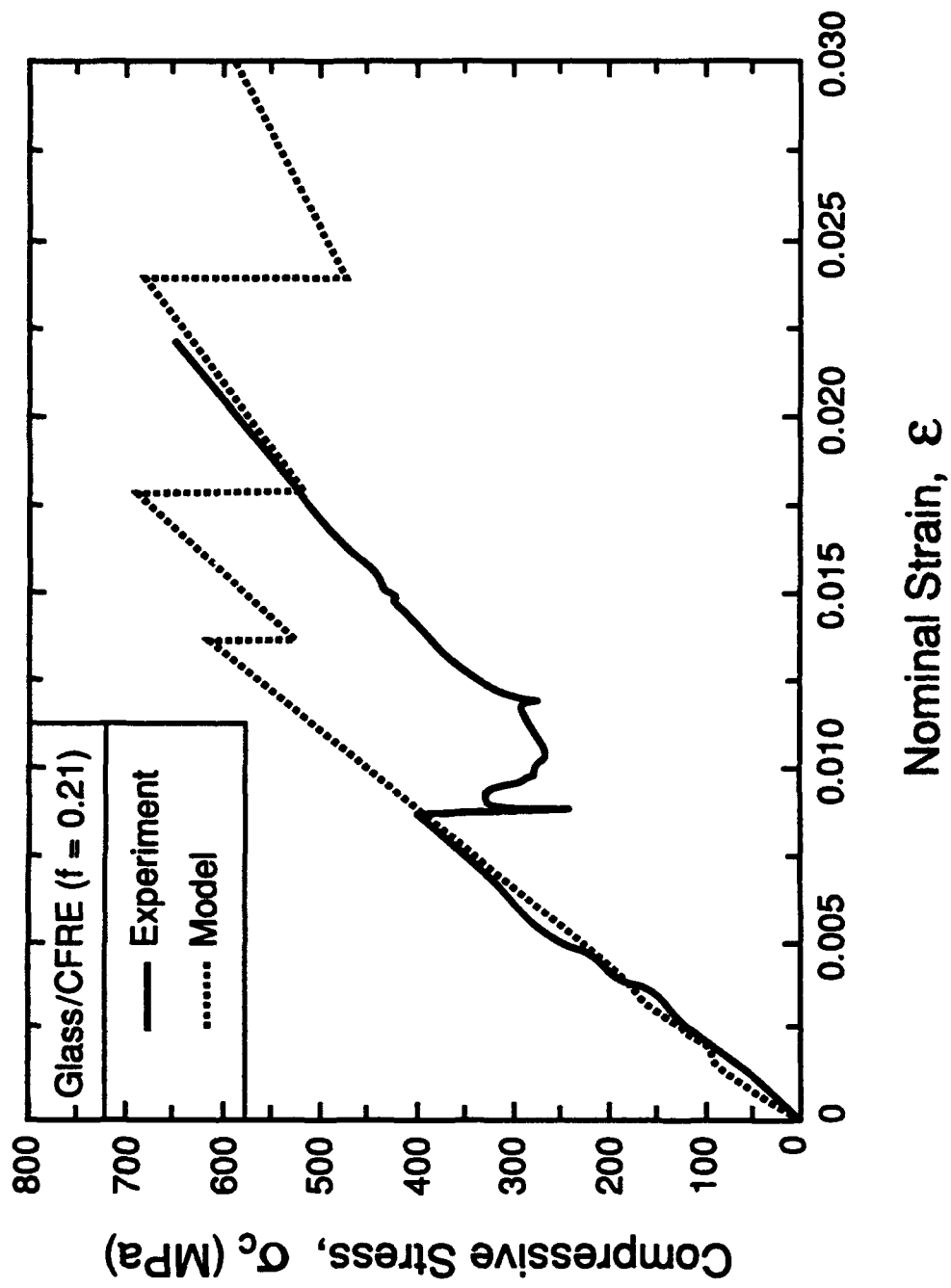


Figure 10

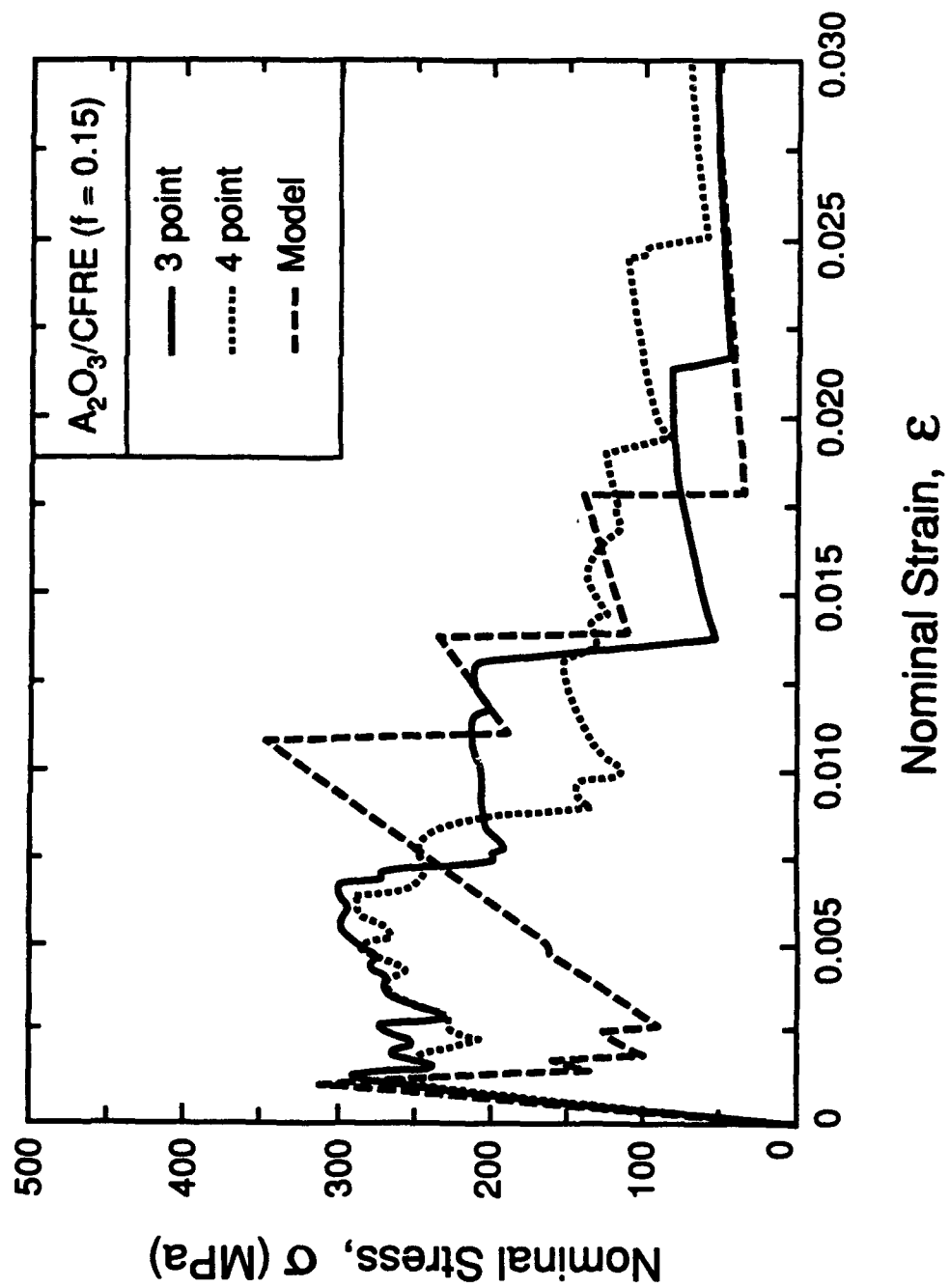
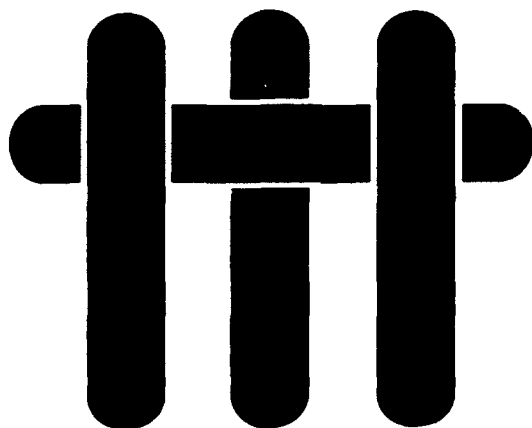


Figure 11

# M A T E R I A L S



## **THE MICROSTRUCTURE OF SiC/C COMPOSITES AND RELATIONSHIPS WITH MECHANICAL PROPERTIES**

by

**X. Bourrat, K.S. Turner and A.G. Evans**  
Materials Department  
College of Engineering  
University of California, Santa Barbara  
Santa Barbara, California 93106-5050



## ABS RACT

Three different 2-D SiC/C composites, analyzed by TEM, have mechanical performances directly controlled by the interfacial structure resulting from processing. Localized attachment of the fibers to a brittle matrix constituent is shown to be responsible for composite weakening by impeding interface debonding and sliding. Moreover, the particulate phase used in the matrix is found to have a strong influence. There is a consequent sensitivity of composite strength to the particulate properties. Finally, it is demonstrated that the hindrance of debonding and sliding caused by the brittle matrix phase can be suppressed by using a C fiber coating.

## 1. INTRODUCTION

Fiber-reinforced composites consisting of combinations of SiC and C have been explored as materials having thermostructural characteristics suitable for elevated temperature applications.<sup>1-6</sup> There are two opposing strategies. One uses C fibers and a matrix of SiC, usually produced by chemical vapor infiltration (CVI). The other uses SiC fibers and a matrix consisting of C; these are designated Ceracarb<sup>TM</sup> materials.<sup>1-3, 6</sup> The former has superior room temperature tensile properties (Fig. 1), because C fibers have a greater strength than SiC fibers, such as Nicalon. However, the latter has unexpected durability, under load, in oxidizing environments. The oxidation problem with C/SiC materials (especially those produced by CVI) relates to the rapid transport path for oxygen through the porous outer skin in C fibers, such as T 300. Consequently, the C fibers are rapidly degraded by oxygen,<sup>4,5</sup> resulting in a diminished tensile strength. The situation with SiC/C is very different. Various processing flaws exist,<sup>6</sup> but these do not provide a continuous conduit for oxygen ingress. Examples of such flaws are shown in Fig. 2. Moreover, the matrix is compliant and has a relatively high fracture toughness. Consequently, matrix cracks do not necessarily develop *within the plies*, even upon loading to failure.<sup>6</sup> These composites can thus be surprisingly resistant to oxidative degradation, especially when inhibiting particles are incorporated into the C matrix.

A number of mechanical measurements and microstructural investigations have now been made on SiC/C composites, showing that a variety of behaviors can be obtained, dependent upon the processing steps used and their sequence.<sup>1-3, 6</sup> These studies have provided insight into the mechanical behavior, but have not explicitly related the damage modes to the C microstructure. The present study uses transmission electron microscopy (TEM) to characterize the microstructure at high resolution and provides relationships with the mechanical behavior.

Among three different grades of Ceracarb™, two have high tensile strength (Fig. 1) and good notch resistance.<sup>1-3</sup> Both materials have a relatively low interface sliding resistance  $\tau$  (10–15 MPa) and satisfy global load sharing (GLS) criteria for the ultimate tensile strength (UTS).<sup>1</sup> The present designations for these materials are LT and LTC. The third material, designated HT, has lower tensile strength and greater notch sensitivity. This material has a relatively large interface sliding resistance<sup>1</sup> ( $\tau \approx 90$  MPa).

In the HT material, mode I matrix cracks form in the 0° plies and extend subject to fiber failure<sup>1, 2, 6</sup> (Fig. 3b). This damage mode is the origin of the relatively low UTS and the notch sensitivity. It is caused by the large  $\tau$ . Conversely, for the LT and LTC materials, mode I matrix cracks have not been found in the 0° plies. Instead, composite fracture occurs by the stochastic failure of fibers in these plies<sup>1, 6</sup> (Fig. 3a), consistent with GLS requirements. Interply shear cracking also occurs in these materials in the vicinity of transply processing flaws (Fig. 3c), but such cracks do not adversely affect the room temperature properties.<sup>6</sup>

## 2. MATERIALS

Three silicon carbide fiber-reinforced carbon composites (Ceracarb™) were provided by BP Chemicals (HITCO), referred to as LT, LTC and HT in this work. They are cross-ply laminates of eight-harness satin weave with Si-C-(O) nanocrystalline fibers (Nicalon™ NLM 202), laid up in a 0°/90° fashion with a nominal fiber volume fraction,  $f \approx 0.43$ . The densification involves two steps. The first comprises impregnation by phenolic resin with a particulate filler, followed by carbonization. This phenolic-based carbon material is referred to as the 'matrix' and designated, M. The filler is carbon black in the LT material and a B<sub>4</sub>C oxidation inhibitor in both the LTC and HT materials. The second step involves the chemical vapor infiltration (CVI) of carbon,

referred to here as 'pyrocarbon' and designated, PyC. An additional fiber coating step is used with the LTC material. This coating is introduced by CVI, prior to resin impregnation.

### **3. CHARACTERIZATION**

#### **3.1 Procedures**

Thin slices of material were cut for TEM characterization, to provide sections normal to the ply stacking. Sample preparation for TEM involved polishing, finishing with 1  $\mu\text{m}$  diamond, then dimpling to 25  $\mu\text{m}$  thickness and finally, ion-milling. Samples were examined with a JEOL 4000 FX (0.22 nm point-resolution) equipped with a Gatan PEELS spectrometer.

#### **3.2 General Observations**

The TEM observations are summarized by using the schematics shown in Fig. 4. The LTC material has a relatively uniform fiber coating  $\sim 0.5 \mu\text{m}$  thick (0.4 to 0.8  $\mu\text{m}$ , depending on location). This coating has the pyrolytic C (PyC) structure, elaborated below. Otherwise, all three materials have the same three generic features.

(i) There are 'matrix' regions, designated M, comprising C plus filler particles. These regions originate from resin impregnation and pyrolysis. The C in the M material is disordered. In some regions of the uncoated (LT and HT) composites, this M material is attached to the fibers.

(ii) Other regions consist of PyC. This material has a bilayer morphology with a mid-plane separating the layers (XX' on Fig. 4a). This morphology arises because the PyC has deposited onto juxtaposed surfaces, present after impregnation and pyrolysis, and grown together. In most cases, there are two such surfaces, such that the PyC bilayer is often interposed between the fibers and the M material.

(iii) Finally, there is axial porosity, designated P. These pores are *always* surrounded by PyC and are evidently regions that have not been filled in the final CVI processing step.

The schematic illustrations associated with the overview are based on the actual micrographs presented on Figs. 5–8. The physical proximities of the fibers, the resin-derived matrix M and the pyrolytic carbon found in the materials without the fiber coatings (LT and HT) are illustrated on Figs. 5, 6. Note that, in Fig. 5, there is no attachment between the M material and the fiber. Moreover, a circumferential debond within the PyC is evident at one of the fibers. Such debonding is further addressed below. Conversely, in Fig. 6, substantial segments exhibit attachment of the M material to the two fiber perimeters (marked with arrows). This figure also illustrates the typical morphology of the residual porosity.

The boundary within the PyC bilayer formed upon CVI by counter growth from both the fiber (F) and the matrix (M) surfaces is illustrated in Fig. 7. A silica island on the fiber surface is also evident in this figure. Such islands are *only* found in the HT material. Their presence had been noted in a previous study, which identified adherent islands on the fibers, after pull-out upon composite rupture.<sup>1</sup> Finally, the typical morphology of the PyC fiber coating layer in the LTC material is shown in Fig. 8. Also evident in this figure are the filler particles (f).

### 3.3 Microstructural Details

#### (i) Fiber Coatings

A cross section of the CVI fiber coating in the LTC composite (Fig. 8) indicates a C layer having thickness  $\approx 0.5 \mu\text{m}$ . The structure is typical of that for PyC. The C layers are densely packed, with good stacking coherence, and aligned parallel to the fiber surface.

### *(ii) Matrices*

Observations of the M material reveal the presence of the filler particles (Fig. 9): either carbon black (LT) or B<sub>4</sub>C (LTC and HT), as established by the diffraction patterns. Lattice fringe images obtained in the vicinity of these particles (Fig. 10b) indicate the structure and texture of the C. The carbon black (Fig. 10a) has a concentric texture (double-bar). The layer dimension ( $\leq 2$  nm) and the structure are characterized by good stacking (5 to 8 layers stacked in coherence). This structure can be ranked as type II-type III upon comparing with a structural classification.<sup>7</sup> The phenolic-resin-based carbon structure is characterized by poorly organized long carbon layers. The layers have a poor stacking in the  $\bar{c}$  direction but have a long-range preferred orientation, especially when close to the particles. Remote from the particles, the structure resembles that of glassy carbon with long-range orientation. This effect is shown by the arc superimposed on the ring in the diffraction pattern. It is known as 'stress-graphitization' and arises during carbonization. In addition, textural featuring occurs in the form of halos around the B<sub>4</sub>C particles. These are suspected to arise from thermal mismatch cracks subsequently filled by CVI impregnation (arrows in Fig. 9b).

### *(iii) Interphases*

A series of thin interphases exists between the fiber and either the M material or the PyC (coating or bilayer). Moreover, the interphases are inhomogeneous around the fiber perimeter. A typical cross section is shown in Fig. 11. The fiber is nanocrystalline, although the outer part (F) is generally carbon-rich. The contrast in this region is given by the carbon layers, which are more or less aligned with the fiber surface. This particular fiber has a silica layer,  $\sim 8.8$  nm thick. Another example has been shown in Fig. 7. There are also regions in which the silica layer is absent (Fig. 12). Where SiO<sub>2</sub> layers are present, debonding is often induced by ion milling experimentally, when M is

directly in contact with the fiber. Conversely, debonds have never been identified in those regions devoid of  $\text{SiO}_2$ . The occurrence of  $\text{SiO}_2$  islands (Fig. 7) predominates in the HT material.

#### (iv) *PyC Bilayers*

Cross sections of the PyC layers (Fig. 13) indicate two 'weak' locations at the gaps indicated by the arrows. These gaps have probably been enlarged by ion milling. The first gap occurs where the bilayers converge during CVI. The infiltration here is incomplete and closed porosity is left in the middle (double arrow). The second gap exists *within* the PyC layer adjacent to the fiber. The thin carbon layer attached to the fiber has different contrast than the bulk (Bragg fringes). It represents the oriented carbon deposited onto the silica layer. The 'weakness' arises at this location because of the change in the structure of the carbon.

In longitudinal section (Fig. 14), the PyC is characterized by a columnar organization of the HM pitch-based type. The layers are densely packed (see the inset), and well-aligned parallel to the interface. Most of the large porosity is an artifact related to milling. The comparison of the PyC structure in cross- and longitudinal-sections shows that the orientation angle is much larger longitudinally. This anisotropy can be attributed to the thermal expansion mismatch.

## 4. MICROSTRUCTURE DEVELOPMENT

Before attempting to interpret specific features of the microstructure, the matrix behavior expected during pyrolysis, after resin infiltration is assessed. At this stage, matrix shrinkage can result in three modes of damage, summarized in Fig. 15. Strong effects of spatial arrangement and of external constraints are evident. (i) When the boundaries of the ply can displace freely and the fibers have a uniform spatial

arrangement, the tensile stresses are in the hoop orientation. Shrinkage cracks, when they occur, will then be radial, between the fibers. (ii) In the absence of constraints, but with a non-uniform spatial arrangement of fibers, the fiber configuration can locally resist inward radial displacements. This results in radial tensile stress, causing local separations between the matrix and fibers. (iii) When a ply is rigidly constrained by neighboring plies, within the preform, the displacements occur radially outward and again separations arise between the matrix and the fibers. In cases (ii) and (iii), separations between the fibers and the matrix occur non-uniformly, because contact must be retained around some portion of the circumference.

Most of the microstructural observations (Fig. 4) are consistent with either (ii) or (iii) having occurred during pyrolysis, following impregnation.<sup>‡</sup> Thereafter, the remaining porosity is partially filled by the final CVI step.

The distribution and morphology of  $\text{SiO}_2$  on the fibers have particular significance. When a continuous  $\text{SiO}_2$  layer is present, the M material appears to debond readily from the fibers. Conversely, the matrix and fiber are much more adherent when  $\text{SiO}_2$  is absent. The presence of  $\text{SiO}_2$  islands, predominantly in the HT material, also has importance for composite properties, discussed below. These variations in  $\text{SiO}_2$  morphology are hypothesized to depend on the filler particle in the M material, particularly the B containing material. When B is present, because it has a high vapor pressure, it can evaporate from the particles during processing and condense onto the  $\text{SiO}_2$ . This addition of B to the  $\text{SiO}_2$  reduces its viscosity, such that surface tension driven viscous flow would then be possible. Such flow could cause island formation, by dewetting of the fiber surface, leaving other regions devoid of  $\text{SiO}_2$ .

---

<sup>‡</sup> There may also be some effects on the M phase distribution associated with incomplete impregnation, because of differences in wetting, with and without the PyC fiber coating.



## 5. MECHANICAL BEHAVIOR

The PyC material, when attached to the fibers, appears to debond readily, whether it is introduced as a fiber coating or during the final processing step. This is evident from the debonding induced upon ion milling (Fig. 5). Conversely, the phenolic derived M material appears to have a higher debond energy when attached to the fiber. This interphase is completely resilient during TEM specimen preparation. The consequence is that, since the fibers in the LTC material are completely surrounded by PyC, the interfaces debond and slide readily (with small  $\tau$ ) when fibers fail. This response eliminates stress concentrations in neighboring fibers and leads to stress/strain characteristics completely consistent with GLS criteria<sup>1, 6</sup> (Fig. 16).

In the HT and LT materials, the region where M is in contact with the fibers, particularly when the SiO<sub>2</sub> layer is absent, represents sections of interface that are more difficult to debond. More importantly, the SiO<sub>2</sub> islands that exist in the HT material, because of the B<sub>4</sub>C filler phase, act as asperities that inhibit interface sliding, leading to the larger  $\tau$ .<sup>1</sup> The high  $\tau$ , in turn, results in a change in cracking mode and a violation of GLS, causing a reduced ultimate strength.

## 6. SUMMARY

Microstructural studies of C matrix composites conducted by TEM have identified critical roles of both the SiO<sub>2</sub> layer on the fibers and the differing C materials produced by pyrolysis and CVI. The SiO<sub>2</sub> layer appears to be affected by the filler phase in the matrix, associated with a diminished viscosity. This viscosity change causes viscous flow upon processing that results in island formation on the fibers, as well as regions of the interface devoid of SiO<sub>2</sub>. These differing SiO<sub>2</sub> morphologies have direct

consequences upon the interface sliding and debonding resistances, which govern the fiber load sharing behavior and the ultimate tensile strength.

The C produced by CVI is in the form of oriented layers with a columnar microstructure, whereas the C formed by pyrolysis is disordered and essentially amorphous. There is a consequent effect on debonding and sliding. When the C contacting the fiber is entirely formed by CVI, as in the LTC material, debonding and sliding occurs readily and the composite has optimum tensile properties, fully governed by global load sharing. However, when some of the contacting C derives from pyrolysis, as in the LT and HT materials, debonding is locally more difficult. Then, the morphology of the  $\text{SiO}_2$  layers, discussed above, has a dominant role.

## REFERENCES

- [1] F.E. Heredia, S.M. Spearing, A.G. Evans, P. Mosher and W.A. Curtin, "Mechanical Properties of Continuous-Fiber-Reinforced Carbon Matrix Composite and Relationship to Constituent Properties," *J. Am. Ceram. Soc.*, 75[11] (1992) 3017-25.
- [2] F.E. Heredia, S.M. Spearing, T.J. Mackin, M.Y. He, A.G. Evans, P. Mosher and P.A. Brøndsted, "Notch Effects in Carbon Matrix Composites," submitted to *J. Am. Ceram. Soc.*, Nov. 1992.
- [3] P.A. Brøndsted, F.E. Heredia and A.G. Evans, "The In-Plane Shear Properties of 2-D Ceramic Matrix Composites," submitted to *J. Am. Ceram. Soc.*, Feb. 1993.
- [4] F. Lamouroux, X. Bourrat, R. Haslain and J. Sévely, "Oxidation Behavior of Carbon Phases in C/SiC Composites," accepted in *Carbon*, June 1993.
- [5] F. Lamouroux, G. Camus and J. Thebault, "Oxidation Resistance and Strength After Oxidation of a 2-D Woven Carbon Fiber/Silicon Carbide Matrix Composite," *Proceed. ECCM-5*, Bordeaux, April 7-10, 1992.
- [6] K. Turner, J.S. Speck and A.G. Evans, "The Mechanisms of Deformation and Failure in Carbon Matrix Composites, submitted to *J. Am. Ceram. Soc.*
- [7] X. Bourrat, "Electrically Conductive Grades of Carbon Black: Structure and Properties," *Carbon*, 31 (1993) 287.
- [8] T. Kohno, K. Kurosaki and T. Herai, "Effect of Ply Thickness on Mechanical Property of 2-Dimensional Carbon/Carbon Composite," *Proceed. 20<sup>th</sup> Biennial Conf. on Carbon*, Santa Barbara, June 23-28, 1991, 394-5, ACS Ed. (1991).

## FIGURE CAPTIONS

- Fig. 1. Tensile stress/strain curves for the carbon matrix composites studied in this work, compared with those for carbon fiber-reinforced SiC.
- Fig. 2. Processing flaws found in C matrix composites: a) Transply, b) Interply.
- Fig. 3. Damage modes found in C matrix composites: a) stochastic failure of fibers, b) mode I matrix crack in  $0^\circ$  plies, c) mode II interply cracks.
- Fig. 4. Schematics showing the overall microstructural characteristics of the materials.
- Fig. 5. Material LT: low magnification: fiber (F), pyrocarbon (PyC), matrix (M) and double arrows (weakness plane).
- Fig. 6. Material HT: fiber (F), silica ( $\text{SiO}_2$ ), CVI carbon matrix phase (PyC) and matrix (M).
- Fig. 7. Material HT: low magnification with fiber (F), CVI carbon matrix phase (PyC) and matrix (M) with its filler (f).
- Fig. 8. Interface region in LTC material showing the fiber (F), the coating (COAT) and the matrix (M) with its filler (f).
- Fig. 9. a) Material LT showing the resin-based carbon and the carbon black filler.  
b) Material HT showing the resin-based carbon (M) and the filler ( $\text{B}_4\text{C}$ ).
- Fig. 10. Lattice fringes image of matrix: a) material LT: carbon black (CB) and matrix (M) showing stress orientation, b) material HT:  $\text{B}_4\text{C}$ .
- Fig. 11. Material LT: fiber surface (F), silica layer ( $\text{SiO}_2$ ) and CVI carbon matrix phase (PyC).
- Fig. 12. Material LT: matrix (M) bonded directly on the fiber surface (F) where silica ( $\text{SiO}_2$ ) is lacking.
- Fig. 13. Material LT at low magnification: fiber (F), matrix (M) and arrows. PyC growth (double arrows: weakness planes).
- Fig. 14. Material LT: longitudinal section of PyC. Inset is a lattice fringe image in the same area.

**Fig. 15.** Schematics illustrating the effects of spatial heterogeneity and constraint on the shrinkage flaws found upon matrix pyrolysis.

**Fig. 16.** A comparison of measured stress/strain curves with those predicted for a analysis based on stochastic fiber failure subject to global load sharing.

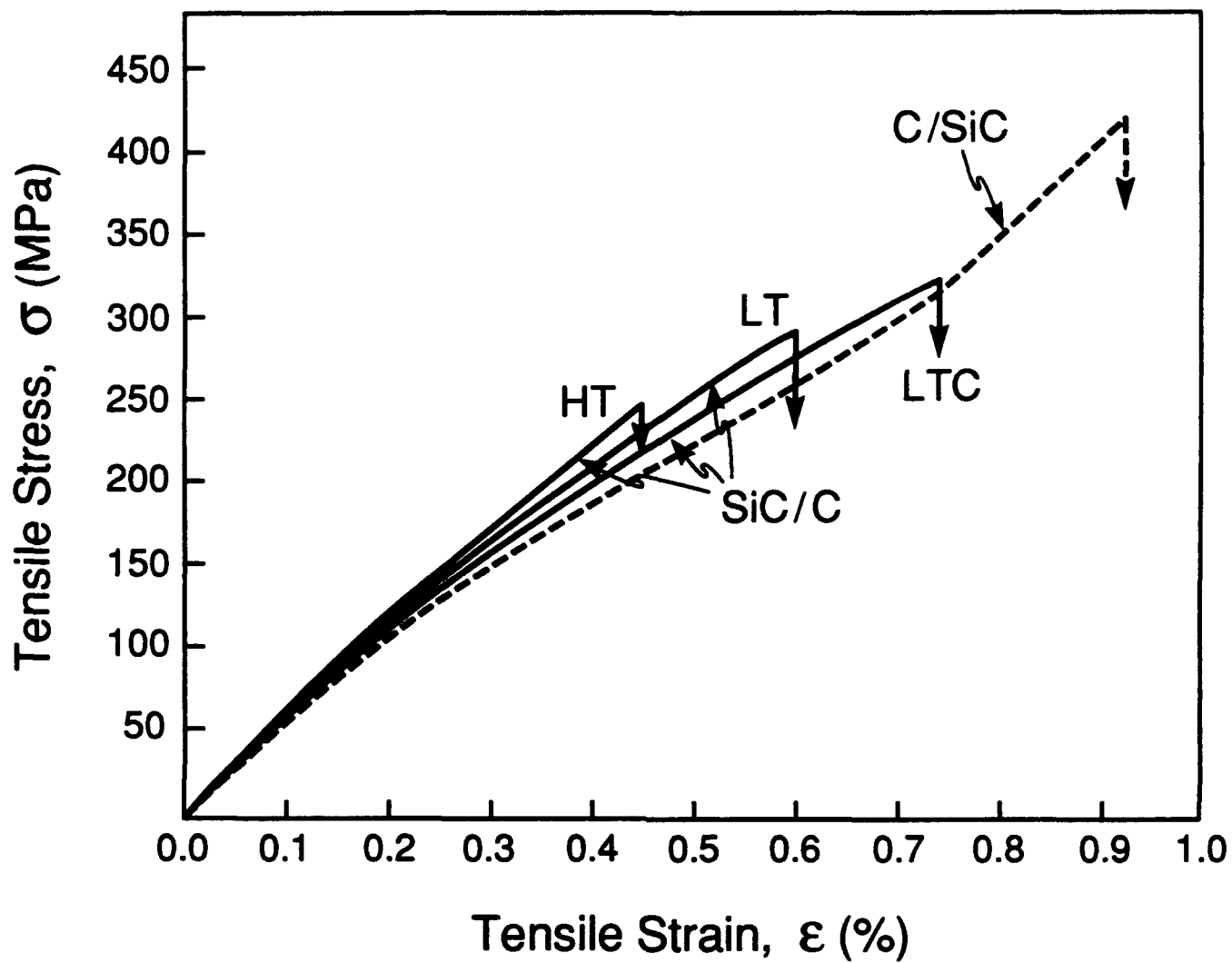


Figure 1

Figure 2a

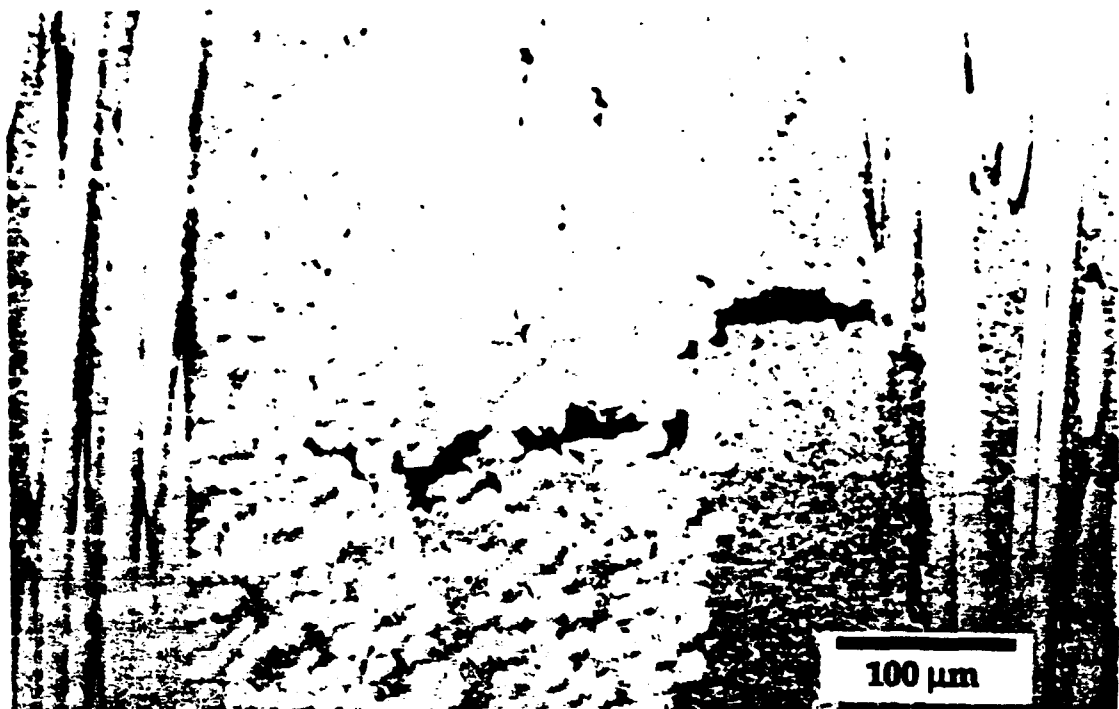
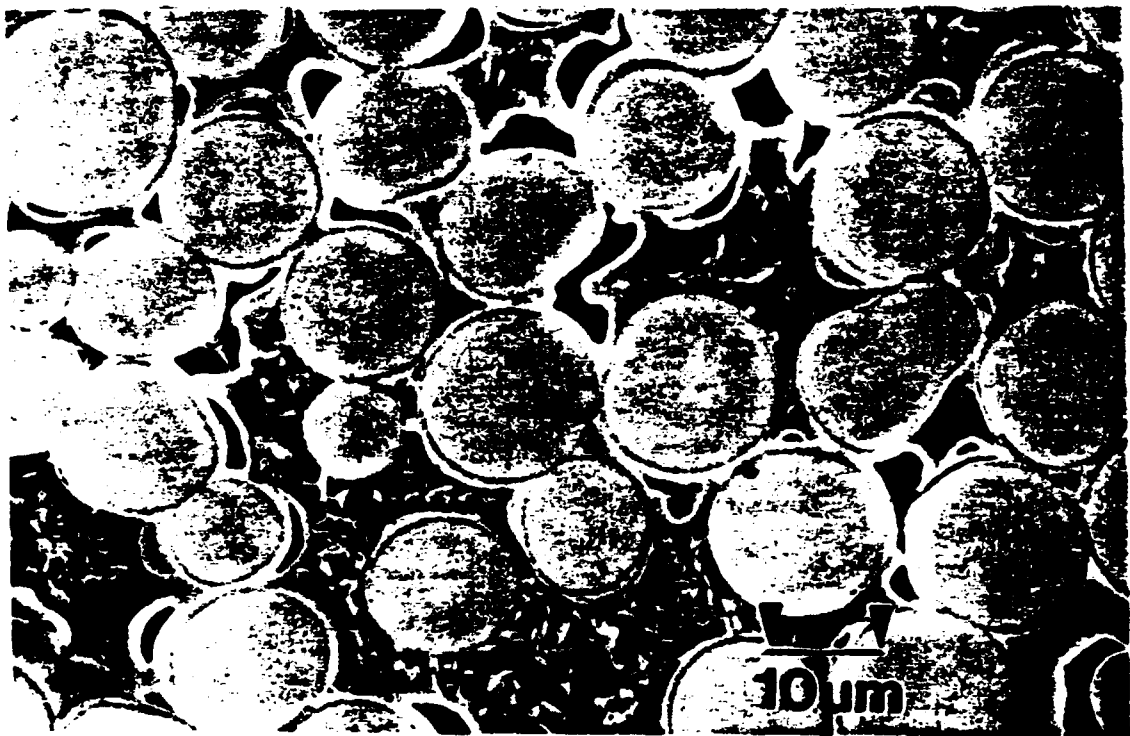
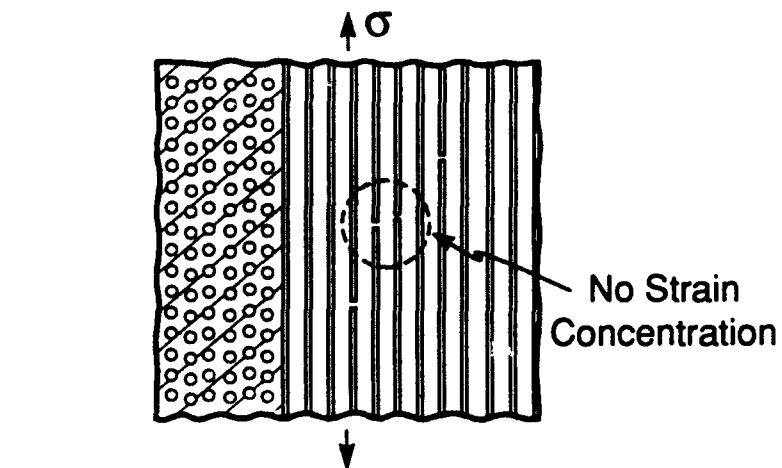
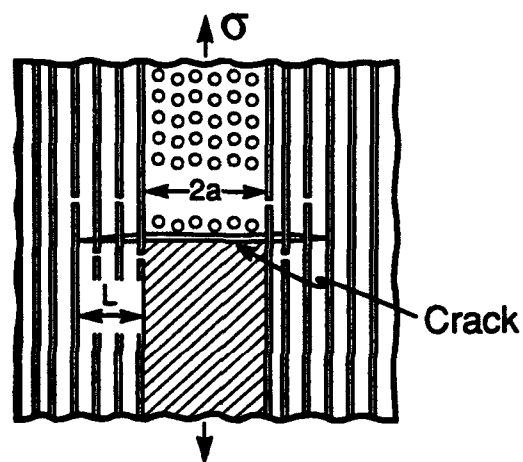


Figure 2b

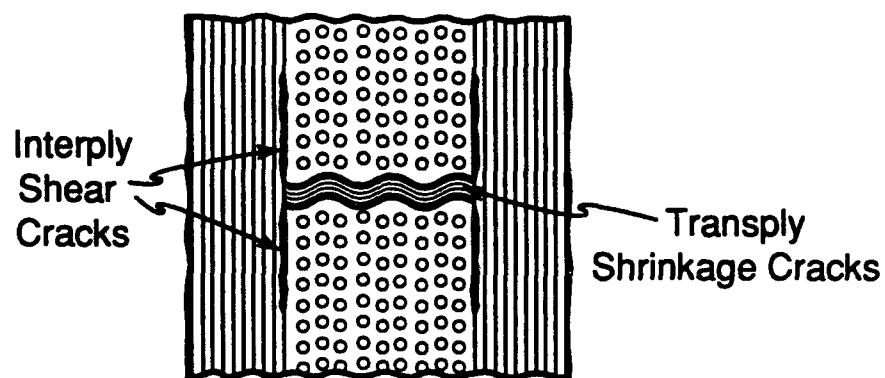




a) Non-Interacting Fiber Bundle Failure



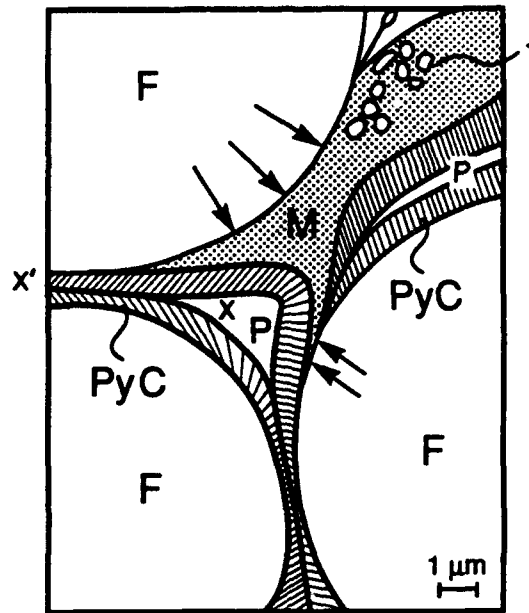
b) Crack Extension with Fiber Pull-Out



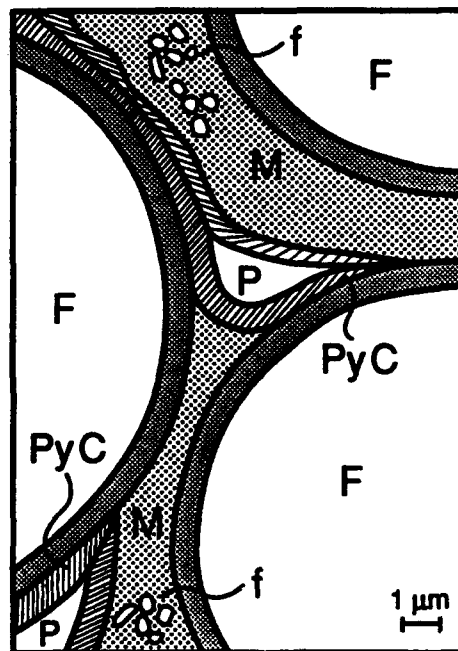
c) Interply Shear Cracks

Figure 3





a) Without Fiber Coating (HT and LT)



b) With Fiber Coating (LTC)

Figure 4. Schematic of the microstructures: F, fiber; M, matrix; f, filler; PyC, pyrocarbon; C, coating; and P, porosity; arrows indicate locations where fibers attached to the matrix.

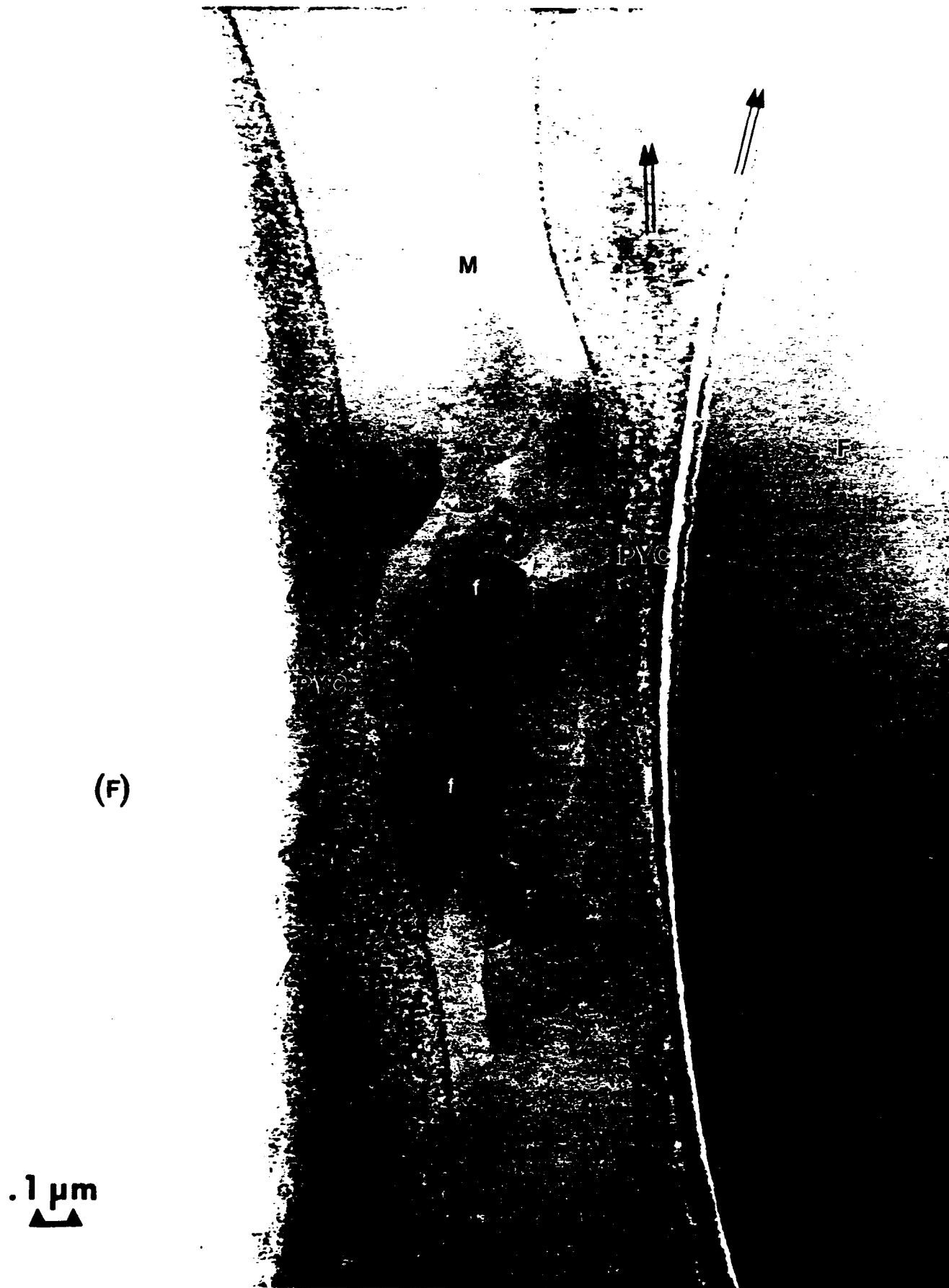


Figure 5

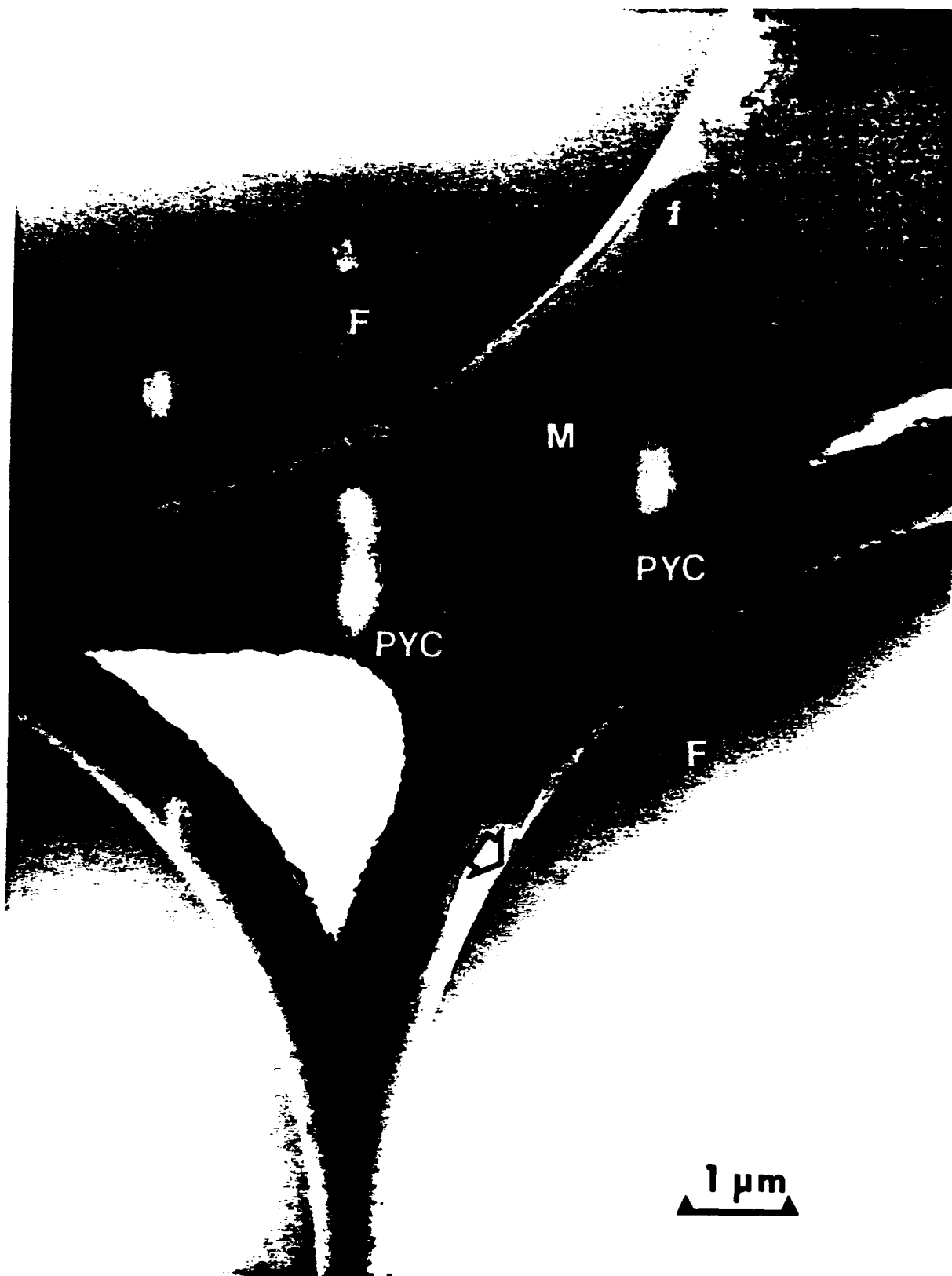


Figure 6



Figure 7



Figure 8



Figure 9a



Figure 9b

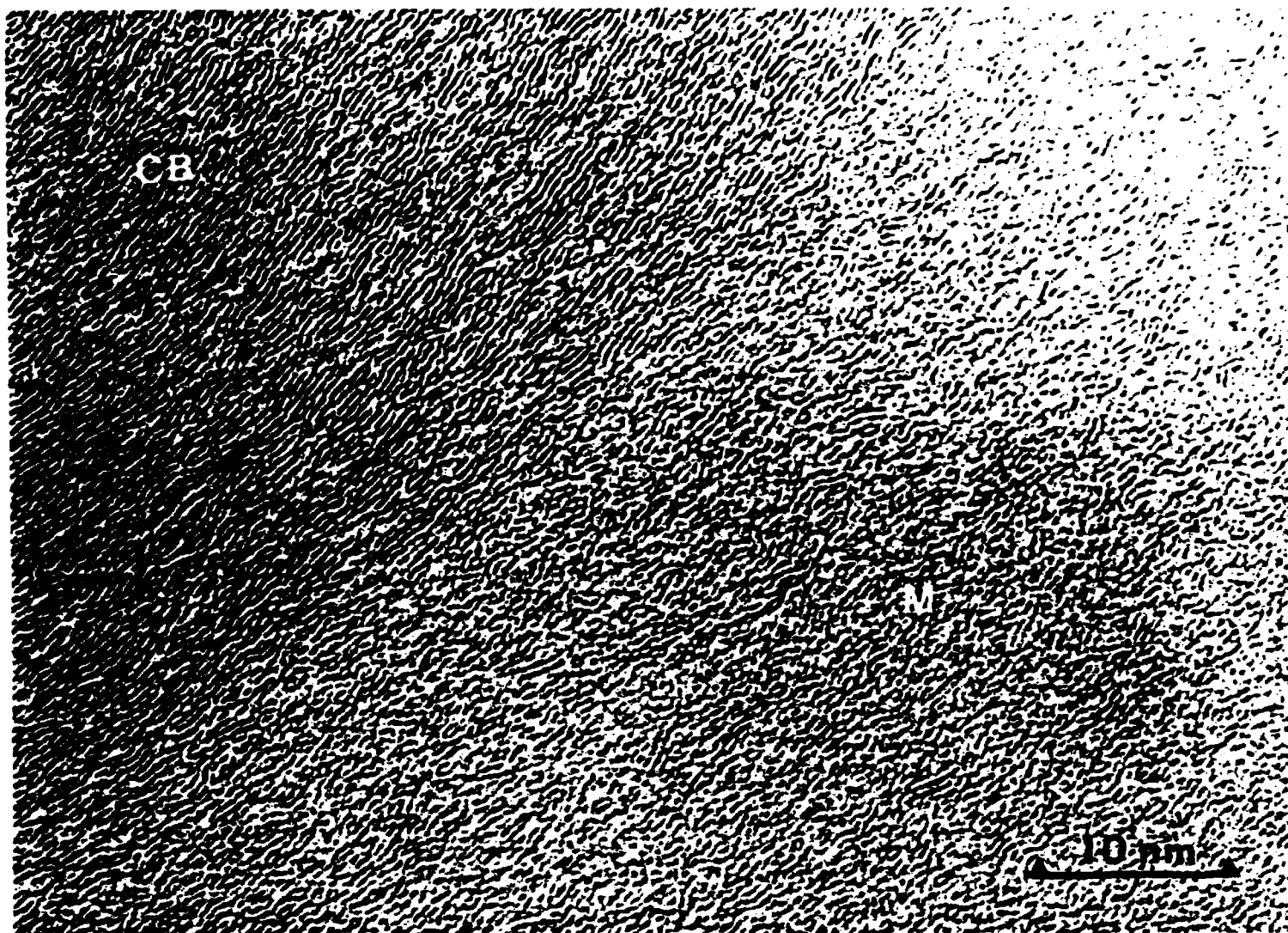


Figure 10a



B<sub>4</sub>C

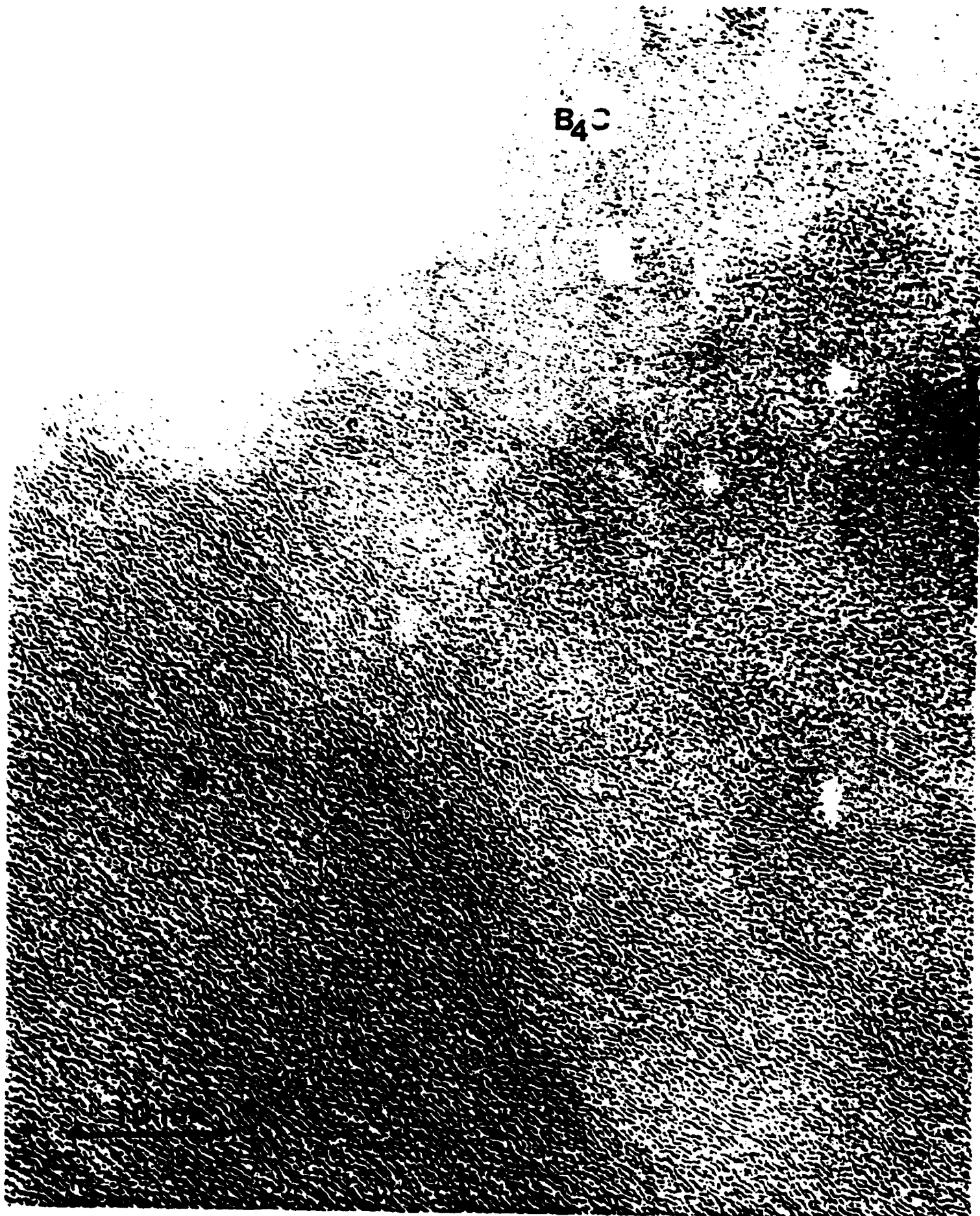


Figure 10b

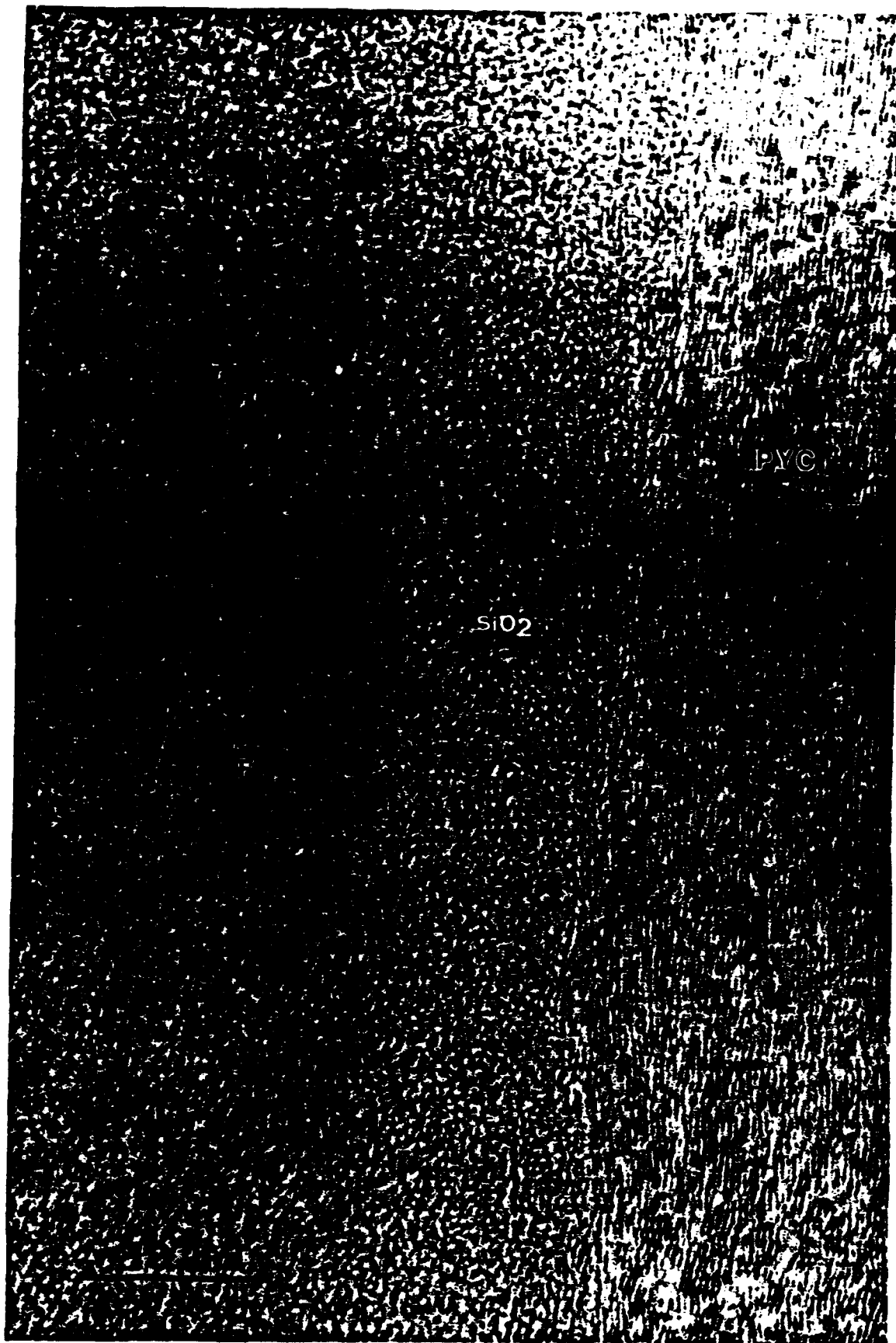


Figure 11



Figure 12



Figure 13



Figure 14

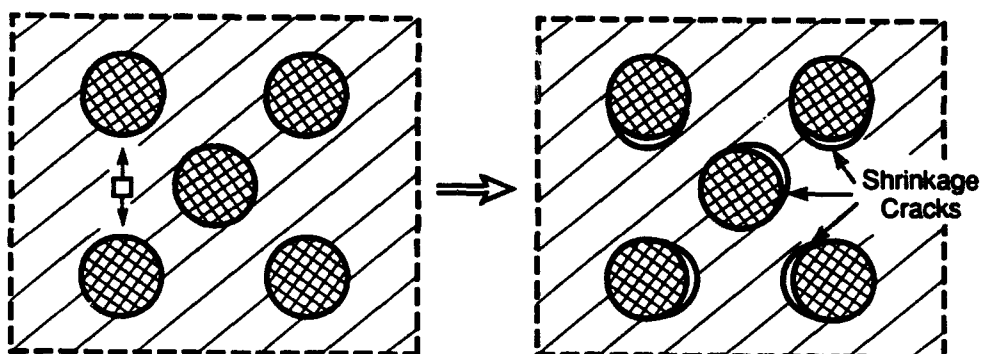
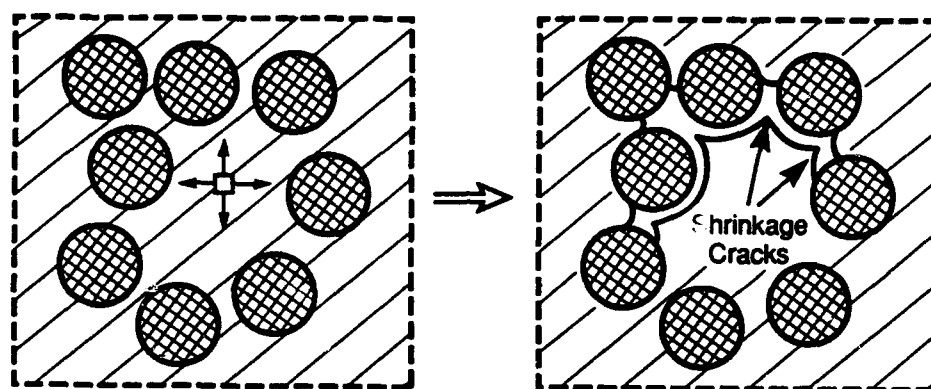
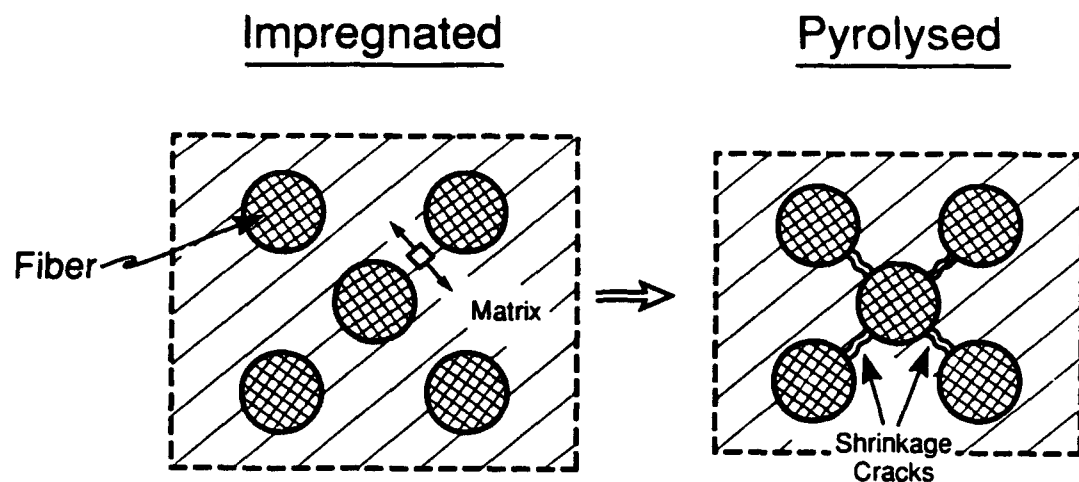
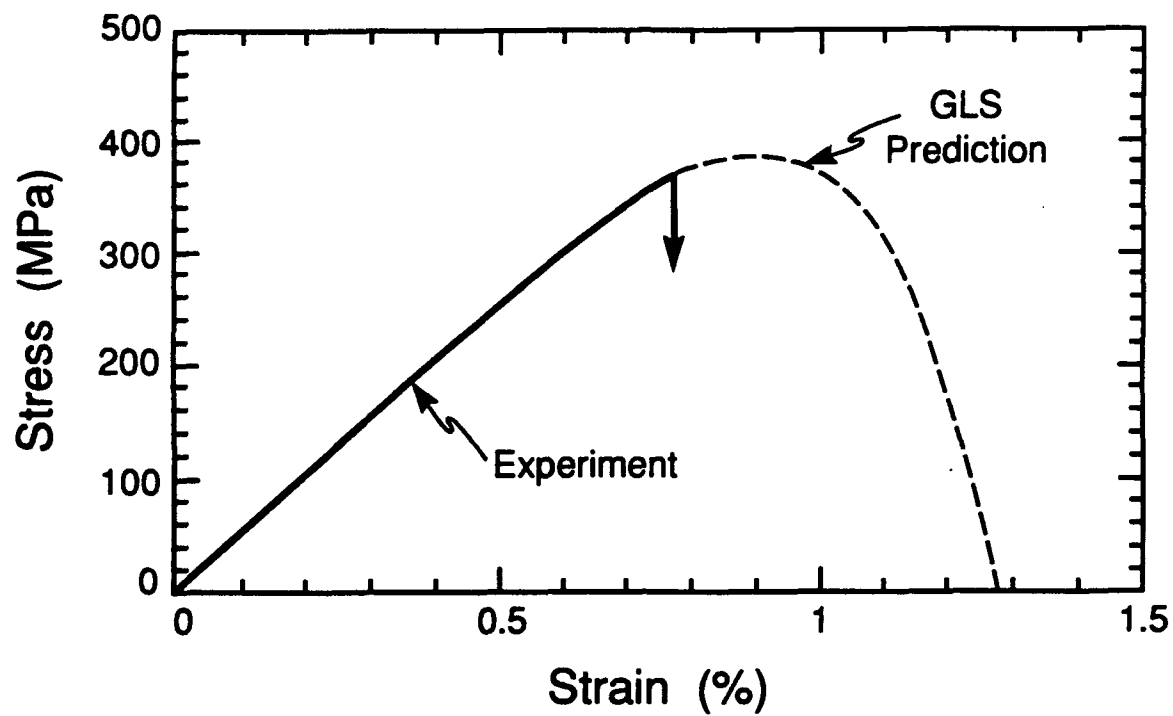
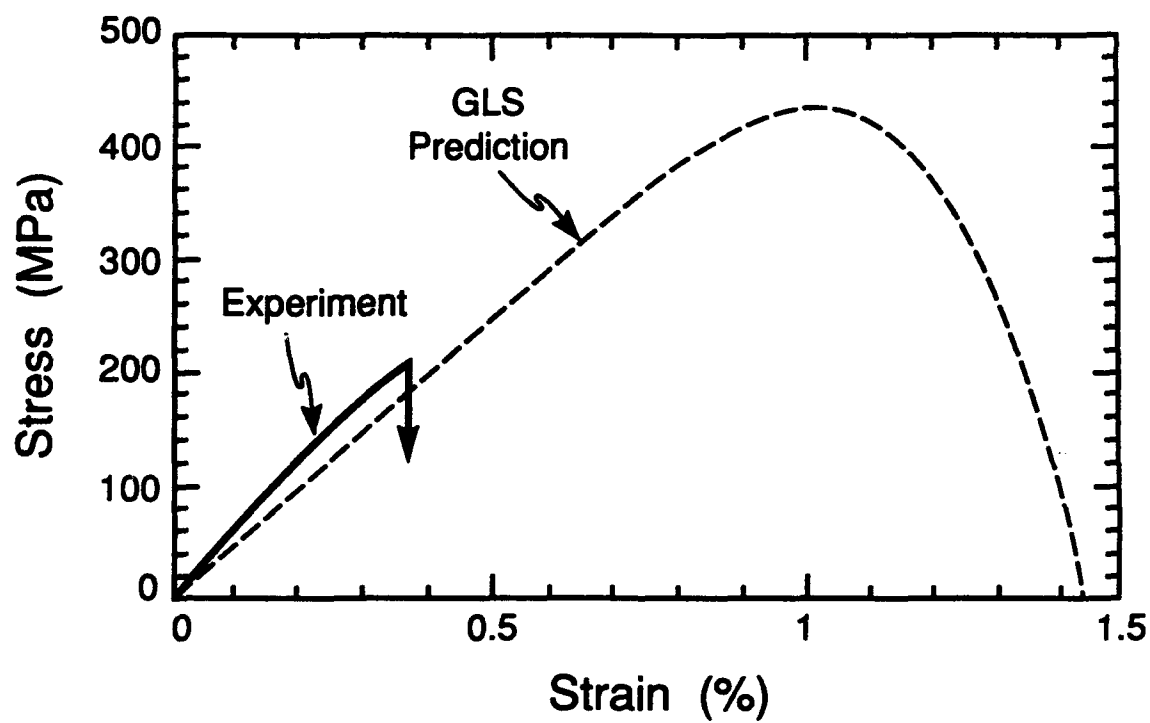


Figure 15



a) LT and LTC Materials



b) HT Material

Figure 16

# Microstructural Observations on Constrained Densification of Alumina Powder Containing a Periodic Array of Sapphire Fibers

David C.C. Lam\* and F.F. Lange

Materials Department  
College of Engineering  
University of California  
Santa Barbara, California 93106

\*Current Address: Hitachi Research Laboratory, Hitachi Ltd., Hitachi-shi, 316 Japan

## Abstract

Alumina powder was packed within and around a square array of 16 sapphire fibers to study the density and microstructure of the matrix powder after different heat treatments. The matrix powder along the cell edges of the array (most closely spaced distance between fiber centers) was observed to become dense and support grain growth before the regions within the centers of the square unit cells. The denser, larger grained material between the fibers forms a continuous network of creep resistant material that constrains the densification of the porous regions.

## 1. Introduction

As reviewed in reference 1, the presence of inclusions within a powder compact can retard the densification of the composite system and lead to the redistribution of voids<sup>2</sup> to form crack-like flaws within the partially dense material. The retardation had been theorized to originate from isolated inclusions,<sup>3</sup> from inclusion pairs,<sup>4</sup> as well as from the interaction of all inclusion, which can be described<sup>5</sup> as a constraining network. In this study, alumina powder was packed within and around a periodic array of sapphire fibers to determine if isolated inclusions can produce the density distributions predicted by the constraining network theory<sup>5</sup> and finite element calculations.<sup>6</sup>

## 2. Experiments

The processing of a composite containing non-touching, sapphire fibers<sup>a</sup> (~100  $\mu\text{m}$  dia. by ~10 cm. long) arranged in a 4 by 4 square array, was initiated by holding each fiber separate with a plastic screen at each end. After centering the

---

<sup>a</sup> Saphikon, Inc, Milford, NH.



bundle within a cylindrical rubber mold (dia.  $\sim 2.5$  cm), alumina powder (average diameter  $\approx 0.2 \mu\text{m}$ <sup>b</sup>) was vibrated around the fibers. (Slurry processing methods, such as slip casting and pressure filtration, were attempted, but differential drying shrinkage produced matrix cracks between the embedded fibers.) The mold was evacuated of air and then iso-pressed at 280 MPa. Experiments with the same powder, without fibers, produced a relative density of 0.58. The consolidated specimen containing the fiber array was heat treated at 1200 °C for 2 h in air<sup>c</sup>. A specimen was removed by diamond cut perpendicular to the fibers and polished for SEM examination.<sup>d</sup> The remaining specimen was further heat treated at 1300 °C for 2 h, sectioned, polished, observed in the SEM and heated again to 1350 °C/0.5h and again examined in the SEM. All specimens were heated and cooled (to 300 °C) at 5 °C/min.

### 3. Results

Figure 1 is a schematic cross-section illustrating the general density distribution observed after 1200 °C/2h, 1300 °C/2h and after thermal etching at 1350 °C/0.5h. Figure 1 also illustrates that the fiber array can itself be considered a single inclusion surrounded by matrix powder. After 1200 °C/2h, regions (4), the matrix material along the edges of the square, unit cells, appeared dense and arguably larger in grain size, whereas all other regions contain similar volume fraction of porosity and similarly sized grains. The difference in microstructure between these regions became more distinct only after further heat treatment.

After 1300 °C/2h, only the matrix within the center of each unit cell, defined as region (5), was porous. Figures 2a and 2b illustrate the grain size of region (1) which was  $>1$  cm from fiber bundle) and (2) after the 1350 °C thermal etch, respectively. It can be seen that the matrix at the interface between the fiber at the edge of the 'single' inclusion (array of fibers) and far from the fiber array are both dense and have the same grain size. Figure 2c illustrates the grain size of material between the inclusions, along the cell edge on the interior of the array, is larger than within the dense matrix. This observation, consistent with the observation that regions (4) were the only dense regions at 1200 °C, shows that regions (4) support grain growth for longer periods relative to other regions. Figure 2d show the porosity in regions (5) after the thermal etch. Figure 3 shows that the grain size between the fibers along the cell edge decreases in the direction towards the cell

<sup>b</sup> AKP-50, Sumitomo Corp., New York, NY.

<sup>c</sup> Lindbergh 1700°C Box Furnace.

<sup>d</sup> Model 840, JEOL, Peabody, MA.

center, and that the interior cell edges (Fig. 3a) appear to be the first to densify and support grain growth, relative to cell edges on the exterior of the array (Fig. 3b).

#### 4. Discussion

Observations presented above show that a periodic, non-touching array of inclusions will constrain the densification of their powder matrix and produce a density distribution that can be predicted purely on the bases of kinematic constraint of differential shrinkage.<sup>5</sup> The kinematic constraint arises because during matrix densification, the composite strain must be isotropic. Isotropy requires all strains within the unit cell be identical. For example, the strain between fiber centers within a unit cell (along both cell edges and cell diagonals) must be identical despite their difference in the fraction of powder, and thus, the expected shrinkage, between these different cell pairs. If both of these different cell pairs were not constrained, the diagonal would shrink more because of the greater ratio (powder : inclusion) of powder between this pair relative to the edge pair. Since all directions must exhibit the same strain, the diagonal pair exerts a compressive strain on the edge pair, likewise, the edge pair exerts a tensile strain on the diagonal pair. These compressive and tensile strains can also be thought of as compressive and tensile stresses.<sup>5,6</sup> The compressive strain exerted on the edge pairs (regions 3 and 4, Fig. 1) cause the matrix between the fibers to densify before the cell centers (diagonal pairs - regions 5), and before the matrix powder that surrounds the fiber array (region 1). The same phenomena, viz., constrained densification and density distributions, were observed in powder matrixes containing randomly distributed inclusions.<sup>2</sup>

Further heat treatment might be expected to cause mass redistribution such that the center of the cells would become dense as well. Experimental observations powder matrices containing randomly distributed inclusions show that the voids within the lower density regions coarsen with only a small amount of additional densification.<sup>7</sup> Coarsening reduces the surface to volume ratio of the void phase within the lower density regions, and thus reduces the driving potential for void disappearance and shrinkage. In addition, as previously pointed out,<sup>2,8</sup> the denser regions within polycrystalline materials will be the first region to support grain growth. That is, coarser grained material is more creep resistant than either the finer grained or less dense material. Thus, the denser, coarser grained material is a continuous network that constrains the shrinkage of the lower density portions of the composite.

Consistent with other observations,<sup>6,9</sup> the current observations also show that a single isolated inclusion (i.e., in this case, the fiber/matrix array itself; Fig. 3b)

will do little to constrain the shrinkage and densification of the surrounding powder matrix (i.e., in this case the powder surrounding the array; Fig. 3a).

### Acknowledgment

This research was supported by the Defense Advanced Research Projects through the University Research Initiative under the Office of Naval Research Contracts No. N00014-86-K-0753 and N00014-92-J-1808.

### Figures

- Fig. 1      Schematic of observed density distribution after heating at 1200 °C to 1350 °C. Darker = denser. Filled, dark circular regions are sapphire fibers.
- Fig. 2a      Matrix grain size in bulk matrix (region 1; ~1 cm from the fiber bundle) after heat treatment at 1300 °C and thermally etched at 1350 °C for 30 min.
- Fig. 2b      Matrix grain size at corner of fiber bundle (region 2) after heat treatment at 1300 °C and thermally etched at 1350 °C for 30 min.
- Fig. 2c      Matrix grain size in between inclusions in interior of bundle (region 4) after heat treatment at 1300 °C and thermally etched at 1350 °C for 30 min.
- Fig. 2d      Matrix grain size center of inclusion square in interior of bundle (region 5) after heat treatment at 1300 °C and thermally etched at 1350 °C for 30 min.
- Fig. 3a      SEM micrograph of region 4 after heat treatment at 1300 °C and thermally etched at 1350 °C for 30 min.. Grain size of matrix in-between two fibers (left side) is dramatically larger than the grain size into cell (right side).
- Fig. 3b      SEM micrograph of region 3 after heat treatment at 1300 °C and thermally etched at 1350 °C for 30 min.. Grain size of matrix in-between two fibers (left side) is dramatically larger than the grain size into cell (right side).

### References

- [1]      R.K. Bordia and G.W. Scherer, "Overview No. 70 On Constrained Sintering I - III," *Acta Metall.*, **36** [9] 2393-2416 (1988).

- [2] O. Sudre and F. F. Lange, "The Effect of Inclusions on Densification. Part I: Microstructural Development in an  $\text{Al}_2\text{O}_3$  Matrix Containing a High Volume Fraction of  $\text{ZrO}_2$  Inclusions," *J. Am. Ceram. Soc.* 75 [3] 519-24 (1992)
- [3] C.H. Hsueh, A.G. Evans R.M. Cannon and R.J. Brook, "Viscoelastic Stresses And Sintering Damage In Heterogeneous Powder Compacts," *Acta Metall.*, 34 [5] 927-36 (1986).
- [4] S. Sundaresan and I.A. Aksay, "Sintering With Rigid Inclusions: Pair Interactions," *J. Am. Ceram. Soc.*, 73 [1] 54-60 (1990).
- [5] F.F. Lange, "Constrained Network Model For Predicting Densification Behavior Of Composite Powders," *J. Mater. Res.*, 2 [1], 59-65 (1987).
- [6] O. Sudre, G. Bao, F. F. Lange, and A. G. Evans, "The Effect of Inclusions on Densification. Part II: Numerical Model," *J. Am. Ceram. Soc.* 75 [3] 525-31 (1992).
- [7] O. Sudre and F. F. Lange, "Constrained Densification: Part III, The Desintering Phenomenon," *J. Am Ceram. Soc.* 75 [12] 3241-51 (1992).
- [8] F. F. Lange, D. C. C. Lam, and O. Sudre, "Powder Processing and Densification of Ceramic Composites," *Mat. Res. Soc. Symp. Proc.* 155 [4] 309-18 (1989).
- [9] F.F. Lange, "Densification of Powder Rings Constrained by Dense Cylindrical Cores," *Acta Metall.*, 37 [2] 697-704 (1989).

Figure 1

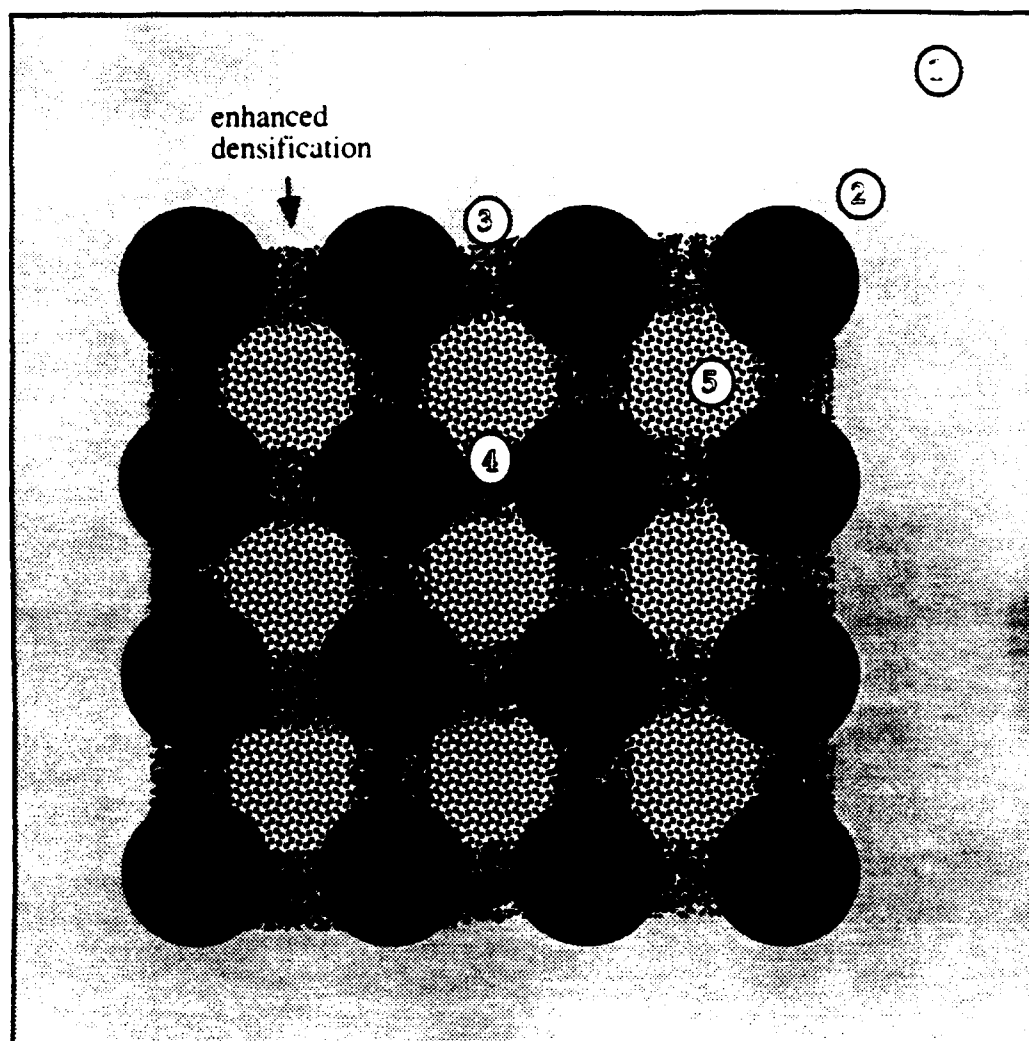


Figure 2

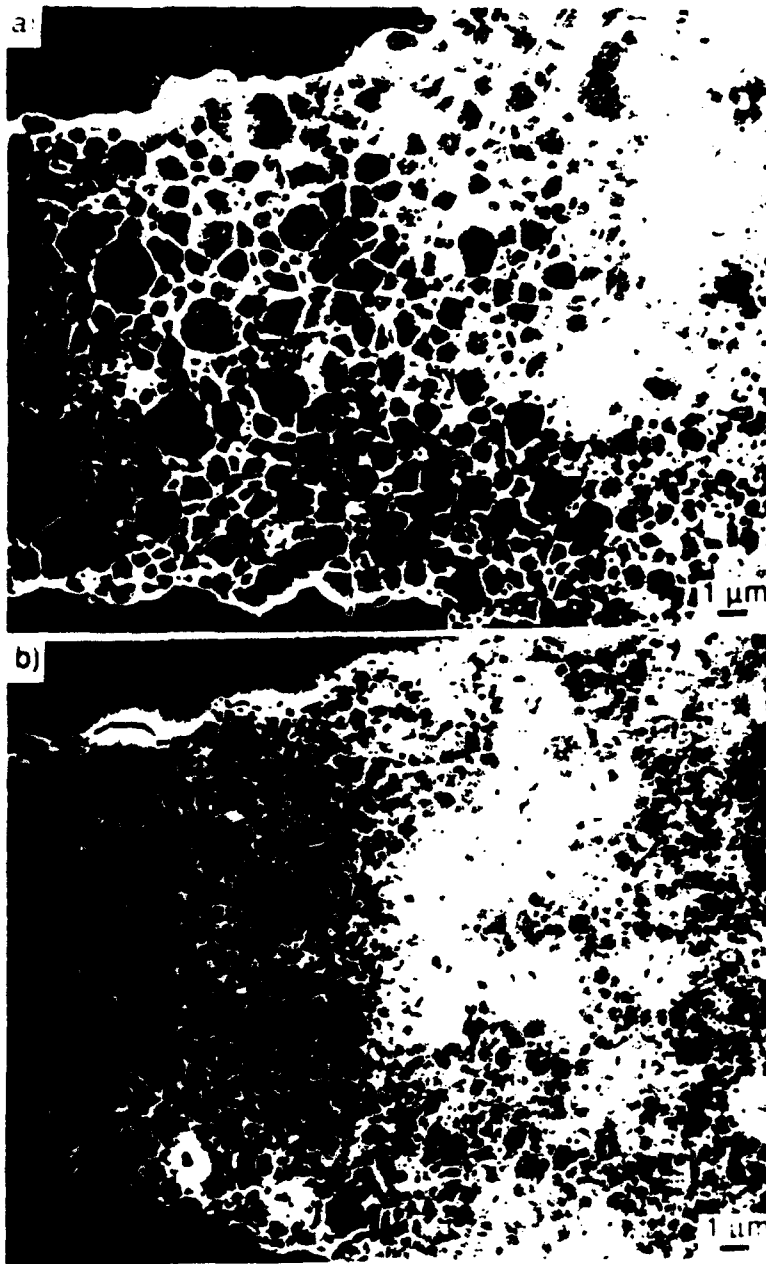
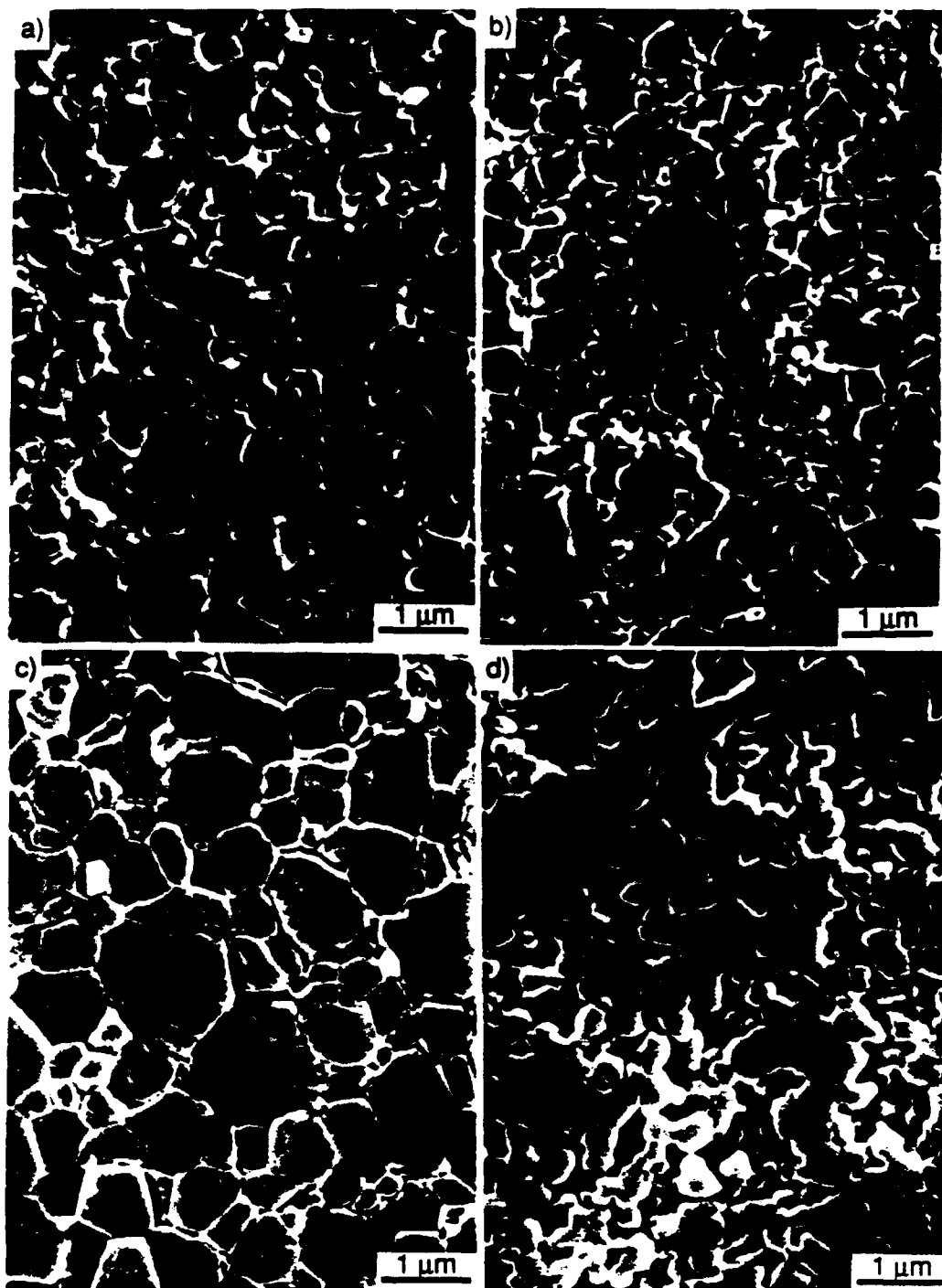


Figure 3



# **Material Issues in Layered Forming**

Christina Amon, Jack Beuth, Helmut Kirchner,  
Robert Merz, Fritz Prinz, Kevin Schmaltz, Lee Weiss

Carnegie Mellon University  
Pittsburgh, PA

## **Abstract**

A brief overview of key issues in layered thermal processing is given. Incremental sintering and layered fusion of powder and molten droplets are discussed. The criteria for remelting the solid substrate are derived from a one dimensional heat transfer model. Temperature gradients which occur during solidification and subsequent cooling are responsible for the build up of internal stresses which can be estimated through establishing an elastic beam model. The difficulties as well as opportunities regarding the generation of multi-layer multi-material structures are also described in this article.

## **Key Words**

Layered manufacturing, sintering, melting, thermal modeling, residual stress, multi material structures, stress cracking.

## **Introduction**

Solid freeform fabrication through layered material deposition appears to be an attractive method for 3D object generation[1,2,3]. This method offers the possibility of expanding the design space with respect to geometric complexity, material diversity, and traditional cost/time constraints. However, building up materials in layers poses significant challenges from material science, heat transfer and applied mechanics viewpoint.

Depositing materials onto a solid substrate can typically be accomplished through sintering, local melting, chemical synthesis (e.g. photo polymerization), or otherwise gluing, brazing, and soldering. The issues associated with each of these processes can be summarized as follows:

- Local melting requires significant energy input to the semi-finished part which may result in the buildup of internal stresses and consequently distortions.
- Sintering requires less energy to establish bonding of the added layers but local voids may be left unless external forces are applied
- The practical applicability of chemical synthesis is limited to certain derivatives of organic substances
- Gluing, brazing, and soldering have the disadvantage of adding bonding materials to the part which are not necessarily desirable for its function or performance.

Some of these difficulties can be overcome by adopting post processing steps such as annealing, sintering, and material infusion. Building parts through layered forming is further complicated if one attempts to deposit dissimilar materials on to the substrate. In particular, differences in the coefficient of thermal expansion (CTE), and misfit dislocations (due to differences in atomic radii) can lead to even greater distortions of the atomic lattice in comparison with layered material structures of the same kind. This paper discusses some of these underlying issues in layered forming rather than attempting to offer specific solutions to these problems.

## **Process Classification**

Common to all layered forming techniques is the incremental nature of the material build up process. Stepwise material build up requires bonding between layers. Obviously, the material



quality of a part is determined by the quality of each deposited layer as well as the quality of the bond between the layers. The following classification for material deposition processing in layered manufacturing is chosen. Processes are listed with respect to the temperature regimes in which they operate at and issues of concern regarding the resulting articles. This list is by no means exhaustive with important problems like speed, surface quality and accuracy not being addressed.

<u>Process</u>	<u>Temperature</u>	<u>Issues</u>
Sintering	$T < T_M$	Density Postprocessing
Melt On	$T > T_M$	Residual Stress Warpage Debonding Postprocessing
Glueing Powder Sheet	$T \sim T_R$	Strength Postprocessing
Photocuring	$T \sim T_R$	Limited Material Range Residual Stress

In the following, we limit our discussion mostly to thermal processing issues (e.g. sintering, melting) some of which are also relevant for processes occurring at room temperature.

### Sintering

Layered powder deposition followed by laser sintering has become an established prototyping process; for more details see [1]. The physics of any sintering process is based on particle fusion at temperatures below the material melting point. During sintering necks form between adjacent powder particles thus reducing the surface area and increasing the density of the powder aggregate. The driving force for this process is the reduction of the particle surface free energy. The densification rate is proportional to that reduction.

In order to change the shape of the powder particles, matter or vacancies need to flow. (Vacancy flow can be considered as the counterflow of matter, both concepts are equivalent). The densification rate depends further on the combination of the transport path of the matter as well as the source of the matter. Ashby [4] distinguishes six different path/source combinations e.g.: surface diffusion from surface, boundary diffusion from boundary, or volume diffusion from boundary. At different temperatures different path/source combinations dominate the flow of matter.

During pressureless sintering (i.e., no external force applied) the densification rate decreases as the aggregate density increases due to a decreasing rate of surface reduction. A quick inspection of the theoretically established sintering maps by Ashby such as the example of copper in Figure 1 indicate that close to full density (i.e. when the neck radius is comparable to the particle radius) can only be reached asymptotically. Also, the times required to achieve high densities are significantly higher than the mean time that a selective heat source (e.g. laser) will for practical reasons dwell in a certain location. Hence, selectively sintered powder aggregates need to be subjected to further postprocessing procedures such as hot isostatic pressing to achieve full density.

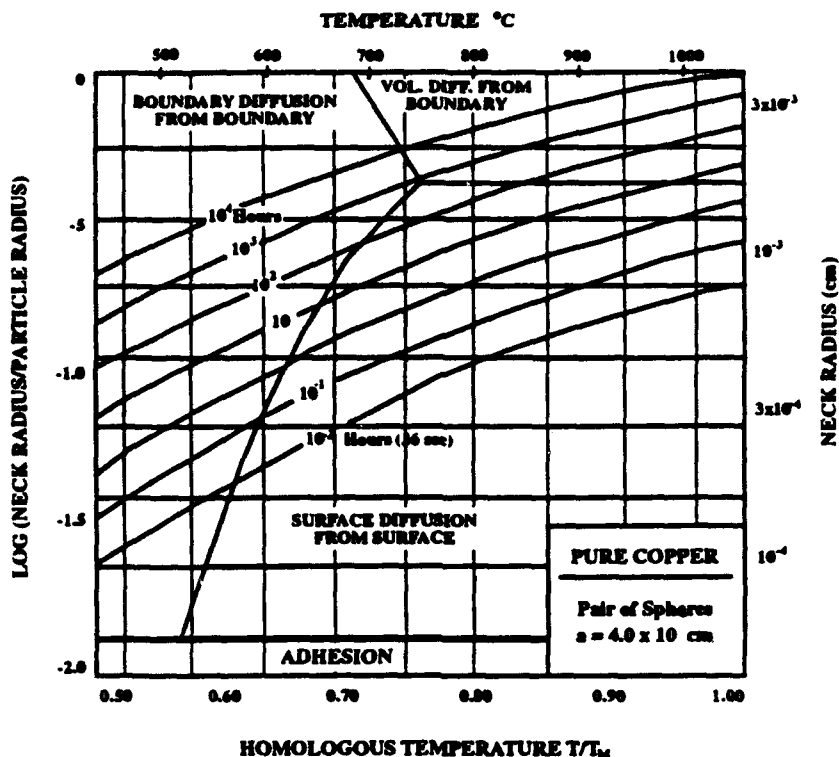


Figure 1: Sintering map of copper particles [4].

### Melting On

To further enhance and accelerate the bonding of a layer to the substrate one can locally melt already deposited powder particles or deposit molten droplets as done for example in thermal spraying [2]. Two scenarios can be envisioned: In the first one the molten droplet adapts to the shape of the underlying substrate. In the second the particle has sufficient energy to remelt the substrate and form a solid bond. In the first case two possibilities for bonding exist. The molten droplets simply form a mechanical interlock as commonly observed in thermal spraying [4]. Alternatively, the droplets may also bond to the substrate through a sinter mechanism in which necking occurs by shape adaptation of the molten droplet and diffusion within or on the surface of the substrate. The rate of bond formation will obviously be higher compared to the pure sinter case as described earlier.

In addition to the structure of the bond, the microstructure resulting from the solidification of the droplets is key to the strength of the layered article. Therefore an understanding of the entire temperature history is important for planing layered manufacturing processes. Also, higher temperature gradients involved in melting compared to pure sintering tends to lead to the formation of higher residual stresses.

In the following sections we address the issue of predicting the thermal history of the melting process as well as the build up of residual stresses after solidification.

### Thermal Modeling

This section presents a numerical modeling of the thermal history of a molten metal particle on a solidified substrate. The particle can be melted by a laser or plasma alternatively, molten droplets can be sprayed on a solidified substrate as depicted in Figures 2a and 2b. This model is useful for investigating the conditions needed to achieve partial substrate remelting, to create an accurate predictive tool of the particle melt of the thermal spray process, and to investigate the effect of operating conditions such as initial molten particle/droplet and substrate temperatures,

size, surface heat transfer and sprayed material properties on the resulting melting front migration rate and thickness, temperature distribution, and overall cooling rates.

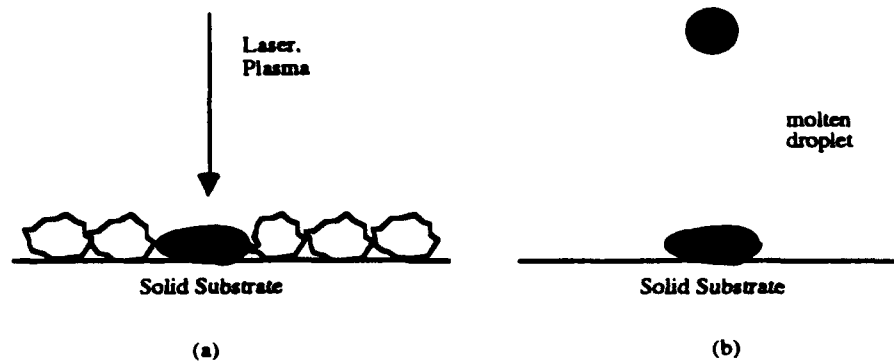


Figure 2 (a) molten powder particle (b) molten droplet deposition.

In the following we refer to molten particles as well as droplets from spraying just as droplets. Application parameters such as laser energy or spray gun power input, and deposition rates may then be modified to optimize the deposited material microstructure.

The numerical model for determining process temperatures and remelting conditions is simplified to a one-dimensional, heat transfer problem by assuming that the impacted droplet width is sufficiently greater than height, and that the droplet flattening time scale is much shorter than the droplet solidification time scale. This phenomena is modeled by the governing equation of the form:

$$\rho c_p \frac{\partial T}{\partial t} = k(T) \left[ \frac{\partial^2 T}{\partial x^2} \right] + \frac{\partial k(T)}{\partial T} \left[ \frac{\partial T}{\partial x} \right]^2 \quad (1)$$

for temperature  $T$ , density  $\rho$ , specific heat  $c_p$ , and thermal conductivity  $k$ . The  $\partial k / \partial T$  term is omitted since the thermal conductivity variation is slight for the materials and temperature ranges considered, although temperature dependent thermal properties are used [6]. This equation is valid for both the liquid region as well as the solid region. Above the top liquid surface, combined convective and radiative boundary conditions exist, while the energy balance:

$$\rho L \frac{\partial x}{\partial t} = k_{sol} \frac{\partial T}{\partial t} - k_{liq} \frac{\partial T}{\partial t} \quad (2)$$

is applied at the interface between the liquid and solid regions, balancing the energy flux into and out of the interface with the release of latent heat ( $L$ ). For the lower boundary of the solid region a constant substrate temperature is assumed at a remote distance from the surface.

The energy equation is discretized using an Eulerian explicit formulation. To track the location of the melting front during the solidification process, a three-point Lagrange interpolation formula is used to approximate the temperature function [7] at the nodes preceding and following the melting point. This assumes a form that can be readily incorporated into the finite difference formulation used, but permits the location of a varying "node" point corresponding to the melting front. The new front location is calculated after each iteration using the discretized interface energy balance equation. To approximate the initial interface temperature when the known liquid droplet first strikes the known solid substrate the analytical Stefan interface solution is used:

$$T_{inter.} = [RATIO * T_{liq} + T_{sol}] / [1 + RATIO] \quad (3)$$

$$\text{RATIO} = \sqrt{(k c_p \rho)_{\text{liq}} / (k c_p \rho)_{\text{sol}}} \quad (4)$$

For the complete duration of the thermal system modeling, the Stefan solution is not an accurate representation of the actual boundary conditions. However, for the initial interface condition the solution above can be used because boundary conditions corresponding to two semi-infinite bodies in contact remain valid until the temperature fluctuation propagates to the liquid surface.

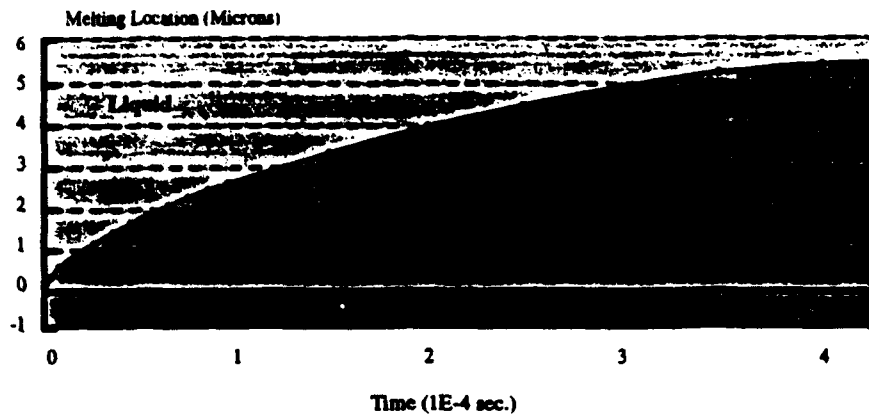
For the first droplet, the initial conditions assumed are uniform droplet and ambient substrate temperatures. When prior molten droplets heat the substrate, the model is then modified to incorporate the two-dimensional effects of substrate preheating arising from the diffusion of energy from previously molten droplets:

$$\rho c_p \frac{\partial T}{\partial t} = k(T) \left[ \frac{\partial^2 T}{\partial x^2} + \frac{\partial^2 T}{\partial y^2} \right] \quad (5)$$

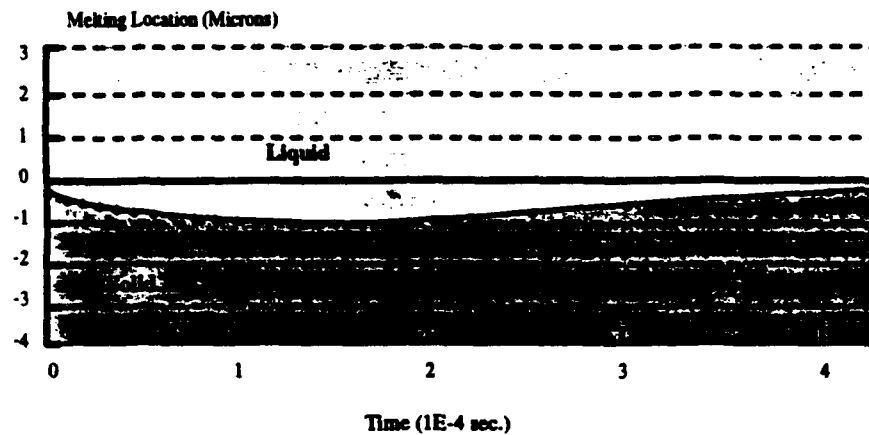
This model reflects the process where the laser source or spray gun is moving across the substrate. As with the one-dimensional solidification model, an Eulerian explicit algorithm is used to solve the two-dimensional energy equation. Because remelting does not occur with this lateral case there is no Lagrangian approximation terms required. The substrate temperature profile resulting from this two-dimensional model is then used as the substrate initial condition for the solidification model.

Simulations are made for the model of single droplets of carbon steel, stainless steel and zinc which are residing or have landed on similar substrates, and for a steel droplet on a zinc substrate. This latter case simulates the building up of sprayed materials onto a sacrificial substrate. Parametric studies of remelting sensitivity to surface convection and radiation changes, variations of impacting droplet temperature, droplet size and existing substrate temperature have been performed. The solidification process is completed so rapidly (on the order of milliseconds) that the heat transfer is basically a conductive process, and the surface convective and radiative effects are negligible. Numerical results also indicate that substrate remelting will not occur with realistic droplet temperatures (having less than several hundred degrees centigrade of superheating) on an *unheated* substrate. A remelting condition requires a substrate heated several hundred degrees above ambient temperature. This condition does exist when the preheating effect caused by previous droplets is included with the two-dimensional model.

For the case of a stainless steel droplet landing on a stainless steel substrate, numerical simulations are performed with initial "droplet" thickness of 100 microns and substrate temperature of 1100°C. The time-dependent solidification of this layer is shown in Figure 3 for two cases: a 1550°C and a 1650°C initial droplet temperature. The y-axis of Figure 3. indicates the location of the melting front; 0 represents the interface between the impinging droplet and the substrate, with the droplet extending in the positive direction.



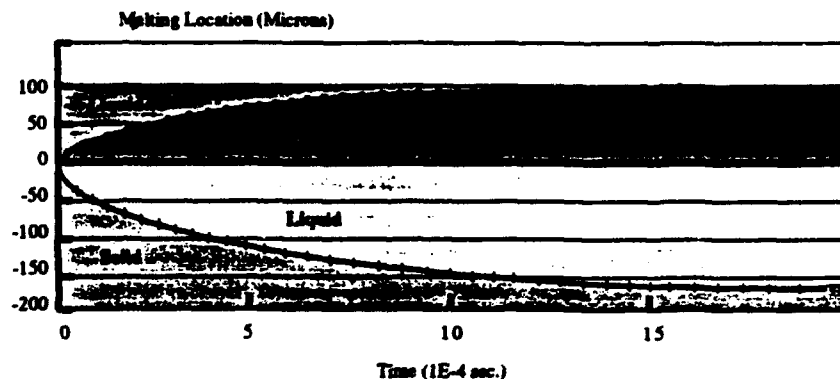
Initial Droplet Temperature 1550 Degrees



Initial Droplet Temperature 1650 Degrees

**Figure 3: Substrate Remelting**  
(304 Stainless Steel Preheated substrate, Drop Size 100 Microns)

At the start of the simulation the entire positive y region is liquid and the negative region solid. For the 1550°C temperature no substrate remelting occurs, while for the 1650°C case a small amount of remelting does occur. In Figure 4 the results for a stainless steel droplet on a zinc substrate are shown.



Melting Front: — Stainless Steel    - - - Zinc  
(Initial 1450 Degree SS droplet on 25 Degree zinc substrate)

**Figure 4: Substrate Remelting (Stainless steel on zinc substrate)**

The stainless steel droplet, initially at its melting temperature, solidifies while the lower melting zinc melts and actually vaporizes slightly. This result demonstrates the need to protect sacrificial support material.

## Mechanics Issues in Shape Deposition Processes

A current limitation of layered processing is the build-up of residual stresses as artifacts are manufactured. Residual stresses can affect artifact performance (response and life) and are also the root cause of specific deleterious effects including artifact warping, artifact delamination and stress cracking of brittle layers. Understanding the build-up of residual stresses and how to minimize them and their effects are thus the focus of current mechanics research into layered manufacturing.

### *Residual Stresses and Artifact Warping*

In the layered processing, residual stresses are built up as new layers are deposited onto existing layers of the artifact. This build-up is due to the contraction each new layer experiences as it solidifies and cools and occurs even in the successive application of layers of the same material. The process is illustrated in Figure 5 where, for simplicity, a single layer of one material is shown applied to a single existing layer of another material. The layer thicknesses may differ, however, it is assumed that each layer is beam-shaped. It is also assumed that the new layer experiences a uniform contraction as it solidifies on the existing layer and that the contraction can be characterized by a temperature-independent coefficient of thermal expansion,  $\alpha$ . Under these assumptions, the elementary analysis of Timoshenko [8] for the stresses in a uniformly heated bimaterial strip can be applied to predict the residual stresses in each layer and the curvature of the two-layered artifact caused by the contraction of the newly applied layer. The predicted curvature,  $\kappa$ , takes the form

$$\kappa \equiv \frac{1}{\rho} = \frac{-\alpha \Delta T}{\frac{(h_1 + h_2)}{2} + \frac{(E_1 h_1^3 + E_2 h_2^3)}{6(h_1 + h_2)} \left( \frac{1}{E_1 h_1} + \frac{1}{E_2 h_2} \right)} \quad (6)$$

where  $\rho$  is the radius of curvature of the artifact. In eq (6)  $\alpha$  is the coefficient of thermal expansion of the new layer and  $\Delta T$  is the difference (negative in sign) between the solidification temperature of the new layer and the operating temperature. The layer thickness is designated by  $h$  and  $E$  is the Young's modulus of the layer.

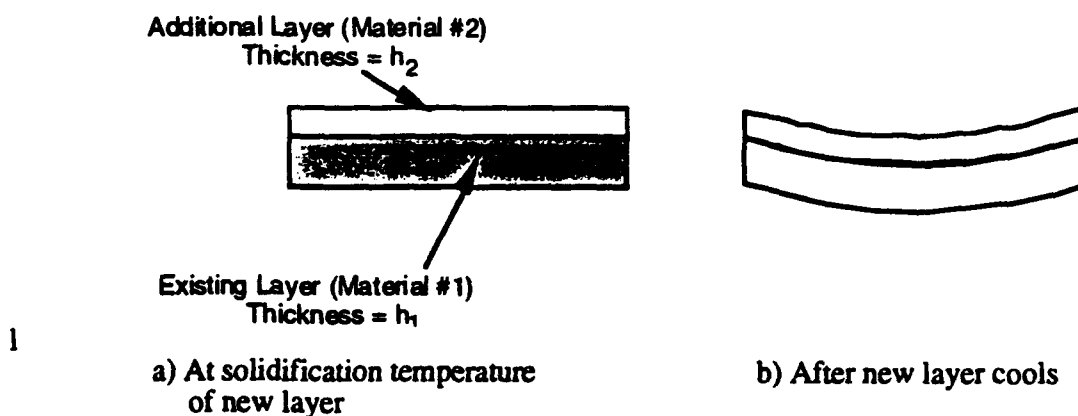


Figure 5 Curvature induced by the thermal contraction of a new layer (material #2) after its application to an existing layer (material #1).

For this simple model the stresses in each layer of the bilayer artifact are composed of axial and bending components and thus vary linearly through the thickness of each layer. In layered manufacturing, this interaction between newly applied and existing layers is repeated for each additional layer applied. The curvature of the artifact and the residual stresses in it are increased with the addition of each new layer.

There is a need in layered manufacturing to experimentally quantify residual stresses created during the process by measuring curvature changes caused by the addition of new layers. Results can be compared to simple models of layer interaction such as the one above. It is expected that enhancements to the model will be necessary, including accounting for the temperature dependency of coefficients of thermal expansion and the modeling of non-uniform thermal contraction of individual layers. In particular, results from thermal modeling of the solidification of layers (see previous section) is expected to yield more precise layer residual stress distributions for use in the solid mechanics model. The goal would be to not only predict residual stress and curvature effects in geometrically complex artifacts, but to also shed light on material combinations and process procedures that minimize them. An example of a layered copper steel tube manufactured by Carnegie Mellon's MD\* process [2] is shown in Figure 6

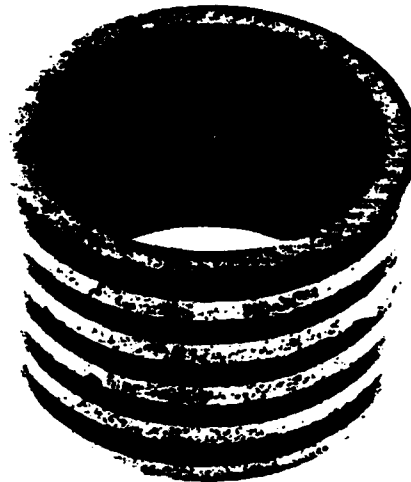
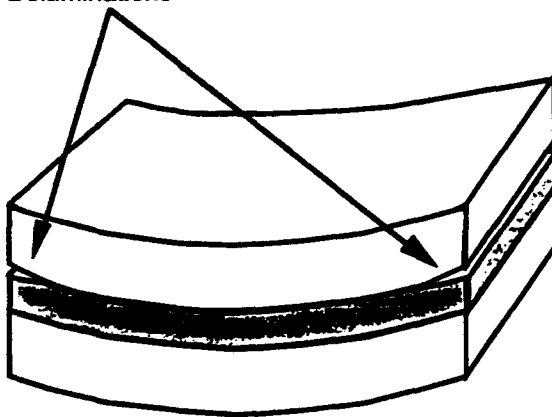


Figure 6. Layered copper steel tube manufactured in MD\*

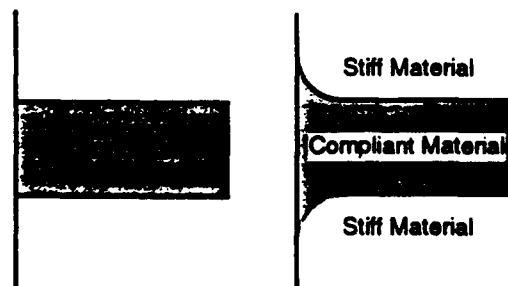
#### *Interfacial Debonding*

In addition to warping, residual stresses can cause delaminations between layers by acting as the driving force in the propagation of interfacial cracks from the edges of the artifact toward its center (see Figure 7 a). The delamination may propagate through the entire length of the artifact, separating it into two pieces. This is particularly a problem in the case of artifacts made of layers of different materials, due to the large stress concentrations that exist at the intersection of an uncracked bimaterial interface and a free edge.

#### *Delaminations*



(a)



(b)

Figure 7 a) Edge delaminations and b) Untailored and tailored bimaterial interfaces

A fully elastic asymptotic analysis of a bimaterial interface intersecting a free edge (see Bogy [9] or Hein and Erdogan [10]) predicts that stresses are, in general, singular there. Using the notation that the stresses vary as  $r^{(\lambda-1)}$  as  $r$  approaches zero, where  $r$  is measured from the intersection point,  $\lambda$  can take on values from  $\lambda=1.0$  (no singularity) to roughly  $\lambda=0.60$ . The value of  $\lambda$  is a function of the relative mismatch in elastic properties of the two materials and the angle that the interface makes with the free edge. The stress singularities that result from an elastic analysis of the bimaterial problem are important for two reasons. First, they indicate that actual interfaces in manufactured artifacts exhibit very high concentrations of stress at their free edges. Second, from an analysis standpoint, because the strength of the singularity in the elastic stresses is a function of the material combination studied, analytical comparisons of delamination driving force between different material combinations is difficult if an uncracked interface model is used.

We are investigating several approaches to help minimize delaminations. For example, one approach involves attempting to tailor the geometry of the interface to eliminate undesirable elastic stress singularities. This approach was suggested to the authors by G. B. Sinclair and follows the work of Okajima [11] on the bimaterial interface problem and the role of interface geometry in adhesive tensile tests. In Okajima [11] it is shown that the stress singularity at a bimaterial free edge in adhesive specimens can be eliminated if the interface is made to intersect the free edge tangentially, as shown in Figure 2b. In fact, the angle of intersection with the free edge need not be tangential and is a function of the relative elastic mismatch between the layers.

### *Stress Cracking*

Another problem associated with residual stresses layered manufacturing is the cracking of newly applied brittle layers as they cool and contract after being applied to existing layers of the artifact (see Figure 8). A separate but related problem is the cracking of brittle layers after they are embedded between ductile layers within the artifact, typically due to a combination of residual and applied tensile stress. It is important to predict, for a particular brittle material, the maximum allowable thickness of a newly applied layer so that stress cracking will not occur. Similarly, for embedded layers, it is desired to determine the relative thickness of an embedded layer so that no cracking will occur.

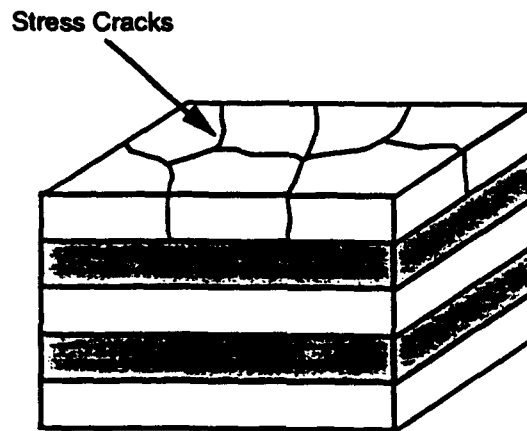


Figure 8. Stress cracking in a newly applied brittle layer.

### *Summary*

Layered manufacturing offers new opportunities for product design. This is true from a geometry and from a materials perspective. Objects of arbitrary geometric complexity can be built from a larger variety of material combinations than with conventional manufacturing methods. However, frequently the quality of the built articles (bond strength between layers and material density) and the rate at which they are created does not meet industrial demands. A better insight into the physics of the underlying bonding processes between layers and the resulting residual stress accumulation due to temperature gradients is expected to lead to improved performance of objects through layered manufacturing.



## ACKNOWLEDGEMENTS:

Financial support by the Advanced Research Agency (ARPA/ESTO) and by the University Research Initiative at University of California at Santa Barbara Grant N00014-92-J-1801 is gratefully acknowledged.

## References

1. Bourell, D.L., Beaman, J.J., Marcus, H.L., and Barlow, J. W., (1990) "Solid Freeform Fabrication: An Advanced manufacturing Approach," *Proc. Solid Freeform Fabrication Symposium*, The University of Texas at Austin, Aug. 6-8, 1-7 (1990).
2. Weiss, L. E., Prinz, F. B., Adams, D. A., and Siewiorek, D. P., (1992) "Thermal Spray Shape Deposition", *Journal of Thermal Spray Technology*, Vol. 1, pp. 231-237.
3. Sachs E., Cima, M., Cornie J., (1990) "Three Dimensional Printing: Rapid Tooling and Prototypes Directly from CAD Representation," *Proc. Solid Freeform Fabrication Symposium*, The University of Texas at Austin, Aug. 6-8, 27-33.
4. Ashby M. F., (1974) "A first Report on Sintering Diagrams," *Acta Met*, Vol. 22, pp. 275-286.
5. Herman, H., "Plasma-sprayed Coatings," (1988) *Scientific American*, Sept. 1988, pp. 112-117.
6. Amon, C.H., Prinz, F.B., and Schmaltz, K.S., (1993) Numerical Modeling of Thermal Spray Systems," Technical Report EDRC 24-10693, Carnegie Mellon University, Pittsburgh, PA
7. Y.S. Touloukian, Y.S. (1967) "Thermophysical Properties of High Temperature Solid Materials," Vol. 3, 1967, Macmillan, New York.
8. Timoshenko, S. (1925), "Bending and Buckling of Bimetal Strips," *J. Optical Soc. Am.*, Vol. 11, p. 233-255.
9. Bogy, D.B. (1971), "Two Edge-Bonded Elastic Wedges of Different Materials and Wedge Angles Under Surface Traction," *J. Appl. Mech.*, Vol. 38, pp. 377-386.
10. Hein, V.L. and Erdogan, F. (1971), "Stress Singularities in a Two-Material Wedge," *Int. J. Fract. Mech.*, Vol. 7, pp. 317-330.
11. Okajima, M. (1985), "Analysis of Tensile Testing Configurations for Assessing the Strength of Butt Joints," Ph.D. thesis, Department of Mechanical Engineering, Carnegie Mellon University.

## THERMAL MODELLING AND EXPERIMENTAL TESTING OF MD\* SPRAY SHAPE DEPOSITION PROCESSES

C.H. Amon, R. Merz, F.B. Prinz and K.S. Schmaltz  
Department of Mechanical Engineering and  
Engineering Design Research Center  
Carnegie Mellon University

### ABSTRACT

MD\* is a thermal spray manufacturing process to rapidly form near net-shape objects. Optimizing the properties of objects manufactured by this process requires the understanding of the thermal history of the deposited material, particularly the occurrence of substrate remelting and substrate cooling rates. A mixed Lagrangian-Eulerian model accounting for remelting has been developed to investigate the effect of operating conditions such as droplet or substrate temperatures and droplet size on the remelting phenomenon and cooling rates experienced. Experiments are performed for molten carbon steel droplets impinging on a similar substrate to acquire input data for the model and results for comparison with numerical simulations.

### INTRODUCTION

Originally, thermal spray techniques applied thin films to provide corrosion resistance or improve thermal properties through the film material. The thermal spray process also offers a novel manufacturing technique with advantages over more conventional forming methods (i.e., casting and machining) by its ability to rapidly free-form near net-shape structures. A spray based process described by Weiss *et al* (1992) developed at Carnegie Mellon is known as MD\*. This process builds up an object (monolith) by spraying successive layers of material, maintaining the monolith's shape by machining each layer. The process permits the manufacture of complex geometric structures, selection of varied materials for composite and laminate structures difficult or impossible to create using traditional methods, rapid prototyping from a computer-aided environment, and integration of electronic components and sprayed interconnecting wiring within the mechanical assemblies. Spray manufacturing has been selected for a specific project, the Navigator, underway at Carnegie Mellon, involving the manufacture of a wearable computer, requiring flexibility in packaging electronics and providing necessary configurations for heat removal.

The thermal spray process modelled numerically and verified experimentally in this paper is a proprietary microcasting process capable of providing individual, millimeter-sized droplets free falling to the substrate surface at a rate of several droplets per second. This process differs considerably from the traditional wire arc or plasma spray methods, where the deposition material is melted (either by a

current arcing or plasma) and gas propelled to the substrate, generating a fine, high velocity mist of 100  $\mu\text{m}$  droplets, in a near Gaussian spray distribution about the nozzle centerline. Droplet melting temperatures are comparable for all of the processes, but the microcasting droplets have a greater impact temperature. With a greater droplet volume-to-surface ratio, microcasting droplet heat transfer to the atmosphere before impact is less complete and impinging droplet temperatures can have several hundred degrees of superheating; plasma and wire arc droplets are cooled during droplet flight to near melting conditions. Of the three processes, microcasting only generates liquid droplet temperatures significantly above the melting point at impact.

Superheat is crucial to improve bonding of successive layers. Proper bonding can be achieved via a mechanical interlocking of the layers; however, improved bonding results when the superheated droplets partially remelt the solid substrate. Ensuing material properties, both thermal and electrical as well as mechanical, are strongly affected by the bonding conditions, necessitating the ability to predict this remelting. The cooling rate also affects resulting properties and can dictate aspects of design configuration such as the Navigator's operating cooling system.

Predicting melting conditions and cooling rates through numerical modelling offers the opportunity to improve the spray process. Resultant properties depend on both the characteristics of the impinging droplets and the cooling rates experienced during manufacturing, making the control of spray application parameters crucial to the mechanical and thermal properties of the structures fabricated. The material properties created in a thermal spray system are improved if remelting conditions exist, though the remelting extent must remain slight to maintain dimensional integrity. Accurate temperature modelling is important for other manufacturing considerations, including protection of supporting structures having lower melting temperatures than the sprayed material, control of application temperatures to protect embedded electronics, and control of thermal stress induced warping or delaminating by successive depositions as detailed by Amon, Beuth *et al* (1993).

While spraying the Navigator's electronic wiring within the monolith, a balance is needed between keeping fabrication temperatures below any manufacturing limits and improving the quality of the bonding between successive layers when the impinging liquid droplets have sufficient energy to slightly remelt the previously deposited layer. Deposited material properties (both mechanical and thermal) vary depending on

application parameters. Beyond remelting, the cooling rate of the deposited material also affects microstructure and, thereby, material properties. These properties can differ significantly from non-sprayed values for the same material. Modelling of temperatures that result from different application techniques allows a prediction of material properties. With better knowledge of the anticipated properties, modifications to the spray process and the system configuration can be proposed to maintain optimal operating temperatures for the device.

Therefore, the primary motivations for modelling the melting/solidification phenomena are to predict conditions producing bonding through substrate remelting, and aid in the selection of process parameters to protect electronics and yield desirable material properties. Additionally, modelling creates an accurate predictive tool of the thermal spray process and can be used to investigate the effect of operating conditions such as initial droplet and substrate temperatures, droplet size and surface heat transfer on the resulting melting front migration rate, thickness of remelting, temperature distribution and overall cooling rate of both the droplet and the substrate. The properties of the sprayed materials also influence these factors. With this knowledge, operating parameters such as spray power input and gas velocities, nozzle-substrate distance and deposition rates may be optimized.

This very complex process involves many thermal properties of the materials such as conductivity and specific heat, phase change energy release, as well as application temperatures and physical conditions such as droplet velocities that are based on application feedrates and power selections. While typical non-dimensional heat transfer parameters such as Fourier and Biot numbers have been used for result comparison, from a manufacturing viewpoint the ability to modify these factors is realistically restricted to droplet size and temperature. Therefore this study focuses on investigations of remelting with regard to the parameters that can be altered during manufacturing, expressing the data in a format most closely related to actual spray application.

Existing models include the classical Stefan melting front problem with two semi-infinite surfaces (solid and liquid phases) in contact, the contact surface at melting temperature and interface heat flux balanced by latent heat release. Crank (1984) presents analytical solutions to this problem, which are used to estimate initial interface conditions for the proposed model. Most literature on the location and movement of a solidification front considers traditional casting processes, where liquids are deposited in a mold and slowly cooled, unlike the rapid cooling of thermal spraying. Thermal models have been developed for the plasma spraying process. Pawlowski (1981) uses an analytical approach to solve the one-dimensional heat transfer problem, using simplifying assumptions regarding the deposit layer interface heat transfer and linear temperature profiles across the deposition layer. Pawlowski *et al* (1982) then use a finite difference solution to the same problem, including effects such as contact resistance. Both treat the latent heat released during solidification as a heat input source term and do not calculate the melting front location. El-Kaddah *et al* (1984) use Stefan results in a temperature based model to derive a one-dimensional analytical solution to the plasma spray process, and then extend the solution to reflect the two-dimensional profile of the spray front using a finite difference technique. Bewlay and Cantor (1991) use a similar numerical formulation, incorporating contact resistance across the substrate boundary and Stefan solution profiles in the formulation for an electric

spray process. Mathur *et al* (1991) model the Osprey continuous casting process, where a gravity fed stream of previously molten metal is atomized by inert gas in a rapid solidification deposition process. An enthalpy energy balance is used, rather than temperature, to handle the sharp variation of enthalpy that exists at the phase change.

For fluid dynamic aspects, Madejski (1976 and 1983) uses the Stefan freezing solution with total energy assumptions (kinetic, friction and surface tension terms) to derive an analytical prediction for the final height of a molten droplet "splat". Trapaga and Szekely (1991) expand Madejski's work by modelling the fluid dynamic effect and relating the splat size and spreading time to the spraying conditions. Trapaga *et al* (1992) include heat transfer considerations for the droplet solidification, although the substrate heat transfer is modelled using constant heat transfer coefficient and does not consider substrate remelting. Trapaga's conclusion, that the spreading process takes place in significantly less time than the solidification process, is used for the proposed model.

The MD<sup>+</sup> microcasting process, involving individual liquid droplets hitting and possibly remelting a substrate before solidifying, is not represented by the models described above. Solidification models do not address the physical process of superheating, rapid deposition and solidification that defines the MD<sup>+</sup> spray process, while temperature models for spray processes do not determine the actual location of the melting front either within the deposition layer or into the substrate if initial remelting occurs.

## PROPOSED NUMERICAL MODEL

The formulation of a model of the MD<sup>+</sup> spray process presented in this paper, which focuses on determining thermal spray process temperatures and remelting conditions, is uncoupled from the fluid dynamics and simplified to a heat transfer problem by making the assumption that an individual droplet strikes the solid surface and flattens much more rapidly than the time required for the droplet to solidify. Therefore, the dynamic effects of the flattening process are considered a precursor to the thermal process. When the times for both processes are of the same order of magnitude, this simplification will not be valid. Because of the discrete nature of the microcasting deposition process, a one-droplet model is used. An assumption that the impacted droplet width is sufficiently greater than its height simplifies the model to a one-dimensional differential equation of the form:

$$\rho c_p \frac{\partial T}{\partial t} = \lambda(T) \left[ \frac{\partial^2 T}{\partial x^2} \right] + \frac{\partial \lambda}{\partial T} \left[ \frac{\partial T}{\partial x} \right]^2 \quad (1)$$

Although temperature-dependent thermal properties are used for the materials and temperature ranges considered, the thermal conductivity ( $\lambda$ ) temperature dependence is slight and the  $\partial \lambda / \partial T$  term is omitted. Equation 1 is valid for both the liquid as well as the solid region. At the top surface of the liquid region, combined convective and radiative boundary conditions are imposed, while the energy balance:

$$\rho L \frac{\partial x}{\partial t} = \lambda_{sol} \frac{\partial T}{\partial x} - \lambda_{liq} \frac{\partial T}{\partial x} \quad (2)$$

with density  $\rho$  and latent heat  $L$ , is applied at the interface between the liquid and solid regions, balancing the energy flux into/out of the interface with latent heat release. For the lower

solid region boundary, constant temperature is maintained at a remote distance from the surface. The initial assumption of a one-dimensional problem may be inaccurate for the geometry of the actual manufacturing process and shape of individual droplets. Also depending on the orders of magnitude of the impaction and cooling process times, modelling that incorporates multi-dimensional effects, together with the dynamic effects of the droplet impaction, may be required.

Equation 1 is discretized using an Eulerian explicit formulation. The explicit form of the finite difference formulation is used for its simplicity, despite the necessity of meeting stability criteria. The remelting aspect of the spray process is sufficiently rapid that the small time steps imposed for stability do not present a significant calculation burden.

To track the location of the melting front during the solidification process, a three-point Lagrange interpolation formula, described by Crank (1984), is used to approximate the temperature function. This assumes a form that can be readily incorporated into the finite difference formulation, but permits the location of a varying mesh point corresponding to the melting front. The Lagrange formulation of the finite difference equation is used for temperature calculations with nodes preceding and following the melting point, detailed in Amon, Prinz *et al* (1993). For the preceding node in the liquid region, the discretization is:

$$\frac{\partial^2 T}{\partial x^2} = \left[ \frac{T_{\text{melt}}}{p(p+1)} - \frac{T(j)}{p} + p \frac{T(j+1)}{(p+1)} \right] \quad (3)$$

The melting parameter,  $p$ , represents the melting front location between the fixed mesh points, and is recalculated after each iteration using a discretized form of Equation 2. For the initial interface temperature, when the droplet first strikes the solid substrate (both liquid and substrate temperatures are known), the analytical Stefan interface solution is used to approximate the temperature as follows:

$$T_{\text{inter}} = [\text{RATIO} \cdot T_{\text{liq}} + T_{\text{sol}}] / [1 + \text{RATIO}] \quad (4)$$

$$\text{RATIO} = \sqrt{(\lambda c_p \rho)_{\text{liq}} / (\lambda c_p \rho)_{\text{sol}}} \quad (5)$$

Initial conditions in the first model correspond to uniform droplet and ambient substrate temperatures, however, during the actual process, prior droplets strike and preheat the substrate as the spray gun moves across the substrate. To include this effect, the initial substrate temperature profile is modified to incorporate the two-dimensional effects of substrate preheating arising from the diffusion of energy from previously deposited droplets.

$$\rho c_p \frac{\partial T}{\partial t} = \lambda(T) \left[ \frac{\partial^2 T}{\partial x^2} + \frac{\partial^2 T}{\partial y^2} \right] \quad (6)$$

As with the one-dimensional solidification model, an Eulerian explicit algorithm is used to solve Equation 6. The transient substrate temperature profile from the prior model is used as one fixed temperature boundary condition, while convection to ambient conditions is used for the remaining three boundaries. A resulting vertical temperature profile from this model at an appropriate time and horizontal distance becomes the solidification model substrate initial condition.

## EXPERIMENTAL TESTS

The microcasting process testing uses 1.5% manganese, low carbon steel droplets and similar substrates to verify actual impacting droplet conditions, provide input for the numerical model, and compare model predictions and experimental results for temperatures and remelting. Three experiments are performed: i) calorimetry determines average droplet impact temperatures over a range of spray process parameters; ii) thermocouples measure droplet and substrate temperatures to measure cooling rates for two spray conditions; and iii) metallographic examinations of previous test samples ascertain remelting depth and steel microstructure.

Calorimetry measures 25 to 100 droplets over a wide range of steel feedrates and power settings, and an average droplet impact temperature is calculated for each spray parameter setting. Adjustments compensate for the water bath temperature rise due to microcasting power source radiation, latent heat of fusion released by the solidifying steel droplets and latent heat of vaporization of a small amount of water boiled away by impacting steel droplets. Temperature dependent carbon steel and water specific heats are used. Figure 1 shows the calorimetry results, each curve represents a group of tests with a constant steel feedrate and varied power. An additional test performed for one feedrate and power setting varied the droplet height. Increasing the distance that the droplets fall from 11 cm (the height used for all of the above results) to 19 cm, decreases the average droplet impact temperature by 300 K. As before, manufacturability considerations constrain the useful range of droplet elevation.

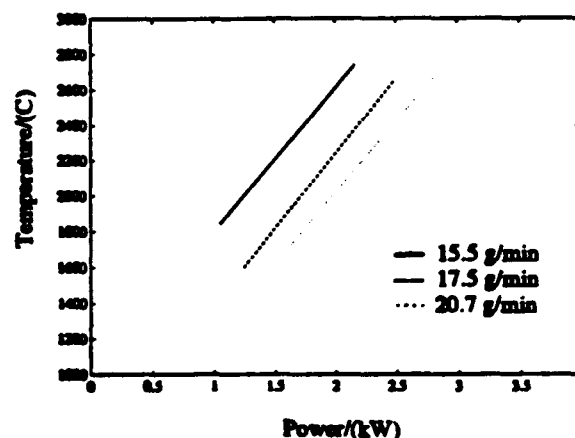


Figure 1. Calorimetry Results—Varied Application Parameters

Uncertainties on the order of 100 K arise from the measurement of the temperatures, weights and actual amount of water vaporized. Rather than considering specific temperature values, the tests indicate that it is possible to alter the impacting temperature by 800 K over the range of parameters explored. However, the entire ranges are not available for material deposition due to operational limitations.

Thermocouple measurements determine individual droplet temperatures and substrate heating. A hole is drilled through the substrate plate and a type C thermocouple (Tungsten with 5% Rhenium/Tungsten with 26% Rhenium) is inserted to the surface (left side of Figure 2) and insulated from the plate with a ceramic spacer. An individual steel

droplet is dripped onto the thermocouple to measure its impact temperature as well as the droplet cooling rate. The thermocouple time constant is approximately 0.05 seconds. The droplets are applied using two feedrate and power settings. The average thermocouple readings is consistently lower than the calorimetry results by a range of 5.6 - 8.6%, which is counter intuitive since most errors associated with calorimetry tend to underestimate droplet temperatures. This can be reconciled by considering the measured droplet temperature decay curve (Figure 5), with an estimated time constant of about one second. Measuring this temperature with a thermocouple having a 0.05 second time constant results in an underestimation of the peak temperature of the rapidly cooling droplet by approximately 10-15%. Above calorimetry uncertainties and temperature fluctuations from test to test also contribute to the difference.

Substrate measurements (right side of Figure 2) are performed by drilling the substrate plate nearly to the surface and measuring the temperature of the steel plate directly below the location where a droplet impacts, using a type K thermocouple (Nickel with 5% Aluminum/Silicon with 10% Chromium). One to four mm spacing depths between the thermocouple and the surface are used to measure the substrate temperature at different depths. Measurements are also collected at a lateral width distance of 6.35 mm from the droplet impact, using the same substrate depths. Insulation is again maintained with ceramic spacers, the thermocouple time constant is approximately 0.003 seconds.

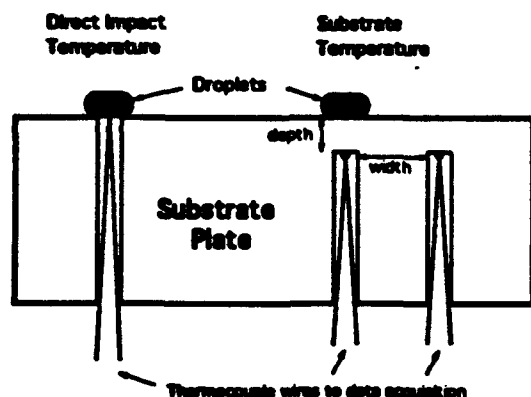


Figure 2. Thermocouple Experiments Setup

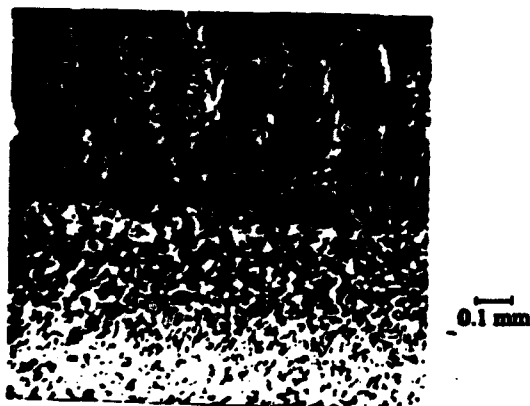


Figure 3. Metallographic Examination (50X Magnification)

Determination of actual substrate remelting, which occurs in about  $10^{-3}$  seconds, is verified by metallographic examination of the sample plates used for the substrate temperatures experiments. This allows the correlation of observed remelting with measured temperatures. The exposed surface is ground and polished to a mirror finish and etched with a nitric acid solution. At 50X magnification, the extent of remelting is measured for each droplet, while greater magnification is used to determine the steel microstructure. Figure 3 shows the martensite microstructure of the droplet, indicative of the rapid cooling. The plate has a ferrite-pearlite structure at a distance from any remelting, shifting from a coarse to a finer structure as the droplet is neared. Where remelting has occurred, martensite, lower bainite, and carbide inclusions appear. For all of the samples measured, the depth of remelting is approximately in the range of 0.1 to 0.2 mm, increasing as the impacting droplet size increases. Cooling rate estimates can also be made from the microstructure examination using carbon steel cooling transformation diagrams. Based on the martensitic structure, the droplet cools from a molten state to below 800 K in less than 2 seconds. The remelting zone resolidifies and cools below 600 K in less than 5 seconds to attain its microstructure.

## NUMERICAL RESULTS

One- and two-dimensional models represent a preliminary attempt to gain insight into the determination of remelting likelihood and sensitivity of remelting to droplet and substrate conditions, as well as the prediction of droplet and surface temperatures and cooling rates. Numerical simulations are performed for models with carbon steel, stainless steel and zinc landing on similar substrates. The primary focus of these simulations is to examine the effect that the droplet temperature and size and substrate temperature have on the remelting phenomenon. For each material, initial conditions are varied in an attempt to achieve partial substrate remelting. Numerical results indicate that conditions permitting substrate remelting do not occur unless droplet impact temperatures approach material vaporization temperature when landing on an unheated substrate, or are superheated several hundred degrees with a substrate preheated above ambient temperature.

Investigating the effect of the impinging droplet temperature, Figure 4 shows the numerical results of melting front migration versus time for a 2 mm carbon steel "droplet" landing on a carbon steel substrate initially at ambient conditions. The positive vertical axis represents the droplet region, the negative portion the substrate. Remelting is only achieved when the droplet temperature reaches 2500°C. Similar results are found for substrate temperature effects. For both cases, the rapid, initial front migration for the lower substrate temperatures is a reflection of the quenching due to the cold substrate. The migration rate slows when the substrate has been heated by the droplet.

The cooling rate, which is important for the deposit material microstructure as well as for residual thermal stress considerations, can also be calculated from the numerical simulations. For carbon steel, the droplet temperature exhibits the greatest rate of cooling, approximately 5000 K/s at the beginning, less than 1000 K/s by 0.5 seconds and significantly less by one second. For the interface, initially at a Stefan calculated temperature, the initial cooling rate is on the order of 1500 K/s and is 500 K/s after 0.5 seconds.

Numerical simulations are performed impinging steel droplets on a zinc substrate model the process involving sacrificial support substrates. Results show that the lower melting point zinc melts to a significant depth and actually vaporizes slightly at the steel/zinc interface during this process, indicating the need to thermally protect support substrate materials having lower melting temperatures.

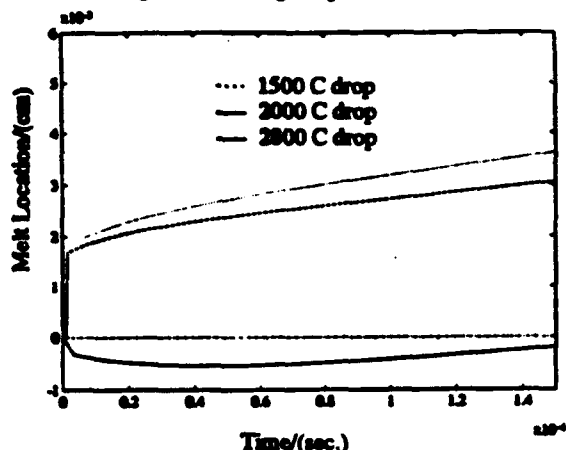


Figure 4. Melting Front Migration vs. Time

Model-related spatial and temporal resolution, as well as boundary conditions, are investigated. Discretization of the mesh spanning the liquid (droplet) and solid (substrate) regions is varied to achieve convergent solutions, avoid excessive computation time, ensure lower boundary condition validity, and maintain accuracy. Theoretical numerical stability for the Eulerian formulation imposes a maximum time step of  $3 \times 10^{-7}$  seconds for the typical node spacing distance; however, the solution only converges for a step size smaller than  $5 \times 10^{-9}$ . This additional time step refinement is probably influenced by the added approximation introduced by the Lagrange temperature interpolation. A sensitivity analysis of the surface convection and radiation effects influencing remelting is performed. The surface heat transfer coefficient is calculated using a correlation for impinging gas forced convection, while radiation is considered as a constant input from the power source. Both of these effects are found to be insignificant compared to the conduction of heat into the substrate. This implies that the substrate melting and resolidification process is completed so rapidly (on the order of  $10^{-3}$  seconds) that the heat transfer is dominated by conduction, and the surface convective and radiative effects are negligible.

#### NUMERICAL/ EXPERIMENTAL COMPARISON

Results from the thermocouple experiments previously discussed and the numerical model are combined for comparison. Using direct impact measurements of droplet temperature as the initial condition for the model liquid region, initial measured substrate temperature for the solid region, and direct measurement of the droplet "splat" height after cooling for model dimensions, numerical simulations are performed that reflect the actual conditions experienced during the carbon steel microcasting process. Thermocouple values also provide cooling rates to compare with numerical simulations, in addition to peak temperature measurements.

Comparing numerically simulated droplet cooling rates with measured values, Figure 5 shows that the cooling predicted by the model is initially comparable to the experimental results; however, the simulated results later in the process reflect a smaller cooling rate than those values seen for the experiments. Results for the first 0.6 seconds differ by less than 3%; by 1.2 seconds, the difference between measured and numerical is about 30%. This divergence begins at  $1400^{\circ}\text{C}$  where the droplet has approximately solidified. The model uses temperature dependent thermal properties taken from measurements of traditionally formed steel, this discrepancy suggests that thermal properties produced by this rapidly cooled droplet may vary from the tabulated values. For the entire simulation, a cooling rate underprediction is expected because the model only considers one-dimensional cooling, while in the actual process, with a single droplet on a large substrate, multi-dimensional cooling takes place.

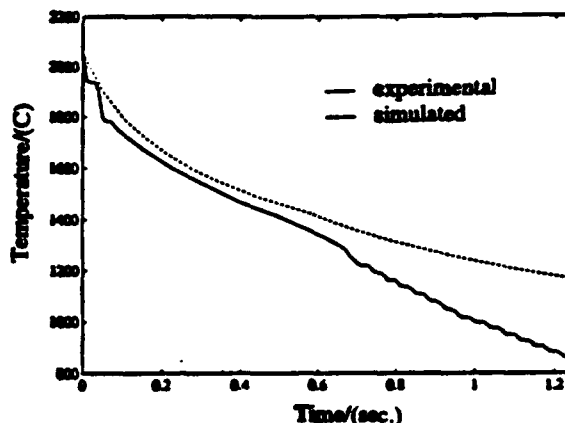


Figure 5. Experimental vs. Simulated - Drop Temperatures

For the measurement of substrate temperature at a depth of 1.27 mm, Figure 6 shows the comparison between the numerical and experimental values. The experimental plot begins at a  $100^{\circ}\text{C}$  substrate temperature as a result of an initial droplet striking (and preheating) the surface before a second droplet lands on the heated substrate above the thermocouple, causes remelting and bonds. The numerical simulation approximates a preheated substrate to match the substrate temperature initial condition for the model of the second droplet. The initial heating rates are comparable, although the numerical results slightly underestimate the peak temperature and then exhibit a slower rate of cooling than the experiment results. Similar results are obtained for the deeper substrate measurements. In order to obtain a comparable temperature history curve, it is necessary to use a model liquid thickness of 0.2 mm, compared to the actual measured "splat" thickness of 2.0 mm. Making this reduction simulates a comparable droplet volume to be considered for the comparison because the actual droplet has a finite width, while the model width does not. Using the actual measured thickness for the model yields a significant simulation overshoot of the peak temperature.

Actual remelting depths measured by metallography of the samples compare poorly with the depths predicted by the model. Although it is difficult to determine the exact depth by microstructure inspection over the transformation from the unmelted ferrite-pearlite plate to the martensite droplet above the substrate, a remelting zone of 0.1 mm seems to exist. The model predicts a remelting depth an order of magnitude

smaller. A primary cause is that the peak initial droplet temperatures are underestimated by the thermocouple measurements, and these lower values are used for the simulations. Convective effects within the liquid region will also increase the energy at the interface for remelting. It is also possible that the uncertainties regarding the actual initial substrate temperature contribute to this difference.

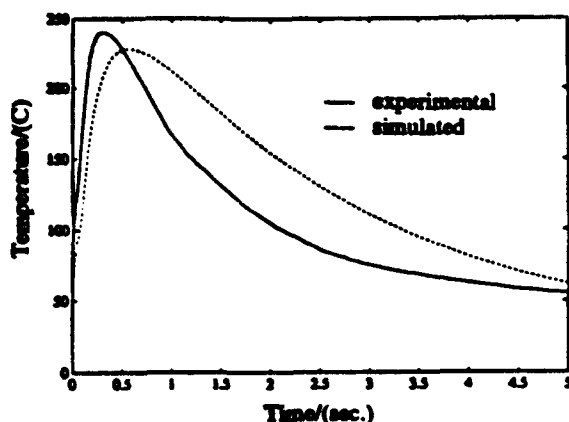


Figure 6. Experimental vs. Simulated - Substrate Temperatures

## CONCLUSION

Experimental measurements of the MD<sup>+</sup> thermal spray microcasting process provide the preliminary information needed to quantify this process as well as understand the effect that the application parameters have on droplet temperature. These experimental results are also used as initial conditions for, and comparison of, one- and two-dimensional numerical simulations. Simplifying the process into a one-dimensional format to examine the remelting phenomenon and cooling rates provides not only useful information regarding the initial stages of solidification, and a qualitative understanding of the microcasting process, but additionally facilitates the model formulation and computational effort. However, it is only modestly accurate in matching the experimental data for carbon steel tests over an extended time.

Numerical simulations, performed for carbon steel, stainless steel and zinc droplets with similar substrates, indicate that substrate remelting can only be achieved when droplet impact temperatures either approach the material vaporization temperature for the case of an unheated substrate, or are several hundred degrees above the melting point for a preheated substrate. Calorimetry results show that for MD<sup>+</sup> microcasting, unlike more traditional methods, it is possible to generate impacting droplets that have significant superheat and a wide range of impact temperatures based on operating parameters. This results in the substrate remelting predicted numerically and verified by metallographic examination.

Although the model does correctly predict remelting, results from both the direct impact and substrate thermocouple temperature measurements, particularly the substrate, indicate that the simplifying assumptions made for the model do affect the accuracy of the results. In particular, the geometry of the process renders a one-dimensional model inaccurate, since the droplets exhibit a cooling rate faster than a one-dimensional model predicts. The inclusion of fluid dynamics in future models is needed to improve the accuracy of the model predictions and to examine whether uncoupling the fluid

dynamic and thermal processes is valid for the droplets typifying the MD<sup>+</sup> microcasting process.

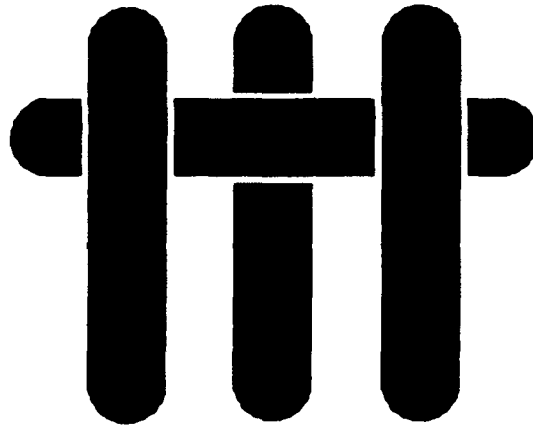
## ACKNOWLEDGMENTS

Financial support by the Advanced Research Project Agency Grant JFBI92195, Office of Naval Research Grant N00014-94-1-0183, and University Research Initiative at the University of California at Santa Barbara Grant N00014-92-J-1808, is gratefully acknowledged.

## REFERENCES

- Amon, C.H., Beuth, J., Kirchner, H., Merz, R., Prinz, F.B., Schmaltz, K.S., and Weiss, L.E. 1993, Material Issues in Layered Forming, Proc. Solid Freeforming Fabrication Symposium, Austin, pp. 1-10.
- Amon, C.H., Prinz, F.B., and Schmaltz, K.S. 1993, Numerical Modelling of Thermal Spray Systems, Technical Report EDRC 24106-93, Carnegie Mellon University, Pittsburgh, PA.
- Bewlay, B.P., and Cantor, B. 1991, The Relationship Between Thermal History and Microstructure in Spray-Deposited Tin-Lead Alloys, *J. of Mat. Res.*, vol. 6, no. 7, pp. 1433-1454.
- Crank, J. 1984, *Free and Moving Boundary Problems*, pp. 1-29, Oxford Press, New York.
- El-Kaddah, N., McKelliget, J., and Szekely, J. 1984, Heat Transfer and Fluid Flow in Plasma Spraying, *Metall. Trans. B*, 15B, pp. 59-70.
- Madejski, J. 1976, Solidification of Droplets on a Cold Surface, *Int. J. Heat Mass Transfer*, vol. 19, pp. 1009-1013.
- Madejski, J. 1983, Droplets on Impact with a Solid Surface, *Int. J. Heat Mass Transfer*, vol. 26, no. 7, pp. 1098-1102.
- Mathur, P., Apelian, D., and Lawley, A. 1989, Analysis of the Spray Deposition Process, *Acta Metallica*, vol. 37, no. 2, pp. 429-443.
- Pawlowski, L. 1981, Temperature Distribution in Plasma-Sprayed Coatings, *Thin Solid Films*, vol. 81, pp. 79-88.
- Pawlowski, L., Vardelle, M., and Fauchais, P. 1982, A Model of the Temperature Distribution in an Alumina Coating During Plasma-Spray, *Thin Solid Films*, vol. 94, pp. 307-319.
- Trapaga, G., and Szekely, J. 1991, Mathematical Modelling of the Isothermal Impingement of Liquid Droplets in Spraying Processes, *Metall. Trans. B*, 22B, pp. 901-914.
- Trapaga, G., Matthys, E.F., Valencia, J.J., and Szekely, J. 1992, Fluid Flow, Heat Transfer and Solidification of Molten Droplets Impinging on Substrates: Comparison of Numerical and Experimental Results, *Metall. Trans. B*, 23B, pp. 701-718.
- Weiss, L.E., Prinz, F.B., Adams, D.A., and Siewiorek, D.P. 1992, Thermal Spray Shape Deposition, *J. Thermal Spray Technology*, vol. 1(3), pp. 231-237.

M A T E R I A L S



**Liquid Precursor Infiltration and Pyrolysis of Powder  
Compacts, I: Kinetic Studies and Microstructure  
Development**

**W. C. Tu and F. F. Lange**

**Materials Department  
College of Engineering  
University of California, Santa Barbara  
Santa Barbara, CA 93106**



# **Liquid Precursor Infiltration and Pyrolysis of Powder Compacts, I: Kinetic Studies and Microstructure Development**

W. C. Tu and F. F. Lange  
Materials Department  
College of Engineering  
University of California, Santa Barbara  
Santa Barbara, CA 93106

## **ABSTRACT**

The kinetics of infiltration of a solution precursor into  $S_3N_4$  powder compacts was studied using either water or an aqueous solution of Zr-nitrate and Y-nitrate that forms a crystalline  $Zr(Y)O_2$  (3mol%  $Y_2O_3$ ) solid-solution during pyrolysis. When the powder compact contained air, the infiltration involves two steps: 1) relatively rapid intrusion of liquid via flow due to capillary pressure and 2) diffusion of entrapped gas to the surface as its pressure becomes equal to the capillary pressure. The kinetics of both processes are described with different parabolic rate laws, Darcy's Law and Fick's Law, respectively. When the intruded precursor is converted to an inorganic during heat treatment, the void space is partially filled with pyrolyzed precursor without shrinkage of the  $S_3N_4$  powder. The kinetics of subsequent cycles depends on the permeability of the pyrolyzed precursor, which depends on its microstructural development during heat treatment subsequent to pyrolysis. Surface cracks can form within the powder compact during either precursor drying or pyrolysis; they can be avoided by strengthening the powder compact by forming small necks between touching particles via evaporation-condensation. Precursor molecules were found to concentrate near the surface as the precursor solvent was removed by drying. The movement of precursor molecules were prevented by gelling the precursor prior to drying, viz., by soaking the infiltrated bodies in an aqueous  $NH_4OH$  solution. Microstructures developed during cyclic precursor infiltration and pyrolysis were characterized to show that crack-like voids are produced within the pyrolyzed precursor due to its large volume change during pyrolysis and densification; the size distribution of the crack-like voids is proportional to the size distribution of the voids within the initial powder compact.

## 1. INTRODUCTION

Liquid precursor infiltration and pyrolysis can be useful for processing ceramics and their composites. As demonstrated by others, [1-7] either the same phase as the powder or a different phase can be formed within a porous ceramic preform by infiltration with a pyrolyzable liquid precursor. A variety of unique microstructures (graded, multi-phase, partially porous to fully dense, etc.) with unique thermo-mechanical properties (designed residual stresses, graded elastic properties, etc.) can be envisaged when processing is performed by infiltration. In addition, the precursor can be used to both increase the relative density and strengthen the powder compact without shrinkage. [8] The lack of powder shrinkage during strengthening is an advantage in forming ceramic composites where conventional strengthening via densification is constrained and leads to the formation of crack-like voids. [9] For other applications, complete densification could be accomplished after multiple infiltration-pyrolysis processing steps.

Although several different materials have been produced and characterized by the precursor infiltration method, [1-6] the infiltration process has not been adequately characterized. Soil researchers, who have great interest in intrusion and flow of liquids through granular beds, [10, 11] report that the infiltration of a dry, porous media containing gas (e.g. air) occurs by two different mechanisms. First, capillary pressure,  $P_c$  (plus any applied pressure,  $P_a$ ) will cause a wetting liquid to flow into the granular media until the opposing internal pressure of the compressed gas,  $P_i$ , becomes equal to the capillary pressure. Second, gas can diffuse through the liquid from the high pressure, entrapped gas to the ambient at the surface; gas diffusion is driven by its greater solubility at higher pressures.

In the first mechanism, the flow of liquid into a porous media by capillary pressure is described by Darcy's law [12,13]

$$h = \left[ \frac{2KP}{\eta} \right]^{1/2} t^{1/2}, \quad (1)$$

where  $h$  is the distance of liquid intruded within a period  $t$ ,  $K$  is the permeability of the porous body,  $\eta$  is the viscosity of liquid, and  $P = P_c + P_a - P_i$ . The capillary (Laplace) pressure is given by:

$$P_c = \gamma \frac{\partial S}{\partial V} = \frac{2\gamma \cos \theta}{r_e} = \frac{6\gamma \cos \theta \rho}{D(1-\rho)}, \quad (2)$$

where the first equality is the general form of Laplace's equation where,  $\gamma$  is the surface energy per unit area of the liquid.  $\frac{\partial S}{\partial V}$  is the change in wetted solid surface area of the porous compact per change in volume of intruded liquid. When the porosity in the porous compact is replaced by equivalent capillaries of radius,  $r_e$ ,  $\frac{\partial S}{\partial V} = \frac{2 \cos \theta}{r_e}$ , where  $\theta$  is the wetting angle. It can be shown [13,14] that when the powder compact is composed of identical spheres (diameter,  $D$ ) packed with a relative density,  $\rho$ ,  $\frac{\partial S}{\partial V} = \frac{6 \rho}{D(1-\rho)}$ . The expression for gas diffusion (and thus concurrent displacement of gas by the liquid) is given by Fick's law [15,16]

$$h = (2D_g \beta P_i)^{1/2} t^{1/2}, \quad (3)$$

where  $h$  is distance of liquid intrusion within a period of  $t$ ,  $D_g$  is the diffusion coefficient of the gas within the liquid,  $\beta$  is Henry's constant and  $P_i$  is the pressure of the entrapped gas. Although both phenomena are concurrent, the flow of liquid due to capillary pressure initially dominates, whereas once the gas within the compact is sufficiently compressed, gas diffusion dominates.

The purpose of the current work is to determine the infiltration kinetics of powder compacts formed with a well characterized  $\text{Si}_3\text{N}_4$  powder infiltrated with either water or an aqueous mixture of Zr-nitrate plus Y-nitrate that pyrolyzes to a  $\text{Zr(Y)O}_2$  solid-solution (3 mole %  $\text{Y}_2\text{O}_3$ ).  $\text{Zr(Y)O}_2$  was chosen because of the much higher atomic number of Zr ( $Z = 40$ ), relative to Si ( $Z = 14$ ), so that the distribution and microstructure of the intruded and pyrolyzed  $\text{Zr(Y)O}_2$  could be easily observed with the scanning electron microscope (SEM). Because preliminary studies showed that powder compacts intruded with the  $\text{Zr(Y)O}_2$  cracked during drying, subsequent powder compacts were first strengthened by forming small necks between touching particles via sintering without shrinkage (via evaporation-condensation). The cracking phenomenon will be detailed elsewhere. [8]

## 2. EXPERIMENTAL

Si<sub>3</sub>N<sub>4</sub> powder compacts (25 mm dia. by 6 mm) were prepared by a previously described pressure filtration technique (5 MPa). [17] To obtain uniform powder compacts, large agglomerates in the as received powder<sup>a</sup> were removed by sedimentation [18] to retain particles ≤ 1 μm. After sedimentation, the average particle size was determined <sup>b</sup> to be 0.8 μm. Bodies with two different relative densities were consolidated by pressure filtering dispersed and flocced aqueous slurries containing 0.20 volume fraction of Si<sub>3</sub>N<sub>4</sub> powder. A dispersed Si<sub>3</sub>N<sub>4</sub> slurry was prepared at pH 10 with additions of NH<sub>4</sub>OH and ultrasonicing <sup>c</sup> the sedimented slurry for ≈ 2 minutes. The flocced slurry was prepared by decreasing the pH of the dispersed slurry from 10 to 6 with additions of HNO<sub>3</sub>. After consolidation, the packing density of the bodies were calculated by determining the volume of water lost during drying by weight measurements before and after drying.

During initial experiments, surface cracks were observed after infiltration and precursor drying. For comparison, no cracks were ever observed when powder compacts were infiltrated with deionized water and dried under identical conditions. As described elsewhere, [8] the reason for this cracking phenomenon is now known to be caused by cracking of a thin film of the precursor material on the surface of the powder compact during drying, and the extension of these cracks into the powder compact.

The cracking phenomenon associated with precursor drying was avoided in the current work by increasing the fracture toughness of the consolidated bodies by first forming sintered necks between touching particles prior to any precursor infiltration. This was accomplished by one of two methods. In the first method, neck formation was accomplished through the evaporation-condensation reaction



The schedule that was found to optimize the strength and prevent the cracking of the powder compact was 1000°C/10 h in air followed by 1300°C/10 h in N<sub>2</sub>. In the second method, a small fraction of Si particles <sup>d</sup> (1 to 5 v/o) was incorporated within the powder compact and nitrided at 1300°C to cause Si<sub>3</sub>N<sub>4</sub> to form in the vapor state to condense at contacting particle positions. Since holes were left where Si particles

---

<sup>a</sup> SN-E3, Ube Industries, New York, NY

<sup>b</sup> 5000ET, Micromeritics, Norcross, GA

<sup>c</sup> Model W-380, Heat Systems Ultrasonics, INC., Farmingdale, NY

<sup>d</sup> 4E, KemaNord Inc., Sweden

existed prior to reaction as shown in Fig. 1, this method was abandoned in favor of the first method due to the obvious introduction on an unwanted flaw population.

The liquid precursor used in this study was a mixture of aqueous Zr-nitrate <sup>e</sup> and yttrium nitrate <sup>f</sup> solutions. Prior to infiltration, the solution was concentrated by evaporation to increase its equivalent ZrO<sub>2</sub> concentration from its initial 19 wt % to 35 wt %. The thermal decomposition behavior of the solution precursor was examined by thermogravimetric analysis (TGA)<sup>g</sup> at a heating rate of 5 °C/min in a N<sub>2</sub> atmosphere (the infiltrated and dried precursor was also pyrolyzed in a N<sub>2</sub> atmosphere). TGA data were similar to those reported by Balmer et. al, [19] viz., weight loss is completed before 500°C. The viscosity <sup>h</sup> of the precursor was strain rate insensitive and 1 poise within the shear rate range of 10 s<sup>-1</sup> and 10<sup>3</sup> s<sup>-1</sup>. Its density was determined with a pycnometer to be 1.6 g/cc. In some experiments, the infiltration kinetics were examined by infiltrating powder compacts with de-ionized water (14MW) at pH = 6.8.

Infiltration kinetics without an applied pressure (P<sub>a</sub> = 0) were determined by directly monitoring the weight change of the immersed powder compact (≈ 6 g) suspended with a wire from an electronic balance (± 0.0001 g). Since the weight change (ΔW) in a given period corresponds to the amount of intruded liquid, the extent of infiltration can be expressed as

$$\text{extent of intrusion (\%)} = \frac{\Delta W}{W_1} \times 100, \quad (5)$$

where W<sub>1</sub> is the total weight of liquid required to completely fill the void space. After each infiltration/pyrolysis cycle, W<sub>1</sub> can be determined with

$$W_1 = W_0 \left( \frac{\Phi_0}{1 - \Phi_0} \right) \left( \frac{\rho_l}{\rho_{\text{Si}_3\text{N}_4}} \right) - (W_s - W_0) \frac{\rho_l}{\rho_{\text{ZrO}_2}}, \quad (6)$$

where W<sub>0</sub> and Φ<sub>0</sub> are the dry weight and volume fraction of porosity in the initial Si<sub>3</sub>N<sub>4</sub> powder compact, W<sub>s</sub> is the dry weight of the infiltrated body containing pyrolyzed Zr(Y)O<sub>2</sub>, and ρ<sub>l</sub>, ρ<sub>Si<sub>3</sub>N<sub>4</sub></sub>, ρ<sub>ZrO<sub>2</sub></sub> are the densities of the Zr(Y)-nitrate precursor (1.6 g/cc), Si<sub>3</sub>N<sub>4</sub> (3.2 g/cc), and Zr(Y)O<sub>2</sub> (6.05 g/cc), respectively.

<sup>e</sup> Nyacol Products Inc., Ashland, MA

<sup>f</sup> Nucor Co., Phoenix, AZ

<sup>g</sup> Model 951, DuPont Instruments, Wilmington, DE

<sup>h</sup> Model RMS-800, Rheometrics Inc., Piscataway, NJ

Infiltration measurements for conditions where the powder compact was first evacuated of air ( $P_i = 0$ ), were performed by placing the specimen in a beaker within a chamber evacuated to 0.1 torr. After evacuation, liquid was introduced through an appropriate port to quickly cover the specimen and fill the beaker. After breaking the air seal to the chamber, the beaker and immersed specimen was then removed to an electric balance to determine the weight changes of the immersed specimen, and thus, the intruded liquid volume as a function of time.

Water infiltration measurements were carried out as a function of an applied pressure, i.e.,  $0.25 \text{ MPa} \leq P_a \leq 1.35 \text{ MPa}$  for powder compacts containing air, i.e.,  $P_i > 0$ . This was accomplished with a centrifugation technique where a thin disc specimen was placed in a centrifuge tube, covered with water and then centrifuged to produce a desired pressure. Because the specimen was thin relative to the head of liquid above the specimen, the pressure differential across the specimen was small ( $\Delta P/P_a \approx 2\%$ ). The centrifugation method was chosen because the direct application of an applied pressure would minimize liquid intrusion via gas diffusion. (A low ambient gas pressure exists within a centrifuge, whereas if an applied pressure was exerted on the liquid through any other method, little pressure differential would exist to drive gas diffusion once the fractional void space was filled by liquid flow.

Initial experiments showed that the  $\text{ZrO}_2$  precursor would concentrate near the surface of the powder compact during evaporation, i.e., a portion of the Zr-nitrate molecules would steam to the surface with its solvent during evaporation. This concentration gradient was prevented by immobilizing the Zr-nitrate molecules (and Y-nitrate) by gelling the precursor prior to drying. Gelling was accomplished by submerged the infiltrated specimen in a  $\text{NH}_4\text{OH}$  solution (15 M) for several hours prior to drying at  $60^\circ\text{C}$  for 1 day. After drying, the specimens were heat treated in a flowing  $\text{N}_2$  atmosphere for 4 hours at either  $1000^\circ\text{C}$  or  $1400^\circ\text{C}$ . Repeated infiltration and pyrolysis was performed using the same procedures.

Microstructural examinations were performed using a scanning electron microscope (SEM)<sup>i</sup> and a mercury porosimeter<sup>j</sup>. Some powder specimens were formulated to contain  $9 \mu\text{m}$  polymer spheres<sup>k</sup> that pyrolysis to produce spherical voids during heat treatment. These large voids helped to characterize the microstructure development of the intruded Zr-precursor and schematically illustrated the volume change associated with the pyrolysis process.

---

<sup>i</sup> Jeol 840-ASM, Peabody, MA

<sup>j</sup> AutoPore 9200, Micromeritics, Norcross, GA

<sup>k</sup> Polystyrene DVB, Duke Scientific, Palo Alto, CA

### 3. RESULTS

#### 3.1 General Behavior of Powder Compacts Prior to Infiltration

When pressure filtration was conducted at high pressures ( $\geq 10$  MPa), consolidated bodies often cracked when the pressure was released after filtration. This was observed for bodies consolidated from both dispersed and flocced  $\text{Si}_3\text{N}_4$  slurries. This cracking phenomenon is related to the rheology of the consolidated bodies, which, determines the strain relaxation processes [17] when the applied pressure is removed and the body needs to expand to release its stored strain during pressure consolidation. Cracks were not present when consolidation was conducted at lower pressures. While the presence of cracks can degrade many properties of the bodies, it also affect the kinetics of infiltration as will be described in a following section.

The relative density of bodies produced from the flocced (pH 6) and dispersed (pH 10) slurries was 0.52 and 0.62, respectively. Mercury intrusion data shown in Fig. 2 illustrates that the equivalent capillary size distribution have a mean diameter of 0.2  $\mu\text{m}$  and 0.35  $\mu\text{m}$  for the relative densities of 0.62 and 0.52, respectively. This data suggests that the mean capillary pressure (see eq. (1)) for liquid intrusion will be higher for the denser powder compact.

The fractured necks formed between touching particles produced during the evaporation-condensation reaction (Eq. (3)) are shown in Fig. 3. As detailed elsewhere, [8] the fracture toughness of such a powder compact, determined by the Single-Edge-Pre-cracked-Beam method [20], is  $K_{\text{IC}} = 0.16 \text{ MPa}\sqrt{\text{m}}$ .

#### 3.2 Infiltration Observations and Results

When air was not evacuated prior to infiltration, bubbles appeared on the surface of the immersed body at a later stage of the infiltration process, consistent with the escape of some trapped, compressed gasses. In some cases a stream of air bubbles were emitting from the body. When the compact contained one or more cracks, streams of bubbles were emitted the moment the body was immersed. To further examine the nature of the infiltration process for cracked and uncracked bodies, a separate infiltration experiment was conducted using a low viscosity red ink.<sup>1</sup> The ink provided a distinct color contrast such that saturated and dry regions could be visually distinguished. Observations revealed that the red ink quickly percolate into the body to

---

<sup>1</sup> McCormick & Co., INC., Hunt Valley, MD

form a red, outer zone, surrounding a colorless core. In contrast, bodies were thoroughly wetted by the red ink when cracks were present. Thus, cracked bodies (those that emitted bubbles at the moment of immersion) were never used to obtain kinetic data.

Representative infiltration data for  $\text{Si}_3\text{N}_4$  powder compacts using either the aqueous  $\text{Zr}(\text{Y})$ -nitrate precursor or water are reported in Figs. 4 through 7; in each figure,  $\Delta W/W_1$  is plotted against the square root of time ( $t^{1/2}$ ).

Figure 4 shows the results for the case where powder compacts containing air and completely immersed in an aqueous  $\text{Zr}(\text{Y})$ -Nitrate solution at ambient pressure. As illustrated, for both high and low relative densities, the infiltration curves are depicted by a salient feature, viz., following a relative rapid intrusion, the initial linear curve departs smoothly to another linear curve. Each linear period appears to correlate to the two steps describe by liquid flow (eq. (1)) and gas diffusion (eq. (3)). It should be noted that although the higher relative density body is expected to have a greater capillary pressure, its rate of liquid intrusion was smaller relative to the lower density body. Consistent with its greater mean capillary pressure for the higher density body, its change from the first linear behavior to the second occurred after a greater relative fraction of void space was filled.

When an external pressure was applied during intrusion via centrifugation for powder compacts containing air, the amount of liquid that can be intruded before the departure to the much slower parabolic behavior increased with applied pressure as shown in Fig. 5. The infiltration behavior of a powder compact without an applied pressure, i.e. at ambient pressure, is also shown for comparison. Since water was used to obtain these data, the initial infiltration step could not be observed due to the very low viscosity of water, and thus, its high intrusion rate.

Figure 6 illustrates the comparison between powder compacts containing air and the specimen where air was evacuated. As expected, although the plot is not perfectly linear to the end of infiltration (suggesting some entrapped gas despite evacuation), all of the pore space appears to fill by a single step process, viz., liquid flow instead of gas diffusion.

The kinetic results for specimens subjected to cyclic infiltration after heat treatments at either 1000 °C and 1400 °C for 4h are shown in Fig. 7. These results illustrate that the kinetics for each cycle is strongly dependence on the heat treatment subsequent to each pyrolysis step (specimens for these experiments were evacuated prior to infiltration with the  $\text{Zr}(\text{Y})\text{O}_2$  precursor). After infiltration and prior to pyrolysis (either 1000 °C or 1400 °C) the intruded specimens were soaked in a  $\text{NH}_4\text{OH}$  solution



for several hours to prevent precursor molecules migrating to the surface. Different microstructures developed for each of the two heat treatment temperatures. Mercury intrusion data shown (Fig. 8) shows that the 1000 °C heat treatment produced a microstructure with much smaller equivalent capillaries, whereas specimens heated to 1400 °C had larger capillaries. It is evident that the intrusion of liquid is slower for subsequent cycles after the initial infiltration and pyrolysis step; this is more substantial for the 1000 °C heat treatment. Although all specimens were evacuated prior to intrusion, Fig. 7 also suggests that the infiltration takes place in two steps; a lower permeability is observed for the initial step.

### 3.3 Microstructural Observations

SEM micrographs (not shown) revealed a higher concentration of  $\text{Zr(Y)O}_2$  near the surface where the infiltrated specimen was simply dried prior to gelation. This phenomenon was prevented when the infiltrated bodies were soaked in a  $\text{NH}_4\text{OH}$  solution to gel the precursor before drying. This observation was further detailed by energy dispersive X-ray spectroscopy (EDS) in the SEM. To avoid misrepresenting the phase content and distribution by this technique, a low magnification of 50x was used to obtain the EDS information. [21] The results, shown in Fig. 9, were plotted by the atomic weight ratio of  $\text{Zr/Si}$  and volume ratio of  $\text{ZrO}_2/\text{Si}_3\text{N}_4$  against the normalized distance from the surface. The volume ratio was calculated from the measured atomic weight ratio with the assumption that both phases are stoichiometric and the density of 6.05 g/cc for  $\text{ZrO}_2$  and 3.2 g/cc for  $\text{Si}_3\text{N}_4$  respectively. The results showed that the migration of Zr-nitrate molecules will occur during drying to produce a concentration gradient within the infiltrated body. The second set of data in Fig. 9 shows that a constant distribution of  $\text{Zr(Y)O}_2$  could be obtained by gelling the intruded nitrate precursor by soaking in  $\text{NH}_4\text{OH}$  prior to drying.

It is obvious that the void phase within the  $\text{Si}_3\text{N}_4$  powder compact is sequentially filled with the  $\text{Zr(Y)O}_2$  second phase after each cyclic of precursor infiltration, gelation, drying and heat treatment. A partially filled large void is shown in Fig. 10 after 4 cycles and heat treatments at 1400 °C. The void shown in Fig 10 was purposely introduced by mixing 9  $\mu\text{m}$  diameter polymer spheres with the powder slurry prior to consolidation. The microstructure of the  $\text{Zr(Y)O}_2$  within the pore is typical of all pores, big and small, within the body. As shown, the large crack-like voids are developed within the large void is a result of the constrained shrinkage that take place during heat treatment (gel shrinkage during drying, shrinkage during pyrolysis as the solid precursor converts to the  $\text{Zr(Y)O}_2$ , and densification of the porous, polycrystalline  $\text{Zr(Y)O}_2$  produced during

pyrolysis). These large volume changes can not be avoided, but the size of the crack-like voids can be minimized to the spacing between packed particles provided no large voids are introduced during powder processing and consolidation.

#### 4. DISCUSSION

As detailed in the soil literature [10, 11] and illustrated here, a powder compact can be completely filled with a liquid despite initial, trapped gas. Figure 5 shows that the time require to remove the trapped gas decreases with increasing applied pressure were centrifugation is used to increase driving pressure for liquid flow. In practice, evacuation of the specimen is desirable to minimize the time for each infiltration cycle.

For identical intrusion conditions, eq. (1) shows that the relative parabolic rate for different compacts will depend on the ratio of both the permeability and capillary pressure for the two bodies. The permeability of a powder compact is commonly expressed with the Kozeny-Carman equation [12]:

$$K = \frac{D^2(1-\rho)^3}{36C\rho^2}, \quad (7)$$

where  $C$  ( $\approx 5$ ) is a constant that defines the shape and tortuosity of the pore channels. The slope of the intrusion vs  $t^{1/2}$  function, expressed with Darcy's Law (eq. (1)) , is proportional to  $KP_c$ . Combining eqs. (2) and (7) and using the mean particles size ( $D = 0.8 \mu\text{m}$ ) determined for the powder, the ratio of  $KP_c$  for the two powder compacts with relative densities of 0.52 and 0.62 is 1.9, whereas the ratio of the slopes for data shown in Fig. 4 is 1.8. The good agreement between the calculated and the experimental ratios shows that a higher relative density produces a lower permeability (greater resistance to fluid flow) relative to a larger capillary pressure, and thus increases the intrusion period.

In our description of the two parabolic phenomena it is assumed that the entrapped gas does not escape from the body. The common observation that gas bubbles from the surface after some intrusion period shows that, in most cases, the period where liquid flows into the body can be much longer than expected. Gas bubbling also means that powder compacts contain connective capillaries of a wide distribution. Larger capillaries must support gas escape to the surface as the internal pressure increases during intrusion. The dye penetration experiments show that even these larger capillaries eventually become isolated after some period, consistent with the observation that bubbling stops although intrusion is not complete. In addition, it

should be noted that large cracks are easily detected during infiltration due to profuse bubbling, suggesting a convenient non-destructive evaluation technique for observing cracks (and other defects) in partially dense bodies.

After the initial infiltration and heat treatment step, the void phase is partially filled with the phase formed by the precursor. The kinetics of subsequent infiltration cycles depends on the permeability of the second phase material, which is governed by its microstructure development during heat treatment. Due to the large difference in the specific gravity of the Zr(Y)-nitrate (1.6 g/cc) and Zr(Y)O<sub>2</sub> (6.05 g/cc) and pyrolysis, a large volume change is associated with precursor conversion to dense Zr(Y)O<sub>2</sub>. Since the large volume change is constrained by the powder network, which does not shrink, the void phase undergoes microstructural changes during densification and grain growth analogous to powders whose densification is constrained by inclusions. [9] Under conditions where shrinkage is constrained, heat treatment at high temperatures results in grain coarsening and void growth. [9] Thus, the intruded second phase in bodies heat treated at 1000 °C are expected and observed to have a much smaller, mean capillary diameter relative to those heat treated at 1400 °C and a much smaller permeability. Thus, the size of the equivalent capillaries within the converted Zr(Y)O<sub>2</sub> will depend on the heat treatment temperature and period.

The migration of mobile Zr-acetate molecules to the surface, for the cases where the precursor was not gelled prior to drying is well known phenomena and has been described for the redistribution of liquid by capillary force within powder compacts during the thermolysis of two-component binders.[22]

## 5. CONCLUSIONS

Prior to infiltration, powder compacts must be strengthened to prevent cracking when the intruded precursor is dried. Strengthening without shrinkage can be accomplished by forming necks between touching particles by the evaporation-condensation reaction,  $\text{Si}_3\text{N}_4 + 1.5 \text{O}_2 \leftrightarrow 3 \text{SiO} + \text{N}_2$ . When powder compacts contain air, the infiltration process involves two steps, viz., a rapid intrusion of liquid driven by capillary pressure and slow intrusion via gas diffusion once the pressure in the entrapped gas become equal to the capillary pressure. Both processes exhibit parabolic kinetics. The extent of intrusion by liquid flow depends on the magnitude of the capillary pressure, which increases with relative density. After the initial infiltration and pyrolysis step, the kinetics of subsequent infiltration depends on the microstructure development of the intruded phase within the pore channels of the powder compact,

which depend on the heat treatment after pyrolysis. Finally, it is shown that a higher concentration of  $\text{Zr(Y)O}_2$  near the surface is due to the migration of precursor molecules toward the surface during drying. This is prevented by gelling the precursor prior to drying.

#### ACKNOWLEDGMENT:

This research was sponsored by the Defense Advance Research Projects Agency through the University Research Initiative at UCSB under ONR contract N00014-92-J-1808.

#### REFERENCES

- [1] S. Yajima, T. Shishido, and K. Okamura, "SiC Bodies Sintered with Three-Dimension Cross-Linked Polycarbosilane," *Am. Ceram. Soc. Bull.*, Vol. 56, No. 12, 1060-1063 (1977).
- [2] S.J. Glass and D.J. Green, "Surface Modification of Ceramics by Partial Infiltration," *Adv. Ceramic Mater.*, 2, 2, 129-131 (1987).
- [3] B.R. Marple and D.J. Green, "Incorporation of Mullite as a Second Phase into Alumina by an Infiltration Technique," *J. Am. Ceram. Soc.*, 71[11]C-471-C-473 (1988).
- [4] M.D. Sacks and S.D. Vora, "Preparation of  $\text{SiO}_2$  Glass from Model Powder Compacts: III, Enhanced Densification by Sol Infiltration," *J. Am. Ceram. Soc.*, 71 [4] 245-49 (1988).
- [5] B.E. Walker, Jr., R.W. Rice, P.F. Becker, B.A. Bender, and W.S. Coblenz, "Preparation and Properties of Monolithic and Composite Ceramics Produced by Polymer Pyrolysis," *Am. Ceram. Soc. Bull.*, Vol. 62, No. 8, 916-23 (1983).
- [6] K.S. Mazdiasni, R. West, and L.D. David, "Characterization of Organosilicon Infiltrated Porous Reaction-Sintered  $\text{Si}_3\text{N}_4$ ," *J. Am. Ceram. Soc.*, 61[11-12] 504-508 (1978).
- [7] D.R. Clarke, "Interpenetrating Phase Composites," *J. Am. Ceram. Soc.*, 75 [4] 739-59 (1992).
- [8] W. C. Tu, Ph. D Thesis, University of California at Santa Barbara (1993); W. C. Tu and F. F. Lange, "Strengthening of Ceramic Powder Compacts by Liquid Precursor Infiltration and Pyrolysis," to be published.

- [9] O. Sudre and F.F. Lange, "Effect of Inclusions on Densification: I, Microstructural Development in an  $\text{Al}_2\text{O}_3$  Matrix Containing a High Volume Fraction of  $\text{ZrO}_2$  Inclusions," *J. Am. Ceram. Soc.*, 75 [3] 519-24 (1992).
- [10] J. Constantz, W.N. Herkelrath, and F. Murphy, "Air Encapsulation during Infiltration," *Soil Sci. Soc. Am. J.*, 52, 10-16 (1988).
- [11] A.R. Jarrett and J.R. Hoover, "Evaluating the Effect of Increased Concentration of  $\text{CO}_2$  on Infiltration Rate," *Trans. ASAE* 28:179-182 (1985).
- [12] A.E. Scheidegger, *The Physics of Flow Through Porous Media*, 3rd ed. University of Toronto Press, Toronto, Canada, 1974.
- [13] F.A. Dullien, *Porous Media-Fluid Transport and Pore Structure*, Academic Press, New York, 1979.
- [14] L. R. White, "Capillary Rise in Powders," *J. Colloid and Interface Science*, Vol. 90, No. 2, 536 - 538 (1982).
- [15] G. H. Geiger and D. R. Poipier, *Transport Phenomena in Metallurgy*, Addison-Wesley Publishing Company (1980).
- [16] L. G. Wilson, "The Effect of Air Flow Ahead of Wetting Front on Infiltration," PH. D. Dissertation, University of California, Davis (1962).
- [17] F.F. Lange and K.T. Miller, "Pressure Filtration: Consolidation Kinetics and Mechanics," *Am. Ceram. Soc. Bull.*, Vol. 66, No. 10, 14948-1504 (1987).
- [18] F.F. Lange, B.I. Davis, and E. Wright, "Processing-Related Fracture Origins: IV, Elimination of Voids Produced by Organic Inclusions," *J. Am. Ceram. Soc.*, 69 [1] 66-69 (1986).
- [19] M. L. Balmer, F.F. Lange, and C. G. Levi, "Metastable Phase Selection and Partitioning in  $\text{ZrO}_2$ - $\text{MgO}$  Processed from Liquid Precursors," *J. Am. Ceram. Soc.*, 75 [4] 946-52 (1992).
- [20] T. Nose and T. Fujii, "Evaluation of Fracture Toughness for Ceramic Materials by a Single-Edge-Pre-cracked-Beam Method," *J. Am. Ceram. Soc.*, 71 [5] 328-33 (1988).
- [21] F.F. Lange and M.M. Hirlinger, "Phase Distribution Studies Using Energy Dispersive X-ray Spectral Analysis," *J. Mater. Sci. Lett.*, 4, 1437-41 (1985).
- [22] M.J. Cima, J.A. Lewis, and A.D. Devoe, "Binder Distribution in Ceramic Greenware during Thermolysis," *J. Am. Ceram. Soc.*, 72 [7] 1192-99 (1989).

## Figure Captions

- Figure 1 Large void created by nitridation of a Si particle embedded in a  $\text{Si}_3\text{N}_4$  powder compact.
- Figure 2 Comparison of the pore size distributions for two  $\text{Si}_3\text{N}_4$  powder compacts with different relative densities.
- Figure 3 SEM micrograph showing sintered necks between  $\text{Si}_3\text{N}_4$  particles produced by the  $\text{Si}_3\text{N}_4 + 1.5 \text{O}_2 \leftrightarrow 3 \text{SiO} + \text{N}_2$  evaporation-condensation reaction.
- Figure 4 Plot showing extent of intrusion vs  $(\text{time})^{1/2}$  for infiltration of a liquid precursor for  $\text{Zr}(\text{Y})\text{O}_2$  into  $\text{Si}_3\text{N}_4$  powder compacts containing air.
- Figure 5 Influence of applied pressure, produced by centrifugation, on the infiltration of water into  $\text{Si}_3\text{N}_4$  powder compacts.
- Figure 6 Comparison of extent of intrusion vs.  $t^{1/2}$  for  $\text{Si}_3\text{N}_4$  powder compacts containing air and evacuated of air prior to intrusion.
- Figure 7 Plot showing extent of intrusion vs.  $t^{1/2}$  for cyclic infiltration of a liquid precursor for  $\text{Zr}(\text{Y})\text{O}_2$  into  $\text{Si}_3\text{N}_4$  powder compacts heat treated at either 1000 °C or 1400 °C after precursor pyrolysis.
- Figure 8 Development of pore size distribution during cyclic infiltration and pyrolysis of a liquid precursor for  $\text{Zr}(\text{Y})\text{O}_2$  into  $\text{Si}_3\text{N}_4$  powder compacts heat treated at either 1000 °C or 1400 °C.
- Figure 9 Distribution of  $\text{Zr}(\text{Y})\text{O}_2$  as a function of distance from the surface for  $\text{Si}_3\text{N}_4$  powder compacts after 5 infiltration/pyrolysis cycles with  $\text{Zr}(\text{Y})$ -nitrate for conditions where precursor was gelled prior to drying (a) and dried without gelling (b).
- Figure 10 A large pore within a  $\text{Si}_3\text{N}_4$  powder compact partially filled with  $\text{Zr}(\text{Y})\text{O}_2$  by cyclic infiltration and pyrolysis of a  $\text{Zr}(\text{Y})$ -nitrate precursor.

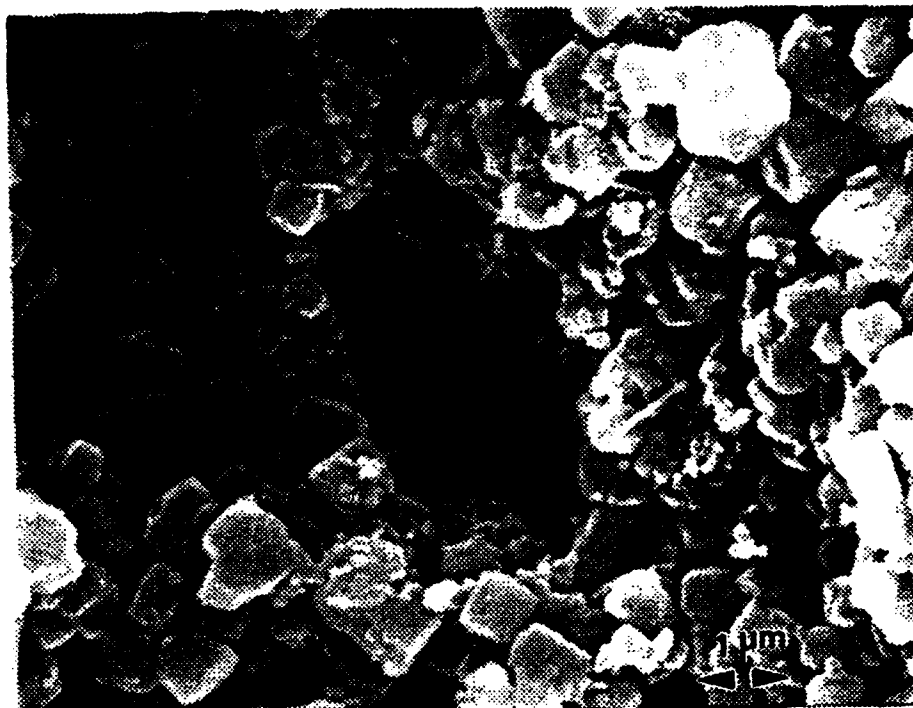


**Fig. 1** Large void created by nitridation of a Si particle embedded in a  $\text{Si}_3\text{N}_4$  powder compact

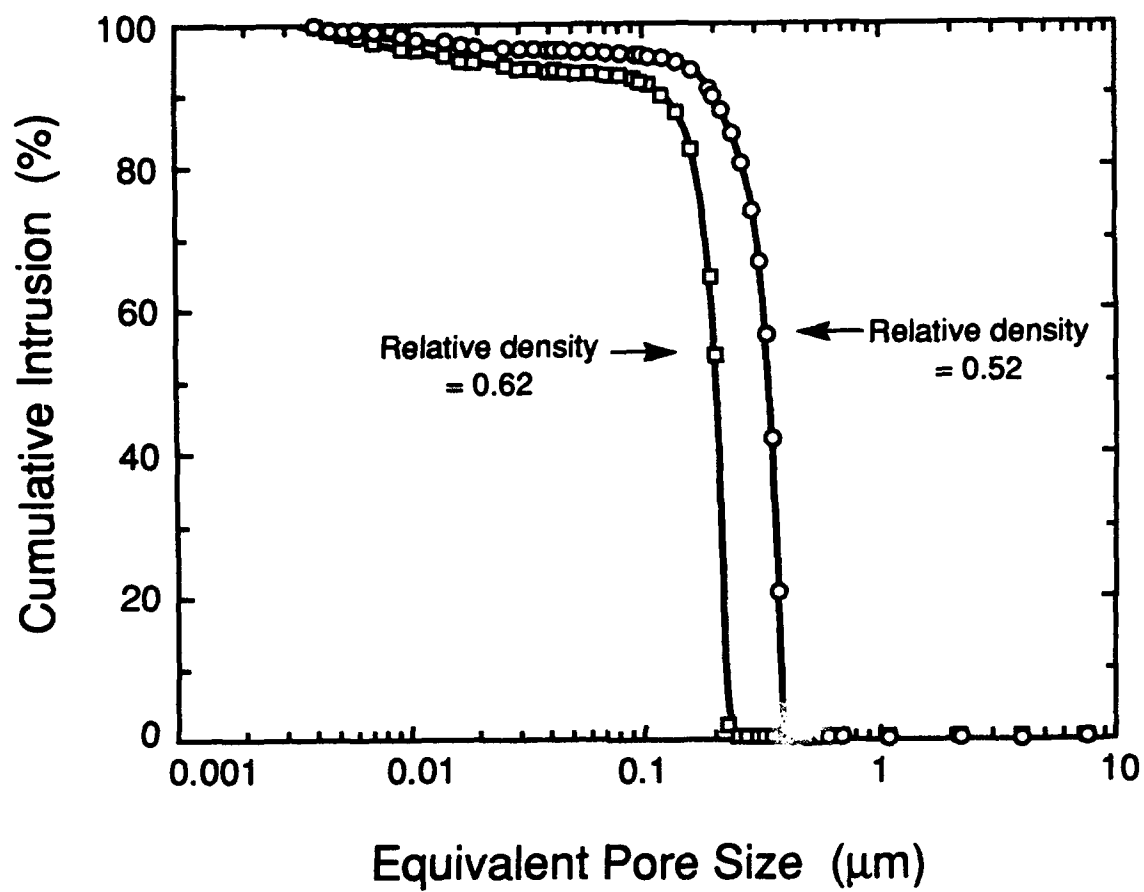


Fig. 2. Comparison of the pore size distributions for two  $\text{Si}_3\text{N}_4$  powder compacts with different relative densities.



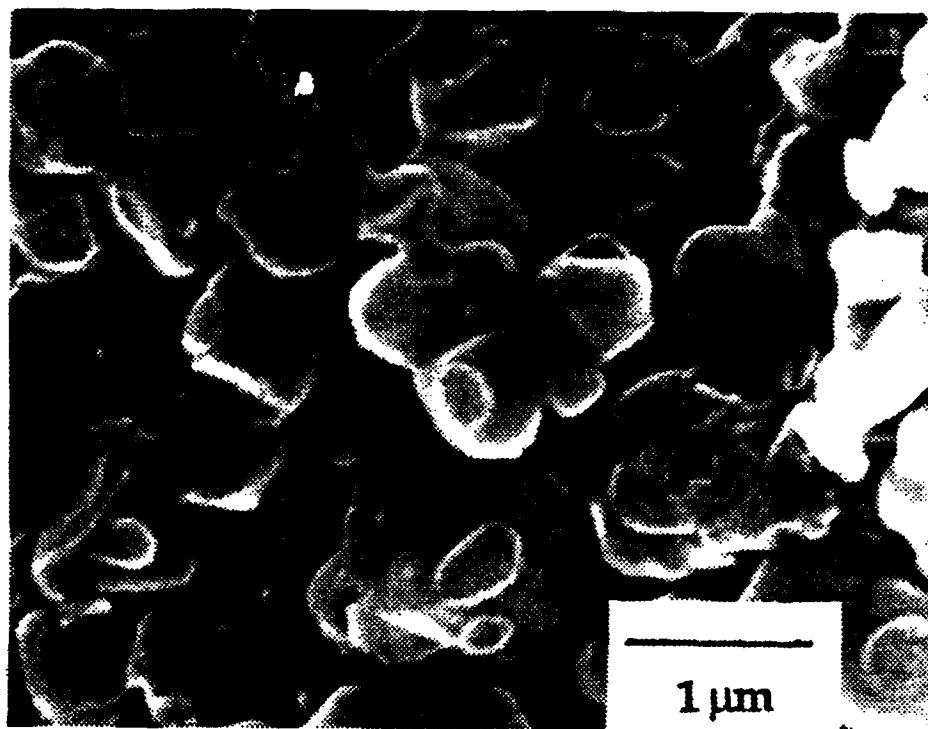


Fig. 3 SEM micrograph showing sintered necks between  $\text{Si}_3\text{N}_4$  particles produced by the  $\text{Si}_3\text{N}_4 + 1.5 \text{O}_2 \leftrightarrow 3 \text{SiO} + 2\text{N}_2$  evaporation-condensation reaction

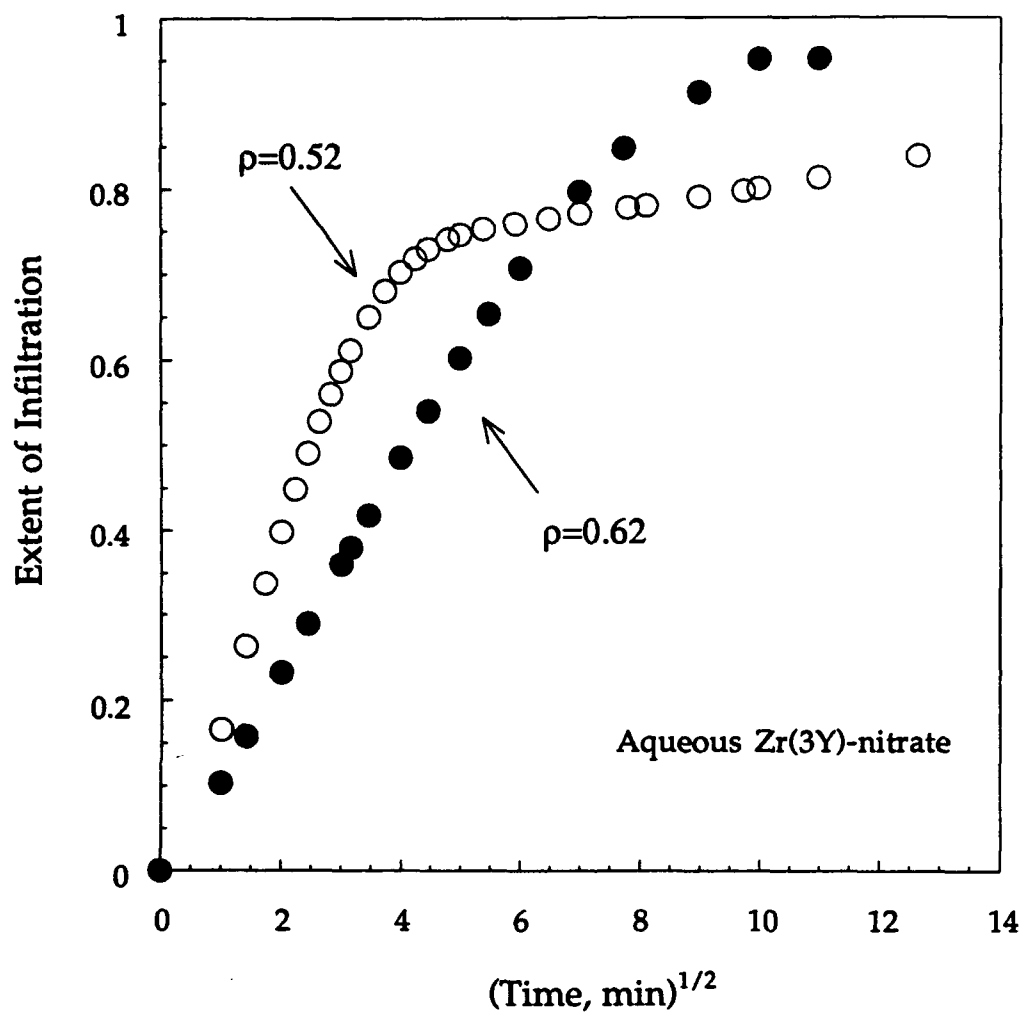


Fig. 4 Plot showing extent of intrusion vs.  $(\text{time})^{1/2}$  for infiltration of a liquid precursor for  $\text{Zr(Y)O}_2$  into  $\text{Si}_3\text{N}_4$  powder compacts containing air

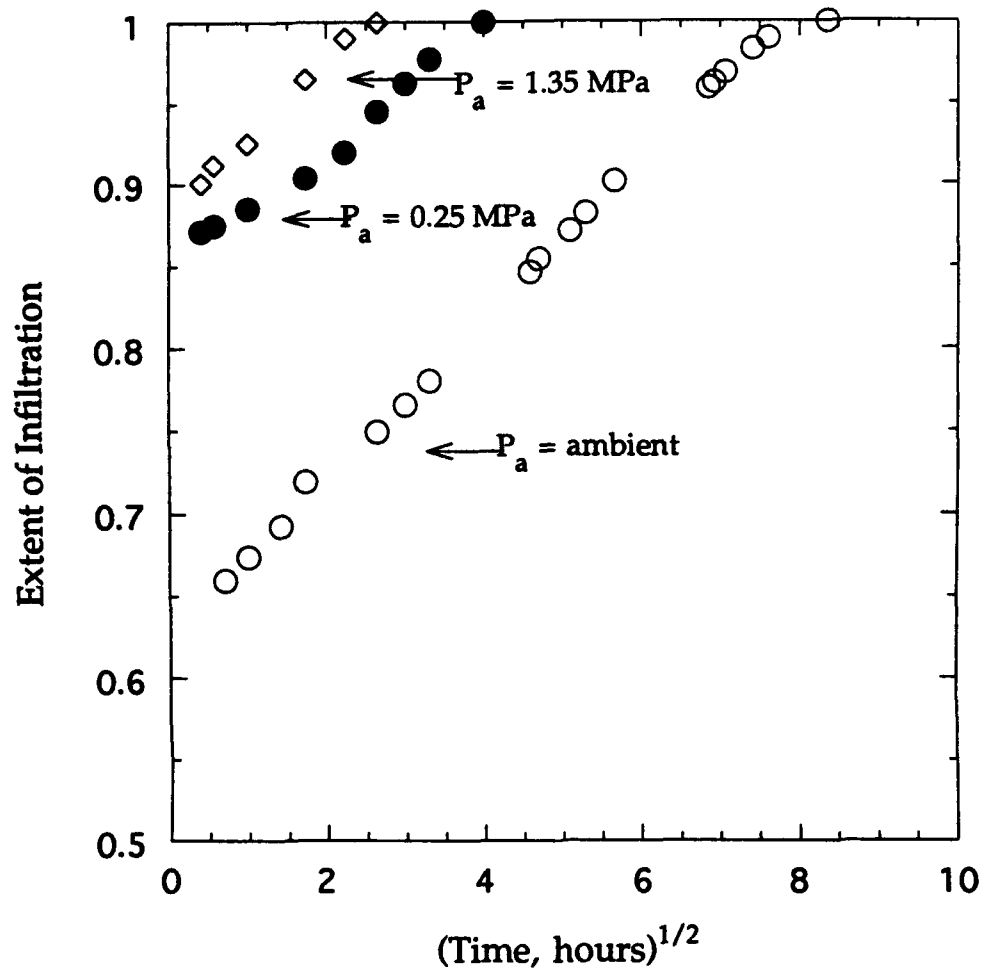


Fig. 5 Influence of applied pressure, produced by centrifugation, on the infiltration of water into Si<sub>3</sub>N<sub>4</sub> powder compacts

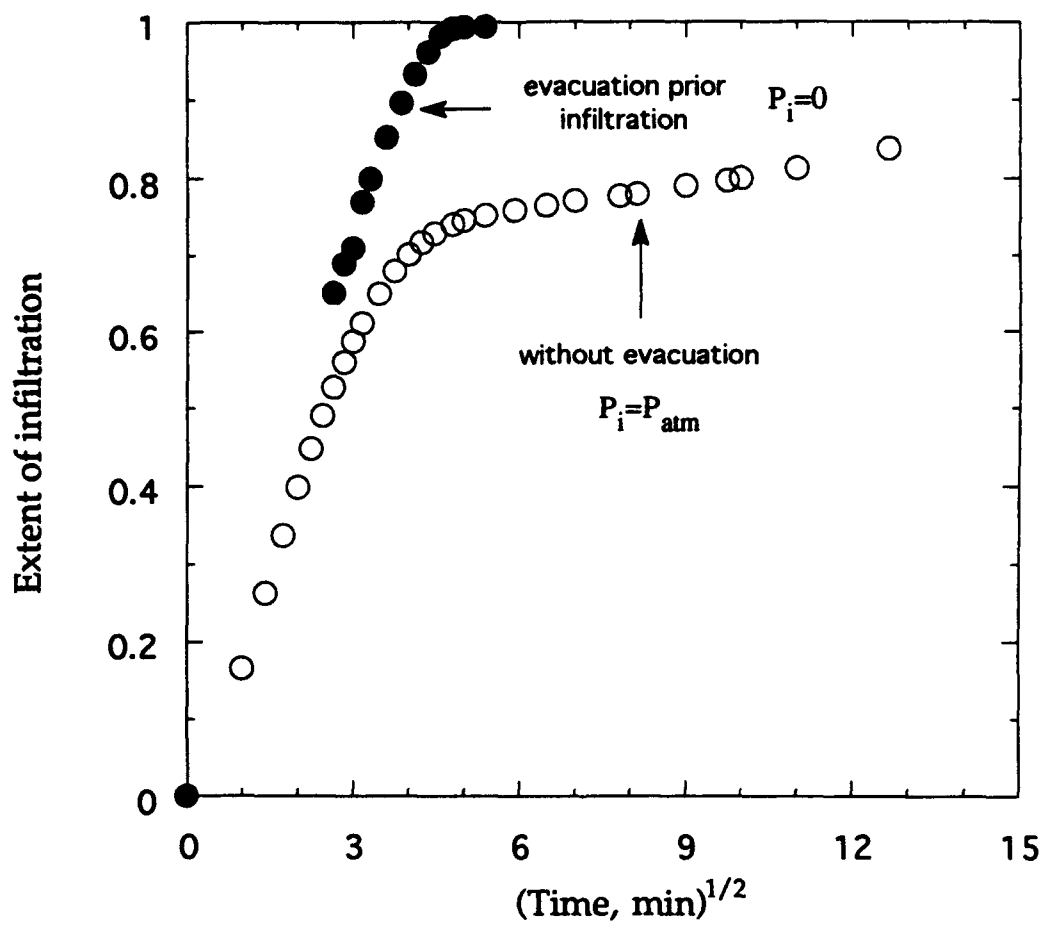


Fig. 6 Comparison of extent of intrusion vs.  $t^{1/2}$  for  $\text{Si}_3\text{N}_4$  powder compacts containing air and evacuated of air prior to infiltration

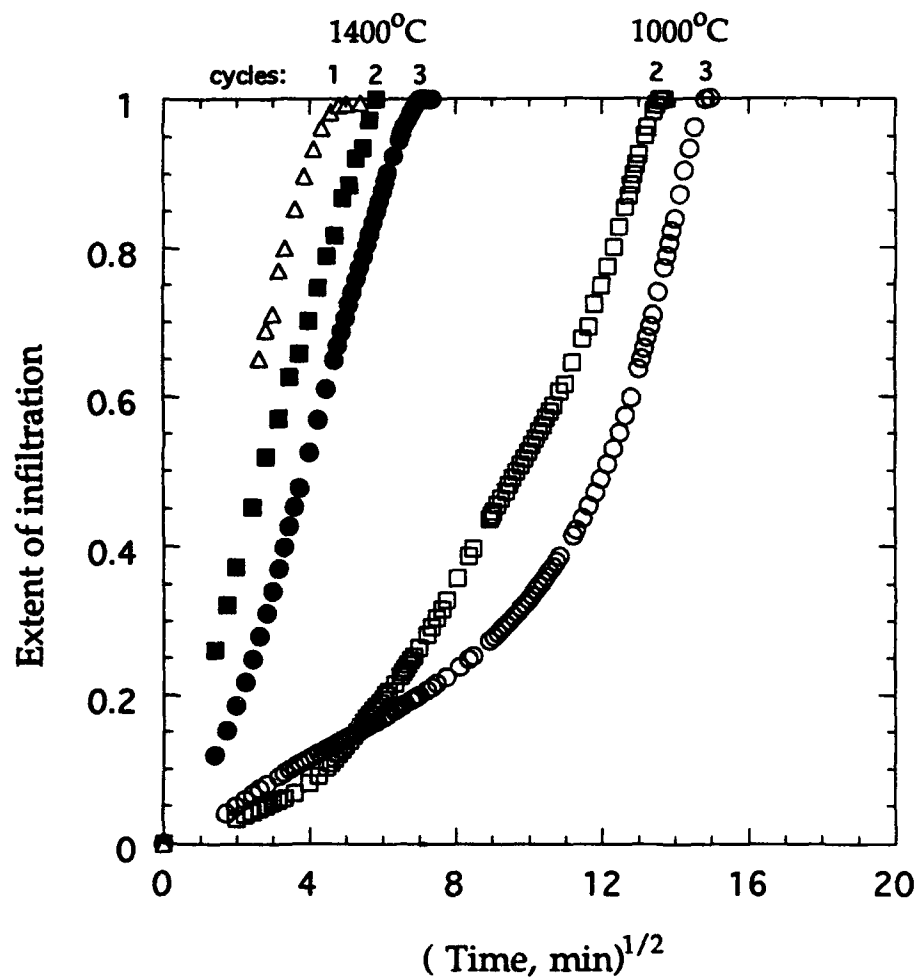


Fig. 7 Plot showing extent of intrusion vs.  $t^{1/2}$  for cyclic infiltration of a liquid precursor for  $\text{Zr}(\text{Y})\text{O}_2$  into  $\text{Si}_3\text{N}_4$  powder compacts heat treated at either 1000°C or 1400°C after precursor pyrolysis

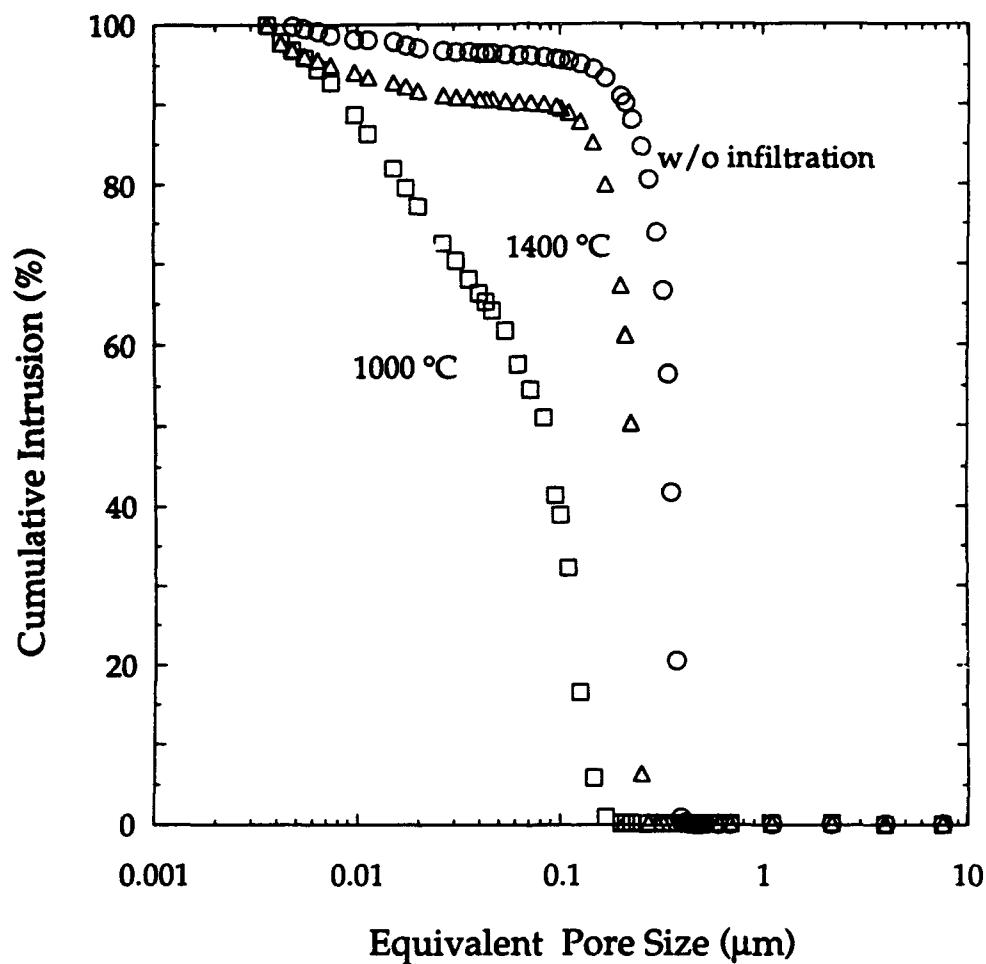


Fig. 8 Development of pore size distribution during cyclic infiltration and pyrolysis of a liquid precursor for  $\text{Zr(Y)O}_2$  into  $\text{Si}_3\text{N}_4$  powder compacts heat treated at either 1000°C or 1400°C

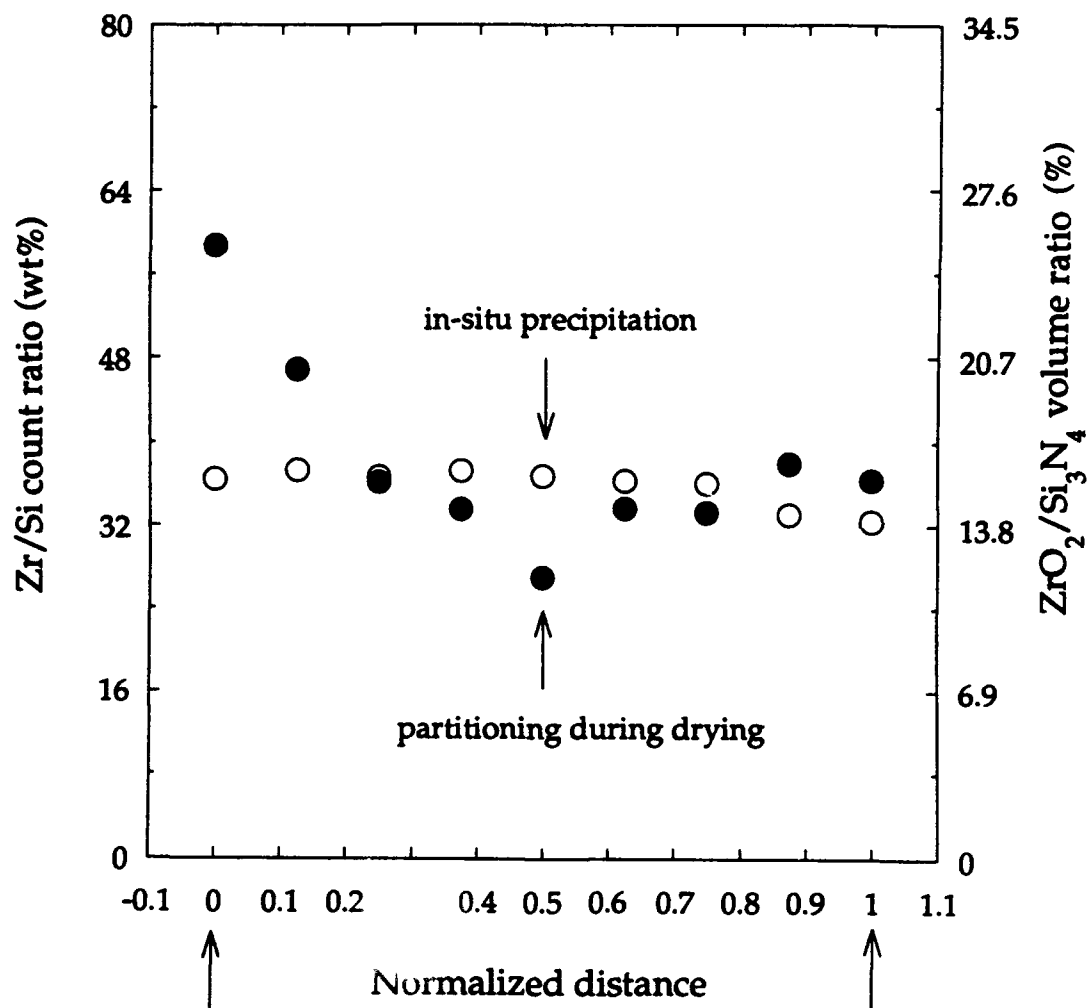


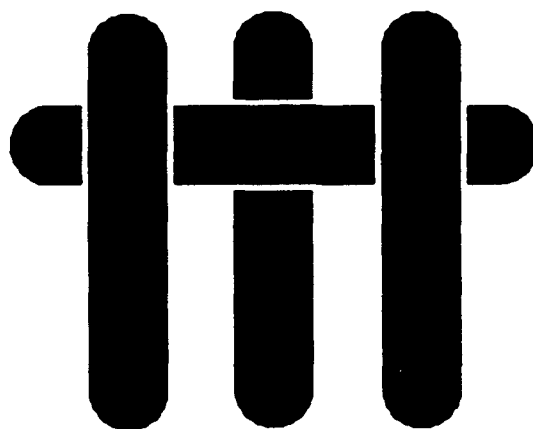
Fig. 9 Distribution of  $\text{Zr(Y)O}_2$  as a function of distance from the surface for  $\text{Si}_3\text{N}_4$  powder compacts after 5 infiltration/pyrolysis cycles with  $\text{Zr(Y)-nitrate}$  for conditions where precursor was gelled prior to drying (a) and dried without gelling (b)



**Fig. 10** A large pore within a  $\text{Si}_3\text{N}_4$  powder compact partially filled with  $\text{Zr(Y)O}_2$  by cyclic infiltration and pyrolysis of a  $\text{Zr(Y)}$ -nitrate precursor



M A T E R I A L S



**Liquid Precursor Infiltration and Pyrolysis of Powder  
Compacts: II, Fracture Toughness and Strength**

**W. C. Tu and F. F. Lange**

**Materials Department  
College of Engineering  
University of California, Santa Barbara  
Santa Barbara, CA 93106**

# **Liquid Precursor Infiltration and Pyrolysis of Powder Compacts,**

## **II: Fracture Toughness and Strength**

W. C. Tu and F. F. Lange

Materials Department

College of Engineering

University of California, Santa Barbara

Santa Barbara, CA 93106

### **ABSTRACT**

$\text{Si}_3\text{N}_4$  powder compacts were infiltrated with liquid precursors to produce either  $\text{Zr}(\text{Y})\text{O}_2$  (3mol%  $\text{Y}_2\text{O}_3$ ) solid-solution or amorphous  $\text{Si}_3\text{N}_4$  after pyrolysis at relative low temperatures and without shrinkage. Cracks that occur within a thin, surface layer of the precursor during pyrolysis can extend into the powder compact. As suggested by theory, this cracking phenomenon could be avoided by either making the powder compact stronger before infiltration and by removing the thin precursor layer before pyrolysis. The mechanical properties of these materials were studied as a function of residual porosity. It was observed that crack extension occurred within the second phase which appeared to govern the critical stress intensity factor ( $K_{\text{IC}}$ ) of the material.  $K_{\text{IC}}$  was found to be a linear function of the ratio between current porosity divided by the porosity in the initial powder compact. Reasonable flexural strengths ( $\approx 300$  MPa) could be achieved despite considerable residual porosity.

## 1. INTRODUCTION

In the first part [1] of this series, the intrusion kinetics of a liquid precursor into a  $\text{Si}_3\text{N}_4$  powder compact was studied. It was shown that when the powder compact contained air, the infiltration involves two steps, each with parabolic kinetics, i.e., relatively rapid intrusion of liquid via flow due to capillary pressure (Darcy's Law) and diffusion of entrapped, pressurized gas to the surface (Fick's Law). When the intruded precursor is converted to an inorganic during heat treatment, the void space is partially filled with pyrolyzed product without shrinkage of the  $\text{Si}_3\text{N}_4$  powder. The kinetics of subsequent cycles depends on the permeability of the pyrolyzed product, which depends on its microstructural development during heat treatment subsequent to pyrolysis. Surface cracks can form within the powder compact during either precursor drying or pyrolysis; this cracking phenomena is detailed in the Appendix.

Partially dense bodies, e.g., those made by the cyclic infiltration and pyrolysis of precursor to an inorganic material, can have advantages that can not be achieved by other conventional techniques. Porous materials can be superior to their fully dense counterparts in applications that require thermal shock resistance and higher specific mechanical properties (properties normalized by density). A recent study [2] of the mechanical properties of partial dense  $\text{Al}_2\text{O}_3$  has shown that high density is not a prerequisite for high strength. The mechanical performance of a porous ceramic can be prescribed by the well known Griffith equation:

$$\sigma_f = Y \frac{K_c}{\sqrt{a}}, \quad (1)$$

where  $\sigma_f$  is the fracture stress,  $K_c$  is the critical stress intensity factor,  $a$  is the critical flaw size and  $Y$  is a dimensionless term which depends on the stress distribution and crack configuration. Eq.(1) shows that porous bodies can be strong provided the critical flaw size,  $a$ , is small, and the material's resistance to crack growth,  $K_c$ , is not greatly reduced by the porosity. As recently shown by Lam et al., [2] for porous materials formed by the partial densification of powders,  $K_c$  is related to the current porosity ( $\rho - \rho_0$ ) divided by the initial porosity ( $1 - \rho_0$ ) by

$$K_c = K_\infty \left( \frac{\rho - \rho_0}{1 - \rho_0} \right), \quad (2)$$

where  $K_{c0}$  is the critical stress intensity factor for the fully dense material,  $\rho$  is the current relative density, and  $\rho_0$  is the initial packing density.

The objective of the present study was to characterize the mechanical properties of  $\text{Si}_3\text{N}_4$  powder compacts made denser and stronger by cyclic liquid precursor infiltration/pyrolysis. In Part I of this study, the liquid precursor was an aqueous Zr-nitrate solution containing Y-nitrate that formed a  $\text{Zr(Y)O}_2$  second phase within the  $\text{Si}_3\text{N}_4$  powder compact. The current study will emphasize the mechanical properties of materials formed with this precursor as well as a bodies infiltrated with a polysilazane precursor that produces an amorphous  $\text{Si}_3\text{N}_4$  second phase. As detailed below, it is shown that crack extension in these bodies occurs within the added, second phase material, which governs the  $K_c$  of the infiltrated material.

## 2. EXPERIMENTAL

Discs (2.5 dia. x 0.5 cm) and rectangular bars (0.5 x 0.5 x 0.35 cm) were prepared separately by either pressure filtration (5 MPa) and slip casting of dispersed (pH = 10) aqueous slurries containing 0.20 volume fraction of  $\text{Si}_3\text{N}_4$ <sup>a</sup> as previously reported. [1] The consolidated bodies were dried at room temperature for 1 day and at 60°C for a second day. Prior to infiltration, the powder compacts were strengthened by forming small necks between touching particles by an evaporation-condensation method described elsewhere. [1]

Two different liquid precursors were used in this study: Zr(Y)-nitrate and polysilazane,<sup>b</sup> which pyrolyzed to  $\text{Zr(Y)O}_2$  and  $\text{Si}_3\text{N}_4$ , respectively. Several physical properties of these precursors are summarized in Table 1. The Zr(Y)-nitrate precursor and its infiltration into pre-strengthened  $\text{Si}_3\text{N}_4$  powder compacts was previously described. [1] The thermal decomposition for both precursors were determined by thermogravimetry analysis (TGA) in flowing  $\text{N}_2$ . The TGA results were used to optimize the heating schedules for precursor pyrolysis. Because the polysilazane precursor is very sensitive to oxygen and water vapor, it had to be handled in a  $\text{N}_2$  filled glove box. Because its viscosity was too high at room temperature, the infiltration of the polysilazane was conducted at 150 °C where its viscosity was sufficiently low (2 poise) and where it was still relatively stable to cross linking and decomposition. Pre-strengthened powder compacts, contained in a beaker, were evacuated of gas within a

---

<sup>a</sup> SN-E3, Ube Industries, New York, NY

<sup>b</sup> Pyrofine PV™, ATOCHEM, Paris, France.

chamber with a mechanical vacuum pump. Prior to introducing the preheated liquid precursor (150°C) into the chamber to cover the specimen, the specimen was also heated to 150°C. After the specimen was covered with the precursor, the chamber was backed filled with N<sub>2</sub>. The temperature of the liquid polysilazane was controlled to 150°C ± 10°C for an infiltration period of 24 h to insure complete infiltration. When the specimens were then removed from the chamber a thick, viscous layer of precursor clung to the specimen as it cooled. As described in the Appendix, to avoid cracks from extending from the thick layer of precursor into the powder compact during pyrolysis, the precursor layer was removed with an abrasive SiC paper prior to pyrolysis. The polysilazane precursor was pyrolyzed in a tube furnace with flowing N<sub>2</sub>. To avoid violent decomposition during precursor cross-linking and pyrolysis, a slow heating schedule of 300°C/h to 150°C, 5°C/h to 350°C, 60°C/h to 800°C, and 120°C/h to 1250°C (4h) was used. Multiple infiltration/pyrolysis cycles were performed. Some specimens were subjected to further heat treatments at 1400°C and 1500°C for 5 hours to characterize microstructural changes within the intruded material. The porosity remaining in the specimens after each infiltration/pyrolysis cycle was measured by the water replacement method [1] which does not require knowledge of the pyrolyzed precursor density.

The fracture strength of the treated powder compacts were measured with diamond machined bar specimens (0.3 × 0.3 × 2.5 cm) using a three point flexural test (span 2.0 cm) in a mechanical testing machine.<sup>c</sup> Before testing, the tensile surface of the specimens were polished to 1µm finish with diamond paste and the edges were beveled to remove severe damage introduced during diamond machining.

The plane strain fracture toughness (K<sub>IC</sub>) was determined using a single edge pre-cracked beam (SEPB) method. [3] A straight, through pre-crack was introduced by the bridge-indentation technique. Beam specimens were ground flat and parallel to each opposite face with a 400 grit diamond wheel to obtain rectangular beams of dimensions 0.3 × 0.4 × 2.0 cm. Both the bottom and side surfaces were further polished to a 1µm finish with a diamond paste on an automatic polishing machine.<sup>d</sup> A row of Vickers indentations (3 to 5) were placed on the center of the polished surface using a hardness tester with a load of 7 kg. The ends of the row of Vickers indentations were made as close to the edge as possible without chipping either edge of the specimen. The indented specimens were then compressed with a bridge using a crosshead speed of 0.1mm/sec. The specimens were unloaded when a desired pre-crack was produced.

---

<sup>c</sup> Model 1123, Instron.

<sup>d</sup> Multipol 2, Malvern Instruments, Malvern, England.

An acoustic emission sensor was attached to the fixture to help detect when the crack popped-in during bridge loading. After pre-cracking, the specimen was inspected with an optical microscopy to ensure the crack lengths to be approximately equal on both side surfaces. For most measurements, a dye penetrant<sup>e</sup> was applied to enhance the visibility of the pre-crack. The pre-cracked specimens were then loaded by three-point flexure in the same testing machine with a cross-head speed of 0.05mm/sec. The  $K_c$  was determined by knowing the maximum load and the dimensions of the beam specimens through a formula [4]:

$$K_c = \frac{PS}{B W^{1/2}} f(a/W), \quad (3)$$

where P is the peak load, B and W are the width and height of the beam respectively, S is the span length, and a is the pre-crack length.

Fracture surfaces were examined by scanning electron microscopy (SEM). The microstructure associated with the intruded phase was also characterized by transmission electron microscopy (TEM).

### 3. RESULTS

The thermal decomposition behavior of the polysilazane precursor is reported in Fig. 1. Pyrolysis associated with the  $Zr(Y)O_2$  precursor is presented elsewhere. [1] The weight loss during heating of the polysilazane precursor occurred in two major steps: a 5 % weight loss between 200 and 275°C and a 30 % weight loss between 400 and 550°C. The first loss is expected to be due to volatile, low molecular weight oligomers. The ceramic yield of the precursor is  $\approx 60$  wt %. After pyrolysis, the precursor appears black, indicative the presence of residual carbon. Large cracks and frozen bubbles are observed for specimens of the pyrolyzed precursor which exhibits a linear shrinkage of  $\approx 10\%$ . An X-ray diffraction analysis shows that the pyrolyzed precursor is amorphous for heat treatments below 1400°C/4h; whereas  $\alpha$ - $Si_3N_4$  is clearly evident when the material was heated to 1500°C/4h.

The relative density ( $\rho$ ) of the infiltrated and pyrolyzed bodies as a function of number of infiltration cycles is shown in Fig. 2. As expected, the higher ceramic yield of polysilazane is more effective in reducing the porosity per infiltration cycle; the porosity

---

<sup>e</sup> Penetrant DP-40, Sherwin Inc., Los Angeles, CA.

decreased from an initial 40 % to 20 % after three infiltration cycles. However, attempts to increase the density with more infiltration cycles was not successful. The microstructural development of a cyclically infiltrated body, after successive heat treatments at 1250 °C, 1400 °C, and 1500 °C for 4 hours, is shown in Fig. 3. As shown, the morphology of  $\text{Si}_3\text{N}_4$  particle network remains unchanged whereas the pyrolyzed phase changes from an apparent glassy appearance to a more discrete particulate-like morphology after the 1500 °C treatment. The development of large crack-like voids due to constrained shrinkage within the pore space is also evident and expected. [1] TEM observations, shown in Fig. 4, for bodies heat treated at 1250°C and 1500°C, illustrate that the phase within the pore space is amorphous by electron diffraction analysis. Microstructure features associated with the  $\text{Zr(Y)O}_2$  intruded phase are presented elsewhere. [1]

The critical stress intensity factor ( $K_{\text{IC}}$ ) and fracture strength ( $\sigma_{\text{f}}$ ) of the infiltrated bodies are presented in Figs. 5 and 6, respectively.  $K_{\text{IC}}$  vs  $(\rho - \rho_0)/(1 - \rho_0)$  ( $\rho_0$  and  $\rho$  = initial and current porosity, respectively) appears to result in a linear function as suggested by Eq. (1). For bodies infiltrated with polysilazane, measurements were only made for up to 3 infiltration cycles because an addition cycle produced no further densification. Bodies infiltrated with polysilazane and subjected to a further heat treatment at 1500°C/4h, did not show any improvement in the mechanical properties over those heat treated at 1250°C/4h. However, as shown in Fig. 7, their fracture surface appears different. In all cases, the fracture path appears to traverse only the amorphous material produced by cyclic pyrolysis as shown in Fig. 8.

#### 4. DISCUSSION

It is obvious that higher yielding inorganic precursors require fewer cycles of infiltration and pyrolysis to increase the density,  $K_{\text{IC}}$  and strength of a powder compact. Further densification of the porous bodies by cyclic infiltration and pyrolysis of polysilazane did not occur after 3 cycles after the porosity was reduced from 40 % to = 20%. Since water could still be intruded into these bodies, it appeared that the flow resistance of the material became too large to allow intrusion of the viscous polysilazane. A close examination of the microstructure shown in Fig. 6 reveals that the pore spaces in the initial powder compact are apparently filled with a second phase with equivalent capillary channel diameters < 5 nm. This fine structure together with the relative high viscosity of polysilazane ( $\approx 2$  Poise), compared to water (0.01 Poise), might explain the observed behavior.

SEM observations (Fig. 10) shows that the crack exclusively traversed the pyrolyzed precursor, viz., no transgranular fracture of  $\text{Si}_3\text{N}_4$  particles is observed. This observation suggests that the fracture resistance ( $K_{\text{IC}}$ ) of the pyrolyzed precursor is less than that of the  $\text{Si}_3\text{N}_4$  suggesting that the fracture resistance of these porous materials is dominated by the pyrolyzed inorganic that bonds the particles together. Thus, the  $K_{\text{IC}}$  of the same powder infiltrated with the transformation toughening  $\text{Zr}(\text{Y})\text{O}_2$  is higher than that for the compacts infiltrated with the amorphous  $\text{Si}_3\text{N}_4$ . As shown in Fig. 7, the  $K_{\text{IC}}$  vs  $(\rho - \rho_0)/(1 - \rho_0)$  plot for bodies infiltrated with  $\text{Zr}(\text{Y})$ -nitrate and polysilazane have different slopes, and thus different intercepts when  $(\rho - \rho_0)/(1 - \rho_0) = 1$ . Since the fracture path only traverses the second phase, the intercept of the  $K_{\text{IC}}$  vs  $(\rho - \rho_0)/(1 - \rho_0)$  plot can be interpreted as the intrinsic fracture toughness of the pyrolyzed ceramic, which for the two different materials is determined from the intercept to be 1.8 and 3.5  $\text{MPa}\cdot\text{m}^{1/2}$  for amorphous  $\text{Si}_3\text{N}_4$  and  $\text{Zr}(\text{Y})\text{O}_2$ , respectively. It is noted that 1.8  $\text{MPa}\cdot\text{m}^{1/2}$  is less than the  $K_{\text{IC}}$  for equiaxed  $\text{Si}_3\text{N}_4$  produced liquid sintering aids (3  $\text{MPa}\cdot\text{m}^{1/2}$ ) [5] and other high toughness  $\text{Si}_3\text{N}_4$  materials (8  $\text{MPa}\cdot\text{m}^{1/2}$ ) [6], but is close to those of CVD amorphous  $\text{Si}_3\text{N}_4$  (1.9  $\text{MPa}\cdot\text{m}^{1/2}$ ) [7] and HIPed fully dense  $\text{Si}_3\text{N}_4$  containing intergranular  $\text{SiO}_2$  (1.9  $\text{MPa}\cdot\text{m}^{1/2}$ ) [8]. The  $K_{\text{IC}}$  of the intruded  $\text{Zr}(\text{Y})\text{O}_2$  phase is larger, but still less than those reported in the literature for bulk,  $t$ - $\text{Zr}(\text{Y})\text{O}_2$  (5  $\text{MPa}\cdot\text{m}^{1/2}$ ) [9].

The strength of the porous powder body is expected to depend on the fracture toughness of the body and the critical flaw size. Therefore, for a similar flaw size, the strength should increase in proportional to the fracture toughness. This trend is observed in Fig. 8 for both  $\text{Zr}(\text{Y})$ -nitrate and polysilazane infiltrated porous bodies, provided that all materials were processed with a similar distribution of flaw sizes.

## 5. CONCLUSIONS

The present study indicated that  $\text{Si}_3\text{N}_4$  bodies with reasonable high strength and toughness can be achieved without shrinkage and at a relatively low temperature by the infiltration of liquid precursor that yields an inorganic material upon pyrolysis. The mechanical properties of infiltrated bodies depend on the amount of fractional porosity filled and the material that bonds particles together.

## ACKNOWLEDGMENTS

This research was sponsored by the Defense Advance Research Projects Agency through the University Research Initiative at UCSB under ONR contract N00014-92-J-1808. The authors thank Dr. Pravin Narwankar for helping with the TEM work and



Prof. Zhigang Suo for discussion concerning the cracking of thin films and crack extension from the thin film into the underlying substrate.

#### **APPENDIX: Crack Extension from Thin Films to Underlying Substrates**

In part I [1] of this series, it was reported that surface cracks were observed after the powder compact, infiltrated with a Zr-nitrate precursor, was dried. Cracking was not observed when the same bodies were dried after infiltrated with water. The cause of cracking was not understood, but cracking could be avoided for the case of the Zr-nitrate precursor infiltration by pre-strengthening [1] the powder compact. Pre-strengthening was accomplished by forming small necks between touching particles via evaporation-condensation prior to precursor infiltration and drying. In the current work, surface cracking of the polysilazane infiltrated bodies was observed after the first cycle of pyrolysis despite the use of pre-strengthened powder compacts. The cause of surface cracking during pyrolysis, and that of the mysterious surface cracking associated with drying bodies infiltrated with Zr-nitrate precursor, was made self evident when some cracks formed during pyrolysis of a thick surface coating of polysilazane were observed to continue into the powder compact, despite the used of pre-strengthened powder compacts.

Unlike the Zr-nitrate precursor, polysilazane is very viscous at room temperature. Thus, when the infiltrated powder compact is removed from its hot (150 °C) polysilazane bath and cooled, a thick coating of precursor is left on the surface. As shown in Fig. 9(a) the coating contains multiple cracks after pyrolysis. Some of these cracks bifurcate along the interface between the coating and powder compact, while a smaller fraction extend into the powder compact. Fig 9(b) shows a portion of the surface of a representative powder specimen after the pyrolyzed precursor layer was removed. As shown, a similar mud-cracking appearance develops but the distance between the multiple cracks on the powder compact is much larger than that for the coating. Also, the cracks within the powder compact only extend to a given depth and tend to propagate parallel to the surface as shown in Fig. 10. This type of crack path is well described by Evans et al. [10] for cracking from thin films. It is caused by the crack seeking a path that minimizes its shear loading at the crack front ( $K_{II} \rightarrow 0$ ). Experiments showed that cracks within the powder compact could be avoided if the precursor layer was removed prior to pyrolysis. All of these observations strongly suggest that the cracks observed in the powder compact after pyrolysis were caused by stresses within the precursor coating.

The conditions for crack extension in thin films under residual, biaxial tension is well known. [10-13] In our case, the tensile stresses arise due to the constrained shrinkage of the precursor film, first during drying, and then, during pyrolysis. The fact that a precursor film is left on the powder compact surface after intrusion was not visually evident for the Zr-nitrate precursor, which is relatively fluid and thus would produce a very thin film, but very evident for the viscous polysilazane.

When thin films contain residual, biaxial tensile stresses, the underlying substrate is in a state of compression. When the film thickness,  $t$ , is very small compared to the substrate thickness, the stresses within the substrate are very small and neglected. Cracking within the film occurs when a small crack,  $c$ , which is much less than the film thickness,  $c < h$ , first extends across the film thickness, viz.,  $c \rightarrow h$ . For this case, the crack is treated as if it were within an infinite body under tension,  $\sigma_r$ . Its extension is thus governed by the usual strain energy release rate function,  $G = Y \frac{\sigma_r^2}{E^*} c > G_c^f$ . Where  $E^*$  and  $G_c^f$  are the elastic modulus (either plane strain conditions or plane stress) and critical strain energy release rate of the film material;  $Y$  is a numerical constant. When the crack encounters the interface between the film and substrate, it can either stop at the interface ( $G_c^s$  and  $G_c^i > G_c^f$ ), bifurcate along the interface ( $G_c^i < G_c^f < G_c^s$ ) or extend into the substrate ( $G_c^s < G_c^f < G_c^i$ ).  $G_c^i$  and  $G_c^s$  are the critical strain energy release rates of the interface and substrate, respectively. For the latter condition, the crack only extends into the substrate for a short distance because its strain energy release rate function rapidly decreases, [13] viz., the residual stresses are localized to the film.

Once the crack spans the film thickness ( $c \approx h$ ) and either stops, extends along the interface or into the substrate, it then traverses the film ( $a \gg h$ ); this type of crack extension is generally called tunneling. The condition for tunneling requires that  $G^t = Z \frac{\sigma_r^2}{E} h > G_c$ , where  $G_c$  is the critical strain energy release rate of the film, interface or substrate and  $Z$  is a numerical constant. The strain energy release rate function for crack extension across the film,  $c \rightarrow h$ , is always larger than that for tunneling. Since the condition for crack tunneling does not depend on the crack length,  $c$ , but depends on the film thickness,  $h$ , it can be shown that neither crack extension within the film ( $c \rightarrow h$ ) nor tunneling ( $c \gg h$ ) can occur when the film thickness is less than a crucial value,  $t < t_c$ .

Thus, as schematically shown in Fig. 11, crack extension from the precursor film into the powder compact (substrate for the precursor film) can be avoided by either

reducing the value of the strain energy release rate function for crack tunneling ( $G^t$ ) by decreasing the film thickness, or by increasing the critical strain energy release rate ( $G_c^s$ ) for the powder compact. In practice, the cracking of the powder compact during polysilazane pyrolysis was avoided by removing the film prior to pyrolysis, whereas, before the problem was fully understood, it was avoided during drying of the Zr-nitrate precursor by strengthening the powder compact prior to infiltration. The critical thickness that induces cracking of thin, precursor films produced from  $ZrO_2$  precursors on sapphire substrates is  $\approx 0.1 \mu m$ . [14]  $ZrO_2$  precursor films of this thickness on  $Si_3N_4$  powder compacts would have gone unnoticed in the current work.

## REFERENCES

- [1] W. C. Tu and F. F. Lange, "Liquid Precursor Infiltration and Pyrolysis of Powder Compacts: I, Kinetics Studies and Microstructure Development," to be published.
- [2] D.C.C. Lam, F.F. Lange, and A.G. Evans, "Mechanical Properties of Partially Dense Alumina Produced from Powder Compacts," to be published.
- [3] T. Nose and T. Fujii, "Evaluation of Fracture Toughness for Ceramic Materials by a Single-Edge-Pre-cracked-Beam method," J. Am. Ceram. Soc., 71[5], 328-333 (1988).
- [4] H. Tada, P.C. Paris, and G. R. Irwin,, The Stress Analysis of Cracks Handbook, Del. Research, St Louis, Mo.
- [5] W. C. Tu and F. F. Lange, unpublished work.
- [6] C. W. Li and J. Yamanis, "Super-Tough Silicon Nitride with R-Curve Behavior," Ceram. Eng. Sci. Proc., 10 [7-8] 632-45 (1989).
- [7] I. E. Reimanis, J. J. Petrovic, H. Suematsu, T. E. Mitchell, and O. S. Leung, "The Mechanical Properties of A Novel  $Si_3N_4$ -Amorphous  $Si_3N_4$  Composite," Mat. Res. Soc. Symp. Proc., Vol. 287, 499-504 (1993).
- [8] G. Pezzotti, " $Si_3N_4/SiC$  Platelet Composite without Sintering Aids: A Candidate for Gas Turbine Engines," J. Am. Ceram. Soc., 76 [5] 1313-20 (1993).
- [9] Y. Okamoto, J. Leuji. et.al., "Creep Deformation of Yttria-Stabilized Tetragonal Zirconia (Y-TZP)," in Advances in Ceramics 24B, Edited by S. Somiya, N. Yamamoto, et al., 565-71 (1988).
- [10] J. Hutchison and Z. Suo, "Mixed Mode Cracking in Layered Materials," Vol. 28 Advances in Applied Mechanics, edited by J. W. Hutchison and T. Y. Wu (1991)

- [11] A. G. Evans, M. D. Drory, and M. S. Hu, "The Cracking and Decohesion of Thin Films," *J. Mater. Res.*, 3, 1043-1049 (1988).
- [12] M. D. Thouless, "Crack Spacing in Brittle Films on Elastic Substrate," *J. Am. Ceram Soc.*, 72 [7] 2144-46 (1990).
- [13] Y. Tao, Z. Suo and A. G. Evans, "Thin Film Cracking and The Roles of Substrate and Interface," *Int. J. Solids Structures*, Vol. 29 [21] 2639-2648 (1992).
- [14] K. T. Miller, F. F. Lange, and D. B. Marshall, "The Instability of Polycrystalline Thin Films: Experiment and Theory," *J. Mat. Res.* 1 [5] 151-60 (1990).

**Table I. Properties of Liquid Precursors**

	Zr(Y)-nitrate	Polysilazane
Physical appearance	liquid	viscous liquid
viscosity (Poise)	1	20 @100°C 1 @150°C
specific gravity (g/c.c)	1.6	1.0
ceramic yield (wt%)	35	58-63
ceramic composition	Zr(Y)O <sub>2</sub>	Si <sub>3</sub> N <sub>4</sub> SiC SiO <sub>2</sub> C

## Figure Captions

- Figure 1 TGA results for polysilazane precursor.
- Figure 2 Relative density vs. number of cycles of infiltration for  $\text{Si}_3\text{N}_4$  powder compacts infiltrated with Zr(Y)-nitrate and polysilazane.
- Figure 3 Microstructure developments of a  $\text{Si}_3\text{N}_4$  powder compact cyclically infiltrated with polysilazane and heated to (a)  $1250^\circ\text{C}$ , (b)  $1400^\circ\text{C}$ , and (c)  $1500^\circ\text{C}$  in  $\text{N}_2$  for 5 hours.
- Figure 4 TEM micrographs of pyrolyzed polysilazane in  $\text{Si}_3\text{N}_4$  powder compacts heated to (a)  $1250^\circ\text{C}$  and (b)  $1500^\circ\text{C}$ .
- Figure 5 Fracture toughness vs. fractional porosity filled for liquid precursors infiltrated  $\text{Si}_3\text{N}_4$  powder compacts.
- Figure 6 Fracture strength vs. porosity for liquid precursors infiltrated  $\text{Si}_3\text{N}_4$  powder compacts.
- Figure 7 SEM micrographs of the fracture surfaces of polysilazane infiltrated  $\text{Si}_3\text{N}_4$  powder compacts of different heat treatments: a)  $1250^\circ\text{C}$  and b)  $1500^\circ\text{C}$ .
- Figure 8 SEM micrograph showing the fracture path of a polysilazane infiltrated  $\text{Si}_3\text{N}_4$ .
- Figure 9 Optical micrographs showing the mud-cracking appearances for (a) the precursor coating and (b) the surface of a powder disk after precursor pyrolysis.
- Figure 10 Optical micrographs showing the crack profiles in the cross-section of a damaged powder compact.
- Figure 11 A schematic diagram showing the effect of substrate fracture toughness on the cracking of thin film/substrate materials under residual stresses.

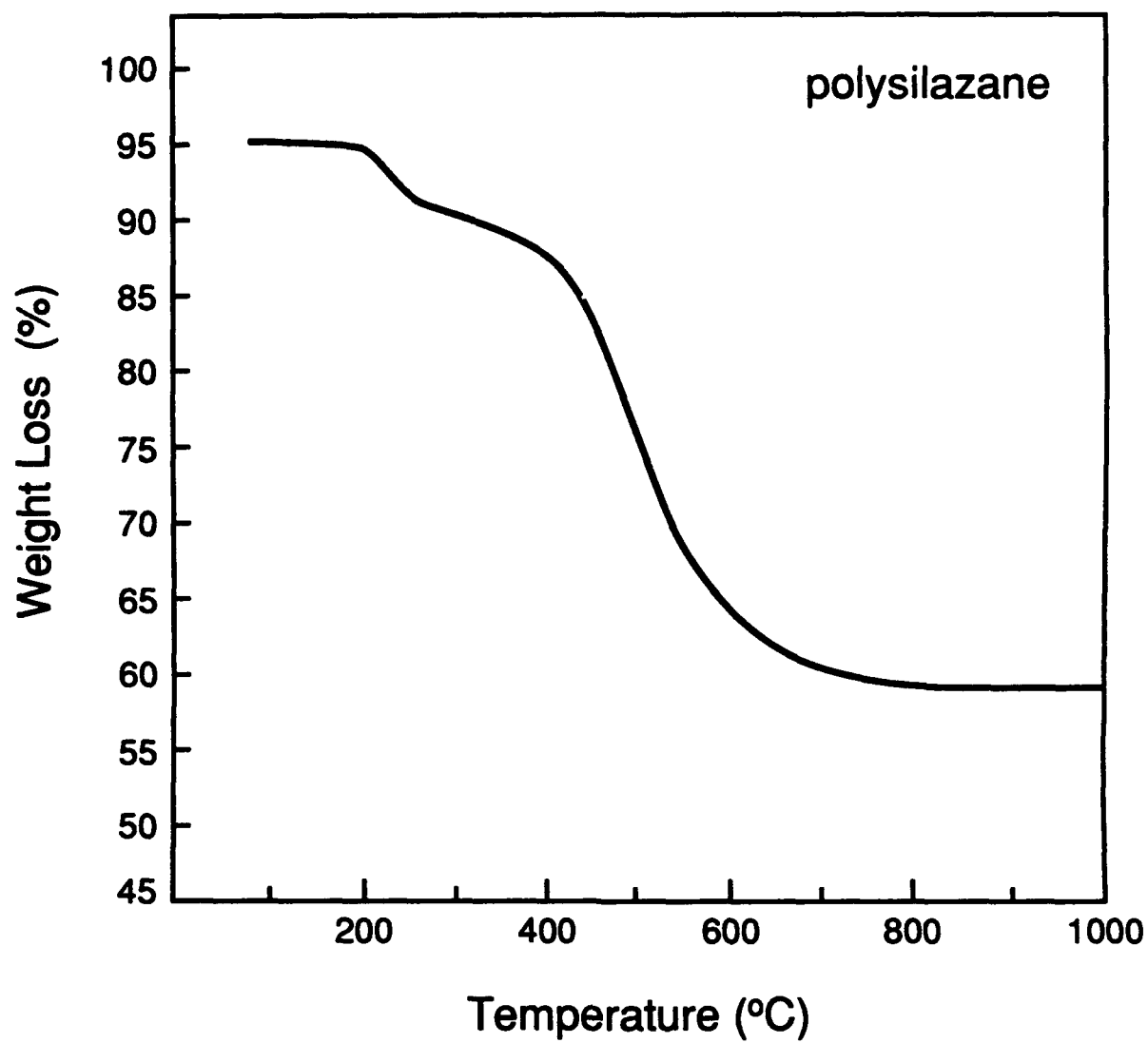


Figure 1

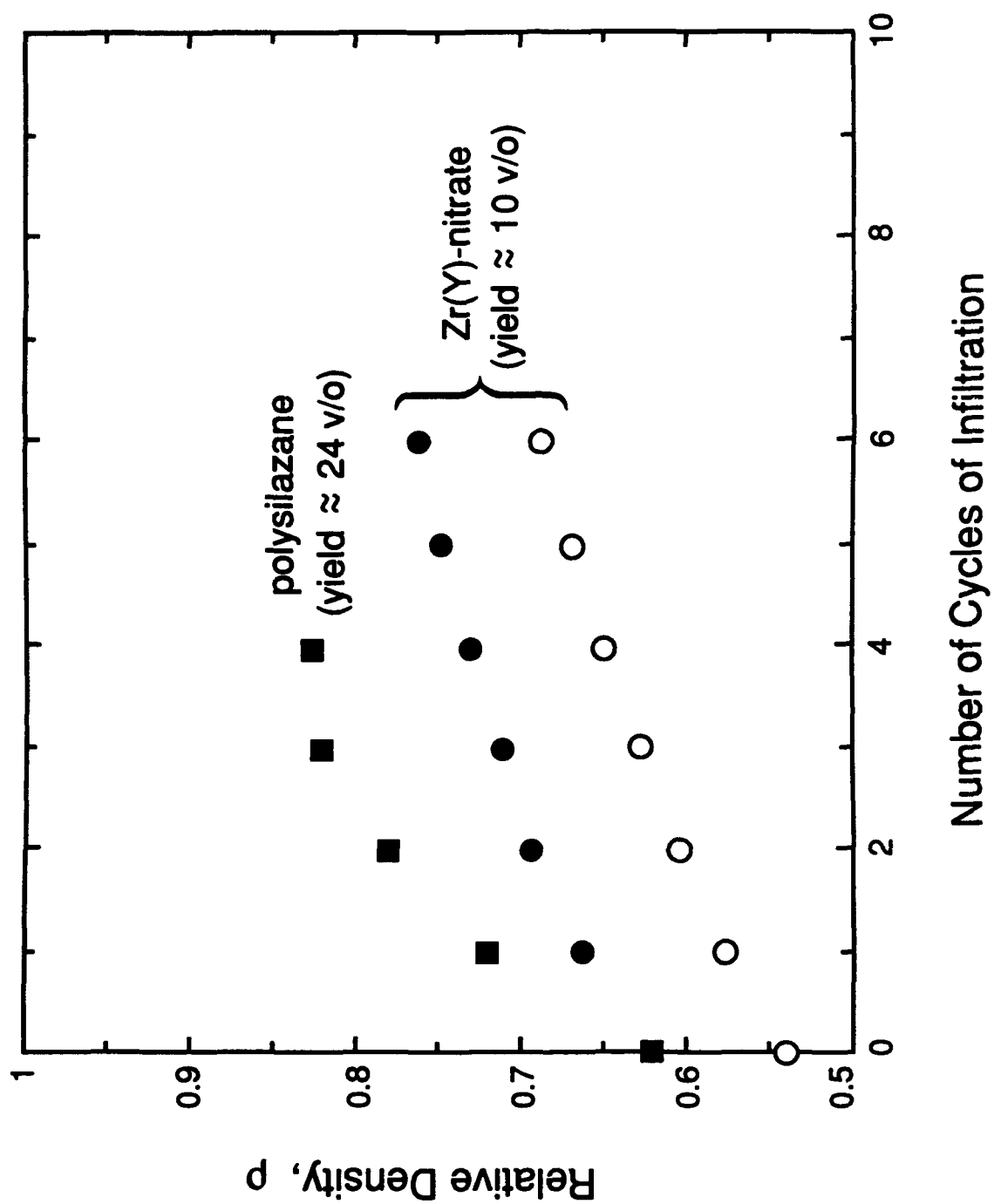


Figure 2



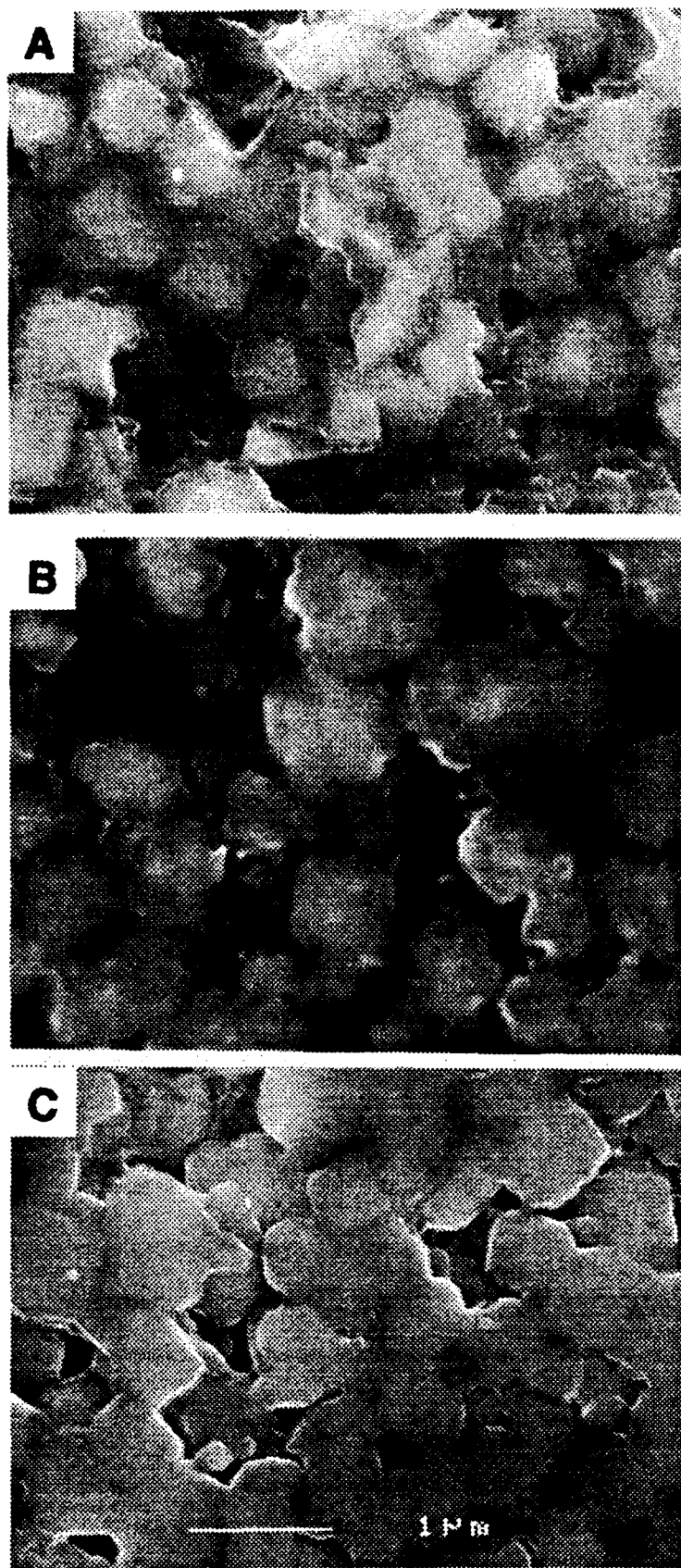


Figure 3

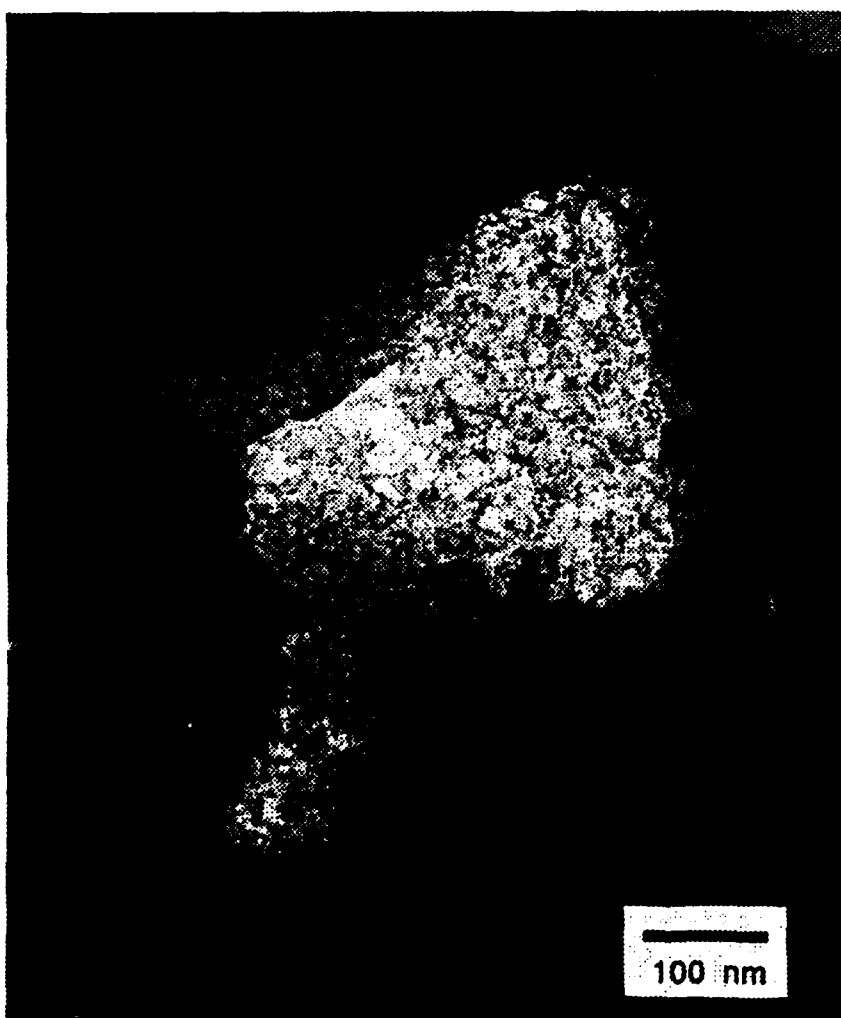


Figure 4 (a)



**Figure 4 (b)**

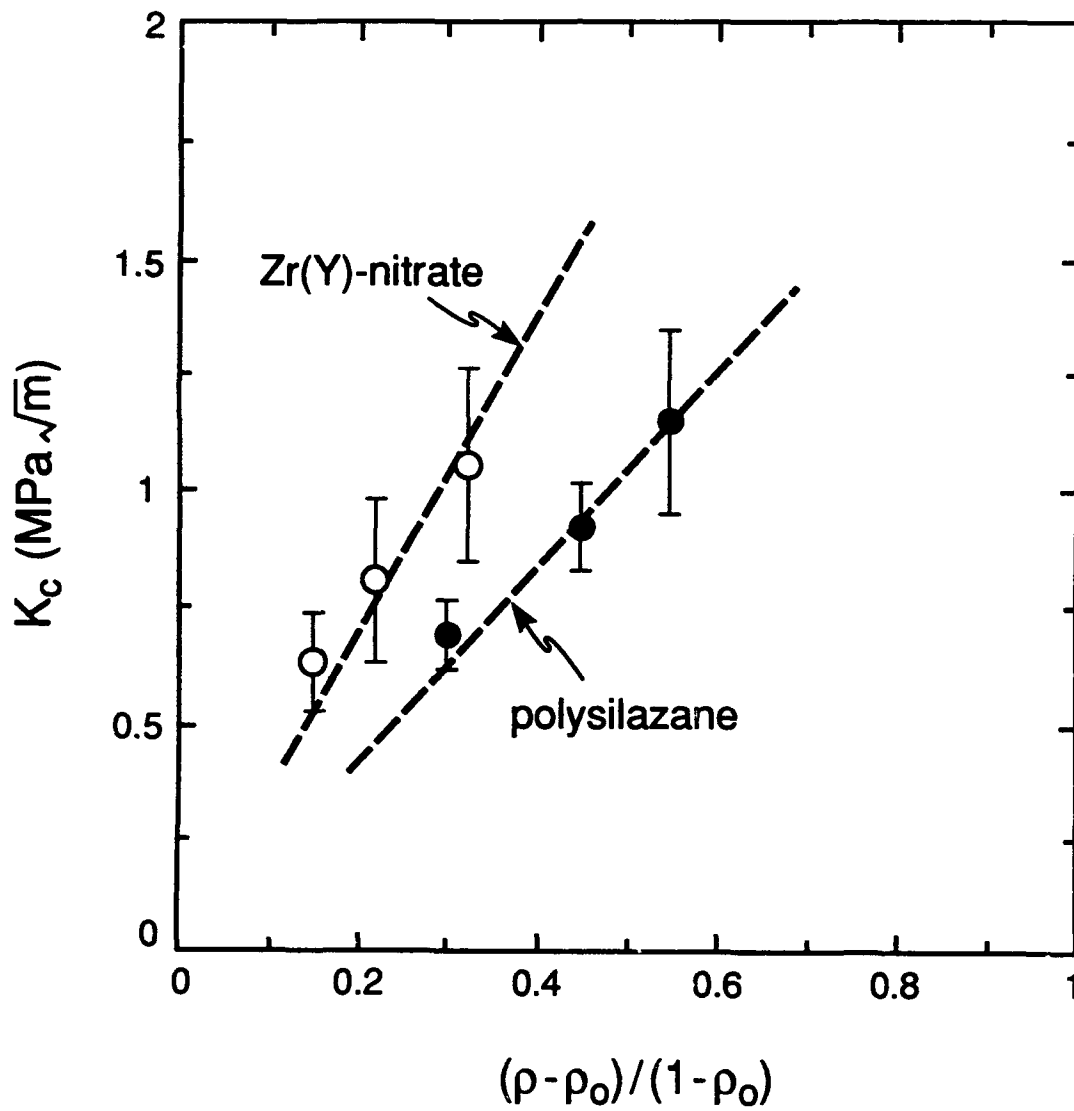


Figure 5

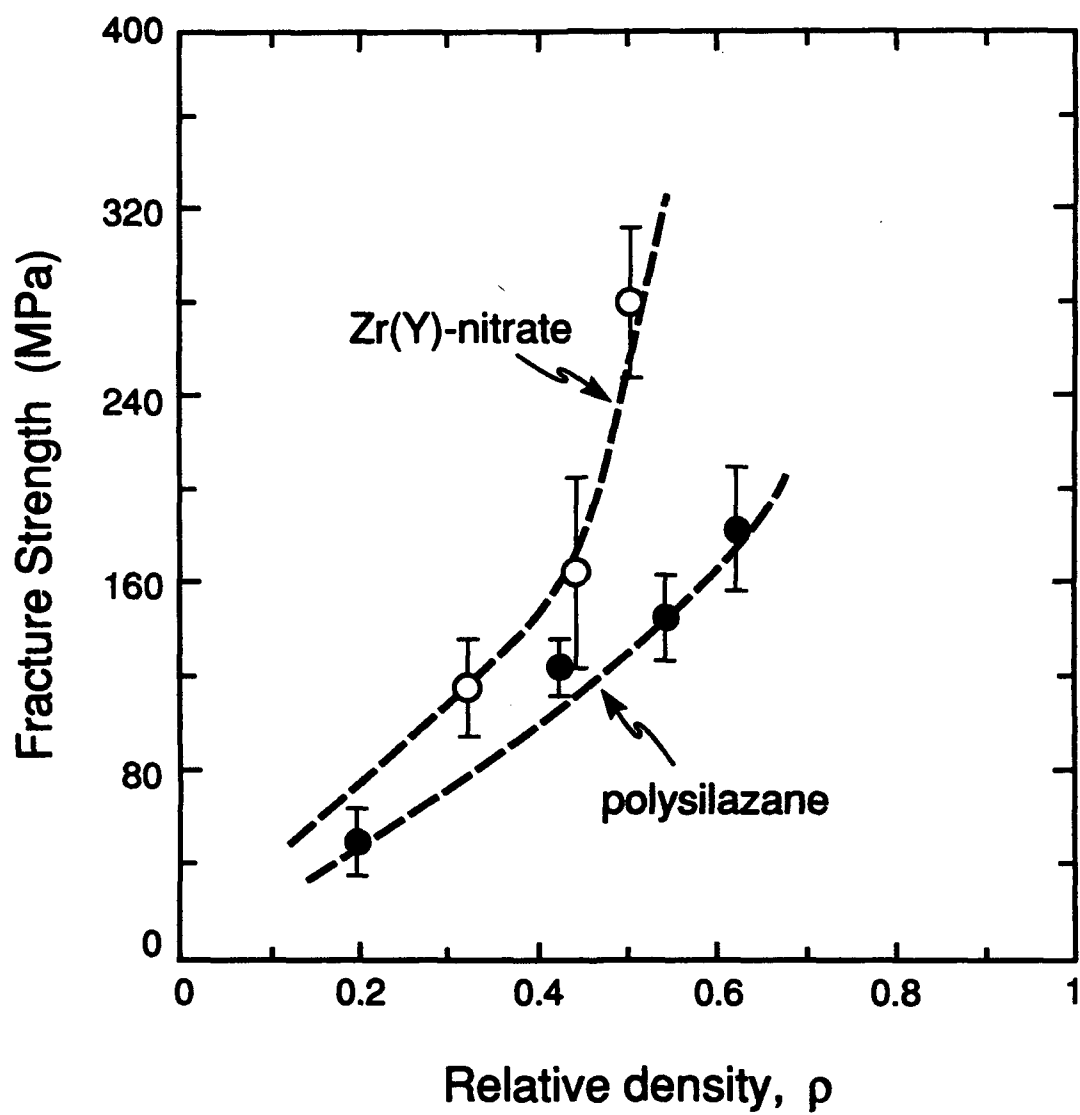
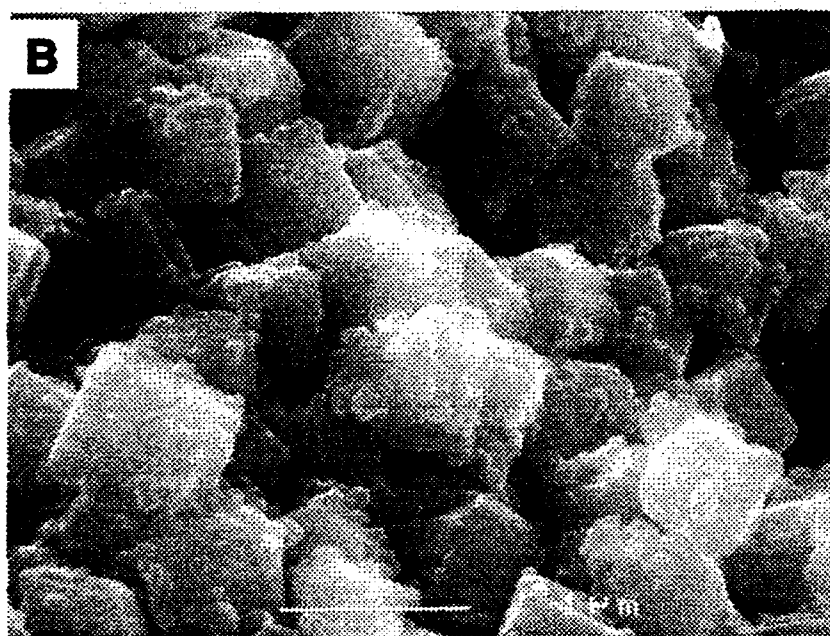
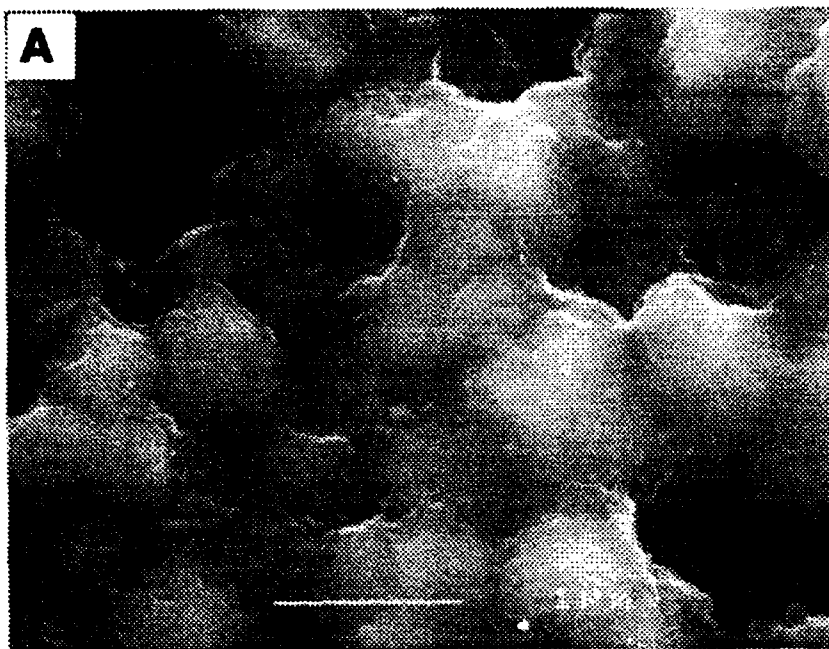
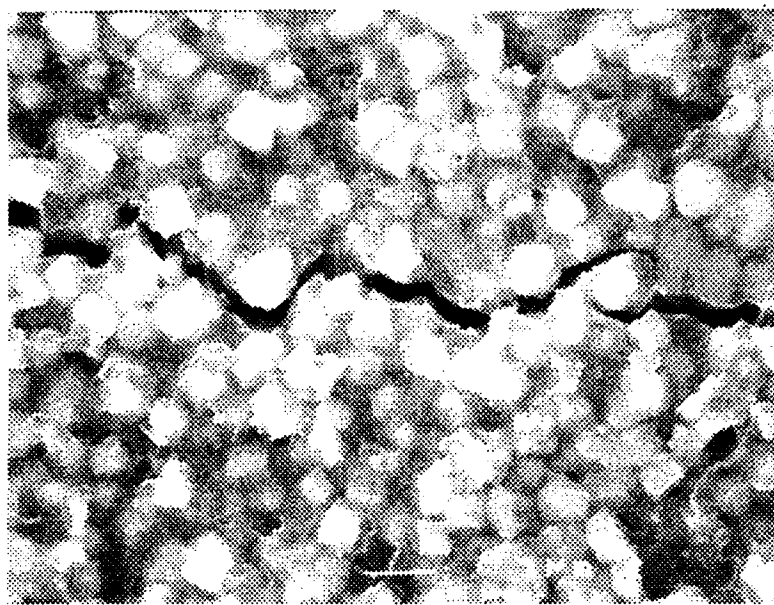


Figure 6



**Figure 7**



**Figure 8**

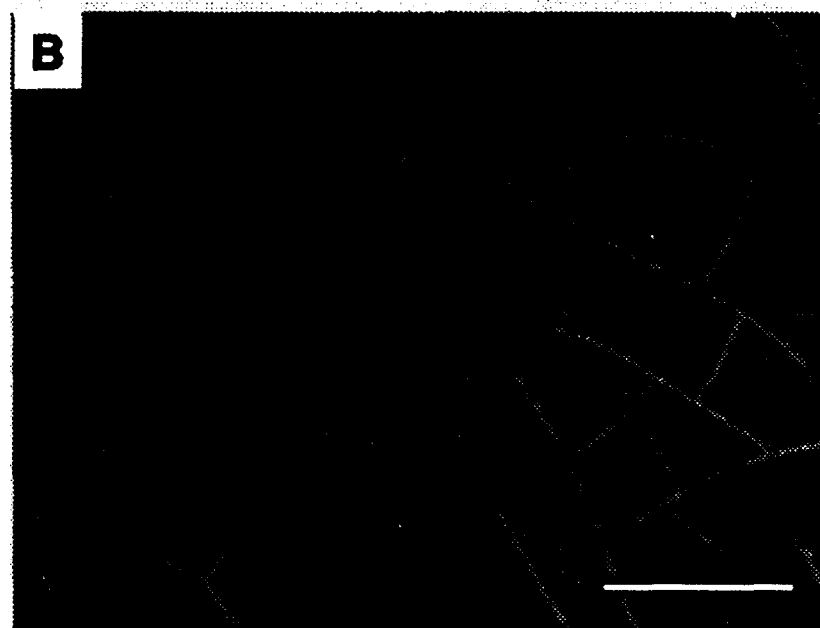
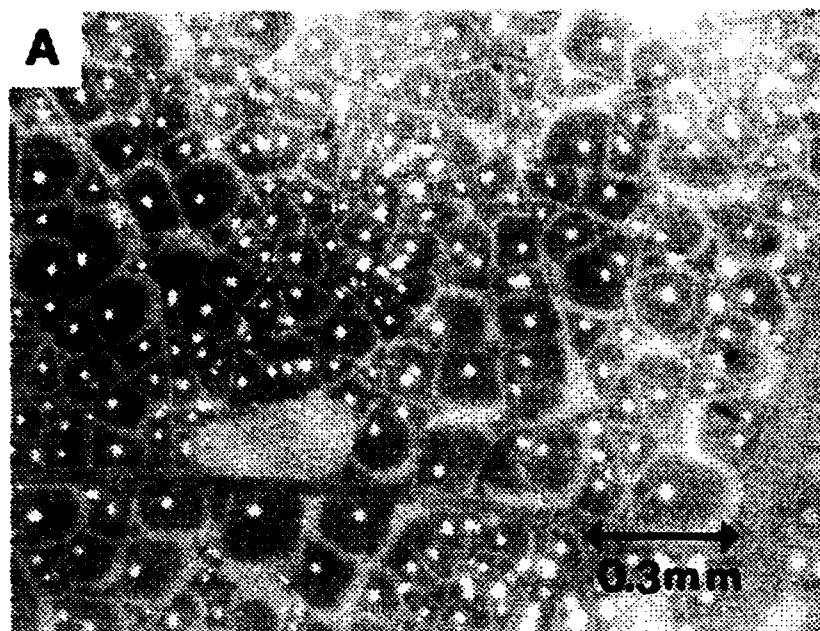


**Figure 9**



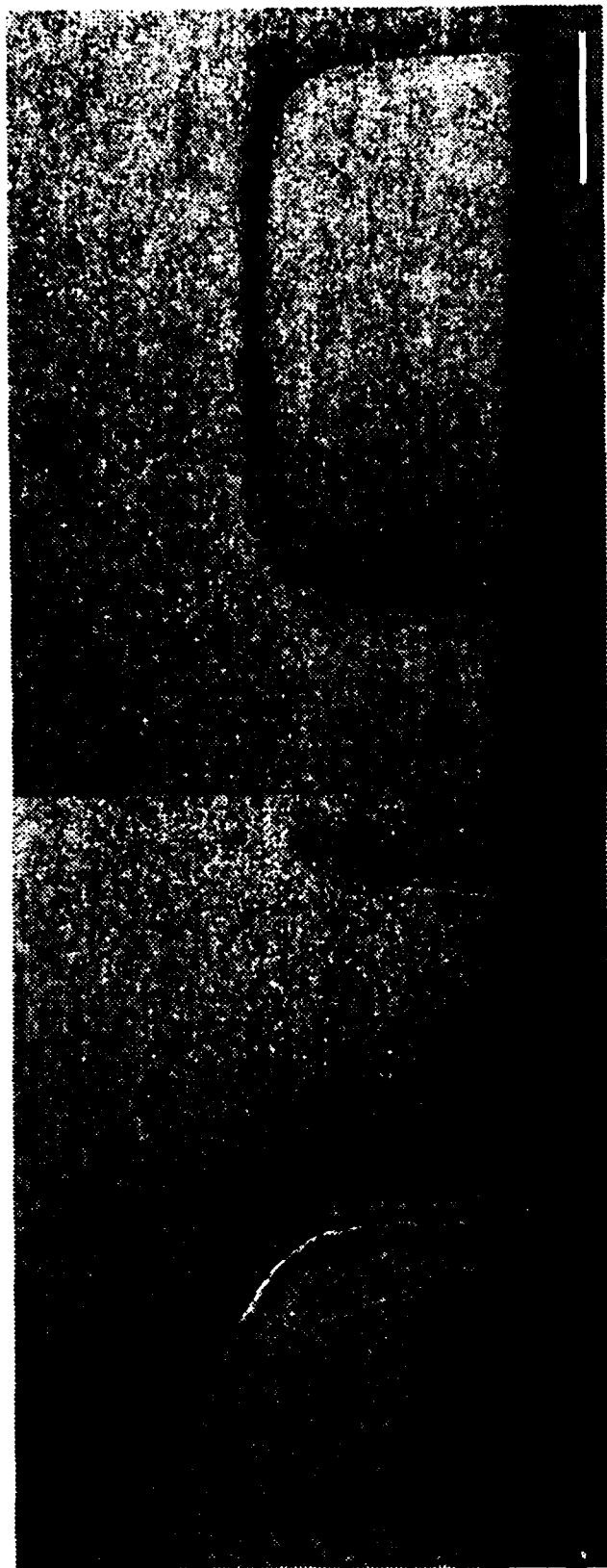


Figure 10

Strain Energy Release Rate,  $= \sigma_R^2 h / E_f$

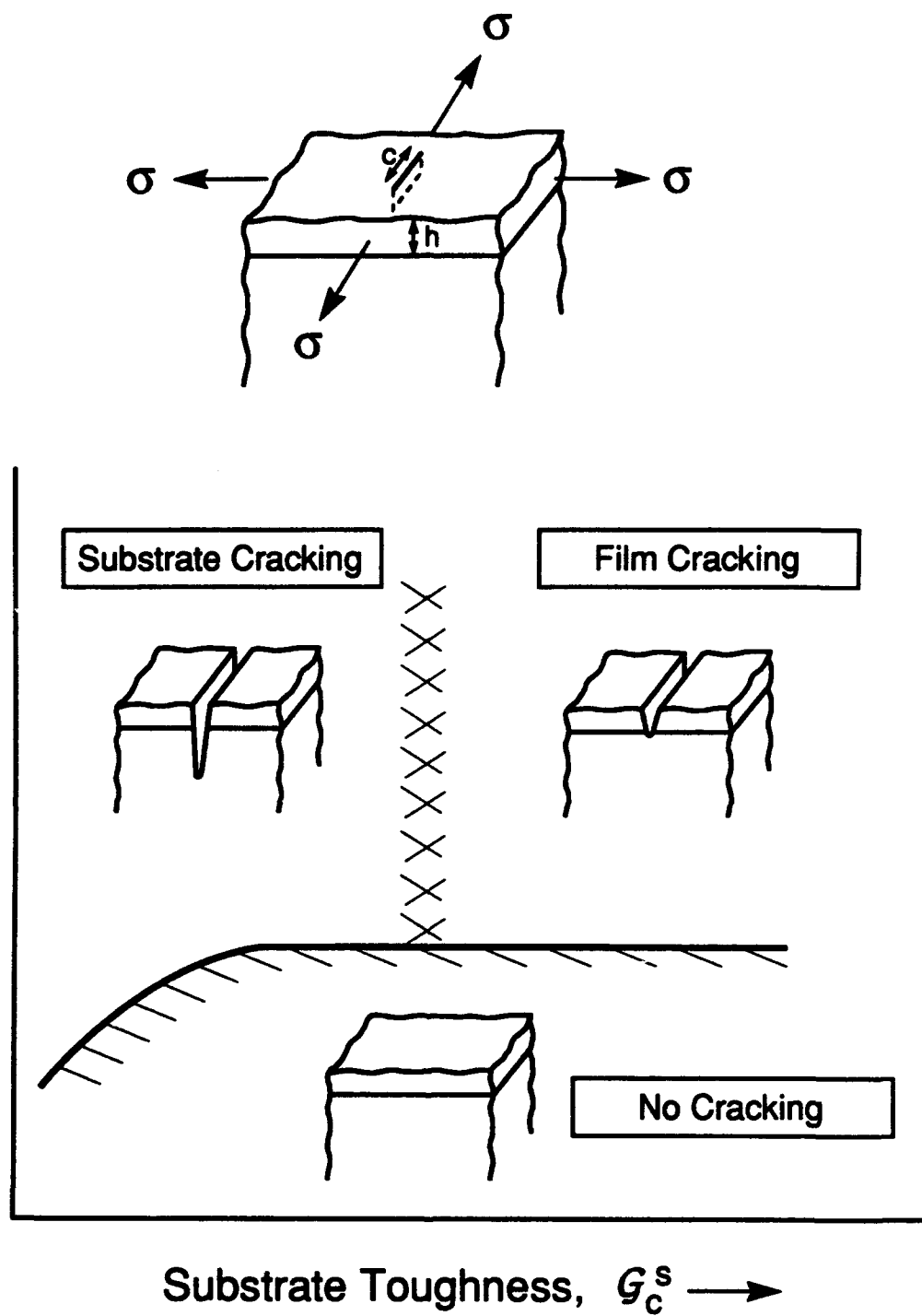


Figure 11

## Influence of Interparticle Forces on the Rheological Behavior of Pressure-Consolidated Alumina Particle Slurries

Bhaskar V. Velamakanni,<sup>\*,†</sup> Fred F. Lange,<sup>\*</sup> Frank W. Zok,<sup>\*</sup> and Dale S. Pearson

Materials Department, University of California, Santa Barbara, California 93106

The stress relaxation behavior of alumina powder compacts, consolidated from aqueous slurries by pressure filtration, is reported. The interparticle forces were controlled prior to consolidation by changing the pH from 3 to 9 and by adding different amounts of salt (0.1 to 2.0M  $\text{NH}_4\text{Cl}$ ) to slurries maintained at pH 4. Disk-shaped bodies were rapidly compressed to an axial strain of 2%, and the resulting stress relaxation data were monitored as a function of time. For bodies formed from dispersed slurries (pH  $\leq 4$  without added salt), the stress relaxation behavior consisted of an irreproducible mixture of plastic and elastic response. The initial stress and the stress retained after long relaxation periods were highest for bodies formed with flocced slurries (pH 9). For bodies formed with coagulated slurries (pH 4 with added salt), the initial stress increased with the addition of 0.1 to 0.5M salt, but the bodies behaved plastically, with more than 90% of the initial stress relaxing within a short period. These results are consistent with a short-range, repulsive interparticle force that lowers the attractive force between particles. They also suggest that interparticle forces in consolidated bodies can be controlled in a way that should prove useful in preventing damage that occurs during processing and reshaping operations.

### I. Introduction

WE HAVE recently<sup>1</sup> shown that weakly attractive interparticle potentials can be achieved in aqueous  $\text{Al}_2\text{O}_3$  slurries. The method begins by adjusting the pH to produce highly repulsive interparticle forces (pH  $\leq 4$ ) in agreement with the Derjaguin-Landau-Verwey-Overbeek (DLVO) theory. Indirect evidence suggested that when an indifferent electrolyte was added to a highly dispersed slurry, a very short-range repulsive potential was developed, as counterions decreased the magnitude of the long-range repulsive electrostatic potential to allow particles to become attractive. This short-range interparticle potential is currently believed to be due to a hydrated layer, similar to that found for mica surfaces<sup>2,3</sup> and clay surfaces.<sup>4</sup> Viscosity measurements indicate<sup>1</sup> that, beyond a certain salt concentration ( $\sim 0.1\text{M}$ , sufficient to lower the repulsive barrier so that particles can coagulate), an attractive network is formed with a strength that increases with salt content. At higher concentrations ( $> 1.5\text{M}$ , where the electrostatic repulsive potential is negligible) the network strength is no longer increased with further additions of salt. The strength of these networks, as determined by viscosity, sedimentation, yield stress, and packing pressure measurements, is considerably lower than that of networks formed at the isoelectric point (pH  $\sim 9$ ). From these

observations, it was concluded that particles in the salted slurries are prevented from contacting each other by the short-range potential. To distinguish the two attractive networks, we call networks formed by adding salt at low pH "coagulated," and networks formed by changing the pH to the isoelectric point "flocced."

Unlike the flocced slurry, where particles form a very strong network, the short-range, repulsive interparticle forces in a coagulated slurry form a weak, but nontouching, network and hence act as a "lubricant" that allows particles to easily rearrange and pack to a high density.<sup>1</sup> Consequently, coagulated slurries can be packed to high densities by centrifugation without particle segregation.<sup>5</sup> Sequential centrifugation of two different coagulated slurries was used recently in a unique way to fabricate a layered, toughened material.<sup>6</sup> In addition, unlike dispersed slurries,  $\text{Al}_2\text{O}_3$  bodies formed from coagulated slurries retain their shape after consolidation, but can be reshaped by plastic flow. In many respects, coagulated slurries and the bodies they form have rheological characteristics similar to clay systems.

The purpose of the present work is to characterize the rheological behavior of water-saturated bodies consolidated by pressure filtration from *dispersed*, *flocced*, and *coagulated*  $\text{Al}_2\text{O}_3$  slurries. Stress relaxation experiments are commonly carried out in conventional rheological instruments to determine the yield strength of slurries formed with attractive potentials.<sup>7</sup> Uniaxial stress relaxation experiments were performed with a servo-hydraulic mechanical testing machine conventionally used to determine the creep behavior of solid materials.

### II. Experimental Methods

#### (1) Slurry Preparation

Aqueous slurries containing 20 vol%  $\alpha$ -alumina powder (Sumitomo Chemical Company, New York, Grade APK-50) (0.2- $\mu\text{m}$  mean particle diameter as described elsewhere<sup>8</sup>) were used in this study. All slurries were prepared by first dispersing the powder in deionized water at pH 4. At this pH, the zeta potential of alumina is sufficiently large to keep the particles dispersed.<sup>9</sup> A high shear-field, obtained by immersing an ultrasonic horn in the slurry, was used to break apart agglomerated particles. The pH was then adjusted with analytical grade  $\text{HNO}_3$  or  $\text{NH}_4\text{OH}$ , and, if salt was used, analytical grade  $\text{NH}_4\text{Cl}$ .

#### (2) Pressure Filtration

Pressure filtration was used to prepare the consolidated bodies. A predetermined volume of slurry was poured into a cylindrical filtration die, 2.54 cm in diameter, to make consolidated bodies which were  $\sim 1$  cm thick after filtration.<sup>9</sup> A pressure of 14.6 MPa was applied to the plunger with an automated hydraulic press. The average particle packing density of consolidated bodies made from dispersed (pH  $< 4$ ) slurries and flocced (pH 8 to 9) slurries were 62% and 54% of theoretical, respectively, prior to fluid removal. As described elsewhere,<sup>8</sup> the packing density of the consolidated bodies decreased from 62% to 54% as the pH increased from 5 to 8. For the coagulated slurries, the packing density was 62%.<sup>1</sup> While removing samples from the

G. L. Messing—contributing editor

Manuscript No. 194935. Received January 18, 1993; approved June 18, 1993.  
Supported by a Grant from the Office of Naval Research under Contract No. N00014-90-J-1441.

<sup>\*</sup>Member, American Ceramic Society.

<sup>†</sup>Now with Corporate Research Processing Technology Laboratory, 3M Company, St. Paul, MN 55144-1000.

die and during subsequent handling, extreme care was exercised to minimize any distortion. After measuring the dimensions, the saturated bodies were immediately sealed in a zip-lock plastic bag containing a moist paper towel. The presence of the towel ensured that there was sufficient humidity (100%) in the bag to prevent the body from drying during testing and storage. (Although stress relaxation experiments were performed within hours after the samples were sealed in the bag, the bodies were found to retain their rheological characteristics for at least one week.)

### (3) Stress Relaxation Measurements

The stress relaxation experiments were performed within a servo-hydraulic mechanical testing machine (MTS Model 850, Minneapolis, MN). The machine was equipped with a micro-profiler for controlling piston displacement, a personal computer for data acquisition, and a 890-N (200-lb) stationary load cell. The cylindrical specimen, contained within the plastic bag, was deformed between two platens with the machine in the displacement control mode. After the consolidated body was placed on the bottom platen, the piston was carefully raised to bring the top portion of the consolidated body in contact with the upper platen. A small compressive load of 0.5 to 2 N was applied to the sample to ensure that both platens were in good contact with the specimen.

An experiment consisted of applying a 2% compressive strain at a strain rate of  $0.17 \text{ s}^{-1}$ . The nominal time to accomplish the loading was 0.12 s. The stress was calculated assuming that the area of the specimen did not change during straining. At least two consolidated bodies were fabricated and tested for each pH and/or salt concentration. The experiment was terminated when the load relaxed to either zero or an apparent saturation value. Some experiments were conducted by applying further increments of strain, 2%, to the same specimen.

## III. Results

A preliminary analysis indicated that the stress relaxation data could not be described by a single exponential function. As a result, the rheological properties of the bodies are characterized here by two experimentally determined parameters: the peak stress,  $\sigma_p$ , obtained at the end of the initial rapid straining period, and the saturation stress,  $\sigma_s$ , obtained from the period where the stress appears constant. A  $\pm 10\%$  scatter in determining  $\sigma_s$  was observed.

### (1) Influence of pH

The first series of stress relaxation experiments were made on the consolidated bodies made from dispersed and flocced slurries. Although the stress relaxation behavior of samples made from flocced slurries was reproducible, the behavior of consolidated bodies made from dispersed slurries (at any pH  $\leq 4.5$ ) was erratic. Neither the shape of the stress relaxation curve nor the values of  $\sigma_p$  and  $\sigma_s$  were reproducible. The rheological behavior ranged from viscous flow (small  $\sigma_p$  and  $\sigma_s \rightarrow 0$ ) to elasticlike behavior (large  $\sigma_p$  and  $\sigma_s > 0$ ). Two possible reasons for this variation are discussed below.

Reproducible data were obtained for bodies prepared from dispersed slurries by adding  $0.1 \text{ M NH}_4\text{Cl}$  to the slurry prior to consolidation. Adding salt did not affect either the stress relaxation behavior or the final packing density of bodies prepared from slurries at pH values near the isoelectric point.<sup>1</sup>

Figures 1(a) and (b) show the average peak stress ( $\sigma_p$ ) and the ratio of the saturation to peak stress ( $\sigma_s/\sigma_p$ ) as a function of pH for bodies consolidated with slurries containing  $0.1 \text{ M NH}_4\text{Cl}$ . These data show a transition between plastic behavior (small  $\sigma_p$ ,  $\sigma_s/\sigma_p \rightarrow 0$ ) to elasticlike behavior (large  $\sigma_p$ ,  $\sigma_s/\sigma_p > 0$ ) between a pH of 4 and 5.

### (2) Influence of Electrolyte Concentration at pH 4

In another study,<sup>10</sup> we report that both the viscosity and the yield stress increase with increasing salt concentration in coagulated slurries. In the present experiments, a similar behavior

was found for the consolidated bodies. Although there was considerable scatter in the experimental measurements, the average  $\sigma_p$  increases rapidly with salt concentration between 0.1 and  $0.5 \text{ M}$  (as shown in Fig. 2). It was also observed that the ratio of relaxed stress increased from  $\approx 0$  to  $0.1 \pm 0.05$  over the same range of salt concentration ( $0.1 \text{ M}$  to  $0.5 \text{ M}$ ) and remains constant for salt concentrations  $\geq 0.5 \text{ M}$ . These data confirm that the strength of the particle network is enhanced when the salt concentration exceeds  $0.1 \text{ M}$ , but over 90% of the peak stress is quickly relaxed.

### (3) Sequential Straining Experiments

Figure 3(a) shows the relaxation behavior of a body consolidated from a slurry at pH 3.8 and containing  $0.1 \text{ M NH}_4\text{Cl}$ . The sample was sequentially subjected to 2 strain cycles of 2% each. As shown, the relaxation occurs much more rapidly after the second strain cycle. This body was then subjected to a third cycle (not shown), but no stress increase was observed. Figure 3(b) shows similar trends for a body consolidated from a pH 4 slurry containing  $2 \text{ M NH}_4\text{Cl}$ . These observations show that the behavior is history-dependent, becoming more plastic in subsequent strain cycles.

Figure 4 shows the effect of repeated strain cycles on the stress relaxation behavior of a consolidated body of pH 6 and containing  $0.1 \text{ M NH}_4\text{Cl}$ . After the initial 2% strain, the body relaxes to a saturation stress of  $\approx 30\%$  of the peak stress. However, upon repeated straining, the saturation stress continues to increase. The same behavior was observed for samples subjected to as many as 16 strain cycles of 2% each.

### (4) Influence of Aging

Aging experiments were performed because bodies consolidated from dispersed slurries (without added salt) exhibited erratic stress relaxation behavior. The effect of aging was investigated for bodies made from both dispersed and coagulated slurries after they had been already subjected to one cycle of strain. After the initial stress relaxation experiment, the body (still contained within its plastic bag) was carefully removed from the testing machine and left undisturbed for a predetermined period. Later, the body was tested again. The rheology of the bodies made from coagulated slurries was still plastic after 7 days. In contrast, bodies made from dispersed slurries (pH 4, without salt) that were very plastic during the first strain cycle became elasticlike after only 24 h of aging. Bodies consolidated from coagulated slurries that had been subjected to repeated strain cycles until no stress response was observed (e.g., a specimen similar to that shown in Fig. 3(a)) remained plastic after aging.

## IV. Discussion

The data clearly show that the maximum stress achieved during rapid straining and the amount of stress relaxation depend strongly on the interparticle potentials. Several basic trends are evident. First, bodies formed with coagulated slurries (and some with dispersed slurries) quickly relax after rapid straining, with  $\sigma_s \approx 0$ . In contrast, bodies formed with flocced slurries are capable of supporting a relatively large stress for long periods, despite their lower packing density, i.e., they have a much higher yield strength. Second, it appears that the particle networks of some bodies formed from dispersed slurries become cohesive during either consolidation or aging, and subsequently behave similarly to flocced networks.

Figure 5 schematically illustrates the expected interparticle potential as a function of particle separation for the three types of slurries used in this study. For flocced and dispersed particles (Figs. 5(a) and (b)) the interaction potentials are expected to conform closely to the well-known DLVO theory. They apply to materials near the isoelectric point (pH range of 7 to 9) and at low pH ( $< 4$ ), where the density of positive surface sites is low and high, respectively.

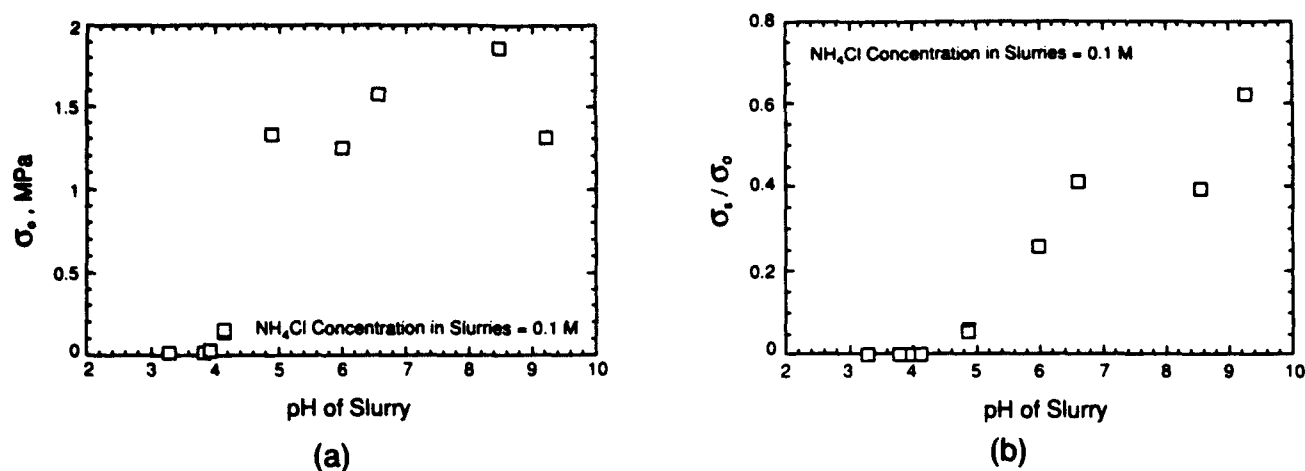


Fig. 1. Plots showing the influence of pH on (a) the peak stress,  $\sigma_0$ , and (b) relaxed stress ratio,  $\sigma_1/\sigma_0$ , for bodies containing 0.1 M NH<sub>4</sub>Cl.

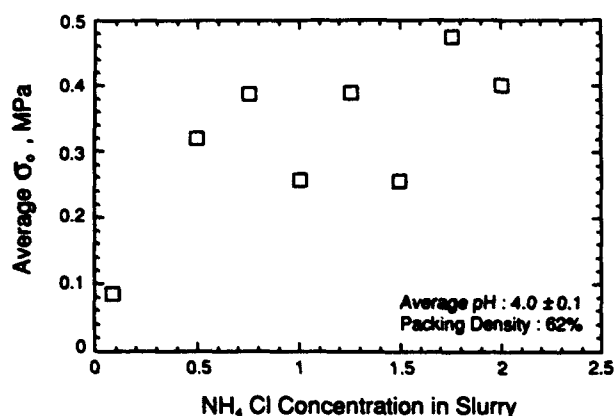


Fig. 2. Plot showing the influence of NH<sub>4</sub>Cl concentration on the peak stress ( $\sigma_0$ ) for bodies consolidated at pH 4.

Particles in a flocced slurry (Fig. 5(a)) are expected to be in contact with each other. This contact and the resulting friction between particles will resist particle rearrangement during consolidation. However, once consolidated to a given packing density, the cohesive network should be capable of supporting a relatively large stress.<sup>11</sup> Beyond the yield stress, particle rearrangement is expected to produce either an increased packing density, if liquid is expelled,<sup>12</sup> or plastic flow, if the liquid volume in the compact remains constant. Unless constrained with hydrostatic pressure, the fracture strength of the flocced bodies can be exceeded prior to plastic flow. The reason for the increase in the apparent yield stress with repeated rapid straining and relaxation testing, which has the appearance of a hardening phenomenon, is currently unknown. A slight increase in particle packing density during each strain cycle could be responsible for this apparent hardening effect.

Particles in a dispersed slurry repel one another. When pushed together during consolidation, their mutual repulsive force (Fig. 5(b)) will act as a "lubricant," easing rearrangement and leading to a high packing density that is relatively pressure-

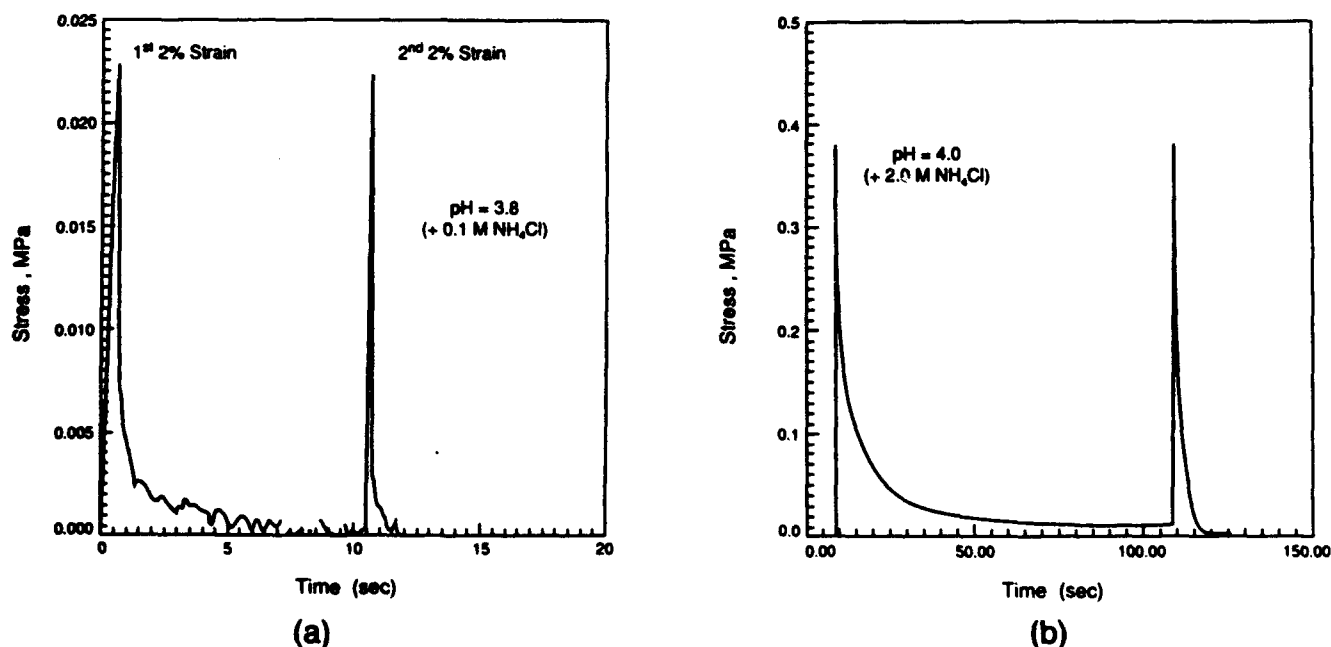


Fig. 3. Stress relaxation behavior for two loading cycles, each with 2% strain: (a) body consolidated from a pH 3.8 slurry containing 0.1 M NH<sub>4</sub>Cl and (b) body consolidated from a pH 4 slurry containing 2 M NH<sub>4</sub>Cl.

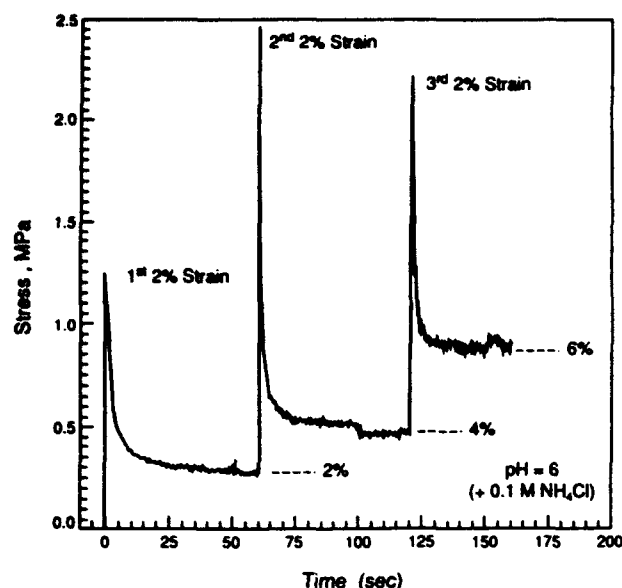


Fig. 4. Stress relaxation behavior for three successive loading cycles, each with 2% strain, for a body consolidated from a slurry at pH 6 containing 0.1 M  $\text{NH}_4\text{Cl}$ .

insensitive. If the repulsive interparticle potential persists after particle packing, then the body is expected to still flow, although with a much higher viscosity relative to the slurry. On the other hand, once a stable packing arrangement has been achieved, the applied force between particles can be increased to exceed the repulsive interparticle force if the body is constrained from flow (e.g., within a die cavity). If this occurs, the particles will be "pushed" into the primary minimum. Under these conditions, the particles will form a touching and strongly cohesive network with flow properties similar to that described above for flocced bodies.

Kuhn *et al.*<sup>11</sup> have shown that when pressure is applied to a powder compact, the force between pairs of particles within a network exhibits a wide range of values. That is, some particles are not stressed while others support a larger than average portion of the applied pressure. Thus, only a fraction of the particles in a dispersed slurry are expected to be pushed into the primary minimum. The remaining particles will still be on the repulsive side of the DLVO maximum. Thus, the rheology of a

body formed from a dispersed slurry will depend on the fraction of particles in the primary minimum which should be a strong function of the consolidation conditions (magnitude of applied pressure, period of pressure application, etc.).

Other effects, generally attributed to aging, can also cause initially repulsive particles to become attractive. For example, when alumina is dispersed at a low pH, the pH drifts, because of chemical reactions of the acidic water with the particles themselves. Bodies consolidated from initially dispersed slurries could do the same, and thus dramatically change their behavior.

The coagulated slurry is described by a combination of interparticle potentials consisting of the van der Waals attractive potential, a residual electrostatic repulsive potential, and a short-range, repulsive potential (see Fig. 5(c)). For mica surfaces, the short-range repulsive potential was termed a "hydration" potential initially described by Israelachvili, Pashley, and co-workers.<sup>2,3,13-15</sup> Certain hydrated cations such as  $\text{Li}^+$ ,  $\text{Na}^+$ ,  $\text{K}^+$ ,  $\text{Mg}^{2+}$  bind to the negatively charged sites on the mica surface to produce a short-range repulsive potential due to the energy needed to dehydrate the bound cations.<sup>2,3</sup> The magnitude of hydration potential appears to exponentially decrease with a characteristic decay length of  $1.0 \pm 0.2$  nm. Measurements between interacting microrough surfaces is exponentially repulsive below 4 to 6 nm.<sup>15</sup> At separations near 2 nm, the repulsive pressure between surfaces can exceed 10 MPa.<sup>15</sup> The short-range repulsive potential also produces a low coefficient of friction between mica surfaces.<sup>16</sup> Such repulsive hydration potentials between surfaces are not a part of the classical DLVO model.

In our initial report on the effect of the added electrolyte on dispersed  $\text{Al}_2\text{O}_3$  slurries,<sup>1</sup> it was hypothesized that the negatively charged, hydrated, counter ions produced a short-range repulsive potential similar to the hydration potential described by Israelachvili, Pashley, and co-workers. The stress relaxation data presented here are consistent with this hypothesis and the interparticle potentials described in Fig. 5. The stress relaxation data strongly suggest that the short-range repulsive potential persists during consolidation and is unaffected by aging. The stress relaxation behavior of coagulated bodies subjected to repeated strain cycles (Fig. 4) further suggests that some of the particles do form cohesive bonds during pressure consolidation, but are broken during subsequent straining. In addition, the increased peak stress with increasing salt content is consistent with the understanding that the particles are in a deeper potential well, making their rearrangement more difficult.

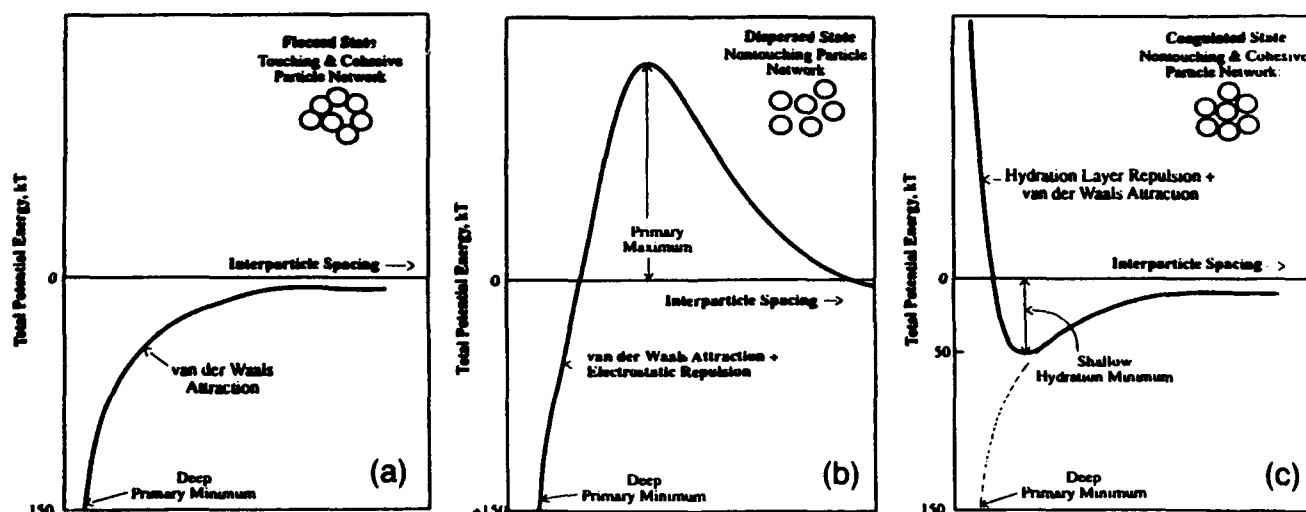
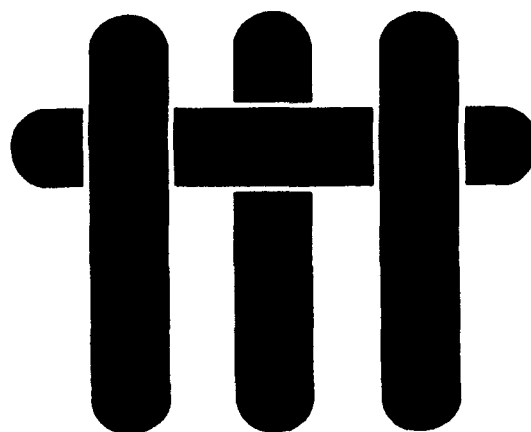


Fig. 5. Schematic representing the interparticle potential vs separation distance for (a) "flocced" slurries (DLVO type), (b) "dispersed" slurries (DLVO type), (c) "coagulated" slurries (DLVO + short-range, repulsive potential).

## References

- <sup>1</sup>B. V. Velamakanni, J. C. Chang, F. F. Lange, and D. S. Pearson, "New Method for Efficient Colloidal Particle Packing via Modulation of Repulsive Lubricating Hydration Forces," *Langmuir*, **6** [7] 1323–25 (1990).
- <sup>2</sup>R. M. Pashley, "DLVO and Hydration Forces between Mica Surfaces in  $\text{Li}^+$ ,  $\text{Na}^+$ ,  $\text{K}^+$ , and  $\text{Cs}^+$  Electrolyte Solutions: A Correlation of Double-Layer and Hydration Forces with Surface Cation Exchange Properties," *J. Colloid Interface Sci.*, **83**, 531–46 (1981).
- <sup>3</sup>R. M. Pashley and J. N. Israelachvili, "DLVO and Hydration Forces between Mica Surfaces in  $\text{Mg}^{2+}$ ,  $\text{Ca}^{2+}$ ,  $\text{Sr}^{2+}$ , and  $\text{Ba}^{2+}$  Chloride Solutions," *J. Colloid Interface Sci.*, **97**, 446–55 (1984).
- <sup>4</sup>H. van Olphen, *An Introduction to Clay Colloid Chemistry*; p. 99, Wiley, New York, 1977.
- <sup>5</sup>J. C. Chang, B. V. Velamakanni, F. F. Lange, and D. S. Pearson, "Centrifugal Consolidation of  $\text{Al}_2\text{O}_3$  and  $\text{Al}_2\text{O}_3/\text{ZrO}_2$  Composite Slurries vs Interparticle Potentials: Particle Packing and Mass Segregation," *J. Am. Ceram. Soc.*, **74** [9] 2201–204 (1991).
- <sup>6</sup>D. B. Marshall, J. J. Rato, and F. F. Lange, "Enhanced Fracture Toughness in Layered Microcomposites of  $\text{Ce-ZrO}_2$  and  $\text{Al}_2\text{O}_3$ ," *J. Am. Ceram. Soc.*, **74** [12] 2979–87 (1991).
- <sup>7</sup>N. Q. Dzuy and D. V. Boger, "Yield Stress Measurement for Concentrated Suspensions," *J. Rheol. (NY)*, **27** [4] 321–49 (1983).
- <sup>8</sup>B. V. Velamakanni and F. F. Lange, "Effect of Interparticle Potentials and Sedimentation on Particle Packing Density during Pressure Filtration," *J. Am. Ceram. Soc.*, **74** [1] 166–72 (1991).
- <sup>9</sup>F. F. Lange and K. T. Miller, "Pressure Filtration: Kinetics and Mechanics," *Am. Ceram. Soc. Bull.*, **66** [10] 1498–504 (1987).
- <sup>10</sup>J. C. Chang, F. F. Lange, and D. S. Pearson, "Viscosity and Yield Stress Behavior of  $\text{Al}_2\text{O}_3$  Slurry Systems as a Function of Interparticle Potentials," *J. Am. Ceram. Soc.*, in press.
- <sup>11</sup>L. T. Kuhn, R. M. McMeeking, and F. F. Lange, "A Model for Powder Consolidation," *J. Am. Ceram. Soc.*, **74** [3] 682–85 (1991).
- <sup>12</sup>C. P. Cameron and R. Raj, "Better Sintering through Green-State Deformation Processing," *J. Am. Ceram. Soc.*, **73** [7] 2032–37 (1990).
- <sup>13</sup>J. N. Israelachvili and G. E. Adams, "Measurement of Forces between Two Mica Surfaces in Aqueous Electrolyte Solutions in the Range 0–1000 nm," *J. Chem. Soc. Faraday Trans. 1*, **74**, 975–1001 (1978).
- <sup>14</sup>J. N. Israelachvili and R. M. Pashley, "Molecular Layering of Water at Surfaces and Origin of Repulsive Hydration Forces," *Nature (London)*, **306** [5940] 249–50 (1983).
- <sup>15</sup>J. N. Israelachvili, "Measurements of Hydration Forces between Macroscopic Surfaces," *Chem. Scr.*, **25**, 7–14 (1985).
- <sup>16</sup>A. M. Homola, J. N. Israelachvili, M. L. Gee, and P. M. McGuigan, "Measurements of and Relation between the Adhesion and Friction of Two Surfaces Separated by Molecularly Liquid Films," *J. Tribol.*, **111**, 675 (1989). □

# M A T E R I A L S



## *Evolution of a Metastable FCC Solid Solution during Sputter Deposition of Ti-Al-B Alloys*

J.P.A. Löfvander\*, U. Ruschewitz† and C.G. Levi

High Performance Composites Center  
and Materials Research Laboratory  
Materials Department, College of Engineering  
University of California at Santa Barbara

\* Now at EKI Industries, Santa Barbara, CA 93109

† Now at Institut für Anorganische Chemie der Rheinisch  
Westfälischen Technischen Hochschule Aachen, 52056 Aachen, Germany

to be submitted for publication to  
*Scripta Metallurgica et Materialia*

April, 1994



# Evolution of a Metastable FCC Solid Solution during Sputter Deposition of Ti-Al-B Alloys

J.P.A. Löfvander\*, U. Ruschewitz†, and C.G. Levi

Materials Department, College of Engineering  
University of California, Santa Barbara, CA 93106, U.S.A.

\* now at EKI Industries, Santa Barbara, CA, 93109

† now at Institut für Anorganische Chemie der Rheinisch  
Westfälischen Technischen Hochschule Aachen, 52056 Aachen, Germany

## Introduction

Continuous-fiber reinforced titanium-matrix composites are conceptually very attractive candidates for advanced high temperature structural applications, but also present some of the most difficult challenges to implementation. One significant problem concerns the optimization of matrix creep properties. Ti alloys of interest have relatively modest creep strengths which, coupled with the weak interfaces used in most current systems, lead to poor transverse properties and exacerbate the inherent anisotropy of these composites [91JDE, 93GJL]. Ongoing modeling work has shown that a low matrix creep strength can also accentuate the degradation of longitudinal properties associated with local fiber failure [94DuM]. Conversely, creep resistant matrices hinder densification and require higher processing temperatures and pressures, increasing the potential for thermochemical interactions or mechanical fiber damage and limiting the achievable composite properties.

B additions to most Ti alloys yield thermochemically stable acicular TiB particulates which can be used in a variety of creep strengthening schemes. For example, TiB reinforcements have been effective in reducing the creep rate of cast  $\gamma$ -TiAl base alloys up to  $\sim 980^\circ\text{C}$  [90KSC, 91Val] and more significantly in  $\beta$ -(Ti,Mo) alloys up to  $600^\circ\text{C}$  [94Phi]. TiB particles on a scale attractive for dispersion strengthening have

also been produced by rapid solidification (RSP) [84Sas, 86Row]. One could envision using TiB-bearing RSP particulate as a matrix in composite fabrication, although fiber damage during consolidation is expected to be an issue and important microstructural features such as interfiber spacing would be difficult to control. An attractive processing alternative involves the physical vapor deposition of the matrix on the fibers, which has the potential to optimize interfiber spacing, reduce damage relative to the powder methods, and yield highly supersaturated solid solutions with enhanced potential for dispersoid refinement and homogeneity [93PWC]. This paper explores the latter issue, focusing on the microstructure evolution of a nominally  $\alpha$ -Ti-Al-B alloy synthesized by sputter deposition.

### Experimental Procedure

Three alloys with nominal compositions Ti-7Al-7B, Ti-7Al, and Ti-7B (at.%) were produced by conventional arc-melting under an inert Ar atmosphere with <0.1 ppb O<sub>2</sub>. Starting materials were high purity Ti (<200 ppm O), 99.99% Al and 99.6% B. Circular sputtering targets, 50 mm in diameter and 6 mm thick, were electro-discharge machined from arc-melted discs weighing ~90 g each. Magnetron sputtering was carried out in 1Pa Ar using an accelerating voltage of 400 V and a current of ~0.5 A. Films with average thicknesses of ~100  $\mu$ m were deposited on substrates made of 50x75 mm Ta sheets, mounted on a Cu chill ~40 mm from the target. A thermocouple was spot welded to the back of the Ta sheet to monitor temperature during deposition.

Microstructures and chemical compositions were analyzed in a JEOL 2000FX transmission electron microscope (TEM) equipped with energy dispersive spectroscopy (EDS). TEM specimens were prepared by standard dimple grinding and ion milling techniques, as well as by jet polishing in a Fishione unit operating at 40 V

with a 4 vol.%  $\text{H}_2\text{SO}_4$  solution in methanol at  $0^\circ\text{C}$ . Pulverized samples for X-ray diffractometry (XRD) were prepared by peeling the sputtered films from the substrates and grinding them with a ceramic mortar and pestle. XRD was performed on a Scintag DMX 2000 diffractometer using Cu radiation ( $\lambda = 154.06 \text{ pm}$ ); analysis focused on the  $25^\circ \leq 2\theta \leq 80^\circ$  range scanning in a step mode with 10 seconds per point and a step size of  $0.03^\circ$ .

## Results

Most of the work focused on the ternary Ti-7Al-7B alloy, with binaries serving as points of comparison. The as-sputtered film had a thickness ranging from  $\sim 50 \mu\text{m}$  at the edges to  $\sim 130 \mu\text{m}$  in a circular region at the center of the substrate, approximately corresponding to the shape of the racetrack in the target. The deposition time was  $\sim 7 \text{ h}$  and the temperature of the Ta foil remained relatively constant, in the range of  $300\text{--}320^\circ\text{C}$ . Similar conditions were maintained in the deposition of the binary films. The films were somewhat brittle but relatively large sections of them could be easily removed from the substrate for sample preparation.

A representative bright field TEM image of the as-sputtered film is shown in Fig. 1(a). The structure is single phase, nanocrystalline, with some evidence of texturing suggested by the selected area diffraction pattern (SADP) in Fig. 1(c). Dark field images using the portion of the rings marked in the SADP suggest a crystallite size on the order of  $2 \text{ nm}$ , as seen in Fig. 1(b). No significant differences were discerned between samples prepared by jet polishing or ion milling. Average measurements of the ring diameters in SADP's recorded from three different areas are summarized in Table 1. The observed reflections could not be indexed to the  $\alpha(\text{HCP})$  or  $\beta(\text{BCC})$  forms of Ti, but agreed quite well with an FCC unit cell with  $a \approx 420 \text{ pm}$ .

X-ray diffraction analysis of pulverized Ti-7Al-7B films in the as-sputtered condition corroborates the TEM results, as indicated by Fig. 2. A family of broad reflections consistent with the FCC-Ti structure is clearly evident over the silicon standard peaks, which are much stronger and sharper. The broad shape of the reflections suggests a crystallite size  $\leq 10$  nm, in agreement with the TEM images. Three smaller but relatively sharp peaks were also noted but could not be reconciled with any of the Ti polymorphs, the Si standard, or any of the known Ti borides or aluminides. Since there was no evidence of a second phase in the TEM analysis, the unidentified peaks were ascribed to impurities possibly introduced during grinding.

Structural information was extracted by fitting the pattern in Fig. 2 to a Lorentzian function, using the peak fitting routine in the DMS software package (Scintag Inc.). The d-spacings from this analysis can be consistently indexed to the major planes of the face centered cubic structure, as shown in Table 2. A  $\chi^2$  square refinement of the diffraction pattern using Si ( $a = 543.088$  pm) as an internal standard leads to a lattice parameter of  $a = 421.(2)$  pm for the FCC solid solution. Calculated d-spacings for the relevant planes, based on the above unit cell dimensions, are listed for comparison in Table 2. Relative peak intensities for a pure Ti FCC phase were calculated using the program LAZY PULVERIX [91YJP] and are compared with the experimental intensities in Table 2. The agreement between the measured and calculated d-spacings and intensities is quite reasonable. It is then concluded that the single phase solid solution evolving during sputter deposition of Ti-7Al-7B has a disordered face centered cubic structure.

XRD of pure Ti, Ti-7Al, and Ti-7B films of comparable thickness produced by sputter deposition under similar conditions revealed that the evolving structure was in all cases hexagonal close packed. Heat-treatment of the sputtered Ti-7Al-7B film at  $900^\circ\text{C}$  for 1 h yields a dispersion of TiB in a single phase  $\alpha$ -Ti matrix, as illustrated in Fig. 3(a), indicating that the FCC phase evolving from sputter deposition is

a supersaturated metastable solid solution. The microstructure shows little evidence of further evolution upon additional thermal exposure, with negligible dispersoid coarsening after 100 h at 700°C, as noted in Figure 3(b).

The boride dispersoids have short dimensions on the order of ~15 nm with aspect ratios of ~10 or greater, and are uniformly distributed through the matrix. Since the residual B solubility in the matrix is minimal, one can readily estimate the volume fraction of TiB dispersoids to be ~9%, which translates into a mean planar interparticle spacing on the order of 50 nm. Coupled with the promising microstructural stability, the dispersion scale offers significant strengthening potential. Small specimens of Ti-7Al-7B matrix composites produced by sputter deposition of the alloy on TiB<sub>2</sub> coated SiC-fibers, followed by HIP consolidation, had matrix hardness values ranging from 800-1100 VHN, compared with 200 VHN for Ti-7Al.

### Discussion

FCC structures in Ti-rich alloys have previously been reported but only as a transformation product of metastable  $\beta$ -(Ti), always in sub-micron foils or particles, and normally mixed with other phases. For example, cubic martensites with lattice parameters ranging from 420 to 450 pm have been observed in Ti-6Al-4V [67WiB], Ti-5.5Cr [69ETP], and Ti-10Mo and Ti-15Mo [69HaK]. These phases were mixed with  $\beta$ -(Ti) and ascribed either to the relief of volume constraint in the thin TEM foil [69WiB], or to hydrogen contamination during the electrochemical thinning process [69HaK]. Since the phases were not detected in the bulk samples, they are considered artifacts of the TEM sample preparation. FCC-Ti has also been observed in rapidly solidified particles,  $\leq 100$  nm in diameter, produced by electrohydrodynamic atomization of a Ti-1.2Er alloy [87Lon]. Although  $\beta$ -(Ti) was not detected, twinning of the

FCC phase suggested that it evolved by solid state transformation of a higher temperature  $\beta$  structure.

In contrast with most previous reports, the Ti-7Al-7B sputtered films show only the FCC solid solution phase, with no evidence of having evolved from the transformation of a parent  $\beta$  structure. In principle, its formation at  $\sim 300^\circ\text{C}$  is consistent with the reported lattice stability for the FCC form of pure Ti, which has a theoretical melting point of  $\sim 868^\circ\text{C}$  [92KLC]. The high B supersaturation is also consistent with reported solubility extensions of up to  $\sim 10$  at.%B in  $\beta$ -(Ti) by rapid solidification [86Wha]. Indeed, one could argue that the solubility extension may be even higher in FCC-Ti based on the relative solubilities of B in  $\alpha$  and  $\beta$  [90MLS].

A recently developed thermodynamic model for the Ti-Al system [92KLC] can be used to assess the relative stabilities of the relevant solid phases in the absence of partitioning. These are plotted as a function of temperature and composition in Fig. 4, wherein the various fields are defined by the  $T_0$  curves for the liquid-solid and solid-solid transformations. The thermodynamically feasible phases and their hierarchy are listed within each field. (One may infer that if a solid phase is stable relative to its melt, it would also have a driving force to form from a vapor of identical composition.) Note that the FCC phase ( $\kappa$ ) is feasible across the entire composition range for temperatures below  $T_0(\text{L}/\kappa)$ , but it is always *the least favorable phase* on the Ti-rich end of the diagram. Addition of Al to Ti increases the valence-electron/atom ratio and would be expected to enhance the relative stability of the phases in the order  $\kappa > \alpha > \beta$  [88Bre]. While this is evident in the rising trend of the  $T_0'(\beta/\alpha)$  curve in Fig. 4, the predominance of  $\alpha$  over  $\kappa$  is not substantially changed until the Al content exceeds  $\sim 50$  at% ( $e/a \geq 2.5$ ). Conversely, it is noted that the calculated stability of  $\gamma$  ( $\text{L}1_0$ ) increases more rapidly with Al addition than that of its disordered counterpart  $\kappa$ , and is always more favorable than the latter on the Ti rich end. However, its evolution would be less competitive from a kinetic viewpoint, espe-

cially since  $\alpha$  is still the thermodynamically preferred phase. B additions can be viewed as equivalent to Al from an e/a ratio perspective, but even at 14 at.%(Al+B) the e/a ratio would be only 2.14, closer to HCP than to FCC [88Bre]. In summary, the selection of FCC over HCP during sputter deposition cannot be justified on thermodynamic arguments and must arise from a kinetic bias. The reasons, however, are not immediately apparent.

Lattice parameter calculations for a FCC-(Ti<sub>86</sub>Al<sub>7</sub>) solid solution based on a hard sphere model with  $r_{Ti}=146.1$  pm and  $r_{Al}=143.2$  pm yield  $a=412.6$  pm, compared with an experimental value of 421.2 pm. An interstitial solubility model for B with octahedral site occupancy of 7:93 would yield a lattice expansion to  $a=417.8$  pm, in qualitative agreement with the experiment. Conversely, substitutional solubility would produce a lattice contraction, even in the case of dimer occupancy. Thus, the high supersaturation of B can be assumed to be accommodated interstitially. One might argue that the attachment of B atoms on growing close packed planes, coupled with their tendency to covalent bonding, could promote FCC over HCP stacking. It is noted, however, that this does not occur in binary Ti-B alloys, suggesting that the atomic rearrangement mechanisms and kinetics at the growth front need better understanding. Further studies are necessary before this issue can be resolved satisfactorily.

### Conclusions

Sputter deposition of Ti-7Al-7B leads to a highly supersaturated single phase solid solution with a face centered cubic structure, identified by both electron and X-ray diffraction analysis. Thermodynamic information reveals that the FCC phase is the least favorable for this composition at the synthesis temperature (300°C), but the reasons for its kinetic selection are yet to be elucidated. The B supersaturation is

accommodated interstitially and leads to precipitation of nano-scale TiB dispersoids under high temperature annealing, while the parent FCC structure transforms to the more stable  $\alpha$ -(Ti,Al) solid solution. Preliminary evaluations of the hardness and microstructural stability of the dispersion reveal promising potential for use as a matrix in high temperature Ti-MMC's.

### Acknowledgments

This investigation was supported by the Advanced Research Projects Agency (ARPA) through a University Research Initiative Grant N00014-92-J-1808, supervised by Dr. W. Coblenz and monitored by Dr. S. G. Fishman of the Office of Naval Research. The authors would like to thank Messrs. Joel Philliber, Deryck Stave and Neil Neighman for technical assistance in producing the targets and sputtered films.

### References

- 67WiB J.C. Williams and M.J. Blackburn: *ASM Trans.*, 60 (1967) 373.
- 69ETP R.H. Ericksen, R. Taggart and D.H. Polonis: *Trans. AIME*, 245 (1969) 359.
- 69HaK C. Hammond and P.M. Kelly: *Acta Metall.*, 17 (1969) 896.
- 84Sas S.M.L. Sastry, T.C. Peng, P.J. Meschter, and J.E. O'Neal: *JOM*, Sept. 1983, 21.
- 86Row R.G. Rowe, T.F. Broderick, E.F. Koch, and F.H. Froes: in *Titanium Rapid Solidification Technology*, ed. F.H. Froes, D. Eylon, and S.M.L. Sastry, The Metallurgical Society of AIME, Warrendale, PA (1986).
- 86Wha S.H. Whang: *J. Mater. Sci.* 21 (1986) 2224.
- 87Lon B. London, S.M.L. Sastry, C.G. Levi, J.J. Valencia, and P.B. Fraundorf: "Microstructural Studies of Rapidly Solidified Sub-micron Titanium Alloy Powders," presented at the Symposium on Elevated Temperature Titanium Alloys, TMS Fall Meeting, Cincinnati, OH, 1987.



- 88Bre L. Brewer: in Alloying, eds. J.L. Walker, M.R. Jackson and C.T. Sims, ASM International, Metals Park, OH (1988).
- 90KSC S.L. Kampe, G.H. Swope, and L. Christodoulou: *MRS Symp. Proc.* 194 (1990) 97.
- 90MLS J.L. Murray, P.K. Liao, and K.E. Spear: in Binary Alloy Phase Diagrams, ed. T.B. Massalski, ASM International, Materials Park, OH (1990) p. 544.
- 91JDE S. Jansson, H.E. Dève, and A.G. Evans: *Metall. Trans. A*, 22A (1991) 2975.
- 91Val J.J. Valencia, J.P.A. Löfvander, C. McCullough, C.G. Levi, and R. Mehrabian: *Mat. Sci. Engr. A*144 (1991) 25.
- 91YJP K. Yvon, W. Jeitschko, and E. Parthé: *J. Appl. Cryst.*, 10 (1977) 73.
- 92KLC U.R. Kattner, J.-C. Lin, and Y.A. Chang: *Metall. Trans. A*, 23A (1992) 2081.
- 93GJL S.R. Gunawardena, S. Jansson, and F.A. Leckie: *Acta Metall. Mater.* 41 (1993) 3147.
- 93PWC P.G. Partridge and C.M. Ward-Close: *Int. Mat. Rev.* 38 (1993) 1.
- 94DuM Z.Z. Du and R. McMeeking: "Creep Models for Metal Matrix Composites with Long Fibers," to be submitted to *Jo. Mech. Phys. Solids* (1994).
- 94Phi J.A. Philliber and C.G. Levi, research in progress.

**Table 1. Comparison of calculated d-spacing ratios for FCC Ti ( $a=420$  pm) with experimental values from SAD patterns of the Ti-7Al-7B solid solution.**

hkl	(111)	(200)	(220)	(311)	(222)	(400)	(331)	(420)	(422)
Calculated	1.00	0.866	0.612	0.522	0.500	0.433	0.397	0.387	0.369
Experimental	1.00	0.877	0.625	0.543	0.502	0.444	0.391	0.391	0.351

**Table 2. Comparison of experimental spacings and intensities with calculated values for FCC Ti.**

hkl	d exp.	d calc.	I exp.	I calc.
111	2.420	2.428	1000	1000
200	2.114	2.103	580	478
220	1.493	1.487	420	282
311	1.270	1.268	250	312
222	1.220	1.214	80	89

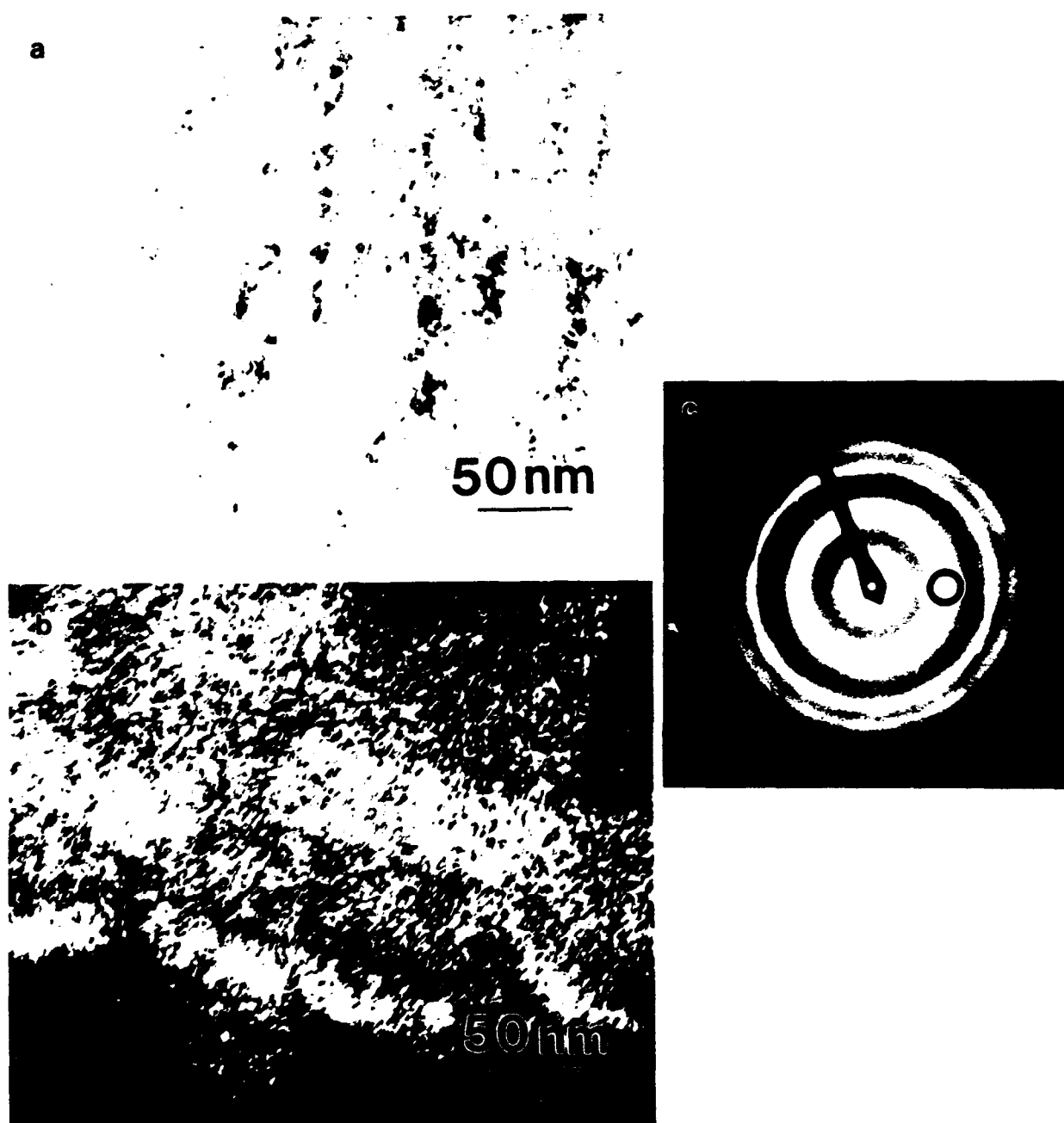


Figure 1. Microstructure of Ti-7Al-7B in the as-sputtered condition: (a) bright field, (b) dark-field, and (c) SAD pattern showing portion of ring used in DF.

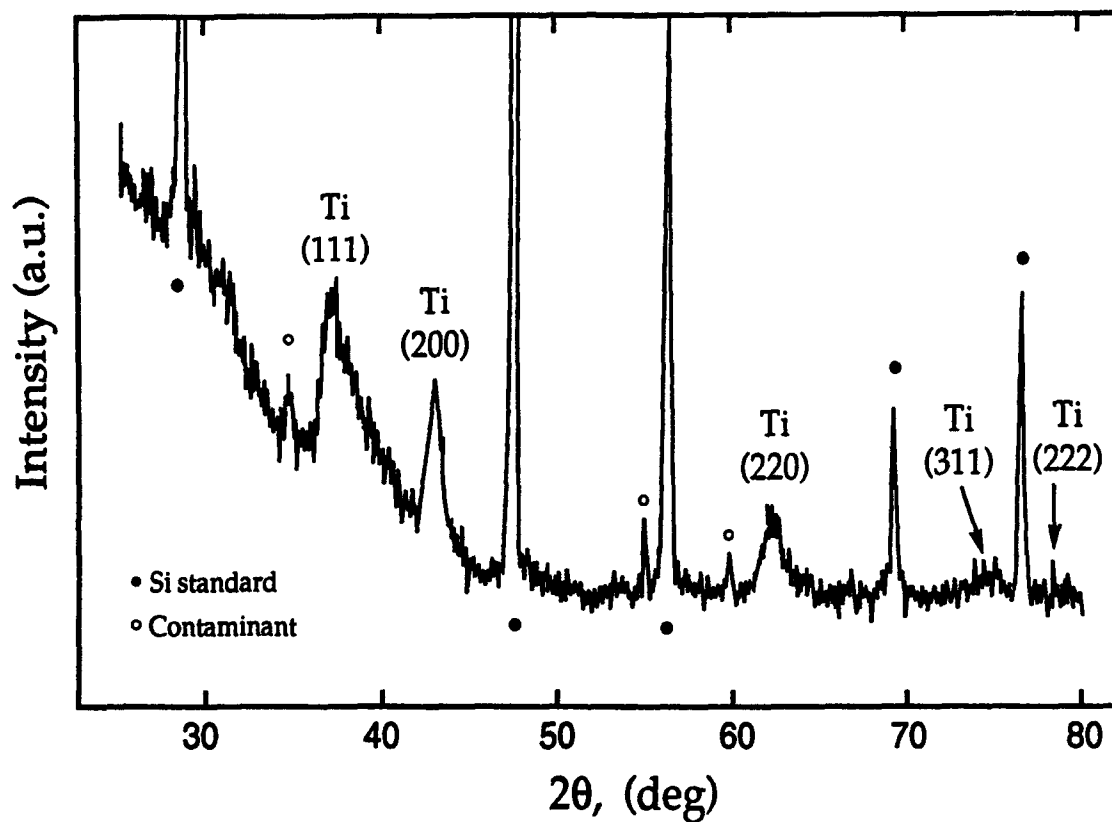


Figure 2. X-ray intensity pattern obtained from as-sputtered Ti-7Al-7B ground to powder. The broad peaks are indexed based on an FCC unit cell. Si peaks are from internal standard. Small contaminant peaks are probably associated with debris from the grinding process.

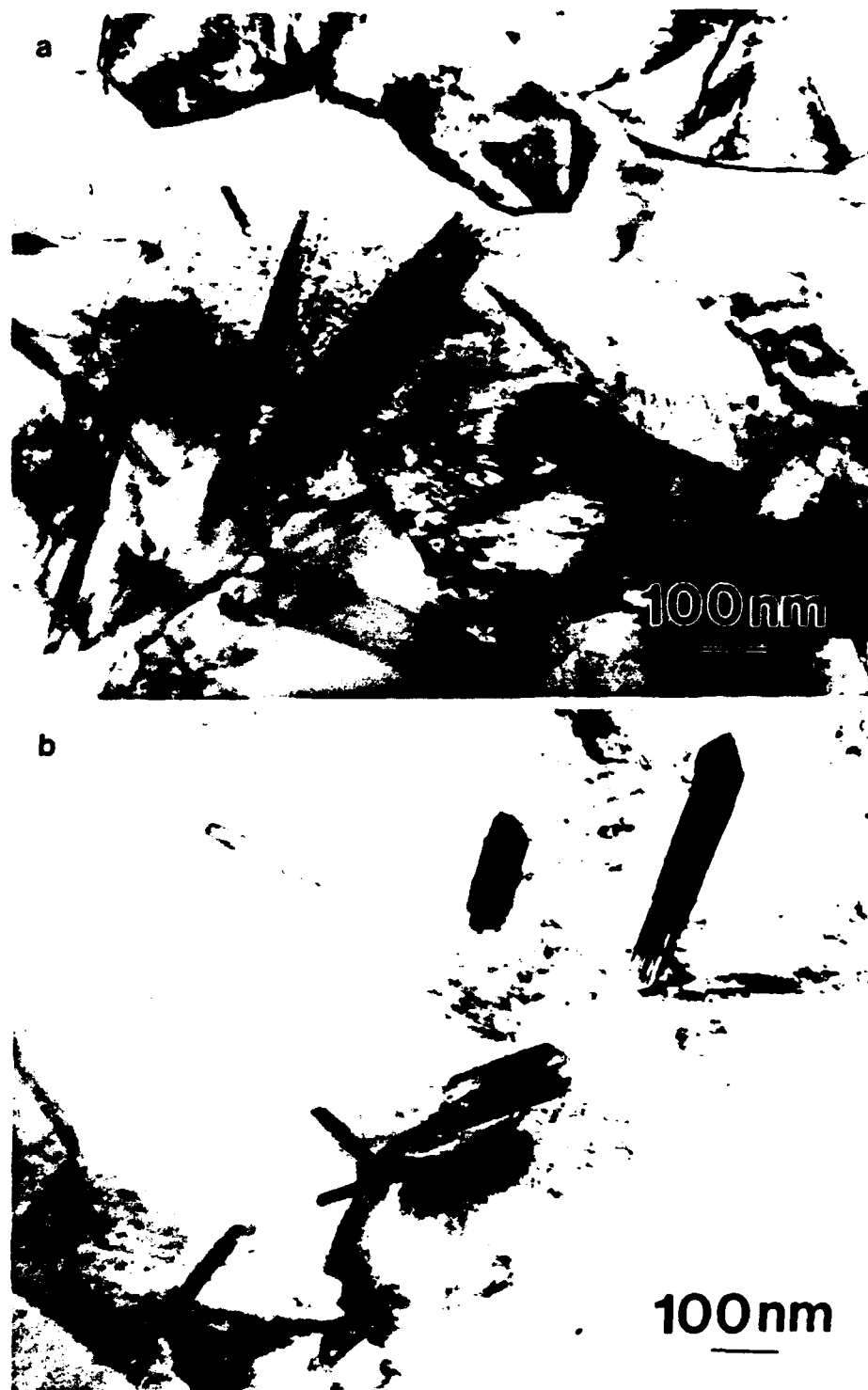


Figure 3. Bright-field TEM micrographs of sputtered Ti-7Al-7B heat-treated in Ar at (a) 900°C for 1h, and (b) 900°C/1h + 700°C/100h. The matrix is  $\alpha$ -(Ti,Al) and the acicular dispersoids are TiB.

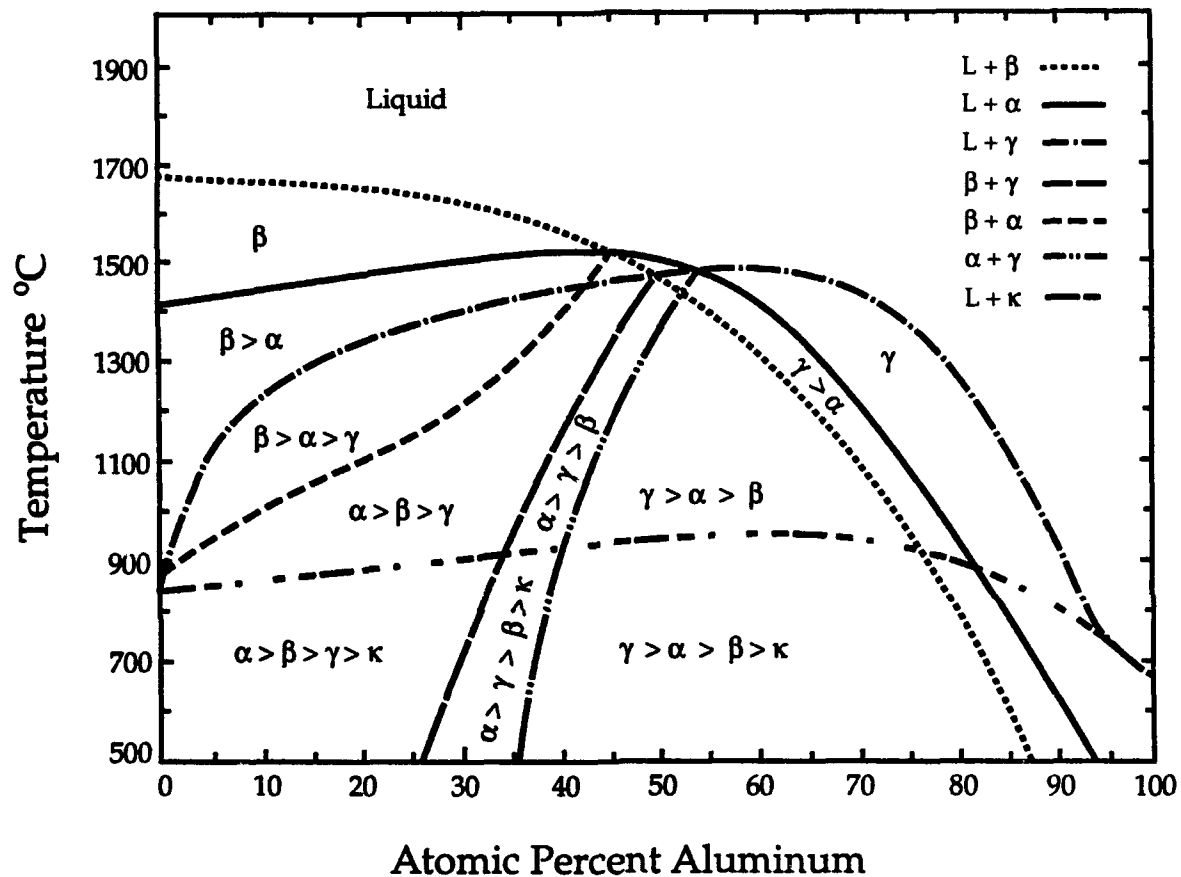
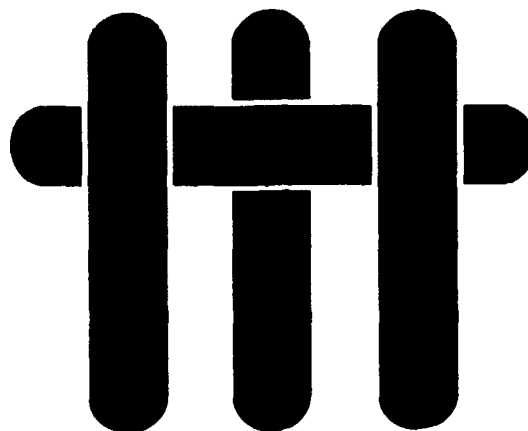


Figure 4. Thermodynamic hierarchy map for the three disordered solid solution phases ( $\alpha$  = HCP,  $\beta$  = BCC,  $\kappa$  = FCC) and the least complex FCC-based ordered phase ( $\gamma$  =  $L1_0$ ). The ordered hexagonal  $DO_{19}$  structure and the more complex FCC-related intermetallics on the Al-rich end are not relevant to this discussion.

# M A T E R I A L S



## *Novel ODS Copper Alloys from Rapidly-Solidified Precursors—I: Microstructural Development*

M.S. Nagorka\*, C.G. Levi, and G.E. Lucas

High Performance Composites Center  
Materials Department  
College of Engineering  
University of California at Santa Barbara

\* Currently at Kaiser Aluminum Corp., Pleasanton, CA.

submitted for publication to  
*Metallurgical and Materials Transactions*  
March, 1994

# Novel ODS Copper Alloys from Rapidly-Solidified Precursors—I: Microstructural Development

by

Michael S. Nagorka, Carlos G. Levi, and Glenn E. Lucas<sup>†</sup>

## ABSTRACT

ZrO<sub>2</sub>, Y<sub>2</sub>O<sub>3</sub>, and rare earth oxides with related structures are attractive candidates for dispersion strengthening of copper alloys but pose significant processing challenges owing to the low solubility of the oxide-forming elements in Cu. It is shown that the problems may be circumvented by a synthesis approach coupling rapid solidification and internal oxidation, followed by standard P/M consolidation. Cu-Zr and Cu-Y alloys were melt spun into ribbons ~50-150 μm thick and internally oxidized at 1023-1223 K to yield ~1 vol.% of ZrO<sub>2</sub> or Y<sub>2</sub>O<sub>3</sub> particles ranging in size from ≤5 nm up to ~150 nm. The coarser oxides result from direct oxidation of the intermetallic segregate, whereas the finer ones are generated by a dissolution-reprecipitation process. The relative proportions of fine and coarse oxides and the homogeneity of the distribution are related to segregation scale in the melt spun ribbon and the relative permeabilities of oxygen and the oxidizable element in the alloy, which depend on the internal oxidation temperature. The oxide dispersoids were predominantly cubic zirconia or cubic yttria and exhibited cube-on-cube orientation relationships with the matrix. Analysis of particle shapes revealed that the dominant interfaces are of the type {100}<sub>Ox</sub> || {100}<sub>Cu</sub> and {111}<sub>Ox</sub> || {111}<sub>Cu</sub>, and could be explained by image charge interaction concepts. Extrusion produced an elongated grain structure but no significant changes in the oxide distribution.

---

<sup>†</sup> M.S. Nagorka, formerly Graduate Research Assistant at the University of California, Santa Barbara (UCSB), is now Staff Research Engineer at Kaiser Aluminum Corp. in Pleasanton, CA. C.G. Levi is Professor of Materials and Mechanical Engineering, and G.E. Lucas is Professor of Nuclear Engineering and Materials, both at UCSB, Santa Barbara, CA, 93106.



## INTRODUCTION

The need for materials with desirable combinations of high electrical/thermal conductivities and high-temperature strength/creep resistance led to the commercial development of oxide-dispersion-strengthened (ODS) copper [76NKS]. Standard ODS copper alloys contain  $\leq 3$  vol.% of  $\gamma$ -Al<sub>2</sub>O<sub>3</sub> dispersoids which are produced by the internal oxidation (IO) of dilute copper-aluminum alloy powders. The IO powder material is subsequently consolidated, densified, and reduced to the desired dimensions by deformation processing methods [84Nad]. While these alloys exhibit superior combinations of conductivity and strength retention with temperature, modest strength values often limit the spectrum of applications [84GLL].

ODS copper alloy design has long been a subject of interest. Different oxides have been investigated [47MeD, 62KoG, 69SwF, 70SwF, 71SCK, 71ScO, 74ShB, 76NKS], alone and in combination with other strengthening agents, e.g. [84GLL]. Dispersoids were viewed initially as simple physical barriers in the dislocation path, whereupon selection was based on achievable size, spacing and high temperature stability. As understanding of the creep mechanisms evolved, it was proposed that the major strengthening effect is associated with an attractive dislocation/dispersoid interaction arising from the diffusional relaxation of dislocation core stresses at the particle/matrix interface [90RöA]. This suggests that interfacial configuration, and hence dispersoid structure, may play a significant role in the dislocation/particle interaction and should be an important parameter of alloy design.

Previous work by the authors [91Nag] suggested that ZrO<sub>2</sub>, Y<sub>2</sub>O<sub>3</sub> and many rare earth oxides were attractive candidates for dispersion strengthening owing to their high thermodynamic stability. The low solubilities and diffusivities of the oxide-forming elements in Cu should also enhance the microstructural stability against coarsening. More importantly, all these oxides have fluorite-related struc-

tures and would inherently form different interfaces with Cu than those developed by  $\gamma\text{-Al}_2\text{O}_3$ , which is a spinel. Thus, they offer interesting opportunities to explore the role of the dispersoid/matrix interface on the creep behavior of ODS copper.

The major hindrance to developing ODS Cu alloys based on Zr, Y or rare earths is the marginal solubility of these elements in Cu. When cast, the oxidizable element forms an intermetallic segregate in the interdendritic spaces, yielding a highly inhomogeneous oxide distribution upon internal oxidation [70SwF, 91Nag]. Swisher and Fuchs [70SwF] utilized extensive deformation processing to refine the structure of the intermetallic and successfully generated ODS materials with attractive properties from Cu-Zr alloys. Their approach, however, is somewhat cumbersome and limited in practice to very thin wires or foils. Nagorka et al. [91Nag] proposed that rapid solidification processing (RSP) could be used more effectively to refine the intermetallic phases to a scale suitable for internal oxidation, and demonstrated the concept on splat-quenched Cu-Y alloys. Scale-up of this idea based on ultrasonic gas atomization of a Cu-1.5Y alloy<sup>1</sup> produced somewhat coarser microstructures than splat cooling and consequently inadequate oxide dispersions. However, the results were sufficiently encouraging to motivate the search for a scale-up RSP technique potentially capable of achieving faster solidification rates than atomization. This led to melt spinning as a source of precursor ribbons which lend themselves easily to standard IO processing.

This investigation focused on the fundamental understanding of microstructural development in relatively dilute Cu-ZrO<sub>2</sub> and Cu-Y<sub>2</sub>O<sub>3</sub> alloys synthesized by internal oxidation of rapidly solidified ribbons, which were subsequently pulverized and consolidated by hot pressing and extrusion. A companion paper [94NLL] reports on the evaluation of the creep behavior of the materials produced in this manner.

---

<sup>1</sup> All alloy compositions in atomic percent unless specified otherwise.

## EXPERIMENTAL PROCEDURE

Copper alloys with low concentrations ( $\leq 1\%$ ) of Y or Zr were prepared by vacuum induction melting OFHC copper with the appropriate amounts of each element (99.9% pure) and casting into 12 mm diameter cylindrical graphite molds. Sections of the cast bars were remelted in  $\sim 100$  g batches and melt spun in a free jet configuration onto a Cu-Be wheel with a peripheral speed of 15 m/s. Argon was used both as the atmosphere in the melt spinning chamber ( $\sim 100$  kPa) and as the pressurizing gas ( $\sim 115$  kPa). Other cast bars were swaged down to 1.7 mm diameter and used to determine the IO kinetics following the approach in Reference [69SwF].

Ribbons and wires were internally oxidized using the Rhines pack method [42RJA]. The material to be oxidized was placed together with fine ( $\sim 325$  mesh) cuprous oxide powder into a stainless steel container which was evacuated, back-filled with purified Ar, sealed, heated to the oxidation temperature and held for a specified time. Oxidation conditions and alloy designations for the different materials are given in Table 1. The residual  $\text{Cu}_2\text{O}$  was removed from the ribbon by ultrasonic cleaning in an aqueous solution of 20 vol%  $\text{HNO}_3$  and a subsequent reduction anneal for 1 hour at 873 K in a He atmosphere containing 4 vol%  $\text{H}_2$ .

Bulk samples for creep testing were prepared by vacuum hot pressing (VHP) and subsequent hot extrusion of the internally oxidized ribbon material. The ribbon was initially "pulverized" to facilitate packing and then VHP at 973 K and 53 MPa into 30 mm diameter billets using high-density graphite dies lined with graphite foil. The billets were cleaned after pressing, sealed in copper cans under vacuum and then hot-extruded at  $\sim 1010$  K using boron nitride for lubrication. The extrusion ratio was 9:1 and the final diameter 9.5 mm.

Microstructural characterization was carried out by optical (OM), scanning electron (SEM), and transmission electron microscopy (TEM). Grain sizes were

determined from standard metallographic specimens following ASTM specification E112 (microstructural variations made full compliance impossible in some cases). Grain aspect ratios in extruded alloys were assessed by counting intercepts parallel and transverse to the extrusion direction and then taking the ratio of these values.

TEM specimens were prepared by sectioning with a slow speed diamond saw, grinding to  $\sim 150\text{ }\mu\text{m}$  thickness, punching out 3 mm diameter disks, and grinding said disks to  $\leq 80\text{ }\mu\text{m}$  thick. Final thinning of as-spun ribbons was accomplished by twin-jet electropolishing with a solution of 30 vol%  $\text{HNO}_3$  in methanol cooled to 238 K under a voltage of 25 V. This approach did not give satisfactory results for the internally oxidized samples, which were dimpled and subsequently ion milled with Ar under an accelerating voltage of 5 kV.

## RESULTS AND DISCUSSION

### *Microstructures produced by Rapid Solidification*

The ribbons produced by melt spinning were typically  $\sim 3$  to 4 mm wide with average thicknesses of  $\sim 100 \pm 50\text{ }\mu\text{m}$ . (Substantial thickness variations arise from surface ripples associated with the widely varying flow pattern of the metal jet.) A longitudinal section through the Cu-0.32Zr ribbon at a location where the thickness is  $\sim 70\text{ }\mu\text{m}$ , Figure 1(a), reveals a small chill zone of equiaxed grains at the surface in contact with the wheel which evolves into a classical columnar microstructure that extends to the free surface of the ribbon. Second phases become clearly distinguishable in OM at  $\sim 50\text{ }\mu\text{m}$  from the chill surface and assume a "cellular" pattern<sup>2</sup> as the solidification front approaches the free surface. TEM images of this ribbon near the

---

<sup>2</sup> The pattern may well be dendritic but the low volume fraction of second phase precludes the clear delineation of secondary arms. This is observed even at low growth velocities [91Nag].

mid-thickness, Figure 1(b), clearly reveal a microcellular structure with segregate spacings of  $\sim 200$  nm. The segregate phase is discontinuous and consists of a Cu-Zr intermetallic particles with an average diameter of  $\sim 12$  nm. The cellular structure becomes coarser in both segregate size ( $\sim 80$  nm) and spacing ( $\sim 500$  nm) in regions closer to the free surface. Nevertheless, the Zr intermetallic was in all cases much finer than the  $1\text{ }\mu\text{m}$  size reported when the precursor microstructure is refined by deformation processing of cast materials [70SwF].

A small amount of ultrafine *intracellular* precipitates ( $\leq 5$  nm) is also found in regions closer to the surface. These are consistent with solid-state precipitation of the Zr intermetallic as the slight solubility of Zr in Cu ( $\sim 0.12\%$  at 1245 K [90ArA]) decreases further during post-solidification cooling. Diffraction patterns from the larger segregate particles could not be conclusively indexed to any of the Cu-Zr intermetallics reported in the literature.

The Cu-0.33Y ribbon, Figure 1(c), exhibits a region of columnar grains  $\sim 3\text{ }\mu\text{m}$  in diameter evolving from the chill face. These are superseded above  $\sim 1/3$  of the ribbon thickness by equiaxed grains  $\sim 5\text{ }\mu\text{m}$  in diameter, which extend to the ribbon surface. Columnar-to-equiaxed transitions are not unusual in melt spun microstructures and were a regular feature of the Cu-Y ribbons, but seldom observed in Cu-Zr. This is consistent with the much wider freezing range of the Cu-0.33Y alloy ( $\sim 220$  K vs  $\sim 110$  K for Cu-0.32Zr) [81ChL, 90ArA]. If the heat extraction rates are comparable, the width of the mushy zone should be considerably greater for the Cu-Y alloy, and consequently the relative volume fraction of solid behind the dendrite/cell tips would be lower<sup>3</sup>. This would imply an increase in the probability of dendrite tip detachment generally associated with convective melt intrusion

---

<sup>3</sup> One could readily show that the maximum gradient in a ribbon would be on the order of  $0.3\text{--}3\text{ K}/\mu\text{m}$  for relatively high interfacial heat transfer coefficients of  $0.1\text{--}1\text{ GW}/\text{m}^2\text{ s}$ . This suggests that a "steady state" mushy zone is unlikely to develop, but the argument should be still qualitatively correct.

(presumably induced by the relative shear between the moving solid and the melt above it) into the mushy zone. In the classical scenario of the columnar-to-equiaxed transition [66Jac] these detached dendrite tips are unconstrained "nuclei" which may evolve into equiaxed grains if the melt is sufficiently undercooled, and eventually occlude the growth of the columnar front [87FIH, 93RaG]. One should obviously question whether this mechanism is applicable when the mushy zone structure is more cellular than dendritic. Massive heterogeneous nucleation in the bulk liquid cannot be discounted, but this would imply the presence of a substantial population of more active "catalysts" in the Cu-Y alloy relative to the Cu-Zr, and/or a higher melt undercooling in front of the dendrite/cell tips. While these issues cannot be elucidated with the available evidence, they are not critical to the primary subject of this paper and will not be further discussed.

TEM analysis of the mid section of the Cu-Y ribbon, Figure 1(d), reveals a microstructure similar to that of the Cu-Zr ribbon, albeit somewhat coarser. Inter-metallic particles had an average size  $\sim 65$  nm and spacings in the range 300-500 nm. Ultrafine precipitates are also visible in the matrix, as in Cu-Zr, but the volume fraction is smaller in agreement with the lower solubility of yttrium in copper. Diffraction patterns obtained from the larger intermetallic segregate particles were consistent with the structure of  $\text{Cu}_7\text{Y}$ , which is the equilibrium second phase for alloys with  $\leq 12\% \text{Y}$  [81ChL].

### *Internal Oxidation Kinetics*

The kinetics of internal oxidation in Cu-Y and Cu-Zr alloys were studied on 1.7 mm diameter wires of Cu-1Y and Cu-1Zr<sup>4</sup> as discussed in the Experimental

---

<sup>4</sup> These studies were performed prior to the selection of leaner alloys for melt spinning. The 1% compositions were more suitable for metallographic examination than the  $\sim 0.3\%$  alloys eventually used for the rest of the work. The difference is not considered critical as Swisher and Fuchs showed that the oxidation times scale linearly with alloy composition [69SwF].

section. A typical cross section of the partially oxidized wires used to measure the oxidation depth as a function of time is depicted in Figure 2. The oxidation front is clearly delineated by the disappearance of the larger intermetallic particles, which produce the dark contrast evident in the unoxidized core. Experimental measurements of oxidation depth as a function of time are given in Table 2.

A solution for the time-dependent position of the IO front has been derived by Swisher and Fuchs [69SwF]. This can be expressed as

$$1 - \phi^2(1 - \ln \phi^2) = \frac{t}{t_c} \quad (1a)$$

$$\phi = \left( \frac{r_u}{R} \right) \quad t_c = \frac{1}{4} \left( \frac{N_B v}{N_o^s} \right) \left( \frac{R^2}{D_o} \right) \quad (1b)$$

where  $r_u$  is the radius of the unoxidized core,  $R$  is the outer radius of the wire (850  $\mu\text{m}$ ),  $N_B$  is the atomic fraction of the oxidizable element in the bulk alloy (0.01),  $v$  is the stoichiometric ratio of oxygen to metal atoms in the oxide (1.5 for Y, 2 for Zr),  $N_o^s$  is the oxygen concentration at the wire surface (assumed constant and equal to the equilibrium solubility of oxygen in the alloy), and  $D_o$  is the diffusion coefficient of oxygen through the matrix. Note that  $R(1 - \phi)$  is the oxidized thickness,  $\phi^2$  is the volume fraction of unoxidized material, and  $t_c$  is the characteristic time for complete oxidation of the wire.

Values of  $t_c$  were estimated using oxygen solubilities and diffusivities reported in the literature [69PaR] and are listed in Table 2. The IO distances and times were then reduced to the form of Equation (1) and are plotted in Figure 3. Also given for comparison are normalized results from the literature for the oxidation of Cu-0.4Zr [70SwF] and Cu-1.2Cr [69SwF] in He/CO<sub>2</sub> mixtures at 1173 K. It is immediately evident that both the present results and those of Swisher and Fuchs cluster around single straight lines, supporting the hypothesis that the underlying

mechanism is correctly described by Equation (1), but the slopes of the lines are different and significantly lower than unity. This indicates that the experimental times for complete oxidation are longer than those predicted using literature values of  $N_O^s$  and  $D_O$ . A linear regression of  $[1-\phi^2(1-\ln\phi^2)]$  vs.  $t$  for the different wires readily yields the experimental values of the characteristic times listed in Table 2.

Analysis of the discrepancy between predicted and experimental IO times provides insight into the process, albeit not definitive conclusions on its origins. It may be argued that the delay is caused by the sluggish dissolution (or in-situ oxidation) of the intermetallic particles. However, one can easily show by analogy with standard heat transfer solutions [59Ca] that, in the absence of an oxygen sink, the oxygen concentration at the core of the wire would reach 1% of the surface value in  $t \approx 0.05(R^2/D_O)$ , and would be essentially saturated in  $t_s \approx (R^2/D_O)$ . By comparison, the time for complete internal oxidation from Equation (1) is  $t_c = 0.25\mu (R^2/D_O)$ , where  $\mu = (N_{BV}/N_O^s)$  represents the "strength" of the sink. Since  $N_B \approx 10^{-2}$  and  $N_O^s \approx 10^{-5}$  for the present experiments,  $\mu$  would be on the order of  $\sim 10^3$  and hence  $t_c \gg t_s$ . If the rate of dissolution (or direct oxidation) of the intermetallic particles were dominant, the oxygen could reach the center of the wire well in advance of the visible oxidation front. The O gradient through the wire would be much smaller than in the case described by Equation (1) and the oxidation front would be "diffuse", in obvious conflict with the microstructural evidence. It also follows that the kinetics would not be described by Equation (1) [69SwF].

The more likely source of uncertainty in the prediction of oxidation kinetics is the oxygen permeability ( $D_O N_O^s$ ); values for this parameter estimated from the experiments are also listed in Table 2. As expected from Figure 3, the effective permeabilities corresponding to the two sets of data are  $\sim 1/3$  (this work) and  $\sim 2/3$  [70SwF] of those calculated from independently determined values of  $N_O^s$  and  $D_O$  [69PaR]. Swisher noted that these lower permeability values are common to IO measure-



ments and ascribed them to counterdiffusion of the oxidizable element and/or blockage of the diffusion path by oxide particles [71Swi]. It was also noted, however, that counterdiffusion should be greatly minimized when the oxidizable element is only marginally soluble in the matrix, as in the present case. Similarly, it would be difficult to ascribe the observed reductions in permeability (30-70%) to blockage caused by oxide contents of  $\leq 3$  vol.%.

Variations of the magnitude observed are not uncommon in diffusivity data, although the relative consistency within each data set suggests that the differences are not simply experimental scatter. It is possible that the oxygen concentration at the surface,  $N_O^s$ , varies from one set of experiments to the other. (Note that results for different alloys in the same atmosphere are consistent, but not for similar alloys with comparable microstructures, e.g. Cu-Zr wires produced by casting and cold working by ~98% [cf. 70SwF] oxidized in different atmospheres.) Since the oxygen partial pressure,  $p_{O_2}$ , in the He/CO<sub>2</sub> atmospheres of Swisher and Fuchs was reported to be well above that necessary to form Cu<sub>2</sub>O on the surface, it might be inferred that the Ar/Cu<sub>2</sub>O mixture used in the present work was not capable of maintaining an equilibrium saturation of O at the wire surface. One would have to question, however, whether  $N_O^s$  could be maintained sufficiently constant during and between experiments to produce the reasonably consistent data in Figure 3.

Notwithstanding the relative uncertainty in the parameters that determine the oxidation kinetics, the practical impact is minimal owing to the small thickness of the rapidly solidified ribbons. Calculated oxidation times for the thicker 150  $\mu$ m ribbons of Cu~0.32Zr, using the appropriate form of Equation (1) for a plate [71Swi], range from ~7 to ~142 min for temperatures between 1223 and 1023 K. Oxygen permeabilities were estimated using an activation energy of ~165 kJ/gr-atom, (compared with a literature value of 193 kJ/gr-atom [69PaR]), deduced from the lower temperature measurements. In principle, times for Cu~0.33Y ribbons of the

same thickness should be approximately 75% of those calculated for Zr. However, the Cu-Y alloy cannot be processed above ~1123 K since the Cu-Cu<sub>7</sub>Y eutectic temperature is only 1133 K. To ensure complete conversion, the times selected for the actual experiments were several times longer than the theoretical predictions.

### *Microstructure of Internally Oxidized Ribbons*

Internal oxidation at the lower temperature (1023 K) yields spatially inhomogeneous dispersions of oxide particles in both alloys, which are less than optimal from a strengthening viewpoint—see Figure 4. A majority of the oxide particles appear in clusters ~200-300 nm across, distributed through the matrix on a scale comparable to that of the original intermetallic segregate, ~500 nm. The clusters exhibit a bimodal distribution of particle sizes, the finer on the order of 5-10 nm, and the coarser ranging from a few tens up to ~150 nm. On average, the relative population of fine particles within the clusters was much higher in Cu-ZrO<sub>2</sub> than in Cu-Y<sub>2</sub>O<sub>3</sub>. Fine oxide particles ≤10 nm across were also observed uniformly distributed throughout the matrix, albeit in a much lower volume fraction than within the clusters, and substantially fewer in number for Cu-Y<sub>2</sub>O<sub>3</sub> than for Cu-ZrO<sub>2</sub>. Some oxide particles on the order of 100 nm were also present at grain boundaries, more commonly in Cu-Y<sub>2</sub>O<sub>3</sub> than in Cu-ZrO<sub>2</sub>.

The Cu-0.32Zr alloy oxidized at 1223 K exhibits a markedly superior distribution of oxide particles, as noted in the TEM micrograph of Figure 5(a). With the exception of a minor fraction of grain boundary oxides, which can be up to ~50 nm in size, the majority of the particles in this material have dimensions of ≤ 10 nm and are quite uniformly dispersed through the matrix with no evidence of clustering. In contrast, the Cu-0.33Y alloy oxidized at 1123 K (the highest temperature allowable in practice by the onset of eutectic melting) still exhibited large particles at the former segregate sites, as illustrated by Figure 5(b), although some improve-

ments were noted in the size and relative population of the finer oxides. Nevertheless, even the non-optimal dispersions produced by this approach had generally finer particle sizes than those reported for internally oxidized wires with "mechanically refined" segregate structures [69SwF, 70SwF].

The presence of oxide clusters and the bimodal particle size distribution arise from the competition between the two IO micromechanisms proposed by Swisher and Fuchs: *in-situ reaction*, wherein the oxide forms directly on the intermetallic particle, and *dissolution-reprecipitation*, wherein the oxide forms away from the intermetallic producing a concentration gradient that tends to dissolve the latter. In the first case, proposed for Cu-Cr [69SwF], the size and spacing of the oxide dispersoids would be comparable to that of the segregate phase in the precursor microstructure (or larger if coarsening of the intermetallic takes place prior to arrival of the oxidation front). The coarser oxides in the present work are likely to have been generated by this mechanism. Conversely, dissolution-reprecipitation inherently leads to finer sizes and spacings than direct reaction, but the dispersion would not necessarily be homogeneous unless the diffusive transport of the oxidizable element away from the intermetallic particle is competitive with the rate of oxygen ingress.

The local time scale of the oxidation process can be defined in terms of the intermetallic spacing,  $\lambda_i$ , and the velocity of the oxidation front for a plate [71Swi] as:

$$\tau_{ox} = \frac{\lambda_i \ell N_B v}{D_o N_o^s} \quad (2)$$

where  $\ell$  is the distance from the ribbon surface. Conversely, the time scale for the dissolution of a spherical intermetallic particle of diameter  $\delta_i$  into a corresponding

volume of diameter  $\lambda_i$  under a concentration gradient on the order of  $\sim 2N_B^*/\lambda_i^5$  can be given as a first approximation by

$$\tau_{\text{dis}} = \frac{\lambda_i \delta_i}{4 D_B N_B^* (1 + \eta)} \quad (3)$$

where  $N_B^*$  is the equilibrium solubility of the oxidizable element B at the Cu/inter-metallic interface, and  $\eta$  is the stoichiometric ratio of Cu to B atoms in the intermetallic. For maximum homogeneity of oxide particle dispersion  $\tau_{\text{dis}} < \tau_{\text{ox}}$ . In a dilute dispersion the intermetallic particle size and spacing may be related to its volume fraction,  $f_i$ , by  $(\lambda_i/\delta_i) \approx \sqrt{\pi/6f_i}$  [90RöA], where  $f_i \approx (1+\eta)N_B$ . Thus, the desirable microstructural scale to ensure dispersion homogeneity should be

$$\frac{\lambda_i}{\ell} \leq f \left( \nu \sqrt{1+\eta} \right) \sqrt{N_B} \left[ \frac{D_B N_B^*}{D_o N_o^s} \right] \quad (4)$$

where  $f$  is a factor that lumps the geometrical assumptions of the problem and the group  $\nu \sqrt{1+\eta}$  accounts for the effect of stoichiometry. For the present discussion  $f \approx 5$ ,  $\nu \sqrt{1+\eta} \approx 4.5$  and  $N_B = 0.003$ ; hence, the group of factors in front of the permeability ratio is of order unity. The ratio  $(\lambda_i/\ell)$  is  $\sim 1$  near the surface and decreases to  $\sim 0.01$  at the center of the ribbons, suggesting that conditions for homogeneous distribution are easier to achieve away from the surface. Conversely, time available for intermetallic coarsening, also a function of  $D_B N_B^*$ , increases with distance from the surface suggesting the existence of an optimum thickness range to produce reasonably homogeneous dispersions.

Since  $D_B < D_o$  but  $N_B^* > N_o^s$ , even for the relatively insoluble Zr and Y, there would be a minimum IO temperature to satisfy Equation (4), provided the activa-

5

Swisher and Fuchs [70SwF] actually proposed that the dissolution occurs over a scale larger than the interparticle spacing, but their own experimental results clearly indicate that the diffusion distances involved are  $\sim 2 \mu\text{m}$  whereas the interparticle spacing estimated from their microstructural data should be  $\sim 5 \mu\text{m}$ .

tion energy for the permeability of the oxidizable element is greater than that of oxygen. At the lower oxidation temperature (1023 K) the permeability ratio is apparently too small for both Zr and Y, and hence only part of the oxidation takes place by dissolution-precipitation whereupon the resulting oxides are clustered near the prior segregate sites. The volume fraction and relative dispersion of the fine oxides is greater in Cu-Zr than in Cu-Y, consistent with the lower permeability expected for the latter on the basis of its much larger atomic size. From the present results and those in [70SwF] it appears that temperatures in the range of 1173-1223 K increase sufficiently the permeability of Zr in Cu to satisfy Equation (4). It is also evident that the conditions for homogeneous dispersion are not satisfied for Cu-Y even at the highest possible IO temperature (1123 K).

#### *Crystallography of Dispersoids and Interfaces in IO Ribbons*

Selected area diffraction (SAD) patterns taken from the clusters and the surrounding areas, Figure 8, reveal that all particles in the Cu-Y<sub>2</sub>O<sub>3</sub> alloy were cubic yttria (D5<sub>3</sub>). In contrast, the ZrO<sub>2</sub> dispersoids exhibited two crystal structures: all the fine particles and the majority in the lower end of the coarser range were cubic zirconia (C1) whereas the rest were monoclinic. The identification of the ZrO<sub>2</sub> particles as cubic rather than tetragonal is based primarily on the absence of {11 $\bar{2}$ } reflections in the SAD patterns [84LHM]. (Fine particles within the matrix could not be conclusively indexed owing to the small volume fraction and hence low intensity of the diffraction patterns. However, analysis of their size and shape suggests they are similar to the finer particles within the clusters.) The monoclinic particles are twinned, suggesting that they evolved from the transformation of a parent tetragonal ZrO<sub>2</sub> phase.

With the possible exception of some particles at grain boundaries, all other oxides consistently exhibited clear crystallographic relationships with the Cu matrix, evident in Figure 8. The dominant one is the classical cube on cube:

$$\{100\}_{\text{Ox}} \parallel \{100\}_{\text{Cu}} \quad \langle 001 \rangle_{\text{Ox}} \parallel \langle 001 \rangle_{\text{Cu}}$$

Monoclinic zirconia particles (mz) located either within the oxide clusters or on some copper grain boundaries, exhibited a pseudo cube-on-cube orientation relationship with the copper in which

$$(\bar{1}11)_{\text{mz}} \parallel \{1\bar{1}1\}_{\text{Cu}} \quad (002)_{\text{mz}} \parallel \{002\}_{\text{Cu}}$$

A second type of orientation relationship was also observed between Cu and some of the coarser cubic  $\text{Y}_2\text{O}_3$  particles ( $\geq 30$  nm). It is given as:

$$\{100\}_{\text{Y}_2\text{O}_3} \parallel \{1\bar{1}1\}_{\text{Cu}} \quad \langle 001 \rangle_{\text{Y}_2\text{O}_3} \parallel \langle 110 \rangle_{\text{Cu}}$$

This is similar to that reported for an internally oxidized Cu-Mn alloy by Ernst [90Ern] who described it as a "55°  $\langle 110 \rangle$  topotaxy". In this orientation yttria would share a common  $\langle 110 \rangle$  zone axis with the copper matrix, wherein the  $[001]_{\text{Y}_2\text{O}_3}$  direction is rotated 55° from the  $[001]_{\text{Cu}}$  axis to bring it into alignment with one of the  $\langle 110 \rangle_{\text{Cu}}$  directions.

The orientation relationships above are not sufficient to deduce the actual crystallography of the interfaces between matrix and dispersoids, which is in principle relevant to the effectiveness of the dislocation/particle interaction. This information must come from careful examination of the shape of the oxide particles, particularly the finer ones, in relation to well defined zone axes of the Cu matrix. In general, particle shapes were found to be similar in both  $\text{ZrO}_2$  and  $\text{Y}_2\text{O}_3$  bearing alloys. Figures 7(a,b) show fine  $\text{ZrO}_2$  dispersoids within a cluster in TEM images taken along the  $[100]_{\text{Cu}}$  and  $[110]_{\text{Cu}}$  zone axes. Many of the particles in Figure 7(a)

have a roughly square or rectangular shape with edges corresponding to  $\{100\}_{\text{Ox}}$  planes facing  $\{100\}_{\text{Cu}}$  planes, as deduced from the Moiré fringe spacing ( $\sim 0.6$  nm), and the zone axis. The particles appear approximately hexagonal upon tilting to the  $[110]$  zone axis, Figure 7(b), as one pair of  $\{100\}_{\text{Ox}}$  facets is replaced by four of the  $\{111\}_{\text{Ox}}$  type. It is inferred that the particles are tetrakaidecahedral in shape, with six  $\{100\}$  and eight  $\{111\}$  facets. Variations in appearance noted in the TEM images arise from differing degrees of development of the  $\{111\}$  and  $\{100\}$  facets. There was no evidence of coherency strains near the particles, in agreement with prior studies on IO copper alloys [91EPH, 90Ern]. Most of the interfaces were expected to be incoherent based on the relatively large lattice disregistry of the various pairs of matching planes observed.

It may be readily shown that the smallest lattice mismatch between copper and the fluorite-type oxides in this study does not correspond to the observed cube-on-cube orientation relationship, but rather to a cube-on-edge, i.e.

$$\{100\}_{\text{Ox}} \parallel \{100\}_{\text{Cu}} \quad \langle 001 \rangle_{\text{Ox}} \parallel \langle 011 \rangle_{\text{Cu}}$$

Fecht and Gleiter [85FeG] reported that noble metals tend to orient themselves in a cube-on-cube relationship when small metal spheres are sintered onto the surface of single crystals of various ionic compounds, regardless of the facet shown by the substrate and irrespective of the lattice mismatch. Studies of interfaces between f.c.c. metals and oxides with f.c.c. anion lattices (spinel or rock salt) consistently show predominance of the  $\{111\}_{\text{Ox}} \parallel \{111\}_{\text{M}}$  planes [68WiS, 88NeM, 90Ern, 90GaM, 90Mus, 91EPH]. In contrast, the cubic  $\text{ZrO}_2$  and  $\text{Y}_2\text{O}_3$  dispersoids in this study exhibit both strongly developed  $\{111\}_{\text{Ox}} \parallel \{111\}_{\text{Cu}}$  and  $\{100\}_{\text{Ox}} \parallel \{100\}_{\text{Cu}}$  interfaces.

The observed orientation relationships and interfaces may be explained by the image charge interaction model of Stoneham and Tasker [88StT]. The strongest interactions in the noble metal-oxide interfaces occur between the closest packed

metal planes and the oxide planes with the highest charge density, which are {111} type in the spinel and rock salt structures [90Ern]. Conversely, the {100} anion planes in fluorite have a higher charge density than those of the {111} type, but the matching {100}<sub>Cu</sub> planes in a cube-on-cube orientation have a lower packing density than {111}<sub>Cu</sub>. In principle, the strongest image force would develop in a {100}<sub>Ox</sub> || {111}<sub>Cu</sub> interface, but such an orientation would allow only one pair of parallel facets to minimize their energy. That such an interface is rarely observed suggests that the observed combination of the lower charge density {111}<sub>Ox</sub> planes with the most densely packed {111}<sub>Cu</sub> planes, and the higher charge density {100}<sub>Ox</sub> planes with the less closely packed {100}<sub>Cu</sub> planes, is more effective in minimizing the overall interfacial energy between matrix and dispersoids.

While orientation relationships of the type {100}<sub>Ox</sub> || {111}<sub>Cu</sub> are never dominant, they were observed more frequently in Cu-Y<sub>2</sub>O<sub>3</sub> than in Cu-ZrO<sub>2</sub>, usually conforming to the 55° <110> topotaxy model. As expected from the discussion above, the particles are in this case platelike in shape. The parallel {100}<sub>Ox</sub> and {111}<sub>Cu</sub> planes are aligned such that <100> rows of oxygen anions are parallel to close-packed <110> rows of copper atoms, as illustrated in Figure 8. Since the true image forces are likely to be lower in yttria owing to the lower packing density of anions on the {100} planes, it is not clear why this orientation relationship is found more frequently in Cu-Y<sub>2</sub>O<sub>3</sub> than in Cu-ZrO<sub>2</sub>. Stoneham and Tasker [88StT] suggested that "lock-in" interfacial configurations, in which close-packed rows of atoms/ions in one phase can fit into valleys between the close-packed rows of atoms/ions in the other phase [85FeG], can optimize image charge interactions because they may allow the corresponding interfacial planes to more closely approach each other. This type of configuration may be achievable in Cu-Y<sub>2</sub>O<sub>3</sub>, as illustrated in Figure 8. However, the anion positions on the {100} planes of the cubic yttria structure are not truly co-



planar as in fluorite [94]DL], suggesting that the image forces should be somewhat lower than anticipated from the lock-in perspective.

### ***Microstructure of Consolidated and Extruded Materials***

All three alloys exhibit grain structures elongated in the extrusion direction, as illustrated by the optical micrograph from alloy Z9 in Figure 9(a). The  $Y_2O_3$  bearing alloy Y7 exhibits a greater number of larger oxide particles than either Z7 and Z9, as well as a substantial proportion of nearly equiaxed grains, suggesting that more extensive dynamic recrystallization may have occurred in Y7. Average grain sizes (GZ), measured transverse to the extrusion direction, and grain aspect ratios (GAR) in the longitudinal direction are listed in Table 3. Note that GZ decreases and GAR increases with increasing the refinement and homogeneity of the oxide dispersion, i.e.  $Z9 > Z7 > Y7$ . Low magnification analysis in the TEM reveals similar grain structures for the three alloys, consisting of small grains in which subgrains are sometimes visible, e.g. Figure 9(b).

Dark field imaging of alloy Z9 revealed a uniform dispersion of oxides ranging from ~5 to ~20 nm in diameter, as depicted in Figure 10(a). The well defined orientation relationships in the IO ribbons are rarely preserved, as expected from the occurrence of recrystallization. However, DF imaging reveals that large numbers of particles still exhibit common orientations. Oxide clusters readily visible in the internally oxidized ribbons of alloys Z7 and Y7 were obscured by dislocation entanglements around them and thus no longer distinguishable in the extruded rods at equivalent TEM magnification. While some cluster breakup may be expected during the relatively severe extrusion, dark field images reveal that many clusters survive the process essentially undeformed, e.g. Figure 10(b). This suggests that the particle density within the cluster is sufficiently high to make it behave as a hard inclusion.

From a classical Orowan perspective, the strengthening potential of a dispersion is primarily a function of the interparticle spacing,  $\lambda_0$ . If the dispersion is reasonably uniform, as in alloy Z9, the spacing may be readily estimated from the same stereological relationship used above,  $(\lambda_0/\delta_0) = \sqrt{\pi/6f_0}$ , where  $\delta_0$  is the average dispersoid diameter from metallographic measurements, and  $f_0$  is the dispersoid volume fraction which is easily estimated from the concentration of oxidizable element in the alloy. This is much more difficult to define properly when the bulk of the oxide particles are clustered, and their sizes vary over a wide range, as in alloys Z7 and Y7. The oxide clusters could in principle act as dislocation pinning points, but their spacing is often too large ( $\geq 500$  nm) to be fully effective for strengthening by the Orowan or Rösler/Arzt mechanisms. There is, however, a small fraction of much finer oxides dispersed relatively uniformly throughout the matrix between clusters. To a first approximation one could estimate the volume fraction of fine "matrix" dispersoids assuming that they arise only from the small, albeit finite, amount of oxidizable element dissolved in Cu. (A finite solubility is supported by the presence of ultrafine intermetallic particles within the cells/dendrites of the rapidly solidified microstructures.) Ignoring for a moment the possibility of solute trapping during RSP, an upper limit would be given by the maximum equilibrium solubility, which is  $\sim 0.12\%$  for Zr and  $\sim 0.04\%$  for Y. This yields "effective" volume fractions of dispersoids of  $\sim 0.32\%$  for Z7 and  $\sim 0.14\%$  for Y7, respectively, well below the  $\sim 1\%$  content calculated for alloy Z9 (admittedly an optimistic estimate, since some of the oxide was present as coarser grain boundary oxide particles).

Notwithstanding the lower effective  $f_0$  values for the materials with clustered oxides, the measured particle sizes are in all cases sufficiently fine (5 ~ 6 nm) to yield interparticle spacings in the range attractive for dispersion strengthening, as shown in Table 3. A companion paper [94NLL] reports on the properties of these materials.

While a reasonably optimum combination of processing conditions yielding suitable oxide dispersions seems to have been identified for dilute Cu-Zr alloys, the same was not true for Cu-Y. One might hypothesize that improvements in the rapid solidification process, e.g. reducing and controlling the ribbon thickness by using planar flow casting instead of free-jet melt spinning, could lead to additional refinement of the intermetallic Cu<sub>7</sub>Y. However, the lower permeability for Y and inherent limitations to the IO temperature suggest that complete elimination of coarser particles and oxide clusters may not be practically achievable. In principle, improved RSP could lead to metastable solubility extensions and hence a greater proportion of Y or Zr in solution or as fine intracellular precipitates. Splat cooling experiments undertaken in a previous investigation [91Nag] failed to suppress partitioning or produce evidence of substantial extensions in solubility relative to melt spinning. However, such a goal may be achieved if the alloy were synthesized by sputtering or vapor deposition. Figure 11 shows an example of a Cu-1Y alloy film, ~100  $\mu\text{m}$  thick, produced by sputter deposition and subsequently oxidized at 1023 K using the same approach described for the melt-spun ribbons [93LöL]. TEM examination revealed no Y-rich second phase in the sputtered film, which was a single phase extended solution with essentially the same composition as the initial target. The internally oxidized film had a remarkably uniform distribution of oxides, all  $\leq 10$  nm in size and in principle ideal for dispersion strengthening. It remains to be seen whether this approach is practical in developing free-standing shapes with desirable mechanical properties.

## CONCLUSIONS

It has been shown that oxide dispersions with attractive potential for creep strengthening of Cu may be produced from nominally insoluble elements by a pro-

cessing approach combining rapid solidification and internal oxidation. The oxidizable element ( $M = \text{Zr}, \text{Y}$ ) is typically present as a Cu-rich intermetallic phase,  $\text{Cu}_\eta\text{M}$ , which can be easily transformed to the corresponding oxide,  $\text{MO}_x$ , by standard IO techniques. The scale and homogeneity of the oxide dispersion are determined, to a first approximation, by the size and spacing of the intermetallic phase. Not surprisingly, the latter can be refined more effectively by RSP than through deformation processing of the cast structure, an approach used by earlier investigators.

The desirable microstructural scale to produce a homogeneous oxide dispersion during IO depends on the competition between the rates of oxygen ingress and dissolution of the intermetallic, which is reflected on the relative permeabilities of oxygen and the oxidizable element. Oxygen ingress predominates at the lower temperatures, leading to the formation of coarser oxides produced by *in-situ oxidation* of the intermetallic, and a varying proportion of finer oxides clustered around the prior intermetallic sites which evolve by a *dissolution-reprecipitation* mechanism. A smaller fraction of fine oxides, more uniformly distributed through the matrix, arises from the low concentration of oxidizable element dissolved in the primary phase during solidification. Increasing the IO temperature enhances preferentially the intermetallic dissolution rate and hence the relative population of finer oxides and their homogeneity of dispersion through the matrix. This approach produces satisfactory microstructures in Cu-Zr, but not in Cu-Y owing to its initially coarser intermetallic distribution, lower permeability and earlier onset of eutectic melting, which limits the maximum IO temperature. An alternate option to improve dispersoid homogeneity when  $D_{\text{B}}N_{\text{B}}^{\bullet} \ll D_{\text{O}}N_{\text{O}}^{\text{S}}$  is to "trap" the oxidizable element in solution prior to IO. While this may be beyond the reach of RSP for the Cu-Y alloys, it is readily achievable by vapor deposition techniques.

The finer oxide particles produced in these alloys were cubic zirconia or cubic yttria and had cube-on-cube orientation relationships with the matrix in the as-oxi-

dized condition. The oxides were tetrakaidecahedral in shape, with well developed {100} and {111} facets facing planes of the same type in the Cu matrix. While these interfaces cannot be explained on the basis of coincident site lattice arguments, they are consistent with simple models based on image charge interactions between anion and metal planes. Deformation processing may change some of the orientation relationships owing to partial recrystallization, but was not sufficiently severe to have a significant effect on the overall oxide distribution.

### ACKNOWLEDGMENTS

This research was supported by the Advanced Projects Research Agency through University Research Initiative Grant N00014-92-J-1808 supervised by Dr. W. Coblenz and monitored by Dr. S.G. Fishman of the Office of Naval Research. Additional support for M. S. Nagorka in the form of a National Defense Science and Engineering Grant fellowship provided by the Advanced Projects Research Agency is gratefully acknowledged. The authors would also like to thank Dr. Alfred Austen of Innovare, Inc. for his assistance in extruding the materials used in this work.

### REFERENCES

- [42RJA] F. N. Rhines, W. A. Johnson, and W. A. Anderson, "Rates of High-Temperature Oxidation of Dilute Copper Alloys," *Transactions of the Metallurgical Society of AIME*, 147(1942) 205-221.
- [47MeD] J.L. Meijering and M.J. Druyvesteyn, "Hardening of Metals by Internal Oxidation. Part II," *Philips Res. Rep.* 2 (1947) 260-280.
- [59CaJ] H.S. Carslaw and J.C. Jaeger: Conduction of Heat in Solids, 2nd Ed., Oxford University Press, 1959, p.200.
- [62KoG] N. Komatsu and N.J. Grant, "Thermal Stability of Cu-SiO<sub>2</sub> and Cu-Al<sub>2</sub>O<sub>3</sub> Alloys," *Trans. Metall. Soc. AIME*, 224(1962) 705-713.

- [66Jac] K.A. Jackson, J.D. Hunt, D.R. Uhlman, and T.P. Seward III, *Trans. Metall. Soc. AIME*, **236** (1966) 149.
- [68WiS] D. M. Williams and G. C. Smith, "A Study of Oxide Particles and Oxide-Matrix Interfaces In Copper," in G. S. Ansell, T D. Cooper, and F. V. Lenel, eds., Oxide Dispersion Strengthening, Gordon and Breach, New York (1968) 509-536.
- [69PaR] R.L. Pastorek and R.A. Rapp, "The Solubility and Diffusivity of Oxygen in Solid Copper from Electrochemical Measurements." *Trans. Metall. Soc. AIME*, **245** (1969) 1711-1720.
- [69SwF] J. H. Swisher and E. O. Fuchs, "Kinetics of Internal Oxidation of Cylinders and Spheres; Properties of Internally Oxidized Cu-Cr Alloys," *Transactions of the Metallurgical Society of AIME*, **245**(1969) 1789-1794.
- [70SwF] J. H. Swisher and E. O. Fuchs, "Dispersion-Strengthening of Copper by Internal Oxidation of Two-Phase Copper-Zirconium Alloys," *Journal of the Institute of Metals*, **98**(1970) 129-133.
- [71SCK] W. Scheithauer, Jr., R.F. Cheney, and N.E. Kopatz, "The Manufacture and Properties of High-Conductivity High-Strength Cu-ThO<sub>2</sub>," in Modern Developments in Powder Metallurgy, Vol. 5, ed. H.H. Hausner, Plenum Press, New York-London (1971) 149-158.
- [71ScO] H. Schreiner and H. Ohmann, "Dispersion Hardened Materials with Copper as a Base Metal," in Modern Developments in Powder Metallurgy, Vol. 5, ed. H.H. Hausner, Plenum Press, New York-London (1971) 125-136.
- [71Swi] J. H. Swisher, "Internal Oxidation," in Oxidation in Metals and Alloys, American Society for Metals, Metals Park, OH (1970) 235-267.
- [74ShB] R.S.W. Shewfelt and L.M. Brown, *Phil. Mag.* **30** (1974) 1135.
- [76NKS] A.V. Nadkarni, E. Klar, and W.M. Shafer, "A New Dispersion Strengthened Copper," *Metals Engineering Quarterly* (1976), 10-15.
- [81ChL] D.J. Chakrabarti and D.E. Laughlin, *Bull. Alloy Phase Diagrams* **2**(3) (1981).
- [83Bra] E.A. Brandes, ed., Smithells Metals Reference Handbook, Butterworths, London (1983) 4-24.

- [84LHM] V. Lanteri, A.H. Heuer, and T.E. Mitchell, "Tetragonal Phase in the System  $\text{ZrO}_2\text{-Y}_2\text{O}_3$ ," in Science and Technology of Zirconia II, N. Claussen, M. Rühle, and A. Heuer, eds., The American Ceramics Society, Columbus OH (1984) 118-130.
- [84GLL] N.J. Grant, A. Lee, and M. Lou, "Multiple Hardening Mechanisms for High Strength, High Temperature, High Conductivity Copper Base Alloys," in High Conductivity Copper and Aluminum Alloys, E. Ling and P. W. Taubenblat, eds., AIME, Warrendale, PA, (1984) 103-117.
- [84Nad] A.V. Nadkarni, "Dispersion Strengthened Copper Properties and Applications," in High Conductivity Copper and Aluminum Alloys, E. Ling and P. W. Taubenblat, eds., AIME, Warrendale, PA, (1984) 77-101.
- [85FeG] H. J. Fecht and H. Gleiter, "A Lock-In Model for the Atomic Structure of Interphase Boundaries Between Metals and Ionic Crystals," *Acta Metallurgica*, 33(1985) 557-562.
- [87FIH] S.C. Flood and J.D. Hunt, "Columnar and Equiaxed Growth. II. Equiaxed Growth Ahead of a Columnar Front," *J. Crystal Growth* 82 (1987) 552-560.
- [88NeM] G. Necker and W. Mader, *Phil. Mag. Letters*, 58, (1988) 205-212.
- [88StT] A. M. Stoneham and P. W. Tasker, "Understanding Oxide-Metal Interfaces," *Journal de Physique*, C5(1988) 99-113.
- [90ArA] D. Arias and J.P. Abriata, in Binary Alloy Phase Diagrams, T. B. Massalski (editor in chief), ASM International, Metals Park, OH (1990) 1511.
- [90Ern] F. Ernst, "HRTEM of the Cu/MnO Interface in an Internally Oxidized Cu-Mn Alloy," *Material Research Society Symposium Proceedings*, 183(1990) 49-54.
- [90GaM] Y. Gao and K. L. Merkle, *J. Mater. Res.*, 5, (1990) 1995-2003.
- [90Mus] T. Muschik, "Final Report: Metal/Ceramic Interfaces In Internally Oxidized Pd-Al Alloys," Materials Department, University of California, Santa Barbara, Santa Barbara, California (1990).
- [90RöA] J. Rösler and E. Arzt, "A New Model-Based Creep Equation for Dispersion Strengthened Materials," *Acta Metallurgica et Materialia*, 38(1990) 671-683.
- [91EPH] F. Ernst, P. Pirouz, and A. H. Heuer, "HRTEM Study of a Cu/ $\text{Al}_2\text{O}_3$  Interface," *Philosophical Magazine A*, 63(1991) 259-277.

- [91Nag] M.S. Nagorka, C.G. Levi, G.E. Lucas, and S.D. Ridder, *Mat. Sci. and Engr.*, **A142**, (1991) 277-289.
- [93LöL] J.P.A. Löfvander and C.G. Levi: unpublished research, University of California at Santa Barbara, 1993.
- [93RaG] M. Rappaz and Ch.-A. Gandin, "Probabilistic Modeling of Microstructure Formation in Solidification Processes," *Acta Metall. Mater.* **41**(2) (1993) 345-360.
- [94JDL] V. Jayaram, M. De Graef, and C.G. Levi, "Metastable Extension of the Fluorite Phase Field in  $Y_2O_3$ - $ZrO_2$  and its effect on Grain Growth," *Acta Metall. Mater.* (1994) in press.
- [94NLL] M.S. Nagorka, G.E. Lucas, and C.G. Levi: "Novel ODS Copper Alloys from Rapidly Solidified Precursors-II: Creep Behavior," submitted to *Metallurgical and Materials Transactions*, 1994.

Table 1. Oxidation Conditions for the Alloys Investigated

Designation	Composition (at.%)	Product Form	IO Temp. (K)	IO Time (h)	Consolidated for Testing?
Z7	0.32 Zr	Ribbon	1023	12	Yes
Z9	0.32 Zr	Ribbon	1223	12	Yes
Y7	0.33 Y	Ribbon	1023	3	Yes
Y8	0.33 Y	Ribbon	1123	3	No*
ZW7	1 Zr	Wire	1023	4 - 64	n/a
ZW8	1 Zr	Wire	1073	4 - 64	n/a
YW7	1 Y	Wire	1023	8 - 32	n/a
YW8	1 Y	Wire	1073	8 - 32	n/a

\* This material was not considered for testing because its microstructure did not represent a significant improvement over that of Y7 (see later discussion.)



**Table 2. Experimental Measurements of Internal Oxidation Kinetics**

Temperature (K)	1023		1073	
Alloy	Cu-1Zr	Cu-1Y	Cu-1Zr	Cu-1Y
Time (h)	Thickness Oxidized ( $\mu\text{m}$ )			
4	48	61		
8	64	81	89	168
16	101	127	127	211
32	122	193	233	314
64	203	284		
	Characteristic Time for Complete Oxidation (h)			
From O Permeabilities in Literature	168	126	58	44
Experimental	629	322	234	139
Correlation Coefficient for Eq. (1)	0.982	0.998	0.959	0.994
	Oxygen Permeability ( $\text{m}^2/\text{s}$ )			
Literature Values	$6 \times 10^{-15}$		$1.7 \times 10^{-14}$	
Estimated from Experiments	$1.6 \times 10^{-15}$	$2.3 \times 10^{-15}$	$4.3 \times 10^{-15}$	$5.4 \times 10^{-15}$

**Table 3. Microstructural Parameters of Extruded Alloys**

Material	Grain Size $d$ ( $\mu\text{m}$ )	Grain Aspect Ratio	Volume Fraction of Oxide†	Oxide Particle Diameter, $\delta_o$ (nm)	Interparticle Spacing, $\lambda_o$ (nm)
Alloy Y7	4.3	1.5	0.0014*	6.0	120
Alloy Z7	3.6	2.2	0.0032*	5.1	66
Alloy Z9	2.4	2.8	0.010‡	6.2	44

† Volume fraction of fine matrix oxides.

\* Estimated based on solubility of yttrium or zirconium in matrix at eutectic temperature.

‡ Actual volume fraction of fine oxides smaller because of grain boundary oxides.

## LIST OF FIGURES

- Figure 1. Microstructure of melt spun Cu-0.32Zr (a,b) and Cu-0.33Y (c,d) ribbons: (a,c) Optical images with the chill face in contact with the wheel at the bottom of the micrographs; (b,d) TEM images taken near the mid-thickness of the ribbons. Note the somewhat coarser segregation scale of the Cu-Y in the TEM micrographs.
- Figure 2. Cu-1Y wire internally oxidized at 1023 K for 64 hours. The lighter microstructure near the periphery is the internally oxidized zone whereas the darker contrast in the core arises from the unoxidized intermetallic particles. Note the sharp boundary delineating the oxidation front.
- Figure 3. Internal oxidation kinetics plotted in terms of Equation (1);  $\phi^2$  is the volume fraction of unoxidized material and  $t_c = (N_{BV}/4N_O^S)(R^2/D_O)$  is the time for complete oxidation of the wire. Results from earlier studies by Swisher and Fuchs [69SwF, 70SwF] are included for comparison.
- Figure 4. TEM views of Cu-0.32Zr (a,b) and Cu-0.33Y (c,d) internally oxidized at 1023 K. The spacing of the oxide clusters in (a,b) is comparable to the scale of the intermetallic segregate dispersion. Note the difference between the particle size distributions within the clusters of (b) and (d). Finer particles ( $\leq 10$  nm) predominate in Cu-Zr (b), but not in Cu-Y (d).
- Figure 5. TEM views of (a) Cu-0.32Zr, and (b) Cu-0.33Y, internally oxidized at 1223 K and 1123 K, respectively. Increased IO temperature is sufficient to practically eliminate oxide clustering in (a), but not in (b). IO temperatures in both cases are slightly below the onset of eutectic melting.
- Figure 6.  $[110]_{Cu}$  zone axis patterns showing dominant orientation relationships in Cu-ZrO<sub>2</sub> (a,b) and Cu-Y<sub>2</sub>O<sub>3</sub> (c,d) ribbons IO at 1023 K: (a) cube-on-cube orientation for c-ZrO<sub>2</sub> particles; (b) "pseudo" cube on cube relationship observed in m-ZrO<sub>2</sub> particles, (c) cube-on-cube orientation for cubic Y<sub>2</sub>O<sub>3</sub> (many of the small spots arise from double diffraction); and (d) 55°(110) topotaxy relationship [90Ern] between Y<sub>2</sub>O<sub>3</sub> and Cu. Note the evidence of twinning in the m-ZrO<sub>2</sub> ZAP suggesting that the actual orientation relationship evolved between a parent t-ZrO<sub>2</sub> phase and Cu.
- Figure 7. High magnification views of ZrO<sub>2</sub> dispersoids: (a) imaged along  $[100]_{Cu}$  zone axis; (b) tilted to  $[110]_{Cu}$  zone axis.
- Figure 8. Schematic of interfacial arrangement corresponding to the 55°  $\langle 110 \rangle$  topotaxy relationship. The  $\{111\}_{Cu}$  plane is superimposed on the  $\{100\}_{Ox}$  plane rotated so that the  $\langle 001 \rangle_{Ox}$  direction is parallel to  $\langle 110 \rangle_{Cu}$ . Two adjoining rows of oxygen anions lie between close-packed rows of copper atoms (arrowed).

- Figure 9.** Microstructure of extruded Cu-ZrO<sub>2</sub> rod produced from ribbon internally oxidized at 1223 K: (a) optical view of longitudinal section showing elongated grains, (b) TEM view of transverse section showing deformation substructure.
- Figure 10.** Dark field TEM images of oxide distributions in the extruded alloys: (a) uniform oxide distribution in Alloy Z9, (b) essentially undeformed oxide cluster in Alloy Z7.
- Figure 11.** ODS Cu-3 vol.%Y<sub>2</sub>O<sub>3</sub> alloy produced by sputter deposition of Cu-1Y and internal oxidation at 1023 K. Deposition thickness was ~100 μm. Note uniform oxide dispersion in bright (a) and dark (b) field images. (c) shows the scale of the typical oxide particles and (d) a well developed cube-on-cube orientation relationship. (Courtesy of J.P.A. Löfvander.)

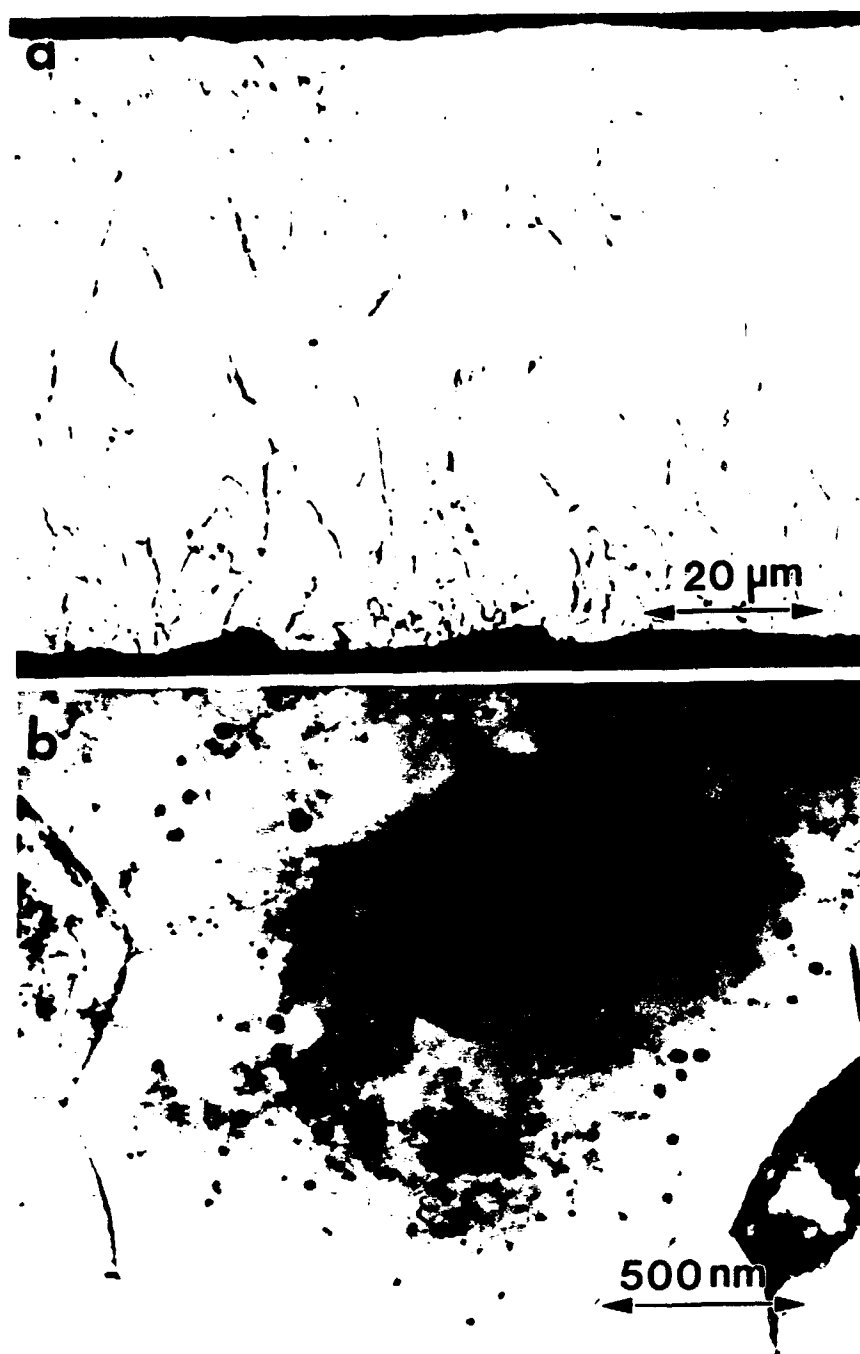


Figure 1. Microstructure of melt spun Cu-0.32Zr ribbons: (a) Optical image with the chill face in contact with the wheel at the bottom of the micrograph; (b) TEM image taken near the mid-thickness of the ribbon.

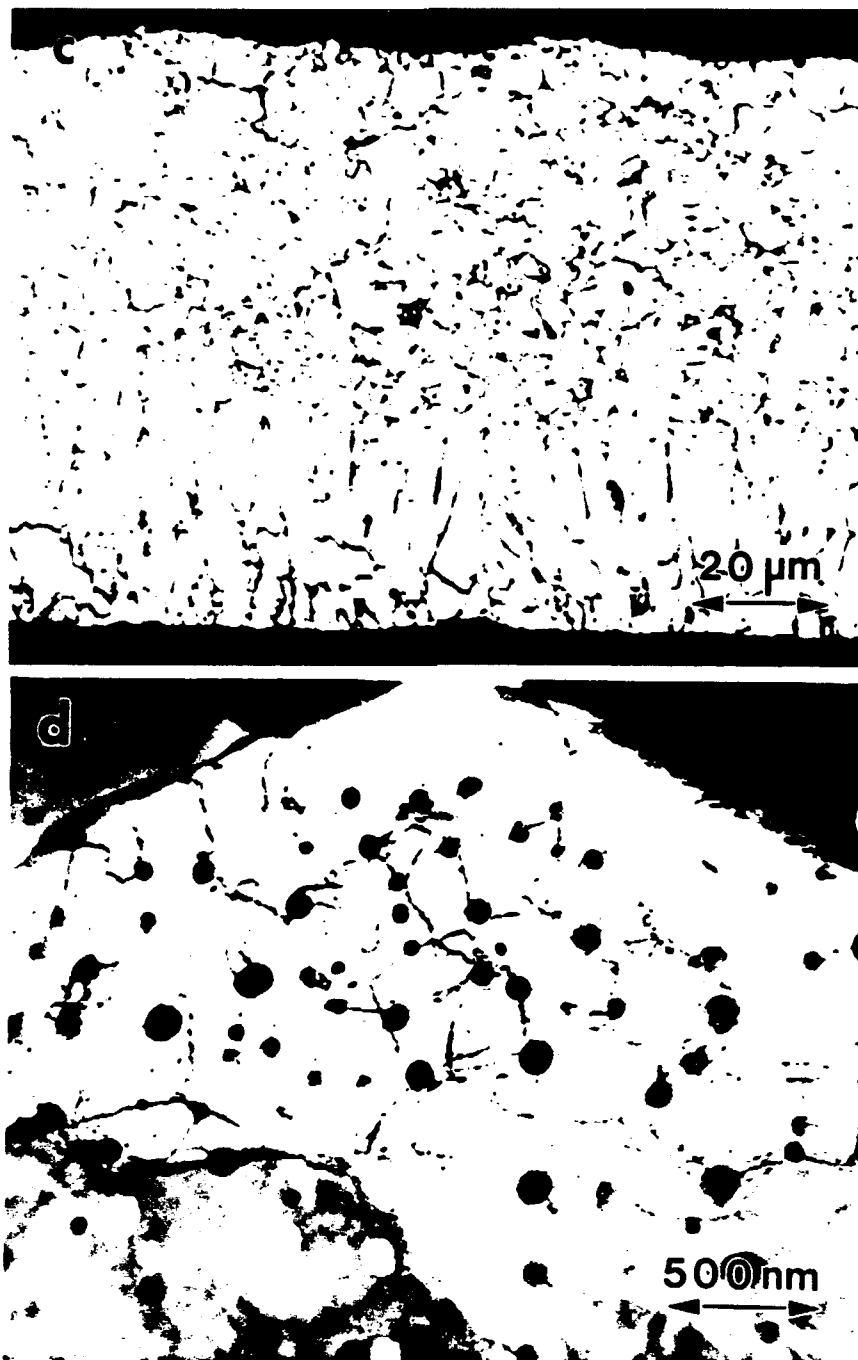
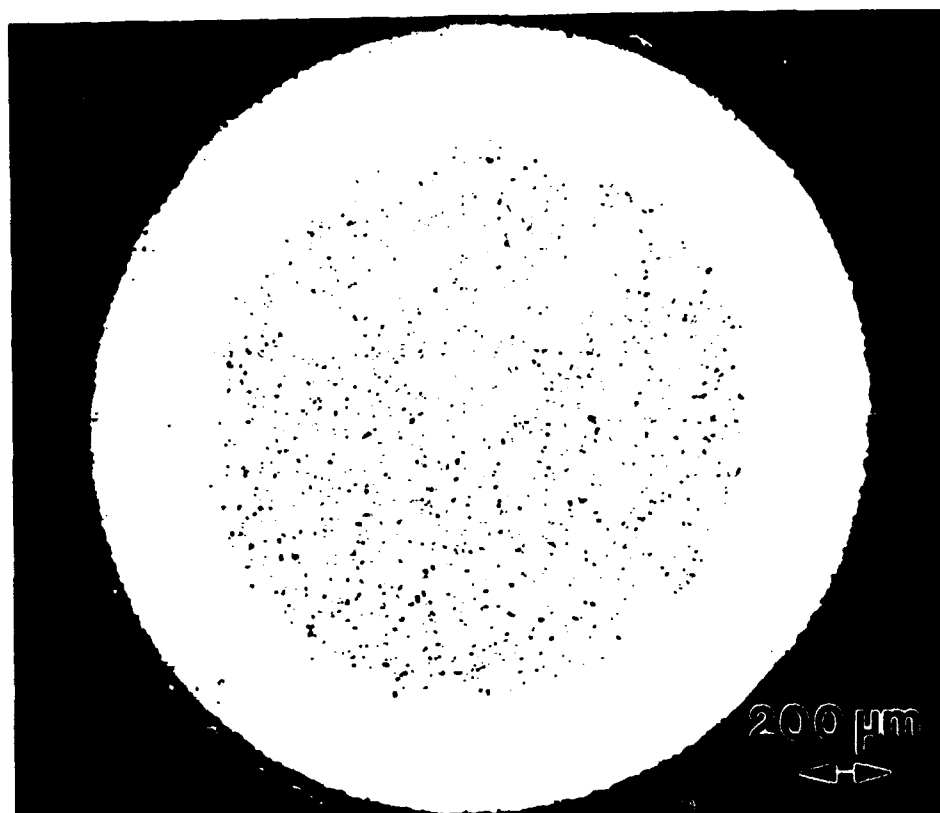


Figure 1. (cont.) Microstructure of melt spun Cu-0.33Y ribbons: (c) Optical image with the chill face in contact with the wheel at the bottom of the micrographs; (d) TEM image taken near the mid-thickness of the ribbon. Note the somewhat coarser segregation scale of the Cu-Y in the TEM micrographs (b,d).



**Figure 2.** Cu-1Y wire internally oxidized at 1023 K for 64 hours. The lighter microstructure near the periphery is the internally oxidized zone whereas the darker contrast in the core arises from the unoxidized intermetallic particles. Note the sharp boundary delineating the oxidation front.

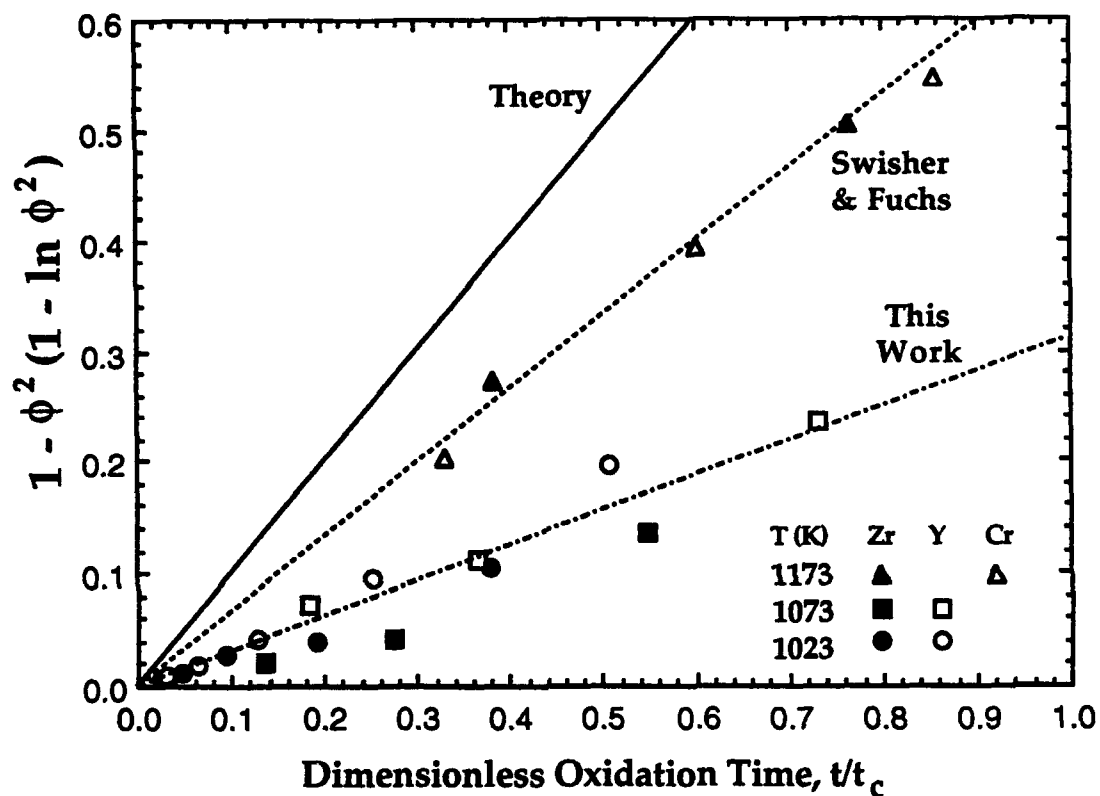


Figure 3. Internal oxidation kinetics plotted in terms of Equation (1);  $\phi^2$  is the volume fraction of unoxidized material and  $t_c = (N_{BV}/4N_0^s)(R^2/D_0)$  is the time for complete oxidation of the wire. Results from earlier studies by Swisher and Fuchs [69SwF, 70SwF] are included for comparison.

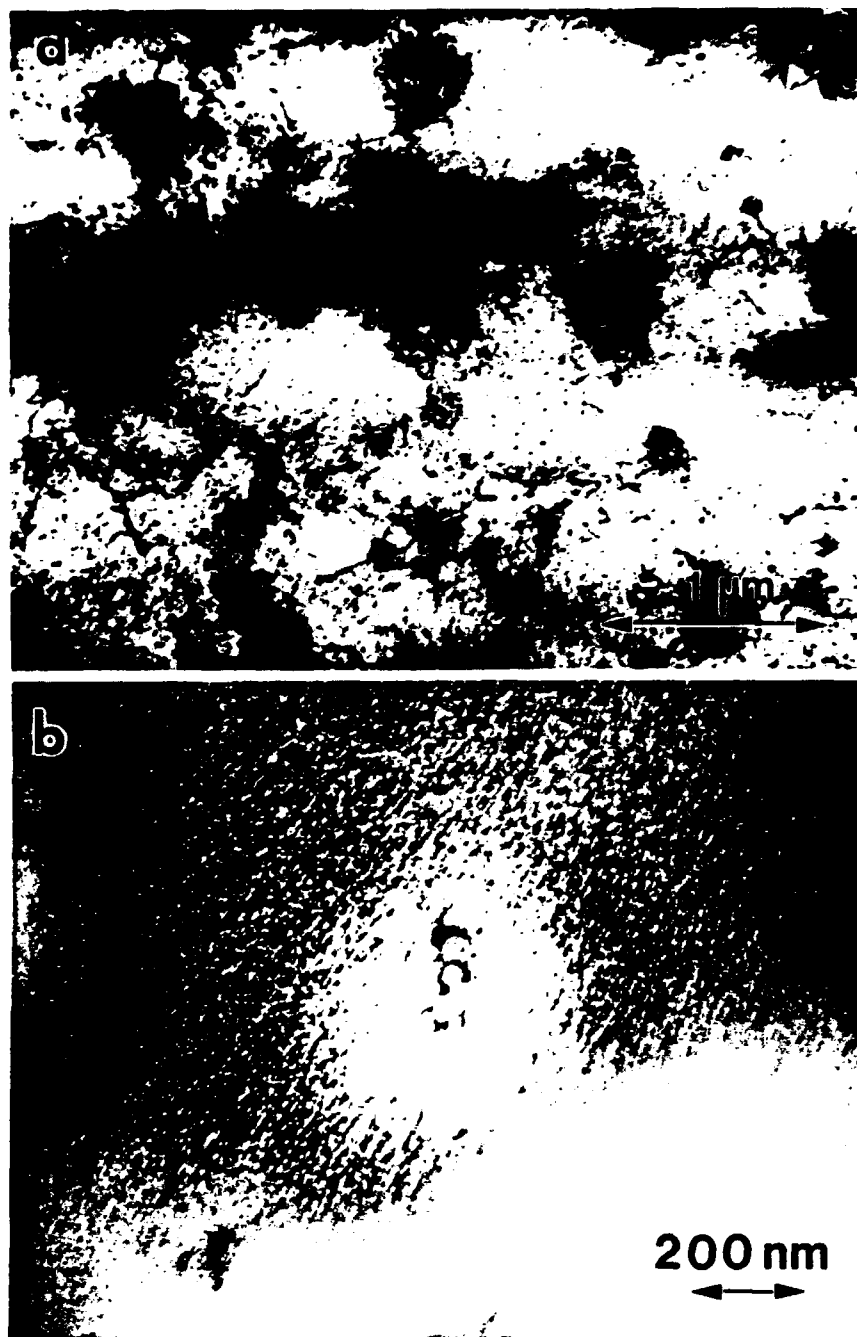


Figure 4. TEM views of Cu-0.32Zr internally oxidized at 1023 K. The spacing of the oxide clusters in (a) is comparable to the scale of the intermetallic segregate dispersion. Note the difference between the particle size distributions within the clusters of (b) and (d). Finer particles ( $\leq 10$  nm) predominate in Cu-Zr (b), but not in Cu-Y (d).



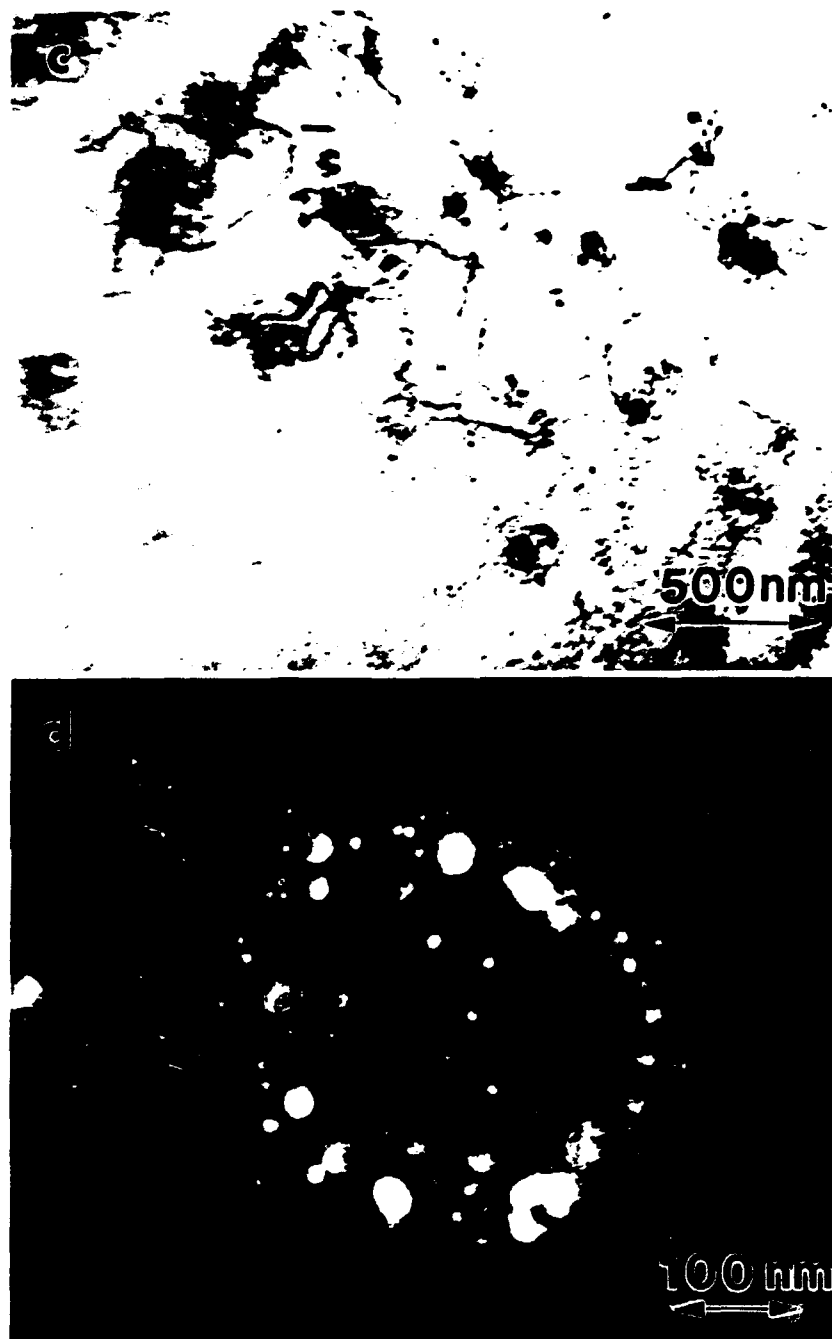


Figure 4. (cont.) TEM views of Cu-0.33Y internally oxidized at 1023 K. The spacing of the oxide clusters in (b) is comparable to the scale of the intermetallic segregate dispersion. Note the difference between the particle size distributions within the clusters in (b) and (d). Finer particles ( $\leq 10$  nm) predominate in Cu-Zr, but not in Cu-Y.

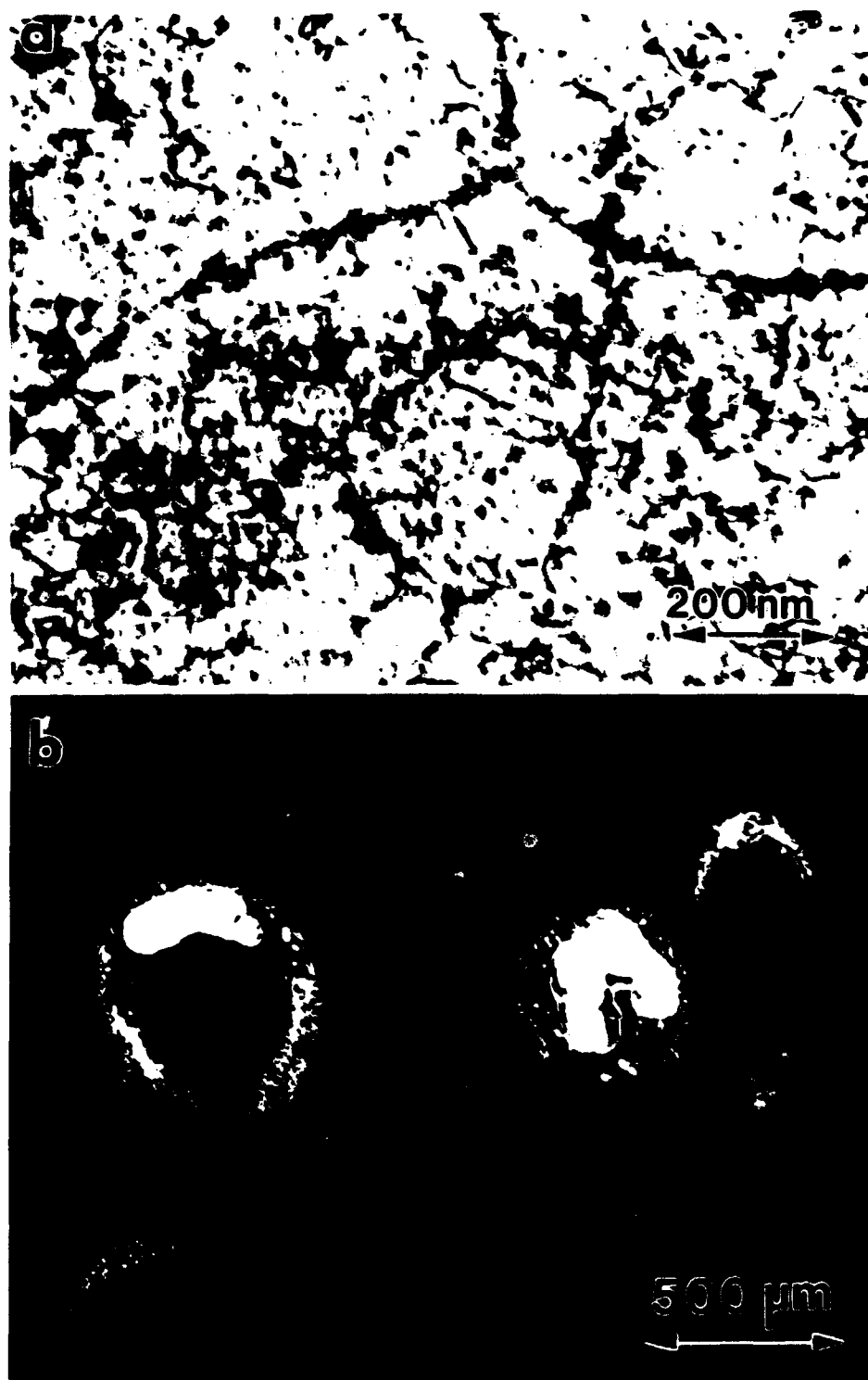


Figure 5. TEM views of (a) Cu-0.32Zr, and (b) Cu-0.33Y, internally oxidized at 1223 K and 1123 K, respectively. Increased IO temperature is sufficient to practically eliminate oxide clustering in (a), but not in (b). IO temperatures in both cases are slightly below the onset of eutectic melting.

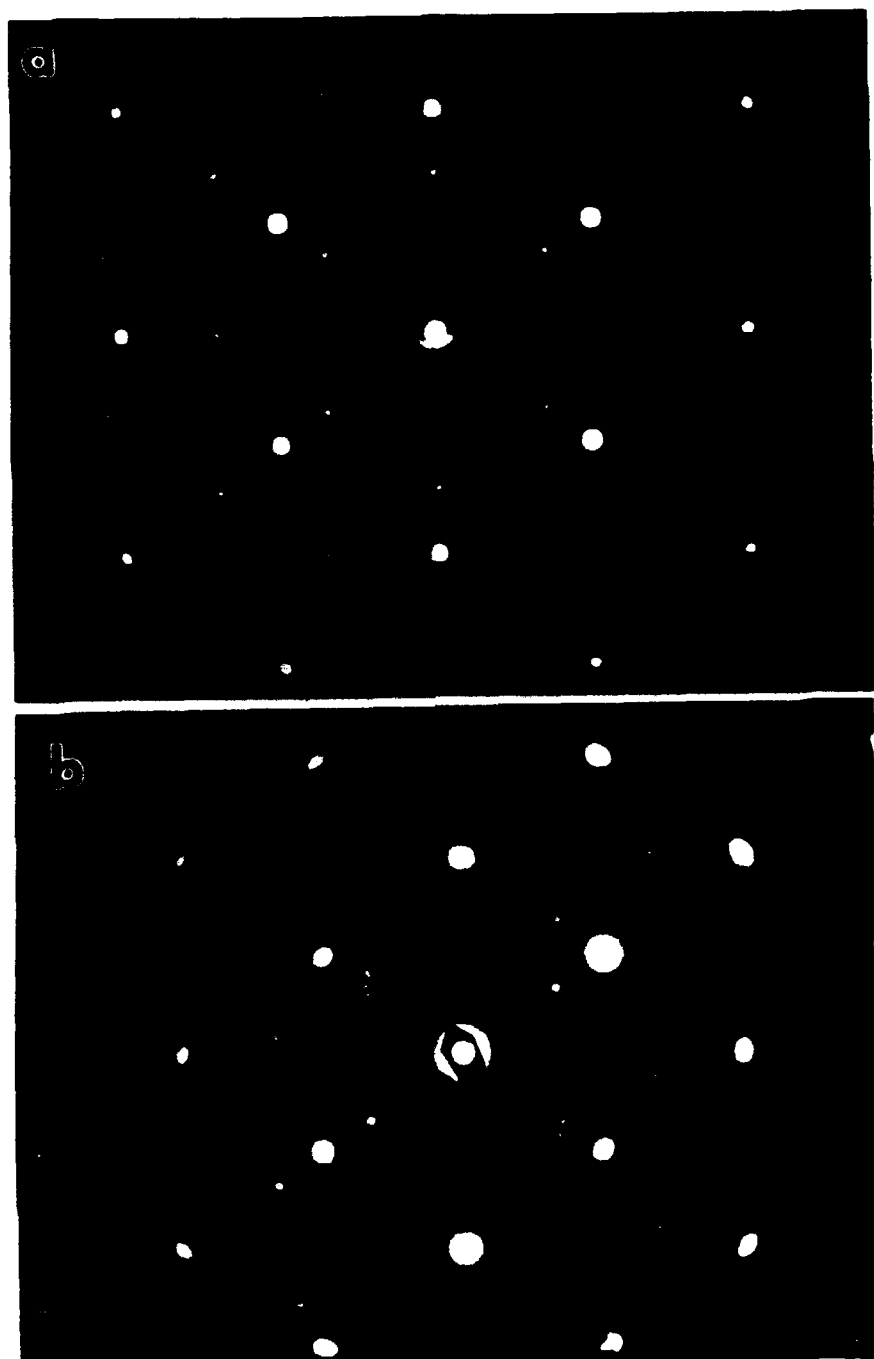


Figure 6.  $[110]_{\text{Cu}}$  zone axis patterns showing dominant orientation relationships in Cu-ZrO<sub>2</sub> ribbons IO at 1023 K: (a) cube-on-cube orientation for c-ZrO<sub>2</sub> particles; (b) pseudo cube on cube relationship observed in m-ZrO<sub>2</sub> particles, Note the evidence of twinning in the m-ZrO<sub>2</sub> ZAP suggesting that the actual orientation relationship evolved between a parent t-ZrO<sub>2</sub> phase and Cu.

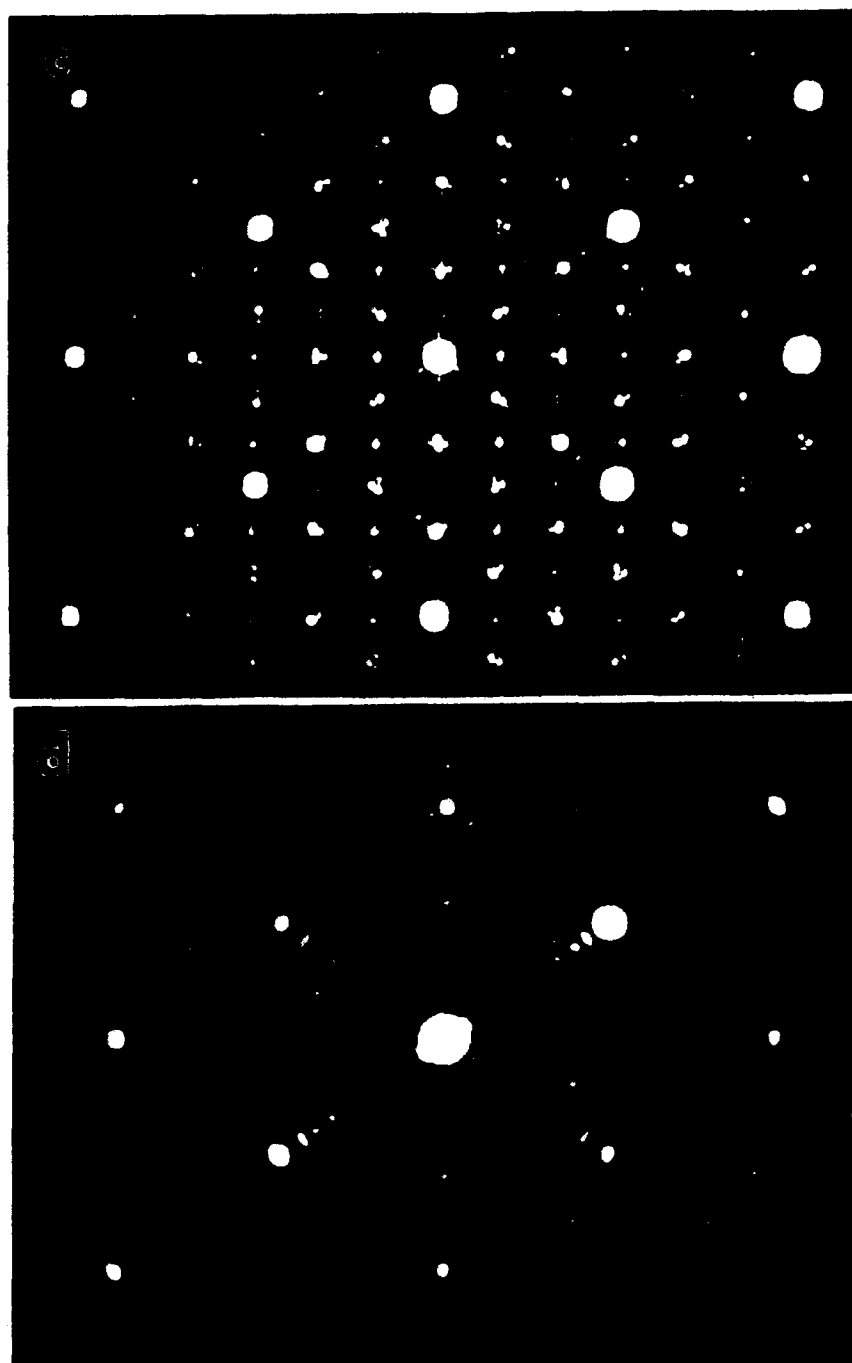


Figure 6. (cont.)  $[110]_{\text{Cu}}$  zone axis patterns showing dominant orientation relationships in Cu- $\text{Y}_2\text{O}_3$  ribbons IO at 1023 K: (c) cube-on-cube orientation for cubic  $\text{Y}_2\text{O}_3$  (many of the small spots arise from double diffraction); and (d)  $55^\circ\langle 110 \rangle$  topotaxy relationship  $[90\text{Er}]$  between  $\text{Y}_2\text{O}_3$  and Cu.

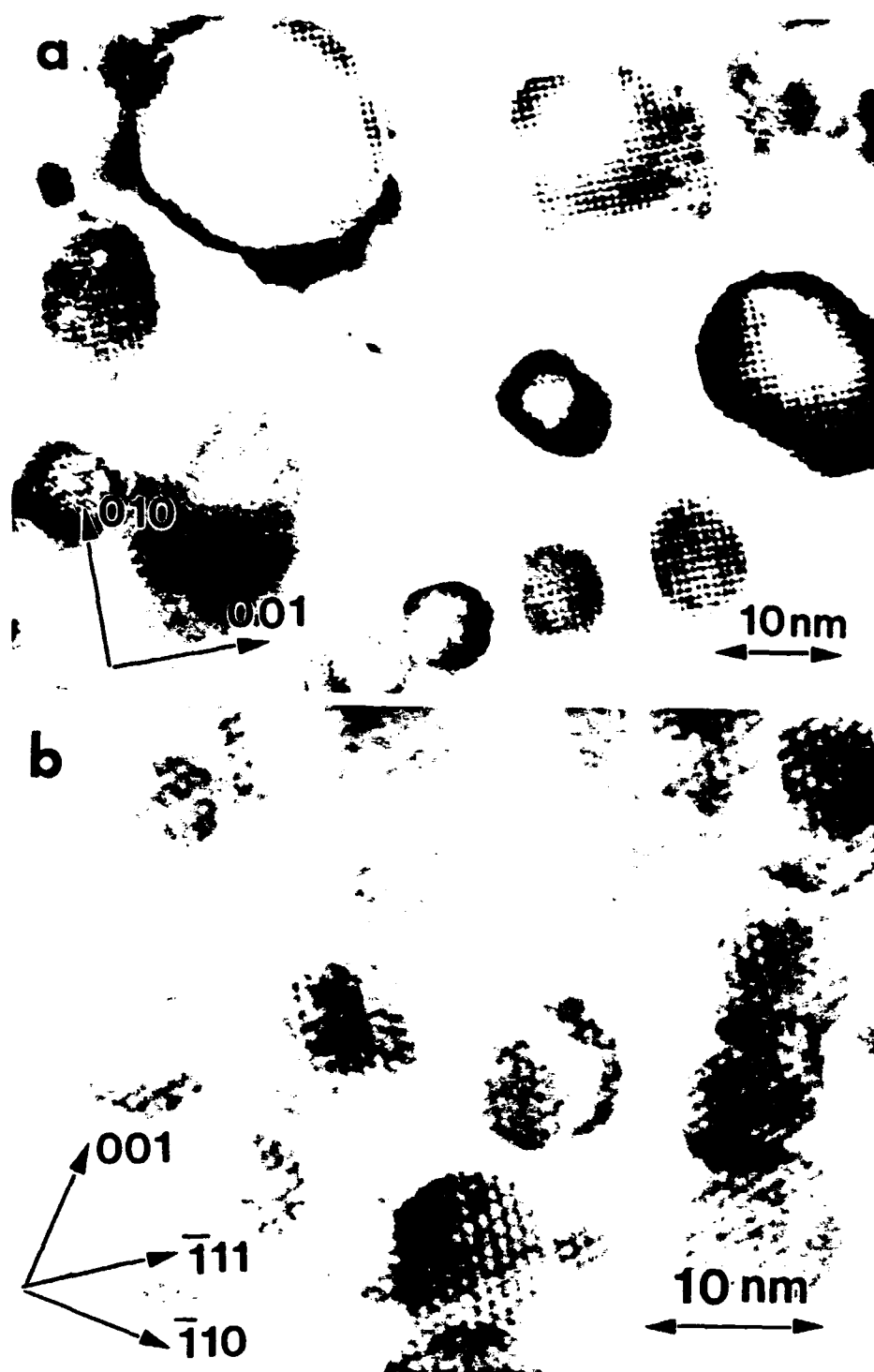
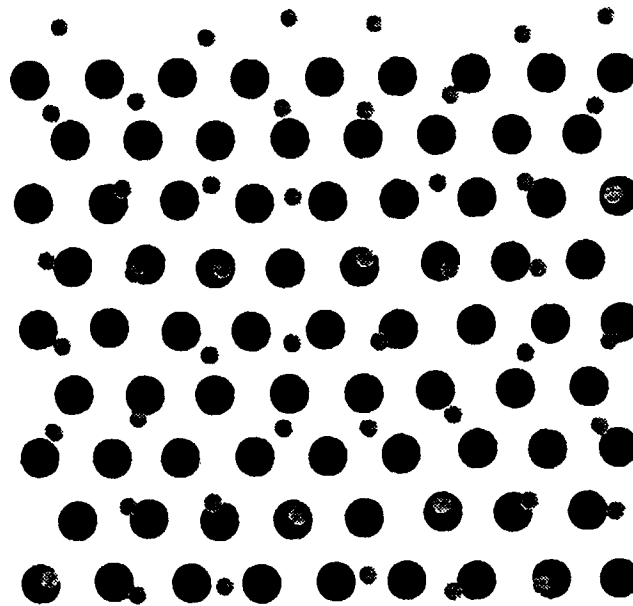


Figure 7. High magnification views of ZrO<sub>2</sub> dispersoids: (a) imaged along [100]<sub>Cu</sub> zone axis; (b) tilted to [110]<sub>Cu</sub> zone axis.



**Figure 8.** Schematic of interfacial arrangement corresponding to the  $55^\circ\langle 110 \rangle$  topotaxy relationship. The  $\{1\bar{1}1\}_{\text{Cu}}$  plane is superimposed on the  $\{100\}_{\text{Ox}}$  plane rotated so that the  $\langle 001 \rangle_{\text{Ox}}$  direction is parallel to  $\langle 110 \rangle_{\text{Cu}}$ . Two adjoining rows of oxygen anions lie between close-packed rows of copper atoms (arrowed).

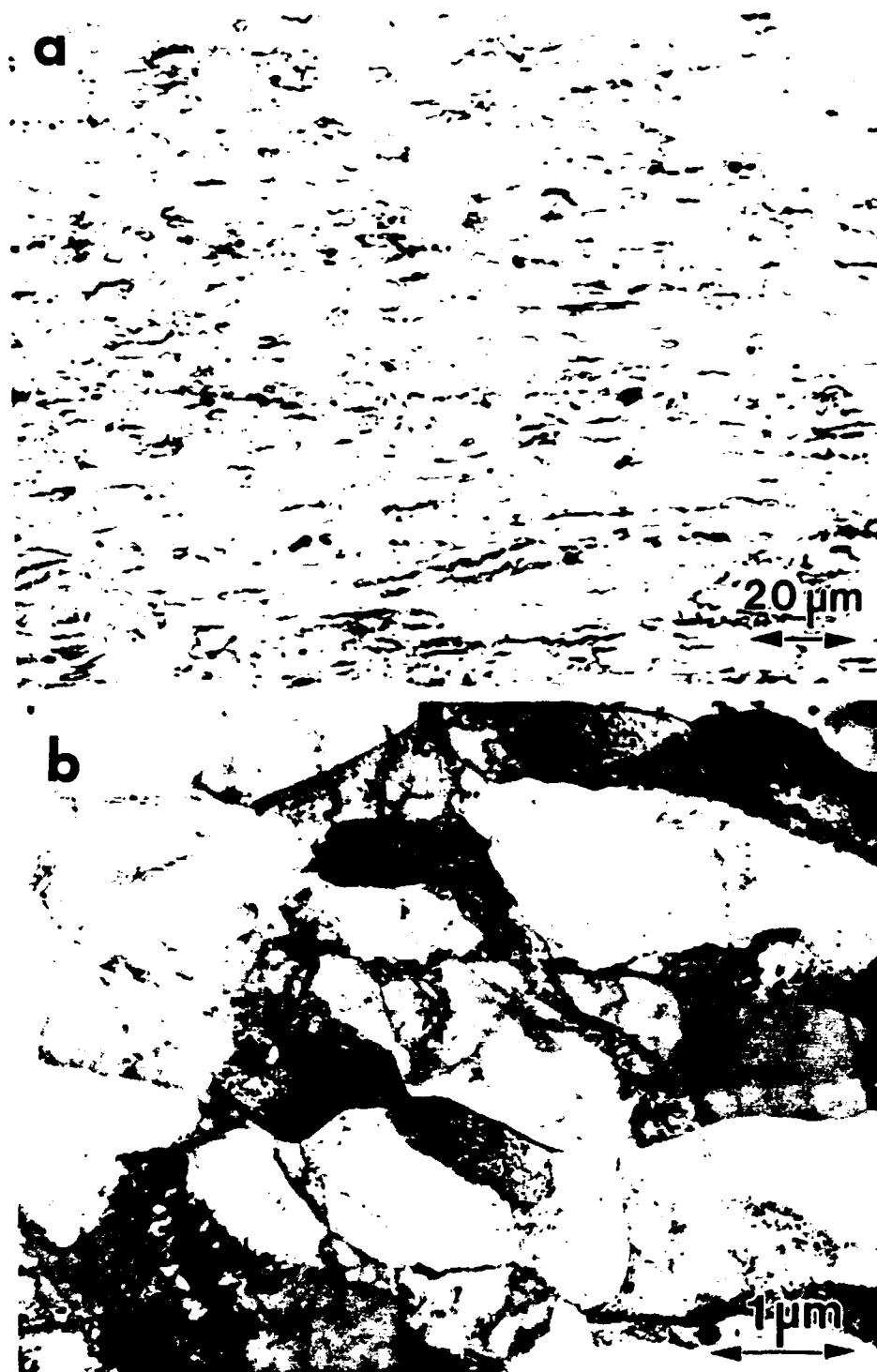


Figure 9. Microstructure of extruded Cu-ZrO<sub>2</sub> rod produced from ribbon internally oxidized at 1223 K: (a) optical view of longitudinal section showing elongated grains, (b) TEM view of transverse section showing deformation substructure.

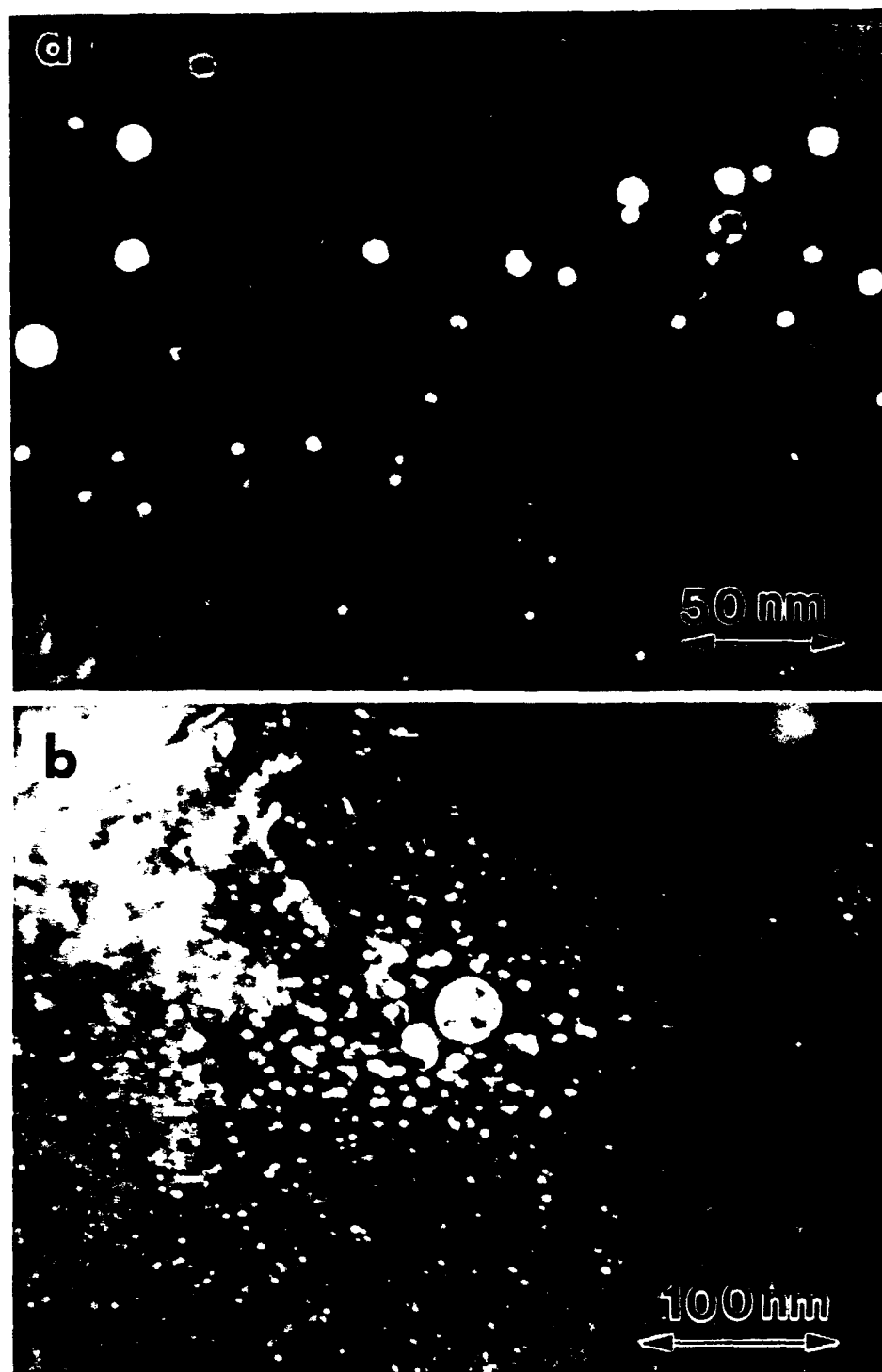


Figure 10. Dark field TEM images of oxide distributions in the extruded alloys: (a) uniform oxide distribution in Alloy Z9, (b) essentially undeformed oxide cluster in Alloy Z7.



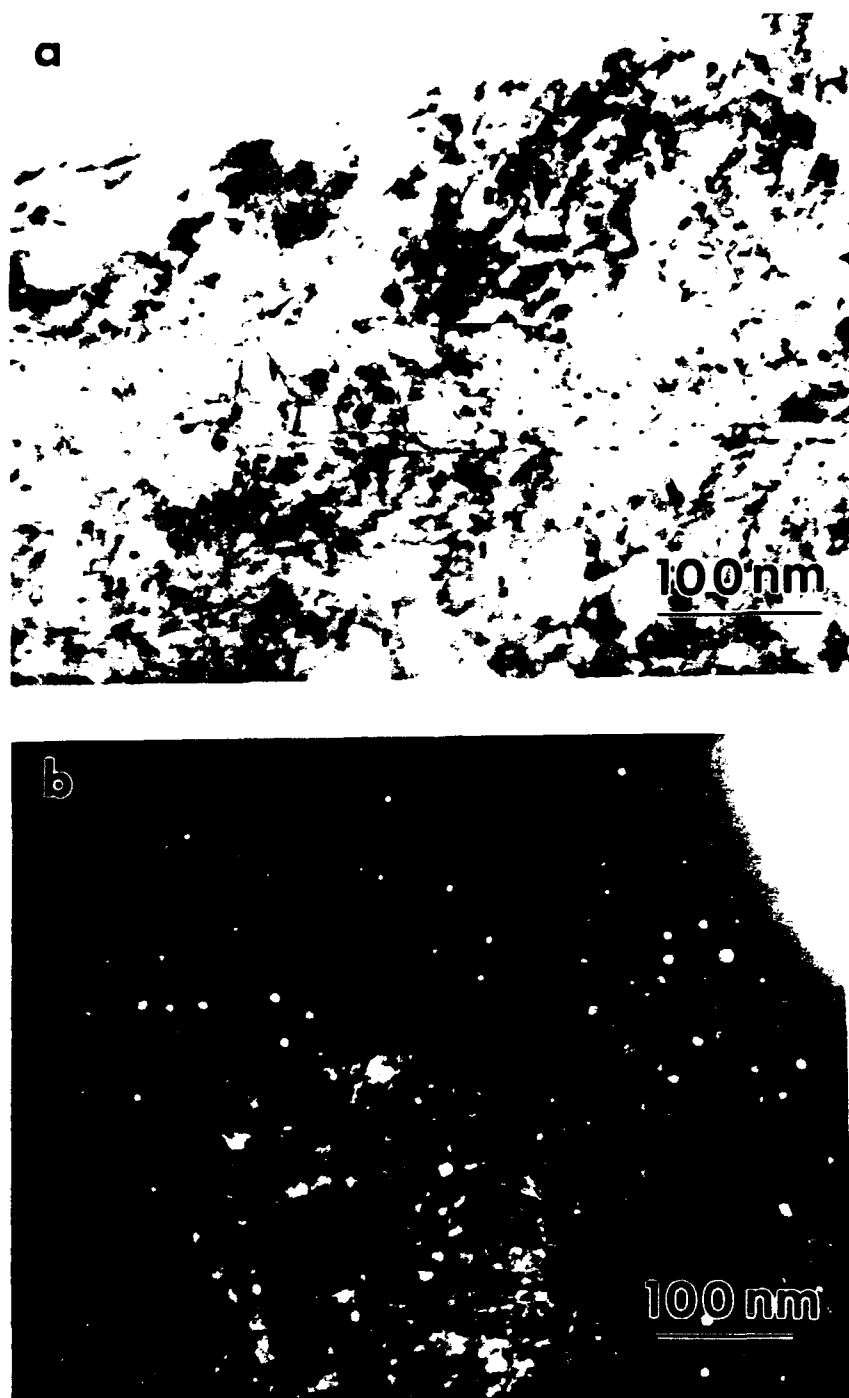


Figure 11. ODS Cu-3 vol.%Y<sub>2</sub>O<sub>3</sub> alloy produced by sputter deposition of Cu-1Y and internal oxidation at 1023 K. Deposition thickness was ~100  $\mu$ m. Note uniform oxide dispersion in bright (a) and dark (b) field images.

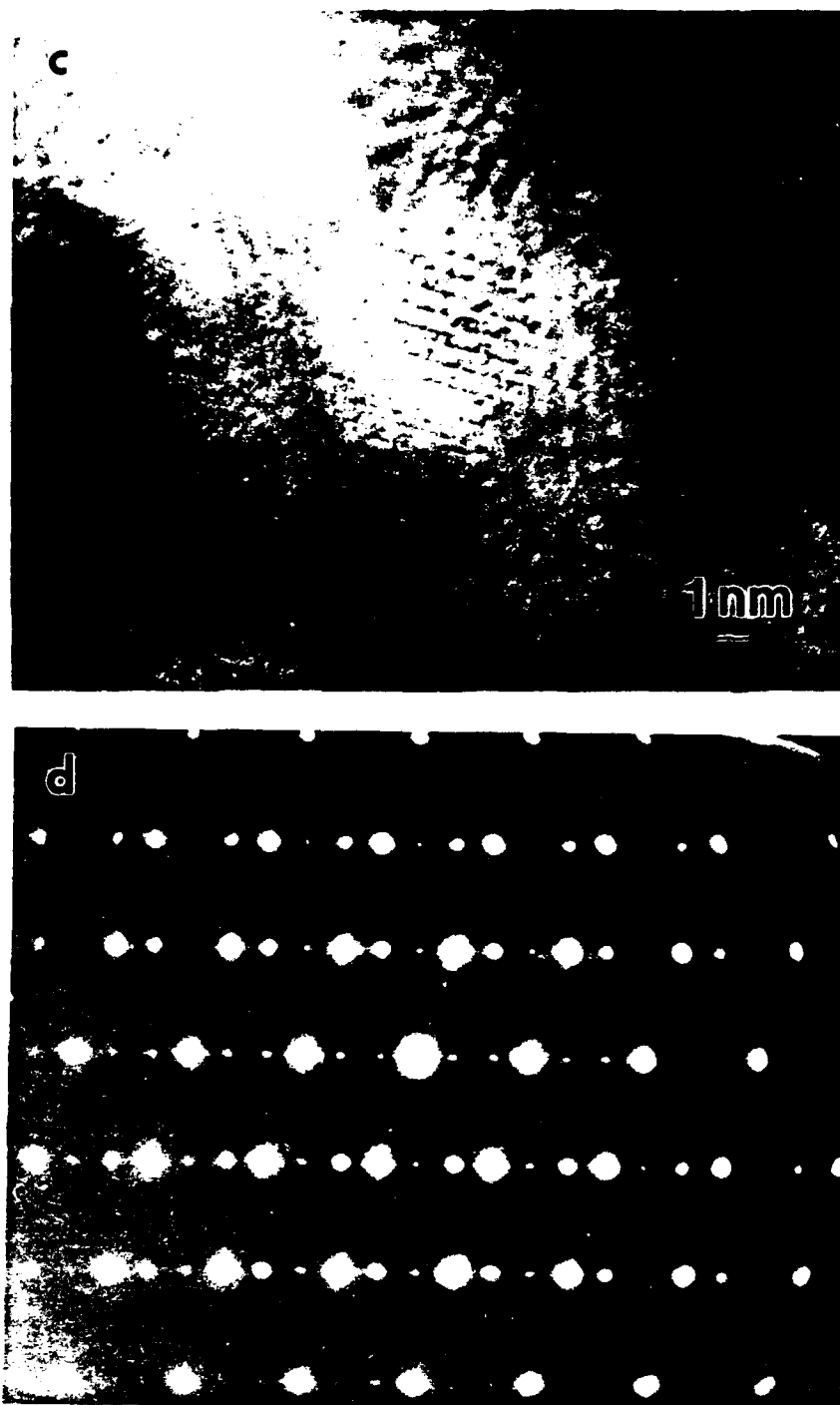
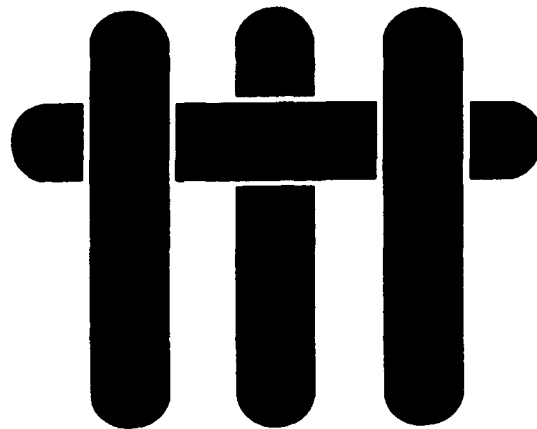


Figure 11. (cont.) ODS Cu-3 vol.%Y<sub>2</sub>O<sub>3</sub> alloy produced by sputter deposition of Cu-1Y and internal oxidation at 1023 K. Deposition thickness was ~100  $\mu$ m. (c) shows the scale of the typical oxide particles and (d) a well developed cube-on-cube orientation relationship. (Courtesy of J.P.A. Löfvander.)

# M A T E R I A L S



## *Novel ODS Copper Alloys from Rapidly-Solidified Precursors—II: Creep Behavior*

M.S. Nagorka\*, G.E. Lucas, and C.G. Levi

High Performance Composites Center  
Materials Department  
College of Engineering  
University of California at Santa Barbara

\* Currently at Kaiser Aluminum Corp., Pleasanton, CA.

submitted for publication to  
*Metallurgical and Materials Transactions*

March, 1994

# Novel ODS Copper Alloys from Rapidly-Solidified Precursors—II: Creep Behavior

by

Michael S. Nagorka, Glenn E. Lucas, and Carlos G. Levi†

## ABSTRACT

Yttria- and zirconia-dispersion strengthened copper alloys produced by hot pressing and hot extrusion of internally-oxidized melt-spun Cu-0.33 at.%Y and Cu-0.32 at.%Zr ribbons were subjected to compressive creep tests at 923 and 973 K. Creep strengths and stress exponents were higher for the Cu-ZrO<sub>2</sub> alloy than for Cu-Y<sub>2</sub>O<sub>3</sub>, and both were higher than those of pure copper. Comparisons of the creep properties with published data for pure copper along with microscopic evidence indicated that at least two creep mechanisms were operating in these alloys. These are: attractive dislocation/particle interactions in the matrix and particle-inhibited diffusional creep. The experimental data at low stresses could be described reasonably well by the Arzt-Ashby-Verral model for particle-restricted diffusional creep, using plausible values for the structure-related parameters. Fitting the higher stress creep data to the Rösler-Arzt model of dislocation/particle interaction resulted in values of the relaxation parameter ( $k$ ) within the bounds predicted by the theory. The estimated  $k$  values for Y<sub>2</sub>O<sub>3</sub> and ZrO<sub>2</sub> are in the vicinity of ~0.8, compared with ~0.9 for the  $\gamma$ -Al<sub>2</sub>O<sub>3</sub> dispersoids in conventional ODS Cu. The analysis suggests that these alternate dispersoids with fluorite-related structures may interact more effectively with dislocations during creep.

---

† M.S. Nagorka, formerly Graduate Research Assistant at the University of California, Santa Barbara (UCSB), is now Staff Research Engineer at Kaiser Aluminum Corp. in Pleasanton, CA. G.E. Lucas is Professor of Nuclear Engineering and Materials, and C.G. Levi is Professor of Materials and Mechanical Engineering, both at UCSB, Santa Barbara, CA, 93106.

## INTRODUCTION

The creep of dispersion-strengthened (DS) alloys has been described in terms of three regimes that depend on the applied stress and temperature [91Arz]. At high modulus-compensated stresses these materials exhibit creep behavior similar to their non-DS counterparts, with relatively low stress exponents,  $4 < n < 8$ , and activation energies on the order of that for bulk diffusion in the material. With decreasing stress the creep exponents become very large,  $20 < n < 100$ , and the activation energy for creep becomes significantly larger than that of bulk diffusion in the matrix. At high homologous temperatures and relatively low stresses the stress exponent returns to relatively small values.

The transition from the low to the intermediate stress regime has been described in terms of the presence of a "threshold stress" below which creep essentially (and in many cases for all practical purposes) ceases in the material. Observations indicate that this threshold stress is in the range of a few tenths of the Orowan stress of the material,  $\sigma_{Or}$ , and increases with decreasing test temperature. This has led to the hypothesis that the creep rate in the second regime is controlled by the time required for dislocations to bypass the dispersoids by a climb mechanism. Shewfelt and Brown [77ShB] suggested that dislocations might "locally" climb over the dispersoids only in their near vicinity, with the remainder of the dislocation remaining in its glide plane. Threshold stresses of  $0.7\sigma_{Or}$  and  $0.4\sigma_{Or}$  were calculated with this model for climb over cuboidal and spherical particles, respectively. Arzt and Ashby [82ArA] discussed an alternate "general" climb geometry in which the length of the climbing segment is on the scale of the dispersoid spacing. Values of the threshold predicted by their model are in the range  $0.04\text{--}0.08\sigma_{Or}$  [82ArA].

Analysis of these models reveals significant shortcomings. The dislocation configuration assumed by Shewfelt and Brown is unlikely to evolve in the absence

of attractive dislocation/dispersoid interactions. Lagneborg [73Lag], and later Rösler and Arzt [88RöA], argued that the sharp bends in the dislocation line near the particle dictated by the local climb model would tend to relax by diffusional flow of vacancies and produce a line geometry more like that of general climb. Conversely, the later climb model predicts threshold stresses that are significantly lower than those observed experimentally.

A more recent model for the creep of DS alloys proposed by Rösler and Arzt [90RöA] postulates that threshold stress-like behavior arises from the need to detach dislocations from dispersoid particles to which they are attracted. This attractive interaction arises from the diffusional relaxation of dislocation core stresses at the matrix/particle interface. Arzt and Wilkinson [86ArW] indicated that only a modest reduction of the dislocation core stresses would cause the attachment/detachment process to predominate the stress required for dislocation climb over the particle. One implication is that different matrix/particle interfaces might promote varying degrees of dislocation attachment and thus affect differently the creep strength of the material. This concept stands in marked contrast to the climb-based models in which interfaces are not expected to have any effect on creep properties.

The premise that interfacial structure may play a significant role in the creep strengthening efficiency of dispersoids motivated the synthesis of ODS Cu alloys based on  $\text{ZrO}_2$  and  $\text{Y}_2\text{O}_3$ . Since Zr and Y are practically insoluble in Cu, a processing approach coupling rapid solidification and internal oxidation was developed for these materials, as discussed in Part I [94NLL]. The resulting alloys contained fine dispersoids that exhibited attractive characteristics for strengthening purposes, as shown by Table 1. This paper reports the creep and strength properties of these materials and discusses them within an analytical framework based on current theoretical models.

## EXPERIMENTAL PROCEDURE

Yttria- and zirconia-dispersion strengthened copper alloys containing ~1 volume percent of oxide particles were prepared by the internal oxidation of rapidly solidified, melt-spun copper-yttrium and copper-zirconium ribbon. The internally-oxidized materials were subsequently consolidated and hot extruded to produce bar stock as detailed in Part I [94NLL]. The materials to be evaluated in this study (Table 1) were identified by a letter corresponding to the oxide type (Y or Z) and a number indicative of the internal oxidation temperature in °C (7 or 9 for 750 or 950°C), as these were the prime parameters in determining the quality of the oxide dispersion [94NLL].

Cylindrical specimens 6.4 mm in diameter and 12.7 mm in length were machined from the as-extruded bars of each material. Room temperature compression tests were carried out on specimens of the three alloys to determine yield strengths, which would subsequently be used to estimate values for  $\sigma_{0.2}$ . Constant load compression creep tests were performed on a closed-loop, servo-hydraulic, instrumented load frame equipped with a high temperature compression apparatus designed and built in-house [93Cas] and a clamshell-type air furnace. An inert atmosphere was provided by the installation of a quartz tube with stainless steel support caps that fit within the furnace and around the compression stage; dry argon gas was trickle-purged through the tube during testing. Test temperature was monitored by a thermocouple located at the lower plate of the compression stage near the specimen. Specimen ends were coated with boron nitride to minimize barrelling during the course of testing.

Load and displacement were monitored by a standard load cell and extensometer in series with the load train, and logged as a function of time onto a desktop computer. The acquisition of multiple creep rate data points from individual speci-

mens was necessary because of the modest amount of material available for testing. Tests were run at constant load until the displacement rate became constant; this constant rate was used to determine the steady-state creep rate at the given load (and hence stress). At that point the load on the specimen was increased and maintained until steady state creep was again achieved. This was repeated until accumulated strains became large (generally, where specimen barreling became obvious). The multiple testing appeared to provide reliable data since data sets of creep rate versus stress that were obtained from different specimens overlapped despite beginning with different initial loads.

All of the alloys were tested at both 923 and 973 K under loads that produced steady-state creep rates between  $\sim 7 \times 10^{-8}$  and  $\sim 5 \times 10^{-5} \text{ s}^{-1}$ . The lower bound was determined by equipment resolution limits, and the upper bound by material availability (rates greater than  $5 \times 10^{-5} \text{ s}^{-1}$  consumed creep specimens too rapidly). Generally, at the termination of a test the specimen was kept under load while the furnace cooled in order to "lock-in" the dislocation structure present during the actual creep conditions. Stress exponents were determined from linear regression analysis of log true creep strain rate versus log true stress at constant temperature, and activation energies for creep,  $Q$ , were obtained at constant modulus-compensated values of true stress; values of temperature-dependent elastic modulus of pure copper were obtained from the literature [82FrA].

Transmission electron microscopy (TEM) was performed on a limited number of creep specimens. Care was exercised during preparation to avoid introducing plastic deformation into the imaged portion of the specimen to preserve the dislocation structure present during creep testing. Final thinning and perforation of the TEM specimens was carried out in an ion mill using Ar under an accelerating voltage of 5 kV.



## RESULTS

### *Initial Materials*

A detailed microstructural description of the extruded bars used in the mechanical behavior study is given in Part I. Briefly, the Cu-ZrO<sub>2</sub> alloy internally oxidized at 1223 K (Z9) had the best microstructure, wherein most of the oxide was present as fine dispersoids with an average size of 6.2 nm and estimated spacing of ~44 nm. A minor fraction of larger oxides, ~50 nm in size, was also present at the grain boundaries. The alloys oxidized at 1023 K (Z7 and Y7) had inhomogeneous distributions of oxides, the majority of which were concentrated in clusters consisting of coarse (~30-150 nm) and fine (≤10 nm) particles. There was also a "background" dispersion of finer oxides through the matrix with average sizes of 5 - 6 nm which was much more homogeneous but comprised only 10 - 30% of the total oxide content [94NLL]. Assuming that the finer particles were generated from the amount of oxidizable element dissolved in the matrix, one could readily estimate spacings for these dispersoids in the range of 60-120 nm—see Table 1. Thus, the background dispersion would be still attractive from a strengthening viewpoint even if the oxides present in clusters had no significant effect.

### *Orowan Stress*

Room temperature Orowan stresses for the three materials were calculated from microstructural data using the following equation from Reference [69Ash]

$$\sigma_{Or} = \frac{1.13M}{2\pi} \left( \frac{Gb}{\lambda_o - \delta_o} \right) \ln \left( \frac{\delta_o}{4b} \right) \quad (1)$$

where  $M = 3$  is a factor to convert shear stress to tensile stress in polycrystalline material,  $G$  is the shear modulus,  $\nu$  is Poisson's ratio,  $b$  the Burgers vector of the mobile dislocations,  $\lambda_0$  the mean planar dispersoid spacing, and  $\delta_0$  the average dispersoid radius. Values of  $\delta_0$  and  $\lambda_0$  were taken from the microstructural data listed in Table 1, and the other values were taken from the literature [82FrA]. The resulting  $\sigma_{Or}$  values are listed in Table 1 and compared with Orowan stress values estimated from the compressive yield strength ( $\sigma_Y$ ) measurements. The latter were calculated by subtracting the yield strength for pure copper with an equivalent grain size from the measured  $\sigma_Y$ . The appropriate grain size correction for pure copper was made by applying Hall-Petch parameters derived from data of Johnston and Feltner [70JoF]. No allowance was made for the hardening contribution of forest dislocations as their density in the consolidated material appeared relatively modest under TEM.

The calculated Orowan stresses seem to be in good agreement with estimated values from room temperature compression tests, except for Z9 wherein the difference is over 100 MPa. This is not of great concern at this stage considering the uncertainty in the assumptions and parameters used in the calculations. The microstructural observations suggest that  $\sigma_{Or}$  should indeed be significantly higher for Z9, rather than similar to that of Z7 as apparently indicated by the estimates based on the experimental yield strengths.

### ***Creep Behavior***

The steady-state strain rate for alloy Y7 is shown as a function of applied stress in Figure 1(a). The stress exponents of this material were 8.8 and 7.1 at 923 K and 973 K, respectively. The activation energy for creep was calculated at a modulus-compensated stress of  $3.75 \times 10^{-4}$  (corresponding to a stress of 20.5 MPa at 923 K and 20 MPa at 973 K) and had a value of 530 kJ/mol.

The creep of the two copper-zirconia materials (Alloys Z7 and Z9) differed from that of copper-yttria in two important respects. First, the creep strengths of both alloys are considerably higher than that of copper-yttria; and second, the stress exponents are consistently higher. The data for alloy Z7 is shown in Figure 1(b). The creep exponents were 11.5 at 923 K and 10.1 at 973 K, and the apparent activation energy for creep was 486 kJ/mol. The data for alloy Z9 is shown in Figure 1(c). The stress exponents were only slightly higher than those of Z7, i.e. 12.2 at 923 K and 11.8 at 973 K. The activation energy for creep was 535 kJ/mol, again similar to Z7 and Y7. However, it is apparent from a comparison of Figures 1(b) and (c) that alloy Z9 has significantly better creep strength than alloy Z7. This is consistent with the superior oxide distribution of the former, and the higher calculated values of the Orowan stress, as noted above.

Both the stress exponents and activation energy for creep of these materials are well above those of pure copper under power law creep, for which the reported  $n = 4.8$  and  $Q = 197$  kJ/mol (for lattice diffusion) [82FrA].

### *Microstructural Features*

After creep, the microstructure of the three alloys was characterized by some degree of subgrain development. Representative TEM micrographs of grains in alloys Z9 and Y7 are shown in Figure 2. The subgrains are roughly 0.5  $\mu\text{m}$  to 1  $\mu\text{m}$  in diameter with subgrain boundaries varying from rather loosely tangled dislocations to well-defined dislocation arrays. Within the subgrains isolated dislocations may be seen, some of which appear to be pinned at oxide particles.

Higher magnification micrographs suggest some attractive interaction between dislocations and the larger dispersoids. Figures 3(a) and (b) are TEM micrographs of the copper-zirconia materials after creep. In both micrographs some dislocations appear to be pinned on the departure side of the particles—see dislocation

"B" in Figure 3(a)—whereas other dislocations appear to undergo typical Orowan bowing—see dislocation "A" in Figure 3(a). It should be recognized, however, that even if detachment is controlling, dislocations could still display an Orowan bowing configuration prior to climbing over a particle, at which point they would become pinned on the departure side. Moreover, according to the Rösler-Arzt model [90RoA], thermal activation can cause dislocations to be more easily detached from very small particles; and, indeed, in the TEM micrographs it does not appear that the very smallest dispersoids are pinning the dislocations.

Such dislocation-dispersoid interactions were not as readily observed in the copper-yttria alloy. Figure 3(c) shows several dislocations which appear to emanate from a large yttria particle, but it is not clear that they are actually pinned to the particle through an attractive interaction. Away from this particle it is clear that dislocations are pinned at some points in the matrix although it is difficult to determine what the pinning entities are. The difficulty of observing dislocation-dispersoid interactions in this alloy may simply be due to the fact that there are relatively fewer oxide particles in the appropriate size range (~10-50 nm) randomly located throughout the matrix; instead, they are almost invariably located at the site of oxide clusters, where the attractive interaction may be more difficult to detect.

Another feature visible in post-creep specimens was apparent pinning of grain boundaries by the oxide particles. An example of such pinning is shown in Figure 4, which is a TEM image of a grain boundary in alloy Z9 tested at 923 K. Localized distortions in the grain boundary fringes appear to be caused by oxide particles restraining the motion of the boundary in their vicinity (see the arrowed regions in Figure 4). The large number of such distortions suggest that many oxide particles are helping to pin this boundary. Grain boundary pinning of the variety seen in Figure 4 is important in terms of the creep strength of the material since it can decrease the rate of diffusional creep significantly, as discussed below.

## DISCUSSION

The alloys investigated in this work received considerably less deformation processing after internal oxidation than most other ODS copper alloys reported in the literature. This was due to the limited capacity of the available extrusion equipment [94NLL]. Since deformation strongly increases the creep strength of ODS Cu (see, for example, [84Nad]), the strength of the materials in this study was not surprisingly lower than that of commercial alloys. However, the creep behavior of the present alloys was generally similar to that reported for other ODS coppers in that the stress exponents and activation energies for creep were well above those of pure Cu. Table 2 summarizes these parameters for the current work, as well as the values obtained by analyzing the data reported in the literature, and compares them with the values for pure Cu cited earlier.

The values of activation energy obtained in this study are similar to those reported for other dispersion-strengthened, polycrystalline materials, and are higher than the one single crystal experiment in the literature for which an activation energy could be calculated. Conversely, the stress exponents of the polycrystalline materials are as a group lower than those obtained for single crystals, and the values for the present materials are lower than those reported in the literature for other ODS Cu alloys. The differences in stress exponents among polycrystalline materials appears to be related to the extent of prior deformation. Materials used in the current work were extruded with a 9:1 reduction ratio before creep testing. In contrast, the Cu-Al<sub>2</sub>O<sub>3</sub> alloys investigated by Preston and Grant [61PrG] underwent a 28:1 reduction in area by extrusion, and those reported by Nadkarni [84Nad] were extruded with ~30:1 to 40:1 reductions and subsequently cold worked 94%. The origin of the higher stress exponent for the single crystals is not immediately obvious but may arise from the contributions of diffusional creep in the polycrystalline

alloys. This was certainly the case in the present work, as discussed below. Hence, materials with lower grain aspect ratios (less prior deformation) are likely to be more sensitive to diffusional creep and exhibit lower stress exponents.

Figure 5 compares the creep data obtained at 973 K for the copper-yttria and the two copper-zirconia rods with predicted creep rates for pure copper with the same grain size (Table 1). The creep rates for pure copper were determined from expressions developed by Frost and Ashby [82FrA] for grain boundary diffusional creep (Coble creep) and power-law creep (with breakdown correction), which dominate the creep behavior in this temperature and stress regime. All of the alloys exhibit considerable reductions in creep rate compared to pure copper, thus demonstrating the feasibility of improving creep strength with  $Y_2O_3$  or  $ZrO_2$  dispersions.

It is also interesting to note that the creep data were obtained in a stress/temperature regime where multiple creep mechanisms (i.e., diffusional and matrix dislocation creep) would be operating in pure copper. Several factors also point to the operation of multiple creep mechanisms in the dispersion strengthened alloys. First, the experimental data obtained in this study did not exhibit a distinct threshold stress behavior near typical threshold stresses of about  $\sim 0.4\sigma_{Or}$ , as observed in coarser-grained dispersion-strengthened alloys [91Arz]. As noted in Table 1, values for the room temperature Orowan stresses calculated from microstructural parameters were about 93, 154 and 270 MPa for alloys Y7, Z7 and Z9, respectively. Accounting for a  $\sim 30\%$  decrease in the Cu shear modulus between room temperature and 973 K [82FrA], the expected threshold stresses should be in the 30-75 MPa range for these alloys, *well above the stresses at which observable creep occurred*. The absence of a distinct threshold stress and measurable creep at small fractions of the Orowan stress has been observed in other small-grained dispersion-strengthened alloys, where it has been suggested that diffusional creep becomes important [72WiC]. Indeed, the microstructural evidence shown in Figures 3 and 4 suggest that two

mechanisms are operating in these alloys: i.e., matrix creep controlled by dislocation/dispersoid interactions and diffusional creep controlled by grain boundary dislocation pinning.

The creep strengths observed in these alloys are possible only if both dislocation creep and diffusional creep processes are suppressed. In the transition region where both power law and diffusional creep make significant contributions, creep would be dominated by the unsuppressed mechanism if only one mechanism were restricted. However, Figure 5 shows that the creep data for the  $\gamma$  alloys falls below predicted values for both dislocation and diffusional creep, which suggests that both mechanisms are substantially suppressed. Although the operation of more than one mechanism complicates the analysis of the data, it is worthwhile examining models of inhibited diffusional creep and particle-detachment controlled matrix creep with the data at hand to gain some insight for future development of these alloy systems.

A model of particle-inhibited diffusional creep has been proposed by Arzt, Ashby and Verral [83AAV]. This model assumes that the sources and sinks for vacancies in diffusional flow are grain boundary dislocations and hence diffusional flow requires the climb of such dislocations. The presence of dispersoids in the grain boundary inhibits this climb by pinning the dislocations in a manner analogous to dislocation/dispersoid interaction with gliding dislocations in the matrix. The strain rates predicted by the model reflect a complex interaction between the mobility of grain boundary dislocations as they climb over the dispersed particles and the number of particles that can be bypassed by the Orowan mechanism for given values of the applied stress.

The AAV model has been applied to the present results adjusting the relevant structure-related parameters to provide a reasonable fit to the experimental data at the low stress end, where diffusional creep is more likely to dominate.

Figure 6 compares the creep data of the three alloys at 973 K with predictions of the model, using the microstructural parameters shown in Table 3. These can be compared with the corresponding parameters of the "background" matrix dispersion determined from both TEM and solubility data—see Table 1 [94NLL]. The estimated average diameters of particles interacting with the boundaries,  $\delta_B$ , are in the same order of magnitude as those determined by TEM analysis ( $\leq 10$  nm). The decreasing trend from Y7 to Z7 to Z9 is qualitatively consistent with the concomitant reduction in the relative proportion of coarser to finer oxides, as discussed in Part I. The volume fraction of particles ( $f_B \approx 0.01$ ) is consistent with the total oxide content of the alloys, implying that the relevant density of particles at the grain boundaries is that of the bulk alloy. This contrasts with the lower  $f_0$  values in Table 1, since the latter include only the finer, uniformly distributed oxides which are relevant to the interaction with the matrix dislocations. The assumed value of grain boundary dislocation density,  $\rho_B$ , is consistent with other observations [82FrA]. Finally, the activation energy for dislocation mobility in the grain boundaries,  $Q_B$ , falls between a lower bound given by the energy for boundary or lattice diffusion—104 kJ/mol and 197 kJ/mol, respectively—and an upper bound given by the observed activation energy for creep of the alloy (Table 2). Within the assumptions of the model and the uncertainty of the data, this is probably an acceptable rationalization of the creep behavior in the low stress regime.

While it is possible to fit the experiments to the AAV model at the lower stresses, the predictions begins to deviate significantly from the data as the stress increases. This is consistent with an alternate creep mechanism, e.g., matrix creep, predominating in the higher stress regime. Given this observation and assuming that the matrix creep is controlled by dislocation/dispersion interactions, the experimental data obtained in the high stress range can be used to determine model parameters in the Rösler-Arzt theory—particularly the relaxation parameter  $k$ .



The method for estimating  $k$  is described in more detail in Appendix A, and the results are presented in Table 1. The  $k$  values are all close to 0.8, well within the range deemed plausible by Rösler and Arzt ( $0.77 < k < 1.0$ ) [88RöA], suggesting that yttria and zirconia provide similar degrees of dislocation/dispersoid attachment. Conversely, values of  $k$  on the order of  $\sim 0.9$  were obtained by analyzing creep data reported by Preston and Grant [61PrG] and Lloyd and Martin [80LlM] for  $\text{Al}_2\text{O}_3$  dispersoids in polycrystalline and single crystal copper, respectively. The smaller values of  $k$  ( $\sim 0.8$ ) for yttria and zirconia imply that these dispersoids exhibit a stronger degree of dislocation stress relaxation than  $\text{Al}_2\text{O}_3$  and could, consequently, provide a higher degree of creep strengthening for a fixed size and volume fraction of dispersoid. In such a case, alloys strengthened with these fluorite-related oxides would have merit in relation to the conventional  $\gamma\text{-Al}_2\text{O}_3$  dispersoids.

In order to obtain more accurate values of  $k$ , the contribution of diffusional creep processes must be strongly suppressed. This could most readily be accomplished by subjecting the alloys to an annealing procedure sufficient to produce a coarse-grained material in which diffusional creep would play a smaller role. Conversely, it would appear that increased deformation processing might improve the performance of both the zirconia- and yttria-dispersion strengthened systems. Deformation would increase the dislocation density in the final product, an obviously important parameter in the achievable strength levels, and may also help break up oxide clusters or the larger grain boundary particles, although the latter effect was not observed under the relatively modest strains achievable in this work. Deformation also produces elongated grain shapes and introduces crystallographic texture, both of which are known to improve creep strength in DS alloys [70Kil] by reducing the contributions of grain boundary sliding and diffusional creep. These issues should be the subject of future work.

## CONCLUSIONS

The extruded products formed from the melt-spun, internally oxidized copper-yttrium and copper-zirconium alloys displayed creep behavior superior to that of unalloyed copper. The behavior was similar to that of other dispersion-strengthened materials, in which both stress exponents and activation energies for creep were well above those of pure copper. The copper-zirconia alloys exhibited superior creep strengths compared to the copper-yttria material due to better oxide distributions in these alloys. Furthermore, the use of higher internal oxidation temperatures provided improved creep behavior in the copper-zirconia alloys.

The improved creep behavior in the alloys examined appears to result from suppression of both matrix and diffusional creep mechanisms. Both microstructural data and mechanical property data corroborated this. The creep behavior at low stresses could be rationalized by a model for particle-inhibited diffusional creep using reasonable values of microstructural and mobility parameters, and the high stress data could be well fit by the Rösler-Arzt model for dislocation/dispersoid interaction-controlled matrix creep.

The estimated relaxation parameters for these alloys,  $k \approx 0.8$ , were smaller than those determined for the conventional  $\gamma\text{-Al}_2\text{O}_3$  dispersoids in commercial ODS Cu, suggesting that both zirconia and yttria may provide improved barrier strengths to creep. Future work will examine ways to verify this and to improve the microstructural characteristics and performance of these systems.

## ACKNOWLEDGMENTS

This work was sponsored by the Advanced Projects Research Agency through University Research Initiative Grant N00014-92-J-1808 supervised by Dr. W Coblenz and monitored by Dr. S. G. Fishman of the Office of Naval Research. Additional

support for M. S. Nagorka in the form of a National Defense Science and Engineering Grant Fellowship provided by ARPA is gratefully acknowledged. The authors would like to thank Mr. E. Spiller and coworkers at Hazen Research Inc., of Golden, Colorado for their valuable assistance with the preparation of the pulverized ribbon material.

## REFERENCES

- [61PrG] O. Preston and N. J. Grant, "Dispersion Strengthening of Copper by Internal Oxidation," Transactions of the Metallurgical Society of AIME, **221**(1961), 164-173.
- [69Ash] M.F. Ashby, "On the Orowan Stress," in Physics of Strength and Plasticity, A.S. Argon, Ed., MIT Press, 1969, pp. 113-131.
- [70JoF] T. L. Johnson and C. E. Feltner, "Grain Size Effects in the Strain Hardening of Polycrystals," Metallurgical Transactions, **1**(1970) 1161-1167.
- [70Kil] D. H. Killpatrick, "Texture and Elevated Temperature Mechanical Properties of Dispersion-Strengthened Nickel-20 Chromium Alloys," 2nd International Conference on the Strength of Metals and Alloys, American Society for Metals, Metals Park, OH (1970) 649-653.
- [72WiC] B. A. Wilcox and A. H. Clauer, "The Role of Grain Size and Shape in Strengthening of Dispersion Hardened Nickel Alloys," Acta Metallurgica, **20**(1972) 743-757.
- [73Lag] R. Lagneborg, "Bypassing of Dislocations Past Particles by a Climb Mechanism," Scripta Metallurgica, **7**(1973) 605-614.
- [77ShB] R. S. W. Shewfelt and L. M. Brown, "High-Temperature Strength of Dispersion-hardened Single Crystals. II. Theory," Philosophical Magazine, **35**(1977) 945-962.
- [80LIM] G. J. Lloyd and J. W. Martin, "The Effect of Dislocation Density on the Creep of Dispersion-strengthened Copper Crystals," Materials Science and Engineering, **46**(1980) 1-13.

- [82ArA] E. Arzt and M. F. Ashby, "Threshold Stresses in Materials Containing Dispersed Particles," Scripta Metallurgica, **16**(1982) 1285-1290.
- [82FrA] Frost, H. J. and Ashby, M. F., Deformation-Mechanism Maps: the Plasticity and Creep of Metals and Ceramics, Pergamon Press, Oxford, (1982) 21.
- [83AAV] E. Arzt, M. F. Ashby, and R. A. Verrall, "Interface Controlled Diffusional Creep," Acta Metallurgica, **31**(1983) 1977-1989.
- [84Nad] A. V. Nadkarni, "Dispersion Strengthened Copper Properties and Applications," in High Conductivity Copper and Aluminum Alloys, E. Ling and P. W. Taubenblat, eds., AIME, Warrendale, PA, (1984) 77-101.
- [86ArW] E. Arzt and D. S. Wilkinson, "Threshold Stresses for Dislocation Climb Over Hard Particles: The Effect of an Attractive Interaction," Acta Metallurgica, **34**(1986) 1893-1898.
- [88RöA] J. Rösler and E. Arzt, "The Kinetics of Delocation Climb Over Hard Particles-I. Climb Without Attractive Particle-Dislocation Interaction," Acta Metallurgica, **36**(1988) 1043-1051.
- [90RöA] J. Rösler and E. Arzt, "A New Model-Based Creep Equation for Dispersion Strengthened Materials," Acta Metallurgica et Materialia, **38**(1990) 671-683.
- [91Arz] E. Arzt, "Creep of Dispersion Strengthened Materials: A Critical Assessment," Res Mechanica, **31**(1991) 399-453.
- [93Cas] A. Casagrande, "The Effect of Shear of the Densification of Alumina," PhD Dissertation, University of California, Santa Barbara, (1993).
- [94NLL] M.S. Nagorka, C.G. Levi, and G.E. Lucas: "Novel ODS Copper Alloys from Rapidly-Solidified Precursors. I: Microstructural Development" submitted to Metallurgical and Materials Transactions, 1994.

**Table 1. Microstructural and Mechanical Behavior Parameters of Extruded Alloys**

Material	Alloy Y7	Alloy Z7	Alloy Z9
Grain Size, $d$ ( $\mu\text{m}$ )	4.3	3.6	2.4
Grain Aspect Ratio (GAR)	1.5	2.2	2.8
Volume Fraction of Fine Matrix Oxides, $f_o$	$\sim 0.0014^*$	$\sim 0.0032^*$	$\sim 0.01^{**}$
Oxide Particle Diameter $\delta_o$ (nm)	6	5.1	6.2
Dispersoid Spacing $\lambda_o = \sqrt{\pi/6f_o} \delta_o$ (nm)	120	66	44
Rösler-Arzt Relaxation Parameter, $k$	0.82	0.80	0.80
Orowan Stress, $\sigma_{Or}$ (MPa) based on microstructural parameter measurements based on room temperature compression yield data	93 (75)	154 (149)	270 (146)

\* Estimated based on maximum solubility of yttrium or zirconium in matrix.

\*\* Neglects small fraction of larger oxide particles at grain boundaries.

**Table 2. Creep Parameters for ODS Copper Alloys**

Dispersoid	Single/ Poly- crystal	Stress Exponent, $n$	Activation Energy, $Q$ (kJ/mol)	Test Temperatures* (K)	Approximate Stress Range† (MPa)	Reference
None	P	4.8	197	923, 973	10-100	[82FrA]
$\text{Y}_2\text{O}_3$	P	7.1-8.8	530	923, 973	10-50	This Work
$\text{ZrO}_2$	P	10.1-12.2	486-535	923, 973	20-70	This Work
$\text{Al}_2\text{O}_3$	P	14.5-21.9	512	923, 1123	55-241	[61PrG]
$\text{Al}_2\text{O}_3$	P	23-26	—	923	130-210	[84Nad]
$\text{Al}_2\text{O}_3$	S	30-49	368	823, 923	17-27	[80LIM]

\* The low and high temperatures used to obtain stress exponents and activation energies.

† Lowest stress at the high test temperature to the highest stress used at the low test temperature.

**Table 3. Values of Adjustable Parameters Used In Model of Arzt et al. [83AAV]**

Parameter	Alloy Y7	Alloy Z7	Alloy Z9
$\delta_B$ (nm)	10.6	5.2	3.4
$f_B$	0.01	0.01	0.01
$\rho_B$ (m <sup>-1</sup> )	10 <sup>7</sup>	10 <sup>7</sup>	10 <sup>7</sup>
$Q_B$ (kJ/mol)	300	289	295

## APPENDIX A. EVALUATION OF THE RELAXATION PARAMETER

The Rosler-Arzt model [90RöA] for matrix creep controlled by dislocation detachment from dispersoids takes the form

$$\frac{\dot{\epsilon}}{\dot{\epsilon}_0} = \exp\left(-\frac{E_d}{RT}\right) \quad (\text{A.1})$$

where  $\dot{\epsilon}$  is the steady state creep rate and  $\dot{\epsilon}_0$  is a pre-exponential term given by

$$\dot{\epsilon}_0 = 3D_v \rho_m \frac{\lambda_0}{b} \quad (\text{A.2})$$

Here,  $D_v$  is the volume diffusivity,  $\rho_m$  the mobile dislocation density in the matrix, and  $\lambda_0$  and  $b$  are defined as before. Finally,  $E_d$  is an activation energy for dislocation detachment, and is given by

$$E_d = \frac{Gb^2\delta_0}{2} \left[ (1-k) \left( 1 - \frac{\sigma}{\sigma_d} \right) \right]^{3/2} \quad (\text{A.3})$$

While  $\sigma$  is the applied stress,  $\sigma_d$  is an athermal detachment stress, related to the Orowan stress by

$$\frac{\sigma}{\sigma_{Or}} = \sqrt{1-k^2} \quad (\text{A.4})$$

and  $k$  is the Rösler-Arzt relaxation parameter, defined as the ratio of the dislocation line tension at the particle/matrix interface to the line tension in the matrix far away from the particle.

If this mechanism predominates at the higher stresses in the present materials, the activation energy and stress exponents measured experimentally are

"apparent" values,  $Q_{app}$  and  $n_{app}$ , respectively, and would be related to Equations (A.1)-(A.4) by

$$Q_{app} = -k_B \left[ \frac{d \ln \dot{\epsilon}}{d(1/T)} \right]_{\sigma} ; \quad n_{app} = \left[ \frac{d \ln \dot{\epsilon}}{d \ln \sigma} \right]_T \quad (A.5)$$

where  $k_B$  is the Boltzmann constant. Combining Equations (A.1) through (A.5) and solving for  $k$  in terms of  $Q_{app}$  and  $n_{app}$  gives

$$k = 1 - \left\{ \frac{4k_B T n_{app}}{3Gb^2 \delta_o (\sigma/\sigma_d) \sqrt{1 - (\sigma/\sigma_d)}} \right\}^{3/2} \quad (A.6)$$

$$\frac{\sigma_d}{\sigma} = 1 + \frac{3(Q_{app} - Q_v)}{2k_B T n_{app} [1 - (T/G)(dG/dT)]} \quad (A.7)$$

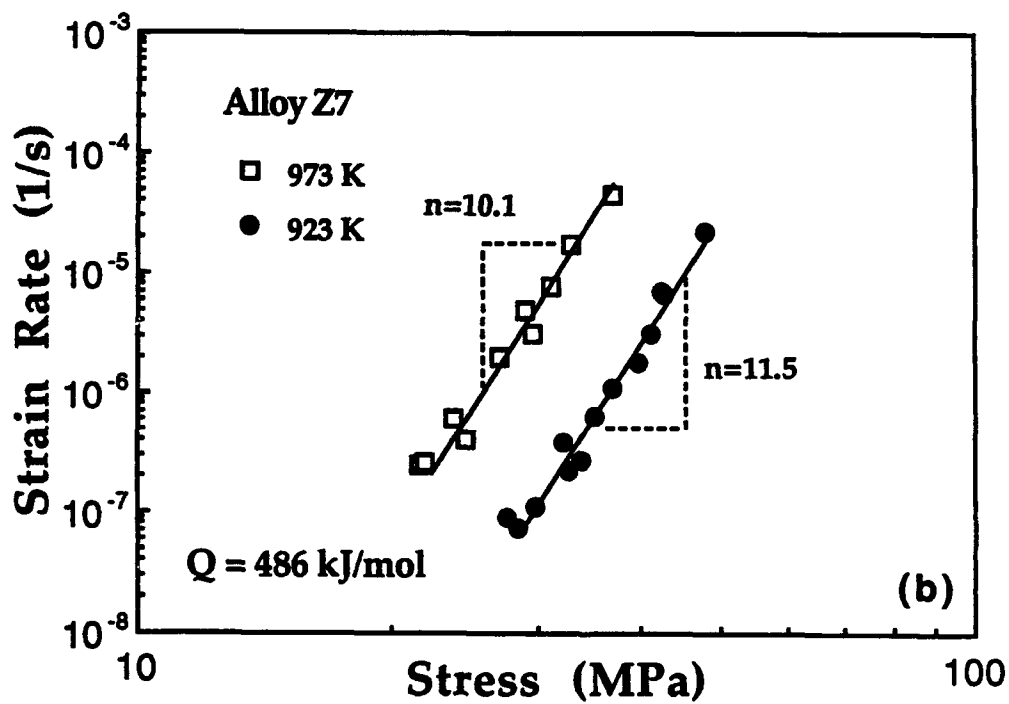
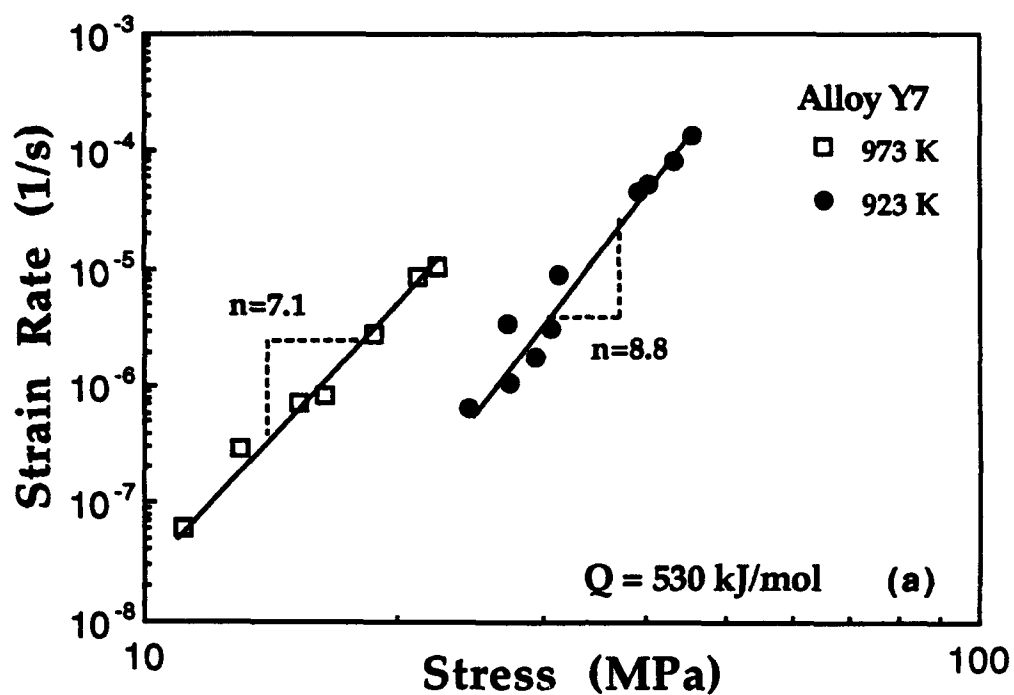
Hence, estimates of the relaxation parameter can be made from measured values of  $n_{app}$ ,  $Q_{app}$ , literature values of  $Q_v$  and  $G(T)$  [82FrA], and microstructurally measured values of the particle size  $\delta_o$ .

Values of  $\delta_o$  obtained directly from analysis of the TEM micrographs and the corresponding estimates of  $k$  are shown in Table 1.



## LIST OF FIGURES

- Figure 1. Log-log plots of steady-state strain rate versus applied stress for: (a) Alloy Y7, (b) Alloy Z7, and (c) Alloy Z9.
- Figure 2. Typical microstructures of as-crept materials tested at 923 K: (a) Alloy Z9, (b) Alloy Y7. Pinned dislocations are noticeable in (b).
- Figure 3. Dislocation-dispersoid interactions in as-crept materials: (a) Alloy Z7 crept at 973 K (dislocation A appears to undergo Orowan bowing while dislocation B appears to be attached to dispersoid particles), (b) weak-beam image of Alloy Z9 crept at 923 K, (c) dark field image of Alloy Y7 crept at 923 K.
- Figure 4. Grain boundary pinned by oxide particles in Alloy Z9 crept at 923 K. Arrows point to locations where grain boundary is clearly restrained by dispersoid particles.
- Figure 5. Strain rate-stress data for alloys tested at 973 K compared with calculated creep rates for Coble and power-law (with breakdown correction) mechanisms for pure copper with the same grain size: (a) Alloy Y7; (b) Alloy Z7; (c) Alloy Z9.
- Figure 6. Strain rate-stress data for (a) Alloy Y7, (b) alloy Z7, and (c) Alloy Z9 crept at 973 K compared with predictions of particle-inhibited diffusional creep model of Arzt et al. [83AAV]. Values of parameters that gave best fit to data are shown in Table 3.



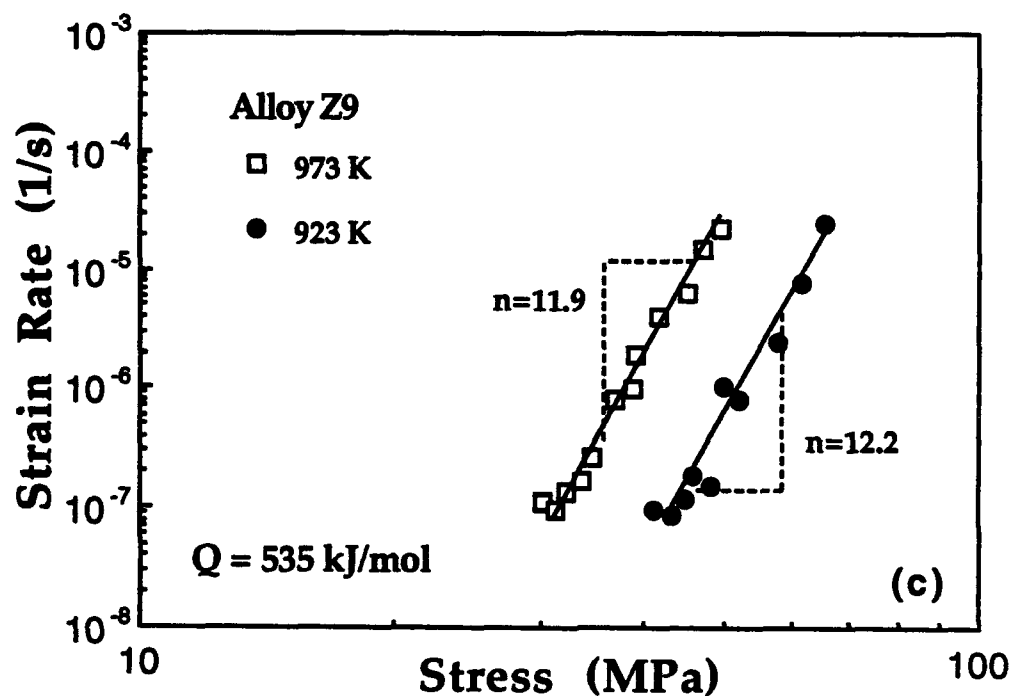


Figure 1. Log-log plots of steady-state strain rate versus applied stress for: (a) Alloy Y7, (b) Alloy Z7, (c) Alloy Z9.

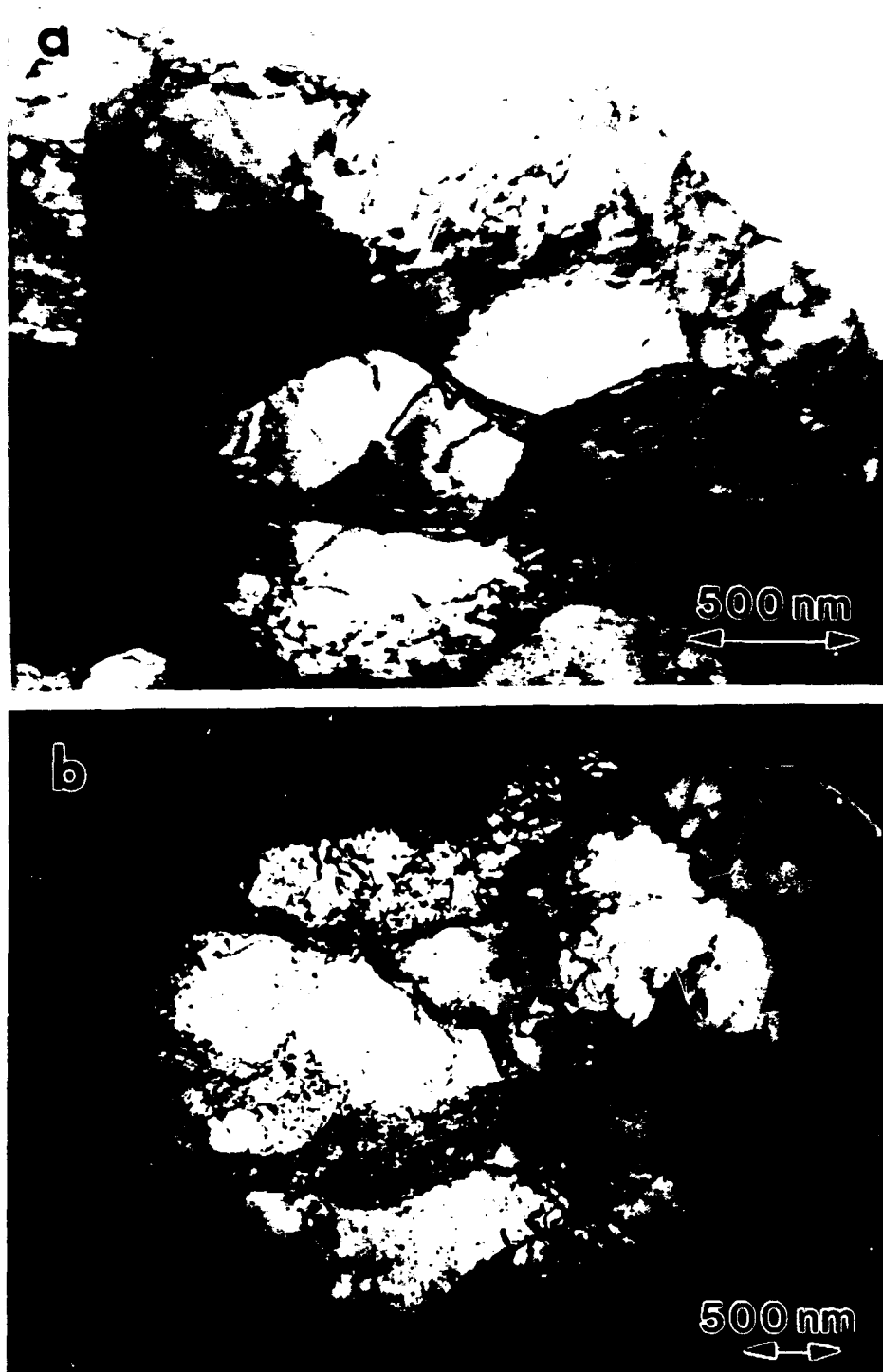


Figure 2. Typical microstructures of as-crept materials tested at 923 K: (a) Alloy Z9, (b) Alloy Y7. Pinned dislocations are noticeable in (b).

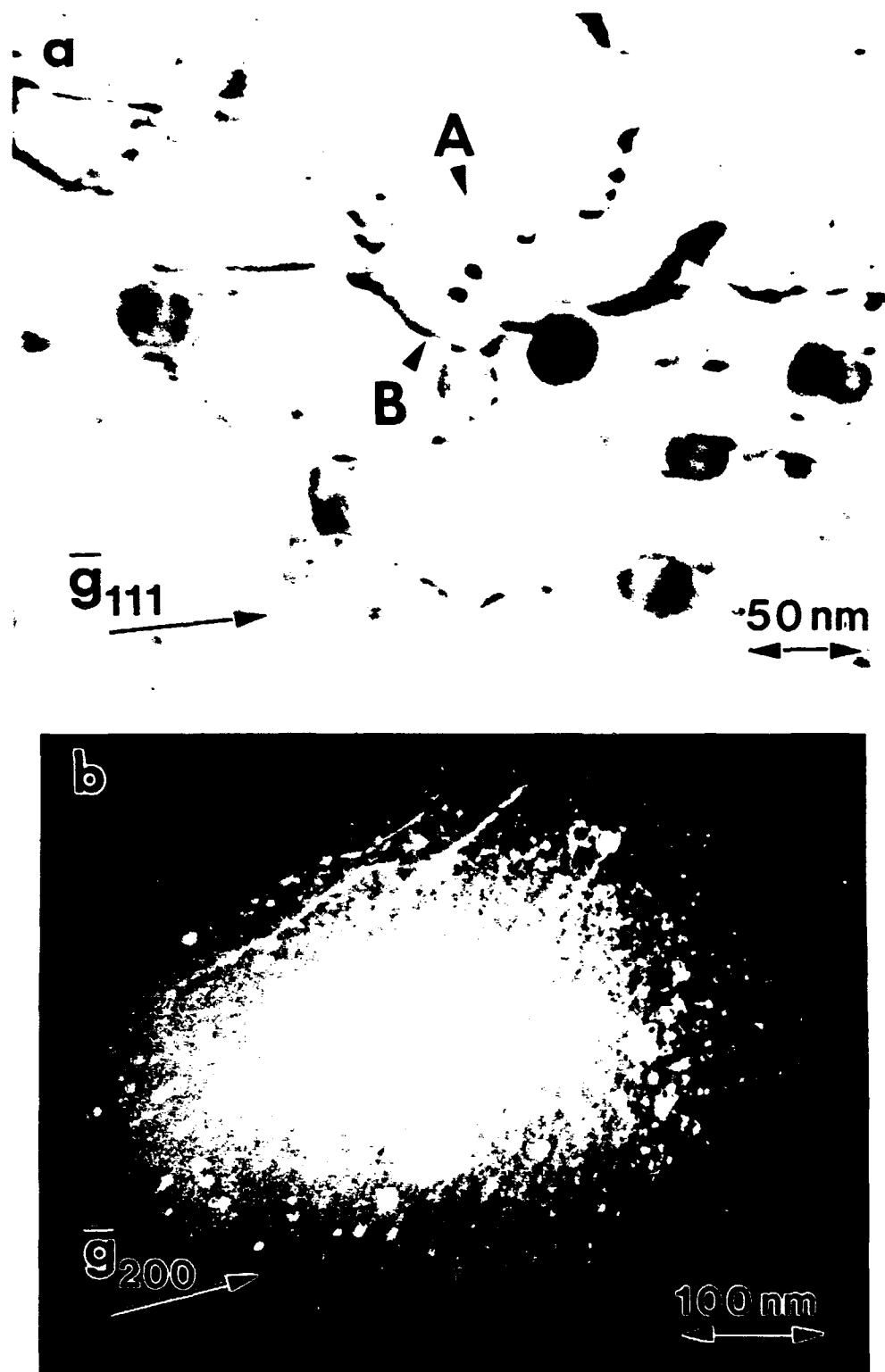


Figure 3. Dislocation-dispersoid interactions in as-crept materials: (a) Alloy Z7 crept at 973 K (dislocation **A** appears to undergo Orowan bowing while dislocation **B** appears to be attached to dispersoid particles), (b) weak-beam image of Alloy Z9 crept at 923 K.



Figure 3. (cont.) Dislocation-dispersoid interactions in as-crept materials: (c) dark field image of Alloy Y7 crept at 923 K.

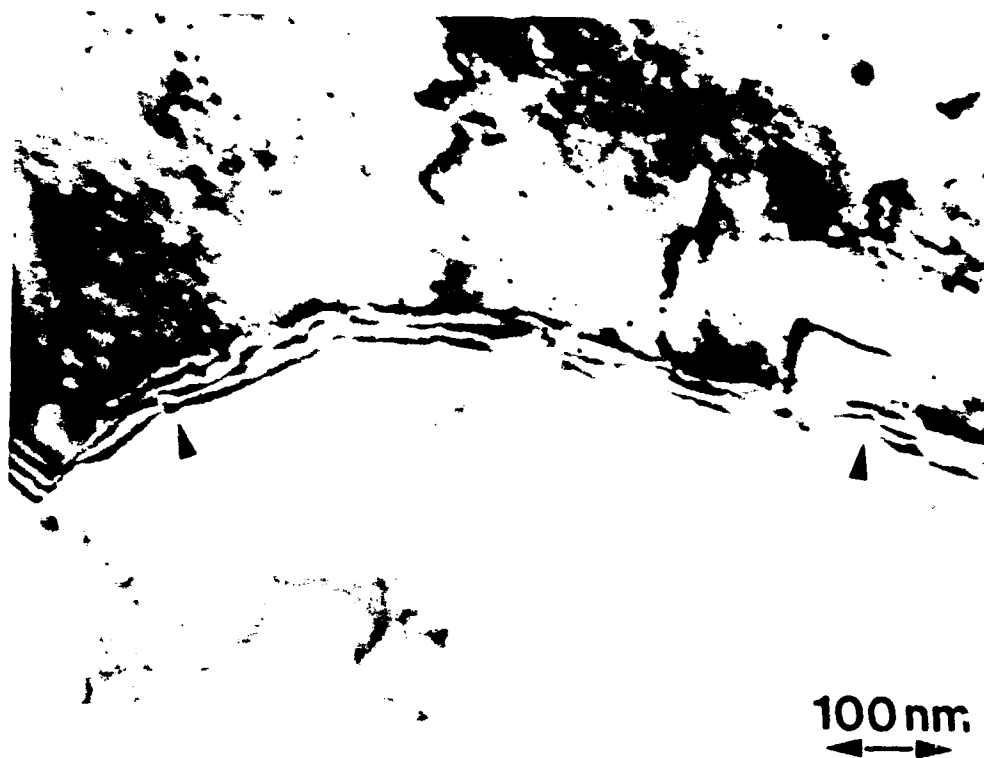
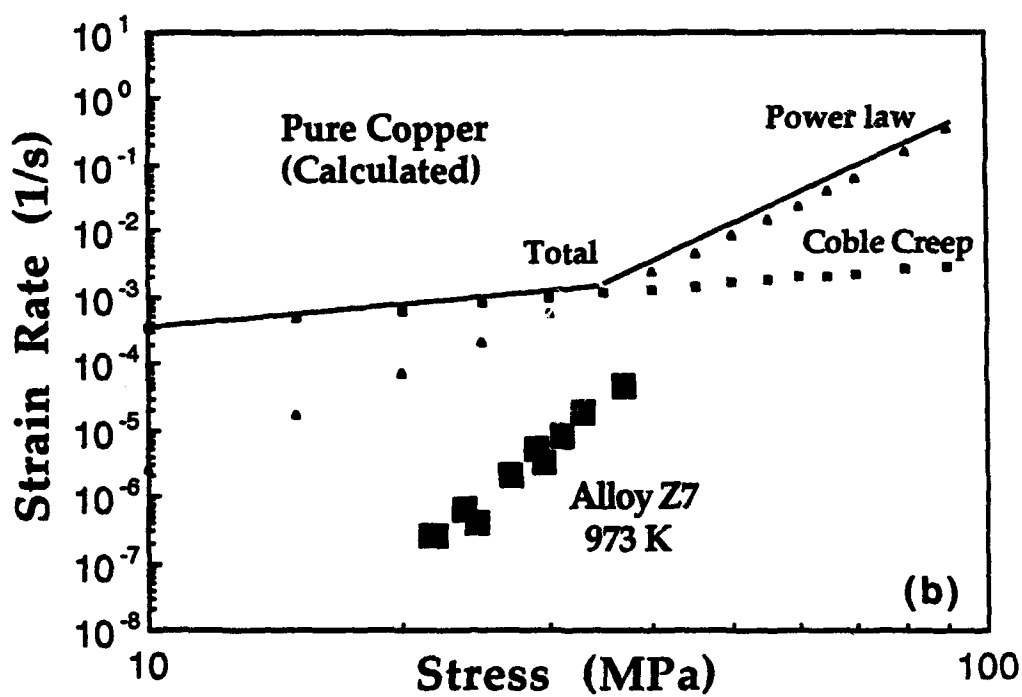
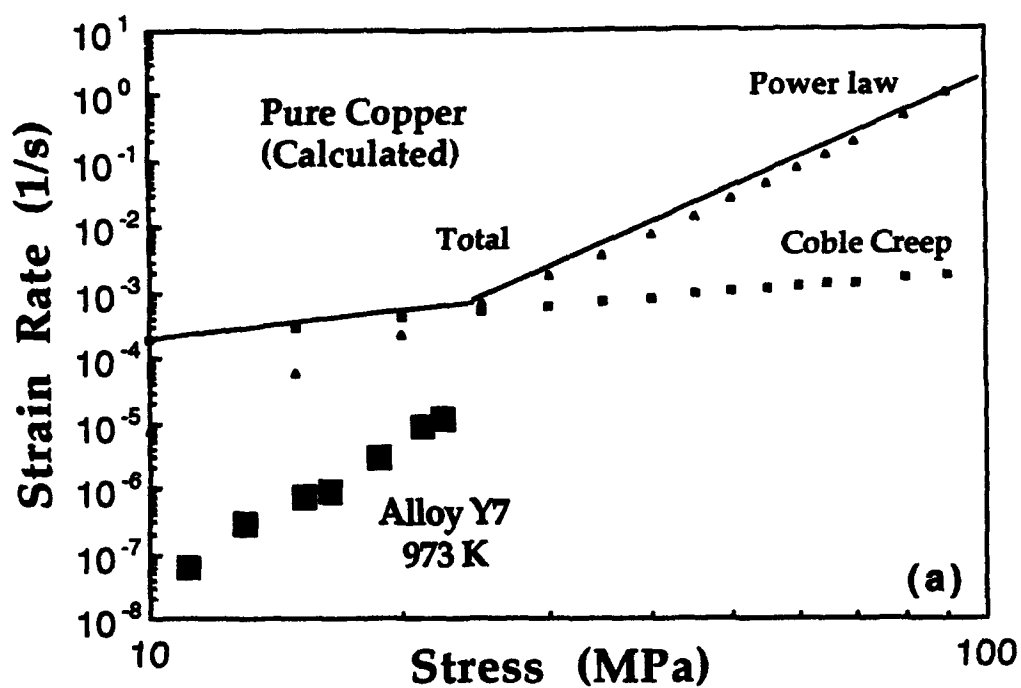


Figure 4. Grain boundary pinned by oxide particles in Alloy Z9 crept at 923 K. Arrows point to locations where grain boundary is clearly restrained by dispersoid particles.





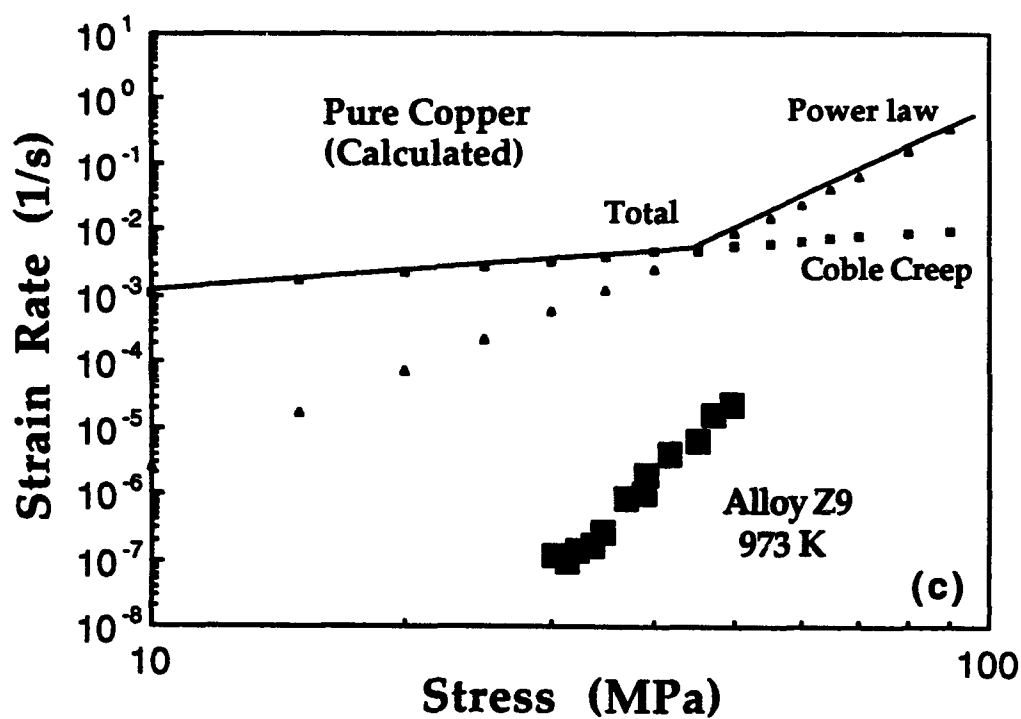
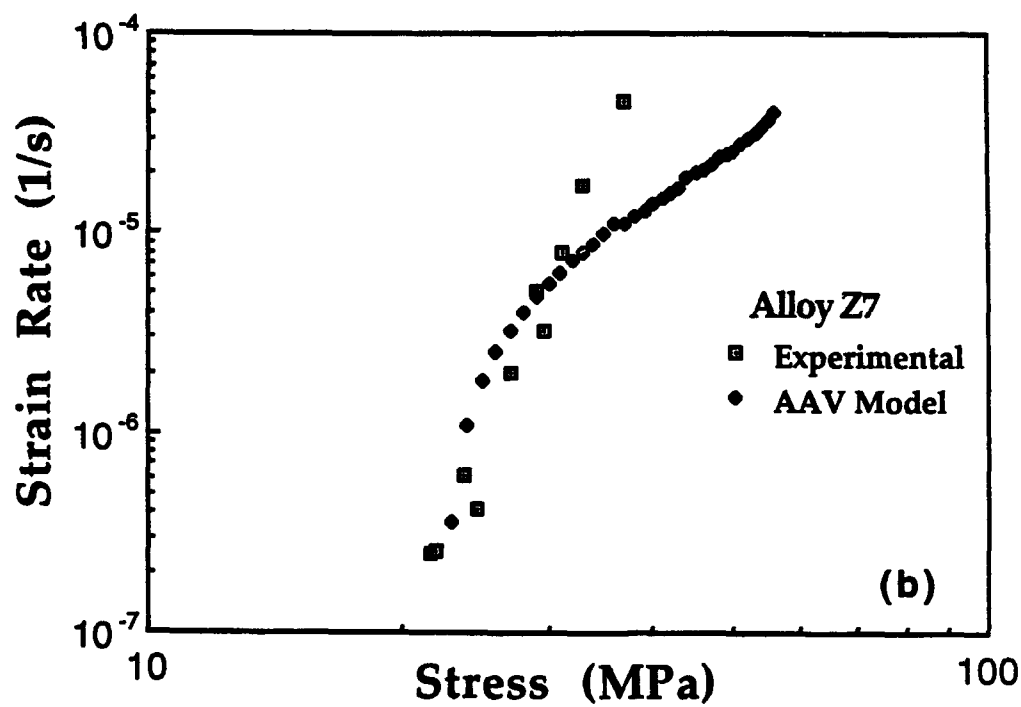
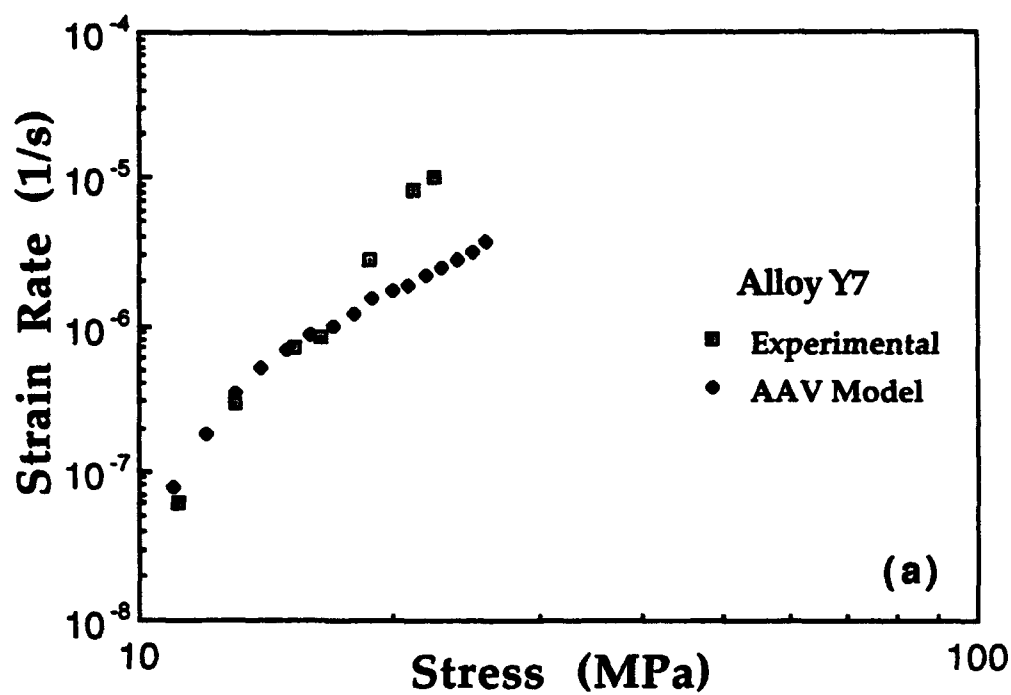


Figure 5. Strain rate-stress data for alloys tested at 973 K compared with calculated creep rates for Coble and power-law (with breakdown correction) mechanisms for pure copper with the same grain size: (a) Alloy Y7, (b) Alloy Z7, (c) Alloy Z9.



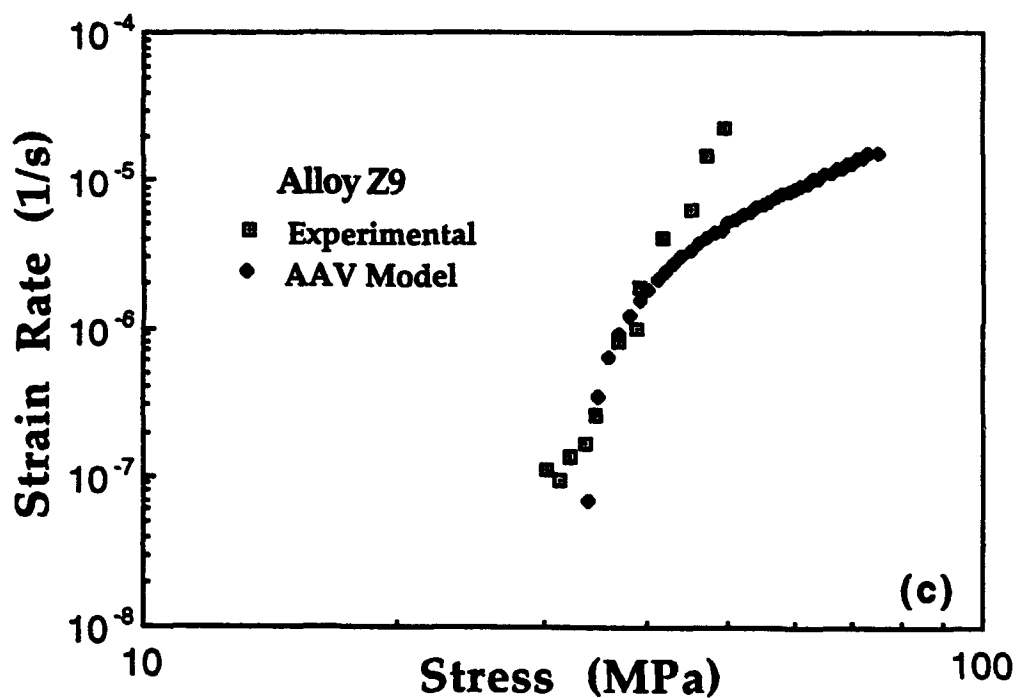
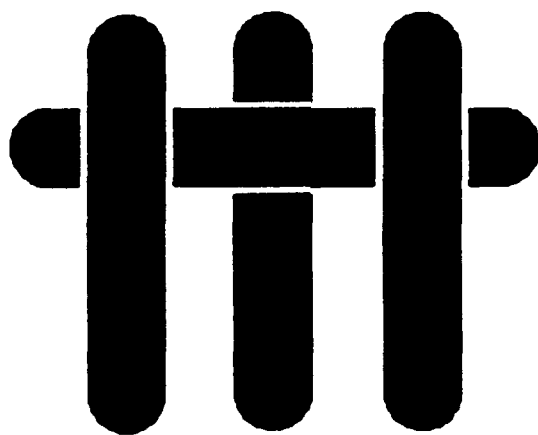


Figure 6. Strain rate-stress data for (a) Alloy Y7, (b) alloy Z7, and (c) Alloy Z9 crept at 973 K compared with predictions of particle-inhibited diffusional creep model of Arzt et al. [83AAV]. Values of parameters that gave best fit to data are shown in Table 3.

# M A T E R I A L S



## Mechanical Properties of Partially Dense Alumina Produced from Powder Compacts

David C.C. Lam\*, F.F. Lange and A. G. Evans

Materials Department  
College of Engineering  
University of California  
Santa Barbara, California 93106

\* Current Address: Hitachi Research Laboratory, 1-1 Saiwaicho 3 chome, Hitachi-shi,  
Ibaraki-ken, 317 Japan

## Abstract

The elastic modulus ( $E$ ), critical strain energy released rate ( $G_c$ ), and flexural strength ( $\sigma$ ) have been determined for two partially dense alumina bodies produced from the same powder but with different initial densities. The mechanical properties were measured for specimens fabricated at four different relative densities. The measured elastic modulus, critical strain energy released rate and a calculated critical stress intensity factor ( $K_c$ ) were observed to be linearly related to  $(\rho - \rho_0)/(1 - \rho_0)$ , where  $\rho$  is the current relative density and  $\rho_0$  is the initial relative density of the powder compact. With the observed linear relations for  $E$ ,  $G_c$  (or  $K_c$ ) and the assumption that the crack length responsible for failure was present in the initial powder compact and shrunk in proportion to the relative density change, a Griffith equation was constructed to estimate the strength at any relative density. This relation was in good agreement with measurements.

## 1. Introduction

A variety of porous ceramics, viz., filters, membranes, electronic substrates, etc., fabricated by the partial densification of powders compacts, require mechanical reliability for their commercial performance. This article examines the effect of porosity on mechanical properties.

In their review of cellular materials, Gibson and Ashby<sup>1</sup> point out that porous materials can have higher specific mechanical properties relative to fully dense materials. Porous solids can also be formed with powders, which compartmentalize the void phase and transmit force through structural units having morphological characteristics which differ from those of cellular materials. Although powder compacts can be stable under applied pressures, neglecting relatively weak, interparticle attractive forces, their mechanical integrity under tension is initially zero, but increases as necks form between touching particles while the void content decreases and changes its morphology.

Although the elastic modulus<sup>2-14</sup> and strength<sup>15</sup> of materials containing isolated pores have been modeled and measured, only Young's Modulus has been extensively researched for porous materials formed with powders. One of the more interesting microstructural features was discovered by Green et al<sup>8</sup> who showed that prior to any densification, the formation of necks between touching particles by surface diffusion can increase the elastic modulus to approximately 10% of the fully dense value.

Further mass transport increased the relative elastic modulus in a manner that appear to be linearly related to relative density, with the zero modulus intercept dependent on the initial density of the powder compact. The fracture resistance ( $G_c$  or  $K_{Ic}$ ) and strength of partially dense powder compacts have received much less attention. Because partially dense powder compacts could be used in a variety of structural applications, e.g., as matrices within continuous fiber composites, our objective was to obtain a greater understanding of how the mechanical properties of partially dense powder compacts are related to relative density.

## 2. Experiments

By controlling the interparticle potential,  $\alpha$ - $\text{Al}_2\text{O}_3$  powder <sup>a</sup> (mean particle diameter, 1  $\mu\text{m}$ , see ref. 16 for size distribution) compacts with an initial relative density,  $\rho_0$ , of either 0.50 or 0.62 were formed by pressure filtration with a method and reagents reported elsewhere <sup>16</sup>. Prior to filtration, the dispersed (pH 4) slurry, containing 20 volume %  $\text{Al}_2\text{O}_3$  was ultrasonicated for 20 minutes in an attempt to break up larger agglomerates. The lower density body was formed from a flocculated slurry (increasing the pH from 4 to 9), whereas the higher density body was formed from a dispersed slurry. Large cylindrical billets with a height of  $\sim 10$  cm. and a diameter of  $\sim 7.6$  cm. were formed. The bodies were dried and heat treated at 800  $^\circ\text{C}$  for 2 hours (shrinkage began at  $\sim 1100^\circ\text{C}$ ) to impart some mechanical integrity to diamond cut bars for Archimedes density measurement. The large bodies were further heat treated at 1100  $^\circ\text{C}$  for 2 hours to further increase the structural integrity of the material so that bars with the dimension 2.5 x 5 x 50 mm could be cut for property measurements. Bars were then heated to temperatures between 1200  $^\circ\text{C}$  to 1500  $^\circ\text{C}$  for two hours for room temperature measurements of relative density, elastic modulus, crack growth resistance and strength.

The elastic modulus was measured with an ultrasonic technique used by Green and coworkers <sup>8</sup>. The sonic velocity of the partially dense bars was measured by gently clamping a set of dry contact transducers across two parallel surfaces. The ultrasonic velocity was measured by a computerized ultrasonic system <sup>b</sup>; 1 MHz transducers were used for lower density bars, while 2 MHz transducers were used for the higher density bars. With the velocity of sound  $v$  through the material, the Young's modulus can be calculated using the well known relation, <sup>17-22</sup>

---

<sup>a</sup> AKP 15, Sumitomo Corp., New York, NY.

<sup>b</sup> Model 7000; Ultrasonics, Inc State College PA.

$$E = \rho v^2 (1 - 2\mu)(1 - \mu^2), \quad (1)$$

where  $\mu$  is the Poisson's ratio which had been experimentally determined by Green ( $\mu \approx 0.17$ ) to be approximately independent of relative density <sup>8</sup>.

The critical stress intensity factor  $K_c$  is a measure of the materials resistance to crack growth and is related to tensile strength ( $\sigma_c$ ) through the Griffith <sup>23</sup> fracture equation:

$$\sigma_c = Y \frac{K_c}{\sqrt{2\pi c}}. \quad (2)$$

$K_c$  is typically measured with a specimen configuration in which the K function is known, e.g., a compact tension specimen configuration that contains a preexisting crack of known dimension. Determination of the crack length in a porous body is subjective and renders conventional  $K_c$  test configurations unreliable.

Alternately, a technique exists for measuring the critical strain energy release rate,  $G_c$ , which does not require knowledge of the initial crack length. In this measurement, the energy released during fracture is determined from the integrated area under the load-displacement curve and the cross sectional area of the fractured surface <sup>24, 25</sup>. In the present study, load-displacement curves are obtained from 3-point bend tests of chevron notched bars tested with a span length of 38 mm. Load was applied with a servo-hydraulic test frame <sup>c</sup> and deflection was measured directly by placing a spring loaded deflection arm on top of the center point of the bar. The chevron notch was sawn into the bar to improve crack propagation stability; in instances where no notch was used, the crack is known to become unstable and propagated catastrophically. In catastrophic failure, the work under the catastrophic load-displacement curve is larger than the real work and therefore overestimates the true energy released during fracture. Representative measurements of fracture energy must be determined from a stable load deflection curve shown in Fig 1; the tail in the load vs deflection curve shows that the crack grew in a stable manner so that the work dissipated during fracture could be properly determined. With knowledge of  $E$  and  $G_c$ ,  $K_c$  was determined using

$$K_c = \sqrt{E G_c}. \quad (3)$$

The strength of unnotched bars was measured using the same three point flexure test. Similar to other specimens, the bars for strength measurements were cut from the

---

<sup>c</sup> Model 810, Material Testing System

billets after the 1100 °C/2h treatment and further heat treated at high temperatures. No additional machining was performed after the initial 1100°C sintering step. Thus no new flaws that were introduced after the 1100 °C heat treatment.

### 3. Results

All data are tabulated in Table 1. Plots for the relative elastic modulus  $\bar{E}$  and the relative critical strain energy release rate  $\bar{G}_c$  as a function of the current, relative density,  $\rho$ , appeared nearly linear as shown in Fig. 2. In these plots, both  $\bar{E}$  and  $\bar{G}_c$  extrapolate to 0 at the respective initial, relative densities,  $\rho_0$  for the two materials. Moreover when  $\bar{E}$  and  $\bar{G}_c$  are plotted against the density function <sup>a</sup>,  $(\rho - \rho_0)/(1 - \rho_0)$  all data appeared to produce the same linear function as shown in Figs. 2 and 3. In Fig. 2, the elastic modulus of the porous material is normalized by the elastic modulus of the fully dense material,  $E = 400$  GPa.<sup>8</sup> Likewise, in Fig. 3, the critical strain energy release rate for the porous material is normalized by the value for the fully dense material,  $G_c = 40$  J/m<sup>2</sup>.<sup>26</sup> Combining  $\bar{E}$  and  $\bar{G}_c$  with eq. (1), the mean  $\bar{K}_c$  is plotted in Fig. 4. Figure 5 reports the flexural strength vs the current, relative density,  $\rho$  for the two materials.

Representative micrographs of fractured surfaces that illustrate the microstructural evolution for material with an initial relative density of 0.50, after 2h heat treatments at 1200 °C, 1300 °C, and 1400 °C, are shown in Fig. 6. At 1200 °C, the grains appear to be nearly identical to the average and distributed <sup>16</sup> size of the initial particles, and the necks between the particles are large. At 1300 °C, the necks between the initial touching particles are fully formed. At 1400 °C, the substantial grain growth has occurred. Thus, it can be concluded that data for  $\bar{E}$ ,  $\bar{G}_c$  and  $\sigma_c$  were recorded for microstructures wherein necks between initial touching particle are fully formed, as well as being subject to grain coarsening.

### 4. Discussion

A linear relation was discovered between the relative elastic modulus and relative density for materials with different initial densities. The density function brings the data sets into coincidence (Fig 2) was determined through the more general relation,

$$\bar{E} = m\rho - k, \quad (4)$$

<sup>a</sup>  $(\rho - \rho_0)/(1 - \rho_0)$  is the current fractional porosity  $(\rho - \rho_0)$  divided by the initial, fractional porosity  $(1 - \rho_0)$



where the boundary conditions  $\bar{E} \rightarrow 1$  when  $\rho \rightarrow 1$  and  $\bar{E} \rightarrow 0$  when  $\rho \rightarrow \rho_0$  was used to give

$$\bar{E} = \frac{\rho - \rho_0}{1 - \rho_0}. \quad (5)$$

To understand the physics behind eq (4), it can be imagined that the first term,  $m\rho$ , represents a material formed with continuous, non-interacting, solid framework with a volume fraction,  $\rho$ . The rest of the material is void space. When all of the framework is oriented in the same direction as the stress (case where the framework is a bundle of unidirectional fibers),  $m = 1$ . Like-wise, when only a fraction of the framework,  $f$ , is oriented in the testing direction (i.e., an orthogonol network of continous fibers, bonded together where they touch),  $m = f$ . The connective network in the partially dense powder compact supports stress only when  $\rho > \rho_0$ . Thus, after necks form between the particles, the connective network supports stress in proportion to the differential density. Unlike low density cellular and random fiber materials <sup>1</sup>, the particle network does not contribute to deformation through large bending moments. Although the isostatic, compressive modulus of unbonded powder compacts are known to exhibit finite values described initially by Hertz, <sup>27</sup> in tension, dry powders are only held together by van der Waals forces. For this reason, we assume that  $\bar{E} = 0$  when  $\rho = \rho_0$ .

A recent review <sup>9</sup> of modulus-density relations has proposed a relation,

$$\bar{E} = \left(1 - \frac{P}{P_c}\right)^n, \quad (6)$$

where  $P$  is the current volume fraction of porosity ( $1 - \rho$ ),  $P_c$  is a critical volume fraction of porosity where  $\bar{E} = 0$ , and  $n$  is an exponent used to fit experimental data. Clearly,  $P_c = (1 - \rho_0)$  and when  $n = 1$ , eqs (5) and (6) are identical. Data for 6 rare-earth oxide systems <sup>10-12</sup> gave <sup>9</sup>  $0.47 < \rho_0 < 0.6$  through extrapolation of the data with eq. (6), which are consistent with values generally achieved for powders ( $\rho_0$  values were not reported by the original authors <sup>10-12</sup>). Values for  $n$  ranged around unity (0.74 and 1.3), suggests that the data could be approximated with a linear relation,  $n = 1$ . Figure 7 shows replots of data obtained for alumina bodies, <sup>8</sup> with two different initial densities illustrate that the data coincide and produce a linear relation when  $(\rho - \rho_0)/(1 - \rho_0)$  is used as the density coordinate.

In a similar manner and reasoning, the relative strain energy release rate can be directly related to the density function

$$\bar{G}_c = \frac{\rho - \rho_o}{1 - \rho_o} \quad (7)$$

For this relation to apply, it is required that the crack front be continuous within the dense framework (as suggested in Fig. 6) and its area fraction be proportional to  $\rho$ .<sup>28</sup> Furthermore, since both  $\bar{E}$  and  $\bar{G}_c$  can be approximated by the same density function, eq (3) requires that the relative, critical stress intensity factor also have the same dependence on relative density, viz.,

$$\bar{K}_c = \frac{\rho - \rho_o}{1 - \rho_o} \quad (8)$$

The strength of the porous body is inversely related to the square root of the flaw size,  $c$ . Consequently, by assuming that the flaws (size  $c_i$ ) are incorporated into the powder compact during processing and shrink as the compact densifies, the current flaw size should be represented by

$$c = \alpha(1 - \epsilon) + \beta, \quad (9)$$

where  $\epsilon$  is the linear shrinkage strain given by

$$\epsilon = 1 - \left( \frac{\rho_o}{\rho} \right)^{1/3}. \quad (10)$$

The coefficients  $\alpha$  and  $\beta$  are determined by requiring that  $c \rightarrow c_i$  when  $\rho \rightarrow \rho_o$ , and  $c \rightarrow 0$  when  $\rho = 1$ . The last assumption ( $c \rightarrow 0$  when  $\rho = 1$ ) is certainly not to be expected, since flawless bodies may never be produced. Yet, as seen by the following, a simpler expression results than if the assumption were  $c \rightarrow$  finite value when  $\rho = 1$ . Thus, our expression is not expected to fit experimental results when  $\rho \rightarrow 1$ . Thus, using eqs (9) and (10) with the bounding assumptions, one obtains

$$\bar{c} = \frac{c}{c_i} = \frac{\left( \frac{\rho_o}{\rho} \right)^{1/3} - \rho_o^{1/3}}{1 - \rho_o^{1/3}}. \quad (11)$$

By combining the preceding relations, the strength can be expressed as a function of the critical stress intensity factor of the dense body,  $K_c$ , the size of the largest initial flaw within the powder compact,  $c_i$ , and density as

$$\sigma_c = Y \frac{K_c}{\sqrt{2\pi c_i}} \frac{\rho - \rho_o}{1 - \rho_o} \left[ \frac{1 - \rho_o^{1/3}}{\left(\frac{\rho_o}{\rho}\right)^{1/3} - \rho_o^{1/3}} \right]^{\frac{1}{2}} \quad (12)$$

Using  $K_c = 4 \text{ MPam}^{1/2}$ ,  $Y = 1$  and the strength data reported in Table 1, eq(12) produces a value of  $c_i = 350 \mu\text{m}$ . This not unreasonable judging that large agglomerates of this size are observed in the dry powder and may not be completely removed by ultrasonification without subsequent sedimentation or filtration. Only one of these agglomerates need be present within the flexural bar. It is also possible that these large flaws were introduced when the specimens, which were slightly strengthened by heating to  $1100^\circ\text{C}$ , were diamond cut. Eq. (12), has been plotted on Fig. 5 to illustrate the reasonable agreement with experimental data for  $\rho < 0.9$ , as expected, due to the simplifying assumption,  $c \rightarrow 0$  when  $\rho = 1$ .

## 5. Conclusion

It has been shown that the elastic modulus and critical strain energy release rate of a partially dense powder compact are linearly proportional to the density function,  $(\rho - \rho_o)/(1 - \rho_o)$ . This function arises because the solid and void phases are interpenetrating, where the solid phase is a framework that supports load without large bending moments, and allows crack extension in proportion to its area fraction (when  $\rho > \rho_o$ ). The variation in strength with relative density is consistent with the Griffith equation when the strength determining cracks within the powder shrink in proportion to the change in relative density.

## Acknowledgment

This research was supported by the Defense Advanced Research Projects through the University Research Initiative under the Office of Naval Research Contracts No. N00014-86-K-0753 and N00014-92-J-1808.

Table I Collective Data

Initial Relative Density,  $\rho_0 = 0.62$ 

Sintering	$\rho$	$\bar{E}$	$\bar{G}_c$	$\sigma_c$
1200°C/2h	0.71	0.25 ± 0.01 (5)	0.38 ± 0.05 (5)	127 ± 21 MPa (9)
1300°C/2h	0.78	0.42 ± 0.01 (5)	0.50 ± 0.03 (3)	168 ± 43 MPa (8)
1400°C/2h	0.85	0.57 ± 0.02 (5)	0.71 ± 0.07 (5)	270 ± 34 MPa (8)
1500°C/2h	0.96	0.91 ± 0.01 (5)	0.78 ± 0.08 (6)	474 ± 67 MPa (5)

Initial Relative Density,  $\rho_0 = 0.50$ 

Sintering	$\rho$	$\bar{E}$	$\bar{G}_c$	$\sigma_c$
1200°C/2h	0.58	0.17 ± 0.01 (5)	0.19 ± 0.03 (4)	34 ± 6 MPa (3)
1300°C/2h	0.65	0.30 ± 0.01 (5)	0.31 ± 0.06 (5)	81 ± 17 MPa (3)
1400°C/2h	0.73	0.46 ± 0.02 (5)	0.43 ± 0.07 (4)	158 ± 23 MPa (5)
1500°C/2h	0.85	0.69 ± 0.02 (5)	0.62 ± 0.07 (3)	318 ± 39 MPa (4)

Elastic modulus is normalized by  $E = 400 \text{ GPa}$  <sup>26</sup>Critical strain energy release rate is normalized by  $G_c = 40 \text{ J/m}^2$  <sup>26</sup>

Number in parentheses indicates number of tests.

## References

1. L.J. Gibson and M.F. Ashby, Cellular Solids, Pergamon Press (1988).
2. R.L. Coble and W.D. Kingery, "Effect of Porosity on Physical Properties of Sintered Alumina," *J. Am. Ceram. Soc.*, 39, 377 (1956).
3. D.P.H. Hasselman and R.M. Fulrath, "Effect of Cylindrical Porosity on Young's Modulus of Polycrystalline Brittle Material," *J. Am. Ceram. Soc.*, 47, 545-5 (1965).
4. J.P. Watt, G.F. Davies and R.J. O'Connell, "The Elastic Properties of Composite Materials," *Rev. Geophys. Space Phys.* 14, 541-63 (1976).
5. B. Budiansky and R.J. O'Connell, "Elastic Modulus of a Cracked Solid," *Int. J. Solids Structures*, 12, 81-97 (1976).
6. F.P. Knudsen, "Effect of Porosity on Young's Modulus of Alumina," *J. Am. Ceram. Soc.*, 45 94-5 (1962).
7. J.C. Wang, "Young's Modulus of Porous Materials, Part I & II," *J. Mater. Sci.*, 19, 801-814 (1984).
8. D. J. Green, C. Nader and R. Brezny, "The Elastic Behavior of Partially-Sintered Alumina," Sintering of Advanced Ceramics, Ceramics Transactions vol 7, ed. C.A. Handwerker, J.E. Blendell and W.A. Kaysser. 345-56.
9. K. K. Phani and S. K. Niyogi, "Elastic Modulus-Porosity Relation in Polycrystalline Rare-Earth Oxides," *J. Am. Ceram. Soc.* 70 [12] C362-66 (1987).
10. M. O. Marlowe and D. R. Wilder, "Elasticity and Internal Friction of Polycrystalline  $Y_2O_3$ ," *J. Am. ceram. Soc.* 48 [5] 227-33 (1965).
11. W. R. Manning, M. O Marlowe and D. R. Wilder, "Temperature and Porosity Dependence of Young's Modulus of Polycrystalline  $Dy_2O_3$  and  $Er_2O_3$ ," *J. Am. ceram. Soc.* 49 [4] 227-28 (1966); with O. Hunter, Jr. and B. R. Powell, Jr. "Elastic Properties of Polycrystalline  $Y_2O_3$ ,  $Dy_2O_3$ ,  $Ho_2O_3$ , and  $Er_2O_3$ : Room Temperature Measurements," *J. Am. ceram. Soc.* 52 [8] 436-42 (1969),
12. B. R. Powell, Jr. and W. R. Manning, "Elastic Properties of Polycrystalline  $Yb_2O_3$ ," *J. Am. Ceram. Soc.* 54 [10] 488-90 (1971).
13. O. Hunter, Jr. H. J. Korklan and R. R. Suchomel, "Elastic Properties of Polycrystalline Cubic  $Sm_2O_3$ ," *J. Am Ceram. Soc.* 57 [6] 267-68 (1974); with G. e. Graddy Jr., "Elastic Properties of Polycrystalline Cubic  $Lu_2O_3$ ," *J. Am Ceram. Soc.* 5 [1-2] 82 (1976).
14. S. L. Dole, O. Hunter, Jr. and F. W. Calderwood, "Elastic Properties of Polycrystalline Scandium and Thulium Sesquioxides," *J. Am Ceram. Soc.* 60 [3-4] 167-68 (1977).

15. R.M. Spriggs, "Expression For Effect Of Porosity on Elastic Modulus of Polycrystalline Refractory Materials, Particularly Aluminium Oxide," *J. Am. Ceram. Soc.* 44, 628-29 (1961); "Effect of Open and Closed Pores on Elastic Moduli of Polycrystalline Alumina," *J. Am. Ceram. Soc.* 45, 454 (1962).
16. B.V. Velamakanni and F.F. Lange, "Effect of Interparticle Potentials and Sedimentation on Particle Packing Density of Bimodal Particle Distribution During Pressure Filtration," *J. Amer. Ceram. Soc.*, 74 [1] 166-72 (1991).
17. J. Krautkramer and H. Krautkramer, Ultrasonic Testing of Materials, 2nd ed. Springer, Berlin (1977).
18. M.C. Bhardwaj, "Principles and Methods of Ultrasonic Characterization of Materials," *Adv. Ceram. Mater.*, 1 [4] 311-24 (1986).
19. M.P. Jones, G.V. Blessing and C.R. Robbins, "Dry-Coupling Ultrasonic Elasticity Measurements of Sintered Ceramics and Their Green States," *Mater. Eval.*, 44 [6] 859-62 (1986).
20. J.A. Brunk, C.J. Valenza and M.C. Bhardwaj, "Applications and Advantages of Dry Coupling Ultrasonic Transducers For Materials Characterization and Inspection," Acousto-Ultrasonics: Theory and Applications, J.C. Duke, Jr. ed. Plenum Press, N.Y. (1988).
22. D.S. Kupperman and H.B. Harplus, "Ultrasonic Wave Propagation Characteristics of Green Ceramics," *Ceram. Bull.*, 63 [12] 1505-9 (1984).
23. A.A. Griffith, "Phenomena of Rupture and Flow In Solids," *Phil. Trans. R. Soc. London.* A221, 163-90 (1920).
24. J. Nakayama, "Direct Measurements of Fracture Energies of Brittle Heterogeneous Material," *J. Amer. Ceram. Soc.*, 48 [11] 583-87 (1965).
25. F.J.P. Clarke, H.G. Tattersall, and G. Tappin, "Toughness of Ceramics and Their Work of Fracture," *Proc. Brit. Ceram. Soc.*, 6 163-72 (1966).
26. B. D. Flinn, F. W. Zok, F. F. Lange, and A. G. Evans, "Processing and Properties of  $Al_2O_3$  Reinforced with Al Alloys," *Mater. Sci. & Engr.* A144, 153-157 (1991).
27. K. Walton, "The Effective Elastic Modulus of a Random Packing of Spheres," *J. Mech. Phys. Solids.* 35 [2], 213-26 (1987).
28. R.W. Rice and S.W. Freiman, "The Porosity Dependence of Fracture Energies," in Ceramics Microstructures '76, ed., R.M. Fulrath and J.A. Pask, 800-9 (1976).

### Figure Captions

Fig. 1      Typical load-displacement curve for fracture energy measurement.

- Fig. 2      Relative elastic modulus for both high and low initial density sets as a function of fractional densification. Fully dense elastic modulus corresponds to 400 GPa.<sup>26</sup>
- Fig. 3      Relative critical strain energy released rate for both high and low initial density sets as a function of fractional densification. Fully dense critical strain energy released rate equals 40 J/m<sup>2</sup>.<sup>26</sup>
- Fig. 4      Mean fracture toughness of porous alumina as a function of fractional densification calculated from elastic modulus and critical strain energy release rate data.
- Fig. 5      Strength of partially densified alumina plotted as a function of fractional densification. The solid circles represents the data set with  $\rho_0 = 0.62$  and the open circle is the set with  $\rho_0 \approx 0.50$ . The proposed strength relation represented as the solid line.
- Fig. 6      SEM micrographs of the fractured surface of porous alumina ( $\rho_0 = 0.5$ ) at the initial stage of densification where necks are just formed (top, 1200 °C/2h); at the intermediate stage where the grain boundaries are fully formed before significant grain growth (middle, 1300 °C/2h); at the final stage where grain growth had taken place (1400 °C/2h).
- Fig. 7      Relative elastic modulus data for polycrystalline alumina<sup>8</sup> plotted as a function of fractional densification.

Fig. 1 Lam et al

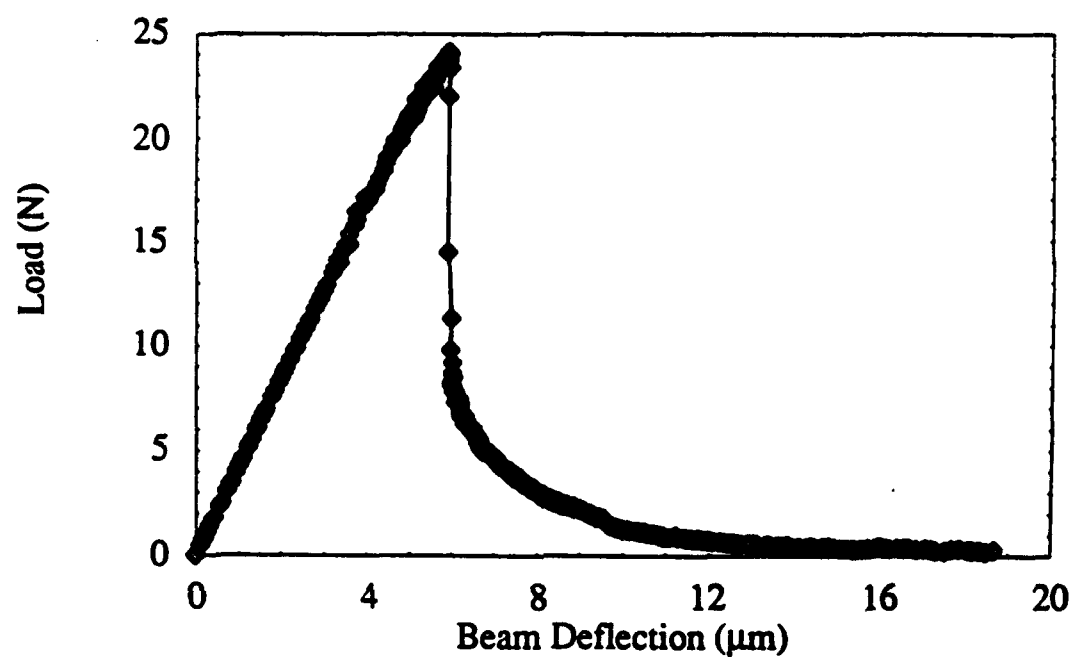




Fig. 2 Lam et al

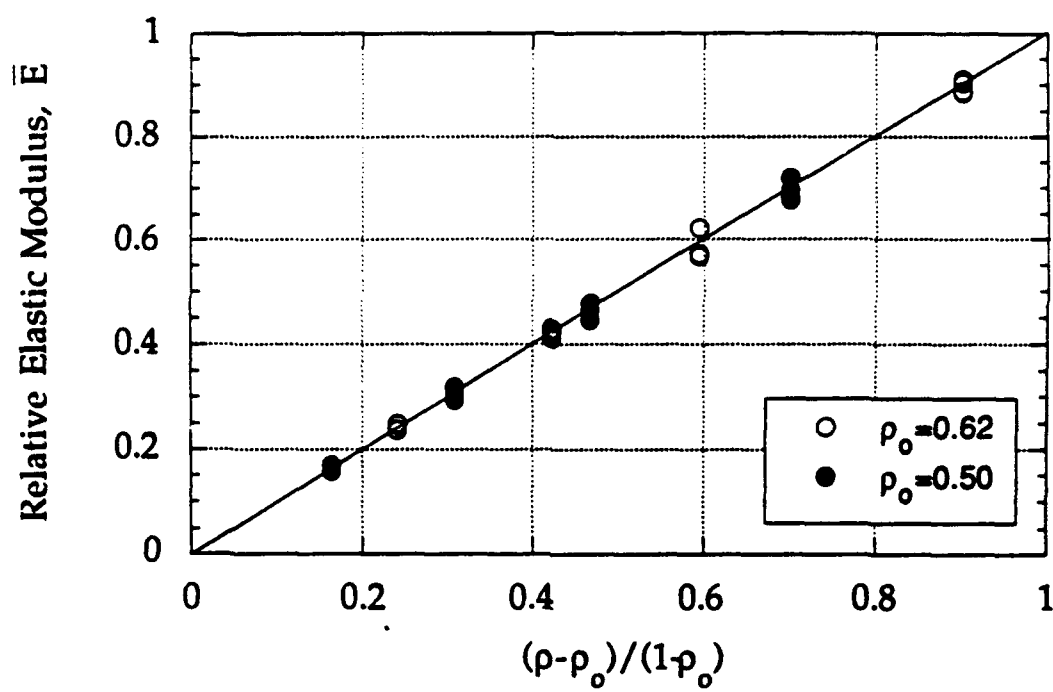


Fig. 3 Lam et al

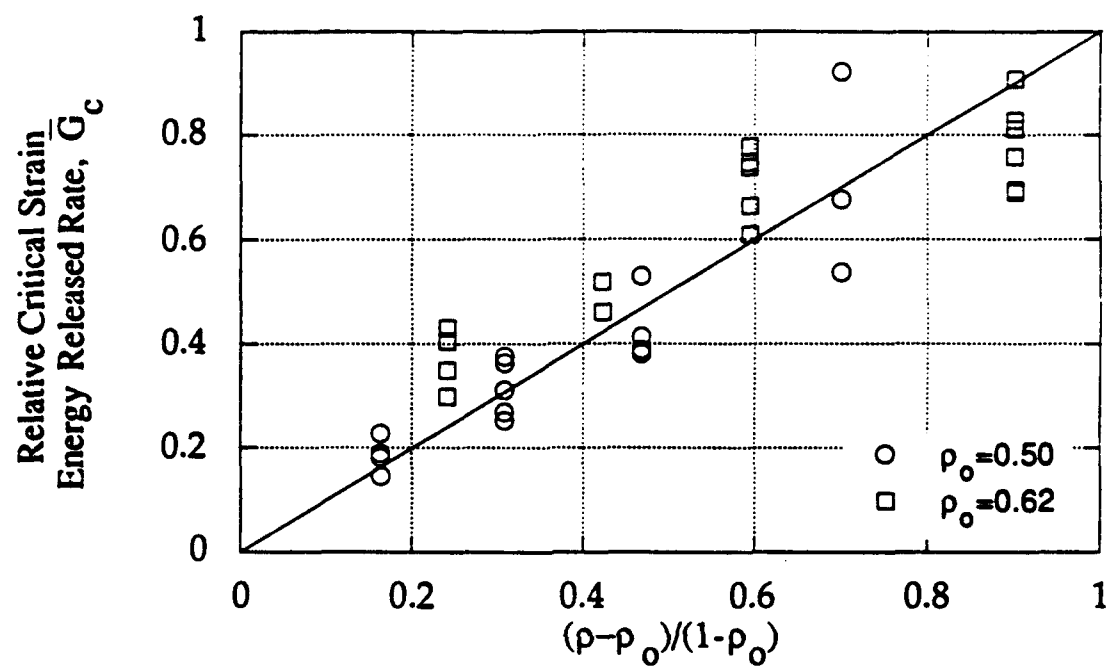


Fig. 4 Lam et al

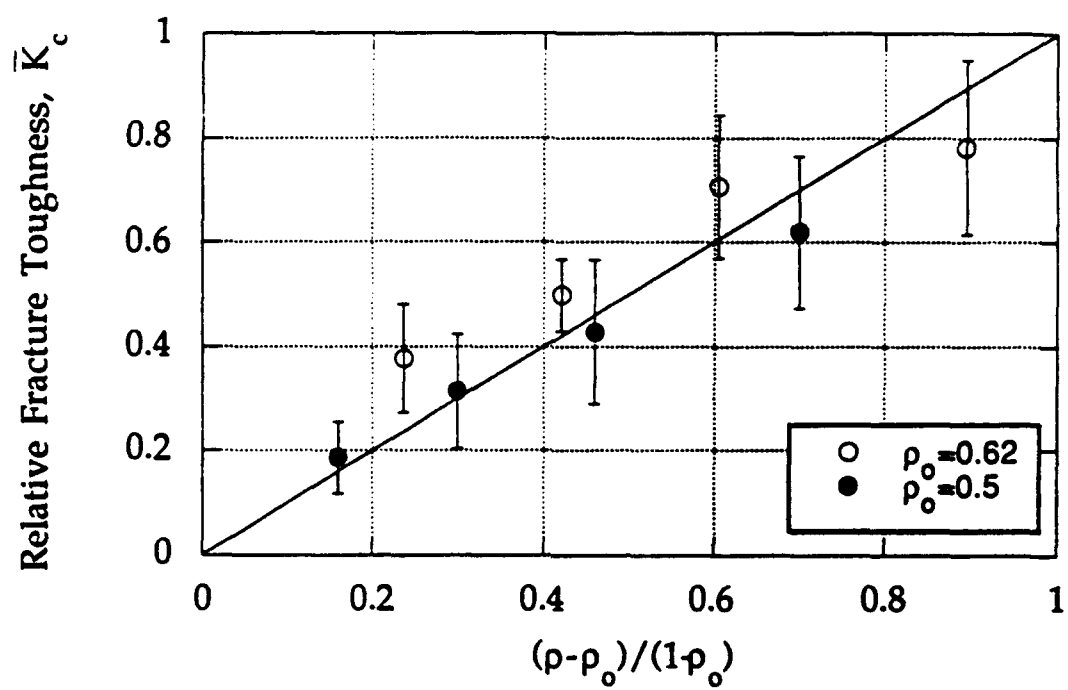
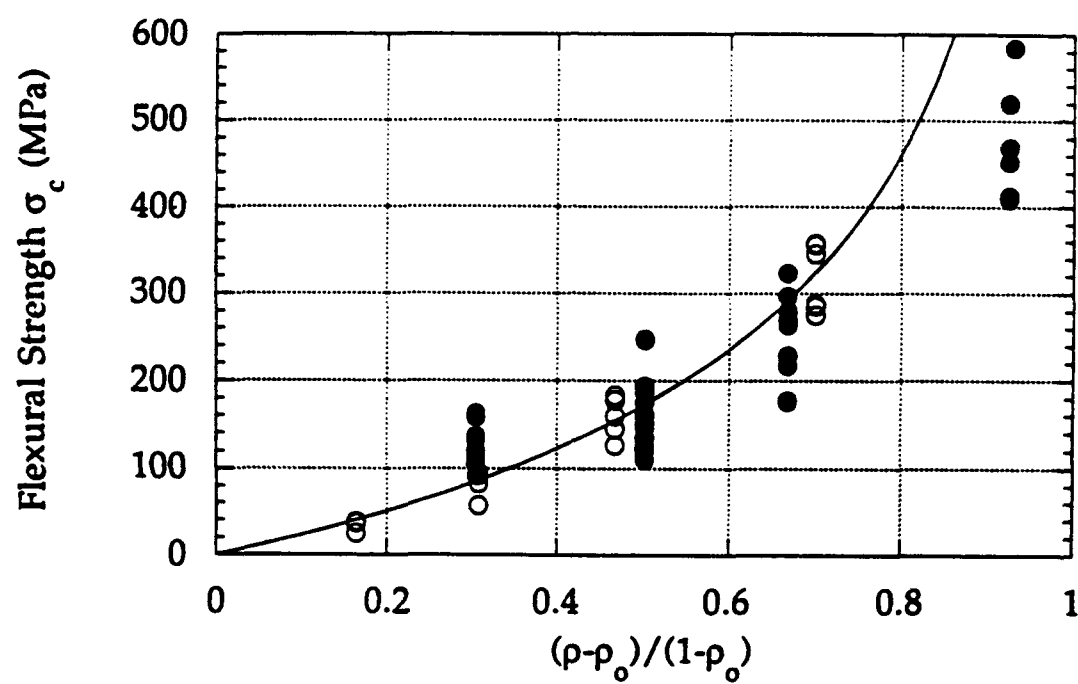


Fig. 5 Lam et al



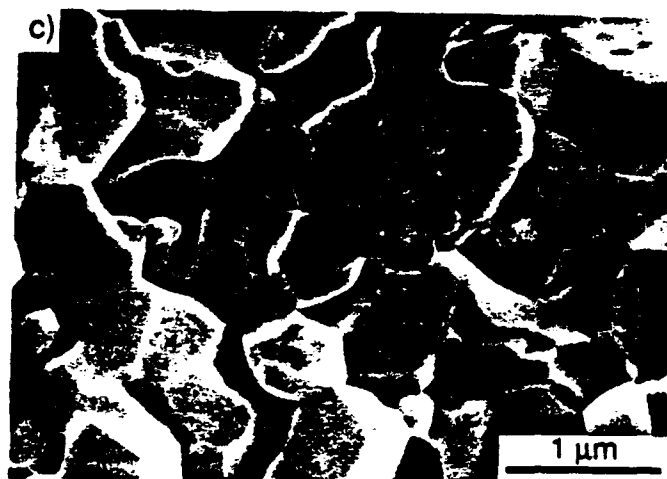
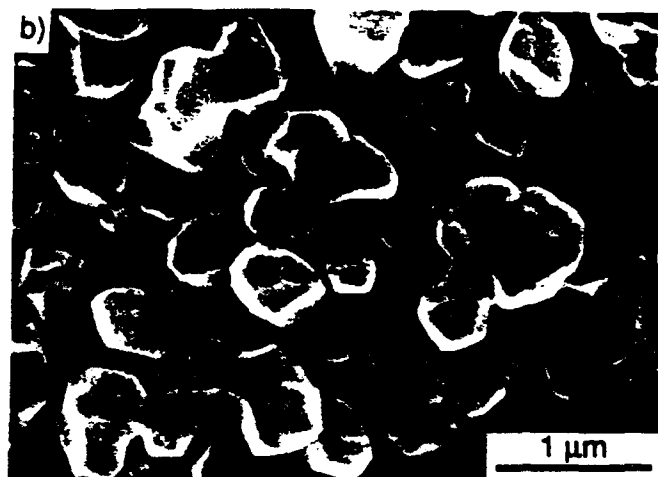
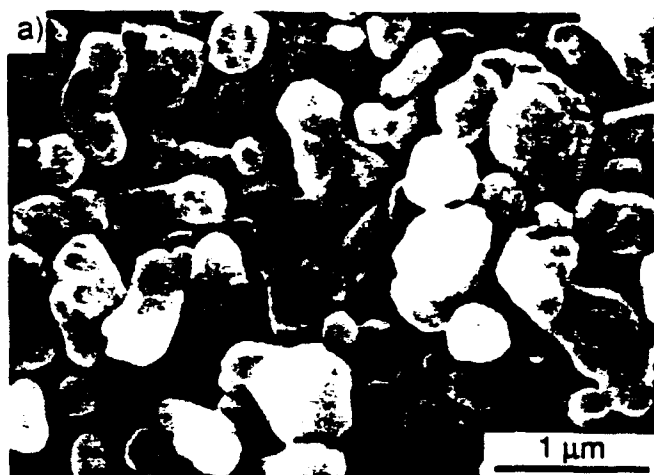


Fig. 7 Lam et al.

